Geological Fieldwork 2015

A Summary of Field Activities and Current Research

BRITISH
COLUMBIA

Ministry of
Energy and Mines

Ministry of Energy and Mines, British Columbia Geological Survey
Paper 2016-1

British Columbia Geological Survey
Ministry of Energy and Mines
www.em.gov.bc.ca/geology

BRITISH
COLUMBIA

Ministry of
Energy and Mines

Geological Fieldwork 2015

A Summary of Field Activities and Current Research

Ministry of Energy and Mines
British Columbia Geological Survey

Paper 2016-1

Ministry of Energy and Mines
Mines and Mineral Resources Division
British Columbia Geological Survey

Recommended citation format for individual papers:

Schiarizza, P., 2016. Toward a regional stratigraphic framework for the Nicola Group: Preliminary results from the Bridge Lake – Quesnel River area. In: Geological Fieldwork 2015, British Columbia Ministry of Energy and Mines, British Columbia Geological Survey Paper 2016-1, pp. 13-30.

Front Cover: On Mount Sinwa, Inklin River area near Atlin. In the foreground and middle ground are massive to locally well-bedded and fossil-bearing Upper Triassic limestones of the Sinwa Formation, in the hanging wall of the King Salmon thrust. In the background is Chakluk Mountain, which is underlain mainly by Early Jurassic arc-derived strata of the Laberge Group.
Magmatic belts of Stikinia project (Porphyry transitions). **Photo by D. Miller.**

Back Cover: Horn Mountain Formation (late Early to early Middle Jurassic) a new formation in northern Stikinia. Resistant lenses of augite-phyric lava flows with marginal autobreccias alternate with recessive polymictic volcanic breccias (middle maroon volcanic unit). East of Dease Lake, south shore of 'Grizzly lake'. View to the southeast; tents for scale.
See: van Straaten, B.I., and Nelson, J., 2016. Syncollisional late Early to early Late Jurassic volcanism, plutonism, and porphyry-style alteration on the northeastern margin of Stikinia, this volume. **Photo by B.I. van Straaten.**

British Columbia Cataloguing in Publication Data

Main entry under title:

Geological Fieldwork: - 1974 -

Annual.

Issuing body varies

Vols. for 1978-1996 issued in series: Paper / British Columbia. Ministry of Energy, Mines and Petroleum Resources; vols. for 1997 - 1998, Paper / British Columbia. Ministry of Employment and Investment; vols. for 1999-2004, Paper / British Columbia. Ministry of Energy and Mines; vols. for 2005-2009, Paper / British Columbia. Ministry of Energy, Mines and Petroleum Resources; vols. for 2010, Paper / British Columbia. Ministry of Forests, Mines and Lands; vols. for 2011, Paper / British Columbia. Ministry of Energy and Mines; vols. for 2012- , Paper / British Columbia. Ministry of Energy, Mines and Natural Gas; vols. for 2014- , Paper / British Columbia. Ministry of Energy and Mines.

Includes Bibliographical references.

ISSN 0381-243X=Geological Fieldwork

1. Geology - British Columbia - Periodicals. 2. Mines and mineral resources - British Columbia - Periodicals. 3. Geology - Fieldwork - Periodicals. 4. Geology, Economic - British Columbia - Periodicals. 5. British Columbia. Geological Survey Branch - Periodicals. I. British Columbia. Geological Division. II. British Columbia. Geological Survey Branch. III. British Columbia. Geological Survey Branch. IV. British Columbia. Dept. of Mines and Petroleum Resources. V. British Columbia. Ministry of Energy, Mines and Petroleum Resources. VI. British Columbia. Ministry of Employment and Investment. VII. British Columbia Ministry of Energy and Mines. VIII. Series: Paper (British Columbia. Ministry of Energy, Mines and Petroleum Resources). IX. Series: Paper (British Columbia. Ministry of Employment and Investment). X. Series: Paper (British Columbia Ministry of Energy and Mines). XI. Series: Paper (British Columbia Ministry of Energy, Mines and Petroleum Resources). XII. Series: Paper (British Columbia Ministry of Forests, Mines and Lands). XIII. Series: Paper (British Columbia Ministry of Energy and Mines). XIV. Series: Paper (British Columbia Ministry of Energy, Mines and Natural Gas). XV. Series: Paper (British Columbia Ministry of Energy and Mines).

QE187.46 622.1'09711 C76-083084-3 (Rev.)

Victoria
British Columbia
Canada

January 2016

Preface

Geological Fieldwork 2015

The 41st edition of Geological Fieldwork is a volume of peer-reviewed papers that present the results of geological research conducted by the British Columbia Geological Survey (BCGS) and its partners in 2015. The papers address various aspects of British Columbia's geology, with many highlighting the mineral wealth of the Province. The Geological Fieldwork publication is one way that the BCGS helps the minerals industry unlock this wealth by providing comprehensive, objective, and up-to-date geoscience information at no cost.

The BCGS undertook a wide variety of geoscience projects in 2015, many of which were done in collaboration with partners to maximize the benefits that come from combined staff and resources. Major partners in 2015 include the Geological Survey of Canada, the University of Victoria, and the Canadian Mining Innovation Council. The Survey also completed many smaller projects in collaboration with faculty and students from universities, with geologists from exploration companies, and with consultants from other geoscience agencies including Geoscience BC.

As is evident from the Table of Contents, this volume contains papers that range from regional mapping of magmatic arcs, to site-specific investigations of mineral deposits, to detailed studies of indicator minerals collected from samples of glacial till. The differing scales and diversity of these projects reflects the growing capacity of the Survey to tackle increasingly complex geological problems posed by the Canadian Cordillera. In 2015, collaboration between the BCGS and Geological Survey of Canada focused on two major programs: the second iteration of the five-year Geo-mapping for Energy and Minerals program (GEM 2) and the fifth iteration of the Targeted Geoscience Initiative (TGI-5) program. The GEM 2 program saw Survey geologists investigating the bedrock geology and crustal architecture of northern British Columbia to better understand the genesis and distribution of Jurassic and Triassic porphyry copper-gold-molybdenum deposits. The TGI-5 projects are largely at the planning stage, although the two-day "Symposium on Critical and Strategic Materials" held in Victoria in November will form the basis of a new TGI-5 project that will investigate these materials. The Symposium immediately followed the annual BCGS Open House and brought together an international group of research scientists and industry professionals to discuss materials of high economic or trade importance (hence 'critical') and those of importance to a nation's security (hence 'strategic'). The BCGS organized the Symposium, which was co-sponsored by the Pacific Section of the Geological Association of Canada (GAC-PAC) and the Geological Survey of Canada, and produced a 273-page proceedings volume of extended abstracts (BCGS Paper 2015-3).

January 2015 also marked the opening of the 'BC Pavilion' at the Vancouver Convention Centre, the new home of the Mineral Exploration Roundup. Designed by Survey staff to function as a one-stop venue for Roundup delegates, the Pavilion affords the Survey and its sister government agencies the opportunity to present program highlights and new geoscience information in addition to assisting delegates with permitting and tenure issues.

The BCGS's extensive rock and geochemical archive was moved in the fall of 2015 to a refurbished building on Victoria's waterfront. The new building is larger and easier to access. This will facilitate the more rapid retrieval of rock samples and geochemical pulps for future re-analysis projects.

Finally, 2015 will be remembered as another year of staff renewal with the addition of Bram van Straaten and Luke Ootes, who joined the BCGS as Project Geologists with expertise in copper and gold metallogeny, respectively.

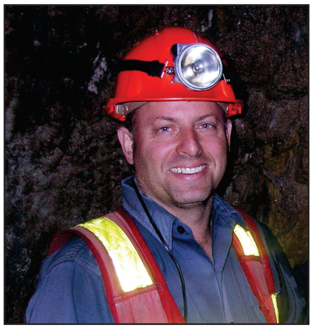

Stephen M. Rowins
Chief Geologist & Executive Director
British Columbia Geological Survey

Table of Contents

British Columbia Geological Survey annual program review 2015-2016

Adrian S. Hickin[1, a], Larry D. Jones[1], and Gordon Clarke[2]

[1] British Columbia Geological Survey, Ministry of Energy and Mines, Victoria, BC, V8W 9N3
[2] British Columbia Geological Survey, Ministry of Energy and Mines, Vancouver, BC, V6Z 2G3
[a] corresponding author: Adrian.Hickin@gov.bc.ca

Recommended citation: Hickin, A.S., Jones, L.D., and Clarke, G., 2016. British Columbia Geological Survey annual program review 2015-2016. In: Geological Fieldwork 2015, British Columbia Ministry of Energy and Mines, British Columbia Geological Survey Paper 2016-1, pp. 1-11.

---

1. Introduction

Providing a summary of projects, events, and accomplishments over the past year, this review highlights activities of the British Columbia Geological Survey (BCGS). Established in 1895, the Survey links government, the minerals industry, and British Columbians to the Province's geology and mineral resources. The key roles of the Survey are to

- create, maintain, and deliver geoscience knowledge to lead informed decision making
- attract companies and individuals to explore British Columbia for new mineral and coal resources
- act as the public steward of mineral and coal resources
- guide public policy by providing assessments on mineral exploration and mining activities.

The BCGS remains committed to producing geoscience data and knowledge that stimulate exploration activity and attract investment. The Survey strives to be a leader in public government geoscience, providing information to all stakeholders and communities through traditional reports, maps, and databases (Fig. 1), which can be freely accessed online. Headquartered in Victoria, the BCGS is a branch in the Mines and Mineral Resources Division of the Ministry of Energy and Mines. The Survey has a permanent staff of 28 people (Fig. 2) operating in three sections: 1) Cordilleran Geoscience; 2) Resource Information; and 3) the Mineral Development Office (MDO). The Cordilleran Geoscience Section is responsible for generating new geoscience knowledge, largely through field-based studies and surveys. The Resource Information Section is responsible for maintaining and developing the provincial geoscience databases and disseminating geoscience data online through MapPlace. This Section is responsible for evaluating, approving, and archiving mineral and coal exploration assessment reports filed by the exploration and mining industry. The MDO links the province's mineral and coal resources to the investment community, distributes and promotes BCGS technical data, and coordinates the technical outputs of the Regional Geologists Program.

2. Cordilleran Geoscience Section

The Cordilleran Geoscience Section consists of resident geologists with expertise in regional bedrock mapping, tectonics, mineral deposits, Quaternary and surficial geology, geochemistry, petrology, mineral exploration methods, copper and gold metallogeny, and geoscience data management. The Survey is happy to announce the hiring of two new project geologists, Dr. Bram van Straaten and Luke Ootes, who joined the Cordilleran Section in 2015, bring expertise in regional mapping and copper and gold metallogeny.

2.1. Projects

British Columbia Geological Survey projects are based on short-term objectives and long-term goals. Many current projects are continuations of multi-year efforts, whereas others are new. Projects in 2015 focused on porphyry initiatives, deposit studies, exploration methods development, and regional synthesis and map compilation (Fig. 3).

2.1.1. Porphyry initiatives

2.1.1.1. Porphyry environment transitions (GEM 2)

The prolific belt of British Columbia's porphyry deposits is difficult to track in the Stikine terrane of northwestern British Columbia. The Porphyry Environment Transition project, a collaboration with the Geological Survey of Canada (through the Geomapping for Energy and Minerals program; GEM 2), completed its second year of fieldwork in 2015. Through mapping and topical work, the project is targeting regional controls on porphyry mineralization by addressing questions of Late Triassic arc productivity, polarity, and paleogeography, and evaluating indicators of arc prospectivity near its apparent northern termination (see Martin et al., and Mihalynuk et al., this volume).

2.1.1.2. Stikinia magmatism: Stratigraphic and structural controls: Red Mountain to Kitsault (GEM 2)

Mesozoic Stikinia is largely known for its Cu-Au porphyry and related mineral endowment. Significant deposits of this type are found throughout the northwestern part of the terrane, from Dease Lake in the north to Stewart in the south. Farther south however, major coeval deposits show epithermal vein and volcanogenic character. This project is designed to increase

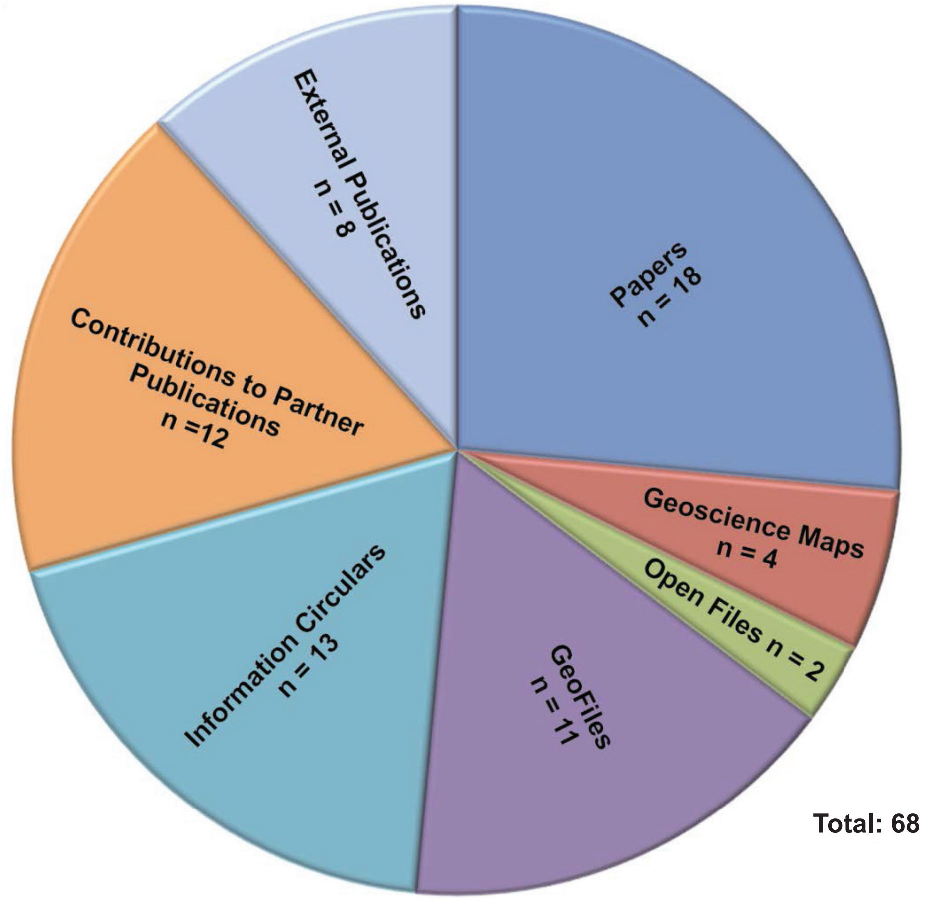

Types of Publications by the British Columbia Geological Survey

Papers*: This series is reserved for reviews and final thematic or regional works. Geological Fieldwork, our annual review of field activities and current research, is released as the first Paper of each year.

Geoscience Maps: This series is the BCGS vehicle for publishing final maps.

Open Files: These maps and reports present the interim results of ongoing research, particularly mapping projects.

GeoFiles: These publications enable rapid release of extensive data tables from ongoing geochemical, geochronologic, and geophysical work. As such, they serve the same function as data repositories provided by many journals, providing immediate access to raw data from specific projects.

Information Circulars: These publications provide accessible geoscience information to a broad audience in government, industry, and the general public. Included in the Information Circular series are the annual Provincial Overview of Mining and Exploration, **Exploration and Mining in British Columbia, and the Coal Industry Overview.

Contributions to partner publications: This category includes reports, maps, and other products published by another agency such as the Geological Survey of Canada or Geoscience BC, but have received contributions from British Columbia Geological Survey staff.

External publications: These are contributions to the peer reviewed literature and published in a recognized national or international scientific journal.

*The count refers to the total number of articles authored by BCGS personnel in a volume.

**Although five articles are included in Exploration and Mining in British Columbia, it is counted as a single volume.

Fig. 1. British Columbia Geological Survey publications in 2015.

Fig. 2. Members of British Columbia Geological Survey.

understanding of both porphyry and non-porphyry mineral occurrences, targeting stratigraphic, structural, and tectonic controls, which will aid in reconstructing the overall tectonic and metallogenetic environment of Stikinia. This project also contributes to the BCGS-Geological Survey of Canada GEM 2 partnership.

2.1.1.3. Stikinia magmatism: Stratigraphic and structural controls: Tanzilla (GEM 2)

An enigmatic Jurassic volcanic succession on the northeastern margin of Stikinia hosts several early-stage mineral exploration projects, including the Tanzilla porphyry system. The Tanzilla alteration zone is large, but poorly explored and with little detailed mapping. As part of the GEM 2 program, the Tanzilla alteration zone was evaluated using ideas generated from previous work in the KSM-Brucejack and emerging KSP (Bronson corridor) regions. Based on new field mapping and preliminary lithogeochemical and geochronological data, these rocks are now considered part of the Hazelton Group and have been formally defined as the Horn Mountain Formation (see van Straaten and Nelson, this volume).

2.1.1.4. Porphyry indicator minerals in till, central British Columbia (TGI-4)

Quesnel, Cache Creek, and Stikine terranes are prospective for porphyry-style mineralization. However, in the Interior Plateau of British Columbia, bedrock is commonly covered by glacigenic sediments. Historically, these sediments have been regarded as a hindrance to mineral exploration. Nonetheless, regional-scale and detailed geochemical surveys by the British Columbia Geological Survey, Geological Survey of Canada, and university researchers have demonstrated that tills can be used to explore for mineralized bedrock. Major, minor, and trace element determinations on the silt-plus-clay fraction of basal tills have successfully detected known sources of mineralization (e.g., Prosperity, Bell, Granisle, Equity Silver, Huckleberry, Mount Milligan) and identified new mineral occurrences (e.g. 3Ts, Huckleberry Mine, Red Sky).

Heavy minerals in basal till have been used extensively to identify buried diamondiferous kimberlite pipes. Recent work by the Mineral Deposits Research Unit (MDRU) at the University of British Columbia has demonstrated that similarly diagnostic minerals occur in ore and alteration zones of alkaline and calcalkaline porphyry deposits in British Columbia. Work by the British Columbia Geological Survey and the Geological Survey of Canada has demonstrated that mineral assemblages considered to be porphyry indicator minerals (PIMs) can be recovered from till samples. The primary objective of this project is to assess the use of these mineral assemblages in basal till samples to explore for concealed base and precious metal deposits in the Province. This three-year project, funded largely by the Geological Survey of Canada's Targeted Geoscience Initiative 4 (TGI-4) program, focuses on characterizing the mineral assemblage of basal tills derived from known porphyry Cu-Mo-Au deposits in central British Columbia.

2.1.1.5. Highland Valley Copper porphyry indicator minerals survey (TGI-4 and CMIC)

A one-year project, funded jointly by the Canadian Mining Innovation Council (CMIC) and the British Columbia Geological Survey, this project focuses on till geochemistry and porphyry indicator minerals at the Highland Valley Mine site. By comparing data from tills and the Highland Valley deposits (and the other deposits studied in the TGI-4 program), the objective of the project is to establish which minerals survive glacial erosion, transport, and deposition, and near-surface oxidation to serve as tools for porphyry deposit exploration.

2.1.1.6. South Nicola arc project (SNAP) compilation

Southern Nicola belt is a Triassic to Early Jurassic intra-

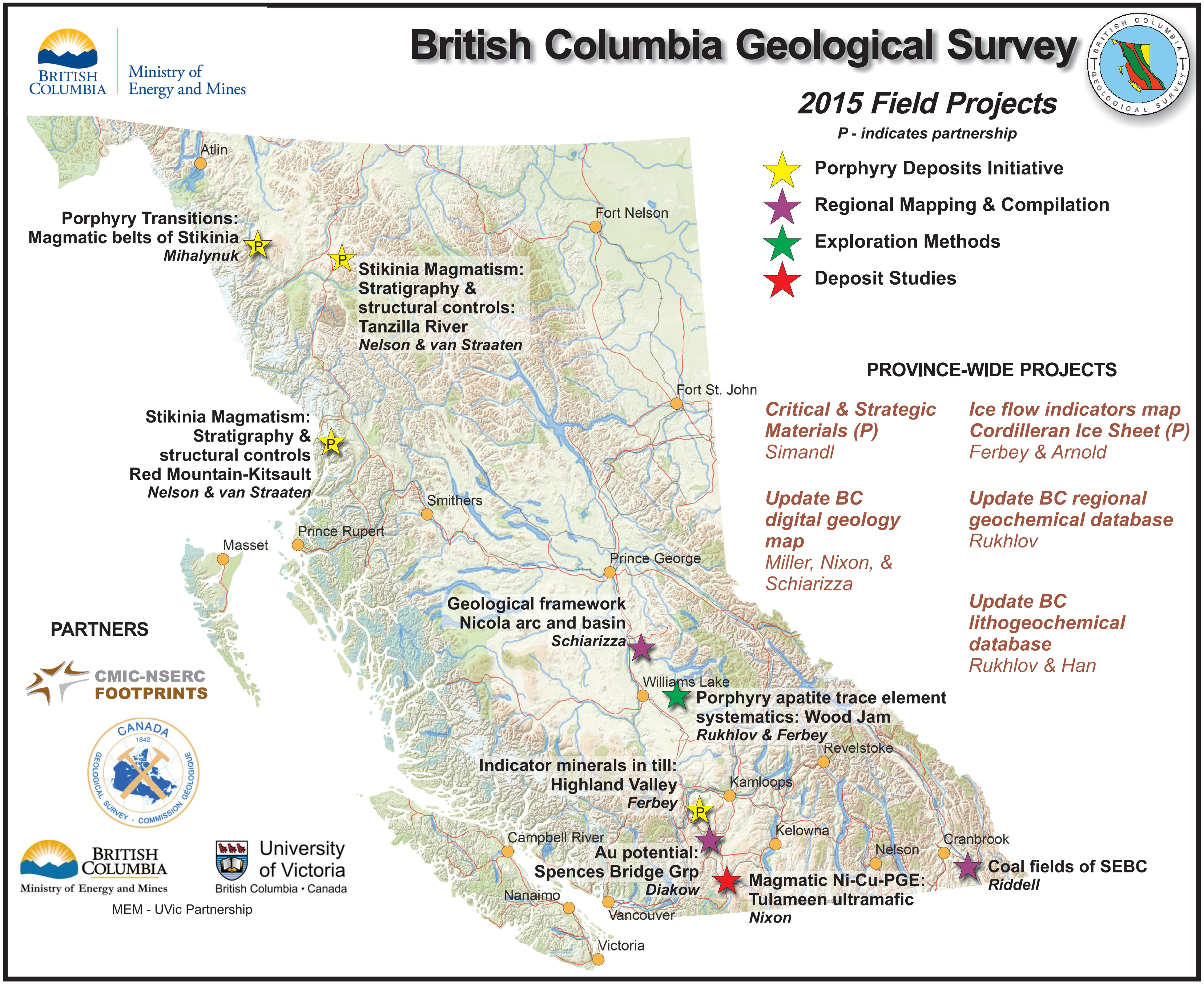

Fig. 3. British Columbia Geological Survey field projects in 2015.

oceanic arc succession that was probably deposited in a setting much like the Fiji-Vanuatu-Solomon-Papuan arc complex of today. It is prolifically mineralized, with most past and present mineral production from porphyry-style mineralization, which commonly contains appreciable Au, Ag and Mo. Mineralization occurs in plutons and their adjacent volcanic and sedimentary country rocks. The British Columbia Geological Survey completed a two-year field mapping program in 2014. In 2015, the project focused on completing 1:50,000 scale maps (from Princeton to the Aspen Grove) and compiling these maps for integration into the British Columbia Digital Geology map.

2.1.2. Deposit studies

2.1.2.1. Epithermal potential of Spences Bridge Group

The Spences Bridge Group is an undeformed and little metamorphosed subaerial volcano-sedimentary succession occupying a northwest-trending belt, up to 25 kilometres wide and 165 kilometres long, between Princeton and Lillooet. It records short-lived Early Cretaceous, continent-margin arc magmatism that developed on an older basement including oceanic rocks of Cache Creek terrane (Carboniferous to Jurassic) and island arc rocks of Quesnel terrane (Late Triassic). Epithermal mineralization was only recently discovered in 2001, a consequence of prospecting following a British Columbia Regional Geochemical survey. These discoveries, and the known epithermal occurrences are in rocks of the Pimainus Formation at the base of the Spences Bridge Group. To test the potential for epithermal mineralization elsewhere in the Spences Bridge Group, a regional mapping project was initiated in selected segments of the belt underlain exclusively by Pimainus Formation rocks.

2.1.2.2. Orogenic Ni-Cu-PGE

This project builds on the now completed TGI-4 'orogenic Ni' deposits studies, conducted as a collaboration between the British Columbia Geological Survey, the Geological Survey of Canada, and the University of British Columbia. New activities by the British Columbia Geological Survey focus on establishing a deposit model for orthomagmatic Ni-Cu±PGE deposits in convergent-margin tectonic settings, such as in British Columbia. With the aim of isolating key ore-forming characteristics of the sulphide-rich intrusions, the most recent activities are directed at completing a geochemical, mineralogical, and geochronological comparison of the Giant Mascot and Turnagain Ni-sulphide deposits with the well-known sulphide-poor intrusion of the Tulameen Alaskan-type complex.

2.1.3. Exploration methods

2.1.3.1. Critical and strategic materials

The demand for strategic and critical materials has grown rapidly in recent years, as ever more technologically advanced devices and industrial processes make use of their unique properties. Interest in specialty metals peaked in 2010 owing to growing global demand, their high value, declining exports from China, and challenges of finding new deposits. These factors created a window of opportunity for Canada to establish itself as a world leader in specialty metal exploration and, potentially, exploitation given the favourable geology in parts of Canada. In November 2015, the British Columbia Geological Survey, with sponsorship from the Pacific Section of the Geological Association of Canada and the Geological Survey of Canada, hosted the Critical and Strategic Materials Symposium, which considered materials of high economic or trade importance (hence 'critical') and those of importance to a nation's security (hence 'strategic'). The Symposium coincided with the end of the 'Specialty Metals Project', a five-year collaborative effort between the British Columbia Geological Survey, the Geological Survey of Canada, and several academic and industry partners. 'Specialty metals', also known as 'rare metals' are uncommon, nonferrous metals used in quantities of typically less than 150,000 tonnes/year or derived from geographically restricted areas. The Specialty Metals Project ran from 2010 to 2015 and was supported by the TGI-4 program.

To accompany the Symposium, the British Columbia Geological Survey produced a volume titled "Symposium on Critical and Strategic Materials Proceedings, November 13-14, 2015, Victoria, British Columbia" (Fig. 4). This volume is a record of the Symposium proceedings, with papers on: the uses, markets, and resources for select critical materials; carbonatites and related mineralization; peralkaline intrusion-related mineralization; rare earth elements; graphite; recent developments in exploration and analytical methods; and a regional geological study.

2.1.3.2. Detrital apatite trace-element compositions: A robust new tool for mineral exploration

Apatite is the most abundant phosphate mineral, occurring as an accessory or rock-forming mineral in many rocks. The crystal structure and chemistry of apatite permit elemental substitution that is sensitive to the environment in which it forms. These properties make apatite a promising indicator for mineral exploration. In this project, a collaboration between the British Columbia Geological Survey and the University of Victoria, apatite grains from the major types of magmatic-hydrothermal mineral deposits (30 localities, mostly in British Columbia) together with apatites from carbonatites (29 intrusive complexes) and unmineralized rocks (11 localities) were analyzed by electron microprobe and laser ablation-inductively coupled plasma mass spectrometry. Discriminant analysis of several elements reveals that apatite grains from mineral deposits can be distinguished from apatite grains in carbonatites and unmineralized rocks. Apatites from the different deposit types also have distinctive trace-element compositions that are readily distinguished by the discriminant functions.

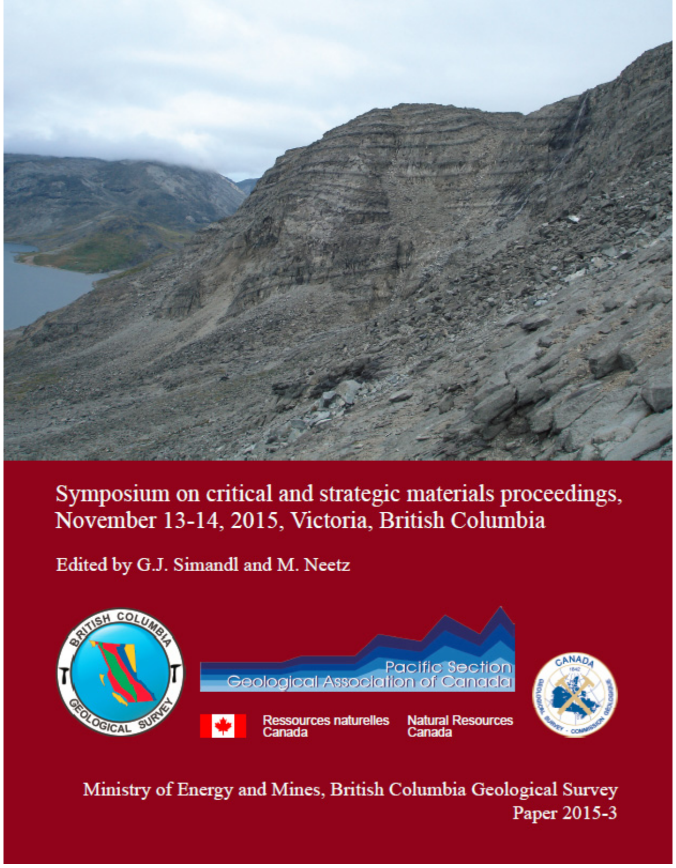
Symposium on critical and strategic materials proceedings,
November 13-14, 2015, Victoria, British Columbia

Edited by G.J. Simandl and M. Neetz

Pacific Section
Geological Association of Canada

Ressources naturelles Canada
Natural Resources Canada

Ministry of Energy and Mines, British Columbia Geological Survey
Paper 2015-3

Fig. 4. British Columbia Geological Survey Paper 2015-3, Symposium on Critical and Strategic Materials Proceedings, November 13-14, 2015, Victoria, British Columbia.

2.1.3.3. Application of trace element composition of detrital apatite from till as a porphyry indicator mineral

Building on work demonstrating that apatite can be used as an indicator mineral to effectively discriminate mineralized systems from barren rocks, and to distinguish different deposit types (see above), this project provides a test by examining detrital apatite grains from TGI-4 till samples collected at the Gibraltar, Mt. Polley, Woodjam, and Highland Valley porphyry deposits. Apatite grains were analyzed by electron microprobe and laser ablation-inductively coupled plasma mass spectrometry. Classification of the examined apatite grains using discriminant functions correctly identified the porphyry deposits in all four study areas. Results show that apatite trace-element chemistry is diagnostic of specific porphyry deposits and their relative oxidation states and thus can be used as an exploration tool for these deposits (see Rukhlov et al., this volume).

2.1.3.4. Application of lead isotopes in till for mineral exploration

The objective of the project was to determine if elemental abundances and Pb isotopic ratios from Chehalis valley basal till samples collected in 2014 could cost effectively highlight the down-ice glacial dispersion of volcanogenic massive sulphide (VMS) occurrences. Despite the relatively young age of the Seneca VMS deposit and surrounding volcanic rocks (Middle Jurassic), the contrast in Pb isotopic ratios between tills derived from country rocks and tills containing ore material is 3-7%. This contrast is 2-3 orders of magnitude above the analytical uncertainties of state-of-the-art multi-collector inductively coupled plasma mass spectrometry (MC-ICP-MS). In this study, a simplified method, in which Pb isotopic ratios are measured by high-resolution inductively coupled plasma mass spectrometry (HR-ICP-MS), is consistent with the MC-ICP-MS results. The relatively inexpensive method of determining Pb isotopic ratios in tills by using HR-ICP-MS constitutes a robust exploration tool for a broad range of concealed Pb-rich deposits including relatively young deposits. This study was published as British Columbia Geological Survey Paper 2015-2 (Fig. 5).

2.1.4. Regional synthesis and map compilation

2.1.4.1. Nicola Arc Stratigraphic Framework

The Nicola Group comprises a diverse assemblage of mainly Upper Triassic volcanic, volcaniclastic, and sedimentary rocks that outcrop over a broad area in southern and central British Columbia. It, and coeval to slightly younger intrusions, are the

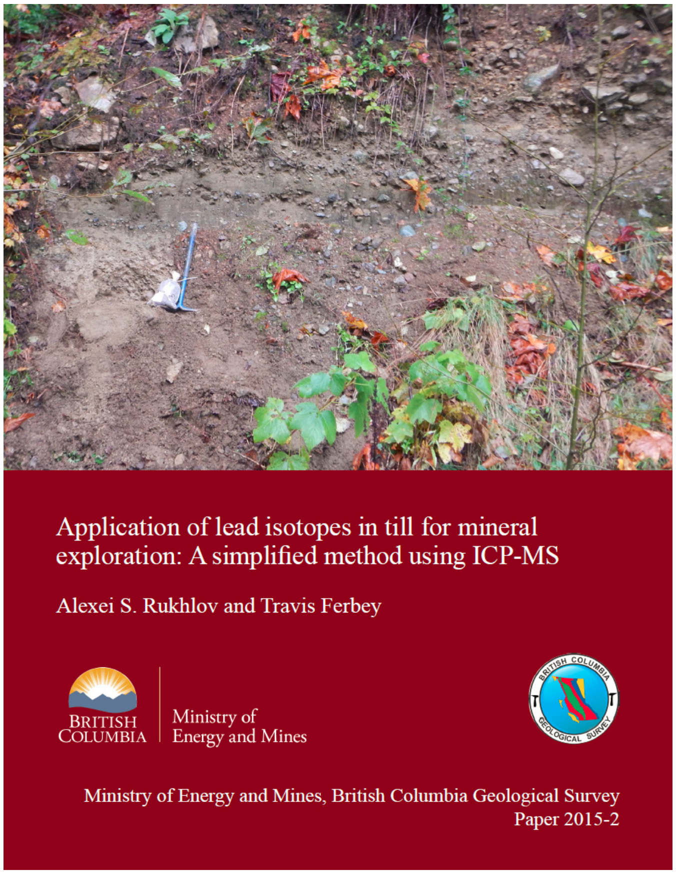
Application of lead isotopes in till for mineral
exploration: A simplified method using ICP-MS

Alexei S. Rukhlov and Travis Ferbey

British Columbia
Ministry of Energy and Mines

Ministry of Energy and Mines, British Columbia Geological Survey
Paper 2015-2

Fig. 5. British Columbia Geological Survey Paper 2015-2, Application of lead isotopes in till for mineral exploration: A simplified method using ICP-MS.

defining elements of the Quesnel arc terrane, an important Cu-Au-Mo metallogenic province that contains numerous porphyry and skarn deposits. However, the stratigraphic architecture of the Nicola group is not well understood. Building on the South Nicola Arc Project (SNAP), this multi-year project initiated in 2015, aims to establish a stratigraphic framework for the group that can be applied at regional and local scales (see Schiarizza, this volume).

2.1.4.2. Ice-flow indicators for the Cordilleran Ice Sheet (GEM 2)

In 2013, the British Columbia Geological Survey compiled a Province-wide ice-flow indicator map. The motivation was to provide the mineral exploration community with a spatial database of ice-flow indicators to assist interpreting till, stream, and soil geochemical surveys. This product was well received by the exploration community and it was decided that, in collaboration the federal GEM 2 program, the database would be expanded to incorporate all mapped ice-flow features for the entire Cordilleran Ice Sheet.

The first phase of the project is now complete, with the integration of ice-flow indicator databases from the British Columbia Geological Survey, Yukon Geological Survey, Geological Survey of Canada, and United States Geological Survey. The second phase is generating new data in northern British Columbia where data are sparse. The compilation will incorporate data captured from digital stereo airphotos, pseudo-stereo orthophoto mosaics, and other imagery. These data will also be used to assess, where possible, the quality of the existing ice-flow data.

2.1.4.3. Coal Fields of British Columbia

The British Columbia Geological Survey has completed coalfield compilation posters for the East Kootenay Coalfields of southern British Columbia and coalfields in the northeastern part of the Province. These posters provide overviews of coalfield geology, coal products, annual and historical production, reserves and resource estimates, and past and current projects.

3. Resource Information Section

The British Columbia Geological Survey serves as the custodian of geoscience data from across the province. These data include bedrock geology, surficial geology, mineral occurrences, and multi-element geochemistry from rock, till, stream-sediment, and water samples. The information resides in databases that are integrated with MapPlace, the free BCGS online service that allows clients to browse, visualize, and analyze multidisciplinary geoscience data and create custom maps. The data and derived products provide baseline geoscience information for mineral exploration, resource assessment, and land use planning. In particular, they increase exploration effectiveness by enabling users to efficiently gather regional information for property-scale evaluation, and help explorers advance projects without duplicating previous work.

Since 1995, MapPlace, has provided open geoscience data and custom map-making tools to help assess the mineral potential of British Columbia, assist exploration, and guide investment decisions. Through MapPlace, BCGS databases talk to each other. ARIS, MINFILE, COALFILE, Property File, geochemical surveys, mineral titles, geological and topographic maps, and the British Columbia Geological Survey publication catalogue can be queried simultaneously, and the output projected onto base imagery of choice (Fig. 6). The next generation of MapPlace, (MapPlace 2), scheduled for release in 2016, is capable of accessing queried BCGS databases to display province-wide maps within seconds.

ARIS is the searchable database of over 34,700 assessment reports submitted to the Ministry of Energy and Mines, in compliance with Mineral Tenure Act (MTA) Regulations. These reports summarize results from exploration programs on mineral claims. After a one-year confidentiality period, the reports become an open resource for planning mineral exploration, investment, research, land use, and resource management. Between 1967 and 2014, ARIS stored work representing expenditures of about $2.8 billion (Fig. 7a). Between 1996 and 2014 most expenditures are a result of drilling (Fig. 8). COALFILE is a library of Coal Assessment Reports submitted by exploration companies since 1900 (Fig. 7b). It includes data from 15,092 boreholes, 541 bulk samples, 995 maps, and 3580 trenches. MINFILE is an inventory documenting metallic mineral, industrial mineral, and coal occurrences in the province. With over 14,000 entries (Fig. 7c), the database is being updated continuously. Users can query MINFILE by location, identification number, mineralogy, commodity, host rock, deposit type, geological setting, age, production, and references. Property File is a collection of over 55,000 government, university, personal, and industry documents donated to the British Columbia Geological Survey over the last 150 years (Fig. 7d). Previously available only in hard copy, these documents can now be searched for, and downloaded from, the Property File database. Property File contains: unpublished reports; theses; field notes; company prospectuses; correspondence; hand-drawn maps; claim maps; mine plans; photographs; and geological, geochemical, geophysical, and drill data. The BC Geological Survey accepts donations to Property File.

The provincial geochemical databases hold field and geochemical data from multi-media surveys by the Geological Survey of Canada, the British Columbia Geological Survey, and Geoscience BC (GBC). The databases are updated regularly and contain results from: 1) the Regional Geochemical Survey program (RGS) including analyses from stream-sediment, lake-sediment, moss, and water samples (Fig. 7e); 2) till surveys; and 3) rock samples. The 2015 version of the RGS database consists of five MS Access tables with locations, field observations, analytical results, and geologic descriptions of sample sites. The determinations include up to 63 analytes from sediment samples and up to 78 analytes from water samples. The provincial rock geochemical database, last released in

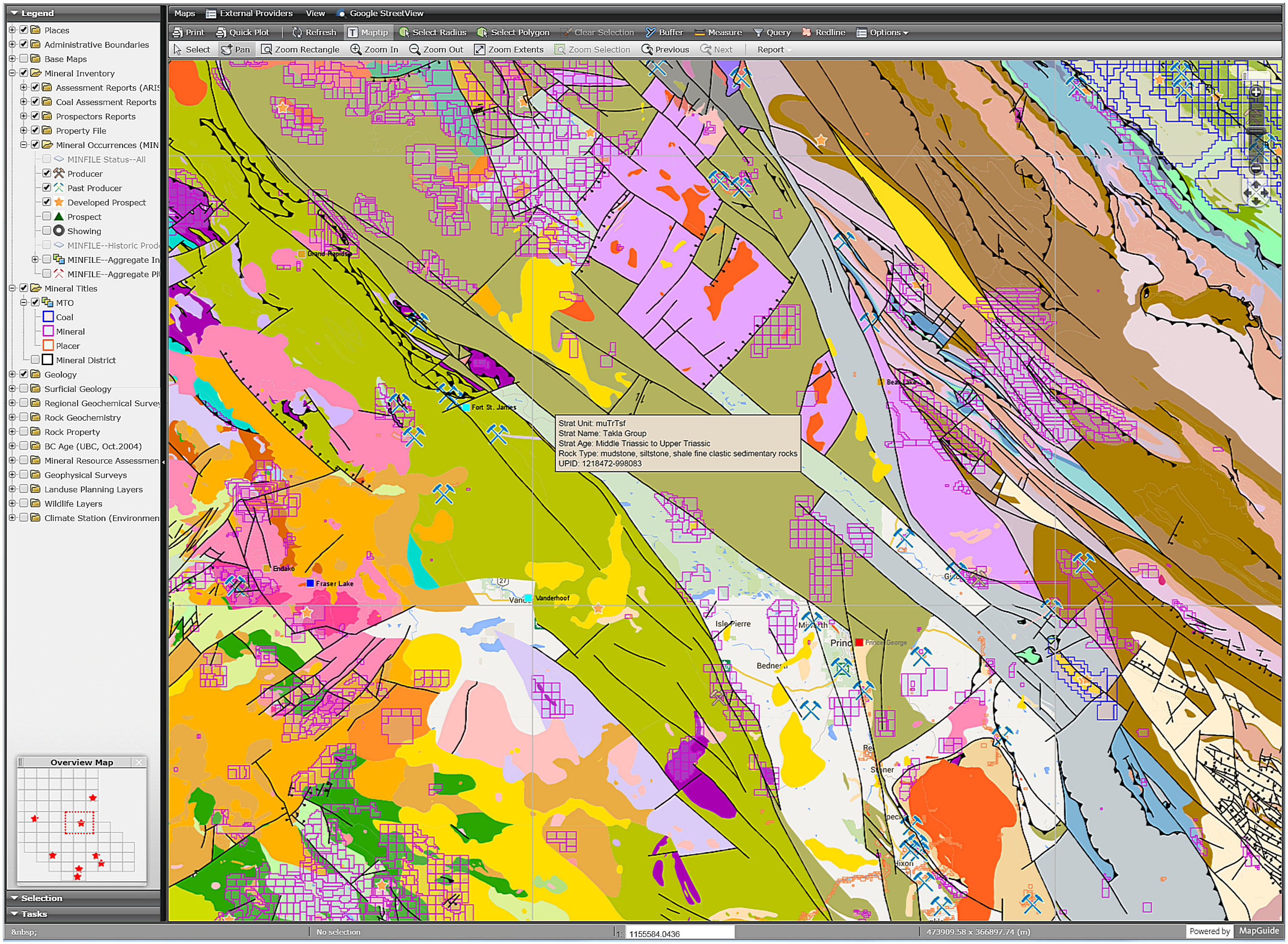

Strat Unit: muTrTsf
Strat Name: Takla Group
Strat Age: Middle Triassic to Upper Triassic
Rock Type: mudstone, siltstone, shale fine clastic sedimentary rocks
UPID: 1218472-998083

Fig. 6. MapPlace 2 screen capture.

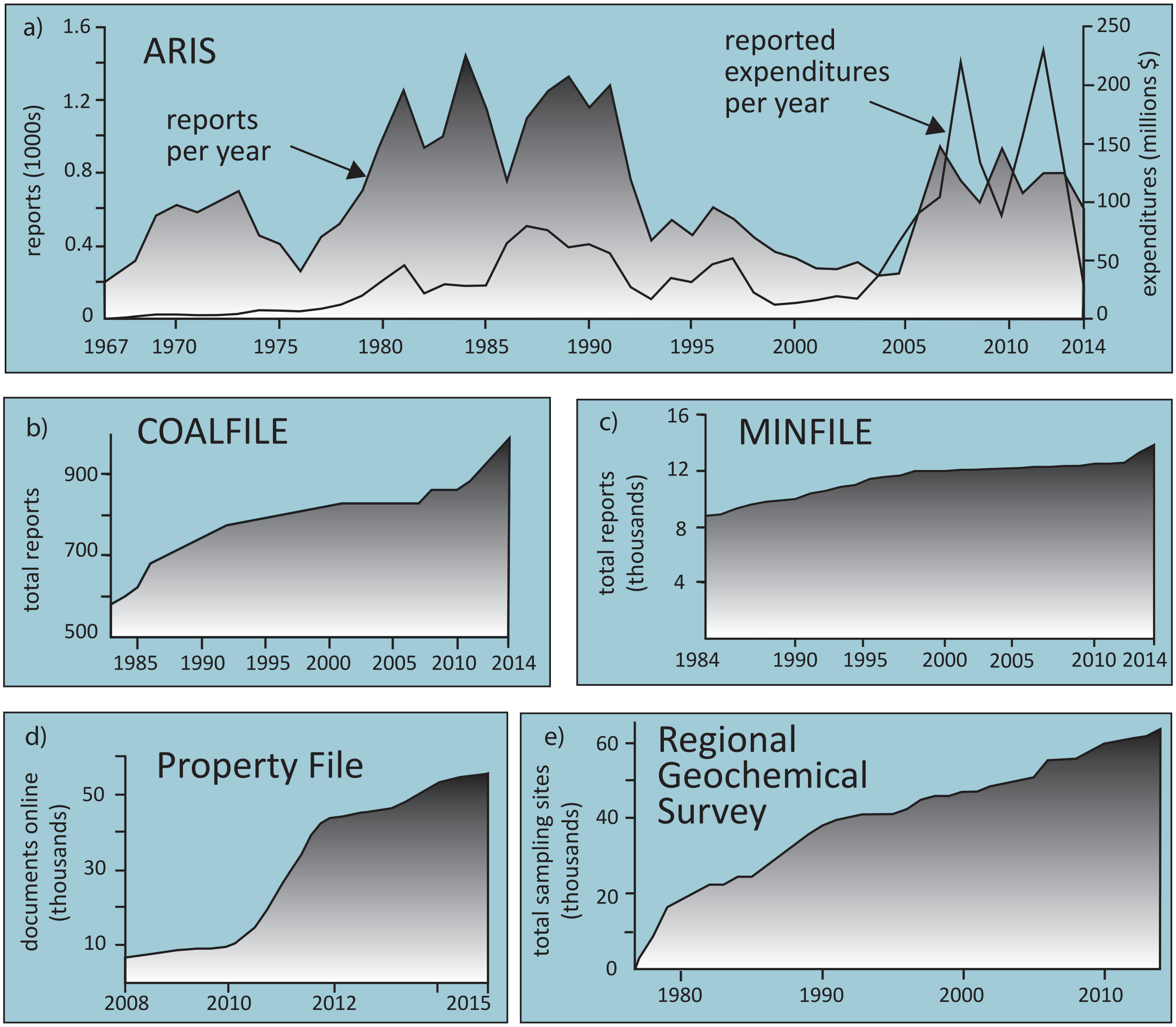

Fig. 7. Growth of some British Columbia Geological Survey databases.

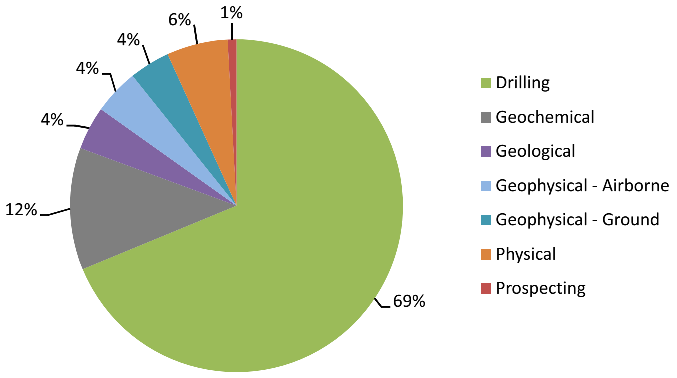

Fig. 8. Assessment report expenditures by type of work from 1996-2014.

2005, was updated and released in January 2016 to include over 10,000 records.

British Columbia Digital Geology is the data source used to create the digital Geological Map of British Columbia (Fig. 9). The October 2015 release integrates five geological maps for northern Vancouver Island.

4. Mineral Development Office

The Mineral Development Office (MDO) is the technical marketing arm of the British Columbia Geological Survey and the Ministry of Energy and Mines. The MDO promotes the mineral and coal industries, domestically and abroad, at conferences, business meetings, investment missions, and over-the-counter contacts. Its location in downtown Vancouver

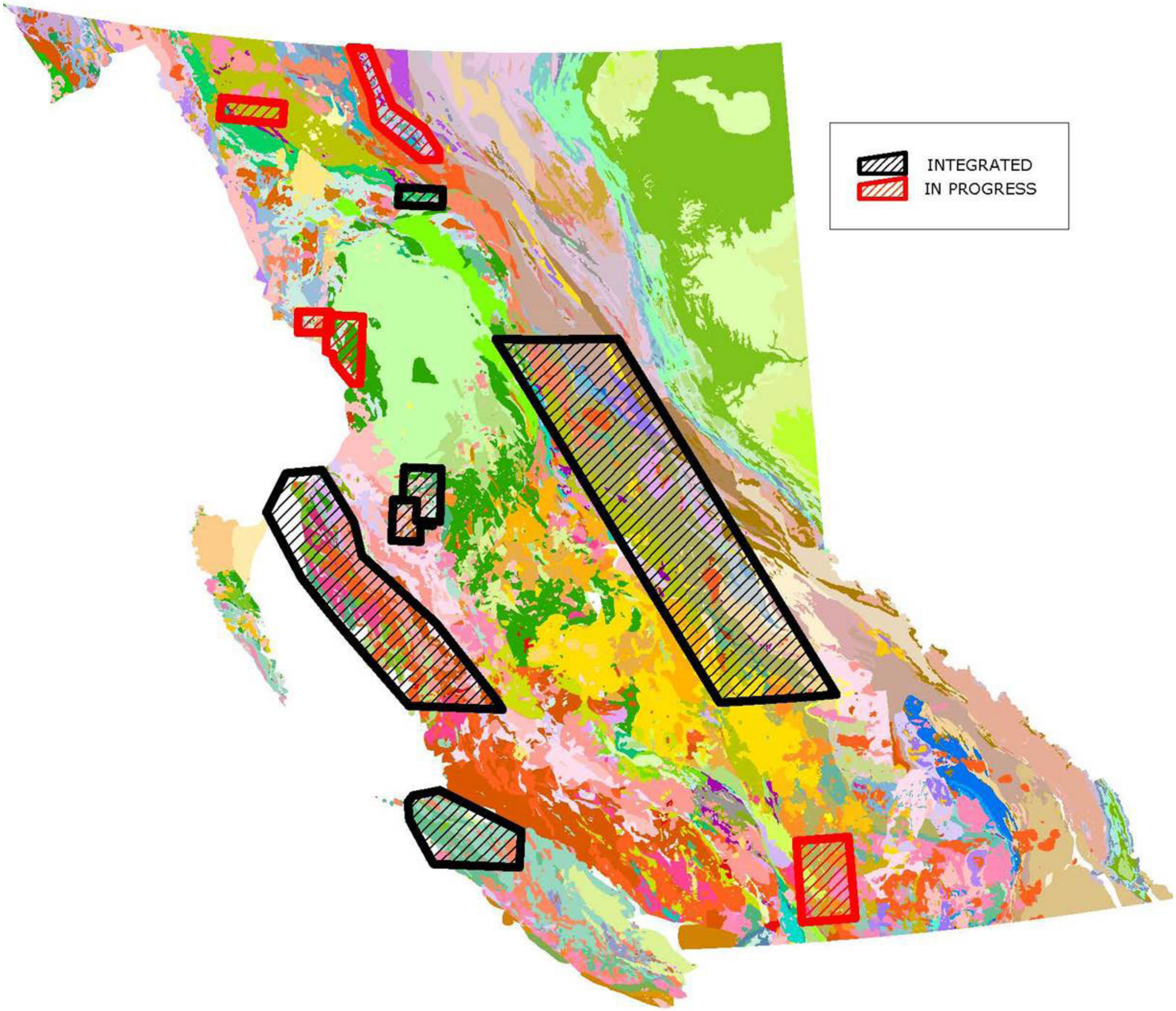

Fig. 9. Areas of British Columbia with recent (black boxes) or ongoing (red boxes) updates to the British Columbia digital geology map (www.empr.gov.bc.ca/Mining/Geoscience/PublicationsCatalogue/DigitalGeologyMaps/Pages/default.aspx).

provides the minerals industry with a point of contact for Survey activities, access to government geoscience products, and advice on mineral and coal opportunities in the Province.

Technical marketing by the MDO targets an audience ranging from large foreign investment groups to independent domestic entrepreneurs, highlighting the Province's mineral and coal potential, geoscience resources, global expertise, and attractive business climate. In 2015 a number of promotional publications were revised, including brochures for copper, gold, molybdenum, coal, nickel, zinc, and jade, which was also produced in Chinese. The MDO office website was redesigned and updated with new publications and revised links to government and industry associations. Website revisions included a Google Earth interactive map showing all British Columbia porphyry deposits with defined resources and comprehensive information about the deposits through a link to MINFILE. In the fall of 2015, the MDO supported the Ministry of International Trade by participating in the China Mining Congress and Expo in Tianjin and the Canada Mineral Investment Forum in Beijing.

The MDO oversees delivering provincial and regional level exploration and mining summary documents from the Regional Geologist Program, maintaining a legacy that dates back to 1874 with the Annual Reports of the Minister of Mines.

5. Regional Geologists Program

The Regional Geologists Program was created in the early 1970s to facilitate economic development in the mineral exploration and mining sector. The British Columbia Regional Geologists represent the provincial government on geological matters at a regional level and capture information on industry activity in their jurisdictions. Within their communities, they provide information on exploration trends, possible investment opportunities, land use processes, First Nation capacity building, and public outreach.

Acknowledgment

We thank George Owsiacki of Total Earth Science Services for desktop publishing of this volume.

Toward a regional stratigraphic framework for the Nicola Group: Preliminary results from the Bridge Lake – Quesnel River area

Paul Schiarizza[1, a]

[1] British Columbia Geological Survey, Ministry of Energy and Mines, 300-865 Hornby Street, Vancouver, BC, V6Z 2G3
[a] corresponding author: Paul.Schiarizza@gov.bc.ca

Recommended citation: Schiarizza, P., 2016. Toward a regional stratigraphic framework for the Nicola Group: Preliminary results from the Bridge Lake – Quesnel River area. In: Geological Fieldwork 2015, British Columbia Ministry of Energy and Mines, British Columbia Geological Survey Paper 2016-1, pp. 13-30.

Abstract

The Nicola Group (Triassic) is the principal volcano-sedimentary unit of the Quesnel arc terrane, well known for its prolific porphyry Cu ±Au-Mo-Ag deposits. Although studied since the late 1800s, a comprehensive regional stratigraphic framework for the Nicola Group, integrating local informal subdivisions introduced by different workers at different times, has hitherto been lacking. In 2015, the British Columbia Geological Survey initiated a multi-year program to establish the regional temporal and spatial variation of Nicola Group subunits. Preliminary investigations were in the Bridge Lake – Quesnel River area of south-central British Columbia, which encompasses a wide belt of Nicola rocks that have been mapped in sufficient detail to allow an initial assessment of stratigraphic divisions over a relatively large area. Some Triassic rocks previously included in the Nicola Group are reassigned to the Slocan Group, and those retained as Nicola Group are separated into four assemblages. Assemblage one, identified only along the northeast margin of the Nicola belt, contains mainly Middle Triassic siltstone and argillite, but also includes volcaniclastic sandstone and pillowed basalt. Assemblage two (Carnian and early Norian) is a widespread and heterogeneous unit that includes basalt flows and basalt breccia, but consists mainly of volcanic sandstone and conglomerate derived from these, or similar, mafic volcanic rocks. Assemblage three is a relatively homogeneous succession of pyroxene-phyric basalt flows and basalt breccia that reflect a major Norian constructional phase of the Nicola arc. Assemblage four (latest Triassic), possibly separated from underlying rocks by an unconformity, contains polymictic conglomerate with abundant hypabyssal and plutonic rock fragments, but also includes red feldspathic sandstone, pyroxene-phyric basalt, and a distinctive coarse, crowded plagioclase-phyric andesite. The four assemblages established in the Bridge Lake – Quesnel River area provide a preliminary framework for ongoing studies of Nicola Group stratigraphy, and will be expanded and modified with further work.

Keywords: Nicola Group, Slocan Group, Triassic, volcanic arc, basalt, basalt breccia, volcanic sandstone, conglomerate, Quesnel terrane, Slide Mountain terrane, Kootenay terrane

---

1. Introduction

Quesnel terrane constitutes an important metallogenic belt that hosts numerous Cu-Au-Mo porphyry and skarn deposits along the length of the Canadian Cordillera (Fig. 1). It is characterized by a Mesozoic arc complex that includes Triassic to Jurassic volcanic and sedimentary rocks, and related calcalkaline and alkaline intrusions. In south-central British Columbia the supracrustal component is represented mainly by the Nicola Group, originally named for exposures of volcanic rocks and limestones on the south side of Nicola Lake (Dawson, 1879), and presently referring to diverse assemblages of mainly Late Triassic volcanic, volcaniclastic, and sedimentary rocks that are exposed over a broad area, including parts of NTS map sheets 82E, 82L, 92H, 92I, 92P, 93A, 93B, and 93G. The Nicola Group has been mapped in reasonable detail in many areas, and numerous informal local subdivisions have been applied by those working in different areas at different times and scales. However, no regional-scale stratigraphy has been established. In 2015, the British Columbia Geological Survey initiated a multi-year program to establish the regional

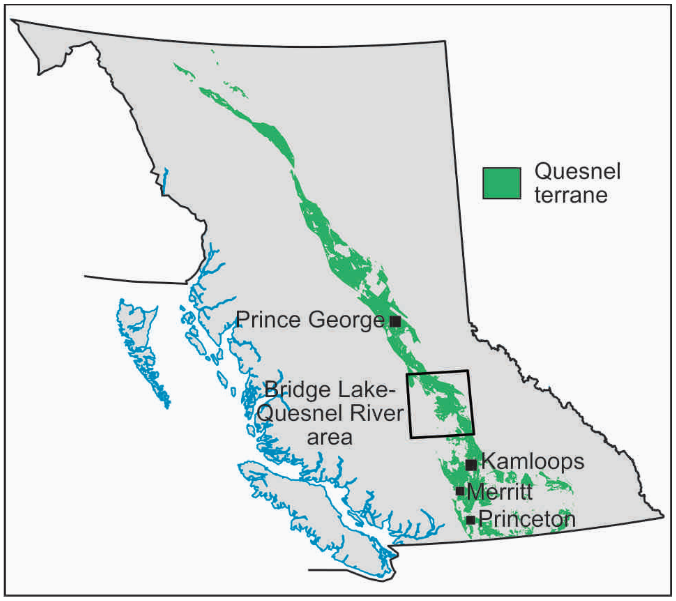

Fig. 1. Location of the Bridge Lake – Quesnel River area and distribution of Quesnel terrane in British Columbia.

temporal and spatial variation of Nicola Group subunits. This regional stratigraphic framework, combined with space-time-composition patterns of associated plutons, will help better define the general architecture of the arc, and improve the geologic framework within which to interpret the settings and controls of mineral occurrences in this important metallogenic domain.

The initial investigations were carried out in the Bridge Lake – Quesnel River area (Figs. 1, 2), an area of subdued topography that is mainly in the Fraser Plateau and Quesnel Highland physiographic provinces, and covers parts of the traditional territories of the Secwepemc, Esk'etemc, and Tsilhqot'in First Nations. This area encompasses a wide belt of Nicola rocks that have been mapped in sufficient detail to evaluate possible stratigraphic divisions over a large area. The geology of the northern part of this area is provided mainly by Panteleyev et al. (1996), which incorporates the work of Campbell (1978), Bailey (1978, 1990), Rees (1987) and Bloodgood (1987, 1990), with subsequent revisions by Logan and Mihalynuk (2005) and Logan et al. (2007). The geology to the south, summarized by Schiarizza et al. (2013), was mapped by Schiarizza and Israel (2001), Schiarizza et al. (2002), Schiarizza and Boulton (2006), Schiarizza and Macauley (2007), Schiarizza and Bligh (2008), and Schiarizza et al. (2009). The preliminary results, presented here, include separation of Triassic rocks into the Nicola and Slocan groups, and dividing Nicola Group rocks into four assemblages.

2. Geologic setting

The Triassic Nicola Group, the main stratigraphic unit of the Quesnel arc terrane, extends across the Bridge Lake – Quesnel River area in a northwest-trending belt that is 30 to 70 km wide (Fig. 2). This belt also includes abundant Late Triassic to Early Jurassic calcalkaline and alkaline arc intrusions, and fault-bounded panels of Lower to Middle Jurassic arc-derived siliciclastic sedimentary rocks of the Dragon Mountain succession (Petersen et al., 2004; Logan and Moynihan, 2009). The Harper Ranch Group, an upper Paleozoic sedimentary and volcanic succession that is well exposed farther south, is represented by two fault-bounded inliers of Permian limestone and siltstone in the southern part of the study area (Fig. 2).

The Nicola Group is flanked to the east by a belt of Triassic sedimentary rocks, mainly black phyllite, slate, and quartz sandstone, which is herein assigned to the Slocan Group. Farther east, the Slocan Group is in contact with the Slide Mountain terrane, including basalt, chert and gabbro of the Fennell Formation south of the Raft batholith, and a narrow, discontinuous belt of mafic schist, referred to as the Crooked amphibolite, to the north. The Slide Mountain terrane is in turn flanked to the east by a wide belt of Proterozoic and Paleozoic siliciclastic, carbonate, and local volcanic and plutonic rocks included in the pericratonic Kootenay terrane. The Cache Creek terrane, including late Paleozoic to early Mesozoic basalt, chert, and limestone, is west of the Nicola belt and is generally interpreted as an accretionary complex genetically related to the subduction that generated the Quesnel magmatic arc. Younger rocks found in the study area include late Middle Jurassic and Early Cretaceous granitic intrusions, Eocene volcanic and sedimentary rocks, and flat-lying Neogene and Quaternary basalt.

Kootenay terrane is commonly interpreted as an outboard facies of the ancestral North American miogeocline (Colpron and Price, 1995; Nelson et al., 2013). Among the youngest units of the terrane are volcanic and plutonic rocks that reflect Devonian-Mississippian initiation of arc magmatism (Schiarizza and Preto, 1987; Paradis et al., 2006). Slide Mountain terrane, the most inboard tract of oceanic rocks in the Canadian cordillera, comprises the remnants of a marginal basin that opened in the late Paleozoic as the locus of arc magmatism migrated westward (Schiarizza, 1989). The active, frontal part of this arc system became the Harper Ranch Group (late Paleozoic; Smith, 1979; Beatty et al., 2006). Collapse of the Slide Mountain marginal basin during the Sonoma orogeny (Permo-Triassic) led to thrust-emplacement of Slide Mountain terrane above Kootenay terrane (Schiarizza, 1989; Ferri, 1997), and may have brought the Harper Ranch Group, and underlying rocks, back into proximity with the pericratonic assemblages of Kootenay terrane. The Slocan Group forms part of a Triassic basin that was deposited unconformably above the thrust-imbricated Slide Mountain and Kootenay terranes (McMullin, 1990; McMullin et al., 1990). The Nicola Group is part of a volcanic arc complex that formed west of the Slocan Group, in response to easterly-dipping subduction that also generated the accretionary complex represented by Cache Creek terrane.

The fault that juxtaposes the Crooked amphibolite of Slide Mountain terrane above Kootenay terrane (Fig. 2) was named the Eureka thrust by Struik (1986), and is equivalent to the Quesnel Lake shear zone of Rees (1987). The kinematic history is best constrained by fabrics preserved in footwall orthogneiss north of Quesnel Lake, where Rees (1987) documented rotated feldspar megacrysts, S-C mylonites, and shear band foliations that indicate a top-to-the-east sense of shear. Struik (1986) and Rees (1987) inferred that the Eureka thrust was an early Jurassic structure that carried both the Crooked amphibolite and the overlying Triassic rocks above Kootenay terrane. The interpretation preferred here, integral to the general tectonic history outlined in the previous paragraph, follows McMullin (1990) and McMullin et al. (1990), who studied a conglomerate unit in the basal part of the Slocan Group a short distance above the Eureka thrust near Wingdam, east of Quesnel. The conglomerate contains clasts derived from both Kootenay terrane and the Crooked amphibolite that were deformed and foliated before being deposited as part of the conglomerate. This suggests that the Eureka thrust is a Permo-Triassic structure that emplaced Slide Mountain terrane above Kootenay terrane, and that the Slocan Group depositionally overlapped these two older terranes after a period of erosion (McMullin et al., 1990). This scenario is consistent with observations and interpretations made elsewhere in the region, as Campbell (1971) documented structural fabrics in the Crooked amphibolite near Crooked Lake that predate deposition of the Slocan Group, and Schiarizza (1989) inferred that east-directed thrust-emplacement and structural imbrication of the Fennell Formation, representing Slide Mountain terrane south of the Raft batholith, occurred in the Late Permian or Early Triassic.

Early Jurassic, east-directed thrust faults are interpreted to imbricate the Slocan Group and western part of the Nicola Group in the Quesnel Lake and Crooked Lake areas (Struik, 1988; Bloodgood, 1990), but are not well documented and are of uncertain extent or regional significance. These structures may correlate with late Early Jurassic east-directed thrust faults that formed during the latter stages of arc magmatism in north-central Quesnel terrane, and juxtapose Quesnel rocks above miogeoclinal rocks (Nixon et al., 1997). A protracted period of contractional deformation and metamorphism that began in early Middle Jurassic time is reflected in polyphase mesoscopic structures in Kootenay terrane, Slide Mountain terrane, the Slocan Group, and eastern parts of the Nicola Group, as well as map-scale structures, including an anticline-syncline pair near Crooked Lake (Fig. 2), that fold these units and their mutual contacts (Campbell, 1971; Rees, 1987; Bloodgood, 1990; Fillipone and Ross, 1990). Correlative structures are not well documented in the central part of the Nicola belt, but it is suspected that a regional syncline (Panteleyev et al., 1996), reflected in the distribution of the younger units of the Nicola Group (Fig. 2), formed at the same time. The youngest structures in the region include systems of Eocene dextral strike-slip and extensional faults (Panteleyev et al., 1996; Schiarizza and Israel, 2001).

3. Triassic rocks of the Bridge Lake – Quesnel River area

Triassic sedimentary and volcanic rocks in the study area are herein assigned to the Slocan Group and the Nicola Group. The Nicola designation was applied to most Triassic rocks in the southern part of the area by Campbell and Tipper (1971), and was used for all Triassic rocks to the north by Panteleyev et al. (1996), including rocks that had previously been referred to as Quesnel River Group (Campbell, 1978; Tipper, 1978) or Takla Group (Rees, 1987). Schiarizza et al. (2013) adopted the approach of Panteleyev et al. (1996) and assigned all Triassic stratified rocks in the southern and central parts of the current study area to the Nicola Group. Sedimentary rocks herein assigned to the Slocan Group were mapped as a distinct unit (the Lemieux Creek succession) in the Nicola Group by Schiarizza et al. (2013), corresponding to rocks that had been excluded from the group by Campbell and Tipper (1971; their unit 10). Likewise, rocks herein mapped as Slocan Group farther north were included in the Nicola Group by Panteleyev et al. (1996) and Bloodgood (1990), but were recognized as a lithologically distinct component (unit Tra), corresponding to rocks that Rees (1987) excluded from the Takla Group and informally referred to as the black phyllite unit. Rees (1987) correlated the black phyllite unit with the Slocan Group of southeastern British Columbia. This correlation is adopted here because, although these rocks are equivalent in age to the Nicola Group, they are lithologically distinct and form a discrete belt to the east of the Nicola Group. Furthermore, as noted by Rees (1987) they: 1) are lithologically identical to the Slocan Group; 2) are, at least in part, the same age as the Slocan Group; and 3) rest unconformably on older rocks (Slide Mountain and Kootenay terrane) that correlate with rocks beneath the Slocan Group (Thompson et al., 2006). The type area of the Slocan Group, near Slocan Lake, is in the Nelson (NTS 82F) and Lardeau (NTS 82K) map areas (Little, 1960), but from there it has been traced northwestward across the entire Vernon (NTS 82L) map area, to a location less than 50 km south-southeast of the Lemieux Creek succession/Slocan Group near Little Fort (Thompson et al., 2006). The Slocan Group in the northwest corner of the Vernon map sheet is juxtaposed with the Nicola Group, to the west, across the Louis Creek fault. This structure tracks northward along the valleys of Louis Creek and the North Thompson River to a system of faults that includes the Lemieux Creek fault, which separates the Lemieux Creek succession/Slocan Group from the Nicola Group north of Little Fort (Fig. 2; Schiarizza et al., 2002).

3.1. Slocan Group

The Slocan Group forms a continuous, relatively narrow belt that extends the full length of the study area, and separates rocks of Slide Mountain and Kootenay terranes to the east from the Nicola Group to the west. Rocks in this belt include the Lemieux Creek succession of Schiarizza et al. (2013), unit Tra of Bloodgood (1990), the black phyllite unit of Rees (1987), and unit uTrp of Struik (1983). The Slocan Group consists mainly of dark grey to black slate and phyllite (Fig. 3), commonly with light to medium grey siltstone laminae, and less commonly with thin interbeds of quartzose siltstone and laminated siltstone. Exposures between Little Fort and the Raft batholith also include thin to thick beds of fine-grained quartzite and quartzose sandstone, locally with conspicuous grains of detrital muscovite and biotite (Schiarizza et al., 2002). A thinly bedded quartzite unit is at the base of the group at several places between Crooked Lake and Horsefly Lake (unit Tra1 of Bloodgood, 1990), and fine-grained, thin- to medium-bedded quartzose sandstone was noted in exposures examined during the 2015 field season, east-southeast of Spanish Lake (Fig. 4). Limestone forms discontinuous lenses, 1-2 m wide, scattered sparsely through parts of the Slocan Group, and is a prominent component near the faulted eastern edge of the group north of Little Fort, where it locally forms thin to thick beds intercalated with siltstone and slate over stratigraphic intervals approaching 100 m (Schiarizza et al. 2002).

Volcanic rocks, generally absent from the Slocan Group, form a local lens, 8 km long and up to 1 km wide, east of Spanish Lake (Struik, 1983; Rees, 1987). This lens includes pale to medium green plagioclase-actinolite-biotite-chlorite (±epidote±calcite) schist that contains flattened quartz amygdules, and 1-2 mm clots of actinolite-biotite-chlorite that may be altered mafic phenocrysts. It also includes plagioclase-quartz-biotite-chlorite-sericite schist, and schist that contains

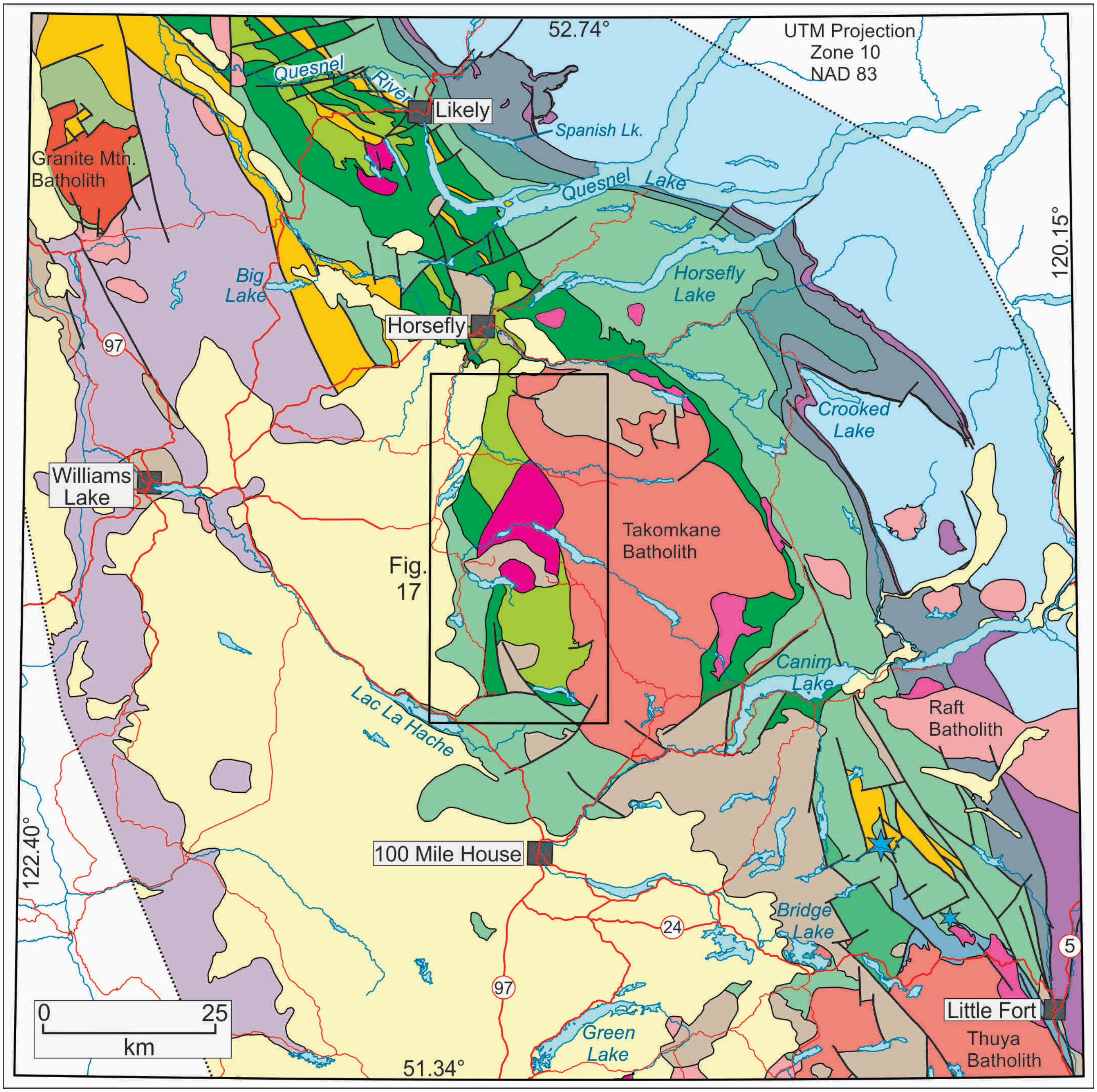

Fig. 2a. Geologic map of the Bridge Lake – Quesnel River area showing the Slocan Group and Nicola Group subdivisions from this study. Based on Struik (1983, 1988), Rees (1987), Bloodgood (1990), Panteleyev et al. (1996), Logan et al. (2007), Schiarizza et al. (2013), Schiarizza (2015), and this study.

flattened fragments of both pale grey quartz-sericite schist and medium green plagioclase-actinolite-biotite-chlorite schist. This lens also includes substantial amounts of well-foliated, platy biotite-sericite-quartz schist that was probably derived from fine-grained quartz-rich sedimentary rocks. The metavolcanic and intercalated metasedimentary rocks are tentatively included in the Slocan Group, but they are very similar to late Paleozoic metavolcanic units found within Kootenay terrane (Schiarizza and Preto, 1987; Ferri, 2001; Paradis et al., 2006). Because contacts with surrounding Slocan phyllites are covered, it is possible that they are an inlier, or fault sliver, derived from that terrane.

Late Triassic macrofossils were collected from the Slocan Group north of Little Fort (Campbell and Tipper, 1971), and conodonts extracted from numerous limestone samples in the same area include Middle and Late Triassic forms (Anisian,

Fig. 2b. Legend for Figure 2a.

Ladinian and early Carnian; Schiarizza et al., 2013). Conodonts have also been extracted from limestone lenses in the group east-southeast of Spanish Lake, and were assigned to the late Anisian-early Ladinian, Ladinian, unrefined Middle Triassic, and unrefined Triassic (Struik, 1988; Panteleyev et al., 1996).

In the southern part of the Bridge Lake – Quesnel River map area, the eastern contact of the Slocan Group is defined mainly by faults, including east-dipping Middle Jurassic thrusts (Campbell and Tipper, 1971) and Eocene normal and dextral strike-slip faults (Schiarizza et al., 2002; Schiarizza and Macauley, 2007; Schiarizza et al., 2013). Farther north, in the Crooked Lake and Spanish Lake areas, the basal contact of the Slocan Group is interpreted as an unconformity that was folded, and variably sheared and transposed, during Jurassic deformation (Campbell, 1971; Rees, 1987). Bloodgood (1990) mapped this contact as a pre-folding, east-directed thrust fault, but this interpretation is based on observations of sheared rock along and near the contact at only a few localities, with little evidence for major displacement, or that these sheared contacts are part of a single fault system. Therefore, following Campbell (1971) and Rees (1987) the basal contact of the Slocan Group is inferred to be an unconformity. This interpretation is consistent with observations made by McMullin et al. (1990), 40 km to the northwest, who identified foliated clasts from the Crooked amphibolite and Kootenay terrane in a conglomerate near the base of the Slocan Group, and concluded that the Slocan Group was deposited unconformably above the Crooked amphibolite after it had been thrust above Kootenay terrane along the Permo-Triassic Eureka thrust fault.

Fig. 3. Dark grey, well-cleaved slate of the Slocan Group, northeast of Canim Lake.

Fig. 4. Thin to medium-bedded, fine-grained quartzose sandstone, with thin interbeds of slaty siltstone; Slocan Group, east-southeast of Spanish Lake. View is northwest; beds dip steeply southwest but are overturned.

3.2. Nicola Group

The Nicola Group in the Bridge Lake – Quesnel River area is subdivided into 4 units (Fig. 5). Assemblage one is mainly Middle Triassic and forms a belt that is juxtaposed against the Slocan Group in the northeastern part of the study area. It corresponds to rocks mapped as unit Trb by Bloodgood (1990), and unit TrJTa by Rees (1987). The other three assemblages form a stratigraphic sequence that spans all of the Late Triassic, and are derived from major map units defined by Schiarizza et al. (2013) in the southern and central parts of the area. Assemblage two corresponds to the Bosk Lake succession, a heterogeneous unit that contains mainly volcanic sandstone but also includes significant proportions of basalt and basalt breccia. Assemblage three corresponds to the Hawkins Lake succession, a relatively homogeneous unit of basalt flows and related breccias. Assemblage four consists of polymictic conglomerate, sandstone and associated volcanic rocks that correspond to the Timothy Creek succession. Other Nicola units mapped by Schiarizza et al. (2013) are considered part of assemblage two (Meridian Lake and Wavey Lake successions), or have been assigned to the Slocan Group (Lemieux Creek succession).

Assemblages two, three and four, defined in the southern part of the area, are easily traced to the north where, with some modifications, they correspond to units 1, 2 and 3 of Panteleyev et al. (1996). Assemblage two includes most rocks assigned to unit 1 by Panteleyev et al. (1996), but excludes some rocks (separated out as units Tra and Trb by Bloodgood, 1990), that are herein assigned to either the Slocan Group (Tra) or assemblage one (Trb). Assemblage three includes most rocks assigned to unit 2 by Panteleyev et al. (1996), but excludes some rocks, stratigraphically beneath their main unit 2 belt, on the west limb of the regional syncline, which are included in assemblage two. Assemblage three also includes analcime-bearing basalts assigned to unit 4 by Panteleyev et al. (1996), following Logan and Mihalynuk (2005) and Logan et al. (2007) who suggest that these distinctive basalt units occur at one, rather than two, stratigraphic levels. Assemblage four includes most rocks assigned to unit 3 by Panteleyev et al. (1996), but excludes Lower Jurassic fossiliferous sedimentary rocks, which are assigned to a separate Jurassic unit (Dragon Mountain succession on Fig. 2), following Logan et al. (2007). Assemblage four, which was assigned a Jurassic age by Panteleyev et al. (1996; their unit 3), is then considered to be mainly or entirely Late Triassic, based on constraints provided in the southern part of the area (Schiarizza et al., 2013).

3.2.1. Assemblage one

Assemblage one is the easternmost element of the Nicola Group in the northern part of the study area. It forms a belt that is bounded by the Slocan Group to the east, and extends from Crooked Lake more than 80 km northwest to the north boundary of the area. Most of this belt comprises rocks mapped as unit Trb by Bloodgood (1990), but in the area north of Quesnel Lake it excludes some rocks of this unit, which are instead assigned to the Slocan Group, and more closely corresponds to rocks mapped as unit TrJTa by Rees (1987), and the basal part of the Quesnel volcanic unit by Struik (1988). Assemblage one is distinguished from the Slocan Group mainly by the presence of feldspathic sandstone that is very similar to sandstone elsewhere in the Nicola Group. The description presented here is biased towards the area north of Quesnel Lake, where the rocks were examined during the 2015 field season.

Assemblage one consists mainly of siltstone, argillite, and slate, but also includes feldspathic sandstone, basalt, and limestone. The most common lithology is dark to medium grey platy argillite to siltstone, comprising beds 1-4 cm thick that are separated by dark greenish grey chloritic partings and/or thin interbeds of dark grey slate (Fig. 6). These beds consist of dark grey argillite in some exposures, and in others are medium to

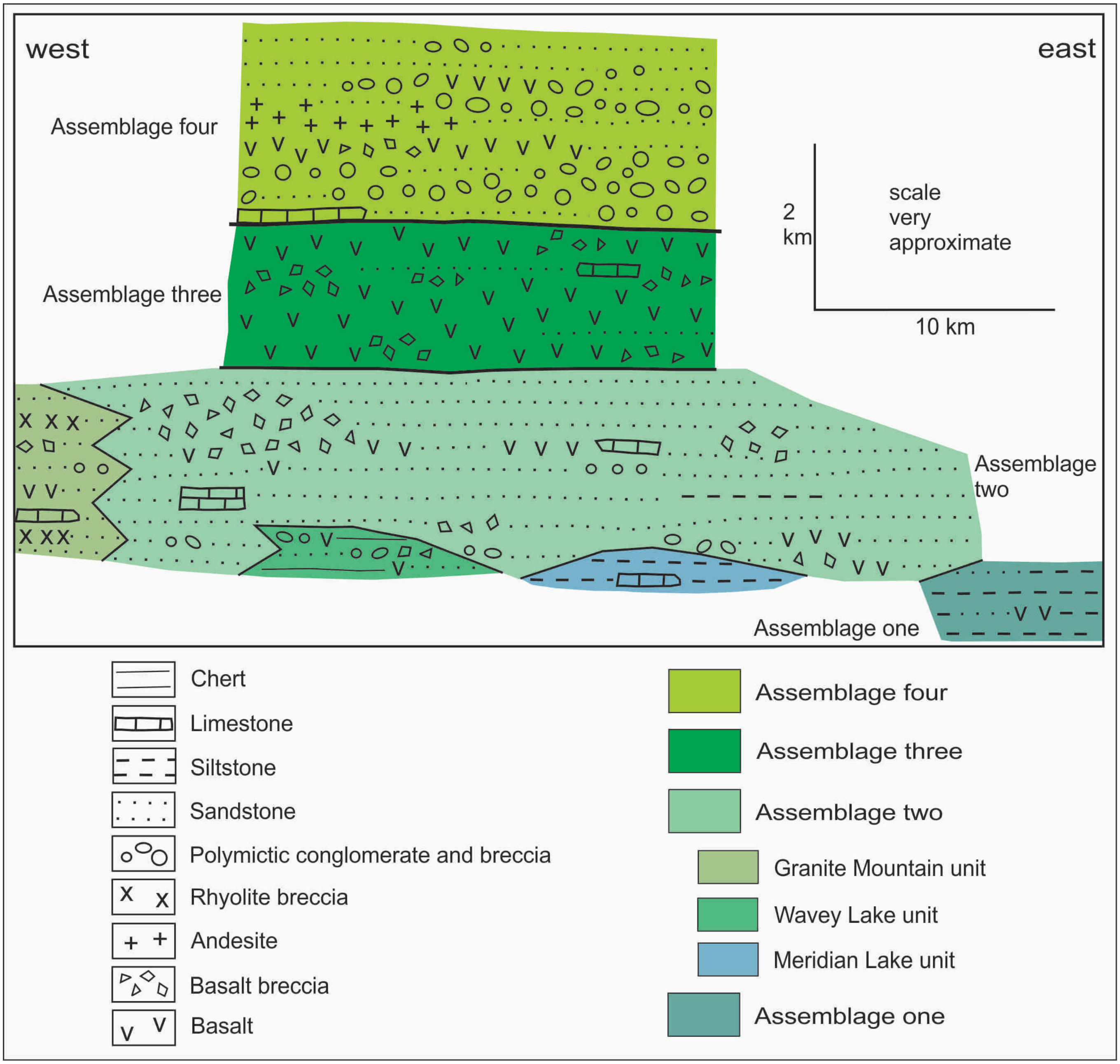

Fig. 5. Schematic stratigraphy of the Nicola Group in the Bridge Lake – Quesnel River study area.

dark grey quartzose siltstone. Less common lithologies include dark grey slate, locally with lighter grey siltstone laminae, and dark grey siltstone and slaty siltstone with thin (2-10 cm) planar beds.

Green to grey, medium to coarse-grained sandstone, very similar to the sandstone of assemblage two, occurs locally within assemblage one, as massive or thin to medium-bedded intervals intercalated with dark grey siltstone. The sandstone is typically feldspathic, but also includes grey to green volcanic lithic grains, and altered mafic mineral or lithic grains. Basalt also occurs locally, as green massive to pillowed units, locally variolitic, that are heavily altered with calcite, epidote and chlorite (Fig. 7). Medium to dark grey limestone forms rare lenses, <1-2 m thick, intercalated with siltstone.

Assemblage one is mainly Middle Triassic, based on conodonts extracted from limestone lenses on the north side of Quesnel Lake. Struik (1988) reported that one collection, from the eastern edge of the assemblage on the north shore of the lake is early-middle Anisian (early Middle Triassic), and another, also from the north shore of the lake but near the western edge of the assemblage, is late Ladinian to Carnian (Middle to Late Triassic). A third collection, from the central part of the assemblage, 2 km south of the east end of Spanish Lake, is early Anisian (Panteleyev et al., 1996; sample 87MB-16-02).

Rees (1987) inferred that assemblage one (his unit TrJTa)

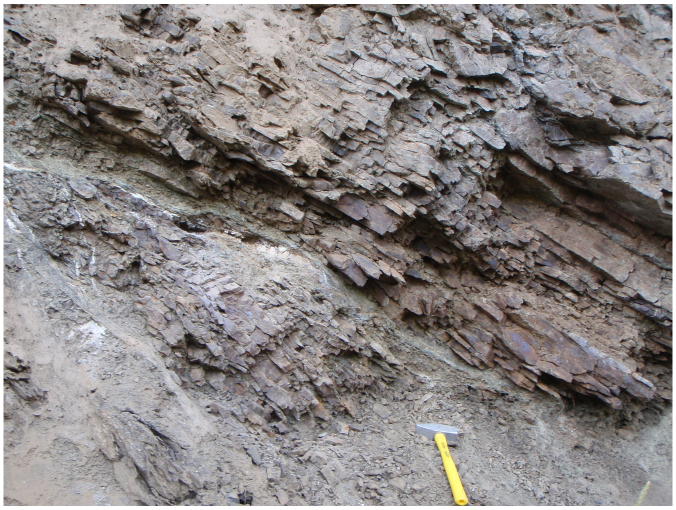

Fig. 6. Platy siltstone, assemblage one of the Nicola Group, 1800 m south of the east end of Spanish Lake.

Fig. 7. Pillowed basalt, assemblage one of the Nicola Group, 1100 m south of Spanish Lake.

overlies the adjacent Slocan Group (his black phyllite unit) across a variably tectonized stratigraphic contact. Struik (1988) noted that the two units are in part the same age, and that conodonts extracted from the lower part of assemblage one on the north shore of Quesnel Lake are older than conodonts extracted from the upper part of the Slocan Group a short distance to the west-northwest. He postulated that the basal contact of assemblage one is a thrust fault along which the Nicola Group was emplaced above the Slocan Group, and suggested that this thrust fault (the Spanish thrust) might have regional extent (Struik, 1988). Observations made during the 2015 field season did nothing to clarify the relationship, but highlighted the difficulties in assessing the nature of the contact because of poor exposure, the similarity of rock types common to both units, and strong deformation expressed as two well-developed cleavages, two or more generations of folds, and ubiquitous outcrop-scale faults of various orientations. External contact relationships provisionally accepted for assemblage one are that it is in thrust contact with the Slocan Group to the northeast (Struik, 1988), and rests stratigraphically beneath assemblage 2 of the Nicola Group to the southwest (Rees, 1987; Struik, 1988), although this latter contact may also, at least locally, be marked by a fault (Bloodgood, 1990).

3.2.2. Assemblage two

Assemblage two is a heterogeneous succession of mainly volcanic sandstone, but with substantial basalt and basalt breccia, and local polymictic conglomerate, siltstone, chert, and limestone. It is the most widespread component of the Nicola Group in the study area, where it forms a continuous belt, locally more than 25 km wide, that extends the full length of the area. On its east side, the belt is juxtaposed against the Slocan Group or assemblage one; to the west it is overlain by assemblage three or is in fault contact with Eocene rocks. Assemblage two also forms a separate western belt, exposed north of 100 Mile House and northwest of Horsefly, which forms the western limb of the regional syncline cored by assemblages three and four (Fig. 2).

Assemblage two consists mainly of rocks referred to as the Bosk Lake succession by Schiarizza et al. (2013), and unit 1 by Panteleyev et al. (1996). It includes 3 separate subunits (Fig. 5): the Meridian Lake unit, comprising siltstone exposed north of the Thuya batholith (Schiarizza et al. (2013); the Wavey Lake unit, a chert-rich unit exposed east and north of Bridge Lake (Schiarizza et al. (2013); and the Granite Mountain unit, unique because it contains substantial amounts of felsic volcanic rock, which is exposed on the margins of the Granite Mountain batholith (Schiarizza, 2014, 2015).

The predominant and characteristic lithology of assemblage two is grey to green, fine- to coarse-grained, commonly gritty, volcanogenic sandstone (Fig. 8). Grains of feldspar, pyroxene, and less common hornblende, together with lithic fragments

Fig. 8. Thick gritty sandstone beds intercalated with thinly bedded sandstone and siltstone, assemblage two of the Nicola Group, 15 km southwest of Crooked Lake.

containing these same minerals, are the main constituents. The sandstone is well bedded in places, but elsewhere forms massive units, up to several tens of metres thick. In well-bedded sections, thin to thick sandstone beds commonly alternate with thin beds of green to grey siltstone or dark grey argillite, and locally display graded bedding, flame structures, and rip-up clasts. Locally, rusty-weathered, thinly bedded to laminated siltstone, intercalated with dark grey slate or slaty argillite, forms intervals up to 10 m thick. The Meridian Lake unit represents a much thicker siltstone sequence that forms the base of the assemblage north of the Thuya batholith.

Pebble conglomerate and pebbly sandstone occur locally in assemblage two, typically as grey-green, medium to very thick beds interspersed with thin intervals of volcanic sandstone and siltstone. Most conglomerates have a sandy matrix and a clast population consisting mainly of pyroxene-feldspar-phyric basaltic fragments. Less common are pebble conglomerates with a rusty-weathered siltstone matrix, and a heterogeneous clast population that includes abundant fragments of limestone, siltstone, and sandstone, as well as pyroxene-plagioclase-phyric basalt, hornblende-feldspar porphyry and aphyric volcanic rock (Schiarizza and Macauley, 2007).

Basalt and basalt breccia are a common component of assemblage two, and in places form accumulations, up to several hundred metres thick, that can be separated out on 1:100,000-scale and more detailed maps (unit uTrNbb of Schiarizza et al., 2013; unit 1a of Panteleyev et al., 1996). One of these mafic volcanic bodies, exposed in several fault panels north of Little Fort, is in the lower part of assemblage two (Schiarizza and Israel, 2001; Schiarizza et al., 2002), whereas others are repeated higher in the section (Schiarizza and Boulton, 2006; Schiarizza and Macauley, 2007). These volcanic units include pillowed and massive pyroxene-plagioclase-phyric basalt (Fig. 9), but volcanic breccia, locally intercalated with lenses and layers of dark green pyroxene-rich sandstone, is predominant. The breccia is typically dark green or grey-green and rusty brown to greenish brown-weathered, but locally the colour is mottled because of varicoloured fragments (light to dark green, grey and maroon). Fragments are typically angular to subangular, and commonly range from a few millimetres to more than 10 cm. In most exposures the fragments are compositionally uniform, consisting almost exclusively of pyroxene±plagioclase-phyryic basalt (Fig. 10), but display considerable textural variation in proportion of phenocrysts, degree of vesiculation, and abundance of amygdules. The matrix is typically sandy, and composed mainly of feldspar, pyroxene, and mafic lithic grains.

Thin intervals of dark grey, brown-weathered limestone and silty limestone, up to a few metres thick, occur rarely in the eastern exposure belt, where they are intercalated with volcanic sandstone or siltstone. Thicker limestone units outcrop locally in the western belt, including an isolated ridge 10 km southeast of Lac La Hache that exposes 30 to 40 m of flaggy bedded limestone (Fig. 11; Schiarizza and Bligh, 2008), and a poorly exposed, but apparently substantial limestone interval west of Antoine Lake, 14 km northwest of Horsefly (Logan et al., 2007).

Chert is a prominent component of the Wavey Lake unit, but is very uncommon elsewhere in assemblage two, where it forms rare thin beds intercalated with siltstone, argillite and sandstone (Schiarizza and Israel, 2001; Schiarizza and Boulton, 2006). Rhyolite-clast volcanic breccia is the defining component of the Granite Mountain unit, because felsic volcanic rocks have been documented at only one locality elsewhere in assemblage two. This occurrence is 23 km northwest of Little Fort, where massive and fragmental feldspar-phyric dacite forms a set of isolated outcrops in an area with mainly basalt and basalt breccia (Schiarizza and Israel, 2001; unit uTrNbf of Schiarizza et al., 2013). Directly beneath these dacites is a succession of volcanic sandstones that enclose a thin unit of fossiliferous lower Carnian limestone.

Conodonts and macrofossils from a few scattered localities

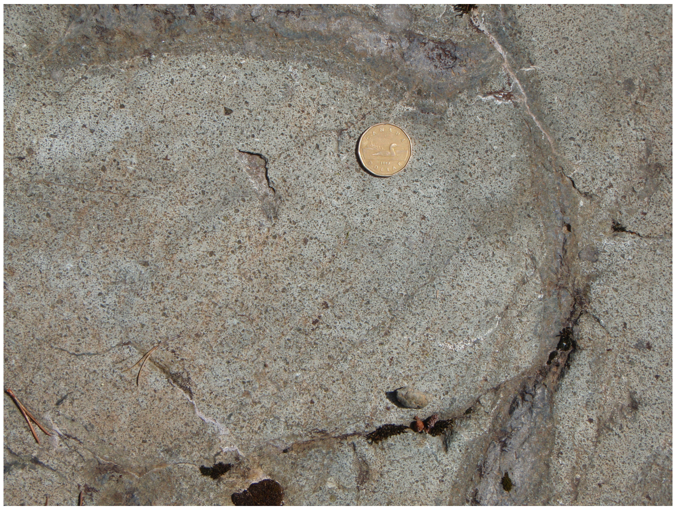

Fig. 9. Pillowed pyroxene-plagioclase-phyric basalt, assemblage two of the Nicola Group, 15 km north-northwest of Little Fort.

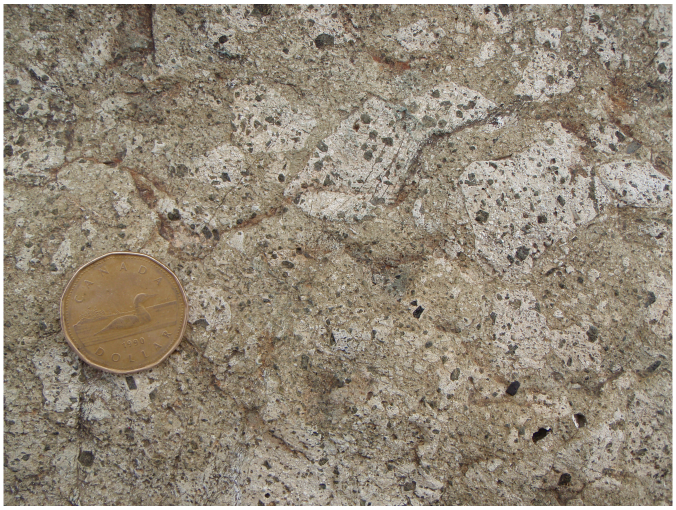

Fig. 10. Pyroxene porphyry breccia, assemblage two of the Nicola Group, Viewland Mountain, 20 km northeast of Horsefly.


Fig. 11. Limestone, assemblage two of the Nicola Group, 10 km southeast of Lac La Hache.

in assemblage two indicate that it is mainly Late Triassic, early Carnian to early Norian. These localities include a narrow limestone unit 10 km northwest of Little Fort with Carnian conodonts and another, 23 km northwest of Little Fort with late Ladinian to early Carnian conodonts and Carnian to middle Norian macrofossils (Schiarizza et al., 2013). Conodonts of probable early Norian age were extracted from limestone west of Antoine Lake (14 km northwest of Horsefly) and a locality 15 km farther to the northwest (6 km northeast of Big Lake) yielded late Carnian conodonts (Panteleyev et al., 1996). Conodonts from a locality 1 km south of the west end of Horsefly Lake are late Carnian, and macrofossils collected 7 km farther south include probable late Carnian or early Norian *Halobia?* (Panteleyev et al., 1996). Conodonts from the Meridian Lake unit are Carnian and late Ladinian to early Carnian (Schiarizza et al., 2013), and a conodont fragment from limestone in the Granite Mountain unit is early Norian (Schiarizza, 2015).

3.2.2.1. Meridian Lake unit

Siltstone that crops out on the north and northeast margins of the Thuya batholith, in the southern part of the study area, is assigned to the Meridian Lake unit (Fig. 2). These rocks are part of the Meridian Lake succession of Schiarizza et al. (2013), but volcanic sandstone and conglomerate that were also included in this succession are excluded, and are incorporated in the adjacent, undivided part of assemblage two (Fig. 5). Thus modified, the Meridian Lake unit consists mainly of rusty-weathered, dark to medium grey, laminated to thinly bedded siltstone and slaty siltstone (Fig. 12), with local thin interbeds of dark grey argillite and chert. Dark grey micritic limestone and limy argillite forms local thin to thick beds intercalated with siltstone and argillite. One of these limestone units yielded Late Triassic (Carnian) conodonts, and another contains Middle or Late Triassic (late Ladinian to early Carnian) conodonts (Schiarizza et al., 2013).

The Meridian Lake unit is cut by Early Jurassic granodiorite of the Thuya batholith, and by a suite of Early Jurassic ultramafic to mafic intrusions. Other contacts are mainly faults, but locally the unit is overlain, to the northeast, by volcanic sandstone and conglomerate typical of assemblage two across an inferred stratigraphic contact. This contact is not well exposed, but seems to be defined by a transitional interval where thin to medium beds of green volcanic sandstone interlayer with dark grey laminated siltstone.

The Meridian Lake unit is provisionally included in assemblage two, apparently representing a siltstone facies in its lower part. Nonetheless, other correlations are possible, given that the unit is markedly similar to the Slocan Group, which includes rocks of the same age, and is also similar to parts of assemblage one, which is mainly older but may also include rocks of the same age.

3.2.2.2. Wavey Lake unit

The Wavey Lake unit (Wavey Lake succession of Schiarizza et al., 2013) forms a distinctive element of assemblage two that is exposed in fault panels east and north of Bridge Lake (Fig. 2). It is characterized by an abundance of grey to green chert (Fig. 13), which occurs as thin-bedded intervals, up to 10 m thick, comprising millimetre to centimetre-scale chert beds separated by partings and thin interbeds of argillite or slate. The chert intervals are interbedded with fine- to medium-grained volcanic sandstones, similar to sandstone elsewhere in assemblage two, which locally form channels that cut into


Fig. 12. Thinly bedded light (quartzose) and dark grey siltstone, assemblage two of the Nicola Group, Meridian Lake unit, north margin of the Thuya batholith.

Fig. 13. Thinly bedded chert, assemblage two of the Nicola Group, Wavey Lake unit, 10 km east-northeast of Bridge Lake.

the chert (Schiarizza et al., 2002). The Wavey Lake unit also includes basalt and basalt breccia, similar to volcanic rocks elsewhere in assemblage two, and bodies of polymictic pebble to cobble conglomerate, up to several tens of metres thick, that are more abundant than elsewhere in the assemblage. The conglomerate contains subangular to rounded clasts of mainly laminated siltstone, cherty argillite, and argillite, but also includes fragments of chert, limestone, pyroxene-plagioclase-phyric basalt, and microdiorite. The Wavey Lake unit is undated, but is suspected to be a relatively old component of assemblage two because the narrow panel north of Bridge Lake is stratigraphically overlain by a thick sandstone sequence in the undivided part of the assemblage. The Meridian Lake unit, or a similar succession, may have been the source of most clasts within the Wavey Lake conglomerates.

3.2.2.3. Granite Mountain unit

Nicola rocks on the margins of the Granite Mountain batholith form an outlier, faulted against Cache Creek terrane, comprising the westernmost part of the group exposed in the Bridge Lake – Quesnel River study area (Fig. 2). Here, the group consists of sandstone and gritty to pebbly sandstone, with local intercalations of conglomerate, mafic and felsic volcanic breccia, siltstone, limestone, and basalt (Schiarizza, 2014, 2015). These rocks are included in assemblage two on the basis of lithology, particularly the predominance of volcanic sandstone, and their early Norian and older age, constrained by conodonts from one limestone unit, and crosscutting plutonic rocks as old as 222.71 ±0.22 Ma (Schiarizza, 2015). This succession is unique, however, because it includes two substantial intervals of felsic volcanic breccia (Fig. 14), with mainly angular to subrounded fragments of pale green, grey or purplish-grey rhyolite, commonly with 1-2 mm phenocrysts of quartz ±feldspar (Schiarizza, 2014). Rhyolites have not been documented in the Nicola Group elsewhere in the Bridge Lake – Quesnel River area, and the Granite Mountain belt may be part of a unique, but poorly-exposed, western facies, with possible affinities to the rhyolite-bearing western Nicola belt exposed in the Princeton-Merritt area farther to the south (Preto, 1979).

Fig. 14. Volcanic breccia with mainly rhyolite fragments, assemblage two of the Nicola Group, Granite Mountain unit, northeast margin of the Granite Mountain batholith.

3.2.3. Assemblage three

Assemblage three is a relatively homogeneous succession of basalt flows and breccias. It includes the Hawkins Lake succession of Schiarizza et al. (2013), most rocks assigned to unit 2, particularly subunits 2a, 2b, 2c and 2e, by Panteleyev et al. (1996), and most rocks assigned to units LTrNvb, LTrNpv and LTrNav by Logan et al. (2007). Assemblage three forms a generally synclinal belt, underlain by assemblage two to the northeast and southwest, which extends 120 km from the southern part of the Takomkane batholith to the northern boundary of the map area (Fig. 2). It is overlain by assemblage four, in the core of the syncline, east of Likely and on the west margin of the Takomkane batholith.

Assemblage three is mainly dark green, locally grey or maroon, brownish-weathered, massive and pillowed basalt (Fig. 15). Textures vary, but most of the basalt is coarsely porphyritic, with large clinopyroxene phenocrysts and smaller plagioclase phenocrysts comprising 30-70% of the rock. The groundmass includes plagioclase laths and small clinopyroxene grains, but commonly displays an alteration assemblage that includes calcite, epidote and chlorite. Amygdules, typically epidote and calcite, may be present, and varioles occur in some pillowed units.

Olivine, typically replaced by iddingsite and other secondary minerals, forms part of the phenocryst assemblage in some basalt units, including those mapped as unit 2a by Panteleyev et al. (1996), which forms the lower part of assemblage three in the Horsefly-Likely area. In this same area, analcime occurs as

Fig. 15. Pillowed pyroxene-plagioclase-phyric basalt, assemblage three of the Nicola Group, 1.5 km north of western Canim Lake.

Fig. 16. Breccia containing pyroxene-phyric basalt fragments, assemblage three of the Nicola Group, 16 km south-southwest of Likely.

phenocrysts in clinopyroxene-plagioclase-olivine-phyric basalt flows and related breccias that are mainly in the upper part of the assemblage, including units 2e and 4 of Panteleyev et al. (1996) and unit LTrNav of Logan et al. (2007). Hornblende-pyroxene-plagioclase-phyric basalt is a minor component of assemblage three, and occurs mainly near the northern boundary of the study area, north of the Quesnel River (unit LTrNhv of Logan et al., 2007).

Breccia, consisting mainly or entirely of basalt fragments, is a common, and locally predominant component of assemblage three. It forms massive to weakly stratified units, up to several tens of metres thick, interlayered with basalt flows. Fragments are angular to subrounded, range from less than 1 cm to more than 20 cm, and are typically supported by a sandy to gritty matrix with predominantly plagioclase, pyroxene and mafic lithic grains (Fig. 16). The fragments are mainly pyroxene-plagioclase-phyric basalt, but they may show considerable variation in size, abundance, and proportion of phenocrysts, and locally are accompanied by other clast-types, including limestone, volcanic sandstone, siltstone, pyroxenite, hornblendite, and diorite (Schiarizza and Boulton, 2006; Schiarizza et al., 2009).

Feldspar-pyroxene sandstone and gritty sandstone is a minor component of assemblage three, and typically forms narrow intervals intercalated with basalt breccia. Lenses of limestone and calcareous mudstone also occur locally (Panteleyev et al., 1996; Schiarizza and Boulton, 2006), and a rusty-weathered laminated siltstone interval, at least 10 m thick, was traced for 1.3 km in the assemblage west of the Takomkane batholith (Schiarizza et al., 2009).

Assemblage three is inferred to be Norian, based on its stratigraphic position between assemblage two (Carnian and early Norian), and assemblage four (latest Triassic). Macrofossils collected from the lower part of the assemblage north of Gavin Lake, 16.5 km southwest of Likely, include *Monotis* sp. (Norian), and a collection from the lower part of the unit east of Lemon Lake, 6 km south of western Horsefly Lake, includes *Halobia* sp. (probably late Carnian or early Norian; Panteleyev et al., 1996).

3.2.4. Assemblage four

Assemblage four contains predominantly polymictic conglomerate and breccia bearing a diverse clast population not seen in older parts of the Nicola Group. It also includes substantial intervals of feldspathic sandstone and volcanic rock, including some volcanic units that are lithologically distinct from those in underlying units. Assemblage four is well exposed locally on the west margin of the Takomkane batholith (Figs. 17, 18) where it was identified as a lithologically distinct, upper unit of the Nicola Group by Schiarizza and Bligh (2008) and Schiarizza et al. (2009), and later referred to as the Timothy Creek succession by Schiarizza et al. (2013). These rocks are equivalent to those included in the lower part of unit 3 by Panteleyev et al. (1996), which are well exposed west of Likely and correspond to units LTrNpt and LTrNvl of Logan et al. (2007).

The conglomerates are commonly medium to dark green or greenish grey, and weather to light shades of brown, greenish brown or beige. In the upper part of the assemblage, and locally elsewhere, they are red to purple, or display patchy colour variations in shades of red, purple, grey and green (Fig. 19). They contain a variety of igneous clasts, including a significant proportion derived from intrusive rocks. Fine-grained, equigranular to weakly porphyritic hypabyssal feldspathic clasts are predominant, but clasts of medium-grained gabbro, diorite, monzodiorite and monzonite are common, as are mafic to intermediate volcanic clasts containing variable proportions of feldspar, pyroxene and hornblende phenocrysts. Angular to subrounded clasts (from a few mm to 20 cm) are supported in a sandy matrix consisting mainly of feldspar, with subordinate mafic mineral grains. The conglomerates are commonly massive, but locally display weak stratification that may be accentuated by intercalations of sandstone and pebbly sandstone.

Medium- to coarse-grained sandstone is predominant in intervals many tens of metres thick in the upper part of the assemblage west of the Takomkane batholith, both in the Mount Timothy area (red sandstone-conglomerate unit of Schiarizza and Bligh, 2008), and the Woodjam Creek area (upper part of the polylithic breccia unit of Schiarizza et al., 2009). Sandstone is also predominant in the lower part of the assemblage west of Likely, and is locally underlain by a substantial limestone interval that marks the base of assemblage four (Logan et al., 2007, section A-A'). The sandstones are mostly green to grey-green, but they may be red, particularly in the upper part of the assemblage, or mottled green and red. They consist largely of feldspar (both plagioclase and pinkish grains that are K-spar and/or hematite-altered plagioclase), along with variably-altered mafic grains (mainly pyroxene) and fine-grained, chlorite-epidote-calcite-altered matrix. Bedding is commonly defined by planar laminations and indistinct platy to flaggy partings (Fig. 20), but thin to medium beds are locally well defined by distinct units of contrasting grain size, ranging from coarse, gritty sandstone to siltstone. In the basal part of the unit, west of Likely, thin to medium beds commonly display normal grading, load casts and flame structures, and locally are deformed by soft-sediment folds (Fig. 21).

Volcanic rocks locally comprise a substantial component of assemblage four, and form mappable bodies west of the Takomkane batholith, in both the Mount Timothy and Woodjam Creek areas (Fig. 17). In each of these areas the volcanic section includes a lower unit of pyroxene-plagioclase-phyric basalt and basalt breccia, and an upper unit of coarse plagioclase-phyric andesite. The lower basalt units are similar to mafic volcanic rocks in assemblages two and three, but the plagioclase-phyric andesites are distinct, and were originally mapped as Eocene by Schiarizza and Bligh (2008). They contain 30-50% plagioclase phenocrysts, commonly 5-10 mm long (locally to 2 cm), in an aphanitic groundmass with mainly randomly oriented plagioclase microlites (Fig. 22). The plagioclase phenocrysts are locally accompanied by smaller pyroxene and/or hornblende phenocrysts, and by scattered amygdules of mainly epidote, calcite and quartz.

Assemblage four is mainly or entirely latest Triassic. This interpretation is based on a U-Pb age of 203.9 ±0.4 Ma on zircons extracted from plagioclase-phyric andesite west of Woodjam Creek (Fig. 17; Schiarizza et al., 2013), and by U-Pb zircon ages ranging from of 203.6 ±0.3 Ma to 205.0 ±0.3 Ma from monzodiorite stocks that crosscut the lower and middle portions of the assemblage east and southeast of Spout Lake (Fig. 17; Schiarizza et al., 2013). Panteleyev et al. (1996; unit 3) considered it Early Jurassic, but this was based mainly on the inclusion of fossiliferous Lower Jurassic sedimentary rocks that Logan et al. (2007) consider a separate unit, shown as Dragon Mountain succession on Fig. 2.

4. Discussion

The preliminary assessment of Nicola stratigraphy presented here indicates that some rocks previously included in the group should be reassigned to the Slocan Group, and that the remaining rocks, retained as Nicola Group, comprise four main units, referred to as assemblages one, two, three, and four. These subdivisions are a starting point for continuing studies on Nicola Group stratigraphy, and are expected to be expanded and modified with further work.

Assemblage one is predominantly Middle Triassic siltstone and argillite, but includes intercalations of volcanic sandstone and pillowed basalt. The age, predominant lithology, and location along the eastern margin of the Nicola belt suggest a possible link to the Slocan Group, a possibility that requires further study. Middle Triassic Nicola rocks are unknown from elsewhere in the Bridge Lake-Quesnel River area, but occur locally in other parts of southern British Columbia, including the Princeton-Merritt area where Nicola Group rhyolites with ~238 Ma U-Pb zircon ages have recently been documented (Mihalynuk et al., 2015, 2016).

Assemblage two (Carnian and early Norian) is a heterogeneous succession that includes virtually all rocks types commonly encountered in the Nicola Group. It includes basalt flows and basalt breccia, but is predominantly volcanic sandstone derived from these, or similar, mafic volcanic rocks. Our current level of understanding in the Bridge Lake – Quesnel River area suggests that mafic volcanic centres of several different ages were distributed across most of the known width of the arc during this time period. Broader-scale features include late Carnian to early Norian rhyolites in the western part of the area (Granite Mountain unit), which may have regional significance if equivalent to rhyolitic rocks (~224 Ma, Mihalynuk et al., 2016) in the western Nicola belt of the Princeton-Merritt area (Preto, 1979).

Assemblage three (Norian) consists mainly of basalt and basalt breccia that reflect a major constructional period in the Bridge Lake – Quesnel River segment of the Nicola arc. Further studies will address if this time interval was one of greater-than-average basalt accumulation in other parts of the arc, the location and arrangement of volcanic centres, and if siliciclastic and carbonate facies that accumulated during this time period can be distinguished from assemblage two. Previous work in the Nicola-equivalent Takla Group of central and northern British Columbia suggest that thick basalt sections of this age accumulated in other segments of the arc (Witch Lake succession of Nelson and Bellefontaine, 1996; Goldway Peak unit of Schiarizza and Tan, 2005).

Assemblage four is characterized by polymictic conglomerate bearing abundant hypabyssal and plutonic clasts, a common red colour, and a volcanic suite that includes distinctive coarse, crowded plagioclase-phyric andesite. It is in part latest Triassic, but neither an upper age limit nor its relationship to Early Jurassic sedimentary rocks (Dragon Mountain succession) have been established. This assemblage reflects significant unroofing of the arc, and it may rest above other parts of the

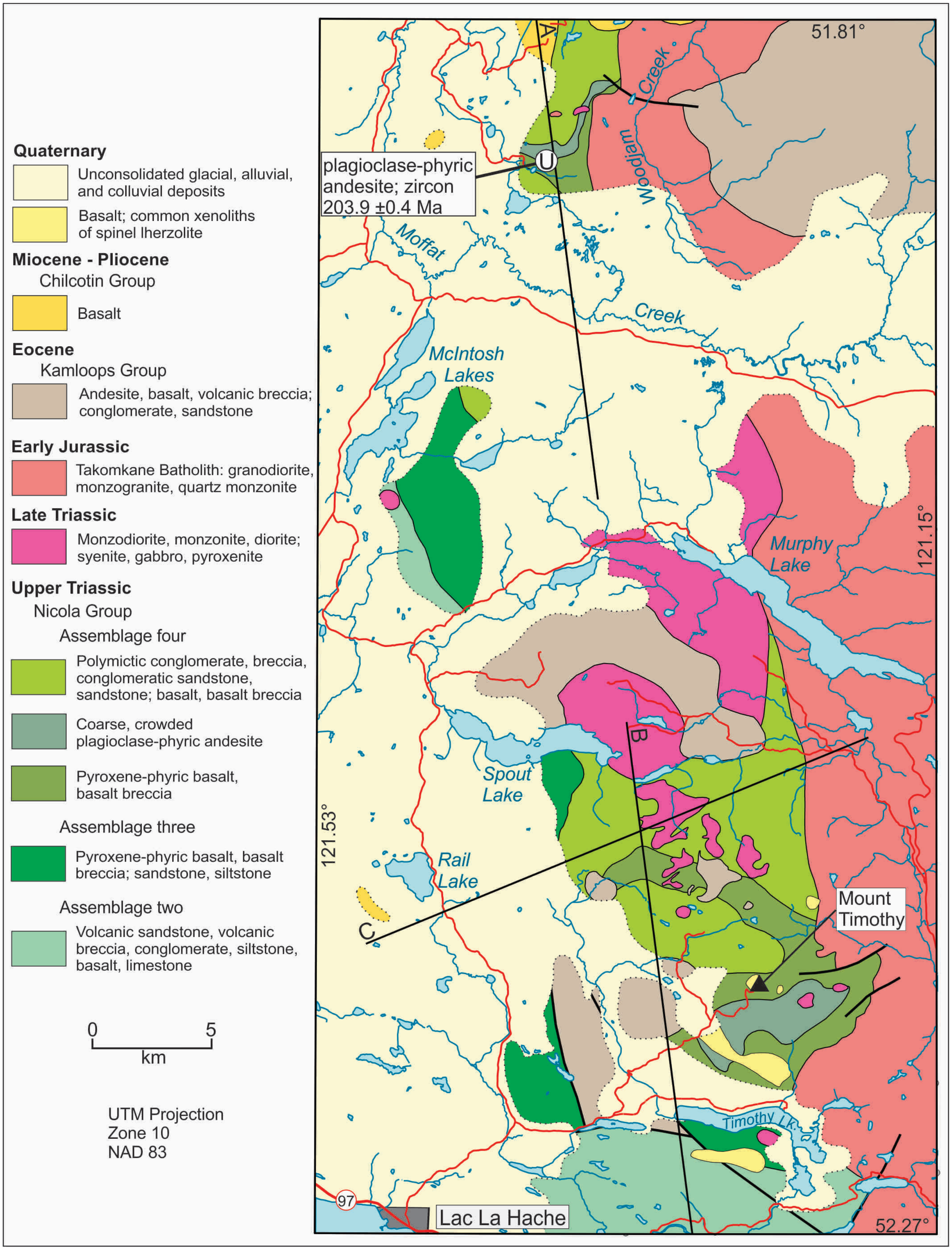

Fig. 17. Geology of the Timothy Lake – Woodjam Creek area. Modified from Schiarizza et al. (2013) mainly by assigning volcanic rocks on Mount Timothy, previously mapped as Eocene, to assemblage 4 of the Nicola Group.

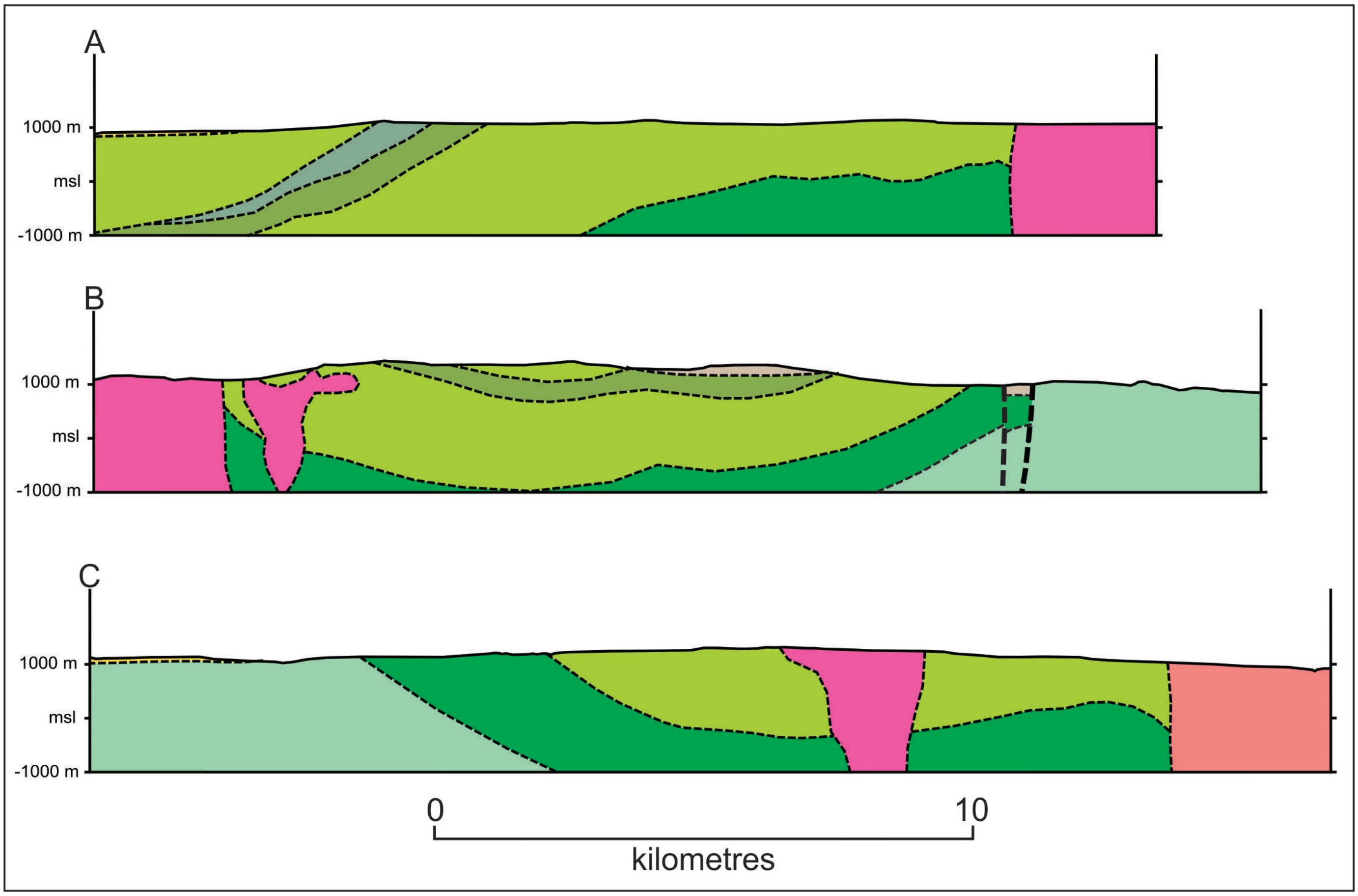

Fig. 18. Schematic vertical cross-sections along lines A, B and C, shown on Figure 17. See Figure 17 for legend.

Fig. 19. Conglomerate, assemblage four of the Nicola Group, 15 km west-southwest of Likely.

Fig. 20. Parallel-stratified red sandstone, assemblage four of the Nicola Group, 6 km northwest of Mount Timothy.

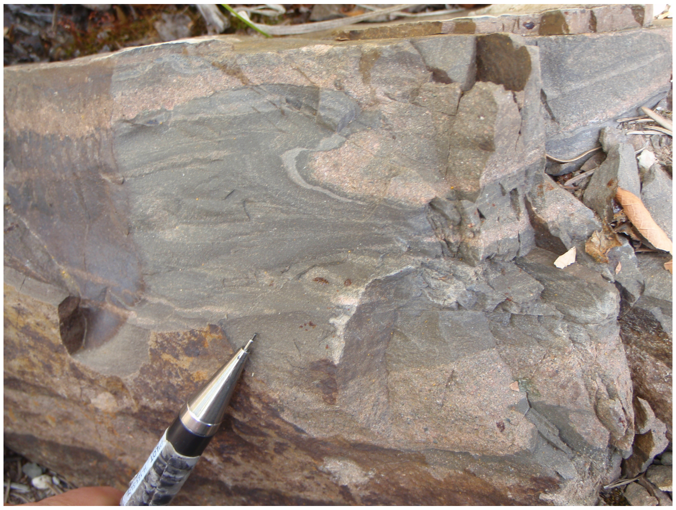

Fig. 21. Graded sandstone beds deformed by soft-sediment folds, assemblage four of the Nicola Group, 15 km west-southwest of Likely.

Fig. 22. Coarse, crowded plagioclase-phyric andesite, assemblage four of the Nicola Group, west of Woodjam Creek.

Nicola group across an unconformity. The present narrow, linear distribution of assemblage four may simply reflect its preservation in the core of a regional syncline, but future studies will address the possibility of sedimentation in an intra-arc rift. Rocks that probably correlate with assemblage four have recently been identified in the Shrimpton Creek area, south of Merritt (Harmon succession; Mihalynuk et al., 2015).

5. Conclusions

Triassic rocks in the Bridge Lake – Quesnel River area are assigned to the Slocan Group and the Nicola Group. The Slocan Group represents a Middle to Late Triassic siliciclastic basin that formed above Paleozoic rocks, including Slide Mountain and Kootenay terranes, which were structurally imbricated in Permo-Triassic time. The Nicola Group is a Middle to Late Triassic volcanic arc succession that accumulated to the west.

The Nicola Group is subdivided into four assemblages that span most of the Middle and Late Triassic. Assemblage one (mainly Middle Triassic), comprises siltstone with local intercalations of volcaniclastic sandstone and pillowed basalt, and is juxtaposed with the Slocan Group in the northeastern part of the study area. Assemblage two (Carnian and early Norian), includes basalt flows and basalt breccia, but is predominantly volcanic sandstone derived from these, or similar, mafic volcanic rocks. Notable variants include an early Carnian siltstone facies (Meridian Lake unit), a chert-rich facies of uncertain age (Wavey Lake unit), and a western facies, early Norian in part, that includes a substantial felsic volcanic component (Granite Mountain unit). Assemblage three is a relatively homogeneous succession of pyroxene-phyric basalt flows and breccias that reflect a major Norian constructional phase. Assemblage four is characterized by polymictic conglomerates that contain abundant hypabyssal and plutonic rock fragments, but also includes red feldspathic sandstone, pyroxene-phyric basalt, and distinctive coarse, crowded plagioclase-phyric andesite. These rocks are, at least in part, latest Triassic, and are suspected to rest unconformably above older assemblages of the group.

The four assemblages established in the Bridge Lake – Quesnel River area provide a preliminary framework for ongoing studies of Nicola Group stratigraphy, and will be expanded and modified with further work.

Acknowledgments

I thank Tim Song, Luke Ootes and Jessica Norris for their cheerful assistance during fieldwork, and Jim Logan who read an earlier version of the manuscript and provided insights into Mesozoic rocks in the Quesnel River area. I also thank Sharon and Skeed Borkowski, of Northern Lights Lodge, for providing excellent accommodation on Quesnel Lake. Lawrence Aspler provided a thorough review that improved the paper.

References cited

Bailey, D.G., 1978. The geology of the Morehead Lake area. Ph.D. thesis, Queen's University, 198p.

Bailey, D.G., 1990. Geology of the central Quesnel belt, British Columbia (parts of NTS 93A, 93B, 93G and 93H). British Columbia Ministry of Energy, Mines and Petroleum Resources, British Columbia Geological Survey Open File 1990-31; scale 1:100,000.

Beatty, T.W., Orchard, M.J., and Mustard, P.S., 2006. Geology and tectonic history of the Quesnel terrane in the area of Kamloops, British Columbia. In: Colpron, M., and Nelson, J. (Eds.), Paleozoic evolution and metallogeny of pericratonic terranes at the ancient pacific margin of North America, Canadian and Alaskan cordillera, Geological Association of Canada, Special Paper 45, pp. 483-504.

Bloodgood, M.A., 1987. Deformational history, stratigraphic correlations and geochemistry of eastern Quesnel Terrane rocks in the Crooked Lake area, central British Columbia, Canada. M.Sc. thesis, The University of British Columbia, 165p.

Bloodgood, M.A., 1990. Geology of the Eureka Peak and Spanish Lake map areas, British Columbia. British Columbia Ministry of Energy, Mines and Petroleum Resources, British Columbia Geological Survey Paper 1990-3, 36p.

Campbell, K.V., 1971. Metamorphic petrology and structural geology of the Crooked Lake area, Cariboo Mountains, British Columbia. Ph.D. thesis, The University of Washington, 192p.

Campbell, R.B., 1978. Quesnel Lake, British Columbia. Geological Survey of Canada, Open File 574; scale 1:125,000.

Campbell, R.B., and Tipper, H.W., 1971. Bonaparte Lake map area, British Columbia. Geological Survey of Canada, Memoir 363, 100p.

Colpron, M., and Price, R.A., 1995. Tectonic significance of the Kootenay terrane, southeastern Canadian Cordillera: An alternative model. Geology, 23, 25-28.

Dawson, G.M., 1879. Preliminary report on the physical and geological features of the southern portion of the interior of British Columbia. In: Report of Progress, 1877-1878, Part B, Geological Survey of Canada, pp. 1B-187B.

Ferri, F., 1997. Nina Creek Group and Lay Range Assemblage, north-central British Columbia: remnants of late Paleozoic oceanic and arc terranes. Canadian Journal of Earth Sciences, 34, 854-874.

Ferri, F., 2001. Geological setting of the Frank Creek massive sulphide occurrence near Cariboo Lake, east-central British Columbia (93A/11, 14). In: Geological Fieldwork 2000, British Columbia Ministry of Energy and Mines, British Columbia Geological Survey Paper 2001-1, pp. 31-49.

Fillipone, J.A., and Ross, J.V., 1990. Deformation of the western margin of the Omineca Belt near Crooked Lake, east-central British Columbia. Canadian Journal of Earth Sciences, 27, 414-425.

Little, H.W., 1960. Nelson map-area, west half, British Columbia (82F W1/2). Geological Survey of Canada, Memoir 308, 205p.

Logan, J.M., and Mihalynuk, M.G., 2005. Regional geology and setting of the Cariboo, Bell, Springer and Northeast porphyry Cu-Au zones at Mount Polley, south-central British Columbia. In: Geological Fieldwork 2004, British Columbia Ministry of Energy, Mines and Petroleum Resources, British Columbia Geological Survey Paper 2005-1, pp. 249-270.

Logan, J.M., and Moynihan, D.P., 2009. Geology and mineral occurrences of the Quesnel River map area, central British Columbia (NTS 093B/16). In: Geological Fieldwork 2008, British Columbia Ministry of Energy, Mines and Petroleum Resources, British Columbia Geological Survey Paper 2009-1, pp. 127-152.

Logan, J.M., Bath, A., Mihalynuk, M. G., Rees, C.J., Ullrich, T.D., and Friedman, R., 2007. Regional geology of the Mount Polley area, central British Columbia. British Columbia Ministry of Energy, Mines and Petroleum Resources, British Columbia Geological Survey Geoscience Map 2007-1; scale 1:50,000.

McMullin, D.W.A., 1990. Thermobarometry of pelitic rocks using equilibria between quartz-garnet-aluminosilicate-muscovite-biotite, with application to rocks of the Quesnel Lake area, British Columbia. Ph.D. thesis, The University of British Columbia, 291p.

McMullin, D.W.A., Greenwood, H.J., and Ross, J.V., 1990. Pebbles from Barkerville and Slide Mountain terranes in a Quesnel terrane conglomerate: evidence for pre-Jurassic deformation of the Barkerville and Slide Mountain terranes. Geology, 18, 962–965.

Mihalynuk, M.M., Diakow, L.J., Logan, J.M., and Friedman, R.M., 2015. Preliminary geology of the Shrimpton Creek area (NTS 092H/15E, 16W) Southern Nicola Arc Project. In: Geological Fieldwork 2014, British Columbia Ministry of Energy and Mines, British Columbia Geological Survey Paper 2015-1, pp. 129-163.

Mihalynuk, M.G., Diakow, L.J., and Friedman, R.M., 2016. Chronology of southern Nicola arc stratigraphy and deformation. In: Geological Fieldwork 2015, British Columbia Ministry of Energy and Mines, British Columbia Geological Survey Paper 2016-1, this volume.

Nelson, J.L., and Bellefontaine, K.A., 1996. The geology and mineral deposits of north-central Quesnellia; Tezzeron Lake to Discovery Creek, central British Columbia. British Columbia Ministry of Employment and Investment, British Columbia Geological Survey Bulletin 99, 112p.

Nelson, J.L., Colpron, M., and Israel, S., 2013. The cordillera of British Columbia, Yukon and Alaska: tectonics and metallogeny. In: Tectonics, metallogeny and discovery: the North American cordillera and similar accretionary settings, Society of Economic Geologists, Special Publication 17, pp. 53-109.

Nixon, G.T., Hammack, J.L., Ash, C.H., Cabri, L.J., Case, G., Connelly, J.N., Heaman, L.M., Laflamme, J.H.G., Nuttall, C., Paterson, W.P.E., and Wong, R.H., 1997. Geology and platinum-group-element mineralization of Alaskan-type ultramafic-mafic complexes in British Columbia. British Columbia Ministry of Employment and Investment, British Columbia Geological Survey Bulletin 93, 141p.

Panteleyev, A., Bailey, D.G., Bloodgood, M.A., and Hancock, K.D., 1996. Geology and mineral deposits of the Quesnel River - Horsefly map area, central Quesnel Trough, British Columbia. British Columbia Ministry of Employment and Investment, British Columbia Geological Survey Bulletin 97, 155p.

Paradis, S., Bailey, S.L., Creaser, R.A., Piercey, S.J., and Schiarizza, P., 2006. Paleozoic magmatism and syngenetic massive sulphide deposits of the Eagle Bay assemblage, Kootenay terrane, southern British Columbia. In: Colpron, M., and Nelson, J. (Eds.), Paleozoic evolution and metallogeny of pericratonic terranes at the ancient pacific margin of North America, Canadian and Alaskan cordillera, Geological Association of Canada, Special Paper 45, pp. 383-414.

Petersen, N.T., Smith, P.L., Mortensen, J.K., Creaser, R.A., and Tipper, H.W., 2004. Provenance of Jurassic sedimentary rocks of south-central Quesnellia, British Columbia: implications for paleogeography. Canadian Journal of Earth Sciences, 41, 103-125.

Preto, V.A., 1979. Geology of the Nicola Group between Merritt and Princeton. British Columbia Ministry of Energy, Mines and Petroleum Resources, British Columbia Geological Survey Bulletin 69, 90p.

Rees, C.J., 1987. The Intermontane - Omineca belt boundary in the Quesnel Lake area, east-central British Columbia: Tectonic implications based on geology, structure and paleomagnetism. Ph.D. thesis, Carleton University, 421p.

Schiarizza, P., 1989. Structural and stratigraphic relationships between the Fennell Formation and Eagle Bay assemblage, western Omineca Belt, south-central British Columbia: Implications for Paleozoic tectonics along the paleocontinental margin of western North America. M.Sc. thesis, The University of Calgary, 343p.

Schiarizza, P., 2014. Geological setting of the Granite Mountain batholith, host to the Gibraltar Cu-Mo porphyry deposit, south-central British Columbia. In: Geological Fieldwork 2013, British Columbia Ministry of Energy and Mines, British Columbia Geological Survey Paper 2014-1, pp. 95-110.

Schiarizza, P., 2015. Geological setting of the Granite Mountain batholith, south-central British Columbia. In: Geological Fieldwork 2014, British Columbia Ministry of Energy and Mines, British Columbia Geological Survey Paper 2015-1, pp. 19-39.

Schiarizza, P. and Bligh, J.S., 2008. Geology and mineral occurrences of the Timothy Lake area, south-central British Columbia (NTS 092P/14). In: Geological Fieldwork 2007, British Columbia Ministry of Energy, Mines and Petroleum Resources, British Columbia Geological Survey Paper 2008-1, pp. 191-211.

Schiarizza, P. and Boulton, A., 2006. Geology and mineral occurrences of the Quesnel Terrane, Canim Lake area (NTS 092P/15), south-central British Columbia. In: Geological Fieldwork 2005, British Columbia Ministry of Energy, Mines and Petroleum Resources, British Columbia Geological Survey Paper 2006-1, pp. 163-184.

Schiarizza, P. and Israel, S., 2001. Geology and mineral occurrences of the Nehalliston Plateau, south-central British Columbia (92P/7, 8, 9, 10). In: Geological Fieldwork 2000, British Columbia Ministry of Energy and Mines, British Columbia Geological Survey Paper 2001-1, pp. 1-30.

Schiarizza, P. and Macauley, J., 2007. Geology and mineral occurrences of the Hendrix Lake area (NTS 093A/02), south-central British Columbia. In: Geological Fieldwork 2006, British Columbia Ministry of Energy, Mines and Petroleum Resources, British Columbia Geological Survey Paper 2007-1, pp. 179-202.

Schiarizza, P. and Preto, V.A., 1987. Geology of the Adams Plateau-Clearwater-Vavenby area. British Columbia Ministry of Energy, Mines and Petroleum Resources, British Columbia Geological Survey Paper 1987-2, 88p.

Schiarizza, P., and Tan, S.H., 2005. Geology and mineral occurrences of the Quesnel Terrane between the Mesilinka River and Wrede Creek (NTS 94D/8, 9), north-central British Columbia. In: Geological Fieldwork 2004, British Columbia Ministry of Energy, Mines and Petroleum Resources, British Columbia Geological Survey Paper 2005-1, pp. 109-130.

Schiarizza, P., Bell, K., and Bayliss, S. (2009): Geology and mineral occurrences of the Murphy Lake area, south-central British Columbia (NTS 093A/03). In: Geological Fieldwork 2008, British Columbia Ministry of Energy, Mines and Petroleum Resources, British Columbia Geological Survey Paper 2009-1, pp. 169-187.

Schiarizza, P., Heffernan, S., and Zuber, J., 2002. Geology of Quesnel and Slide Mountain terranes west of Clearwater, south-central British Columbia (92P/9, 10, 15, 16). In: Geological Fieldwork 2001, British Columbia Ministry of Energy and Mines, British Columbia Geological Survey Paper 2002-1, pp. 83-108.

Schiarizza, P., Israel, S., Heffernan, S., Boulton, A., Bligh, J., Bell, K., Bayliss, S., Macauley, J., Bluemel, B., Zuber, J., Friedman, R.M., Orchard, M.J., and Poulton, T.P., 2013. Bedrock geology between Thuya and Woodjam creeks, south-central British Columbia, NTS 92P/7, 8, 9, 10, 14, 15, 16; 93A/2, 3, 6. British Columbia Ministry of Energy, Mines and Natural Gas, British Columbia Geological Survey Open File 2013-05; 4 sheets, scale 1:100,000.

Smith, R.B., 1979. Geology of the Harper Ranch Group (Carboniferous-Permian) and Nicola Group (Upper Triassic) northeast of Kamloops, British Columbia. M.Sc. thesis, The University of British Columbia, 211p.

Struik, L.C., 1983. Bedrock geology, Spanish Lake and adjoining areas, British Columbia. Geological Survey of Canada, Open File 920; scale 1:50,000.

Struik, L.C., 1986. Imbricated terranes of the Cariboo gold belt with correlations and implications for tectonics in southeastern British Columbia. Canadian Journal of Earth Sciences, 23, 1047-1061.

Struik, L.C., 1988. Regional imbrication within Quesnel Terrane, central British Columbia, as suggested by conodont ages. Canadian Journal of Earth Sciences, 25, 1608-1617.

Tipper, H.W., 1978. Northeastern part of Quesnel (93B) map-area, British Columbia. In: Current Research, Part A, Geological Survey of Canada, Paper 78-1A, pp. 67-68.

Thompson, R.I., Glombick, P., Erdmer, P., Heaman, L.M., Lemieux, Y., and Daughtry, K.L., 2006. Evolution of the ancestral Pacific margin, southern Canadian Cordillera: Insights from new geologic maps. In: Colpron, M., and Nelson, J. (Eds.), Paleozoic evolution and metallogeny of pericratonic terranes at the ancient Pacific margin of North America, Canadian and Alaskan cordillera, Geological Association of Canada, Special Paper 45, pp. 433-482.

Chronology of southern Nicola arc stratigraphy and deformation

Mitchell G. Mihalynuk[1, a], Larry J. Diakow[1], Richard M. Friedman[2], and James M. Logan[3]

[1] British Columbia Geological Survey, Ministry of Energy and Mines, Victoria, BC, V8W 9N3
[2] Pacific Centre for Geochemical and Isotopic Research, University of British Columbia, Vancouver, BC, V6T 1Z4
[3] JLoGeologic, Victoria, BC, V8L 5Z9
[a] corresponding author: Mitch.Mihalynuk@gov.bc.ca

Recommended citation: Mihalynuk, M.G., Diakow, L.J., Friedman, R.M., and Logan, J.M., 2016. Chronology of southern Nicola arc stratigraphy and deformation. In: Geological Fieldwork 2015, British Columbia Ministry of Energy and Mines, British Columbia Geological Survey Paper 2016-1, pp. 31-63.

Abstract

Field observations and new isotopic age determinations from the Southern Nicola Arc Project (SNAP) necessitate further revision of the Nicola arc stratigraphy. New U-Pb CA-TIMS dates significantly extend igneous limits of the Nicola Group. Volcanic crystallization ages now range from ~238 Ma, latest Middle Triassic (Ladinian), to ~202 Ma, latest Triassic (Rhaetian). The youngest age marks the end of Nicola arc development in southern Quesnellia, culminating an interval that started in the late Norian during which volcanism was sporadic and sedimentation of arc-derived detritus was predominant. Late erosion that cuts down to early Norian carbonate rocks, combined with a predominance of mafic magmatism, might account for a lack of datable material between ~223 Ma and ~210 Ma. Resurgence in arc volcanism and eruption of the Harmon succession developed above oxidized basal conglomerate in the late Norian, after ~208 Ma. It is closely timed and possibly succeeded by emplacement of intrusions hosting Cu-Au porphyry mineralization, but also by denudation of the Nicola magmatic arc and accumulation of volcanic and plutonic detritus. A period of Early Jurassic plutonism separates the Nicola Group from a newly defined ~162 Ma volcanic succession, to our knowledge the first to be documented in south-central British Columbia. Named the Osprey unit, and composed of rhyolite and andesite volcanic rocks, they are cut by the nearly coeval and presumably comagmatic Osprey batholith.

The Nicola arc strata were deformed at least three times. First, thick beds of maroon conglomerate containing clasts derived from Nicola arc strata as young as Norian (~210 Ma) were deposited between 208 and 201 Ma in the central part of the study area, coeval with fine-grained deposits to the east, presumably recording uplift. Variable magmatism ranges from strongly alkalic basalts to calc alkaline apatite-biotite-quartz-phyric pyroclastic strata (~202 Ma) with associated copper mineralization. Second, we speculate that Nicola strata were folded and thrusted and overlain by conglomeratic strata (Shea conglomerate). Detrital zircon ages from the conglomerate and youngest underlying strata indicate that this deformation was between 201 and 185 Ma, when Quesnel terrane was docking at the margin of North America. Third, thrust-imbrication of chert pebble conglomerate and Nicola Group strata is constrained by detrital zircon ages from the conglomerate and by crystallization ages from undeformed Spences Bridge Group volcanic strata to between ~134 and 104 Ma, possibly related to docking of the Insular Superterrane.

Keywords: Stratigraphy, geochronology, Nicola Group, Nicola arc, porphyry copper gold, Princeton, Merritt, Spences Bridge Group, Quesnel terrane, Intermontane Superterrane, subduction, collision, deformation, biogeochronology, paleogeography

---

1. Introduction

Late Triassic porphyry deposits are well known in the conjoined Stikine and Quesnel terranes, which comprise most of the accreted crust along the length of British Columbia (Fig. 1). Prolific porphyry mineralization at 205 ±6 Ma produced >90% of the known copper resource in these terranes (Logan and Mihalynuk, 2014). Owing in part to its spectacular metal endowment, the southern Nicola arc in Quesnel terrane has been extensively explored (reviews of exploration can be found in Preto, 1979; Mihalynuk and Logan, 2013b; Mihalynuk et al., 2014a, 2015; and references therein). Since 2012, fieldwork of the Southern Nicola Arc Project (SNAP) has built upon this body of knowledge, particularly between the producing deposits at Copper Mountain (south), Highland Valley (northwest) and Iron Mask (Afton, northeast; Fig. 1). Geochronologic studies at each of these deposits have defined the age of mineralization at ~204 Ma (Mihalynuk et al., 2010; Ash et al., 2007; Logan et al., 2007, although the apparent mineralizing phase of the Guichon batholith at the Highland Valley deposit (Bethsaida phase) has returned older ages of ~209 Ma, Davis in Logan and Mihalynuk, 2014).

Magmatic and sedimentary units of the southern Nicola arc have been classically thought of as forming three subparallel belts separated by northerly trending faults: the Western belt distinguished by felsic volcanic rocks and limestone; the Central belt with mainly mafic volcanic rocks, comagmatic plutons, and locally prominent coarse siliciclastic rocks; and the Eastern belt containing the highest proportion of sedimentary rocks (Preto, 1979, and extended more regionally by Monger, 1989; Figs. 2, 3). All were thought to be strictly Late Triassic and relatively unaffected by contractional deformation. Using isotopic dating techniques unavailable to earlier workers, our work has shown that initial growth of the southern Nicola arc started in the Middle Triassic and continued episodically to latest Triassic,

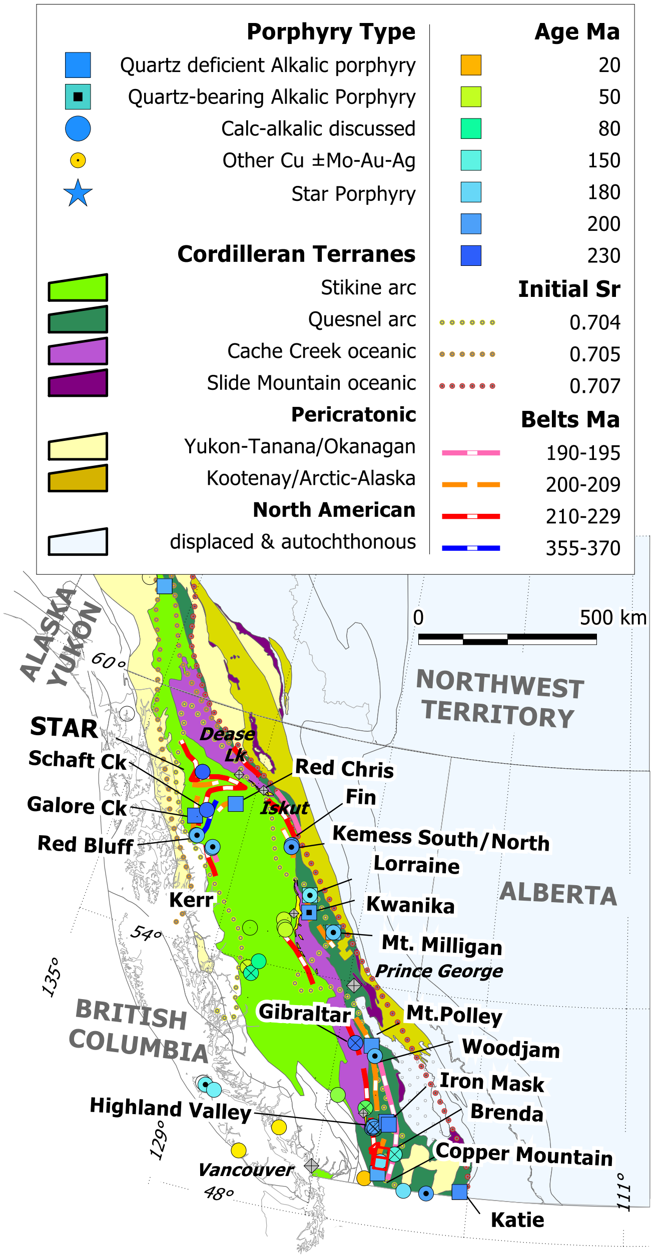

Fig. 1. Tectonostratigraphic terranes of interior British Columbia and major porphyry Cu-Au deposits (modified after Logan and Mihalynuk, 2014). Porphyry deposits are colour coded according to age to show Late Triassic-Early Jurassic porphyry events (shades of blue). Red outline between Copper Mountain and Iron Mask corresponds to the study area outlined on Figure 2.

and that late shortening, affected the entire arc (Mihalynuk et al., 2015). Recent U-Pb zircon data now extend the age and distribution of Nicola magmatism, with felsic pulses at ~238 Ma and ~202 Ma in the Central belt, and ~239 and ~224 Ma in the Western belt (Figs. 2, 3). The youngest detrital zircons from maroon sandstones in the Central belt (Harmon succession) yielded ages of ~208 to 204 Ma (Mihalynuk et al., 2015) consistent with the magmatic ages suggesting that Nicola arc magmatism ceased near the Triassic-Jurassic boundary (~201 Ma; Cohen et al., 2015).

Herein we summarize the results of 15 new isotopic age determinations (see Friedman et al., 2016 for details), and focus on the stratigraphic revisions they necessitate. In some instances, the new data lead to significant revisions of the age relationships in the Central and Eastern belts that were inferred by Mihalynuk et al. (2014, 2015). For example, although Mihalynuk et al. (2015) acknowledged interfingering of volcanic and sedimentary strata in the Eastern belt, they considered that the main sedimentary succession served as basement to the arc. As shown below, the youngest detrital zircon ages require that at least the western exposures of the Eastern belt are coeval with youngest arc magmatism (~202 Ma) and hence the notion of an arc constructed above thick turbiditic deposits remains unsubstantiated. Knowledge of the timing, style, and magnitude of folding and faulting is key to discovering the offset parts of known deposits such as the Boundary fault, which truncates mineralization in the Copper Mountain deposit (Preto, 1972). We also focus in this paper on using the new ages to further refine the chronology of deformation in the mineralized arc.

2. Regional geology

Most rocks of the southern Nicola arc in the study area belong to more than a dozen lithostratigraphic units that can be traced for many kilometres along the arc, and in some cases, across the arc, in either the Central or Eastern belts. Plutons and stocks of various ages have traditionally provided relative age brackets for these units, augmented by relatively few fossil ages from sedimentary units. More detailed descriptions of these units than provided below can be found in the pioneering work of Preto (1979) and in Mihalynuk et al. (2014a, 2015). Readers seeking more regional lithologic information are directed to Monger (1984). Lithologic descriptions herein focus primarily on the Western belt.

2.1. Triassic layered rocks, Eastern and Central belts

The distribution and age relationships of Triassic units in the Eastern and Central belts along a transect at the latitude of ~50°N are presented in Figure 3. Abrupt and non-systematic changes of unit ages in laterally adjacent parts of the transect reflect levels of exposure, largely a consequence of faults. The transect crosses, from east to west (red boxes Fig. 3): 1) the Eastern sedimentary belt, containing mainly well-bedded siltstone and sandstone (<210 Ma in part, this paper); 2) the Paradise succession of polymictic conglomerate with volcanic (and commonly abundant monzonitic) clasts, and including the Boot Lake subdivision, with mainly coarse augite- and hornblende-phyric clasts; 3) the Shrimpton succession of massively-bedded, coarse feldspathic wacke and tuffaceous rocks, calcareous argillaceous volcanic siltstone, limestone-clast bearing conglomerate, and analcime-rich flows; 4) coarse augite porphyry breccia (commonly reworked) and rare flows; 5) Ketcham rhyolite clast sharpstone conglomerate and quartz-

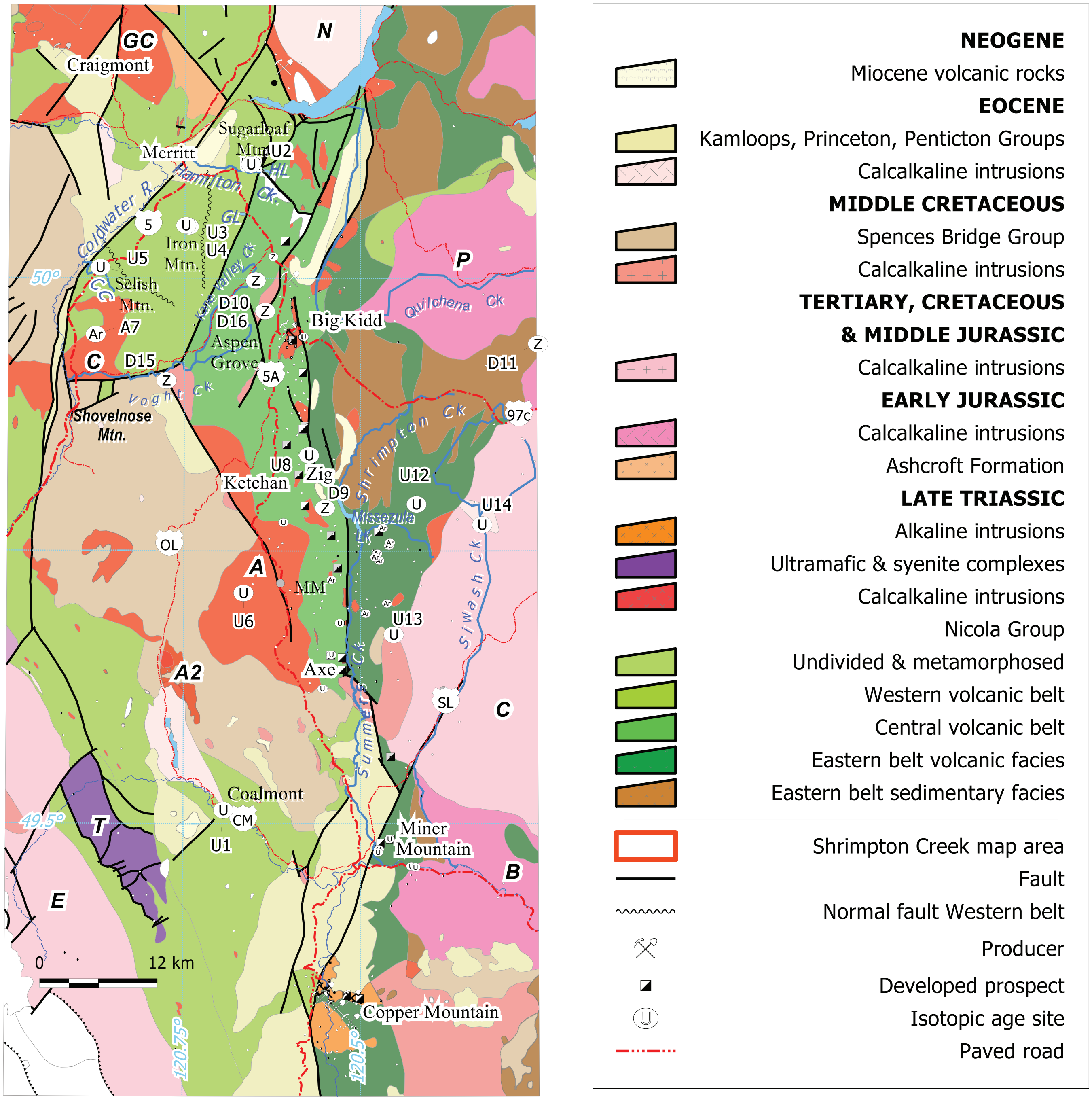

Fig. 2. Geological setting of field mapping and geochronology samples presented in this report. Extents of Preto's (1979) Eastern belt (mafic submarine volcanic and sedimentary rocks), Central belt (arc axis, mafic volcanic and coeval intrusive rocks) and Western belt (intermediate to felsic volcanic and sedimentary rocks) are shown for reference, after Massey et al. (2005); modified from Mihalynuk and Logan (2013b). Abbreviations for major plutons: A = Allison Lake, A2 = newly mapped southwest extension of the Allison pluton, B = Bromley, BI = Boulder intrusion, E = Eagle, GC = Guichon Creek, MM = Missezula Mountain, N = Nicola, O = Osprey Lake, P = Pennask, S = Summers Creek, T = Tulameen complex. See Figure 1 for context. Orange box = 2013 mapping, red box = 2014 mapping, yellow outline = 2015 mapping and Diakow and Barrios (2008). Labels beside geochronologic sampling sites correspond to those in Figure 3 and Table 1. Small isotopic age site symbols are from previously published data.

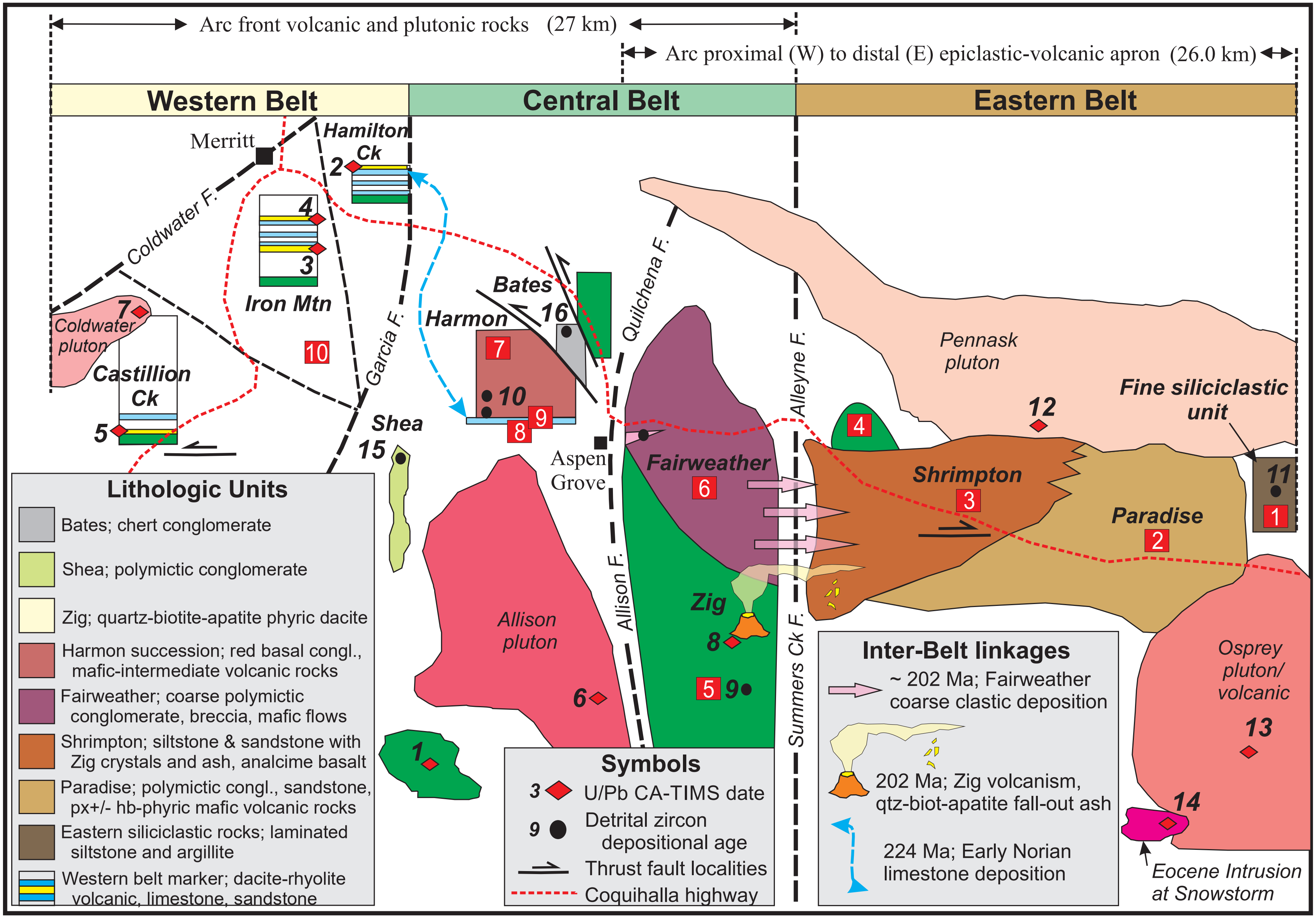

Fig. 3. Schematic diagram showing the general distribution of the Nicola Group at the latitude of ~50°N (Coquihalla Highway 5 and 97C) near Merritt, which transects mainly volcanic rocks in the Western and Central belts, and largely siliciclastic rocks that pass from the Central belt into the Eastern belt. Dated units demonstrate temporal continuity between the Nicola belts. Ages are identified by bold black numbers cross-referenced to Table 1. Red squares represent areas 1-10 referred to in text.

rich sandstone (<= 239 Ma, this study); 6) the Fairweather unit of coarse-grained siliciclastic rocks (Lefebure, 1976), which contains Zig apatite-, biotite-, and sparse quartz-phyric tuffaceous rocks (~202 Ma this study) with 215 Ma calcite-quartz-epidote-chalcocite veins (Re-Os chalcocite; R.A. Creaser, unpublished); 7) bladed feldspar porphyry flows that are intercalated with maroon volcanic sandstone to aphanitic tuff, and rare cherty limestone beds (Voght unit of Harmon succession) and overlie volcanic clast-bearing conglomerate (<210 Ma, this study) and coarse augite porphyry breccia; all overlain by feldspar porphyry volcanic breccia to ash fall tuff (Tillery unit, <201 Ma, possibly Early Jurassic Mihalynuk et al., 2015; see below); 8) the Hendriks fossiliferous limestone and fine-grained calcareous siliciclastic beds, early Norian (~224 Ma; Diakow, Friedman and Orchard, unpublished fossil data; Monger, 1989); 9) Aphanitic green finely vesicular basalt interdigitated with upper parts of the Hendriks limestone;10) Western belt felsic volcanic facies (224 Ma, this study) and siliciclastic facies (Carnian to Early Norian) which are described in more detail below.

2.2. Triassic layered rocks, Western belt

Western belt strata are separated from the Central belt by the Garcia fault, trending northeast between Garcia and Hamilton lakes (Fig. 2), and also form a fault-bounded wedge southwest of Aspen Grove (Preto, 1979). Rocks of the belt extend continuously from Hamilton Creek southwest, for 20 km to Selish Mountain where the Coldwater pluton cuts and terminates bedded strata presumed to be a younger part of the Western belt (Diakow and Barrios, 2008). The tract is about 9 km wide, bound in part or wholly by inferred faults; the Coldwater fault (Eocene) to the northwest and the Garcia fault to the southeast, which was mapped in the Hamilton Creek area (Preto, 1979), and projected southwest (Monger, 1989). Homoclinal stratified rocks throughout the tract dip moderately southeast.

Crudely bedded mafic flows and lesser volcaniclastic rocks of undetermined thickness are at the base of the homocline. Everywhere, these basalts and andesites (lower mafic unit) are overlain by a variety of bedded sedimentary and volcanic rocks (upper stratified unit). In this upper stratified unit are distinctive micritic limestones and dacite to rhyolite volcanic rocks which, recognized throughout the homocline, constitute a marker unit.

Several high-angle faults striking north and west-northwest subdivide the homocline into three major blocks. Clear offset of the lower mafic and upper stratified units show successive up-to-the-north motion resulting in deeper levels of exposure northward. In the northern block, mainly the lower mafic unit is exposed and the upper stratified unit is comparatively thin (400 m), as it increases southward to 1100 m in the central block and 1600 m in the southern block.

2.2.1. Western belt rocks at Hamilton Creek

The upper stratified unit forms a narrow band, faulted against rocks of the Central belt (Preto, 1979). Upper stratified rock units extend discontinuously northward for at least 7 km from Garcia Lake to north of Hamilton Creek (west of Sugarloaf Mountain) where they are about 400 metres thick. In this section, grey limestone forms a series of low-lying ridges, some up to 50 metres wide. Medium to coarse feldspathic wacke and granule conglomerate, and minor basaltic flows occupy recessive areas between resistant limestone ridges. Dacitic, quartz-phyric lapilli tuffs crop out in layers several metres thick at the top of the limestone sections. Nearer Garcia Lake, these tuffs alternate with thicker limestone beds in intervals up to 25 metres thick.

Massive, crudely-layered purplish oxidized and epidote-altered dark green lava flows typify the mafic unit in the Western belt, and are extensive throughout the north block. They contain medium-grained plagioclase and augite phenocrysts and are interlayered with mafic tuff containing dark, aphanitic, indistinct fragments. The contact with the overlying stratified unit is gradational.

2.2.2. Western belt rocks at Iron Mountain

In the central block, the upper stratified unit of the Western belt may be as thick as 1100 m, as estimated from a transect originating at the crest of Iron Mountain that passes through semi-continuous exposures (see Nicola Group Iron Mountain Inset Map in Diakow and Barrios, 2008). The lithologic variability of the marker unit, which starts about 500 m above the base of the upper stratified unit, is well displayed on the southeast-facing slope of Iron Mountain (Fig. 4).

Mafic to intermediate massive flows and fragmental rocks of the lower mafic unit are predominant on the northwest slope of Iron Mountain. At the crest of the mountain, these strata are abruptly overlain by the upper stratified unit, with basal

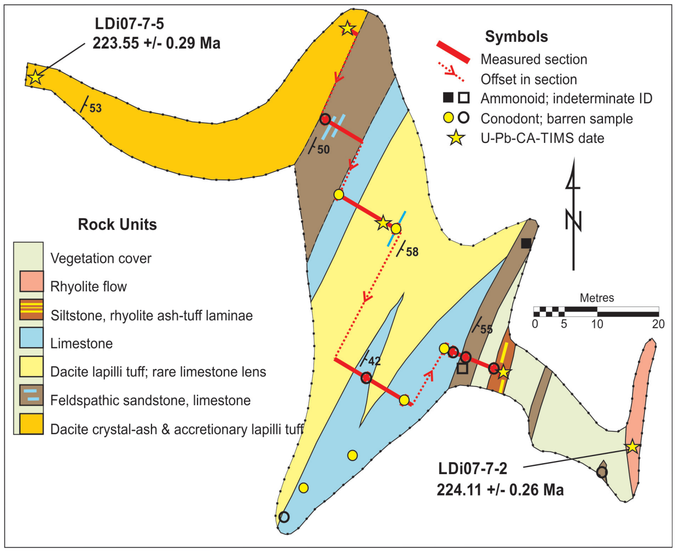

Fig. 4. Geology of the marker interval in the upper stratified unit at Iron Mountain, Western belt of the Nicola Group. Locations of samples reported herein are shown: U-Pb TIMS ages (stars) and fossil collections: conodonts (circles); ammonoids (squares). Results from other samples labelled will be presented in a future publication.

strata consisting of a dense rhyodacite flow lense, 200 to 250 m thick. These flows are overlain by a comparable thicknesses of felsic tuffs, distinguished by common aphanitic rhyolite lapilli and quartz grains, and thin layers of crystal-ash tuff. Multiple layers of accretionary lapilli tuff up to 50 cm thick are in the upper 60 metres of this felsic tuff member. These accretionary lapilli-bearing beds form the lower volcanogenic component of the marker interval (200 m thick; Fig. 4). Marker strata extend upwards for an additional 140 m through a series of limestones up to 3 m thick, and interbedded feldspathic wacke with thin lenses of carbonate and dacitic lapilli tuff. The top of the marker interval is arbitrarily set at a sharp contact with an overlying rhyolite flow unit about 40 m thick. This rhyolite in turn is overlain by a varied sequence including (from base to top): a resistant ridge-forming monolithic andesite breccia overlain by andesite porphyry flows (aggregate thickness to 200 m); maroon oxidized lapilli tuff and interlayered polymictic volcanic clast-bearing conglomerate (175 to 225 m thick), and pink-weathering limestone (10 to 30 m thick). Above this limestone, rock exposure diminishes into isolated occurrences of fine-grained quartz-bearing dacitic tuffs considered the uppermost rock unit of the central block.

2.2.3. Western belt rocks at Castillion Creek

In the south block, the upper stratified unit might be as thick as 1600 m, estimated from a transect that starts at the marker interval along the Coquihalla Highway at Castillion Creek, passing southeast, upslope through isolated exposures to Selish Mountain, then downslope through semi-continuous exposures, ending at the hydro-electric powerline corridor (Diakow and Barrios, 2008).

The marker unit at Castillion Creek is similar to that at Iron Mountain, but with several notable differences. At Castillion Creek, the marker is about 140 m thick and generally contains fewer and thinner volcanic and limestone layers, and more feldspathic wacke than at Iron Mountain. Unique to the Castillion Creek area, are stratiform siliceous beds, which occur in the mafic unit and the marker interval.

Augite-phyric mafic flows typical of the mafic unit extend upward into the lower part of the marker, interleaving with sedimentary rocks. The sedimentary rocks consist mainly of siltstone and sandstone containing angular plagioclase grains and conglomerate interbeds containing abundant angular felsic volcanic pebbles. These clastic beds typically are less than 30 cm thick, in intervals up to 12 metres thick. Carbonate rocks are scarce, comprising two units at different stratigraphic levels. The lower micritic limestone, 1.5 m thick, separates welded felsic vitric tuff layers at the base of the marker. It is grey to grey-black, with argillaceous parting between medium thick beds. More than 100 m upsection, the upper limestone overlies a second felsic pyroclastic unit. This limestone (20 m thick) is dirty grey to light grey, recrystallized and contains abundant shelly fossils.

The felsic rocks comprise sparse, relatively thin, widely spaced pyroclastic layers. The lowest layer consists of tuff in direct contact with underlying mafic lavas; the second is 1.5 m higher, separated by limestone (Fig. 5). These vitric tuffs, each less than 30 cm thick, exhibit a welded fabric. Farther upsection, but within 12 m of the marker's base, ash-tuff occurs as parallel thin beds and laminations in feldspathic sandstone, which alternate regularly between grey, siliceous beds. Felsic tuffs recur near the middle of the marker beneath limestone beds. This upper tuff unit is 25 m thick and contains angular rhyolitic lapilli-sized fragments in a green matrix with broken plagioclase crystals. In this tuff, zones with flattened and aligned lithic fragments define a weak welded fabric suggesting deposition as a subaerial ash-flow. A rhyolite flow unit that displays fine parallel flow laminations crops out at the same elevation as the base of the Castillion marker apparently deposited on the lower mafic flow unit.

Three stratiform siliceous occurrences are widely separated within a vertically aligned, crudely stacked sequence spanning nearly a 100 m change in elevation. Internally, they vary in character and thickness, the longest traced for a maximum of 600 metres along strike. The medial and upper occurrences occur within and at the top of the marker, respectively, and the lowest occurrence is in the underlying mafic unit.

The lowest occurrence consists of a stratiform chert bed that consists of jasper and minor carbonate layers in otherwise massive white silica. It is about 5 m thick and can be followed laterally in isolated exposures for about 120 m. The middle siliceous occurrence is about 15 m above the base of the marker interval and exhibits numerous dcm-scale vuggy, frothy-looking siliceous beds that alternate with feldspathic sandstone and tuffaceous siltstone (Fig. 6). Parallel, cm-scale felsic ash-rich layers mimic the irregular upper surfaces of some sandstone and siliceous beds, possibly from water-settled airborne ash. Capping the uppermost limestone in the marker

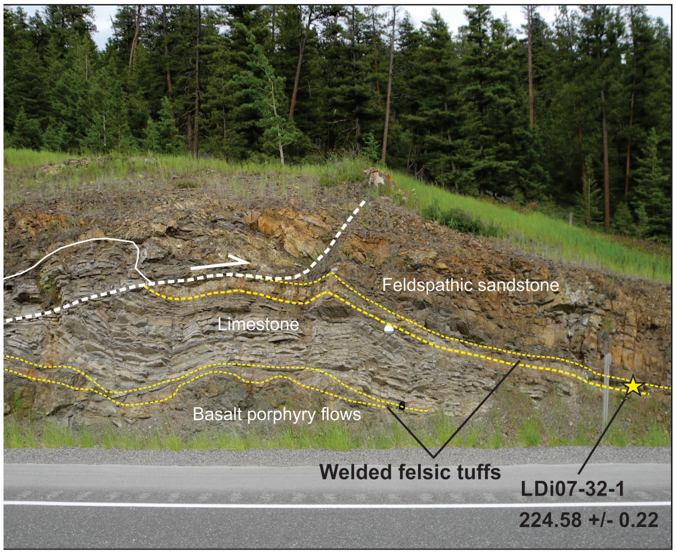

Fig. 5. Rhyolite tuff interlayered with sedimentary and volcanic beds at the base of the marker interval in the upper stratified unit at Castillion Creek, Western belt of the Nicola Group. Sample LDI07-32-1 from welded tuff band with U-Pb TIMS age (see below).

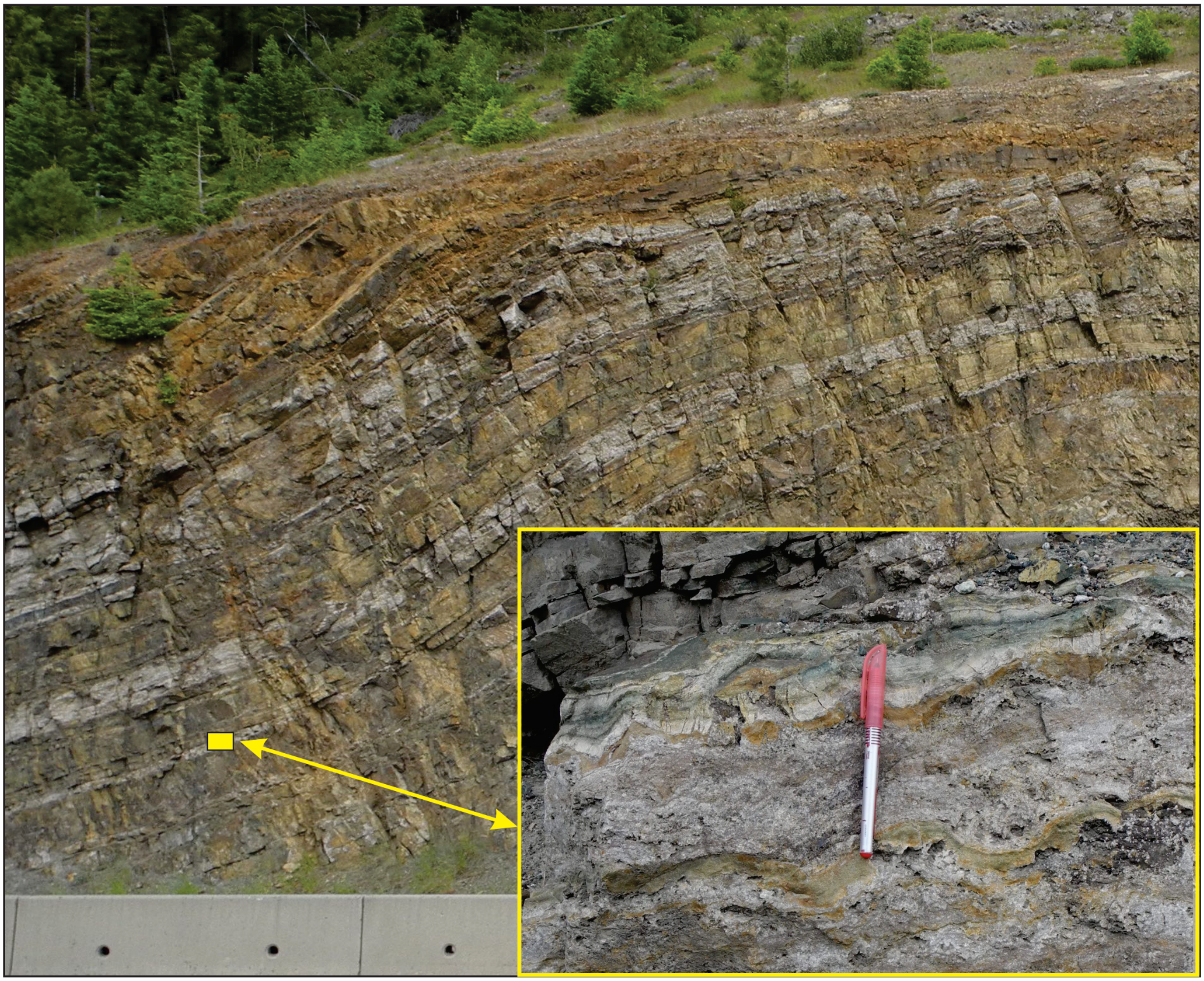

Fig. 6. Grey chert layers interbedded with sandstone and frothy silica (greyish layers) regularly interbedded in the lower part of the marker interval at Castillion Creek, adjacent to the Coquihalla Highway. Height of the exposure is approximately 15 metres. Inset: grey vuggy silica forming frothy-textured layers and interspersed off white ash mantling frothy silica layers with tan siltstone lenses.

unit is a massive 1.5 m thick chert bed, with a basal siliceous mudstone-clast breccia about 25 cm thick. Collectively, these siliceous occurrences are interpreted as repeated exhalations pooled in a relative shallow submarine environment.

Above the marker unit at Castillion Creek is a >1400 m-thick section of mainly volcanic rocks assigned to the upper stratified unit. Dacite and andesite lava flow deposits and related lapilli tuffs are predominant along the east-west ridge leading to Selish Mountain. The flows are commonly finely layered and the tuffs locally display welding. Notably, accretionary lapilli tuff beds are repeated in the section above the marker unit to Selish Mountain and beyond, suggesting much of the section might be subaerial.

2.3. Triassic intrusions

Triassic intrusions that cut the Nicola Group include the Allison pluton (~223 Ma, this study), the Coldwater pluton (~210 Ma, this study) and stocks of the Copper Mountain suite (~205 Ma).

2.3.1. Allison pluton

The Allison pluton underlies the west-central part of the study area where recent mapping shows that it is more extensive than previously recognized (Fig. 2). It is a composite intrusive body, comprising felsic and mafic hornblende-bearing phases. Mafic-rich units range from quartz diorite to hornblende-plagioclase pegmatite. Felsic units range from pink, coarse-grained granite with smoky quartz, to medium-grained, white-weathering tonalite, which tends to cross-cut mafic units. However, evidence for mingling of mafic and felsic melts is common (see Mihalynuk et al., 2015). In the west-central part of the study area, the Allison pluton cuts and/or thermally alters older rocks consisting mainly of augite porphyry and calcareous sedimentary rocks with felsic tuffaceous intervals and probably provided detrital zircons for younger Nicola Group strata. It is a composite body for which we report the first crystallization age of 223 Ma on a synkinematic granitic phase.

2.3.2. Coldwater pluton

At the south end of the Western belt, intermediate and felsic volcanic rocks thought to be stratigraphically continuous with, but well above the marker unit at Castillion Creek are cut by the Coldwater pluton. The intrusive contact is inferred from local exposures along the south-facing slope of Selish Mountain and from several volcanic rafts on the pluton roof. Bleaching and local chlorite alteration caused by thermal metamorphism appears restricted to be relatively narrow zones, perhaps only 10s of metres wide. The Coldwater pluton is homogeneous, consisting of medium- to coarse-grained equigranular diorite containing plagioclase, and variable amounts of fresh biotite (5-15%) and pyroxene (10-35%). Near the pluton margin the concentration of biotite increases to 20% with a corresponding reduction in grain size. Exposures along the Coquihalla Highway generally weather to a light greyish and appear granodioritic in composition; however, they maintain the same primary mafic mineralogy, roughly in similar proportions as dioritic phases. Rare dikes composed of pink, fine grained granite (20 cm wide) and fine grain diorite (3 m wide) cut the pluton.

2.3.3. Copper Mountain suite

Kilometre-scale dioritic stocks intrude strata along the Central belt and commonly are associated with at least minor porphyry copper-style mineralization. Based on lithology, mineralization and arc-axial location, they are presumed to belong to the ~205 Ma (Logan and Mihalynuk, 2014) Copper Mountain suite (Woodsworth et al., 1992); however, attempts to obtain isotopic crystallization age determinations have so far been unsuccessful.

2.4. Jurassic strata

Youngest Nicola Group strata are apparently overlain by the Shea polymictic conglomerate (<= 190 Ma, this study), containing abundant intrusive boulders in a maroon, sandy matrix. The Shea conglomerate is lithologically similar to an older conglomerate layer near the base of the Harmon succession that Mihalynuk et al. (2015) also referred to as the ‘Shea conglomerate’, a practice that is abandoned herein (see Section 3.2.2.4 below). The Harmon conglomerate is restricted to the coarse-grained basal part of maroon epiclastic strata with a detrital zircon maximum age of between ~208 Ma (Mihalynuk et al., 2015) and ~213 Ma (this study).

A conspicuous chert pebble conglomerate (Bates unit; Mihalynuk et al., 2015; <164, Ma, this study), is in apparent thrust contact with various units of the Harmon succession, and is apparently overthrust by Nicola Group. Lack of a local source for the chert clast-rich conglomerate is puzzling, but the clasts were likely derived from extensive ribbon cherts of the Cache Creek terrane, the closest exposures of which are now 75 km to the northwest. The conglomerate may be tectonostratigraphically analogous to the Tantalus chert clast-bearing conglomerate, which was deposited in mainly alluvial and shallow deltaic settings atop northern Quesnellia and Stikinia, also far from present-day Cache Creek terrane sources (Long, 2015).

2.5. Jurassic intrusions

Throughout most of the northeastern part of the study area, all Eastern belt strata are cut by non-foliated rocks of the Pennask batholith. A 193 Ma U-Pb age from a sample of the intrusion (this study) confirms a previous crystallization age from a locality farther northeast (194 ±1 Ma, Parrish and Monger, 1992). Pennask batholith is part of a regional suite including the batholithic-scale Bromley pluton and related pegmatite in the southeast part of the study area (193 ±1 Ma, Parrish and Monger, 1992; 193.6 ±0.3 Ma, Mihalynuk et al., 2015).

2.6. Cretaceous and Eocene rocks

Unconformably overlying Nicola Group units, volcano-sedimentary strata of the Spences Bridge Group form a continuous belt along the western flank of the Nicola arc (Fig. 2). Revising nomenclature of previous studies, Thorkelson and Rouse (1989) divided the group into a lower unit (Pimainus Formation) consisting of andesitic to rhyolitic volcanic flows and related pyroclastic and epiclastic rocks, and an upper unit (Spius Formation) consisting mainly of amygdaloidal andesitic volcanic flows with minor pyroclastic and epiclastic rocks. The Pimainus Formation is the most common in the study area, where it consists mainly of felsic volcanic rocks and derived epiclastic strata. Volcanic strata in the Spences Bridge Group have consistently yielded isotopic ages of 104 Ma (Thorkelson and Rouse, 1989; Diakow, unpublished data). Dikes presumed to be feeders to the Spences Bridge Group (Mihalynuk et al., 2010, 2015) might point to Pimainus Formation magmatism continuing for a added 1.5 m.y. Thorkelson and Smith (1989) interpreted the Pimainus Formation as a continent margin magmatic arc sequence formed during subduction of a narrow basin, and that the Spius Formation records intraplate shield-type magmatism.

Relicts of a once more extensive veneer of Princeton Group (Eocene) felsic volcanic strata are found sporadically throughout the area, but intrusive centres related to this magmatism are uncommon. One such stock is related to mineralization at the Snowstorm prospect (ca. 1917) which, produced minor base metals from sulphides in a quartz vein stockwork (Groves, 1989). Snowstorm adits are drifted into an extensively clay-altered porphyritic intrusion that crystallized at ~53 Ma (this study). This age is consistent with previous Eocene cooling ages (Armstrong and Petö, 1981) and the intrusion is probably comagmatic with Princeton Group volcanic strata (Ickert et al., 2009; Mihalynuk et al., 2014a, b).

3. Geochronology

Below we present seven new U-Pb zircon ages from the Eastern and Central belts, one ^{40}Ar/^{39}Ar age from the Western belt, and five unpublished U-Pb zircon ages from a previous study of the Western belt (Diakow and Barrios, 2008). We also present ages from three post-Nicola Group units (the Pennask batholith, Osprey volcanic unit, and the Snowstorm porphyry). These data compliment previous results reported in Mihalynuk and Logan (2013 a,b) and Mihalynuk et al. (2014a, b). The analyses were completed at the Pacific Centre for Geochemical and Isotopic Research (University of British Columbia, Vancouver).

3.1. Methods

Complete procedures are reported in a companion publication (Friedman et al., 2016) and only abridged methods are presented here.

3.1.1. U-Pb zircon chemical abrasion thermal ionization mass spectrometry (CA-TIMS)

CA-TIMS procedures are modified from Mundil et al. (2004), Mattinson (2005) and Scoates and Friedman (2008). Rock samples underwent standard mineral separation procedures, and zircon separates were handpicked in alcohol. The clearest, crack- and inclusion-free grains were selected, photographed, and then annealed at 900˚C for 60 hours. Annealed grains were chemically abraded, spiked with a $^{233\text{-}235}$U-^{205}Pb tracer solution (EARTHTIME ET535), and then dissolved. Resulting solutions were dried and loaded onto Re filaments (Gerstenberger and Haase, 1997).

Isotopic ratios were measured by a modified single collector VG-54R or 354S thermal ionization mass spectrometer equipped with analogue Daly photomultipliers. Analytical blanks were 0.2 pg for U and up to 1.0 pg for Pb. U fractionation was determined directly on individual runs using the ET535 mixed $^{233\text{-}235}$U-^{205}Pb isotopic tracer. Pb isotopic ratios were corrected for fractionation of 0.30%/amu, based on replicate analyses of NBS-982 reference material and the values recommended by Thirlwall (2000). Data reduction used the Excel™-based program of Schmitz and Schoene (2007). Standard concordia diagrams were constructed and regression intercepts and weighted averages calculated with Isoplot (Ludwig, 2003). All errors are quoted at the 2σ or 95% confidence level, unless otherwise noted. Isotopic ages were calculated with the decay constants λ^{238}=1.55125E^{-10} and λ^{235}=9.8485E^{-10} (Jaffe et al, 1971). EARTHTIME U-Pb synthetic solutions were analysed on an ongoing basis to monitor accuracy.

3.1.2. U-Pb zircon LA – ICPMS

Sample material selected was preferentially medium to coarse-grained sandstones which are expected to have the best likelihood of containing detrital zircons. Following collection, samples were isolated, double wrapped in plastic bags and placed in buckets. Samples were cleaned by washing followed by air abrading. Zircons were analyzed using laser ablation (LA) ICPMS methods using the techniques described by Tafti et al. (2009). Instrumentation comprised a New Wave UP-213 laser ablation system and a ThermoFinnigan Element2 single collector, double-focusing, magnetic sector ICP-MS. All zircons greater than about 50 microns in diameter were picked from the mineral separates and mounted in an epoxy puck along with several grains of the Plešovice (337.13 ±0.13 Ma, Sláma et al., 2007), and Temora2 (416.78 ±0.33 Ma) zircon standards and brought to a very high polish. Before analysis, the surface of the mount was washed for 10 minutes with dilute nitric acid and rinsed in ultraclean water. The highest quality portions of each grain selected for analysis were free of alteration, inclusions, or possible inherited cores. Line scans rather than spot analyses were employed in order to minimize elemental fractionation during the analyses. A laser power level of 40% and a 25 mm spot size was used. Backgrounds were measured with the laser shutter closed for ten seconds, followed by data collection with the laser firing for approximately 35 seconds. The time-integrated signals were analysed using Iolite software (Patton et al, 2011), which automatically subtracts background measurements, propagates all analytical errors, and calculates isotopic ratios and ages. Corrections for mass and elemental fractionation are made by bracketing analyses of unknown grains with replicate analyses of the Plešovice zircon standard. A typical analytical session consisted of four analyses of the Plešovice standard zircon, followed by two analyses of the Temora2 zircon standard, five analyses of unknown zircons, two standard analyses, then five unknown analyses. Each session was completed with two Temora2 zircon standards and four Plešovice standard analyses. The Temora2 zircon standard was analysed as an unknown to monitor the reproducibility of the age determinations on a run-to-run basis (see Friedman et al., 2016).

For plotting and interpretation of detrital zircon analytical results the ISOPLOT software of Ludwig (2003) is commonly used. Acceptance of the youngest probability density peak generated by Isoplot 4.15 as the minimum depositional age is typically a conservative approach, but not always (e.g., young single grain outlier in GMC14-60-2 identified by Isoplot as a sub-population). A more common issue may be the inclusion of multiple populations within a single peak. Bandwidth is an important consideration in resolving population peaks, and proper bandwidth selection is important in identification of sub-populations. Routines such as Unmix in Isoplot 4.15 can be applied to help identify sub-populations, but this routine was not used herein. To evaluate probability density distribution plots, we examined each sample dataset and considered criteria like smallest error envelopes and % discordance of individual zircon analyses in an attempt to reveal the youngest real zircon population(s). We applied a filter to some samples such that the youngest sub-population grains selected have 2σ errors less than 5% of the zircon age determination, and with ^{207}Pb/^{235}U and ^{206}Pb/^{238}U age determinations that differ by less than 1σ. We also considered zircon spot chemistry, placing more confidence in young sub-populations with homogeneous Pb, Th and U isotope contents as a percentage of the analytical counts per second compared to the range of values for that sample.

3.1.3. ^{40}Ar/^{39}Ar

Mineral separates were hand picked, washed in nitric acid, rinsed in de-ionized water, dried, wrapped in aluminum foil and stacked in an irradiation capsule with similar-aged samples and neutron flux monitors (Fish Canyon tuff sanidine, 28.02 Ma; Renne et al., 1998). The samples were irradiated at the McMaster Nuclear Reactor in Hamilton, Ontario, for 90 MWh, with a neutron flux of approximately 3 by 1016 neutrons/cm^2/s.

The sample was analyzed at the Noble Gas Laboratory, Pacific Centre for Isotopic and Geochemical Research, The University of British Columbia, Vancouver. The mineral separate was step heated at incrementally higher powers in the defocused beam of a 10 W CO$_2$ laser (New Wave Research MIR10) until fused. The gas evolved from each step was analyzed by a VG5400 mass spectrometer equipped with an ion-counting electron multiplier. All measurements were corrected for total system blank, mass spectrometer sensitivity, mass discrimination, radioactive decay during and subsequent to irradiation, as well as interfering Ar from atmospheric contamination and the irradiation of Ca, Cl and K (isotope production ratios: $[^{40}\mathrm{Ar}/^{39}\mathrm{Ar}]_K$=0.0302 ±0.00006; $[^{37}\mathrm{Ar}/^{39}\mathrm{Ar}]_{Ca}$=1416.4 ±0.5; $[^{36}\mathrm{Ar}/^{39}\mathrm{Ar}]_{Ca}$=0.3952 ±0.0004, Ca/K=1.83 ±0.01 $[^{37}\mathrm{Ar}_{Ca}/^{39}\mathrm{Ar}_K]$).

The plateau and correlation ages were calculated using Isoplot v. 3.00 (Ludwig, 2003). Errors are quoted at the 2σ (95% confidence) level and are propagated from all sources except mass spectrometer sensitivity and age of the flux monitor. The best statistically justified plateau and plateau age were picked based on the following criteria.

- three of more contiguous steps comprising more than 30% of the 39Ar
- the probability of fit of the weighted mean age greater than 5%
- the slope of the error-weighted line through the plateau ages equals zero at 5% confidence
- the ages of the two outermost steps on a plateau are not significantly different from the weighted-mean plateau age (at 1.8σ, six or more steps only)
- the outermost two steps on either side of a plateau must not have nonzero slopes with the same sign (at 1.8σ, nine or more steps only).

3.2. Results

An overview of geochronologic results is presented in Table 1 and a synthesis of all Triassic age data is presented in Figure 7. Complete raw data tables along with UTM coordinates, procedural blanks and standards, cathode luminescence imagery for many of the zircons analyzed, and supporting diagrams such as detrital zircon isochron plots, and Ar release spectra can be found in Friedman et al. (2016).

3.2.1. Zircon CA-TIMS crystallization and ^{40}Ar/^{39}Ar cooling ages

Sampling for high resolution TIMS geochronology focused on intrusive rocks or felsic extrusive rocks of primary volcanic origin or very immature, reworked volcanic strata in which quartz phenocrysts are present and felsic clasts predominate.

3.2.1.1. Sample MMI14-55-13 (U1), Western belt rhyolite tuffite near Coalmont; 238.6 ±0.3 Ma

Between Princeton and Tulameen (Fig. 2), rhyolite flows and tuffs form a belt >10 km long and <2 km wide. Rhyolite flows are rarely quartz-phyric, but typically pyritic and altered with secondary white mica and clays in white, rust and yellow weathered exposures. Immediately east of Coalmont (adjacent the old town dump) the felsic unit appears to be slightly reworked into pebbly sandstone (tuffite) and interlayered with locally pillowed basalt flow and breccia. In one outcrop, the felsic unit has laminae of Fe>Cu sulphides, interpreted as exhalite (Mihalynuk et al., 2014a). Geochronological analysis of the felsic volcaniclastic unit would provide an age of the felsic belt and possible volcanogenic sulphide mineralization. In addition, an age would test a suspected correlation with very similar rhyolitic rocks at Missezula Mountain (Mihalynuk et al., 2015) and farther north, near the Ketchan porphyry prospect (see below; Sample MMI14-23-15) about 30 km to the northeast, across the Nicola arc.

Sample MMI14-55-13 was collected from the base of a cliff on the eastern outskirts of Coalmont. Although zircons were sparse and fine grained (<50 microns in diameter), they provided a precise U-Pb age of 238.6 ±0.3 Ma (Fig. 8, Table 2). This age is nearly identical (within the limits of error) to the 238.1 ±0.3 Ma age of pyritic felsic lapilli tuff on the east flank of Missezula Mountain (see Sample MMI13-30-4; Mihalynuk et al., 2015) providing compelling support for the lithological correlation. Together, these determinations provide the oldest crystallization ages known from the Nicola Group.

3.2.1.2. Sample LDi12-1-9 (U2), Western belt, dacite tuff at top of marker unit at Hamilton Creek; 224.51 ±0.15 Ma

Sample LDi12-1-9 is from a dacitic lapilli tuff marking the highest exposure in the Hamilton Creek section. This dacite contains light colored felsic-lithic fragments and scarce quartz grains. Five overlapping analyses give a weighted ^{206}Pb/^{238}U age of 224.51 ±0.15 Ma (Fig. 9, Table 3). Limestone sampled stratigraphically below the dated tuff, contain a diverse fauna, including the bivalve *Halobia* sp., and conodont species with an age range of latest Carnian to early Norian (see collection F4, Table 1 in Preto, 1979).

3.2.1.3. Sample LDi07-7-5 (U3), Western belt, dacite near base of marker unit at Iron Mountain; 223.55 ±0.29 Ma

Sample LDi07-7-5 was collected from a accretionary lapilli tuff bed 8 m above the base of the marker interval at Iron Mountain (Fig. 4). The weighted ^{206}Pb/^{238}U age, determined

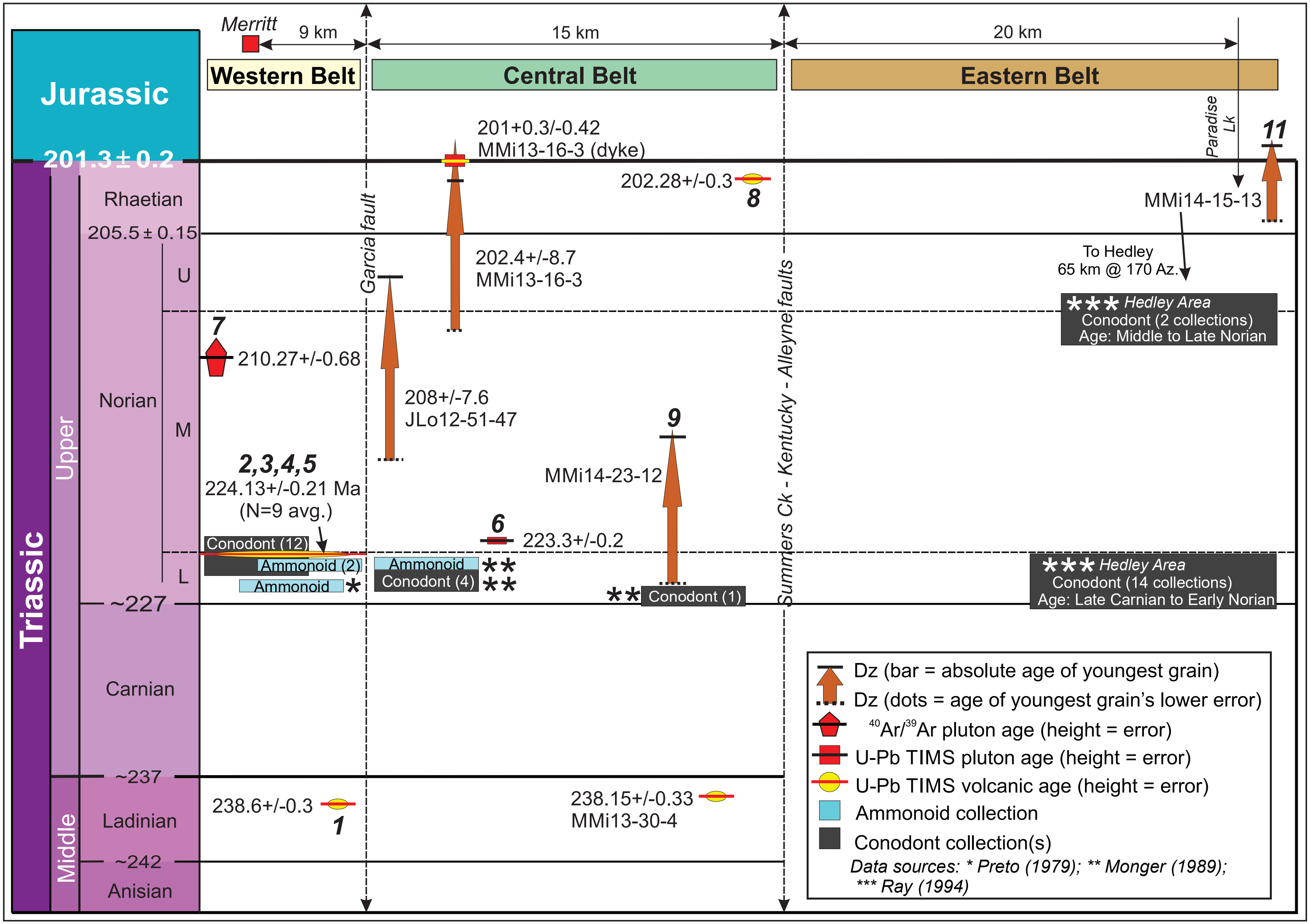

Fig. 7. Time-space distribution of radiometric and biogeochronologic ages for the southern Nicola arc, including unpublished fossil determinations and those reported in Ray and Dawson (1994), and new data presented in this report. Nicola arc belts are those of Preto (1979). Crystallization ages are shown with 2σ errors (solid bars). Detrital zircon ages are from the youngest grains, with the lower extent of arrows portraying 2σ error and the maximum age of deposition. Time scale after Cohen et al. (2013) showing an updated time pick for the Rhaetian lower boundary (Wotzlaw et al., 2014). Isotopic ages are identified by sample numbers cross referenced to Table 1.

Table 1. Synopsis of new ages presented herein; for details see Friedman et al. (2016).

Map No.	Sample No.	Type	Unit / Problem Addressed	age
Magmatic crystallization ages, Nicola Group				
U1	MMI15-53-13	U-Pb	Western belt; rhyolite tuffite near exhalite at Coalmont	238.6 ± 0.3 Ma
U2	LDi12-1-9	U-Pb	Western belt; dacite tuff at top of Hamilton Creek marker	224.51 ± 0.15 Ma
U3	LDi07-7-5	U-Pb	Western belt; dacite near base of Iron Mountain marker	223.55 ± 0.29 Ma
U4	LDi07-7-2	U-Pb	Western belt; rhyolite at the top of Iron Mountain marker	224.11 ± 0.26 Ma
U5	LDi07-32-1	U-Pb	Western belt; welded rhyolite tuff at base of Castillion Creek marker	224.58 ± 0.22 Ma
U6	MMI14-50-2	U-Pb	Central belt; Allison pluton; synkinematic pegmatitic dike cuts border phase only K-Ar determinations previously	223.3 ± 0.2 Ma
A7	LDi07-20-3	Ar/Ar	Western belt; Coldwater pluton cuts and thereby constrains age of upper stratified unit; biotite cooling age	210.27 ± 0.68 Ma
U8	MMI14-62-4	U-Pb	Central belt; Zig dacite lapilli tuff	202.28 ± 0.26 Ma
Sedimentary units, detrital zircon maximum depositional ages; Nicola Group				
D9	MMI14-23-15	U-Pb	Central belt; sharpstone conglomerate derived from Nicola felsic source Confirm source is felsic arc component which so far are ~239 Ma	<227 Ma
D10	LDi14-60-3	U-Pb	Central belt; Harmon succession; sandstone immediately below Voght basalt marker – determine age range of Voght clastic strata	<213 Ma
D11	MMI14-15-13	U-Pb	Eastern belt; fine siliciclastic unit presumed mid to upper Triassic	<202 Ma
Magmatic crystallization ages; intrusions cutting Nicola Group				
U12	MMI14-19-3	U-Pb	Pennask batholith gabbroic pegmatite with minor copper mineralization	193.1 ± 0.2 Ma
U13	MMI14-59-12	U-Pb	Osprey volcanic unit	163.2 ± 0.2 Ma
U14	MMI14-53-2	U-Pb	Snowstorm altered “Otter intrusive suite”, cut by base metal sulphide-quartz stockwork, with open space textures	53.36 ± 0.07 Ma
Sedimentary units, detrital zircon maximum depositional ages; younger than Nicola Group				
D15	MMI14-62-1	U-Pb	Shea conglomerate, extensive erosional deposit above Nicola	<190, possibly ~185 Ma
D16	GMC14-60-2	U-Pb	Bates conglomerate, predominantly chert pebbles lacking a local source	<163, possibly ~134 Ma

*Sample details UTM Easting and UTM Northing as well as complete data tables can be found in Friedman et al. (2016).

from four overlapping zircon fractions on concordia is 223.55 ±0.29 Ma (Fig. 10, Table 4).

3.2.1.4. Sample LDi07-7-2 (U4), Western belt, rhyolite at top of marker unit at Iron Mountain; 224.11 ±0.26 Ma

Sample LDi07-7-2 is from a lenticular rhyolite unit (80 m wide by 220 m long) believed to depositionally overlie the mainly sedimentary upper part of the marker unit at Iron Mountain (Figs. 3 and 4). A 25 m wide vegetated area separates underlying feldspathic sandstones from aphanitic light grey-green rhyolite. The rhyolite gives a weighted ^{206}Pb/^{238}U age of 224.11 ±0.26 Ma interpreted from two overlapping analyses of a younger group (Fig. 11, Table 5). This age is older than the age determined from the dacite near the base of the marker interval at Iron Mountain (see above) which, together with the slightly older population (Fig. 11), may indicate that the zircons are xenocrysts or antecrysts from an older partly crystallized melt from which the rhyolite later erupted.

3.2.1.5. Sample LDi07-32-1 (U5), Western belt, welded rhyolite tuff near base of marker unit at Castillion Creek; 224.58 ±0.22 Ma

At the base of the marker interval at Castillion Creek, are two rhyolite welded tuff beds that are separated by a limestone layer; Sample LDi07-32-1 is from the upper of the two tuffs (Fig. 5) . The weighted ^{206}Pb/^{238}U age on four overlapping U-Pb TIMS zircon analyses is 224.58 ±0.22 Ma (Fig. 12, Table 6).

3.2.1.6. Sample MMI14-50-2 (U6), Central belt, Allison pluton; 223.3 ±0.2 Ma

Sample MMI14-50-2 was collected from the interior of a northeast-oriented dioritic zone (2.5 km wide) near the contact with a screen of mafic country rock (minimum dimension of ~100 m wide), possibly a part of the pluton floor. A weak to moderate fabric in the country rock is strongly overprinted by granoblastic mafic minerals (predominantly hornblende ±pyroxene, magnetite, garnet and sparse clots of very coarse biotite), and these grade into zones of varitextured diorite. Leucogranitic dikes cut the diorite. Planar dikes (decimeters wide) coalesce in the area sampled, and display medium-grained to pegmatitic textures with oriented tabular quartz-feldspar crystal growth on their margins and ribboned quartz in their interiors (Figs. 13 a, b, c). Quartz ribbons have sutured grain boundaries with strained subgrains along them. These textures are evidence of solid state ductile deformation (Duke et al., 1988; Paterson et al., 1989) and a change from magmatic fabrics to tectonic fabric development.

Although the regional importance of this synkinematic fabric

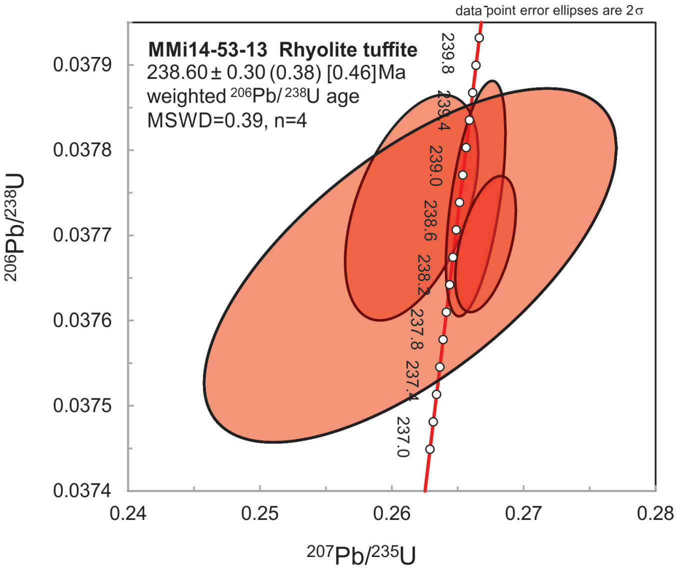

Fig. 8. U-Pb concordia diagram showing TIMS zircon U-Pb age results from sample MMI14-53-13, rhyolite lapilli tuff at Coalmont, Western belt.

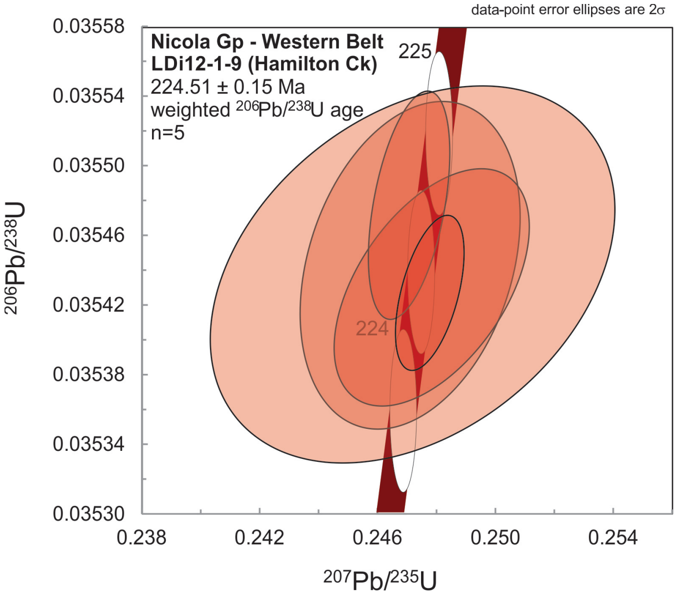

Fig. 9. Concordia plot for U-Pb TIMS data from single zircons, sample LDi12-1-9 (dacite tuff at top of Hamilton Creek marker, Western belt). Weighted age 224.51 ±0.15 Ma based on ^{206}Pb/^{238}U ages of 5 grains. Concordia bands include 2σ errors of U decay constants.

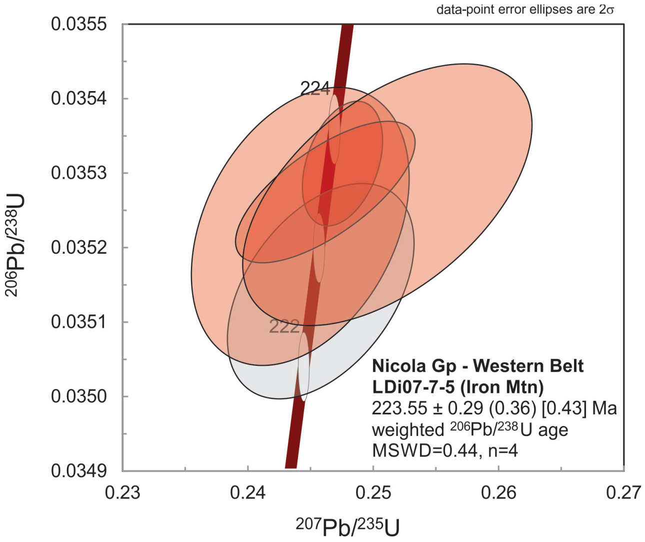

Fig. 10. Concordia plot for U-Pb TIMS data from single zircons, sample LDi07-7-5 (dacite at base of the marker interval at Iron Mountain, Western belt; see Fig. 4). Weighted age 223.55 ±0.29 Ma based on ^{206}Pb/^{238}U ages of 4 grains. Concordia bands include 2σ errors of U decay constants.

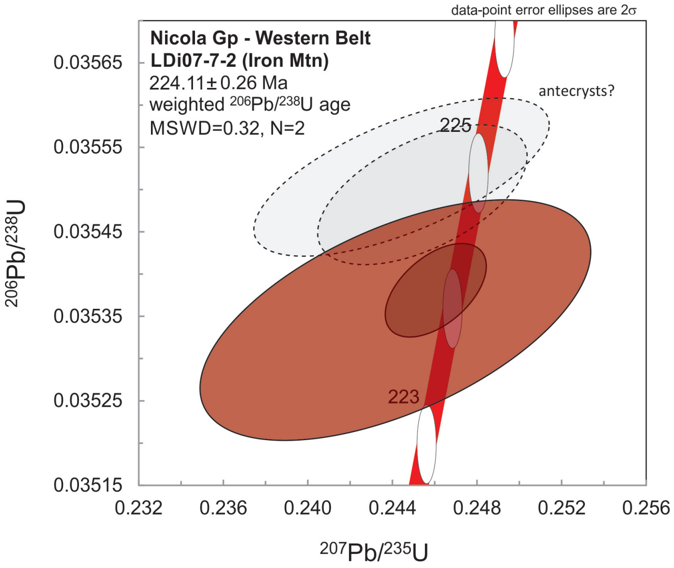

Fig. 11. Concordia plot for U-Pb TIMS data from single zircons, sample LDi07-7-2 (rhyolite at the top of the marker interval at Iron Mountain, Western belt; see Fig. 4). Weighted age 224.11 ±0.26 Ma based on ^{206}Pb/^{238}U ages of 2 grains from the younger population. Concordia bands include 2σ errors of U decay constants.

has yet to be established, dating a cross-cutting leucocratic phase of the Allison pluton provided an opportunity to corroborate existing hornblende and muscovite K-Ar cooling ages of 204 ±10 to 207 ±10 Ma (Preto, 1979; recalculated by Breitsprecher and Mortensen, 2004), while dating the deformational fabric. Chlorite alteration is ubiquitous at the sample site and elsewhere in the pluton, together with lesser epidote, rendering analysis of K-bearing phases unreliable.

A crystallization age has been determined from three zircns overlapping concordia at 223.3 ±0.2 Ma (Fig. 14, Table 7). It is older than the oldest limit of error for previously reported K-Ar cooling ages, but consistent with a population of detrital zircons from basal conglomerate of the Spences Bridge Group unconformably overlying the pluton's eastern margin (see Mihalynuk et al., 2014). This age is very similar similar to ages (e.g., 222.71 ±0.22 Ma) from Burgess Creek tonalite to diorite stock at the northeast margin of the Granite Mountain batholith (adjacent the Gibraltar Cu-Mo porphyry deposit, Fig. 1), which

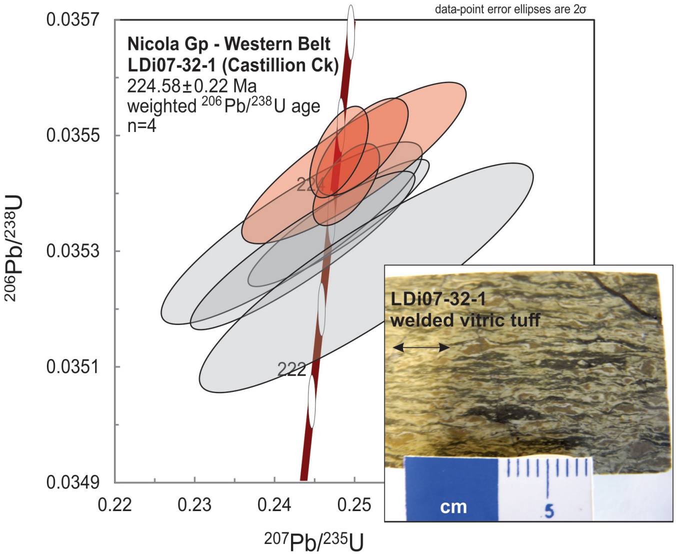

Fig. 12. Concordia plot for U-Pb TIMS data from single zircons, sample LDi07-32-1 (welded rhyolite tuff at base of the marker interval at Castillion Creek, Western belt). Weighted age 224.58 ±0.22 Ma based on ^{206}Pb/^{238}U ages of 4 grains. Concordia bands include 2σ errors of U decay constants. Inset: Collapsed vitriclasts define eutaxitic texture in welded tuff.

also displays synplutonic deformation fabrics cut by younger undeformed intrusive phases (Schiarizza, 2014, 2015, pers. comm. 2016).

3.2.1.7. Sample LDi07-20-3 (A7), Western belt, Coldwater pluton; 210.27 ±0.68 Ma

Sample LDi07-20-3, from near the centre of the Coldwater pluton, is a medium-grained equigranular quartz diorite containing 20% vitreous biotite. A biotite separate yields a plateau, formed by 80.7% of ^{39}Ar gas in 10 steps from which an age of 210.27 ±0.68 Ma is calculated (Fig. 15, Table 8). Because the pluton lacks evidence of secondary alteration, or structural disruption leading to thermal resetting, we infer that the cooling age approximates a crystallization age for the pluton.

The Coldwater pluton cuts the upper stratified unit of the Western belt at Selish Mountain, bracketing deposition to between ~224 Ma (age from the base of the marker interval at Castillion Creek) and ~210 Ma.

3.2.1.8. Sample MMI14-62-4 (U8), Central belt, Zig volcanic unit, dacite 202.3 ±0.3 Ma

In the northern part of the Central belt are pyroclastic deposits of high-silica andesite to dacite composition, readily distinguished by phenocrysts including biotite, quartz and apatite. It is referred to as the Zig unit (Mihalynuk et al., 2015), after the Zig mineral prospect (specifically NOR30), where several old pits excavated calcite-quartz-chalcocite veins up to 20 cm thick. Re-Os isotopic analysis of semi-massive chalcocite in these veins has returned an age of 215 ±2 Ma (R.A. Creaser, unpublished data).

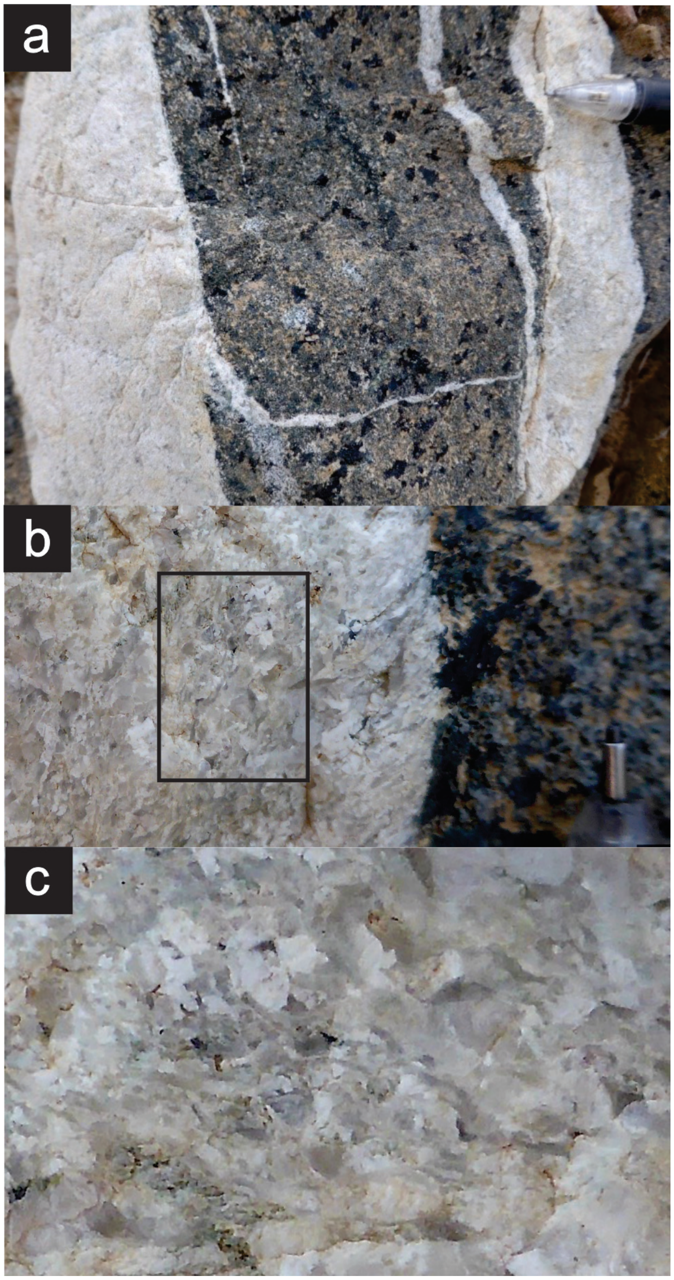

Fig. 13. Allison pluton; leucogranite dikes at sample site MMI14-50-2. **a)** Coalescing dikelets. **b)** Dike close-up showing comb texture mineral growth at the margin (0.5 mm mechanical pencil point for scale). **c)** subsolidus ribbon quartz near the dike centre.

Sample MMI14-62-4 was collected about 5 km to the south along strike of the NOR30 prospect (Fig. 2), in a bluff section of medium-grained plagioclase-bearing tuff containing ~1% red apatite grains (≤3mm in diameter), commonly euhedral with grey rims, and ~0.5% euhedral biotite booklets (≤ 4 mm in diameter). Where sampled, the unit displays characteristic weak and patchy chlorite and epidote alteration, but unlike the unit near NOR30, quartz phenocrysts are conspicuously lacking. Lithic fragments are rounded, perhaps indicating reworking,

Table 2. U-Th-Pb analytical results for MMI14-53-13.

		Compositional Parameters								Radiogenic Isotope Ratios								Isotopic Ages					
Sample	Wt. mg	U ppm	Pb ppm	$\frac{Th}{U}$	^{206}Pb* x10^{-13} mol	mol % ^{206}Pb*	$\frac{Pb^*}{Pb_c}$	Pb$_c$ (pg)	$\frac{^{206}Pb}{^{204}Pb}$	$\frac{^{208}Pb}{^{206}Pb}$	$\frac{^{207}Pb}{^{206}Pb}$	% err	$\frac{^{207}Pb}{^{235}U}$	% err	$\frac{^{206}Pb}{^{238}U}$	% err	corr. coef.	$\frac{^{207}Pb}{^{206}Pb}$	±	$\frac{^{207}Pb}{^{235}U}$	±	$\frac{^{206}Pb}{^{238}U}$	±
(a)	(i)	(j)	(j)	(b)	(c)	(c)	(c)	(c)	(d)	(e)	(e)	(f)	(e)	(f)	(e)	(f)		(g)	(f)	(g)	(f)	(g)	(f)
MMI14-53-13																							
A	0.0013	114	4.9	0.298	0.2334	95.91%	7	0.82	452	0.093	0.0503	1.463	0.2615	1.578	0.03773	0.287	0.478	207.3	33.9	235.9	3.3	238.76	0.67
B	0.0016	106	4.1	0.255	0.2664	98.65%	21	0.30	1369	0.081	0.0512	0.582	0.2664	0.693	0.03774	0.299	0.556	249.1	13.4	239.8	1.5	238.83	0.70
C	0.0018	92	3.7	0.337	0.2612	98.17%	16	0.40	1014	0.108	0.0514	0.637	0.2671	0.705	0.03769	0.173	0.495	258.8	14.6	240.4	1.5	238.50	0.41
E	0.0009	47	2.3	0.112	0.0661	90.08%	2	0.60	186	0.035	0.0503	4.598	0.2614	4.885	0.03766	0.451	0.664	210.5	106.6	235.8	10.3	238.34	1.05

(a) A, B etc. are labels for fractions composed of single zircon grains or fragments; all fractions annealed and chemically abraded after Mattinson (2005) and Scoates and Friedman (2008).

(b) Model Th/U ratio calculated from radiogenic ^{208}Pb/^{206}Pb ratio and ^{207}Pb/^{235}U age.

(c) Pb* and Pbc represent radiogenic and common Pb, respectively; mol % ^{206}Pb* with respect to radiogenic, blank and initial common Pb.

(d) Measured ratio corrected for spike and fractionation only. Mass discrimination of 0.30% ± 0.05%/amu based on analysis of NBS-982; all Daly analyses.

(e) Corrected for fractionation, spike, and common Pb; up to 1 pg common Pb was assumed to be procedural blank: ^{206}Pb/^{204}Pb = 18.50±1.0%; ^{207}Pb/^{204}Pb = 15.50±1.0%; ^{208}Pb/^{204}Pb = 38.40±1.0% (1σ errors).

(f) Errors are 2-sigma, propagated using the algorithms of Schmitz and Schoene (2007) and Crowley et al. (2007).

(g) Calculations are based on the decay constants of Jaffey et al. (1971). ^{206}Pb/^{238}U and ^{207}Pb/^{206}Pb ages corrected for initial disequilibrium in ^{230}Th/^{238}U using Th/U [magma] = 3.

(h) Corrected for fractionation, spike, and blank Pb only.

(i) Nominal fraction weights estimated from photomicrographic grain dimensions, adjusted for partial dissolution during chemical abrasion.

(j) Nominal U and total Pb concentrations subject to uncertainty in photomicrographic estimation of weight and partial dissolution during chemical abrasion.

Table 3. U-Th-Pb analytical results for LDi12-1-9.

		Compositional Parameters								Radiogenic Isotope Ratios								Isotopic Ages					
Sample	Wt. mg	U ppm	Pb ppm	$\frac{Th}{U}$	^{206}Pb* x10^{-13} mol	mol % ^{206}Pb*	$\frac{Pb^*}{Pb_c}$	Pb$_c$ (pg)	$\frac{^{206}Pb}{^{204}Pb}$	$\frac{^{208}Pb}{^{206}Pb}$	$\frac{^{207}Pb}{^{206}Pb}$	% err	$\frac{^{207}Pb}{^{235}U}$	% err	$\frac{^{206}Pb}{^{238}U}$	% err	corr. coef.	$\frac{^{207}Pb}{^{206}Pb}$	±	$\frac{^{207}Pb}{^{235}U}$	±	$\frac{^{206}Pb}{^{238}U}$	±
(a)	(i)	(j)	(j)	(b)	(c)	(c)	(c)	(c)	(d)	(e)	(e)	(f)	(e)	(f)	(e)	(f)		(g)	(f)	(g)	(f)	(g)	(f)
LDi12-1-9																							
A	0.0052	74	2.7	0.257	0.5723	98.42%	18	0.75	1172	0.081	0.050557	1.200	0.247068	1.246	0.035443	0.219	0.293	220.70	27.75	224.19	2.51	224.52	0.48
B	0.0036	54	2.0	0.228	0.2890	97.93%	13	0.50	893	0.072	0.050728	1.031	0.247809	1.103	0.035430	0.158	0.509	228.47	23.82	224.79	2.22	224.44	0.35
C	0.0048	137	4.9	0.353	0.9720	99.65%	83	0.28	5298	0.112	0.050501	0.413	0.247036	0.460	0.035478	0.152	0.459	218.14	9.56	224.17	0.93	224.74	0.33
D	0.0023	50	1.8	0.214	0.1690	97.89%	13	0.30	876	0.068	0.050582	2.216	0.247151	2.290	0.035438	0.251	0.344	221.83	51.25	224.26	4.61	224.49	0.55
E	0.0063	146	8.3	2.495	1.3558	99.21%	59	0.88	2352	0.793	0.050718	0.345	0.247739	0.387	0.035427	0.104	0.517	228.02	7.98	224.74	0.78	224.42	0.23

(a) A, B etc. are labels for fractions composed of single zircon grains or fragments; all fractions annealed and chemically abraded after Mattinson (2005) and Scoates and Friedman (2008).

(b) Model Th/U ratio calculated from radiogenic ^{208}Pb/^{206}Pb ratio and ^{207}Pb/^{235}U age.

(c) Pb* and Pbc represent radiogenic and common Pb, respectively; mol % ^{206}Pb* with respect to radiogenic, blank and initial common Pb.

(d) Measured ratio corrected for spike and fractionation only. Mass discrimination of 0.25%/amu based on analysis of NBS-982; all Daly analyses.

(e) Corrected for fractionation, spike, and common Pb; all common Pb (up to ~0.9 pg) was assumed to be procedural blank: ^{206}Pb/^{204}Pb = 18.50 ± 1.0%; ^{207}Pb/^{204}Pb = 15.50 ± 1.0%; ^{208}Pb/^{204}Pb = 38.40 ± 1.0% (all uncertainties 1-sigma).

(f) Errors are 2-sigma, propagated using the algorithms of Schmitz and Schoene (2007) and Crowley et al. (2007).

(g) Calculations are based on the decay constants of Jaffey et al. (1971). ^{206}Pb/^{238}U and ^{207}Pb/^{206}Pb ages corrected for initial disequilibrium in ^{230}Th/^{238}U using Th/U [magma] = 3.

(h) Corrected for fractionation, spike, and blank Pb only.

(i) Nominal fraction weights estimated from photomicrographic grain dimensions, adjusted for partial dissolution during chemical abrasion.

(j) Nominal U and total Pb concentrations subject to uncertainty in photomicrographic estimation of weight and partial dissolution during chemical abrasion.

Table 4. U-Th-Pb analytical results for LDi07-7-5.

	Compositional Parameters									Radiogenic Isotope Ratios								Isotopic Ages					
Sample	Wt. mg	U ppm	Pb ppm	Th/U	^{206}Pb* x10^{-13} mol	mol % ^{206}Pb*	Pb*/Pb$_c$	Pb$_c$ (pg)	^{206}Pb/^{204}Pb	^{208}Pb/^{206}Pb	^{207}Pb/^{206}Pb	% err	^{207}Pb/^{235}U	% err	^{206}Pb/^{238}U	% err	corr. coef.	^{207}Pb/^{206}Pb	±	^{207}Pb/^{235}U	±	^{206}Pb/^{238}U	±
(a)	(i)	(j)	(j)	(b)	(c)	(c)	(c)	(c)	(d)	(e)	(e)	(f)	(e)	(f)	(e)	(f)		(g)	(f)	(g)	(f)	(g)	(f)
LDi07-7-5																							
C	0.0019	181	6.9	0.466	0.5049	98.52%	20	0.62	1250	0.148	0.050720	2.364	0.245740	2.494	0.035140	0.339	0.444	228.11	54.60	223.11	5.00	222.64	0.74
D	0.0036	103	3.8	0.400	0.5484	99.15%	34	0.39	2173	0.128	0.050830	1.010	0.247486	1.066	0.035312	0.195	0.371	233.15	23.30	224.53	2.15	223.71	0.43
E	0.0022	128	4.9	0.479	0.4126	98.40%	19	0.55	1155	0.151	0.050255	2.809	0.244098	2.930	0.035227	0.436	0.347	206.82	65.14	221.77	5.84	223.18	0.96
G	0.0027	54	2.2	0.413	0.2142	95.76%	7	0.78	435	0.131	0.050602	2.246	0.246105	2.396	0.035274	0.221	0.701	222.74	51.94	223.41	4.81	223.47	0.49
H	0.0016	104	4.1	0.356	0.2442	96.46%	8	0.74	521	0.115	0.051633	3.585	0.251093	3.786	0.035270	0.410	0.532	269.18	82.19	227.46	7.72	223.45	0.90

(a) A, B etc. are labels for fractions composed of single zircon grains or fragments; all fractions annealed and chemically abraded after Mattinson (2005) and Scoates and Friedman (2008).

(b) Model Th/U ratio calculated from radiogenic ^{208}Pb/^{206}Pb ratio and ^{207}Pb/^{235}U age.

(c) Pb* and Pbc represent radiogenic and common Pb, respectively; mol % ^{206}Pb* with respect to radiogenic, blank and initial common Pb.

(d) Measured ratio corrected for spike and fractionation only. Mass discrimination of 0.25%/amu based on analysis of NBS-982; all Daly analyses.

(e) Corrected for fractionation, spike, and common Pb; up to 0.78 pg of common Pb was assumed to be procedural blank: ^{206}Pb/^{204}Pb = 18.50 ± 1.0%; ^{207}Pb/^{204}Pb = 15.50 ± 1.0%; ^{208}Pb/^{204}Pb = 38.40 ± 1.0% (all uncertainties 1-sigma). Excess over blank was assigned to initial common Pb, using the Stacey and Kramers (1975) two-stage Pb isotope evolution model at 224 Ma.

(f) Errors are 2-sigma, propagated using the algorithms of Schmitz and Schoene (2007) and Crowley et al. (2007).

(g) Calculations are based on the decay constants of Jaffey et al. (1971). ^{206}Pb/^{238}U and ^{207}Pb/^{206}Pb ages corrected for initial disequilibrium in ^{230}Th/^{238}U using Th/U [magma] = 3.

(h) Corrected for fractionation, spike, and blank Pb only.

(i) Nominal fraction weights estimated from photomicrographic grain dimensions, adjusted for partial dissolution during chemical abrasion.

(j) Nominal U and total Pb concentrations subject to uncertainty in photomicrographic estimation of weight and partial dissolution during chemical abrasion.

Table 5. U-Th-Pb analytical results for LDi07-7-2.

	Compositional Parameters									Radiogenic Isotope Ratios								Isotopic Ages					
Sample	Wt. mg	U ppm	Pb ppm	Th/U	^{206}Pb* x10^{-13} mol	mol % ^{206}Pb*	Pb*/Pb$_c$	Pb$_c$ (pg)	^{206}Pb/^{204}Pb	^{208}Pb/^{206}Pb	^{207}Pb/^{206}Pb	% err	^{207}Pb/^{235}U	% err	^{206}Pb/^{238}U	% err	corr. coef.	^{207}Pb/^{206}Pb	±	^{207}Pb/^{235}U	±	^{206}Pb/^{238}U	±
(a)	(h)	(i)	(j)	(b)	(c)	(c)	(c)	(c)	(d)	(e)	(e)	(f)	(e)	(f)	(e)	(f)		(g)	(f)	(g)	(f)	(g)	(f)
LDi07-7-2																							
A	0.002	70	2.8	0.272	0.1669	96.33%	7	0.52	504	0.086	0.050145	1.554	0.245405	1.651	0.035494	0.191	0.551	201.73	36.07	222.84	3.30	224.84	0.42
E	0.001	343	12.5	0.274	0.4553	98.59%	20	0.54	1308	0.087	0.050436	0.737	0.246039	0.795	0.035381	0.128	0.516	215.12	17.06	223.35	1.59	224.14	0.28
H	0.001	102	4.2	0.234	0.1516	94.95%	5	0.66	367	0.073	0.049914	2.200	0.244417	2.337	0.035515	0.216	0.663	190.99	51.17	222.03	4.66	224.97	0.48
K	0.001	84	3.5	0.271	0.0992	94.51%	5	0.47	337	0.085	0.050094	2.922	0.244127	3.096	0.035345	0.330	0.567	199.35	67.85	221.79	6.17	223.92	0.73

(a) A, B etc. are labels for fractions composed of single zircon grains or fragments; all fractions annealed and chemically abraded after Mattinson (2005) and Scoates and Friedman (2008).

(b) Model Th/U ratio calculated from radiogenic ^{208}Pb/^{206}Pb ratio and ^{207}Pb/^{235}U age.

(c) Pb* and Pbc represent radiogenic and common Pb, respectively; mol % ^{206}Pb* with respect to radiogenic, blank and initial common Pb.

(d) Measured ratio corrected for spike and fractionation only. Mass discrimination of 0.25%/amu based on analysis of NBS-982; all Daly analyses.

(e) Corrected for fractionation, spike, and common Pb; all common Pb was assumed to be procedural blank: ^{206}Pb/^{204}Pb = 18.50 ± 1.0%; ^{207}Pb/^{204}Pb = 15.50 ± 1.0%; ^{208}Pb/^{204}Pb = 38.40 ± 1.0% (all uncertainties 1-sigma).

(f) Errors are 2-sigma, propagated using the algorithms of Schmitz and Schoene (2007) and Crowley et al. (2007).

(g) Calculations are based on the decay constants of Jaffey et al. (1971). ^{206}Pb/^{238}U and ^{207}Pb/^{206}Pb ages corrected for initial disequilibrium in ^{230}Th/^{238}U using Th/U [magma] = 3.

(h) Nominal fraction weights estimated from photomicrographic grain dimensions, adjusted for partial dissolution during chemical abrasion.

(i) Nominal U and total Pb concentrations subject to uncertainty in photomicrographic estimation of weight and partial dissolution during chemical abrasion.

Table 6. U-Th-Pb analytical results for LDi07-32-1.

	Compositional Parameters									Radiogenic Isotope Ratios								Isotopic Ages						
Sample	Wt. mg	U ppm	$\frac{Th}{U}$	Pb ppm	^{206}Pb* x10^{-13} mol	mol % ^{206}Pb*	$\frac{Pb*}{Pb_c}$	Pb$_c$ (pg)	$\frac{^{206}Pb}{^{204}Pb}$	$\frac{^{208}Pb}{^{206}Pb}$	$\frac{^{207}Pb}{^{206}Pb}$	% err	$\frac{^{207}Pb}{^{235}U}$	% err	$\frac{^{206}Pb}{^{238}U}$	% err	corr. coef.	$\frac{^{207}Pb}{^{206}Pb}$	±	$\frac{^{207}Pb}{^{235}U}$	±	$\frac{^{206}Pb}{^{238}U}$	±	% disc
(a)	(b)	(c)	(d)	(c)	(e)	(e)	(e)	(e)	(f)	(g)	(g)	(h)	(g)	(h)	(g)	(h)		(i)	(h)	(i)	(h)	(i)	(h)	
LDi07-32-1																								
B	0.004	288	0.289	10.9	1.5775	97.73%	12	3.01	817	0.092	0.050838	0.863	0.248552	0.948	0.035459	0.183	0.538	233.49	19.92	225.40	1.92	224.62	0.40	3.80
C	0.004	180	0.283	6.9	1.1712	97.02%	9	2.95	622	0.090	0.050784	1.120	0.248522	1.243	0.035493	0.367	0.466	231.04	25.86	225.38	2.51	224.83	0.81	2.68
D	0.004	343	0.307	13.1	1.7710	97.47%	11	3.78	730	0.097	0.050512	0.900	0.246597	1.008	0.035407	0.293	0.495	218.62	20.82	223.81	2.02	224.30	0.65	-2.60
E	0.003	163	0.286	6.4	0.7142	96.13%	7	2.36	478	0.092	0.051280	1.620	0.247682	1.747	0.035030	0.293	0.503	253.43	37.24	224.69	3.52	221.96	0.64	12.42
CA6	0.002	97	0.405	4.7	0.2845	90.44%	3	2.47	194	0.129	0.050834	3.544	0.247755	3.775	0.035348	0.256	0.908	233.31	81.79	224.75	7.61	223.93	0.56	4.02
CA7	0.002	79	0.280	4.4	0.2337	85.56%	2	3.24	128	0.087	0.049642	5.247	0.241829	5.564	0.035331	0.367	0.873	178.26	122.30	219.92	11.00	223.83	0.81	-25.57
CA8	0.002	92	0.288	4.8	0.2729	87.85%	2	3.10	152	0.092	0.051078	4.362	0.249684	4.635	0.035453	0.325	0.851	244.37	100.47	226.32	9.40	224.59	0.72	8.09
CA9	0.001	71	0.204	3.5	0.1039	88.52%	2	1.11	161	0.064	0.049968	4.477	0.243208	4.766	0.035301	0.320	0.910	193.51	104.07	221.04	9.47	223.64	0.70	-15.57
CA10	0.001	194	0.317	7.7	0.2868	96.45%	8	0.87	522	0.101	0.050934	1.290	0.248714	1.387	0.035416	0.164	0.628	237.83	29.75	225.53	2.81	224.35	0.36	5.67
CA11	0.001	89	0.222	5.1	0.1308	83.63%	1	2.11	113	0.072	0.051690	6.452	0.251251	6.856	0.035254	0.463	0.880	271.71	147.88	227.59	13.98	223.34	1.02	17.80
ET-A	0.003	151	0.301	6.5	0.6907	93.53%	4	3.93	285	0.096	0.051250	1.759	0.250724	1.887	0.035481	0.196	0.683	252.10	40.46	227.16	3.84	224.76	0.43	10.85
ET-B	0.007	85	0.301	3.3	0.8901	96.85%	9	2.38	588	0.096	0.050665	1.117	0.247798	1.210	0.035472	0.183	0.566	225.61	25.81	224.79	2.44	224.71	0.40	0.40

(a) A, B etc. are labels for fractions composed of single zircon grains or fragments; all fractions annealed and chemically abraded after Mattinson (2005).

(b) Nominal fraction weights estimated from photomicrographic grain dimensions, adjusted for partial dissolution during chemical abrasion.

(c) Nominal U and total Pb concentrations subject to uncertainty in photomicrographic estimation of weight and partial dissolution during chemical abrasion.

(d) Model Th/U ratio calculated from radiogenic ^{208}Pb/^{206}Pb ratio and ^{207}Pb/^{235}U age.

(e) Pb* and Pbc represent radiogenic and common Pb, respectively; mol % ^{206}Pb* with respect to radiogenic, blank and initial common Pb.

(f) Measured ratio corrected for spike and fractionation only.

Daly analyses, based on analysis of NBS-982.

(g) Corrected for fractionation, spike, and common Pb; up to 3 pg of common Pb was assumed to be procedural blank: ^{206}Pb/^{204}Pb = 18.50 ± 1.0%; ^{207}Pb/^{204}Pb = 15.50 ± 1.0%; ^{208}Pb/^{204}Pb = 38.40 ± 1.0% (all uncertainties 1-sigma). Excess over blank was assigned to initial common Pb with a Stacey-Kramers model composition at 224 Ma..

(h) Errors are 2-sigma, propagated using the algorithms of Schmitz and Schoene (2007) and Crowley et al. (2007).

(i) Calculations are based on the decay constants of Jaffey et al. (1971). ^{206}Pb/^{238}U and ^{207}Pb/^{206}Pb ages corrected for initial disequilibrium in ^{230}Th/^{238}U using Th/U [magma] = 3. (j) Corrected for fractionation, spike, and blank Pb only.

CA = single grains, chemically abraded; ET = weighted ^{206}Pb/^{238}U age (not included in CA); B - E = more than one grain analyzed, air abraded (not chemically abraded)

Table 7. U-Th-Pb analytical results for MMI14-50-2.

	Compositional Parameters									Radiogenic Isotope Ratios								Isotopic Ages					
Sample (a)	Wt. mg (i)	U ppm (j)	Pb ppm (j)	$\frac{Th}{U}$ (b)	$^{206}Pb^*$ x10^{-13} mol (c)	mol % $^{206}Pb^*$ (c)	$\frac{Pb^*}{Pb_c}$ (c)	Pb_c (pg) (c)	$\frac{^{206}Pb}{^{204}Pb}$ (d)	$\frac{^{208}Pb}{^{206}Pb}$ (e)	$\frac{^{207}Pb}{^{206}Pb}$ (e)	% err (f)	$\frac{^{207}Pb}{^{235}U}$ (e)	% err (f)	$\frac{^{206}Pb}{^{238}U}$ (e)	% err (f)	corr. coef.	$\frac{^{207}Pb}{^{206}Pb}$ (g)	± (f)	$\frac{^{207}Pb}{^{235}U}$ (g)	± (f)	$\frac{^{206}Pb}{^{238}U}$ (g)	± (f)
MMI14-50-2																							
A	0.0020	92	3.6	0.382	0.2619	96.34%	8	0.81	505	0.123	0.051014	1.689	0.241254	1.770	0.034299	0.191	0.469	241.45	38.92	219.45	3.49	217.40	0.41
B	0.0020	1220	47.7	0.730	3.5815	99.80%	164	0.58	9420	0.232	0.050662	0.127	0.245984	0.290	0.035214	0.213	0.917	225.50	2.93	223.31	0.58	223.10	0.47
C	0.0016	94	3.6	0.364	0.2220	97.80%	13	0.41	841	0.116	0.050688	0.807	0.246643	0.893	0.035291	0.169	0.576	226.67	18.65	223.85	1.79	223.58	0.37
E	0.0008	572	22.5	0.530	0.6720	98.06%	15	1.09	954	0.168	0.050557	0.636	0.245617	0.714	0.035235	0.149	0.601	220.67	14.70	223.01	1.43	223.23	0.33

(a) A, B etc. are labels for fractions composed of single zircon grains or fragments; all fractions annealed and chemically abraded after Mattinson (2005) and Scoates and Friedman (2008).

(b) Model Th/U ratio calculated from radiogenic $^{208}Pb/^{206}Pb$ ratio and $^{207}Pb/^{235}U$ age.

(c) Pb* and Pbc represent radiogenic and common Pb, respectively; mol % $^{206}Pb^*$ with respect to radiogenic, blank and initial common Pb.

(d) Measured ratio corrected for spike and fractionation only. Mass discrimination of 0.30% ± 0.05%/amu based on analysis of NBS-982; all Daly analyses.

(e) Corrected for fractionation, spike, and common Pb; up to 1 pg common Pb was assumed to be procedural blank: $^{206}Pb/^{204}Pb = 18.50\pm1.0\%$; $^{207}Pb/^{204}Pb = 15.50\pm1.0\%$; $^{208}Pb/^{204}Pb = 38.40\pm1.0\%$ (1σ errors). Excess over blank was assigned to initial common Pb, using the Stacey and Kramers (1975) two-stage Pb isotope evolution model at 223 Ma.

(f) Errors are 2-sigma, propagated using the algorithms of Schmitz and Schoene (2007) and Crowley et al. (2007).

(g) Calculations are based on the decay constants of Jaffey et al. (1971). $^{206}Pb/^{238}U$ and $^{207}Pb/^{206}Pb$ ages corrected for initial disequilibrium in $^{230}Th/^{238}U$ using Th/U [magma] = 3.

(h) Corrected for fractionation, spike, and blank Pb only.

(i) Nominal fraction weights estimated from photomicrographic grain dimensions, adjusted for partial dissolution during chemical abrasion.

(j) Nominal U and total Pb concentrations subject to uncertainty in photomicrographic estimation of weight and partial dissolution during chemical abrasion.

Table 8. Argon analytical results for LDi07-20-3.

Laser							*Isotope Ratios*							
Power(%)	*$^{40}Ar/^{39}Ar$*	2σ	*$^{36}Ar/^{39}Ar$*	2s	*$^{39}Ar/^{40}Ar$*	2σ	*$^{36}Ar/^{40}Ar$*	2σ	*Rho*	*K/Ca*	*%^{40}Ar rad*	*$f\,^{39}Ar$*	*$^{40}Ar^*/^{39}Ar$*	*K Age ± 2σ*
2.00	172.99	2.72	0.58	0.02	0.01	0.00	0.00	0.00	0.009	0.78	0.21	0.11	0.358	3.37 ± 43.42
2.30	27.56	0.34	0.07	0.00	0.04	0.00	0.00	0.00	0.002	2.09	22.54	0.76	6.214	57.61 ± 6.98
2.60	23.49	0.15	0.02	0.00	0.04	0.00	0.00	0.00	0.007	10.66	79.54	6.32	18.687	167.97 ± 1.71
2.90	23.50	0.15	0.00	0.00	0.04	0.00	0.00	0.00	0.001	25.02	95.70	12.09	22.487	200.30 ± 1.23
3.10	24.20	0.13	0.00	0.00	0.04	0.00	0.00	0.00	0.002	31.99	97.35	10.11	23.561	209.33 ± 1.51
3.20	24.31	0.16	0.00	0.00	0.04	0.00	0.00	0.00	0.000	30.25	96.84	9.37	23.546	209.20 ± 1.83
3.30	24.59	0.13	0.00	0.00	0.04	0.00	0.00	0.00	0.001	24.18	96.03	3.61	23.614	209.78 ± 2.95
3.40	24.47	0.12	0.00	0.00	0.04	0.00	0.00	0.00	0.001	24.82	97.22	7.19	23.787	211.22 ± 1.52
3.50	24.45	0.11	0.00	0.00	0.04	0.00	0.00	0.00	0.000	20.49	97.08	6.84	23.734	210.78 ± 2.08
3.60	24.45	0.10	0.00	0.00	0.04	0.00	0.00	0.00	0.001	17.92	97.24	5.47	23.777	211.14 ± 1.79
3.80	24.09	0.15	0.00	0.00	0.04	0.00	0.00	0.00	0.000	15.76	98.03	12.67	23.613	209.76 ± 1.80
4.00	24.12	0.16	0.00	0.00	0.04	0.00	0.00	0.00	0.000	12.76	98.26	6.81	23.698	210.47 ± 1.56
4.30	24.03	0.16	0.00	0.00	0.04	0.00	0.00	0.00	0.000	11.77	98.44	9.45	23.655	210.12 ± 1.44
4.60	23.91	0.15	0.00	0.00	0.04	0.00	0.00	0.00	0.000	10.63	99.14	9.20	23.703	210.52 ± 1.37

Analysis by Janet Gabites, Pacific Centre for Isotopic and Geochemical Research

1. J = 0.00522800 ± 0.00000784 Volume 39A 1.779 x E-13 cm3 NPT
2. Integrated Date = 204.98 ± 0.47 Ma

Plateau age = 210.27 ± 0.68 Ma(2s, including J-error of . MSWD = 0.70, probability=0.71 Includes 80.7% of the 3steps 5 through 14

Inverse isochron (correlation age) results, plateau steps: Model 1 Solution (±95%-conf.) on 10 points

07LDI-20.3 Biotite age = 210.5 ± 1.3 Ma Initial $^{40}Ar/^{36}Ar$ =441 ± 120 MSWD = 1.4 Probability = 0.19

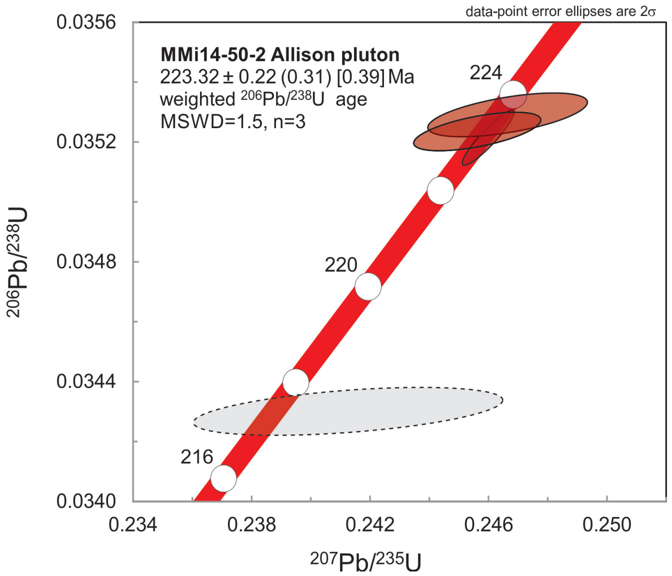

Fig 14. U -Pb concordia diagram showing TIMS zircon U-Pb age results from sample MMI14-50-2 of the Allison pluton. Weighted age 223.32 ±0.22 Ma based on ^{206}Pb/^{238}U ages of 4 grains. Concordia bands include 2σ errors of U decay constants.

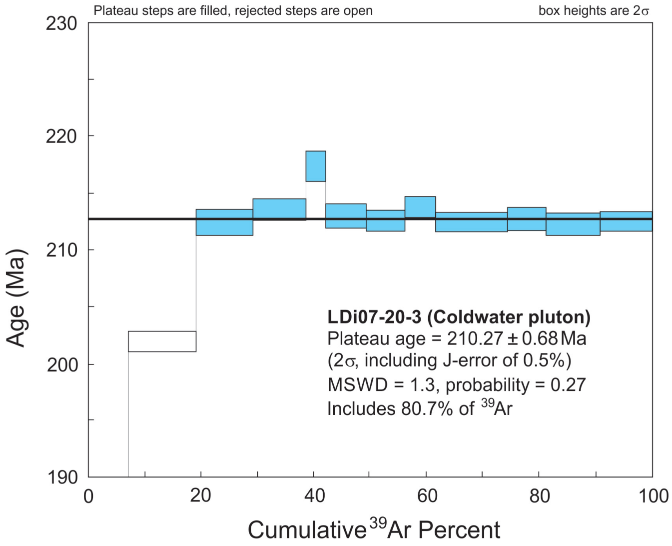

Fig. 15. ^{40}Ar/^{39}Ar step heating gas release spectra from sample LDi07-20-3, a biotite separate from quartz-diorite near the centre of the Coldwater pluton. A plateau age of 210.27 ±0.68 Ma dates crystallization of the pluton and time of emplacement into upper stratified rocks of the Western belt.

but no good bedding or sedimentary sorting could be detected.

Based on a weighted mean ^{206}Pb/^{238}U date for 5 concordant and overlapping single zircon grains, the Zig andesite is 202.3 ±0.3 Ma (Fig. 16, Table 9), considerably younger than the 215 Ma Re-Os chalcocite age. Three explanations should be considered: 1) the unit spans an age of nearly 13 m.y.; 2) one of the ages is in error; or 3) Zig unit has been reworked and mixed with a younger tuffaceous component which included the most attractive zircons for analysis. While we consider the third option as the most likely, U-Pb analysis of the Zig unit at NOR30, and a analysis of a broader selection of zircon morphologies from sample MMI14-62-4 will be required to resolve this problem.

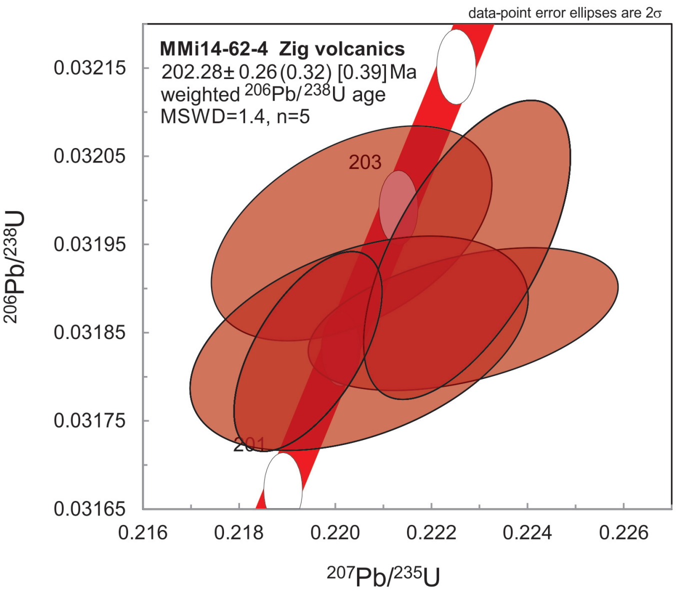

Fig. 16. U-Pb concordia diagram showing TIMS zircon U-Pb age results from sample MMI14-62-4, sparsely quartz-phyric andesite tuff, correlated with host rocks near the Zig (NOR 30) mineral prospect. Weighted age 202.3 ±0.3 Ma based on ^{206}Pb/^{238}U ages of 5 grains. Concordia bands include 2σ errors of U decay constants.

3.2.1.9. Sample MMI14-19-3 (U12), western Pennask batholith, gabbro from border phase; 193.1 ±0.2 Ma

Interior portions of the Pennask batholith tend to be homogeneous and isotropic, white-weathering, medium- to coarse-grained hornblende-biotite granodiorite to tonalite (see descriptions in Mihalynuk et al., 2015). However, near its southwest margin, the batholith is highly variable in composition, ranging from granodiorite to varitextured, locally pegmatitic, hornblende gabbro (Fig. 17).

The gabbro contains 30-70% hornblende, with intragranular plagioclase comprising most of the remainder of the rock. In places, plagioclase is intergrown with pink perthitic K-feldspar; both have been moderately to strongly epidote altered. Fine- to medium-grained magnetite comprises ~10%, and also comprises ~80% of centimeter-thick bands. Fine-grained biotite occurs as scattered booklets and glomerocrysts (<~2%). Trace titanite is fine to medium grained. Irregular voids up to 5cm across may be miarolitic cavities or possibly dissolved mineral matter. Locally, the gabbro contains up to a few percent pyrite and traces chalcopyrite. Because some biotite and K-feldspar textures could have been produced by potassic alteration, and sulphides are locally conspicuous, we sampled the gabbro to test if isolated outcrops interpreted as Pennask border phase might be part of the Copper Mountain suite (Late Triassic), which has considerably higher mineral potential.

Mineralized gabbro sample MMI14-19-3 yielded both abundant zircon and titanite. Three zircon grains analyzed

Fig. 17. Representative outcrop of varitextured hornblende gabbro of the Pennask batholith border phase near geochronology sample site MMI14-19-3.

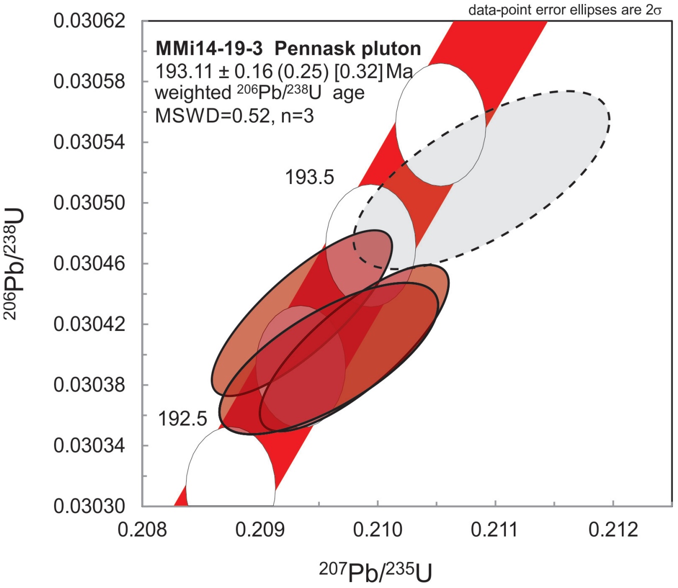

Fig. 18. U-Pb concordia diagram showing TIMS zircon (shaded) and titanite age results from sample MMI14-19-3 of undeformed Pennask batholith. Weighted age 193.1 ±0.2 Ma based on ^{206}Pb/^{238}U ages of 3 zircon grains. TIMS titanite age results are slightly younger than zircon age results. Concordia bands include 2σ errors of U decay constants.

overlap concordia at 193.11 ±0.16 Ma. Titanite from the same sample are slightly younger with a weighted ^{206}Pb/^{238}U date for 4 overlapping and concordant fractions yielding 192.9 ±0.4 Ma (Fig. 18, Table 10). This age couple is consistent with rapid cooling following crystallization.

These new Early Jurassic ages confirm assignment of the border rocks to the Pennask batholith (Mihalynuk et al., 2015) and are the same as previous crystallization ages farther northeast (194 ±1 Ma; Parrish and Monger, 1992).

3.2.1.10. MMI14-59-12 (U13), post-Nicola rhyolite 'Osprey volcanic unit'; 163.2 ±0.2 Ma

In the study area north of Princeton, grey porphyritic granodiorite intrudes andesite breccia and flow banded rhyolite that strongly resembles the Pimanus Formation of the Spences Bridge Group (Early Cretaceous). Mihalynuk and Logan (2014a) included this porphyritic granodiorite with the Summers Creek suite of intrusions, thought to be ~99 Ma (K-Ar cooling ages of Preto, 1979; recalculated in Breitsprecher and Mortensen, 2005). However, zircons extracted from the intrusion overlap concordia between 160 Ma and 164 Ma (see Osprey Lake batholith: Sample MMI 13-4-8, Mihalynuk et al., 2015) indicating that the volcanic package is Late Jurassic or older. To test for an inherited component we analyzed the central and perimeter zones of ten zircons by laser ablation (LA-ICPMS). These analyses confirmed the TIMS results, with a weighted age for 9 of the 10 zircons at 162 ±2 Ma. The youngest concordant grain gave a ^{206}Pb/^{238}U age of 160.67 ±0.21 Ma, which we take as a maximum crystallization age for the intrusion, given that the grains were chemically abraded.

Sample MMI14-59-12 was collected from the rhyolite unit as far from the intrusive contact as possible without losing outcrop continuity (Fig. 2). Five zircon grains gave results that overlap concordia to give a weighted ^{206}Pb/^{238}U age of 163.22 ±0.15 Ma (Fig. 19, Table 11). Not only is this age consistent with the geological requirement that it be older than

Table 9. U-Th-Pb analytical results for MMI14-62-4.

	Compositional Parameters									Radiogenic Isotope Ratios								Isotopic Ages					
Sample	Wt. mg	U ppm	Pb ppm	$\frac{Th}{U}$	^{206}Pb* x10^{-13} mol	mol % ^{206}Pb*	$\frac{Pb^*}{Pb_c}$	Pb$_c$ (pg)	$\frac{^{206}Pb}{^{204}Pb}$	$\frac{^{208}Pb}{^{206}Pb}$	$\frac{^{207}Pb}{^{206}Pb}$	% err	$\frac{^{207}Pb}{^{235}U}$	% err	$\frac{^{206}Pb}{^{238}U}$	% err	corr. coef.	$\frac{^{207}Pb}{^{206}Pb}$	±	$\frac{^{207}Pb}{^{235}U}$	±	$\frac{^{206}Pb}{^{238}U}$	±
(a)	(i)	(j)	(j)	(b)	(c)	(c)	(c)	(c)	(d)	(e)	(e)	(f)	(e)	(f)	(e)	(f)		(g)	(f)	(g)	(f)	(g)	(f)
MMI14-62-4																							
A	0.0115	39	1.4	0.394	0.5933	97.64%	12	1.18	782	0.124	0.049774	0.926	0.219353	1.036	0.031962	0.312	0.482	184.45	21.57	201.37	1.89	202.82	0.62
B	0.0056	56	2.1	0.452	0.4172	95.99%	7	1.44	460	0.144	0.050361	1.010	0.221264	1.096	0.031865	0.208	0.495	211.69	23.39	202.96	2.02	202.21	0.41
C	0.0071	53	2.3	0.321	0.4972	90.75%	3	4.18	199	0.102	0.049962	1.146	0.219324	1.250	0.031838	0.312	0.445	193.24	26.64	201.35	2.28	202.04	0.62
D	0.0057	94	3.2	0.389	0.7173	98.45%	19	0.93	1191	0.124	0.050401	0.571	0.221985	0.752	0.031944	0.434	0.655	213.51	13.22	203.56	1.39	202.70	0.87
E	0.0039	194	6.6	0.432	1.0042	98.77%	24	1.03	1501	0.137	0.050000	0.462	0.219425	0.573	0.031828	0.291	0.599	194.99	10.73	201.43	1.05	201.98	0.58

(a) A, B etc. are labels for fractions composed of single zircon grains or fragments; all fractions annealed and chemically abraded after Mattinson (2005) and Scoates and Friedman (2008).

(b) Model Th/U ratio calculated from radiogenic ^{208}Pb/^{206}Pb ratio and ^{207}Pb/^{235}U age.

(c) Pb* and Pbc represent radiogenic and common Pb, respectively; mol % ^{206}Pb* with respect to radiogenic, blank and initial common Pb.

(d) Measured ratio corrected for spike and fractionation only. Mass discrimination of 0.30% ± 0.05%/amu based on analysis of NBS-982; all Daly analyses.

(e) Corrected for fractionation, spike, and common Pb; up to 1 pg common Pb was assumed to be procedural blank: ^{206}Pb/^{204}Pb = 18.50±1.0%; ^{207}Pb/^{204}Pb = 15.50±1.0%; ^{208}Pb/^{204}Pb = 38.40±1.0% (1σ errors). Excess over blank was assigned to initial common Pb, using the Stacey and Kramers (1975) two-stage Pb isotope evolution model at 202 Ma.

(f) Errors are 2-sigma, propagated using the algorithms of Schmitz and Schoene (2007) and Crowley et al. (2007).

(g) Calculations are based on the decay constants of Jaffey et al. (1971). ^{206}Pb/^{238}U and ^{207}Pb/^{206}Pb ages corrected for initial disequilibrium in ^{230}Th/^{238}U using Th/U [magma] = 3.

(h) Corrected for fractionation, spike, and blank Pb only.

(i) Nominal fraction weights estimated from photomicrographic grain dimensions, adjusted for partial dissolution during chemical abrasion.

(j) Nominal U and total Pb concentrations subject to uncertainty in photomicrographic estimation of weight and partial dissolution during chemical abrasion.

Table 10. U-Th-Pb analytical results for MMI14-19-3.

	Compositional Parameters									Radiogenic Isotope Ratios								Isotopic Ages					
Sample	Wt. mg	U ppm	Pb ppm	$\frac{Th}{U}$	^{206}Pb* x10^{-13} mol	mol % ^{206}Pb*	$\frac{Pb^*}{Pb_c}$	Pb$_c$ (pg)	$\frac{^{206}Pb}{^{204}Pb}$	$\frac{^{208}Pb}{^{206}Pb}$	$\frac{^{207}Pb}{^{206}Pb}$	% err	$\frac{^{207}Pb}{^{235}U}$	% err	$\frac{^{206}Pb}{^{238}U}$	% err	corr. coef.	$\frac{^{207}Pb}{^{206}Pb}$	±	$\frac{^{207}Pb}{^{235}U}$	±	$\frac{^{206}Pb}{^{238}U}$	±
(a)	(i)	(j)	(j)	(b)	(c)	(c)	(c)	(c)	(d)	(e)	(e)	(f)	(e)	(f)	(e)	(f)		(g)	(f)	(g)	(f)	(g)	(f)
MMI14-19-3																							
B	0.0040	465	15.4	0.619	2.3578	99.52%	65	0.94	3842	0.197	0.049902	0.200	0.209352	0.299	0.030427	0.147	0.807	190.42	4.66	193.01	0.53	193.22	0.28
C	0.0025	603	20.4	0.693	1.9114	99.50%	63	0.79	3677	0.221	0.050046	0.217	0.209797	0.313	0.030404	0.148	0.784	197.12	5.05	193.38	0.55	193.08	0.28
D	0.0029	282	9.3	0.550	1.0388	99.20%	38	0.69	2314	0.175	0.050121	0.337	0.210879	0.421	0.030515	0.157	0.671	200.60	7.81	194.29	0.75	193.77	0.30
E	0.0025	343	11.4	0.608	1.0866	99.42%	53	0.53	3182	0.194	0.050005	0.284	0.209580	0.363	0.030397	0.134	0.705	195.24	6.60	193.20	0.64	193.03	0.26
T2	0.0413	18	1.4	1.590	0.9370	73.06%	1	28.46	68	0.508	0.050200	3.736	0.209424	3.862	0.030257	0.540	0.298	204.27	86.69	193.07	6.79	192.15	1.02
T3	0.0522	39	2.3	1.411	2.5914	84.47%	2	39.26	119	0.447	0.049762	1.650	0.208185	1.743	0.030342	0.302	0.384	183.91	38.43	192.03	3.05	192.69	0.57
T4	0.0370	50	3.2	1.377	2.3583	80.91%	2	45.88	96	0.439	0.050124	1.921	0.210606	2.014	0.030473	0.378	0.335	200.77	44.60	194.06	3.56	193.51	0.72
T5	0.0435	17	1.7	2.425	0.9474	66.70%	1	38.99	55	0.773	0.050040	4.304	0.209310	4.433	0.030337	0.742	0.254	196.84	100.01	192.97	7.79	192.66	1.41

(a) A, B etc. are labels for fractions composed of single zircon grains or fragments; all fractions annealed and chemically abraded after Mattinson (2005) and Scoates and Friedman (2008).

(b) Model Th/U ratio calculated from radiogenic ^{208}Pb/^{206}Pb ratio and ^{207}Pb/^{235}U age.

(c) Pb* and Pbc represent radiogenic and common Pb, respectively; mol % ^{206}Pb* with respect to radiogenic, blank and initial common Pb.

(d) Measured ratio corrected for spike and fractionation only. Mass discrimination of 0.30% ± 0.05%/amu based on analysis of NBS-982; all Daly analyses.

(e) Corrected for fractionation, spike, and common Pb; up to 1 pg common Pb was assumed to be procedural blank: ^{206}Pb/^{204}Pb = 18.50±1.0%; ^{207}Pb/^{204}Pb = 15.50±1.0%; ^{208}Pb/^{204}Pb = 38.40±1.0% (1σ errors). Excess over blank was assigned to initial common Pb, using the Stacey and Kramers (1975) two-stage Pb isotope evolution model at 193 Ma.

(f) Errors are 2-sigma, propagated using the algorithms of Schmitz and Schoene (2007) and Crowley et al. (2007).

(g) Calculations are based on the decay constants of Jaffey et al. (1971). ^{206}Pb/^{238}U and ^{207}Pb/^{206}Pb ages corrected for initial disequilibrium in ^{230}Th/^{238}U using Th/U [magma] = 3.

(h) Corrected for fractionation, spike, and blank Pb only.

(i) Nominal fraction weights estimated from photomicrographic grain dimensions, adjusted for partial dissolution during chemical abrasion.

(j) Nominal U and total Pb concentrations subject to uncertainty in photomicrographic estimation of weight and partial dissolution during chemical abrasion.

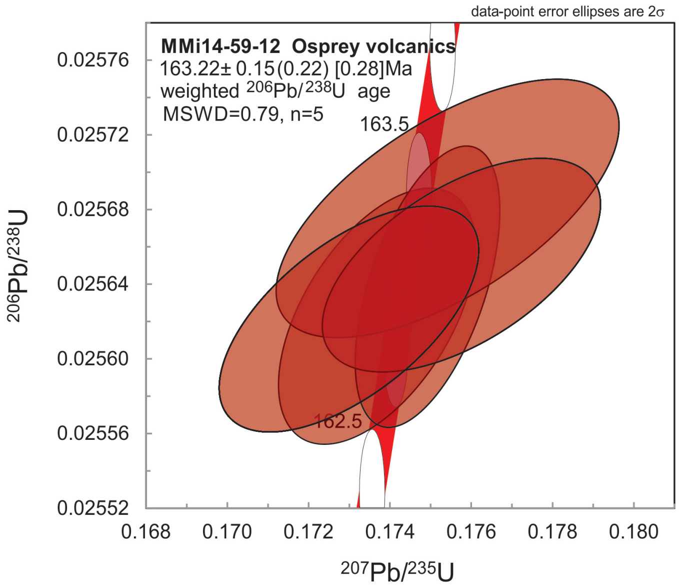

Fig. 19. U-Pb concordia diagram showing TIMS zircon U-Pb age results from sample MMI14-59-12, from rhyolite in a newly-defined volcanic unit, comagmatic with the Osprey batholith. Weighted age 163.2 ±0.2 Ma based on $^{206}Pb/^{238}U$ ages of 5 grains. Concordia bands include 2σ errors of U decay constants.

the crosscutting 162 ±2 Ma (or 160.7 ±0.2 Ma based on the youngest concordant grain) granodiorite, but it strongly hints of an intrusion that cuts its comagmatic volcanic carapice. This is the first example of demonstrable Late Jurassic volcanic rocks presumably overlying older Nicola arc strata in the study area.

We include the granodiorite with the Osprey Lake batholith; a younger phase than the most widespread and distinctive K-feldspar megacrystic granite phase dated at 166 ±1 Ma (U-Pb zircon; Parrish and Monger, 1992). We introduce the informal name 'Osprey volcanic unit' for the comagmatic andesite and rhyolite rocks cross cut by the batholith which, despite a lithologic similarity, are unrelated to the Pimanus Formation.

3.2.1.11. Sample MMI14-53-2 (U14), Snowstorm quartz-feldspar porphyry; 53.36 ±0.07 Ma

Base metal sulphide vein mineralization at the Snowstorm prospect is developed in yellow and rust-weathering, coarse quartz-eye feldspar porphyry of the 'Otter intrusions'. Disseminated fine cubes of pyrite (~1-2%) are widespread and clay-alteration is pervasive. Where least altered, phenocrysts of orthoclase (up to 1 cm across and 15-20%) and hornblende (medium to coarse-grained, up to 15%) are are visible but largely replaced by clay minerals and chlorite-?pyrophyllite. Coarse quartz phenocrysts (~25%) are little affected by alteration.

Limited production of gold, silver and lead from tracked adits at the Snowstorm property date from 1917 to 1927 (Groves, 1989). At least two adits were drifted along mineralized zones. Analysis of mineralized quartz stockwork veining revealed >1% zinc and, in one grab sample, 22.7 ppm indium (Mihalynuk et al., 2015). Although the mineralization has been classified as shear-related veining (MINFILE 092HNE032), open space quartz stockworks and shallow intrusive host rocks are more consistent with intrusion-related vein mineralization. If related to the quartz-eye feldspar porphyry host intrusion, a crystallization age would provide an approximate age for mineralization (or maximum age for shear-related veining). Sample MMI14-53-2, collected at creek level and upstream of the two major adits, returned a U-Pb zircon crystallization age of 53.36 ±0.07 Ma from three grains that overlap concordia (Fig. 20, Table 12). The age is consistent with K-Ar cooling ages from other quartz-feldspar porphyry dikes and stocks that cluster ~53 Ma, including some associated with gold mineralization at the Siwash mine (Armstrong and Petö, 1981 and Hunt and Roddick, 1990; recalculated in Breitsprecher and Mortensen, 2005).

3.2.2. LA-ICPMS detrital zircon ages

3.2.2.1. Sample MMI14-23-15 (D9), Nicola Group, Central belt, Ketcham rhyolite sharpstone conglomerate (<239 Ma, possibly <227 Ma)

Between Missezula Lake and Missezula Mountain (Fig. 2), well-bedded sandstone, conglomerate (containing angular clasts of aphanitic to feldspar- and quartz-phyric rhyolite, Fig. 21), and lesser argillite up to tens of metres thick, are interlayered with reworked ash and lesser lapilli tuff. Because felsic rocks are atypical of the Central belt, Mihalynuk et al. (2014) speculated on possible correlatives including the Skwel Pecken Formation (Early to Middle Jurassic) as defined near Hedley (Ray and Dawson, 1994) or a lithologically similar Nicola unit at Coalmont.

A sample was collected from the north of the Ketchan copper

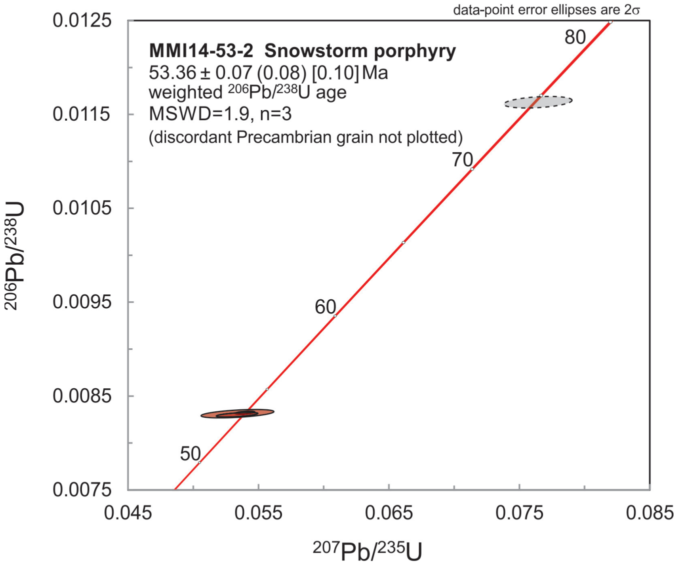

Fig. 20. U-Pb concordia diagram showing TIMS zircon U-Pb age results from sample MMI14-53-2, altered quartz-feldspar porphyry intrusion at the old Snowstorm mine. Weighted age 53.36 ±0.07 Ma based on $^{206}Pb/^{238}U$ ages of 3 grains. Concordia bands include 2σ errors of U decay constants.

Table 11. U-Th-Pb analytical results for MMI14-59-12 Osprey.

		Compositional Parameters								Radiogenic Isotope Ratios								Isotopic Ages					
Sample	Wt. mg	U ppm	Pb ppm	Th/U	^{206}Pb* x10^{-13} mol	mol % ^{206}Pb*	Pb*/Pb$_c$	Pb$_c$ (pg)	^{206}Pb/^{204}Pb	^{208}Pb/^{206}Pb	^{207}Pb/^{206}Pb	% err	^{207}Pb/^{235}U	% err	^{206}Pb/^{238}U	% err	corr. coef.	^{207}Pb/^{206}Pb	±	^{207}Pb/^{235}U	±	^{206}Pb/^{238}U	±
(a)	(i)	(j)	(j)	(b)	(c)	(c)	(c)	(c)	(d)	(e)	(e)	(f)	(e)	(f)	(e)	(f)		(g)	(f)	(g)	(f)	(g)	(f)
MMI14-59-12																							
A	0.0020	157	4.3	0.293	0.3351	97.25%	10	0.78	673	0.093	0.049160	1.041	0.173675	1.141	0.025623	0.219	0.535	155.47	24.36	162.60	1.71	163.09	0.35
B	0.0021	159	4.3	0.359	0.3562	98.10%	15	0.57	975	0.115	0.049481	0.730	0.174918	0.831	0.025639	0.240	0.539	170.69	17.05	163.68	1.26	163.19	0.39
C	0.0013	129	3.8	0.257	0.1789	94.91%	5	0.79	363	0.082	0.049539	1.832	0.175411	1.966	0.025681	0.221	0.640	173.44	42.75	164.10	2.98	163.46	0.36
D	0.0015	168	5.0	0.440	0.2691	96.42%	8	0.83	517	0.141	0.049694	1.495	0.175752	1.592	0.025650	0.183	0.570	180.73	34.84	164.40	2.42	163.27	0.29
E	0.0015	162	4.5	0.285	0.2602	96.96%	9	0.67	608	0.090	0.048967	1.399	0.172982	1.508	0.025621	0.193	0.609	146.24	32.80	162.00	2.26	163.08	0.31

(a) A, B etc. are labels for fractions composed of single zircon grains or fragments; all fractions annealed and chemically abraded after Mattinson (2005) and Scoates and Friedman (2008).
(b) Model Th/U ratio calculated from radiogenic ^{208}Pb/^{206}Pb ratio and ^{207}Pb/^{235}U age.
(c) Pb* and Pbc represent radiogenic and common Pb, respectively; mol % ^{206}Pb* with respect to radiogenic, blank and initial common Pb.
(d) Measured ratio corrected for spike and fractionation only. Mass discrimination of 0.30% ± 0.05%/amu based on analysis of NBS-982; all Daly analyses.
(e) Corrected for fractionation, spike, and common Pb; up to 1 pg common Pb was assumed to be procedural blank: ^{206}Pb/^{204}Pb = 18.50±1.0%; ^{207}Pb/^{204}Pb = 15.50±1.0%; ^{208}Pb/^{204}Pb = 38.40±1.0% (1σ errors).
Excess over blank was assigned to initial common Pb, using the Stacey and Kramers (1975) two-stage Pb isotope evolution model at 163 Ma.
(f) Errors are 2-sigma, propagated using the algorithms of Schmitz and Schoene (2007) and Crowley et al. (2007).
(g) Calculations are based on the decay constants of Jaffey et al. (1971). ^{206}Pb/^{238}U and ^{207}Pb/^{206}Pb ages corrected for initial disequilibrium in ^{230}Th/^{238}U using Th/U [magma] = 3.
(h) Corrected for fractionation, spike, and blank Pb only.
(i) Nominal fraction weights estimated from photomicrographic grain dimensions, adjusted for partial dissolution during chemical abrasion.
(j) Nominal U and total Pb concentrations subject to uncertainty in photomicrographic estimation of weight and partial dissolution during chemical abrasion.

Table 12. U-Th-Pb analytical results for MMI14-54-4 Snowstorm.

		Compositional Parameters								Radiogenic Isotope Ratios								Isotopic Ages					
Sample	Wt. mg	U ppm	Pb ppm	Th/U	^{206}Pb* x10^{-13} mol	mol % ^{206}Pb*	Pb*/Pb$_c$	Pb$_c$ (pg)	^{206}Pb/^{204}Pb	^{208}Pb/^{206}Pb	^{207}Pb/^{206}Pb	% err	^{207}Pb/^{235}U	% err	^{206}Pb/^{238}U	% err	corr. coef.	^{207}Pb/^{206}Pb	±	^{207}Pb/^{235}U	±	^{206}Pb/^{238}U	±
(a)	(i)	(j)	(j)	(b)	(c)	(c)	(c)	(c)	(d)	(e)	(e)	(f)	(e)	(f)	(e)	(f)		(g)	(f)	(g)	(f)	(g)	(f)
MMI14-54-4																							
A	0.0034	287	53.5	0.138	7.5852	99.91%	318	0.57	20246	0.051	0.107700	0.083	2.763932	0.173	0.186127	0.127	0.890	1760.87	1.52	1345.85	1.29	1100.36	1.28
B	0.0033	682	8.2	0.352	1.0909	99.09%	32	0.82	2039	0.113	0.047651	2.678	0.076419	2.793	0.011631	0.432	0.339	81.98	63.52	74.77	2.01	74.55	0.32
C	0.0021	224	2.4	0.855	0.1625	95.59%	7	0.62	420	0.272	0.046600	4.073	0.053378	4.272	0.008308	0.442	0.491	28.79	97.59	52.80	2.20	53.33	0.23
D	0.0025	492	4.6	0.586	0.4260	97.90%	14	0.75	883	0.188	0.047044	1.075	0.053959	1.136	0.008319	0.153	0.456	51.46	25.64	53.36	0.59	53.40	0.08
E	0.0038	239	2.3	0.561	0.3137	97.01%	10	0.80	618	0.178	0.046639	2.305	0.053349	2.436	0.008296	0.241	0.582	30.79	55.19	52.77	1.25	53.26	0.13

(a) A, B etc. are labels for fractions composed of single zircon grains or fragments; all fractions annealed and chemically abraded after Mattinson (2005) and Scoates and Friedman (2008).
(b) Model Th/U ratio calculated from radiogenic ^{208}Pb/^{206}Pb ratio and ^{207}Pb/^{235}U age.
(c) Pb* and Pbc represent radiogenic and common Pb, respectively; mol % ^{206}Pb* with respect to radiogenic, blank and initial common Pb.
(d) Measured ratio corrected for spike and fractionation only. Mass discrimination of 0.30% ± 0.05%/amu based on analysis of NBS-982; all Daly analyses.
(e) Corrected for fractionation, spike, and common Pb; up to 1 pg common Pb was assumed to be procedural blank: ^{206}Pb/^{204}Pb = 18.50±1.0%; ^{207}Pb/^{204}Pb = 15.50±1.0%; ^{208}Pb/^{204}Pb = 38.40±1.0% (1σ errors).
Excess over blank was assigned to initial common Pb, using the Stacey and Kramers (1975) two-stage Pb isotope evolution model at 53 Ma.
(f) Errors are 2-sigma, propagated using the algorithms of Schmitz and Schoene (2007) and Crowley et al. (2007).
(g) Calculations are based on the decay constants of Jaffey et al. (1971). ^{206}Pb/^{238}U and ^{207}Pb/^{206}Pb ages corrected for initial disequilibrium in ^{230}Th/^{238}U using Th/U [magma] = 3.
(h) Corrected for fractionation, spike, and blank Pb only.
(i) Nominal fraction weights estimated from photomicrographic grain dimensions, adjusted for partial dissolution during chemical abrasion.
(j) Nominal U and total Pb concentrations subject to uncertainty in photomicrographic estimation of weight and partial dissolution during chemical abrasion.

Fig. 21. Ketcham conglomerate adjacent to the Ketcham stock, with angular to subrounded clasts of aphanitic to feldspar- and quartz-phyric rhyolite (altered with epidote and chlorite). These conglomerates are some of the oldest dated rocks in the Nicola Group.

porphyry prospect, selecting from the coarsest, quartz-rich sandstone matrix (note that the Ketchan prospect is near Ketchan Creek and Ketcham Lake, we used these geographic places to name for the important conglomeratic unit). Zircons recovered were very fine-grained, but 56 grains were sufficiently large that a 15mm spot size could be analyzed. Zircons dated have a distribution peak at 239 Ma, with a sparse older population at ~255 Ma and a younger shoulder to the age distribution at ~227 Ma (Fig. 22). One orphan grain gave a $^{206}Pb/^{238}U$ age of 217 ±8.5 Ma, but a significantly different $^{207}Pb/^{235}U$ age of 256 ±20 Ma (see Friedman et al., 2016). Given this analytical variability, the fine grain size, and proximity of the cross-cutting Ketchan diorite body, there is a real possibly of post-depositional lead-loss causing an erroneously young age. We consider ~227 Ma the likely maximun age of the sandstone matrix, and that it was mainly sourced from felsic bodies formed at ~239 Ma, such as the 238.15 ±0.33 Ma rhyolite tuff from nearby Missezula Mountain (sample MMI13-30-4, Mihalynuk et al., 2015; Fig. 2) and coeval rhyolite tuffite at Coalmont (238.6 ±0.3 Ma, sample MMI14-53-13, see above).

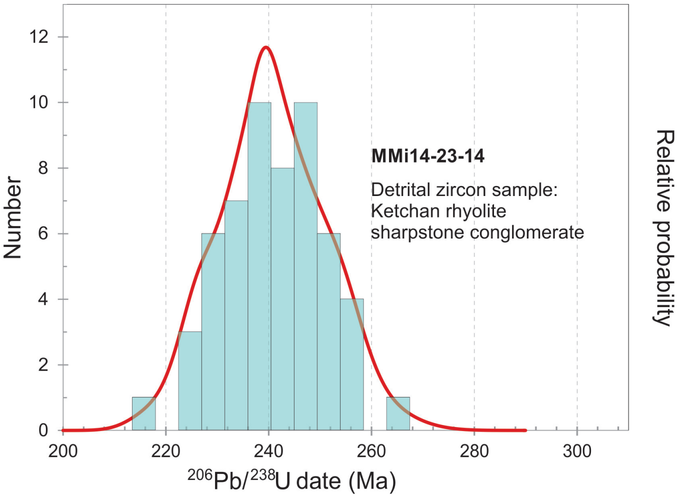

Fig. 22. Probability density plot for sample MMI14-23-15, Ketcham rhyolite clast-bearing conglomerate. A conservative maximum depositional age can be interpreted from the peak shoulder as ~227 Ma, from a protolith that is mainly ~239 Ma, but may range to 255 Ma.

3.2.2.2. Sample LDI14-60-3 (D10), Nicola Group, Central belt, Voght sandstone, Harmon succession <220 Ma, probably <213 Ma

Sample LDI14-60-3 is an oxidized reddish brown sandstone with granulestone layers (Fig. 23) that encloses, and is interbedded with, the Voght unit flows (Mihalynuk et al., 2015) positioned between an underlying basal polymictic conglomerate unit (Harmon conglomerate), and an overlying sequence of distinctive bladed basalt flows Figs. 2, 3). Assuming consistent bed orientation, about 150m of covered section separates the sample site from the lowest coarse bladed feldspar porphyry flow which, together with interbedded maroon sandstone, characterize the Voght unit.

We previously correlated the Voght sandstone with other exposures of maroon sandstone and matrix-supported polymictic

Fig. 23. Maroon sandstone and granule conglomerate sampled for detrital zircons from an interval between conglomerate at the base of the Harmon succession and overlying coarsely bladed plagioclase porphyritic basalt in the Voght unit.

conglomerate ~3 km along strike to the northeast near Corbett Lake (sample 12JLO51-4), and ~8 km across strike to the east (sample MMI13-16-5; Mihalynuk et al., 2015). These were correlated with the upper and lower parts of the Voght unit. Only twenty zircons were recovered and analyzed from each sample, but they fell into strong populations with maximum depositional ages of 208 ±4 Ma and 202 ±4 Ma. Consistency of the younger age with a cross-cutting dike dated at 201 +0.3/-0.4 Ma (Mihalynuk et al., 2015) supports the interpreted age of the top of the section of ~202 Ma. Our expectation was that dating zircons from the base of the Voght flows would help constrain the flow age and confirm correlation with strata to the north.

Sixty-five grains were analyzed. Disregarding the youngest orphan grain at 206 Ma (Fig. 24) five grains with 2σ errors less than 5% of the zircon age determination, and with $^{207}Pb/^{235}U$ and $^{206}Pb/^{238}U$ age determinations that differ by less than 1σ (averaged), form a sub-population between 210 and 215 Ma (average ~213 Ma). We interpret this as the maximum depositional age of the sample, consistent with the ~208 Ma age for the base of the Voght determined previously (Mihalynuk et al., 2015). All other zircons analyzed have ages consistent with local derivation from the Nicola arc, including the sub-population of the three oldest grains at ~236 Ma.

3.2.2.3. Sample MMI14-15-13 (D11), Nicola Group Eastern belt, fine siliciclastic unit, ≤214 Ma, possibly <208 or even <202 Ma

Sample MMI14-15-13 was collected along the far eastern boundary of the northern part of the study area from the Eastern belt sedimentary rocks. Here the succession is mainly well-bedded turbiditic siltstone and argillite with lesser coarse wacke (see Mihalynuk et al., 2015). A carbonate-cemented arkose bed with a minimum thickness of ~15 cm was sampled (Fig. 25).

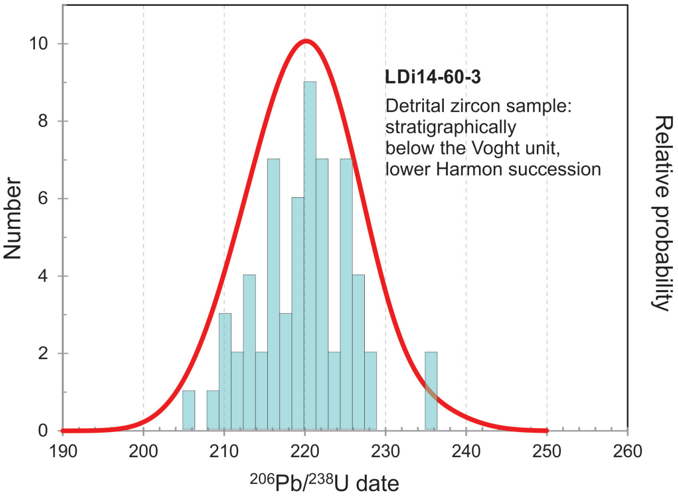

Fig. 24. Histogram of LA-ICPMS age determinations from individual detrital zircons from sample LDI14-60-3. Superimposed red curve is the cumulative age distribution showing resolved populations and their relative probabilities as determined by the ISOPLOT software of Ludwig (2003).

Fig. 25. U-Pb sample MMi14-15-13 of a light-weathering, coarse-grained arkose bed that is carbonate cemented (between the clipboard and hammer).

Sixty-two zircons analyzed yield a probability distribution peak at ~214 Ma (Fig. 26); however, if we use the same multigrain population reliability criteria as for Sample GMC14-50-2 (2σ less than 5% of the zircon age determination, and with $^{207}Pb/^{235}U$ and $^{206}Pb/^{238}U$ age determinations that differ by less than 1σ), then a 208 Ma subpopulation can be identified, but so too can a two-grain population with an average age of 202 Ma and very similar Pb, Th and U isotopic compositions (Friedman et al., 2016). This 202 Ma $^{206}Pb/^{238}U$ determination pair may provide the youngest reliable maximum depositional age. Either way, the strata are clearly too young to underly the Nicola arc and must instead represent deposition coeval with arc growth. All zircons analyzed have ages that are consistent with derivation from the Nicola arc, with the oldest grains around 230 Ma. No grains from an old continental source were detected.

3.2.2.4. Sample MMI14-62-1 (D14), post-Nicola Group conglomerate near Shea Lake, ≤190 Ma, probably <185 Ma

Sample MMI14-62-1 was collected from a sandstone layer in a section of oxidized reddish brown conglomerate outcrop about 3 km west of Shea Lake (Figs. 2, 27). Analyses of 62 grains (Fig. 28) indicate a peak at in the probability density distribution of ~190 Ma (maximum depositional age) and ~215 Ma (age of most common source). A subpopulation of four grains with tightest errors of run at ~185 Ma may provide a younger maximum depositional age. A conspicuous lack of zircons between ~201 and ~197 Ma is consistent with the lack of known magmatism in the region during this period.

In the northwest part of the study area, a polymictic, maroon conglomerate unconformably overlies Late Triassic limestone (Hendriks unit) and is overlain by interbedded maroon epiclastic sandstone and bladed feldspar porphyry flows of the Voght unit (>202 Ma; see above). Mihalynuk et al. (2015) referred to this conglomerate as the ‘Shea conglomerate’ and included it in the upper part of the Nicola Group. However, at the western edge

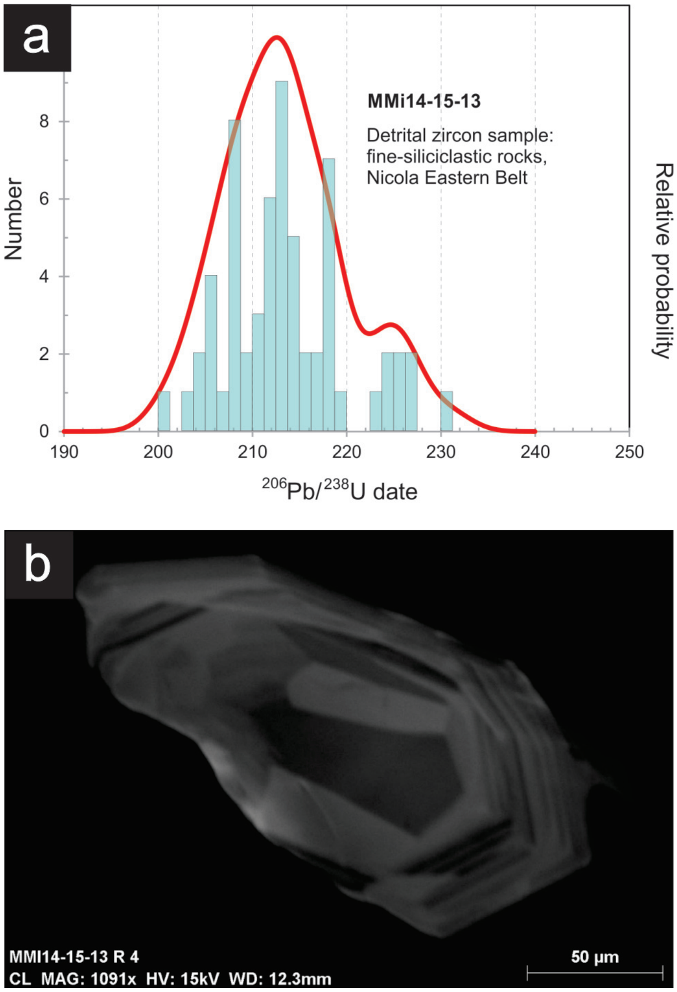

Fig. 26. a) Histogram of LA-ICPMS age determinations for individual detrital zircons from sample MMI14-15-13. Superimposed red curve is the cumulative age distribution showing resolved populations (~214 and ~225 Ma) and their relative probabilities as determined by the ISOPLOT software of Ludwig (2003). However, a younger age is possible, based upon an average of the two youngest grains that have nearly identical U, Pb, and Th compositions (Friedman et al., 2016). **b)** Image of cathodoluminescence of the largest of the two young grains, a broken euhedral crystal.

of the study area similar conglomerates appear to sit above the Nicola Group (unit Kc in Diakow and Barrios, 2008; unit Ks in Monger, 1989) and, as indicated by the detrital ziron ages above, the conglomerates near Shea Lake are younger than ~190 Ma. We now restrict use of the name 'Shea conglomerate' to the conglomerate near Shea Lake, which contains a higher proportion and greater diversity of plutonic clasts, and includes siliceous clasts resembling chert (Diakow and Barrios, 2008). 'Harmon conglomerate' is used to refer to the older Nicola Group conglomerate, which contains rhyolite and limestone as major clast types.

Fig. 27. Oxidized reddish brown, massive sandstone interbed in conglomerate near Shea Lake.

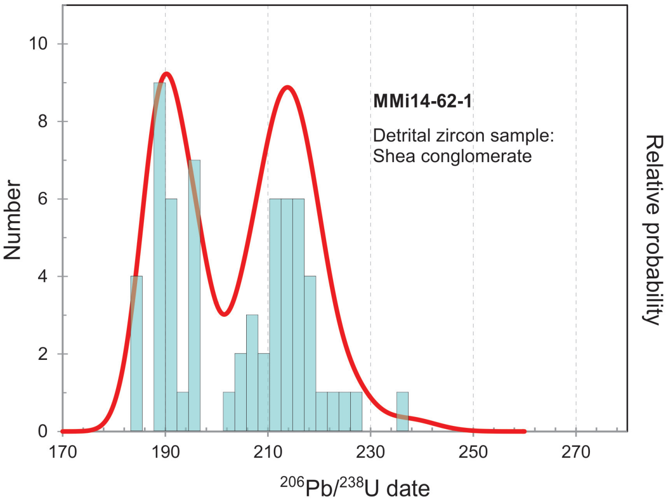

Fig. 28. Histogram of LA-ICPMS age determinations from individual detrital zircons from sample MMI14-62-1. Superimposed red curve is the cumulative age distribution showing resolved populations and their relative probabilities as determined by the ISOPLOT software of Ludwig (2003).

3.2.2.5. Sample GMC14-60-2 (D15), post-Nicola Group Bates chert pebble conglomerate; <163 Ma possibly <134 Ma

The Bates unit, comprising tabular beds of granule to boulder conglomerate, with abundant well-rounded black chert clasts, is at least 420 m thick, and forms a belt west of Aspen Grove that extends for about 17 km (Fig. 2; Mihalynuk et al., 2015). Clasts of litholgies other than black chert are significant only in northern exposures (Mihalynuk et al., 2015). Sample GMC14-60-2 was collected from a chert granule to pebble-rich bed of the Bates conglomerate, uncharacteristically fine-grained for the cobble and boulder-rich conglomerate (Fig. 2). Geological constraints on the age of the conglomerate are based on its unconformable relationship with youngest dated Nicola strata (<201 Ma Tillery unit) near the northern margin of Allison pluton. Farther south, the Spences Bridge Group (104 Ma; Early Cretaceous) is deposited on the Allison pluton without any intervening Bates conglomerate. If Bates conglomerate was deposited and then eroded prior to the sub-104 Ma unconformity, the geologically-constrained conglomerate age would be between ~201, and 104 Ma.

A total of 65 grains were analyzed, resulting in a multi-peaked spectrum with a main population at 163 Ma, and multi-grain subpopulations at 153, 188, 210, 240 and, perhaps, at 305 Ma (Fig. 29a). Two old grains were analyzed: 1400 and 2750 Ma (Friedman et al., 2016). Both ^{207}Pb/^{235}U and the more reliable ^{206}Pb/^{238}U determinations on the youngest grain (Fig. 29b) suggest ages 134 ±15 Ma and 134 ±7.3 Ma (2σ errors) Accepting the age of this single zircon would support assigning the Bates unit to unit Ks of Monger (1989; Early Cretaceous); if the age is spurious then main 163 Ma population peak would confirm assigning the conglomerate to unit 9 of Preto (1979; Late Jurassic).

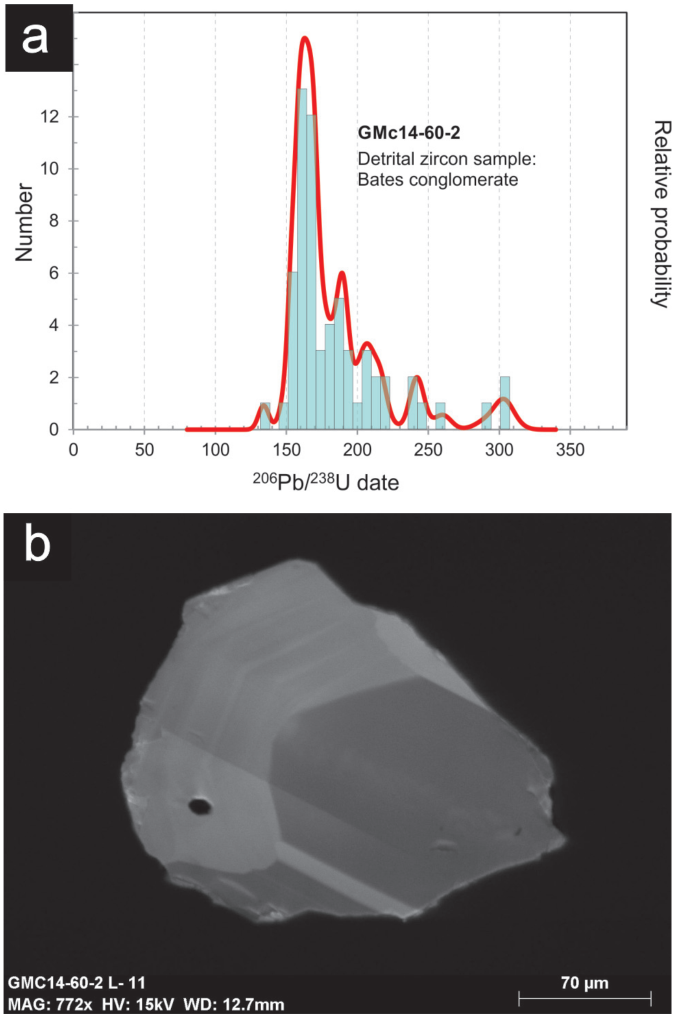

Fig. 29. a) Sample GMC14-60-2, Bates conglomerate zircon age spectra. Not shown are two Precambrian grains with ^{207}Pb/^{235}U ages of 1400 ±36 Ma and 2753 ±53 Ma. **b)** Cathodoluminescence image of the youngest grain. It yielded coeval ^{207}Pb/^{235}U and ^{206}Pb/^{238}U ages of 134 ±15 Ma and 134 ±7.3 Ma (2σ errors).

The main 163 Ma detrital zircon population peak coincides with the age of the Osprey batholith and the newly defined Osprey volcanic unit (sample MMI14-59-12, 163.2 ±0.2 Ma; see above), the closest occurrences of which are now 19 km away. Given the paucity of clasts other than black chert, the 163 Ma zircons may represent air fall material derived from Osprey-related volcanism. The Triassic zircon populations are readily explained by derivation from Nicola arc lithologies (see discussion of other TIMS ages above and Mihalynuk et al., 2015). However, no source of chert is known in the region between the Osprey batholith and the Bates conglomerate, and the sparse latest Carboniferous and single Mesoproterozoic and Archean grains require distant external sources.

4. Discussion: Implications for southern Nicola arc evolution

Acknowledged challenges to our understanding of the Nicola arc have historically been poor exposure and incomplete preservation, but probably even more problematic has been the lack of tight geochronological control. To address this problem, the SNAP objectives were rooted in establishing a better geochronological framework. A significant body of new age data are presented here, and implications of these data can be regional in scope.

Late Carnian to late Norian were previously thought to be the interval for Nicola arc development (Late Triassic; Schau, 1968; Preto. 1979), but arc development can now be shown to extend from latest Middle Triassic (Ladinian) to latest Late Triassic (Rhaetian). Moreover, distinctive stratigraphic units, dated isotopically or by fossils, demonstrate Early Norian stratigraphic links across the Western and Central belts proposed by Preto (1979) and that, by the Rhaetian, the arc was mainly eroding, as recorded by volcano-sedimentary lithofacies that extend continuously eastward from Central into the Eastern belt.

4.1. Proximity of Nicola arc to North America

The Nicola arc was constructed on a variety of basement rocks mainly of island arc character, the oldest with Late Silurian fossils (Read and Okulitch, 1977). However, the underpinnings of the Quesnel terrane have long-been debated with some workers arguing that North American crust extends unbroken beneath the Nicola arc (e.g., Erdmer et al., 2002; Thompson et al., 2006). Lack of Precambrian detrital zircons from analyses of samples reported here and in previous reports on the southern Nicola arc (Mihalynuk et al., 2014; Mihalynuk et al., 2015) support geographic separation from North America through the Triassic. Not one of the detrital zircons in the Triassic samples examined is older than Carboniferous, and the first appearance of Precambrian zircons is in post-Nicola rocks (Bates conglomerate, Late Jurassic-Early Cretaceous). While not a conclusive test, lack of Precambrian zircons is inconsistent with the idea that craton underpins the Nicola arc. Yet just to the north of the study area, in the Nicola Horst, clasts up to 1038 Ma are reported (Erdmer et al., 2001, 2002; Moore, 2000; Moore et al., 2000), demonstrating that Precambrian domains may have existed beneath the Nicola arc, at least as local crustal fragments.

4.2. Nicola arc flares to life in the Middle Triassic

Rhyolite lava and fragmental rocks, with pillowed basalts, mark initial volcanic activity in the Nicola arc (238.15 ±0.33 Ma, sample MMI13-30-4 in Mihalynuk et al., 2015; 238.6 ±0.3 Ma, sample MMI15-55-13, this paper), that produced the rhyolite-rich epiclastic unit yielding a population of detrital zircons at ~239 Ma (sample MMI14-23-15; see Fig. 22). These rocks extend across the Central belt, scattered for 30 km between Coalmont and Missezula Mountain. They represent a pulse of nascent submarine arc magmatism. A similar age for arc initiation in northern Stikinia is recorded by the Joe Mountain volcanic rocks in Yukon (Hart, 1997; Piercey, 2004) which are Ladinian (242-235 Ma timescale of Ikeda and Tada, 2014), supporting a link between Stikinia and Quesnellia by that time (e.g., Mihalynuk et al., 1994). Inception of calc-alkalic porphyry-style mineralization by ~229 Ma in northern Stikinia (Mihalynuk et al., this volume) suggests that the Stikine arc was sufficiently thick to form porphyry deposits by late Middle Triassic.

In the northern part of the Nicola arc near Quesnel Lake, conodonts extracted from the base of the volcanic unit are early to middle Anisian (Struik, 1988). Nicola arc initiation could, therefore, be even older than recorded herein (see Fig. 7). It is possible that futher dating will push the age of southern Nicola arc initiation to older ages.

4.3. Nicola arc growth

Following the early rhyolitic event (~239 Ma), accelerated arc growth is reflected in a heterogeneous accumulation of plagioclase-augite phyric basalt and andesite lava and fragmental rocks interstratified with subordinate epiclastic rocks that are found throughout much of the Central and Western belts. The initial age of this volcanic episode has not been established. However, conodonts from a limestone-bearing conglomerate sampled in the Central belt (site TNe 10-1, Monger, 1989, GSC collection C88062; M.J. Orchard, p. comm, 2015) and a reassessment of conodont collections in the Geological Survey of Canada archive, indicate that carbonate sedimentation in the study area started near the Carnian-Norian boundary (~227 Ma chronostratigraphic chart of Cohen et al., 2013, updated 2015). Multiple carbonate beds in the marker interval, which are interspersed with felsic tuffs throughout the Western belt, extend without tuffs into the Central belt. The age of the marker interval (224-223 Ma) is well established by conodont and U-Pb TIMS data (Fig. 7). The age data also confirm continuity between Western and Central belt units, and establish earliest emergence of parts of the Nicola arc to photic depths in the Carnian and likely subaerial exposure by mid-Early Norian (Fig. 7).

Carbonate deposition marks a period of reef construction supporting a rich fauna (Schau, 1968) in shoaling sectors of the emergent Nicola arc. The style of volcanism also changed during carbonate sedimentation, with the introduction of rhyolite and dacite flows and fragmental rocks that provide the first evidence of subaerial eruptions. At times, phreatic eruptions produced ash-clouds charged with water vapor giving rise to accretionary lapilli tuff, and small-volume welded ash-flow tuffs, and rhyolite flows. Interbedding of subaqueous (fossil-bearing limestone; exhalative chert beds) and subaerial (welded rhyolite tuffs) deposits in the marker interval at Castillion Creek (224.58 ±0.22 Ma) provides evidence for frequent changes in relative sea level.

Because of the restricted range of isotopic ages and the relatively small volume of felsic rocks preserved in the Western belt marker interval, the duration of felsic volcanic activity is thought to be brief. However, a broader time span of volcanic activity is suspected from the substantial volume of mafic and intermediate volcanic and epiclastic rocks with thin accretionary lapilli tuff beds above the marker interval at Castillion Creek (estimate of 1100 to 1300 m exposed at Selish Mountain). The intrusive contact of the Coldwater pluton and thermal aureole developed adjacent to this section indicates that volcanism ceased by ~210 Ma.

4.4. Early Norian cross-arc correlation

Identical middle-Early Norian limestones, confirmed mainly by conodont fauna and few ammonoids (M.J.Orchard, 2016, unpublished fossil report; and fossil identifications in Preto, 1979), are now demonstrated to extend across the northwestern structural boundary between Western and central belts. However, generally interspersed felsic rocks have not been found with exposures of Hendriks limestone in the Central belt, adjacent to Kane Valley (Mihalynuk et al., 2015). Here the apparent absence of these distinctive quartz-bearing tuffs is tentatively attributed to removal during uplift and erosion affecting part of the up-thrown Central belt.

4.5. Deformation of Nicola arc preceding Cu-Au porphyry epoch

Evidence of a Late Triassic collision is widespread throughout Quesnellia and Stikinia (e.g., Logan and Mihalynuk, 2014). In the study area, it is manifested by thrusts and conglomeratic redbed deposition and concomitant changes in the arc chemistry, from predominantly basaltic to pulses of alkalic basalt and high-silica andesite (apatite-biotite-quartz-phyric) volcaniclastic strata (~202.3 ±0.3 Ma, MMI14-62-4) with copper mineralization (Logan and Mihalynuk, 2014). Deformation led to uplift of the Central belt in the Norian and erosion to the level of Hendriks limestone (middle-Early Norian). Erosion apparently obliterated the entire record of pre-210 Ma volcanic strata that are still preserved throughout the

Western belt. Evidence of this erosion is recorded by locally thick, oxidized polymictic conglomerates in the Harmon succession that contain felsic volcanic and limestone clasts, both probably derived from the distinctive early Norian marker strata (~223 to 224 Ma), and abundant granitic clasts that potentially signal exhumation and erosion of the nearby Allison pluton (~223 Ma, sample MMI14-50-2, this paper) and older country rocks.

Deformation leading to uplift and erosion occurred after ~215 Ma, based on the age of the youngest dated rocks that are incised, and probably between ~208 Ma and ~201 +0.31/-0.4 Ma when arc aggradation resumed. The latter ages are based on the youngest detrital zircons (conglomerate sample 12JLO51-47 in Mihalynuk et al. 2015; sandstone sample LDi12-60-3, this study) and age of a crosscutting dike (sample MMI13-16-3 in Mihalynuk et al., 2015).

East-vergent thrust faults, best displayed along highway roadcuts in the study area (Mihalynuk et al., 2015), may provide some indication of the duration of collision because they apparently cut Shrimpton unit strata in the Eastern belt, presumably derived from the ~202 Ma arc. Latest Triassic detrital zircons recovered from arkosic strata of the Eastern belt suggest a link between quartz-phyric eruptions from the Zig area in the Central belt. This connection is strengthened if the youngest two-grain population of Eastern belt sample MMI14-15-13 at 202 Ma (mean) is a depositional age recording direct pyroclastic fallout sedimentation or resedimentation of material immediately reworked from Zig tuffs, (202.3 ±0.3 Ma, sample MMI14-5-62-4). Projected along-strike to the north, these thrusts should be cut by the undeformed ~193 Ma Pennask batholith (sample MMI14-19-3; see also Mihalynuk et al., 2015 and Fig. 2). Extensive overburden obscures any such relationship; although no thrust faults or folds have been recognized within the Pennask batholith.

More regionally, this deformation may be manifested in the Mount Lytton complex, about 50 km to the west, where strongly deformed quartzo-feldspathic gneiss is cut by a locally foliated granodiorite. U-Pb ages from these units are 225 ±5 and 212 ±1 Ma (Parrish and Monger, 1992), suggesting that onset of deformation is possibly older than in the study area.

4.6. Nicola arc wasting

The late arc history is recorded in strata previously described as part of the Eastern belt, which spans more than 20 km across the northern part of the study area (Figs. 2, 3). Rocks of the Central belt (Fairweather unit) extend eastward into mainly clastic and lesser volcanic components of the Eastern belt (Shrimpton, Paradise, Eastern fine siliciclastic units) speculated to represent lateral facies equivalents (Mihalynuk, et al., 2015). Magmatic activity appears to have waned as the Nicola arc was dissected to the level of epizonal plutons, with detritus transported to the arc flanks. Coarse conglomerate of the Fairweather unit, mostly on the eastern flank of the arc, is composed of subequal proportions of massive basaltic flows and, oxidized volcanic breccia and conglomeratic deposits. To the east, the Shrimpton is generally finer grained and better stratified, with sandstones that contain marine fauna in rare limey layers, monzonite-clast conglomerate, and generally thinner mafic flow deposits, including thin (<1m to several m) alkaline basalt flows. Farther east, the Paradise unit is mainly volcanic and pluton clast-bearing conglomerate (commonly with pyroxene- and hornblende-bearing clasts), and flows. Mafic flow deposits comprise local thick accumulations within conglomerate. Farthest east, and not in contact with other facies, are parallel bedded, interstratified siltstone and minor mudstone, presumed to represent deposition in relatively deep marine waters.

Detrital zircon geochronology supports this correlation if the youngest zircon subpopulation (~202 Ma; sample MMI14-15-13) represents the depositional age of the Eastern fine siliciclastic unit. If so, it is coeval with the Fairweather unit, which was dated previously as ~201-202 Ma based on detrital zircons from maroon tuffaceous siltstone, and U-Pb TIMS from a cross-cutting dike (samples MMI13-16-6, Mihalynuk, et al., 2015).

The youngest absolute ages for magmatism in the Nicola arc are from the ~201 Ma dike (sample MMI13-16-3, Mihalynuk et al., 2015) cutting the Fairweather unit, and andesites from Zig unit (Mihalynuk et al., 2015), which has a U-Pb TIMS age of ~202 Ma (sample MMI14-62-4). These rocks may represent terminal volcanism in the Nicola arc. Diagnostic phenocrysts from high-silica andesitic fragmental rocks at Zig, that include quartz, biotite, and fine- to medium-grained apatite prisms, were incorporated in the Shrimpton unit, probably due to dispersal as components of air-borne ash falls. Analcime basalts, localized in the Fairweather and Shrimpton units as relatively thin flows, represent a distinctive alkaline volcanic pulse late in the arc's history, confirming stratigraphic continuity between units.

4.7. Early Jurassic (late Pliensbachian) deformation

A second stage of deformation may be recorded by the <190 Ma (possibly ~185 Ma) Shea conglomerate. No folding, faulting or fabrics can be directly attributed to this event. It is possible that many of the 25 detrital zircons (of the 62 analyzed) that overlap the age of the 193.11 ±0.16 Ma Pennask batholith (see MMI14-19-3) were derived from this or a coeval volcano-intrusive complex. If the age is correct, the Shea conglomerate may be regionally important; its depositional agecorresponding with the age of Quesnel docking in the south (e.g., Parrish and Wheeler, 1983, Archibald et al., 1983; Murphy et al., 1995; Colpron et al., 1996) and north (e.g., Nixon et al., 1995) and development of a regional unconformity in both Quesnellia and Stikinia (e.g., Nelson and Bellefontane, 1996; Brown et al., 1996; Hart, 1997; and see summary in Logan and Mihalynuk, 2014). In the Ashcroft area to the west, carbonaceous marine shale and lesser sandstone of the Lower Jurassic Ashcroft Formation strata were overthrust by Nicola Group rocks around this same time (Travers, 1978).

4.8. Source of black chert clasts in Bates conglomerate?

The source of the chert clasts in the Bates conglomerate remains a mystery. Perhaps chert-rich pelagic deposits of the oceanic Cache Creek terrane were thrust over the Nicola arc, like in northern British Columbia, where Cache Creek overthrust Stikinia during final collision of Stikinia (Monger and Ross, 1971; Ricketts et al., 1992) as it rotated into alignment with the Quesnellian backstop (Mihalynuk et al., 1994). In northern British Columbia, this event is well dated as Middle Jurassic ~173 Ma (Mihalynuk et al., 2004), but a northern hinge produces a geometric constraint requiring collision at the southern latitude of the Nicola Arc during later times. In the south, early-middle Callovian chert deposition (based on radiolarian data; Cordey and Schiarizza, 1993) requires that Stikinia-Quesnellia docking, if it even occurred at the latitude of Merritt, did not happen until after ~165 Ma (2015 IUGS time scale, Cohen et al., 2013). Such timing is consistent with the main age distribution peak at 163 Ma (Fig. 29) and possible derivation from coeval Osprey volcanism (163.2 ±0.2 Ma, sample MMI14-59-12), and Osprey batholith (~162-166 Ma) rocks. To the immediate north, in the Nicola Horst, north of Nicola Lake (Fig. 2), rhyodacite and felsic porphyry clasts of 157 and 161 Ma may be part of a correlative conglomerate (Erdmer et al., 2002). Here the Nicola Group is structurally removed and the conglomerate lies above the Bob Lake assemblage, which contains clasts of 1.04 Ga felsic metaporphyry and is cut by 230 and 219 Ma tonalite and diorite (Erdmer et al., 2002).

4.9. Early Cretaceous deformation

Two pulses of Eartly Cretaceous deformation are recognized regionally, but in the study area no structures can be conclusively related to the older pulse. In the Vernon area to the immediate east, the oldest pulse is represented by intense deformation fabrics in the 162 Ma Kalamalka shear zone that overprint 171 Ma orthogneiss (Glombick et al., 2006). Immediately southwest of the study area, are east vergent thrusts (with a dextral component) and late syn-kinematic tonalite gneisses of the Eagle Complex (157 ±4 Ma), and Zoa complex volcanic strata that are cut by a possibly comagmatic quartz diorite (153 ±10 Ma; U-Pb zircon, Greig et al., 1992).

A younger pulse of Early Cretaceous deformation is manifested in the study area by west-vergent thrust imbrication of the Bates conglomerate with Nicola arc strata. If the youngest reliable detrital zircon age in the Bates conglomerate is 134 Ma, as argued above, then deformation is bracketed between 134 and 104 Ma, the younger age constraint provided by the largely undeformed Spences Bridge Group (Diakow and Barrios, 2008), although west of the study area, the Spences Bridge is deformed within the Nicoamen syncline (Monger, 1985). This deformation may be related to interaction between the Insular and Intermontane superterranes between 135 Ma and the oldest probable stratigraphic link at 130 Ma (Umhoefer and Schiarizza, 1996). Further study of the Bates conglomerate, testing for youngest detrital zircons, and extracting radiolaria from its clasts are required before concrete conclusions can be drawn.

5. Conclusions

Thanks to an ever-expanding network of logging roads and a growing geochronological dataset not available to earlier workers, a more detailed picture of Nicola arc evolution is emerging. Nicola arc construction began by ~239 Ma as recorded by regional felsic pulse of magmatism. Ensuing arc aggradation was mainly by accumulation of mafic, pyroxene and pyroxene-hornblende-phyric volcanic flows and flow breccia as recorded in the Central belt. Felsic volcanic strata were important at ~224 Ma. Well preserved in the Western belt, felsic strata were likely more important regionally, but were removed in other areas by erosion during terrane collision and uplift at ~210 Ma. Strata were deposited on the broad unconformity surface after ~208 Ma (upper part of the Harmon succession), but magmatism seemed to wane until termination of Nicola arc volcanism at ~202 Ma. Copper-gold porphyry-style mineralization was emplaced during the collision and uplift, and early waning magmatic arc stages, when arc wasting predominated and thick coarse clastic deposits formed to the east. Shortening of the arc, attributed to the ~210 Ma and later defomation, is in evidence as folds and thrust faults, including thrust imbrication of Late Jurassic or Early Cretaceous chert pebble conglomerate with Nicola arc strata. Nicola Arc construction, destruction, and deformation are coeval with those in other arc segments within Quesnel and Stikine terranes providing further bases for correlation and prediction of porphyry mineralization along the length of British Columbia.

Acknowledgments

We are indebted to past workers in the southern Nicola arc, especially J.W.H. Monger and V.A. Preto, both of whom have generously shared their time and knowledge with us in the field. Fieldwork in 2013 and 2014 benefitted from the diligent work of G. McEwan and M. Henderson, and in 2015 by T. Findley. Reviews by P. Schiarizza and L. Aspler, neither of whom agree with all of our interpretations, significantly improved this contribution.

References cited

Archibald, D.A., Glover, J.K., Price, R.A., Farrar, E. and Carmichael, D.M., 1983. Geochronology and tectonic implications of magmatism and metamorphism, southern Kootenay arc and neighbouring regions, southeastern British Columbia, Part 1: Jurassic to mid-Cretaceous. Canadian Journal of Earth Sciences, 20, 1891-1913.

Armstrong, R.L. and Petö, P., 1981. Eocene quartz-feldspar porphyry intrusions west of Okanagan Lake, southern B.C.: K-Ar dates and Sr isotopic composition. Northwest Geology, 10, 13–19.

Ash, C.H., Reynolds, P.H., Creaser, R.A. and Mihalynuk, M.G., 2007. ^{40}Ar/^{39}Ar and Re-O Isotopic Ages for hydrothermal alteration and related mineralization at the Highland Valley Cu-Mo deposit (NTS 092I), southwestern British Columbia; In: Geological Fieldwork 2006, British Columbia Ministry of Energy Mines and Petroleum Resources, British Columbia Geological Survey Paper 2007-1, 19-24.

Breitsprecher, K. and Mortensen, J.K., 2004. BC Age 2004A-1: A database of isotopic age determinations for rock units from British Columbia; British Columbia Ministry of Energy, Mines and Petroleum Resources, British Columbia Geological Survey Open File 2004-03.

Cohen, K.M., Finney, S.C., Gibbard, P.L., Fan, J.-X., 2013; updated. The ICS International Chronostratigraphic Chart. Episodes 36, 199–204.

Cordey, F. and Schiarizza, P., 1993. Long-lived Panthalassic remnant; the Bridge River accretionary complex, Canadian Cordillera. Geology, 21, 263–266.

Crowley, J.L., Schoene, B. and Bowring, S.A. 2007. U-Pb dating of zircon in the Bishop Tuff at the millennial scale. Geology, 35, 1123-1126.

Diakow, L.J. and Barrios, A., 2008. Geology and mineral occurrences of the mid-Cretaceous Spences Bridge Group near Merritt, southern British Columbia (Parts of NTS 092H/14, 15, 092I/02, 03). In: Geological Fieldwork 2008, British Columbia Geological Survey, British Columbia Ministry of Energy Mines Petroleum Resources Paper 2009–1, 63-80.

Duke, E.F., Redden, J.A. and Papike, J.J., 1988. Calamity Peak layered granite-pegmatite complex, Black Hills, South Dakota: part 1. Structure and emplacement. Geological Society America Bulletin, 100, 825–840.

Erdmer, P., Heaman, L., Creaser, R.A., Thompson, R.I. and Daughtry, K.L., 2001. Eocambrian granite clasts in southern British Columbia shed light on Cordilleran hinterland crust. Canadian Journal of Earth Sciences, 38, 1007–1016.

Erdmer, P., Moore, J.M., Heaman, L., Thompson, R.I., Daughtry, K.L. and Creaser, R.A., 2002. Extending the ancient margin outboard in the Canadian Cordillera: record of Proterozoic crust and Paleocene regional metamorphism in the Nicola Horst, southern British Columbia. Canadian Journal of Earth Science, 39, 1605–1623.

Friedman, R.M., Mihalynuk, M.G., Diakow, L.J. and Gabites, J.E., 2016. Southern Nicola Arc Project 2015: Geochronologic data constraining Nicola Arc history along a transect near 50°N. British Columbia Ministry of Energy and Mines, British Columbia Geological Survey, Geofile 2016-3.

Gerstenberger, H. and Haase, G. 1997. A highly effective emitter substance for mass spectrometric Pb isotopic ratio determinations. Chemical Geology, 136, 309-312.

Glombick, P., Thompson, R.I., Erdmer, P., Heaman, L., Friedman, R.M., Villeneuve, M., Daughtry, K.L., 2006. U-Pb constraints on the thermotectonic evolution of the Vernon Antiform and the age of the Aberdeen gneiss complex, southeastern Canadian Cordillera. Canadian Journal of Earth Sciences, 43, 213–244. doi:10.1139/E05-096.

Greig, C.J., Armstrong, R.L., Harakal, J.E., Runkle, D., van der Heyden, P., 1992. Geochronometry of the Eagle Plutonic Complex and the Coquihalla area, southwestern British Columbia. Canadian Journal of Earth Sciences, 29, 812–829.

Groves, E.W., 1989. Geological report and work proposal on the Siwash Creek Property. In: British Columbia Ministry of Energy, Mines and Petroleum Resources, Assessment Report 19472.

Hunt, P.A. and Roddick, J.C., 1990. A compilation of K-Ar ages: Report 19. In: Radiogenic Age and Isotopic Studies, Report 3. Geological Survey of Canada Paper 89-02, 153-190.

Ickert, R.B., Thorkelson, D.J., Marshall, D.D. and Ullrich, T.D., 2009. Eocene adakitic volcanism in southern British Columbia: Remelting of arc basalt above a slab window. Tectonophysics, 464, 164–185.

Ikeda, M., and Tada, R., 2014. A 70 million year astronomical time scale for the deep-sea bedded chert sequence (Inuyama, Japan): Implications for Triassic–Jurassic geochronology. Earth and Planetary Science Letters, 399, 30–43.

Jaffey, A.H., Flynn, K.F., Glendenin, L.E., Bentley, W.C. and Essling, A.M., 1971. Precision measurement of half-lives and specific activities of ^{235}U and ^{238}U. Physics Review, C4, 1889-1906.

Lefebure, D.V., 1976. Geology of the Nicola Group in the Fairweather Hills, British Columbia. M.Sc. Thesis, Queen's University, 179p.

Logan, J.M. and Mihalynuk, M.G., 2014. Tectonic controls on early Mesozoic paired alkaline porphyry deposit belts (Cu-Au ±Ag-Pt-Pd-Mo) within the Canadian Cordillera. Economic Geology, 109, 827–858.

Logan, J.M., Mihalynuk, M.G., Ullrich, T., and Friedman, R.M., 2007. U-Pb ages of intrusive rocks and ^{40}Ar/^{39}Ar plateau ages of copper-gold-silver mineralization associated with alkaline intrusive centres at Mount Polley and the Iron Mask batholith, southern and central British Columbia. In: Geological Fieldwork 2006, British Columbia Ministry of Energy, Mines and Petroleum Resources, British Columbia Geological Survey Paper 2007-1, 93–116.

Long, D.G., 2015. Provenance and depositional framework of braided and meandering gravel-bed river deposits and associated coal deposits in active intermontane piggyback basins: The Upper Jurassic to Lower Cretaceous Tantalus Formation, Yukon. Yukon Geological Survey, Open File 2015-23.

Ludwig, K.R., 2003. Isoplot 3.09: a geochronological toolkit for Microsoft Excel. Berkeley Geochronology Center, Special Publication 4, Berkeley.

Massey, N.W.D., MacIntyre, D.G., Desjardins, P.J., Cooney, R.T., 2005. Geology of British Columbia (whole province digital map), British Columbia Ministry of Energy, Mines and Petroleum Resources, British Columbia Geological Survey Geofile 2005-1.

Massey, N.W.D., Gabites, J.E., Mortensen, J.K., 2012. LA-ICP-MS geochronology of the Greenwood gabbro, Knob Hill complex, southern Okanagan, British Columbia. Geol. Fieldwork 2013–1.

Mattinson, J.M., 2005. Zircon U-Pb chemical abrasion (CA-TIMS) method: combined annealing and multi-step partial dissolution analysis for improved precision and accuracy of zircon ages. Chemical Geology, 220, 47-66.

Mihalynuk, M.G. and Logan, J.M., 2013a. Geological setting of Late Triassic Cu-Au porphyry mineralization at the Dillard Creek property near Merritt. In: Geological Fieldwork 2012, British Columbia Ministry of Energy and Mines, British Columbia Geological Survey Paper 2013-1, 97–114.

Mihalynuk, M.G. and Logan, J.M., 2013b. Geological setting of Late Triassic Cu-Au porphyry mineralization at Miner Mountain, Princeton southern British Columbia. In: Geological Fieldwork 2012, British Columbia Ministry of Energy and Mines, British Columbia Geological Survey Paper 2013-1, 81–96.

Mihalynuk, M.G., Nelson, J. and, Diakow, L.J., 1994. Cache Creek Terrane entrapment: oroclinal paradox within the Canadian Cordillera. Tectonics, 13, 575–595.

Mihalynuk, M.G., P. Erdmer, Ghent, E.D., Cordey, F., Archibald, D.A., Friedman, R.M., Johannson, G.G., 2004. Coherent French Range blueschist: Subduction to exhumation in < 2.5 m.y.? Geological Society of America Bulletin, 116, 910–922. doi:10.1130/b25393

Mihalynuk, M.G., Logan, J.M., Friedman, R.M. and Preto, V.A., 2010. Age of mineralization and "Mine Dykes" at Copper Mountain alkaline copper-gold-silver porphyry deposit (NTS 092H/07), south-central British Columbia. In: Geological Fieldwork 2009, British Columbia Ministry of Energy and Mines, British Columbia Geological Survey Paper 2010-1, 163–171.

Mihalynuk, M.G., Logan, J.M., Diakow, L.J., Friedman, R.M. and Gabities, J., 2014a. Southern Nicola Arc Project (SNAP): preliminary results. In: Geological Fieldwork 2013, British Columbia Ministry of Energy and Mines, British Columbia Geological Survey Paper 2014-1, 29–57.

Mihalynuk, M.G., Friedman, R.M., Gabites, J.E. and Logan, J.M., 2014b. Southern Nicola Arc Project 2013: Geochronological data. British Columbia Ministry of Energy and Mines, British Columbia

Geological Survey, GeoFile 2014-3.

Mihalynuk, M.G., Diakow, L.J., Logan, J.M. and Friedman, R.M., 2015. Preliminary geology of the Shrimpton Creek area (NTS 092H/15E, 16W) Southern Nicola Arc Project. In: Geological Fieldwork 2014, British Columbia Ministry of Energy and Mines, British Columbia Geological Survey Paper 2015-1, 129–163.

Monger, J.W.H., 1977. Upper Paleozoic rocks of northwestern British Columbia. Geological Survey of Canada, Paper , pp. 255-262.

Monger, J.W.H. 1985. Structural Evolution of the Southwestern Intermontane Belt, Ashcroft and Hope Map Areas, B.C.. In: Current Research, Part A, Geological Survey of Canada, Report 85-1A, 349-358.

Monger, J.W.H., 1989. Geology, Hope, British Columbia. Geological Survey of Canada, Map 41-1989.

Monger, J.W.H. and Ross, C.A. 1971. Distribution of fusilinaceans in Western Canadian Cordillera. Canadian Journal of Earth Sciences, 8, 259-278.

Monger, J.W.H., Souther, J.G., Gabrielse, H., 1972. Evolution of the Canadian Cordillera; a plate-tectonic model. American Journal of Science, 272, 577–602.

Moore, J.M., 2000. Nicola Horst, southern British Columbia: window into the pre-Triassic margin of North America? In: Current Research, Geological Survey of Canada, Paper 2000-A16, 6p.

Moore, J.M., Gabites, J.E., Friedman, R.M., 2000. Nicola horst: toward a geochronology and cooling history. In: Slave–Northern Cordillera Lithospheric Evolution (SNORCLE) Transect and Cordilleran Tectonics Workshop Meeting, pp. 25–27, f” http://wmsmir.cits.rncan.gc.ca/index.html/pub/geott/ess_pubs/211/211139/cr_2000_a16.pdf , accessed December, 2015.

Mundil,R., Ludwig, L.R., Metcalfe, I. and Renne, P.R., 2004. Age and timing of the Permian mass extinctions: U/Pb dating of closed system zircons. Science, 305, 1760-1763.

Murphy, D.C., van der Heyden, P., Parrish, R.R., Klepacki, D.W., McMillan, W., Struik, L.C. and Gabites, J., 1995. New geochronological constraints on Jurassic deformation of the western edge of North America, southeastern Canadian Cordillera. In: Jurassic Magmatism and Tectonics of the North American Cordillera, Geological Society of America, Special Paper 299, 159–171.

Nelson, J.L., and Bellefontaine, K.A., 1996. The geology and mineral deposits of north-central Quesnellia; Tezzeron Lake to Discovery Creek, central British Columbia. British Columbia Ministry of Energy, Mines and Petroleum Resources, British Columbia Geological Survey Bulletin 99, 112p.

Nixon, G.T., Archibald, D.A. and Heaman, L.M., 1993. ^{40}Ar-^{39}Ar and U-Pb geochronometry of the Polaris Alaskan-type complex, British Columbia; precise timing of Quesnellia-North America interaction. In: Geological Association of Canada / Mineralogical Association of Canada; Annual Meeting, Program with Abstracts, p. 76.

Parrish, R.R. and Wheeler, J.O., 1983. A U-Pb zircon age from the Kuskanax Batholith, southeastern British Columbia. Canadian Journal of Earth Sciences, 20, 1751-1756.

Parrish, R.R. and Monger, J.W.H., 1992. New U-Pb dates from southwestern British Columbia. Radiogenic Age Isotopic Studies, Geological Survey of Canada, Report 5, 87–108.

Paterson, S.R., Vernon, R.H. and Tobisch, O.T., 1989. A review of criteria for the identification of magmatic and tectonic foliations in granitoids. Journal of Structural Geology, 11, 349–363.

Patton, C., Hellstrom, J., Paul, B., Woodhead, J. and Hergt, J., 2011. Iolite: freeware for the visualization and processing of mass spectrometry data. Journal of Analytical Atomic Spectroscopy, 26, 2508-2518.

Piercey, S.J., 2004. Reconnaissance geological and geochemical studies of the Joe Mountain Formation, Joe Mountain region (NTS 105D/15), Yukon. In: Yukon Exploration and Geology, 213–226.

Preto, V.A., 1972. Geology of Copper Mountain. British Columbia Department of Mines and Petroleum Resources, Bulletin 59, 95 p.

Preto, V.A. 1979. Geology of the Nicola Group between Merritt and Princeton: British Columbia Ministry of Energy, Mines and Petroleum Resources, British Columbia Geological Survey, Bulletin 69, 90p.

Ray, G.E. and Dawson, G.L., 1994. The geology and mineral deposits of the Hedley gold skarn district, southern British Columbia. British Columbia Ministry of Energy, Mines and Petroleum Resources, Bulletin 87, 156p.

Read, P.B. and Okulitch, A.V., 1977. The Triassic unconformity of south-central British Columbia. Canadian Journal of Earth Sciences, 14, 606-638.

Renne, P.R., Swisher, C.C., III, Deino, A.L., Karner, D.B., Owens, T. and DePaolo, D.J., 1998. Intercalibration of standards, absolute ages and uncertainties in ^{40}Ar/^{39}Ar dating. Chemical Geology, 145, No. 1-2, 117-152.

Ricketts, B.D., Evenchick, C.A., Anderson, R.G., and Murphy, D.C., 1992. Bowser Basin, northern British Columbia; constraints on the timing of initial subsidence and Stikinia-North America Terrane interactions. Geology, 20, 1119–1122.

Schau, M.P. 1968. Geology of the Upper Triassic Nicola Group in south central British Columbia. Ph.D. Thesis, The University of British Columbia, Vancouver, Canada, 211p.

Schiarizza, P., 2014. Geological setting of the Granite Mountain batholith, host to the Gibraltar porphyry Cu-Mo deposit, south-central British Columbia. In: Geological Fieldwork 2013, British Columbia Ministry of Energy and Mines, British Columbia Geological Survey Paper 2014-1, 95-110.

Schiarizza, P., 2015. Geological setting of the Granite Mountain batholith, south-central British Columbia. In: Geological Fieldwork 2014, British Columbia Ministry of Energy and Mines, British Columbia Geological Survey Paper 2015-1, 19-39.

Schmitz, M.D. and Schoene, B., 2007. Derivation of isotope ratios, errors, and error correlations for U-Pb geochronology using ^{205}Pb-^{235}U(^{233}U)-spiked isotope dilution thermal ionization mass spectrometric data. Geochemistry, Geophysics, Geosystems, 8, Q08006.doi:10.1029/2006GC001492.

Scoates, J.S. and Friedman, R.M., 2008. Precise age of the plantiniferous Merensky Reef, Bushveld Complex, South Africa, by the U-Pb ID-TIMS chemical abrasion technique, Economic Geology, 103, 465-471

Slama, J., Kosler, J., Condon, D.J., Crowlley, J.L., Gerdes, A., Hanchar, J.M., Horstwood, M.S.A., Morris, G.A., Nasdala, L., Norberg, N., Schaltegger, U., Xchoene, B., Tubrett, M.N. and Whitehouse, M. J., 2007. Plesovice zircon – A new natural reference material for U-Pb and Hf isotopic microanalysis. Chemical Geology, 249, 1-35.

Struik, L.C., 1988. Regional imbrication within Quesnel Terrane, central British Columbia, as suggested by conodont ages. Canadian Journal of Earth Sciences, 25, 1608-1617.

Tafti, R., Mortensen, J.K., Lang, J.R., Rebagliati, M. and Oliver, J.L., 2009. Jurassic U-Pb and Re-Os ages for newly discovered Xietongmen Cu-Au porphyry district, Tibet: implications for metallogenic epochs in the southern Gangdese Belt. Economic Geology, 104, 127-136.

Thirlwall, M.F. 2000. Inter-laboratory and other errors in Pb isotope analyses investigated using a ^{207}Pb-^{204}Pb double spike. Chemical Geology, 163, 299-322.

Thompson, R.I., Glombick, P., Erdmer, P., Heaman, L.M., Lemieux, Y., Daughtry, K.L., 2006. Evolution of the ancestral Pacific margin, southern Canadian Cordillera: insights from new geologic maps. In: Paleozoic Evolution and Metallogeny of Pericratonic Terranes at the Ancestral Pacific Margin of North America, Canadian and Alaskan Cordillera, M. Colpron and J.L. Nelson (editors), Geological Association of Canada, Special Paper 45, pp. 433–482.

Thorkelson, D.J. and Rouse, G.E., 1989. Revised stratigraphic nomenclature and age determinations for mid-Cretaceous volcanic rocks in southwestern British Columbia. Canadian Journal of Earth Sciences, 26, 2016-2031.

Thorkelson, D.J. and Smith, A.D., 1989. Arc and intraplate volcanism in the Spences Bridge Group: implications for Cretaceous tectonics in the Canadian Cordillera. Geology, 17, 1093–1096.

Travers, W.B., 1978. Overturned Nicola and Ashcroft strata and their relation to the Cache Creek Group, southwestern Intermontane Belt, British Columbia. Canadian Journal of Earth Sciences, 15, 99-116.

Umhoefer, P.J., Schiarizza, P., 1996. Latest Cretaceous to early Tertiary dextral strike-slip faulting on the southeastern Yalakom fault system, southeastern Coast Belt, British Columbia. Geological Society of America Bulletin, 108, 768–785.

Woodsworth, G.J., Anderson, R.G., Armstrong, R.L., Struik, L.C. and van der Heyden, P., 1992. Plutonic regimes. In: Gabrielse, H. and Yorath, C. J., (Eds.), Geology of the Cordilleran Orogen in Canada, 493–531.

Wotzlaw, J.F., Guex, J., Bartolini, A., Gallet, Y., Krystyn, L., McRoberts, C.A., Taylor, D., Schoene, B. and Schaltegger, U., 2014. Towards accurate numerical calibration of the Late Triassic: High precision U-Pb geochronology constraints on the duration of the Rhaetian. Geology, doi:10.1130/G35612.1.

Age of magmatism and mineralization at the Star (Sheslay, Copper Creek) copper porphyry prospect: Inception of the Late Triassic mineralized arc

Mitchell G. Mihalynuk[1, a], Alexandre Zagorevski[2], Nancy L. Joyce[2], and Robert A. Creaser[3]

[1] British Columbia Geological Survey, Ministry of Energy and Mines, Victoria, BC, V8W 9N3
[2] Geological Survey of Canada, 601 Booth Street, Ottawa, ON, K1A 0E8
[3] Department of Earth and Atmospheric Sciences, University of Alberta, Edmonton, AB, T6G 2R3
[a] corresponding author: Mitch.Mihalynuk@gov.bc.ca

Recommended citation: Mihalynuk, M.G., Zagorevski, A., Joyce, N.L., and Creaser, R.A., 2016. Age of magmatism and mineralization at the Star (Sheslay, Copper Creek) copper porphyry prospect: Inception of the Late Triassic mineralized arc. In: Geological Fieldwork 2015, British Columbia Ministry of Energy and Mines, British Columbia Geological Survey Paper 2016-1, pp. 65-75.

Abstract

Cu-Mo porphyry style mineralization near the Star prospect was likely discovered during construction of the Telegraph Trail in the early 1900s, but it was probably not until about 1976 that the main Dick Creek zone was discovered. Previously, all mineralization was attributed to the Kaketsa pluton (~226 Ma), a small body extending across an area of ~20 km^2, and related satellite intrusions. New U-Pb zircon magmatic (229 ±3 Ma) and Re-Os mineralization (227.2 ±1.0 Ma) ages from the main Dick zone confirm this affiliation. Cu-Mo calc-alkalic style porphyry mineralization of this age is uncommon in the Canadian Cordillera. Although the Star mineralization is broadly similar in style to the huge Schaft Creek deposit (~222 Ma), Dick Creek zone mineralization is significantly older. It is perhaps the oldest well-dated Triassic porphyry mineralization in the Canadian Cordillera, and marks inception of porphyry mineralization in the Late Triassic arc.

Keywords: Copper, gold, molybdenum, silver, porphyry mineralization, Star, Sheslay, Copper Creek, Dick Creek, Kaketsa pluton, Schaft Creek, U-Pb, Re-Os, geochronology

---

1. Introduction

The Star Cu-Mo porphyry (Fig. 1) is the northernmost resource-bearing porphyry deposit in British Columbia. Why similar mineralization seems to be lacking in Late Triassic and Early Jurassic (~230-175 Ma) volcanic arc rocks between Star and allied deposits in Yukon, about 300 km to the north-northwest (Fig. 2), remains unclear. This problem is being addressed by projects forming part of the Geo-mapping for Energy and Minerals (GEM2) program. These projects are designed to characterize volcanic and intrusive rocks across the BC-Yukon border and to establish the regional temporal, tectonostratigraphic, and structural controls on copper-gold porphyry formation. Herein we report new U-Pb zircon magmatic and Re-Os mineralization ages for the Star porphyry prospect (Fig. 3; Dick Creek MINFILE 104J 035). These ages permit comparisons with deposits of similar age and help to define and extend prospective magmatic belts, especially northward.

2. Location and access

The Star porphyry prospect is in northwest British Columbia about 100 km west-southwest of Dease Lake and 50 km northwest of Telegraph Creek (Fig. 1). Access is by helicopter, or by fixed-wing aircraft that are capable of landing on a ~700 m-long gravel runway near the confluence of the Hackett and Sheslay rivers. A network of exploration roads links the

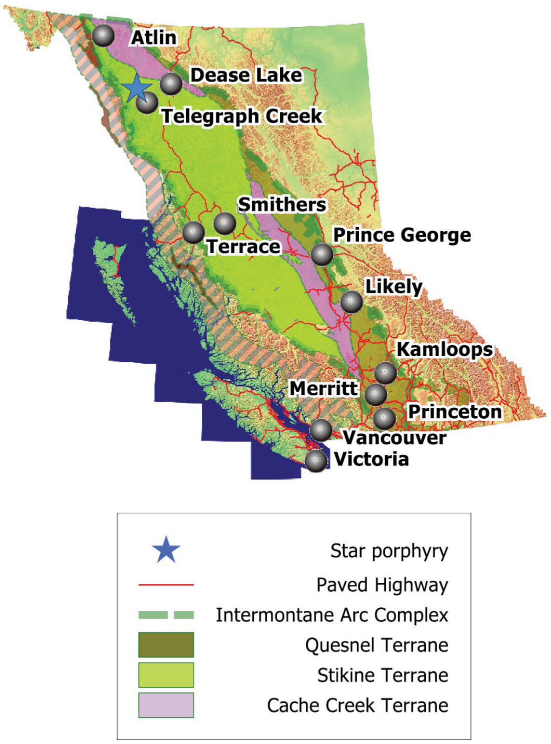

Fig. 1. Location and tectonic setting of the Star Cu-Mo porphyry prospect, which includes the Dick Creek, Hat (Copper Creek), and Pyrrhotite Creek mineralized areas.

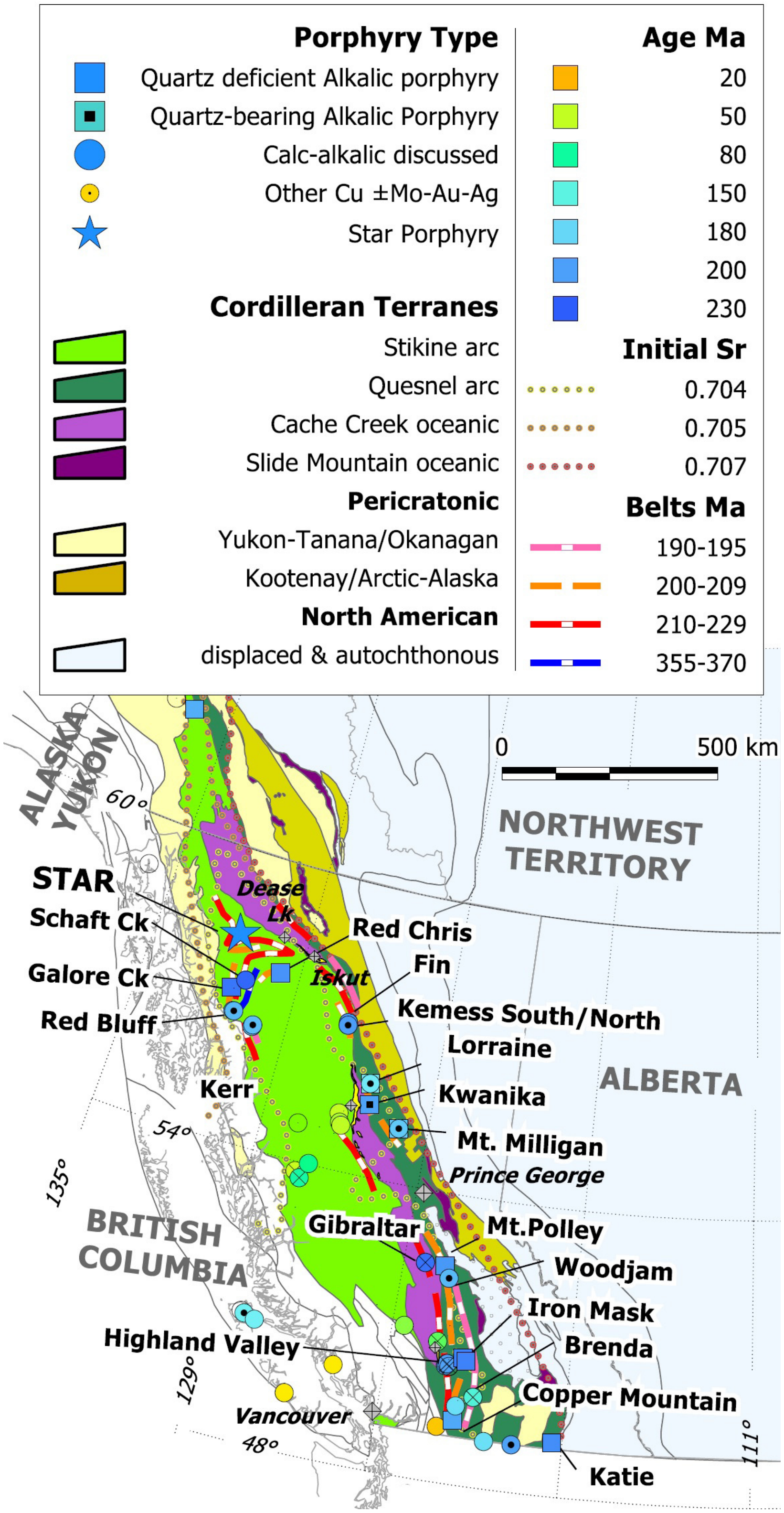

Fig. 2. Star porphyry (star symbol) among porphyry deposits colour coded according to age to show Late Triassic-Early Jurassic porphyry events (shades of blue). Schematic representation of Late Triassic and Early Jurassic arc pluton belts (modified after Logan and Mihalynuk, 2014) as discrete N-trending belts with eastward-progressing axes of magmatism along Quesnel terrane (QN). However, this pattern breaks down in northwestern Stikine terrane (ST), as indicated by Devonian-Mississippian, Late Triassic, and Early Jurassic arc plutons that show westward migration of magmatism and an apparent oroclinal folding along the northern margin of the Bowser basin. Initial strontium isopleths shown for Mesozoic plutons (Armstrong, 1988) mimic the distribution of pericratonic strata that envelop the QN-ST arc complex to the north (cf. Mihalynuk et al., 1994).

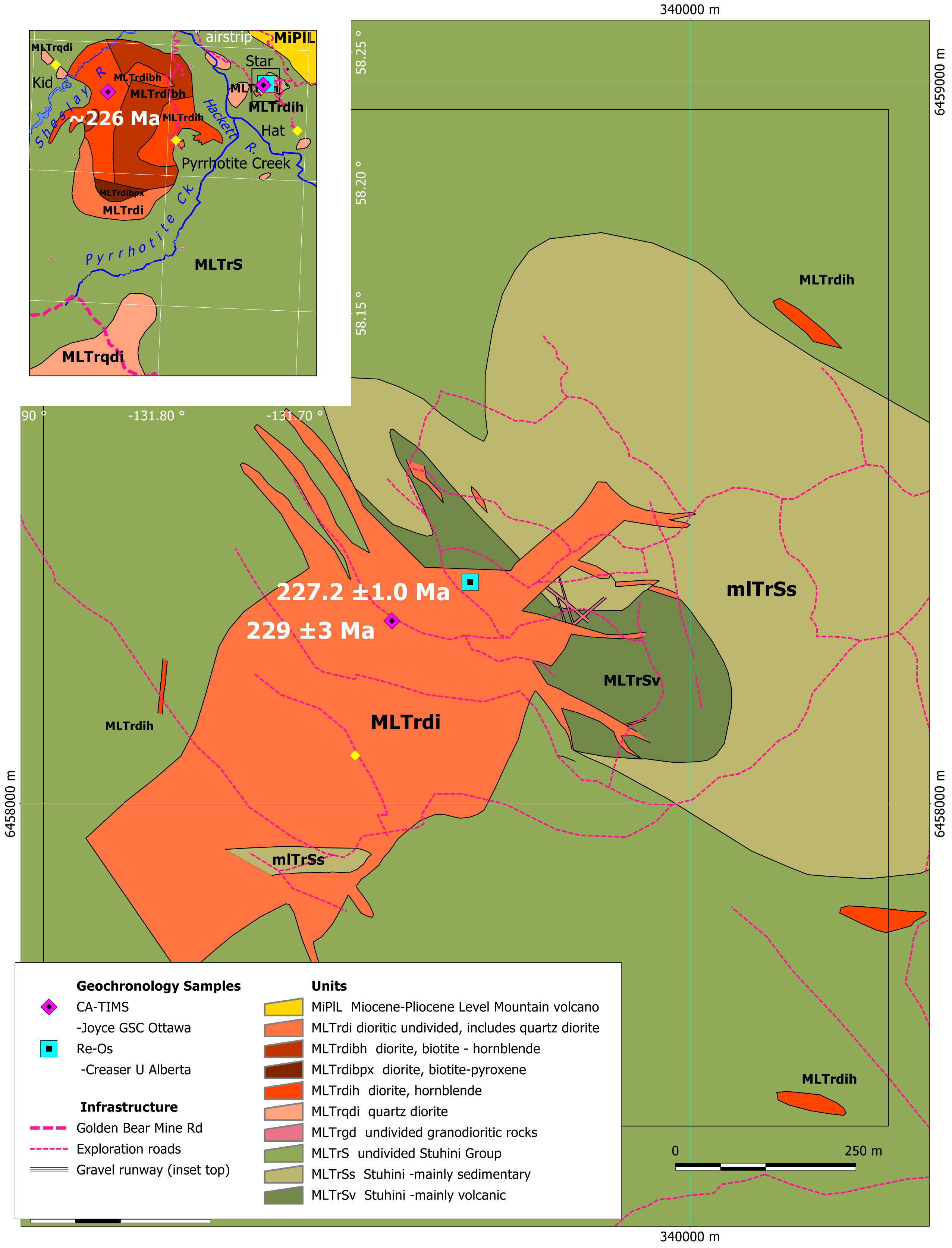

Fig. 3. Property scale geology at the Star prospect based on reconnaissance mapping, data from T.E. Lisle in Panteleyev (1983), and Lane (2005), and drill logs (Prosper Gold Corp., 2015). Most contacts are inferred. Inset shows regional geology and the polyphase, elliptical Kaketsa pluton (after Massey et al., 2005). See text for age data sources. Location of property geology on inset is shown by the rectangle. Both figures are Universal Transverse Mercator (zone 9) projections using North American Datum 1983.

airstrip with the two principal mineralized areas, Dick Creek (MINFILE 104J 035) and Copper Creek (MINFILE 104J 005, currently referred to as 'Hat'), about 3 and 6.5 km southeast, respectively. Old roads also extend from the airstrip to the Pyrrhotite Creek (MINFILE 104J 018) developed prospect, which is included in the Star Property tenures, about 5 km southwest of the Dick Creek mineralized area, and on the opposite side of the Hackett River.

If future road linkage to the provincial highway network is warranted, it would most likely be via the Golden Bear mine access road which, at its closest point, is within 8 km of the Star (Fig. 3). Presently, however, the Golden Bear road is washed out about 23 km from its junction with the Telegraph Creek road (80 km from the community of Dease Lake).

3. Geological setting

Most of British Columbia is underlain by island arc terranes that accreted to the North American margin in Triassic to Cretaceous times (e.g. Monger et al., 1982; Dickinson, 2004). The largest of these terranes is Stikinia (Stikine terrane, Figs. 1, 2), which consists of arc successions ranging from Early Devonian, based on the oldest fossil-bearing strata intercalated with volcanic rocks (Logan et al., 2000), to early Middle Jurassic (Cutts et al., 2015). Stikinia may have been loosely attached to North America by the Early Jurassic (~185 Ma, e.g., Murphy et al., 1995; Colpron et al., 1998), but it did not fully collapse against the margin until the early Middle Jurassic, when subduction in northern Stikinia ceased (Mihalynuk et al., 2004; possibly later in the south, Cordey and Schiarizza, 1993).

Most porphyry-style mineralization in British Columbia is related to Late Triassic and Early Jurassic intrusions in Stikinia and its continent-ward sister terrane, Quesnellia, from which it is separated along much of its southern length by oceanic crustal rocks and mantle slices of the exotic Cache Creek terrane (Fig. 2). Stikinia and Quesnellia appear to be joined at their northern ends where they are also enveloped by pericratonic strata as old as Proterozoic (Watson et al., 1981). This hairpin arrangement of Stikinia-Quesnellia with intervening exotic oceanic rocks and an enveloping belt of craton-derived strata has been attributed to oroclinal folding of once continuous, adjacent arc segments about a northern hinge (Mihalynuk et al., 1994). As a possible analogue, a similar arrangement of arc terranes separated by exotic oceanic rocks, may result if the Pacific Ocean between Asia and North America closes completely, trapping the Hawaii-Emperor seamounts between Japan-Kurile and the Aleutian arcs.

A particularly prolific ~6 m.y. pulse of Late Triassic Cu-Au-Ag porphyry production occurred in Stikinia and Quesnellia, centered on ~205 Ma (Logan and Mihalynuk, 2014). Intrusive activity associated with this pulse of mineralization is alkalic, and attributed to diachronous collision of another arc, the Kutcho-Sitlika arc, with Stikinia-Quesnellia (see Logan and Mihalynuk, 2014 for details). Worldwide, the best developed belts of these quartz-deficient alkalic Cu-Au-Ag porphyry deposits are in British Columbia. Porphyry-style mineralization of the Kaketsa stock and related quartz-saturated intrusions at the Star and nearby Hat prospect is of the Cu-Mo ±Au type, similar to the huge Highland Valley deposit in southern British Columbia (Fig. 2). As we show here, Star porphyry mineralization significantly predates the main ~205 ±3 Ma pulse of alkalic mineralization, consistent with the more variable ages of calc-alkalic deposits elsewhere in the province. Other calc-alkalic deposits older than ~205 include: Highland Valley (~210-206 Ma); Gibraltar (~210 Ma); Fin (~218 - 221 Ma; Dickinson, 2006); and Schaft Creek (222 Ma; see Logan and Mihalynuk, 2014 for a discussion of deposit ages).

Published regional geological maps of the area near the Star and Hat prospects are available at 1:250,000 scale (Gabrielse, 1998; or smaller and in digital format, Massey et al., 2005) and show the area as underlain by undivided volcanic and sedimentary rocks of the Stuhini Group (Late Triassic; Fig. 3). Property scale mapping generally confirms this gross subdivision (e.g., Panteleyev, 1983; Lane, 2005), as does our reconnaissance mapping (Fig. 3). However, future systematic mapping should permit further subdivision of the volcano-sedimentary succession into discrete units and their intrusive equivalents. For example, intrusive rocks, some with evidence of potassic alteration and copper mineralization, are exposed in new roadcuts along the Golden Bear Mine in an area previously mapped as the undivided volcano-sedimentary unit (Fig. 3; Mihalynuk and Zagorevski, 2016).

4. Exploration history

Mineralization near the Star prospect may have been known as early as 1899, when the Canadian Government began constructing the Ashcroft-Yukon telegraph line, linking the Atlin-Klondike goldfields to areas in the south. Earlier surveys for the ill-fated Collins Overland telegraph line in 1867 travelled north along the Tahltan and Hackett River valleys, a route later used by the Hudson's Bay Company, beginning ca. 1891 (Gauvreau, 1893), to access its post at Egnell, at the junction of the Hackett and Sheslay rivers (later known as 'Sheslay'). A track survey of northwest British Columbia commissioned by the Provincial Government began along this route in 1892 (Gauvreau, 1893); it encountered evidence of unsuccessful placer operations, but Gauvreau reported neither base metal occurrences nor exploration thereof. Similarly, from his reconnaissance geological survey along this same route in 1887, Dawson (1888) made no mention of significant mineralization. Not until 1937 are the first written reports of mineralization uncovered by prospecting in Copper Creek (now 'Hat', for a summary of more recent exploration see Caron, 2013). A long history of additional exploration in the area commenced with trenching, mapping, and drilling at Copper Creek in 1955-56 (James, 1956). Copper mineralization discoveries at the Star were staked in 1976, and the most recent diamond drilling was conducted in 2014 by Prosper Gold Corporation (Bernier, 2015). At the nearby Hat prospect, Doubleview Capital Corp. was preparing for a drill program in the fall of 2015 (Shirvani, 2015).

5. Mineralization

Mineralization at the Star property was attributed to the Katetsa pluton and related intrusions (Panteleyev and Duda, 1973). The pluton is a polyphase elliptical body that cuts the Stuhini Group and underlies an area of ~20 km^2 (inset, Fig. 3). We did not map mineralization at the eastern margin of the pluton (Pyrrhotite Creek, also known as Go, G), and the following descriptions are from Panteleyev (1983). The pluton is foliated and zoned, with a biotite-hornblende granodiorite core and hornblende diorite margins. Contact zones may include hornblende-pyroxene gabbro, in some cases as dikes within and outside of the pluton. A stock cutting the northeast contact zone is biotite-hornblende quartz diorite (Fig. 3). Younger dikes vary in composition: quartz diorite, monzonite, syenite and aplite. Panteleyev (1983) described alteration as K-feldspar flooding along fractures with quartz, siderite, and calcite. Pyrite and subordinate chalcopyrite occur as fracture-controlled veinlets in volcanic country rocks and as disseminations in the diorite dikes. Chalcopyrite is concentrated in fractures and shear zones, and in thin bands of mylonite in the main Pyrrhotite Creek prospect (~60 m by 90 m area).

The Dick Creek (Star) prospect is approximately 5km east of the main Kaketsa pluton (Fig. 3). Dick Creek (Star) was the focus of exploration by Prosper Gold Corporation in 2014. Based on work by Prosper Gold Corporation, copper mineralization at the Star prospect occurs in acicular hornblende ±quartz diorite, monzodiorite and adjacent volcano-sedimentary strata, mainly as veinlets, blebs, and disseminations of chalcopyrite together with magnetite and pyrite. Alteration mineralogy includes secondary K-feldspar, and secondary biotite, which is only rarely coarse enough for individual crystals to be seen in hand sample. In some areas, extensive quartz stockworks are developed; some veins are banded and carry molybdenite (see below). Locally, quartz has also flooded the host rock. Late epidote, chlorite and carbonate veinlets are common. The presence of late, cross-cutting, unmineralized hornblende-feldspar porphyritic monzodiorite indicates that there were several pulses of magmatism at the Star property.

6. Previous ages of intrusion and mineralization

Previously published geochronology from the Star tenures is limited to two K-Ar cooling ages. Hornblende from a sample of quartz diorite collected ~800 m west of the Pyrrhotite Creek prospect on the eastern margin of the Kaketsa pluton (Fig. 3) yielded an age reported by Panteleyev and Dudas (1973) as 218 ±8 Ma. Biotite from a similar quartz diorite (Panteleyev, 1976) yielded an age of 214 ±6 Ma, which was recalculated using more modern decay constants as 218 ±12 Ma (Breitsprecher and Mortensen, 2004). A sample from the west side of Kaketsa pluton yielded a U-Pb zircon age of ~226 Ma (Friedman unpublished, in Zagorevski et al., 2015) confirming earlier suggestions (Panteleyev and Dudas, 1973) that the mineralized intrusive rocks at Dick Creek and Pyrrhotite Creek are broadly parts of the same intrusive and mineralizing event.

7. Geochronology

To determine more precise crystallization and mineralization ages at the Star property, we selected two samples for geochronological analysis (Fig. 3). A sample of the quartz diorite that hosts porphyry mineralization at the main Dick Creek zone was taken from diamond-drill hole (DDH) SH028 (sample 14ZE-920A, Fig. 4) to determine the U-Pb zircon age of the magmatic event. A sample of quartz stockwork veining containing molybdenite partings up to ~2 mm thick in and on the margins of cm-thick quartz veins (Fig. 5) was selected for Re-Os age determination to test if mineralization is the same

Fig. 4. Ragged hornblende quartz diorite porphyry, a mineralized intrusive phase in DDH SH028 at the Dick Creek zone, sampled for U-Pb-zircon SHRIMP geochronology (sample 14ZE920A).

Fig. 5. a) Drill core of altered quartz diorite cut by stockworks of quartz-pyrite-molybdenite ±chalcopyrite-epidote-chlorite veinlets and veins up to ~1.5 cm wide. Indicated on the core box is the segment of the core collected for molybdenite extraction and Re-Os age determination (DDH S040, 89.7-90.3m). **b)** Close up of a) with blue-grey molybdenite concentrated along vein margins.

age as the intrusion (sample MMI14-35-11 from DDH S040, 89.7-90.3 m).

7.1. U-Pb zircon methods

Zircon separates were obtained using standard crushing, disk mill, Wilfley table, heavy liquid, and magnetic separation techniques. Analytical procedures and calibration details for the Sensitive High Resolution Ion Microprobe (SHRIMP) at the Geological Survey of Canada in Ottawa followed those described by Stern (1997) and Stern and Amelin (2003). Briefly, zircons were cast in a 2.5 cm diameter epoxy mount along with the Temora 2 zircon primary standard, the accepted $^{206}Pb/^{238}U$ age of which is 416.8 ±0.33 Ma (Black et al., 2004). Fragments of the GSC laboratory zircon standard (z6266, with $^{206}Pb/^{238}U$ age=559 Ma) were also included on the mount as a secondary standard, analyses of which were interspersed among the sample analyses throughout the data session to verify the accuracy of the U-Pb calibration. The mid-sections of the zircons were exposed using 9, 6, and 1 µm diamond compound, and the internal features of the zircons (such as zoning, structures, and alteration) were characterized in both back-scattered electron mode (BSE) and cathodoluminescence mode (CL) using a Zeiss Evo 50 scanning electron microscope. The mount surface was evaporatively coated with 10 nm of high purity Au. Analyses were conducted using an 16O- primary beam, projected onto the zircons at 10 kV. Before analysis, the ion beam was rastered over the area of interest for 2 minutes in order to locally remove the Au coating and eliminate effects of surface common lead. The sputtered area used for analysis was ca. 16 µm in diameter with a beam current of ca. 3.5 nA. The count rates at ten masses including background were sequentially measured over 6 scans with a single electron multiplier and a pulse counting system with deadtime of 23 ns. The 1σ external errors of $^{206}Pb/^{238}U$ ratios reported in the data table incorporate a ±1.39% error in calibrating the standard Temora 2 zircon. Additional details of the analytical conditions and instrument settings are presented in the footnotes of the Table 1. Off-line data processing was accomplished using customized in-house software. Isoplot v. 3.00 (Ludwig, 2003) was used to generate concordia plots and to calculate weighted means. Errors for isotopic ratios in Table 1 are given at 1σ uncertainty, as are the apparent SHRIMP ages. Age errors reported in the text are at the 2σ uncertainty level, and encompass the combined statistical uncertainty of the weighted mean age for the population and the 2σ error of the mean of the Temora 2 zircon calibration standard. No fractionation correction was applied to the Pb-isotope data; common Pb correction used the Pb composition of the surface blank (Stern, 1997). All ages are reported as the ^{207}Pb-corrected weighted mean $^{206}Pb/^{238}U$ age. The error ellipses on the concordia diagrams and the weighted mean errors are reported at 2σ.

7.2. Re-Os methods

A molybdenite mineral separate was prepared by metal-free crushing followed by gravity and magnetic concentration methods, as described in detail by Selby and Creaser (2004). The ^{187}Re and ^{187}Os concentrations in molybdenite were determined by isotope dilution mass spectrometry using Carius-tube, solvent extraction, anion chromatography and negative thermal ionization mass spectrometry techniques. A mixed double spike containing known amounts of isotopically enriched ^{185}Re, ^{190}Os, and ^{188}Os analysis was used (Markey et al., 2007). Isotopic analysis used a ThermoScientific Triton mass spectrometer by Faraday collector. Total procedural blanks for Re and Os are less than <3 picograms and 2 picograms, respectively, which are insignificant for the Re and Os concentrations in molybdenite. The molybdenite powder HLP-5 (Markey et al., 1998), was analyzed as a standard, and

Table 1. SHRIMP U-Pb zircon results.

Spot name	U (ppm)	Th (ppm)	$\frac{Th}{U}$	^{206}Pb* (ppm)	$\frac{^{204}Pb}{^{206}Pb}$	% ±	f(206)^{204} %	$\frac{^{208*}Pb}{^{206*}Pb}$	% ±	$\frac{^{238}U}{^{206}Pb}$	% ±	$\frac{^{207}Pb}{^{206}Pb}$	% ±	$\frac{^{207*}Pb}{^{235}U}$	% ±	$\frac{^{206*}Pb}{^{238}U}$	% ±	Corr Coeff	$\frac{^{207*}Pb}{^{206*}Pb}$	% ±	Apparent Ages (Ma) 204 corrected $\frac{^{206}Pb}{^{238}U}$	Apparent Ages (Ma) 204 corrected $\pm\frac{^{206}Pb}{^{238}U}$	Apparent Ages (Ma) 207 corrected $\frac{^{206}Pb}{^{238}U}$	Apparent Ages (Ma) 207 corrected $\pm\frac{^{206}Pb}{^{238}U}$
Sample Number: 14ZE920A (Z11315) Star quartz diorite																								
11315-027.1	419	210	0.52	12.9	2.7E-4	50	0.59	0.176	7.3	27.6	1.5	0.0554	3.6	0.26	5.7	0.036	1.5	0.3	0.0514	5.5	228	3	**228**	**3**
11315-033.1	327	132	0.42	10.0	1.7E-4	71	1.24	0.137	10.2	27.8	1.5	0.0606	3.9	0.29	5.3	0.036	1.5	0.3	0.0581	5.1	227	3	**225**	**3**
11315-034.1	228	87	0.39	7.0	5.5E-4	50	1.47	0.109	15.3	27.5	1.6	0.0624	5.0	0.27	9.7	0.036	1.7	0.2	0.0544	9.5	228	4	**227**	**4**
11315-037.1	344	166	0.50	10.8	1.6E-4	71	0.76	0.144	8.9	27.2	1.5	0.0569	3.8	0.28	5.2	0.037	1.5	0.3	0.0546	5.0	232	3	**231**	**3**
11315-042.1	566	418	0.76	17.8	*bdl*		0.10	0.271	5.1	27.3	1.5	0.0516	5.3	0.26	5.5	0.037	1.5	0.3	0.0516	5.3	232	3	**232**	**3**
11315-046.1	336	121	0.37	10.6	-2.5E-4	58	0.01	0.112	10.4	27.3	1.8	0.0509	4.2	0.28	5.7	0.037	1.8	0.3	0.0545	5.4	233	4	**232**	**4**
11315-047.1	395	175	0.46	12.3	2.1E-4	58	0.54	0.138	8.6	27.3	1.5	0.0551	3.7	0.26	5.4	0.036	1.5	0.3	0.0521	5.2	231	3	**230**	**3**
11315-049.1^{a}	*99*	*23*	*0.24*	*3.0*	*3.6E-3*	*29*	*5.84*	*0.030*	*127.4*	*26.3*	*1.8*	*0.0974*	*10.4*	*0.21*	*45.6*	*0.036*	*2.7*	*0.1*	*0.0437*	*45.5*	*225*	*6*	*227*	*5*
11315-053.1	238	92	0.40	7.4	*bdl*		0.96	0.111	15.1	27.2	1.9	0.0585	5.2	0.30	5.6	0.037	1.9	0.3	0.0585	5.2	233	4	**231**	**4**
11315-054.1	226	95	0.43	6.9	-3.1E-4	71	1.33	0.129	16.8	27.6	1.6	0.0613	8.6	0.33	9.4	0.036	1.7	0.2	0.0659	9.3	231	4	**226**	**4**
11315-060.1^{a}	*163*	*51*	*0.32*	*5.1*	*2.5E-3*	*27*	*2.43*	*0.092*	*21.7*	*27.0*	*2.1*	*0.0702*	*5.2*	*0.16*	*33.5*	*0.035*	*2.5*	*0.1*	*0.0332*	*33.4*	*224*	*5*	*229*	*5*
11315-070.1	315	140	0.46	9.9	3.2E-4	58	0.83	0.118	12.5	27.1	1.6	0.0574	4.5	0.27	7.3	0.037	1.6	0.2	0.0528	7.1	232	4	**231**	**4**
11315-077.1	419	188	0.46	13.1	-8.2E-5	100	0.20	0.142	9.1	27.5	1.5	0.0524	4.2	0.27	5.0	0.036	1.5	0.3	0.0536	4.7	230	3	**230**	**3**

Notes (see Stern, 1997):

Mount IP747, K100a spot size (13x16μm), 2 minute raster, 6 mass scans

Primary beam intensity ~3-3.5 nA,Weighted mean ^{207}Pb-corrected ^{206}Pb/^{238}U age of the analyses of secondary standard z6266 zircon was determined to be 563 ±5 Ma (2σ), MSWD=0.77, n=23 (no rejections) (accepted ^{206}Pb/^{238}U age is 559 Ma).

Spot name follows the convention x-y.z; where x = lab number, y = grain number and z = spot number

Uncertainties reported at 1σ, unless otherwise indicated, and are calculated by using SQUID 2.50.11.10.15, rev. 15 Oct 2011

f(206)^{204} refers to mole percent of total ^{206}Pb that is due to common Pb, calculated using the ^{204}Pb-method; common Pb composition used is the surface blank (4/6: 0.05770; 7/6: 0.89500; 8/6: 2.13840)

* refers to radiogenic Pb (corrected for common Pb)

Calibration standard Temora2; Age = 416.8 +/-0.33 Ma (Black et al., 2004)

Error in ^{206}Pb/^{238}U calibration 1.39% (1σ, included)

Standard Error in Standard calibration was 0.37% (1σ, not included in above errors but required when comparing data from different mounts).

Apparent ages shown in bold font are those which were used in the weighted mean age calculations

a: analysis was not included in the age calculation because of high common Pb content (f(206)^{204} > 2%)

bdl : below detection limit

over a period of two years an average Re-Os age of 221.56 ±0.40 Ma (1SD uncertainty, n=10) was obtained. This Re-Os age is identical to that reported by Markey et al. (1998) of 221.0 ±1.0 Ma.

7.3. U-Pb zircon results

Sample 14ZE920A was collected from Prosper Gold diamond-drill hole SH028 at approximately 85 m depth (Ganton, 2014). The sample comprises an interval of mineralized and veined 'ragged hornblende' quartz diorite that is locally cut by unmineralized hornblende-feldspar porphyry. The sample yielded abundant clear and colourless, equant to elongate, euhedral prismatic, 50-300 µm zircon crystals with very few clear bubble- or rod-shaped inclusions (Fig. 6). Most grains are needle-shaped with aspect ratios of up to 6:1. Backscatter SEM images of the grains mounted for SHRIMP analysis reveal few internal textures, with the exception of minor inclusions and fractures. Under cathodoluminescence, most grains exhibit c-axis-parallel broadly banded or striped zoning patterns. Distinct oscillatory zoning and faint sector zoning is visible in the more equant and stubby prisms. The central regions of four stubby prismatic grains showed disturbed zoning patterns that may represent earlier zircon growth; however these apparent cores were too small to be analyzed with the ~16 µm ion beam. Uranium content ranged between 99 and 566 ppm and Th/U values were moderate (0.24-0.76). Thirteen grains were analyzed (Table 1); however, two grains were excluded from the age calculation because of elevated common Pb content. Eleven spot analyses on individual grains formed a single population of zircon with a weighted mean $^{206}Pb/^{238}U$ age of 229 ±3 Ma (MSWD=0.44). This age is interpreted to represent the crystallization age of the quartz diorite.

7.4. Re-Os results

Sample MMI14-355-11 was collected from an altered quartz diorite cut by a stockwork of quartz-pyrite-molybdenite ±chalcopyrite-epidote-chlorite veinlets and veins up to ~1.5 cm thick (DDH S040, 89.7-90.3 m; Fig. 5). Molybdenite partings occurred on the margins of cm-thick quartz veins. Molybdenite contained high concentrations of both Re and Os (Table 2). Age uncertainty is quoted at the 2σ level, and includes all known analytical uncertainty, including uncertainty in the decay constant of ^{187}Re. A model age calculated as 227.2 ±1.0 Ma is within error of the U-Pb zircon age of the host intrusion.

8. Discussion

The U-Pb crystallization age (229 ±3 Ma) of the host quartz diorite and Re-Os molybdenite age (227.2 ±1.0 Ma) of mineralization in the Dick Creek zone are coeval within analytical error, supporting previous assertions by Panteleyev (1983) that intrusion and porphyry-style mineralization at the zone are related. Panteleyev (1983) also suggested that the

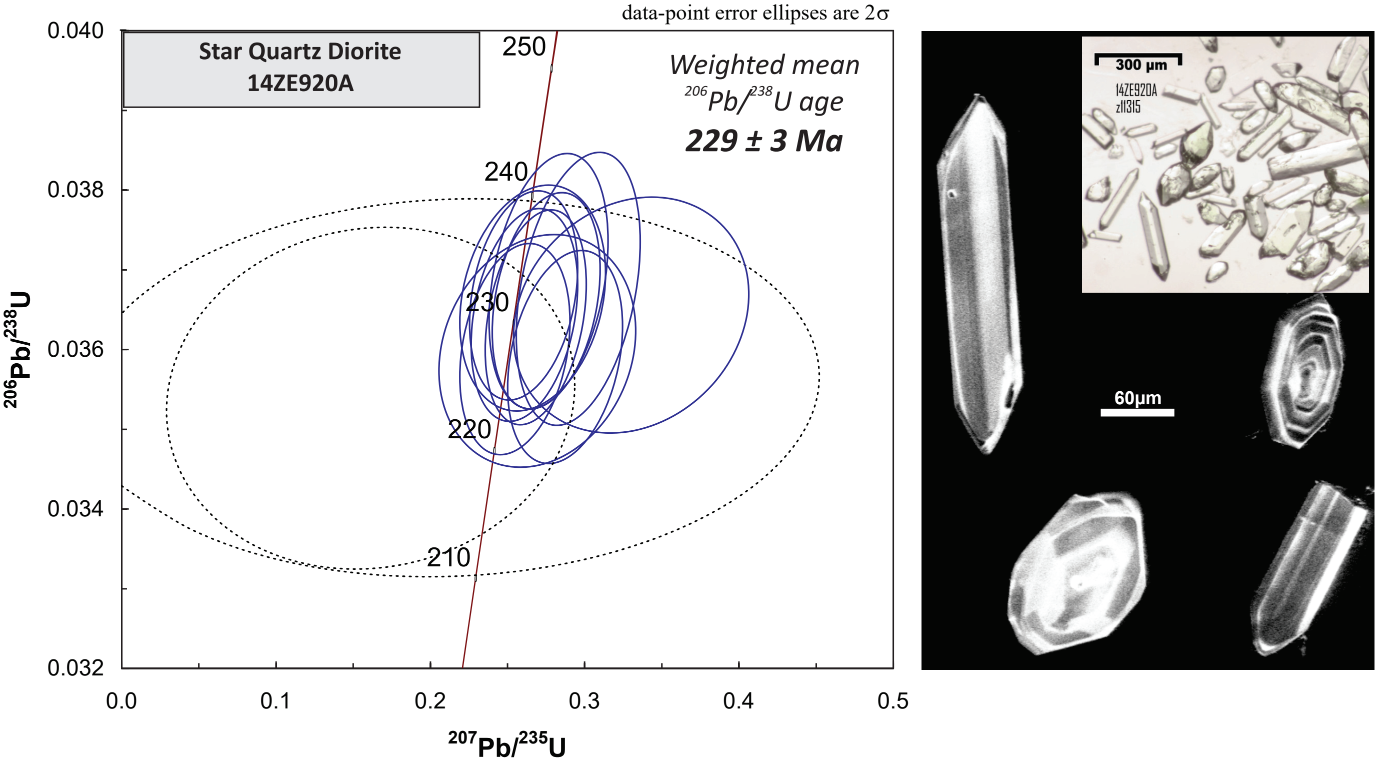

Fig. 6. Concordia plot of 12 zircon grains from sample 14ZE920A. Ellipses are shown with 2σ errors. Their combined age is 229 ±3 Ma. The dotted ellipses are the analyses for grains 49 and 60, which contained elevated common lead and were not included in the age calculations. Right: representative SEM-CL image of 14ZE920A zircons. Inset: photo in transmitted light of 14ZE920A zircons showing clarity, colour, and diverse grain sizes and habits.

Table 2. Re-Os results.

	Re ppm	± 2σ	^{187}Re ppm	± 2σ	^{187}Os ppb	± 2σ	Model age (Ma)	± 2σ (Ma)
MM114-35-11	1665	5	1046	3	3968	4	227.2	1.0

Kaketsa pluton and intrusions at the Star are cogenetic. The new crystallization age at the Star property (229 ±3 Ma) may support this suggestion because it overlaps the preliminary age from the Kaketsa pluton (~226 Ma, Friedman unpublished in Zagorevski et al., 2015) at their limits of error. The new crystallization ages are also older than K-Ar cooling ages of the Kaketsa pluton and satellite intrusions reported in Panteleyev (1976, and recalculated by Breitsprecher and Mortensen, 2004), which were interpreted to date mineralization at Pyrrhotite Creek. If mineralization at Pyrrhotite Creek is related to the small stock that cuts the main Kaketsa pluton, and the stock's relative cooling age (Panteleyev, 1976) is a reliable proxy for the crystallization age, mineralization there may be several m.y. younger than at the Dick Creek zone. Further work to constrain the age of the mineralization at Pyrrhotite Creek will be required to test this supposition.

Mineralization and magmatism at the Star property also overlap the age of magmatism (within the limits of error) at the Eagle property, approximately 17 km to the south (225.45 ±0.31, 227.2 ±0.7 Ma; U-Pb zircon, Takaichi and Johnson, 2012; Takaichi, 2013). Intrusions in the Sheslay area form part of the Stikine plutonic suite (Woodsworth et al., 1992), the emplacement of which is now known to extend from ~229 Ma to 215 Ma (Zagorevski et al., 2014; 2015). Intrusions and mineralization at the Dick Creek zone, Kaketsa Mountain, and Eagle property comprise the oldest phase of Stikine plutonic suite magmatism in the Stuhini arc. These ages demonstrate that birth of the arc occurred significantly before ~229 Ma, perhaps before ~238 Ma as is constrained in Quesnellia by the Nicola arc (Mihalynuk et al., 2015, 2016) and northern Stikinia by the Joe Mountain volcanic rocks in Yukon (Hart, 1997; Piercey, 2004) of Ladinian age (242-235 Ma timescale of Ikeda and Tada, 2014). Inception of porphyry-style mineralization by ~229 Ma suggests requisite crustal thickness of Stuhini arc by that time.

The Star property mineralization is older than the Schaft Creek deposit (222.0 ±0.8 Ma, Re–Os molybdenite, Scott et al., 2008) which was previously thought to be the oldest porphyry deposit in northern Stikinia, and significantly older than the Red Chris and Galore Creek Cu-Au porphyry deposits (~204-210 Ma; Logan and Mihalynuk, 2014).

9. Summary

New geochronological data on the host intrusion and Cu-Mo calc-alkalic porphyry-style mineralization at the Star property (Dick Creek zone) yielded 229 ±3 Ma U-Pb zircon and 227.2 ±1.0 Ma Re-Os molybdenite ages. Affiliation with the mineralized zones surrounding the Kaketsa pluton (~10 km to the west; Panteleyev, 1975), is confirmed with a new U-Pb ziron crystallization age determination from that body of ~226 Ma (Friedman unpublished in Zagorevski et al., 2015). Together with ages from the Eagle Property (Takaichi and Johnson, 2012; Takaichi, 2013), these ages confirm and extend the age range of the Stikine plutonic suite and associated mineralization back to ~229 Ma. Identification of widespread episodic magmatism and mineralization (at ~227, 222, 211, 205 Ma) highlights the need to develop robust regional frameworks that will guide identification of prospective magmatic suites and their trends. Future GEM2 work will acquire additional high quality isotopic ages and will integrate them with geochemical and isotopic studies to identify the characteristics of magmatic episodes during evolution of the Stuhini arc and its mineral deposits.

Acknowledgments

This project is part of the Geo-mapping for Energy and Minerals (GEM2) program, jointly funded by the federal government (Geological Survey of Canada) and the BC Ministry of Energy and Mines (British Columbia Geological Survey). We thank Prosper Gold Corp., especially Dirk Tempelman-Kluit and Bob Lane, for use of camp facilities, and Kimberly Martin and Anne-Sophie Corriveau, for field assistance. Pat Hunt at GSC Ottawa is thanked for the zircon SEM imaging. We thank Tom Pestaj, Bill Davis and Nicole Rayner for their expert guidance and assistance at the GSC SHRIMP facility. This paper was improved by reviewer Andre Panteleyev.

References cited

Armstrong, R.L., 1988. Mesozoic and early Cenozoic magmatic evolution of the Canadian Cordillera. In: Clark, S.P. Jr., Burchfiel, B.C. and Suppe, J. (Eds.), Processes in continental lithospheric deformation. Geological Society of America Special Paper 218, pp. 55–91.

Bernier, P., 2015. February 24, 2015 Prosper Gold Corp. Earns 51% of Star Porphyry Copper Gold Project-Northwestern BC. Available from http://www.prospergoldcorp.com/s/NewsDetails.asp?ID=1926957.

Black, L.P., Kamo, S.L., Allen, C.M., Davis, D.W., Aleinikoff, J.N., Valley, J.W., Mundil, R., Campbell, I.H., Korsch, R.J., Williams, I.S., and Foudoulis, C.F., 2004. Improved ^{206}Pb/^{238}U microprobe geochronology by the monitoring of a trace-element-related matrix effect; SHRIMP, ID–TIMS, ELA–ICP–MS and oxygen isotope documentation for a series of zircon standards. Chemical Geology, 205, 115-140.

Breitsprecher, K., and Mortensen, J.K., 2004. BCAge 2004A-1-a database of isotopic age determinations for rock units from British Columbia. British Columbia Ministry of Energy and Mines, British Columbia Geological Survey Open File, Open File 2004-03.

Caron, L.J., 2013. Sheslay property. National Instrument 43-101, Prosper Gold Corporation, 82p. Available from http://www.prospergoldcorp.com/i/pdf/reports/Sheslay_NI-43101_20130726.pdf, accessed December, 2015.

Colpron, M., Warren, M.J., and Price, R.A., 1998. Selkirk fan structure, southeastern Canadian Cordillera; tectonic wedging against an inherited basement ramp. Geological Society of America Bulletin, 110, 1060-1074.

Cordey, F., and Schiarizza, P., 1993. Long-lived Panthalassic remnant; the Bridge River accretionary complex, Canadian Cordillera. Geology, 21, 263-266.

Cutts, J.A., McNicoll, V.J., Zagorevski, A., Anderson, R.G., and Martin, K., 2015. U-Pb geochronology of the Hazelton Group in the McTagg anticlinorium, Iskut River area, northwestern British Columbia. In: Geological Fieldwork 2014, British Columbia Ministry of Energy and Mines, British Columbia Geological Survey Paper 2015-1, pp. 87–101.

Dawson, G.M., 1888. Report on an exploration in the Yukon District, N.W.T. and adjacent northern portion of British Columbia. In: Geological Survey of Canada Annual Report 1887-8, Annual Report III Parts 1 and 2, p. 5B–277B.

Dickinson, W.R., 2004. Evolution of the North American Cordillera. Annual Review of Earth and Planetary Sciences, 32, 13-45, WOS:000221752500003. doi: 10.1146/annurev.earth.32.101802.120257.

Gabrielse, H., 1998. Geology of the Cry Lake and Dease Lake map areas, north-central British Columbia. Geological Survey of Canada Bulletin 504, 147p.

Gauvreau, N.B., 1893. Exploration of the north-western portion of the Province. In: Crown Land Surveys for the year ending 31st December, 1892, pp. 483-503.

Hart, C.J.R., 1997. A transect across northern Stikinia: Geology of the northern Whitehorse map area, southern Yukon Territory (105D/13-16). Exploration and Geological Services Division, Yukon Region, Indian and Northern Affairs Canada. Bulletin, 8, 112p.

Ikeda, M., and Tada, R., 2014. A 70 million year astronomical time scale for the deep-sea bedded chert sequence (Inuyama, Japan): Implications for Triassic–Jurassic geochronology. Earth and Planetary Science Letters, 399, 30-43.

James, A.R.C., 1956. Callison Copper (Brikon Explorations Limited). In: Minister of Mines Annual Report 1955, pp. 13-14.

Lane, R.W., 2005. Diamond drilling, trenching and rock sampling report, 2004 exploration program - DK Creek west. Assessment Report AR27778, British Columbia Ministry of Energy and Mines, 234p.

Logan, J.M., Drobe, J.R., and McClelland, W.C., 2000. Geology of the Forest Kerr - Mess Creek Area, northwestern British Columbia . British Columbia Ministry of Energy and Mines, British Columbia Geological Survey Bulletin 104, 164p.

Logan, J.M., and Mihalynuk, M.G., 2014. Tectonic controls on early Mesozoic paired alkaline porphyry deposit belts (Cu-Au ±Ag-Pt-Pd-Mo) within the Canadian Cordillera. Economic Geology, 109, 827-858.

Ludwig, K.R., 2003. User's manual for Isoplot/Ex rev. 3.00: a Geochronological Toolkit for Microsoft Excel. Special Publication 4, Berkeley Geochronology Center, Berkeley.

Markey, R., Stein, H., and Morgan, J., 1998. Highly precise Re–Os dating for molybdenite using alkaline fusion and NTIMS. Talanta, 45, 935–946.

Markey, R., Stein, H.J., Hannah, J.L., Zimmerman, A., Selby, D., and Creaser, R.A., 2007. Standardizing Re–Os geochronology: a new molybdenite reference material (Henderson, USA) and the stoichiometry of Os salts. Chemical Geology, 244, 74–87.

Massey, N.W.D., MacIntyre, D.G., Desjardins, P.J., and Cooney, R.T., 2005. Digital Geology of British Columbia: Whole province. British Columbia Ministry of Energy and Mines, British Columbia Geological Survey Digital map Geofile 2005-1.

Mihalynuk, M.G., Nelson, J., and Diakow, L.J., 1994. Cache Creek Terrane entrapment: oroclinal paradox within the Canadian Cordillera. Tectonics, 13, 575-595.

Mihalynuk, M.G., Erdmer, P., Ghent, E.D., Cordey, F., Archibald, D.A., Friedman, R.M., and Johannson, G.G., 2004. Coherent French Range blueschist: Subduction to exhumation in <2.5 m.y.? Geological Society of America Bulletin, 116, 910-922.

Mihalynuk, M.G., Diakow, L.J., Logan, J.M., and Friedman, R.M., 2015. Preliminary geology of the Shrimpton Creek area (NTS 092H/15E, 16W) Southern Nicola Arc Project. In: Geological Fieldwork 2014, British Columbia Ministry of Energy and Mines, British Columbia Geological Survey Paper 2015-1, pp. 129–163.

Mihalynuk, M.G., Diakow, L.J., and Friedman, R.M., 2016. Chronology of southern Nicola Arc stratigraphy and deformation. In: Geological Fieldwork 2015, British Columbia Ministry of Energy and Mines, British Columbia Geological Survey Paper 2016-1, this volume.

Mihalynuk, M.G., and Zagorevski, A.,2016. Geochemical results from GEM2 Reconnaissance surveys between the Stikine River and Atlin, British Columbia Ministry of Energy and Mines, British Columbia Geological Survey GeoFile 2016-2.

Monger, J.W.H., Price, R.A., and Tempelman-Kluit, D.J., 1982. Tectonic accretion and the origin of the two major metamorphic and plutonic welts in the Canadian Cordillera. Geology, 10, 70-75.

Murphy, D.C., van der Heyden, P., Parrish, R.R., Klepacki, D.W., McMillan, W., Struik, L.C., and Gabites, J., 1995. New geochronological constraints on Jurassic deformation of the western edge of North America, southeastern Canadian Cordillera. In: Miller, D.M. and Busby C., (Eds.), Jurassic magmatism and tectonics of the North American Cordillera. Geological Society of America Special Paper 299, pp. 159–171.

Panteleyev, A., 1983. 1977 - Star copper prospect (104J/4, 5). In: Geology in British Columbia 1977 - 1981, British Columbia Ministry of Energy, Mines and Petroleum Resources, British Columbia Geological Survey, pp. 175–180.

Panteleyev, A., 1976. Geochemistry and age of the Kaketsa stock (104J/4W). In: Geological Fieldwork 1975, British Columbia Ministry of Energy, Mines and Petroleum Resources, British Columbia Geological Survey Paper 1976-1, pp. 77–78.

Panteleyev, A., and Dudas, B.M., 1973. Go, G. In: Exploration in British Columbia 1972 1973, British Columbia Ministry of Energy, Mines and Petroleum Resources, British Columbia Geological Survey, pp. 547–549.

Piercey, S.J., 2004. Reconnaissance geological and geochemical studies of the Joe Mountain Formation, Joe Mountain region (NTS 105D/15), Yukon. Yukon Exploration and Geology, 213–226.

Prosper Gold Corporation, 2015. Star Project. http://www.prospergoldcorp.com/s/Star_Project.asp , Accessed December, 2015.

Scott, J.E., Richards, J.P., Heaman, L.M., Creaser, R.A., and Salazar, G.S., 2008. The Schaft Creek Porphyry Cu-Mo-(Au) Deposit, Northwestern British Columbia. Exploration and Mining Geology, 17, 163-196.

Selby, D., and Creaser, R.A., 2004. Macroscale NTIMS and microscale LA-MC-ICP-MS Re-Os isotopic analysis of molybdenite: Testing spatial restrictions for reliable Re-Os age determinations, and implications for the decoupling of Re and Os within molybdenite. Geochimica et Cosmochimica Acta, 68, 3897–3908.

Shirvani, F., 2015. Doubleview Resumes Exploration Program at its Hat Project. Doubleview Capital Corp.. Available from http://www.doubleview.ca/doubleview-resumes-exploration-program-hat-project/.

Stern, R., 1997. The GSC Sensitive High Resolution Ion Microprobe (SHRIMP): Analytical techniques of zircon U-Th-Pb age determinations and performance evaluation. In: Geological Survey of Canada Radiogenic Age and Isotopic Studies, Report 10, 1997-F, pp. 1–31.

Stern, R.A., and Amelin, Y., 2003. Assessment of errors in SIMS zircon U–Pb geochronology using a natural zircon standard and NIST SRM 610 glass. Chemical Geology, 197, 111-142.

Takaichi, M., 2013. Assessment Report on the 2012 Geological, Geochemical, and Geophysical Program at the Eagle Property, BC, Canada. British Columbia Ministry of Energy and Mines, Assessment Report AR34266, Victoria, BC, Canada.

Takaichi, M., and Johnson, C., 2012. Assessment Report on the 2011/2012 Geological, Geochemical, and Geophysical program at the Eagle Property, BC, Canada. British Columbia Ministry of Energy and Mines, Assessment Report AR33330, 383p.

Watson, P.H., Godwin, C.J. and Armstrong, R.L., 1981, Geology, mineralization and K-Ar and Rb-Sr isotopic study of the Ram zinc-lead-silver property, Yukon Plateau, southwest Yukon Territory (105D/4). In: Yukon Geology and Exploration 1979-80, Indian and Northern Affairs Canada, pp. 123-127.

Woodsworth, G.J., Anderson, R.G., Armstrong, R.L., Struik, L.C., and van der Heyden, P., 1992. Plutonic regimes. In: Gabrielse, H. and Yorath, C. J., (Eds.), Geology of the Cordilleran Orogen in Canada, Geological Society of America DNAG volume G-2, pp. 493–531.

Zagorevski, A., Mihalynuk, M.G., Joyce, N., and Martin, K., 2014. Characterization of volcanic and intrusive rocks across the British Columbia - Yukon border, GEM 2 Cordillera. Geological Survey of Canada Open File 7697.

Zagorevski, A., Mihalynuk, M.G., Joyce, N., Kellett, D.A., and Milidragovic, D., 2015. Characterization of volcanic and intrusive rocks across the British Columbia – Yukon border, GEM 2 Cordillera; Geological Survey of Canada Open File 7956, 13p. doi:10.4095/297272.

Circa 180 Ma Ag-Bi-Pb-Mo-Cu-bearing quartz veins in a post-thrust calc-alkaline intrusion near Surprise Mountain, Iskut River area, northwestern British Columbia

K. Martin[1], A. Zagorevski[2, a], M.G. Mihalynuk[3], N.L. Joyce[2], and R. Creaser[4]

[1] Department of Earth Sciences, University of Ottawa, Ottawa, ON, K1N 6N5
[2] Geological Survey of Canada, 601 Booth Street, Ottawa, ON, K1A 0E8
[3] British Columbia Geological Survey, Ministry of Energy and Mines, Victoria, BC, V8W 9N3
[4] Department of Earth and Atmospheric Sciences, University of Alberta, Edmonton, AB, T6G 2R3
[a] corresponding author: alexandre.zagorevski@canada.ca

Recommended citation: Martin, K., Zagorevski, A., Mihalynuk, M.G., Joyce, N.L., and Creaser, R., 2016. Circa 180 Ma Ag-Bi-Pb-Mo-Cu-bearing quartz veins in a post-thrust calc-alkaline intrusion near Surprise Mountain, Iskut River area, northwestern British Columbia. In: Geological Fieldwork 2015, British Columbia Geological Survey Paper 2016-1, pp. 77-94.

Abstract

Polymetallic mineralized quartz veins are hosted by quartz diorite to quartz monzodiorite near Surprise Mountain, western Iskut River area. The intrusion is a homogeneous calc-alkaline, magnetite series granitoid that crosscuts an Early Jurassic thrust. New ^{40}Ar/^{39}Ar hornblende ages (178 ±2 and 179 ±2 Ma) from quartz diorite and a Re-Os molybdenite (180.2 ±0.8 Ma) age from a mineralized quartz vein provide minimums for the time of pluton emplacement. Both age and composition suggest affiliation with the Cone Mountain plutonic suite. Polymetallic quartz veins contain pyrite, galena, and molybdenite; minor bismuthinite, covellite, chalcocite, chalcopyrite and pyrrhotite; and traces of sphalerite. Geochemical analysis of veins reveals elevated Ag, Bi, Cu, Mo, Pb and Zn. Overall, the sporadic mineralization lacks clear horizontal metal zonation but may be related to polymetallic Ag-Pb-Zn±Au or Cu±Ag quartz deposit types, or may be peripheral to skarn or porphyry mineralization. Weak alteration, erratic and weak Au enrichment, and lack of metal zonation differentiates this occurrence from other Jurassic deposits in the area.

Keywords: Iskut River, Stikinia, Early Jurassic, Surprise Mountain, polymetallic vein, Cone Mountain plutonic suite

---

1. Introduction

Northern Stikinia (Fig. 1) has a rich and diverse metal endowment from a variety of mineral deposit types that reflect the varied tectonic history of the Canadian Cordillera. Deposits in northwestern Stikinia range from Mississippian volcanogenic massive sulphides to Triassic-Jurassic Cu-Au porphyry and Eocene epithermal vein systems (e.g., Logan and Koyanagi, 1994; Logan and Mihalynuk, 2014; Nelson and Kyba, 2014). The Late Triassic to early Middle Jurassic is one of the most important time intervals in the northern Cordillera, and is recorded by regionally extensive volcano-sedimentary rocks of the Hazelton Group (Tipper and Richards, 1976) and coeval plutons (Fig. 2). In the Iskut River region, the Hazelton Group exhibits a short but significant magmatic lull between ~185 and 178.5 Ma and an unconformity (Fig. 3; Lewis, 2013; Cutts et al., 2015). This magmatic lull marks the transition from porphyry and epithermal deposits formed during deposition of the lower part of the Hazelton Group and volcanogenic massive sulphide deposits in the upper part (e.g., Anderson and Thorkelson, 1990; Lewis, 2013; Nelson and Kyba, 2014; Kyba and Nelson, 2015). This magmatic lull is absent in the Telegraph Creek area, where the Cone Mountain plutonic suite was emplaced (Fig. 2; Brown et al., 1996). The duration and aerial extent of this magmatic gap and the distribution of Jurassic plutonic suites are important considerations for mineral exploration and for unravelling the tectonic history of Stikinia.

Herein we present field, petrographic, geochemical, and ^{40}Ar/^{39}Ar and Re-Os geochronologic data from a polymetallic quartz vein-bearing quartz diorite intrusion near Surprise Mountain in the western Iskut River area (Fig. 4), and relate the intrusion to the Cone Mountain suite. Our geochronologic data also show that a thrust fault juxtaposing Permian to Late Triassic marbles above Early Jurassic volcaniclastic rocks and cut by the Surprise Mountain intrusion was active during the magmatic lull.

2. Regional geology

The Iskut River area is along the western margin of the Stikine terrane in northwestern British Columbia (Figs. 1, 2). The oldest rocks in the area are part of the Stikine assemblage (Monger, 1977), which consists of Carboniferous bimodal arc magmatic rocks and Permian sedimentary strata. The Stikine assemblage is unconformably overlain by Triassic volcano-sedimentary rocks of the Stuhini Group; both are cut by the Stikine and Copper Mountain plutonic suites (e.g., Logan et al., 2000; Mihalynuk et al., 2012). Above a regional unconformity bevelled into these rocks are volcanic and sedimentary strata of the Hazelton Group (uppermost Triassic and Lower to Middle Jurassic), which are cut by the Texas Creek (Early Jurassic) and Cone Mountain (late Early Jurassic) plutonic suites (Fig. 2; e.g., Evenchick et al., 2010; Gagnon et al., 2012; Nelson and Kyba, 2014; Cutts et al., 2015). The Hazelton Group represents

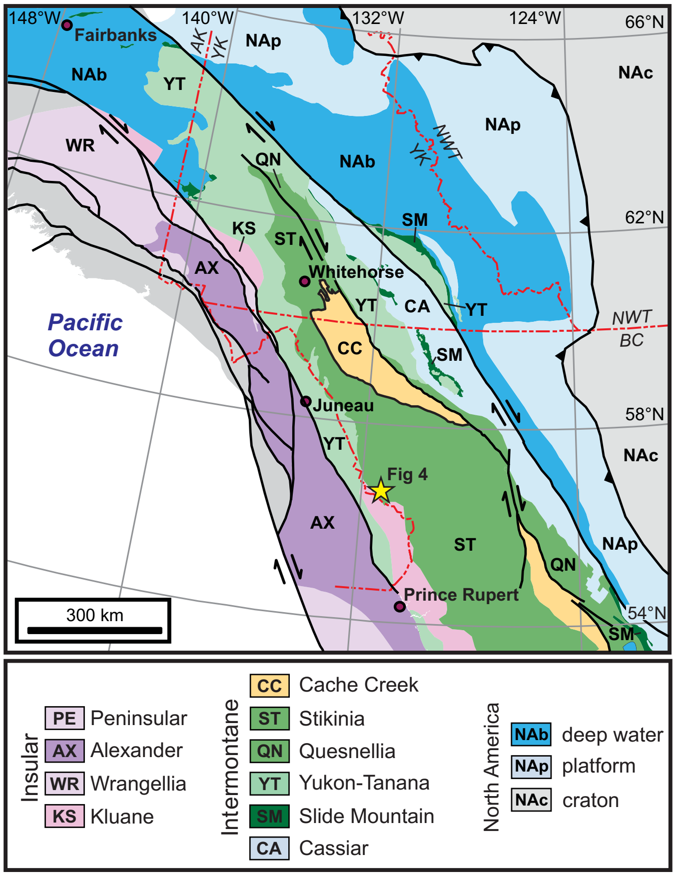

Fig. 1. Geological map of the Canadian Cordillera (from Colpron and Nelson, 2011). Study area (star) is in the Iskut River area of the Stikine terrane.

the final stages of Stikine terrane magmatism before final amalgamation of Stikine, Quesnel, and Cache Creek terranes with North America and deposition of overlap Middle Jurassic to Lower Cretaceous sedimentary rocks of the Bowser Lake Group (Fig. 2; e.g., Evenchick et al., 2007, 2010). Stocks and dikes of the Sloko-Hyder plutonic suite (Eocene) and related volcanic rocks are common in the study area.

The Iskut River area is well known for its prolific mineralization (Fig. 2) including the Eskay, KSM, Brucejack, Snip and Johnny Mountain deposits (Jurassic) and the Burgundy Ridge and Galore Creek deposits (Triassic; e.g., Macdonald et al., 1996). Much of the mineral endowment is spatially associated with hypabyssal porphyritic intrusions (Anderson, 1993) of diverse composition. These plutonic suites include Forrest Kerr and More Creek (Devono-Mississipian), Stikine (Late Triassic), Texas Creek (Early Jurassic), Cone Mountain (late Early Jurassic), Three Sisters (Middle Jurassic) and Sloko-Hyder (Eocene; e.g., Anderson, 1993; Logan and Koyanagi, 1994; Logan et al., 2000; Mihalynuk et al., 2012; Logan and Mihalynuk, 2014). Some members of the Copper Mountain and Texas Creek plutonic suites are distinctive. The Copper Mountain (Late Triassic to Early Jurassic) plutonic suite is conspicuously quartz undersaturated, and includes stocks of foid-bearing syenite, syenite, pyroxenite, gabbro, and monzodiorite compositions (210-195 Ma; Brown et al., 1996; Zagorevski et al., 2015). The Texas Creek plutonic suite consists of calc-alkaline and alkaline intrusions that vary from granodiorite, to quartz monzonite, and quartz monzodiorite, but includes distinctive crowded plagioclase-phyric diorite, K-feldspar megacrystic monzogranite and syenite (195-189 Ma; Macdonald et al., 1996; Febbo et al., 2015).

3. Surprise Mountain

The Surprise Mountain area is underlain by Triassic to Jurassic epiclastic rocks and marble that are cut by equigranular hornblende quartz diorite (Fig. 4).

3.1. Country rocks

The contact between the epiclastic rocks and marbles is a high-strain zone that includes isoclinal folds in the marble (Fig. 5a) and is interpreted as a thrust fault (Mihalynuk et al., 2012). Along strike to the west are limestones that yielded Permian to Late Triassic conodont fauna (Orchard, 1993). Along the eastern margin of the intrusion, the marble defines a garnet, diopside, actinolite ±wollastonite, quartz, carbonate and pyrite exoskarn (Fig. 5b). Euhedral, zoned garnet has optically isotropic cores and anisotropic rims, typical of skarn garnet that form along the grossular-andradite garnet solid solution series (Deer et al., 1997). Early Jurassic volcaniclastic sedimentary rocks (Mihalynuk et al., 2012) structurally beneath the marble (Fig. 4) consist of buff to green weathering, medium bedded, graded tuffaceous wacke. The tuffaceous component is represented by angular plagioclase fragments and altered mafic minerals.

3.2. Hornblende quartz diorite intrusion

Unfoliated, medium- to coarse-grained equigranular intrusion consists of quartz, plagioclase, K-feldspar, and hornblende (Figs. 6a-c). Although the intrusion is relatively homogeneous, the relative proportion of these minerals varies. Hornblende prisms generally range from <1 mm to 4 mm, but are locally as large as 1 cm (Fig. 6b). Feldspars display carlsbad, polysynthetic, and tartan twinning with discontinuous and oscillatory zoning. Offsets of twin lamellae indicate some deformation of the feldspar grains. Very fine myrmekite is locally present between feldspar and quartz grains. Accessory minerals include magnetite, hematite, pyrite, titanite, apatite, and zircon. Magnetite, abundant in most samples, is partially to extensively replaced by, and/or is intergrown with, high-temperature hematite (Fig. 6d). Locally, zones of magnetite-hematite exsolution are well developed. Pyrite disseminations are common.

The intrusion contains angular to rounded diorite to gabbro enclaves that range from decimetres to a metre in diameter (Fig. 6a). These enclaves may represent cognate xenoliths and/or disaggregated syn-magmatic sills, typical of Cordilleran batholiths (Foster and Hyndman, 1990; Brown et al., 1996). The intrusion is cut by rare mafic dikes, leucocratic dikes that locally form subparallel and conjugate arrays, and a K-feldspar and quartz porphyritic dike. Polymetallic mineralized quartz,

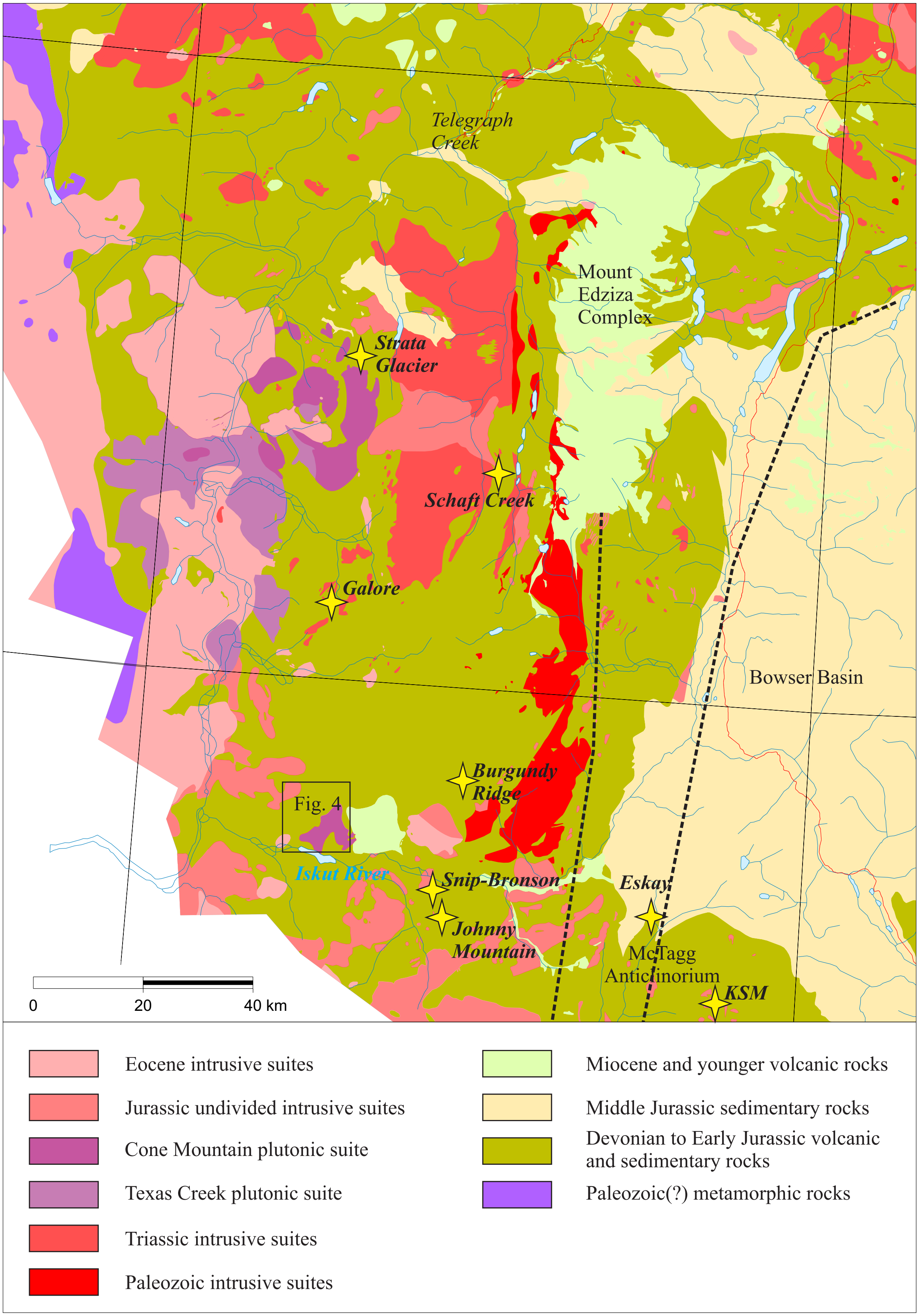

Fig. 2. Simplified geological map of Iskut River – Telegraph Creek area highlighting Mesozoic plutonic suites. Black dashed line is approximate location of the Eskay Rift.

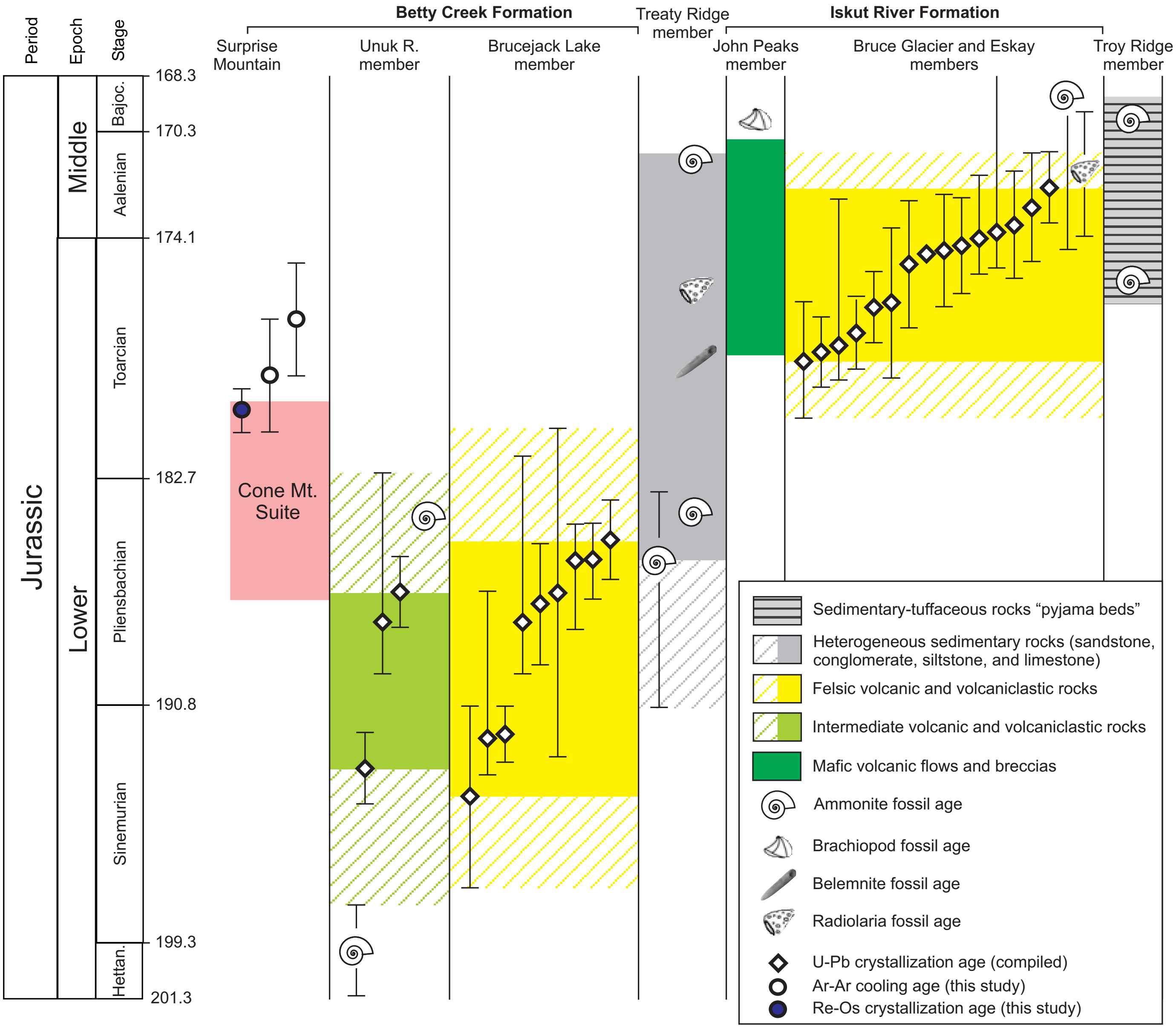

Fig. 3. Summary of Hazelton Group geochronologic and fossil data from the Iskut River area (modified after Cutts et al., 2015) shows a prominent magmatic lull. Data compiled from Macdonald (1993), Childe (1994, 1996), Macdonald et al. (1996), Lewis et al. (2001), Evenchick et al. (2010), Gagnon et al. (2012) and Cutts et al. (2015). Stage boundaries are from Cohen et al. (2013). Age range of the Cone Mountain plutonic suite is from Brown et al. (1996).

and barren epidote and quartz-epidote veins are locally abundant (see below).

3.3. Alteration of the hornblende quartz diorite intrusion

Alteration of quartz diorite is neither pervasive nor intense and generally forms cm- to mm- scale haloes around mineralized quartz veins (Figs. 7a-c). Alteration only partially replaces the primary mineralogy, and consists of sericite, saussurite, epidote, chlorite, carbonate, and Fe-oxide. Alteration intensity varies throughout the intrusion. Some parts contain mainly sericite and saussurite, with minor epidote and no chlorite. Elsewhere, epidote, saussurite, and sericite alteration is predominant, and chlorite is abundant. Alteration of plagioclase to sericite, saussurite, and epidote is particularly obvious in zoned plagioclase crystals where only cores are altered. Hornblende ranges from pristine to completely replaced by chlorite and minor epidote. Carbonate, Fe-oxide, and clay minerals occur along fractures and in-fill brecciated zones. Pyrite is consistently rimmed by iron hydroxides. Alteration of the quartz diorite is particularly intense near quartz veins as narrow selvages of sericite-saussurite. Overall, the quartz diorite body exhibits a macroscopic bleaching towards the most intensely veined part of the intrusion, probably due to a combination of lower modal hornblende abundance, replacement of hornblende by light-weathering chlorite, and increased sericite and saussurite alteration of feldspar.

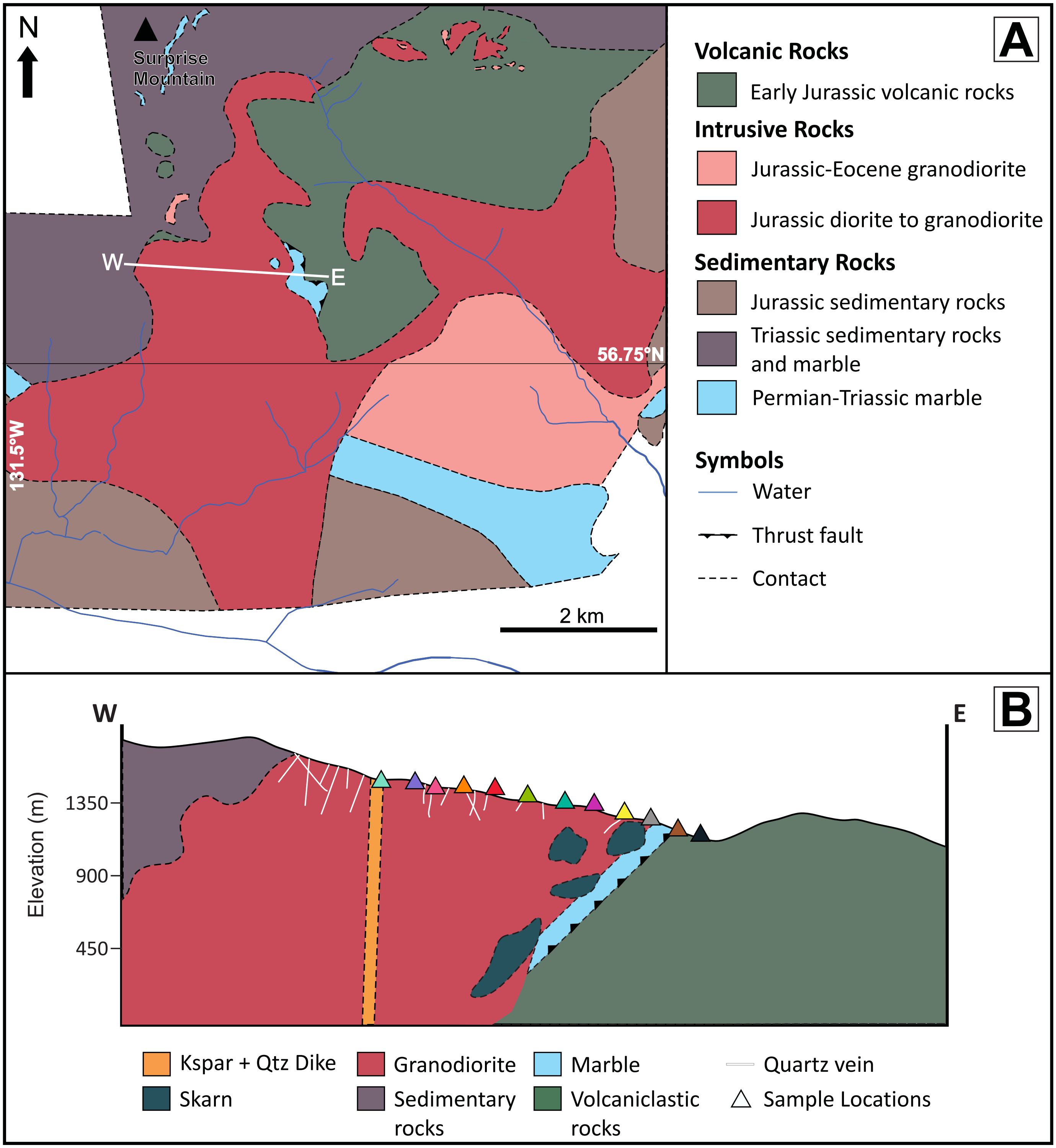

Fig. 4. a) Simplified geological map of the Surprise Mountain area (modified from Mihalynuk et al., 2012). **b)** Schematic cross-section of quartz diorite and host sedimentary rocks. Approximate sample positions indicated by coloured triangles.

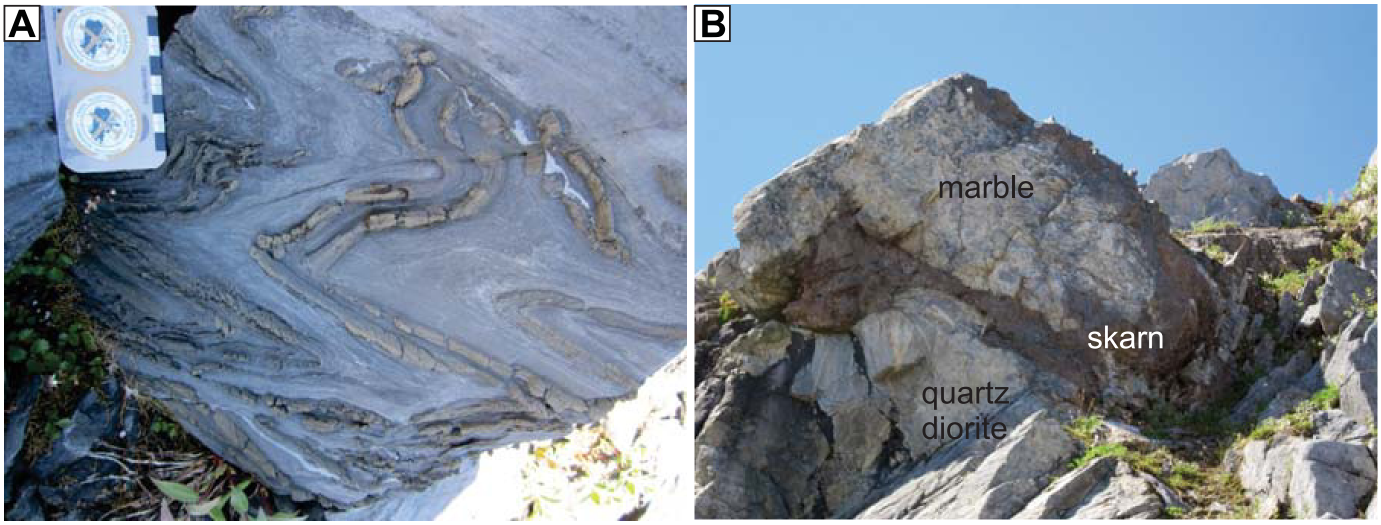

Fig. 5. Permian-Triassic marble, Surprise Mountain area. **a)** Folded (in part isoclinal) layering in immediate hanging wall of thrust fault. Compositional layering in the marble consists of alternating silica and calcite-rich bands. **b)** Marble pod (light toned) in contact with quartz diorite and enveloped by exoskarn.

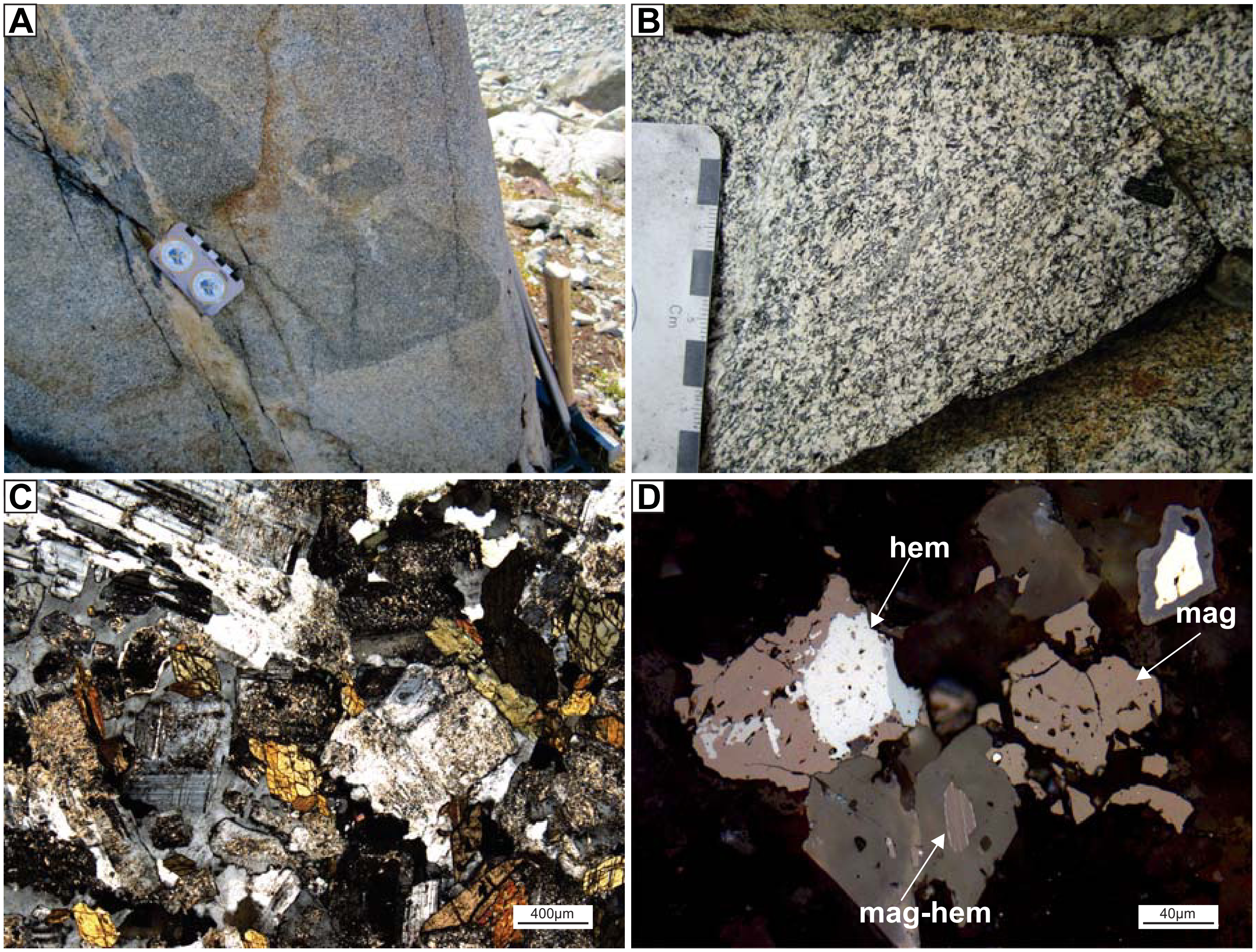

Fig. 6. Hornblende quartz diorite. **a)** Enclaves of diorite in quartz diorite. **b)** Equigranular hornblende quartz diorite (sample ZE573) with sparse hornblende phenocrysts. **c)** Cross-polarized transmitted light view of partially altered quartz diorite. **d)** Polarized reflected light view of magnetite (mag) and hematite (hem), locally exhibiting exsolution texture.

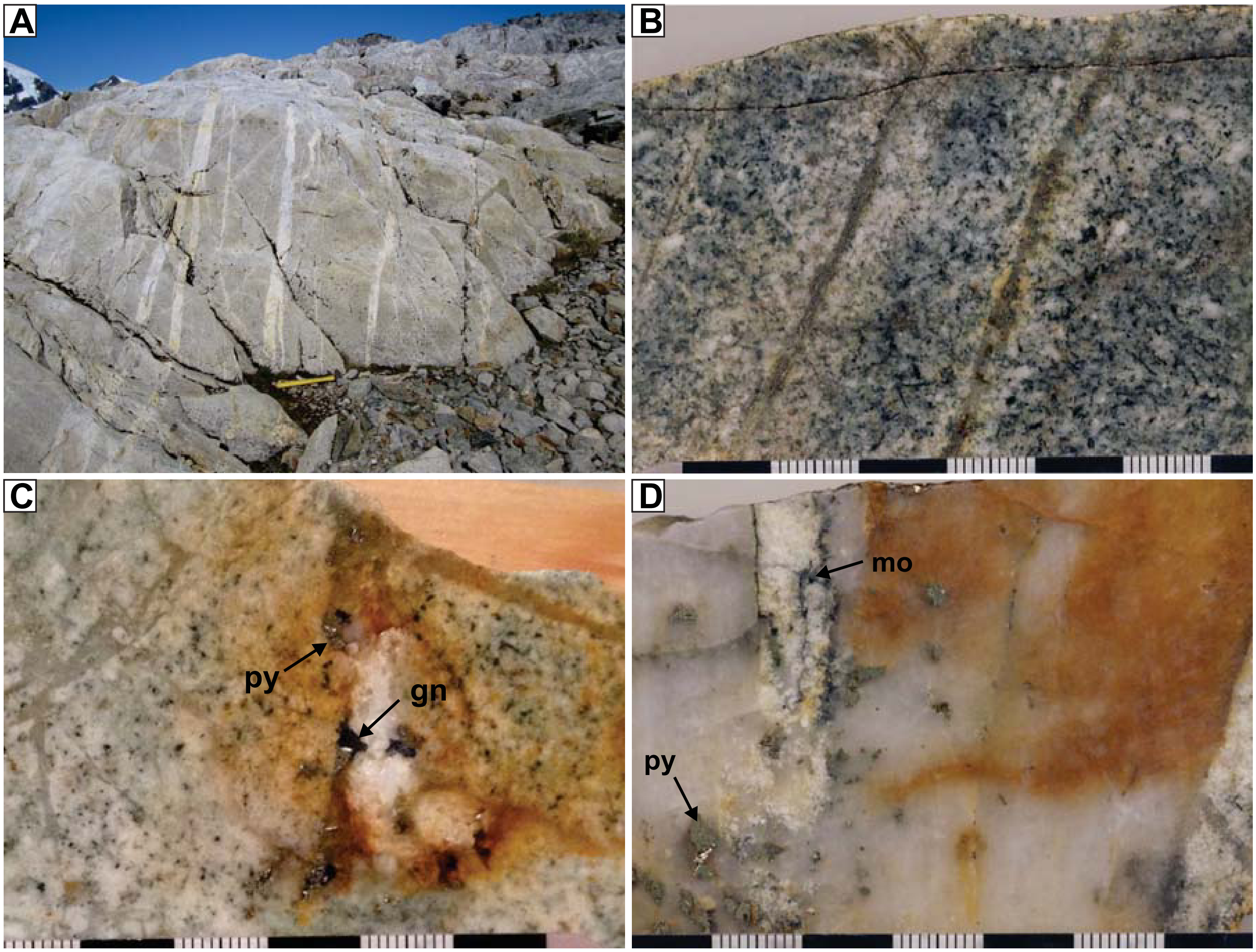

Fig. 7. Quartz veins in quartz diorite intrusion. **a)** Subparallel quartz veins cutting quartz diorite. **b)** Equigranular hornblende quartz diorite cut by thin (4 mm) mineralized quartz veins with narrow alteration haloes (sample K010B). **c)** Bleached granodiorite cut by weakly developed thin quartz vein stockwork, with pyrite (py) and galena (gn) (sample K012A). **d)** Molybdenite (mo) and pyrite (py) mineralization in a 10 cm thick quartz vein (sample K012B).

3.4. Polymetallic veins in the hornblende quartz diorite intrusion

Millimetre- to decimetre- scale quartz veins generally form parallel sets, but also crosscut and form weakly developed stockworks (Figs. 7a, b). The veins trend predominantly ENE-WSW, display moderate to steep dips (~55-70°), and are subparallel to minor ductile shear zones and deformed dikes in the intrusion. Polymetallic sulphides in the quartz veins (Figs. 7c, d) tend to form clots and commonly weather recessively. Mineralized quartz veins tend to be massive and locally fractured and altered by Fe-oxide and hydroxides. Microstructures observable in quartz include deformation lamellae, bulging subgrains and subgrain rotation indicating elevated temperature during deformation (e.g., Passchier and Trouw, 1998).

Mineralization in the quartz veins consists mainly of pyrrhotite, chalcopyrite, and pyrite with subordinate galena, molybdenite, bismuthinite, covellite, chalcocite, magnetite, ilmenite, and sphalerite. Pyrrhotite, commonly intergrown with chalcopyrite, forms blebs in pyrite (Fig. 8a). Pyrrhotite blebs locally contain sphalerite and bismuthinite. Covellite and chalcocite occur as rims on galena, and inclusions in pyrite (Figs. 8b, c), suggesting replacement of chalcopyrite. Bismuthinite inclusions within pyrite may display zonation from bismuthinite, to native bismuth, with rare zones of Bi-Pb-sulphides (Fig. 8d). Pyrite overprints all minerals except molybdenite and Fe-oxides, which replace pyrite along fractures (Figs. 8e, f). Overprinting of pyrite seems to increase towards the middle of the intrusion where galena, bismuthinite, and molybdenite abundance increases with intensity of pyrite overprint. Replacement of chalcopyrite by covellite and chalcocite, and replacement of pyrite by Fe-oxide and hydroxide is interpreted as late stage alteration.

4. Geochronology

We analyzed hornblende from two quartz diorite samples

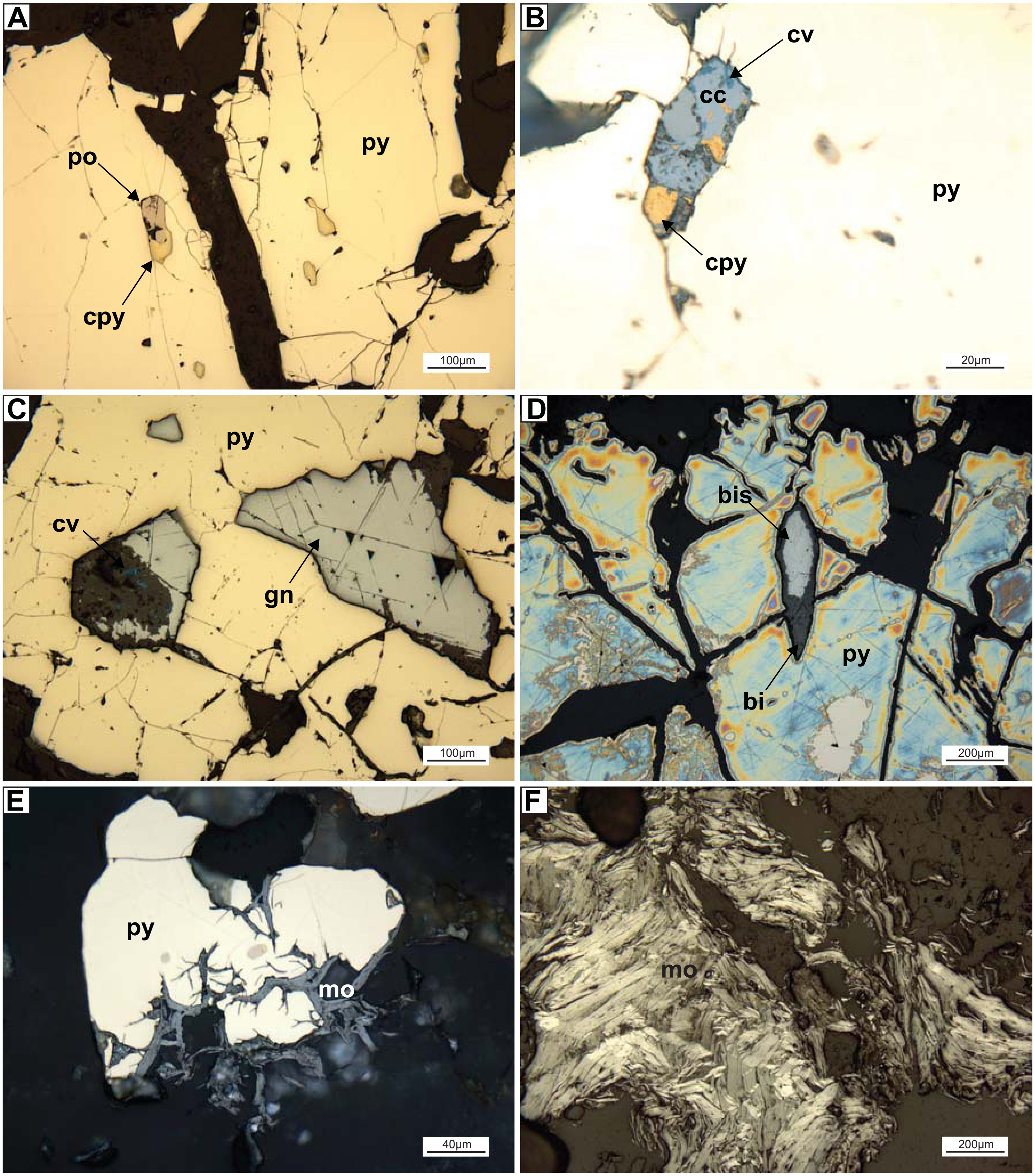

Fig. 8. Mineralization in polymetallic veins. **a)** Polarized reflected light view of chalcopyrite (cpy) and pyrrhotite (po) in pyrite (py). **b)** Polarized reflected light view of covellite (cv) and chalcocite (cc) replacing chalcopyrite (cpy) in pyrite (py). **c)** Polarized reflected light view of pyrite (py) enclosing galena (gn) with late(?) covellite (cv). **d)** Polarized reflected light view of bismuthinite (bis) and bismuth (bi) included in tarnished pyrite (py). **e)** Partly uncrossed polarized reflected light view of molybdenite (mo) replacing py along fractures; pinkish blebs in pyrite are pyrrhotite (po). **f)** Crossed polarized reflected light view of molybdenite (mo) in gangue.

of the Surprise Mountain intrusion using laser $^{40}Ar/^{39}Ar$ step-heating and molybdenite from one sample of a crosscutting quartz vein that contains disseminated sulphides using Re-Os isotopes.

4.1. $^{40}Ar/^{39}Ar$ methods

Samples 14ZEK009 and 11ZE573 were processed for $^{40}Ar/^{39}Ar$ analysis by standard preparation techniques, including hand-picking of fresh unaltered grains of hornblende in the size range 0.25 to 1.0 mm. Individual hornblende separates were loaded into aluminum foil packets along with grains of Fish Canyon Tuff Sanidine (FCT-SAN) to act as flux monitor (apparent age = 28.201 ±0.023 Ma; 1σ, Kuiper et al., 2008). The sample packets were arranged radially inside two separate aluminum canisters; sample 14ZEK009 was included in sample batch GSC #69 and sample 11ZE573 was included in sample batch GSC #70. Both sample batches were submitted for 160 MWh irradiations (Cd-shielded) in the medium flux position 8B at the research reactor of McMaster University in Hamilton, Ontario, Canada.

Laser $^{40}Ar/^{39}Ar$ step-heating analysis was carried out at the Geological Survey of Canada Noble Gas laboratory in Ottawa, Ontario. Upon return from the reactor, samples were split into one or more aliquots each and loaded into individual 1.5 mm-diameter holes in a copper planchet. The planchet was then placed in the extraction line and the system evacuated. Heating of individual sample aliquots in steps of increasing temperature was achieved using a Photon Machines, Inc. Fusions 10.6 55W CO_2 laser equipped with an optical beam-flattening homogenizer lens. The released Ar gas was cleaned in the extraction line over two hot SAES^{TM} NP-10 getters of St 707 alloy (Zr-V-Fe) held at ~400°C (to remove nitrogen, oxygen, hydrocarbons, water and other active gases) and a room-temperature getter containing HY-STOR$^{®}$ 201 calcium-nickel alloy pellets (to remove hydrogen), and then analyzed isotopically using a Nu Instruments multicollector Noblesse mass spectrometer, equipped with a Faraday detector and three ion counters. The analyses were run in ion counter multicollection mode ('MC-Y' mode; additional analytical details provided in Kellett and Joyce, 2014). Blank measurements were made throughout the analytical sessions, the values for which are included in the footnotes of Table 1. Mass fractionation and detector efficiencies were determined from repeated measurements of air aliquots carried out throughout the analytical sessions, whereby ^{40}Ar and ^{36}Ar signals were measured on all collectors. $^{40}Ar/^{36}Ar$ ratios were then determined for each collector individually, and for each combination of collectors. Detector inter-calibration methods are described in further detail in Kellett and Joyce (2014). Data reduction and age calculations were performed using Mass Spec software version 7.93; details regarding data reduction, error propagation and age calculation are outlined in Deino (2001). The software applies and propagates errors for all corrections, including detector inter-calibration factors.

Corrected argon isotopic data are listed in Table 1, and presented in Figure 9 as spectra of gas release or on inverse-isochron plots. For gas release spectra, both the apparent ages and plateau ages calculated from the step-heating analyses rely on the assumption that atmospheric argon has a $^{40}Ar/^{36}Ar$ ratio of 298.56 (Lee et al., 2006; Mark et al., 2011). For this report, a plateau age is defined as an age derived from three or more consecutive heating steps that are statistically equivalent at 95% confidence level, and comprise greater than 50% of the total ^{39}Ar released. In cases where excess ^{40}Ar is suspected in a sample, data are plotted on the inverse isochron diagram, where $^{36}Ar/^{40}Ar$ is plotted against $^{39}Ar/^{40}Ar$ for each analysis (after correction for irradiation-produced interfering isotopes and mass spectrometer discrimination; Roddick, 1988).

Neutron flux gradients throughout the sample canister were evaluated by analyzing the FCT-SAN sanidine flux monitors included with each sample packet and interpolating a linear fit against calculated J-factor and sample position. The error on individual J-factor values is conservatively estimated at ±0.6% (2σ). Because the error associated with the J-factor is systematic and not related to individual analyses, correction for this uncertainty is not applied until calculation of dates from isotopic correlation diagrams (Roddick, 1988). Errors in the plateau and inverse isochron ages do not include the errors of decay constants. Nucleogenic interference corrections were $(^{40}Ar/^{39}Ar)_K = 0.025 \pm .005$, $(^{38}Ar/^{39}Ar)_K = 0.011 \pm 0.010$, $(^{40}Ar/^{37}Ar)_{Ca} = 0.002 \pm 0.002$, $(^{39}Ar/^{37}Ar)_{Ca} = 0.00068 \pm 0.00004$, $(^{38}Ar/^{37}Ar)_{Ca} = 0.00003 \pm 0.00003$, $(^{36}Ar/^{37}Ar)_{Ca} = 0.00028 \pm 0.00016$. The decay constant used was $^{40}K\lambda_{total} = 5.463 \pm 0.214 \times 10^{-10}/a$ (2σ) from Min et al. (2000). All errors are quoted at the 2σ level of uncertainty. The 'MSWD' is defined as the mean square of weighted deviates.

4.2. $^{40}Ar/^{39}Ar$ results

4.2.1. Sample 14ZEK009; hornblende quartz diorite

Hornblende from this sample is clean, fresh, and dark brown to black. One aliquot was analyzed, yielding a flat four-step plateau, giving an age of 178 ±2 Ma (Fig. 9a; MSWD = 1.14, 96.8% of total ^{39}Ar). This age overlaps within error with the inverse isochron hornblende age of sample 11ZE573 and Re-Os age (see below).

4.2.2. Sample 11ZE573; equigranular hornblende quartz diorite

Hornblende grains from this sample are clean, fresh, and dark brown. The degassing behaviour of the hornblende was unpredictable and inconsistent from one aliquot to the next, with most of the gas commonly being released in one or two heating steps. Four aliquots were analyzed, each with slightly different heating schedules, with hopes of achieving more evenly-distributed gas releases. An evenly-distributed pattern was not obtained, and three of four aliquots yielded downward-stepping spectra, best exhibited in Aliquot #1 (Fig. 9b, inset 1). Aliquots #2 and #4 gave plateau and pseudo-plateau ages of 183 and 182 Ma, respectively. However, when plotted on the inverse isochron diagram, most data points from all four aliquots fall below the atmospheric line, confirming the

Table 1. ^{40}Ar/^{39}Ar data for hornblende samples 11ZE573 and 14ZEK009.

			Isotopic Abundances[c] (cps)										Background Isotopic Abundances (cps)																	Inverse Isochron Data				
Run ID#[a]	**Step Used[b]**	**Watts**	**^{40}Ar**	**±1σ**	**^{39}Ar**	**±1σ**	**^{38}Ar**	**±1σ**	**^{37}Ar**	**±1σ**	**^{36}Ar**	**±1σ**	**^{40}Ar Bkgd**	**±1σ**	**^{39}Ar Bkgd**	**±1σ**	**^{38}Ar Bkgd**	**±1σ**	**^{37}Ar Bkgd**	**±1σ**	**^{36}Ar Bkgd**	**±1σ**	**^{39}Ar % of total**	**%(^{36}Ar)$_{Ca}$**	**Ca/K**	**±1σ**	**%^{40}Ar***	**Age (Ma)**	**±1σ**	**^{36}Ar/^{40}Ar**	**±%1σ**	**^{39}Ar/^{40}Ar**	**±%1σ**	**^{36}Ar/^{39}Ar Er. Corr.**
14ZEK009, Hornblende, J = 3.147 ± 0.020 x 10^{-3} (1σ)[e]																																		
Aliquot 1																																		
3334-02A		0.60	125369	79	265.19	3.40	77.97	2.46	1124.5	17.4	378.93	4.14	10216	20	16.65	0.93	28.30	0.82	36.3	1.1	48.71	1.90	1.3	0.1	8.3	0.2	9.8	252.3	23.7	0.003020	1.10	0.002109	1.29	0.002837
3334-02B		0.80	6610	44	166.77	3.65	2.77	1.52	660.2	15.1	17.04	2.44	10216	20	16.65	0.93	28.30	0.82	36.3	1.1	48.71	1.90	0.8	1.1	7.8	0.2	23.9	54.2	24.5	0.002550	14.48	0.025164	2.29	0.013270
3334-02C		1.00	7100	38	222.63	4.63	3.05	1.29	653.4	15.1	9.36	3.15	10216	20	16.65	0.93	28.30	0.82	36.3	1.1	48.71	1.90	1.1	1.9	5.8	0.2	61.4	110.3	23.1	0.001293	34.36	0.031299	2.15	0.003948
3334-02D	*	1.30	345132	166	10132.90	31.50	211.38	3.77	67327.9	296.1	83.06	2.81	10236	29	18.82	0.79	26.76	0.79	39.6	1.0	51.16	1.10	49.3	22.6	13.0	0.1	94.4	**178.4**	**1.1**	0.000186	4.38	0.029230	0.32	0.001675
3334-02E	*	1.60	12456	65	389.08	13.88	11.20	1.43	2197.6	25.5	3.55	1.98	10236	29	18.82	0.79	26.76	0.79	39.6	1.0	51.16	1.10	1.9	17.3	11.1	0.4	93.0	**165.5**	**9.9**	0.000236	67.54	0.031119	3.62	0.001106
3334-02F	*	2.00	232525	107	7125.89	16.39	145.61	2.97	45392.8	171.7	21.90	2.30	10236	29	18.82	0.79	26.76	0.79	39.6	1.0	51.16	1.10	34.7	57.8	12.5	0.1	98.8	**178.8**	**1.1**	0.000040	24.98	0.030517	0.24	0.000361
3334-02G	*	6.00	72461	48	2232.33	6.48	42.19	2.10	15368.6	90.0	9.98	2.83	10256	20	18.14	0.86	27.46	0.83	38.6	1.2	52.92	1.30	10.9	43.0	13.5	0.1	97.7	**176.0**	**2.2**	0.000079	49.80	0.030667	0.30	0.000299
11ZE573, Hornblende, J = 3.511 ± 0.010 x 10^{-3} (1σ)[d]																																		
Aliquot 1																																		
3377-01A		0.60	104541	110	1631.18	5.70	54.68	1.74	7588.3	57.5	129.35	2.46	11396	22	16.98	0.59	36.65	0.76	42.6	0.9	52.92	0.95	4.8	1.6	9.1	0.1	63.7	245.7	2.8	0.001217	1.93	0.015555	0.37	0.015777
3377-01B		0.80	157006	140	4087.66	9.59	85.02	1.98	37595.2	172.8	71.57	1.99	11396	22	16.98	0.59	36.65	0.76	42.6	0.9	52.92	0.95	12.1	14.7	18.0	0.1	88.4	207.3	1.6	0.000389	3.26	0.025875	0.25	0.009694
3377-01C		0.90	694824	579	21071.77	32.76	427.11	4.07	172164.5	744.5	240.00	3.07	11396	22	16.98	0.59	36.65	0.76	42.6	0.9	52.92	0.95	62.3	20.0	16.0	0.1	91.8	185.7	1.3	0.000276	1.60	0.030162	0.18	0.024464
3377-01D		1.00	23980	79	741.99	3.45	16.99	1.60	5834.2	49.0	12.49	1.65	11396	22	16.98	0.59	36.65	0.76	42.6	0.9	52.92	0.95	2.2	13.0	15.4	0.1	86.5	172.2	4.2	0.000453	15.25	0.030781	0.57	0.012358
3377-01E	#	1.10	28372	45	928.68	3.94	14.44	1.71	9227.0	59.8	6.36	1.68	11946	25	16.86	1.10	39.22	0.76	45.2	0.9	57.35	1.00	2.7	40.5	19.5	0.2	96.0	**180.5**	**3.6**	**0.000133**	**44.51**	**0.032516**	**0.46**	**0.001257**
3377-01F		1.20	14051	39	479.05	3.34	9.33	1.45	4728.2	36.6	5.68	1.68	11946	25	16.86	1.10	39.22	0.76	45.2	0.9	57.35	1.00	1.4	23.2	19.3	0.2	90.7	164.5	6.5	0.000311	38.58	0.033871	0.75	0.002676
3377-01G		1.30	63014	48	1302.80	5.04	35.32	1.63	10913.0	70.5	88.92	2.34	11946	25	16.86	1.10	39.22	0.76	45.2	0.9	57.35	1.00	3.8	3.4	16.4	0.1	59.3	176.6	3.5	0.001363	2.73	0.020559	0.40	0.005473
3377-01H		2.00	56124	47	1924.87	6.27	34.76	1.86	16590.7	105.5	23.48	1.56	11946	25	16.86	1.10	39.22	0.76	45.2	0.9	57.35	1.00	5.7	19.7	16.9	0.1	90.0	162.1	2.0	0.000336	8.30	0.034100	0.34	0.002540
3377-01I		6.00	86535	54	1671.88	5.73	54.47	1.77	13823.5	95.7	153.62	3.18	11818	19	18.84	0.84	41.51	0.91	49.2	0.9	51.39	1.50	4.9	2.5	16.2	0.1	48.3	154.9	3.6	0.001731	2.12	0.019213	0.35	0.005205
Aliquot 2																																		
3377-02A	#	0.60	224662	140	4832.15	15.14	127.14	2.84	31641.3	192.3	175.41	2.44	9646	23	18.98	0.78	37.44	0.89	45.1	0.8	50.60	0.86	6.6	5.0	12.8	0.1	77.9	**219.9**	**1.4**	**0.000742**	**1.47**	**0.021415**	**0.32**	**0.008295**
3377-02B	#	0.80	1756653	1041	58258.68	110.30	1260.00	14.83	395214.5	#####	156.19	18.92	9646	23	18.98	0.78	37.44	0.89	45.1	0.8	50.60	0.86	79.2	70.6	13.3	0.1	99.2	**183.6**	**1.2**	**0.000026**	**41.38**	**0.033016**	**0.20**	**0.000426**
3377-02C	#	0.83	14979	59	473.14	4.23	9.59	1.55	3010.4	37.6	2.05	1.53	9646	23	18.98	0.78	37.44	0.89	45.1	0.8	50.60	0.86	0.6	40.9	12.5	0.2	97.6	**189.2**	**6.0**	**0.000081**	**126.63**	**0.031453**	**0.98**	**0.001242**
3377-02D	#	0.86	10712	51	341.57	2.76	5.48	1.55	2369.9	29.6	2.63	2.30	9646	23	18.98	0.78	37.44	0.89	45.1	0.8	50.60	0.86	0.5	25.2	13.6	0.2	94.5	**182.0**	**11.9**	**0.000184**	**117.23**	**0.031741**	**0.94**	**0.002043**
3377-02E	#	0.90	13934	69	448.66	6.31	17.48	1.61	3422.5	37.7	0.28	1.84	9987	17	18.47	1.30	33.31	0.73	45.9	0.9	49.05	0.83	0.6	343.9	15.0	0.3	101.5	**193.0**	**7.7**	**- 0.000049**	**-270.92**	**0.032035**	**1.50**	**0.000602**
3377-02F	#	1.00	21587	70	723.98	4.12	19.04	1.40	5328.6	48.3	1.15	1.53	9987	17	18.47	1.30	33.31	0.73	45.9	0.9	49.05	0.83	1.0	128.9	14.4	0.2	100.5	**183.9**	**4.0**	**- 0.000016**	**-454.65**	**0.033374**	**0.66**	**0.000353**
3377-02G	#	1.10	33501	39	1097.71	4.72	28.11	1.52	8714.3	73.8	5.26	1.54	9987	17	18.47	1.30	33.31	0.73	45.9	0.9	49.05	0.83	1.5	46.2	15.6	0.1	97.5	**182.7**	**2.8**	**0.000084**	**54.53**	**0.032594**	**0.45**	**0.000559**
3377-02H	#	1.30	60990	76	1995.71	11.48	41.15	1.74	15501.0	101.7	9.07	1.65	9901	18	19.66	0.66	36.68	0.95	47.0	0.9	47.06	0.87	2.7	47.7	15.2	0.1	97.7	**183.3**	**2.1**	**0.000078**	**34.82**	**0.032553**	**0.59**	**0.000762**
3377-02I	#	2.00	61761	70	2033.74	10.86	42.07	1.74	15608.4	93.2	9.87	1.65	9901	18	19.66	0.66	36.68	0.95	47.0	0.9	47.06	0.87	2.8	44.1	15.0	0.1	97.3	**181.6**	**2.0**	**0.000089**	**29.92**	**0.032762**	**0.55**	**0.000790**
3377-02J	#	6.00	97979	67	3356.67	10.35	73.80	1.90	22343.9	141.5	15.28	2.55	9901	18	19.66	0.66	36.68	0.95	47.0	0.9	47.06	0.87	4.6	40.8	13.0	0.1	97.2	**174.6**	**1.7**	**0.000092**	**28.24**	**0.034109**	**0.32**	**0.000517**
Aliquot 3																																		
3377-03A	#	0.60	71317	63	504.53	3.46	29.56	1.30	2657.6	49.6	110.87	2.23	9967	17	14.86	1.10	26.53	0.53	33.0	0.7	47.42	0.85	0.9	0.7	10.3	0.2	53.9	**435.2**	**7.3**	**0.001544**	**2.02**	**0.007049**	**0.69**	**0.005523**
3377-03B		0.70	16280	86	425.38	3.10	10.73	1.27	1132.0	41.2	27.33	1.77	9967	17	14.86	1.10	26.53	0.53	33.0	0.7	47.42	0.85	0.7	1.2	5.2	0.2	50.5	120.2	7.7	0.001660	6.58	0.026084	0.90	0.047065
3377-03C		0.75	13116	40	454.91	2.75	10.10	1.08	1252.0	44.1	24.54	2.10	9967	17	14.86	1.10	26.53	0.53	33.0	0.7	47.42	0.85	0.8	1.4	5.4	0.2	44.9	81.5	8.5	0.001845	8.67	0.034623	0.68	0.016010
3377-03D		0.80	16682	74	662.90	4.18	9.91	1.13	2832.6	51.7	11.14	1.54	9967	17	14.86	1.10	26.53	0.53	33.0	0.7	47.42	0.85	1.1	7.1	8.4	0.2	81.5	127.6	4.3	0.000621	14.92	0.039628	0.77	0.016981
3377-03E		0.85	4759	33	283.58	2.85	2.76	1.03	664.5	34.9	0.91	1.38	10081	18	18.51	0.64	25.90	0.54	34.2	0.6	48.32	0.88	0.5	20.4	4.6	0.2	95.5	100.3	8.9	0.000152	190.33	0.059507	1.22	0.002073
3377-03F		0.90	9293	38	403.50	3.09	10.10	1.24	1797.7	47.5	3.08	1.46	10081	18	18.51	0.64	25.90	0.54	34.2	0.6	48.32	0.88	0.7	16.3	8.7	0.2	91.7	131.3	6.6	0.000277	56.59	0.043294	0.87	0.003469
3377-03G		1.00	23331	84	793.81	3.59	17.39	1.22	5449.7	73.6	7.17	1.67	10081	18	18.51	0.64	25.90	0.54	34.2	0.6	48.32	0.88	1.4	21.2	13.5	0.2	92.8	168.1	3.9	0.000242	29.53	0.033869	0.58	0.007547
3377-03H	#	1.30	756020	554	24448.19	37.81	477.54	4.39	209902.0	997.8	151.46	2.49	10081	18	18.51	0.64	25.90	0.54	34.2	0.6	48.32	0.88	42.0	38.7	16.8	0.1	96.3	**183.0**	**1.3**	**0.000123**	**2.70**	**0.032154**	**0.17**	**0.011591**
3377-03I	#	2.00	330130	125	10715.68	15.18	211.50	2.59	87565.4	479.3	52.62	1.64	11377	21	20.32	1.30	29.17	0.65	35.3	0.8	52.60	0.90	18.4	46.4	16.0	0.1	97.5	**184.4**	**1.3**	**0.000085**	**5.84**	**0.032283**	**0.15**	**0.001668**
3377-03J		6.00	525963	265	19551.49	31.53	380.53	3.79	145390.7	727.8	84.20	2.42	11377	21	20.32	1.30	29.17	0.65	35.3	0.8	52.60	0.90	33.6	48.2	14.6	0.1	97.5	162.0	1.2	0.000083	5.57	0.036990	0.17	0.002687
Aliquot 4																																		
3377-04A	#	0.60	613988	328	19863.17	36.57	453.36	4.96	140596.5	941.4	115.64	3.73	10501	19	18.80	0.92	20.47	0.57	26.0	0.7	47.29	0.95	72.1	33.9	13.9	0.1	96.3	**182.7**	**1.1**	**0.000124**	**4.90**	**0.032199**	**0.19**	**0.003023**
3377-04B	#	0.70	31028	84	1119.73	6.74	25.22	1.35	6980.0	129.4	4.73	1.70	10501	19	18.80	0.92	20.47	0.57	26.0	0.7	47.29	0.95	4.1	41.2	12.2	0.2	97.3	**166.2**	**3.0**	**0.000090**	**61.07**	**0.035940**	**0.66**	**0.001812**
3377-04C	#	0.80	29221	55	1088.15	7.87	22.19	1.65	5923.4	95.2	1.32	2.12	10501	19	18.80	0.92	20.47	0.57	26.0	0.7	47.29	0.95	4.0	125.2	10.7	0.2	100.3	**166.0**	**3.7**	**- 0.000012**	**-629.77**	**0.037105**	**0.75**	**0.000075**
3377-04D	#	1.00	14766	63	489.22	3.89	12.50	1.29	3516.0	85.1	2.71	1.53	10501	19	18.80	0.92	20.47	0.57	26.0	0.7	47.29	0.95	1.8	36.1	14.1	0.4	96.5	**179.0**	**5.8**	**0.000117**	**88.58**	**0.032974**	**0.91**	**0.002290**
3377-04E	#	1.10	23158	36	796.79	6.63	16.71	1.30	5090.3	99.3	2.33	2.21	10626	18	21.82	1.00	22.89	0.64	29.7	0.8	49.90	0.90	2.9	60.8	12.5	0.3	98.8	**176.5**	**5.1**	**0.000039**	**242.73**	**0.034261**	**0.85**	**0.000119**
3377-04F	#	1.30	40638	36	1369.82	5.02	30.26	1.33	10447.7	129.7	5.11	1.67	10626	18	21.82	1.00	22.89	0.64	29.7	0.8	49.90	0.90	5.0	57.0	14.9	0.2	98.4	**179.4**	**2.5**	**0.000054**	**76.09**	**0.033538**	**0.38**	**0.000276**
3377-04G	#	1.60	32343	45	1086.08	5.02	25.10	1.23	11088.7	127.8	4.04	1.44	10626	18	21.82	1.00	22.89	0.64	29.7	0.8	49.90	0.90	3.9	76.5	20.0	0.2	99.1	**181.7**	**2.9**	**0.000029**	**153.08**	**0.033351**	**0.49**	**0.000264**
3377-04H	#	2.00	24047	38	869.52	4.77	17.81	1.28	9894.2	131.5	1.62	1.57	10626	18	21.82	1.00	22.89	0.64	29.7	0.8	49.90	0.90	3.2	170.1	22.3	0.3	101.4	**173.1**	**3.7**	**- 0.000048**	**-137.77**	**0.035884**	**0.58**	**0.000323**
3377-04I	#	6.00	23284	30	852.70	5.72	17.29	1.04	6420.3	107.8	-3.33	1.52	10679	18	17.99	0.70	20.98	0.59	25.6	0.6	50.16	0.86	3.1	-53.8	14.8	0.3	106.6	**178.9**	**3.5**	**- 0.000220**	**-29.70**	**0.036440**	**0.69**	**0.000812**

Notes:

a: 4-digit number indicates the RunID number in MassSpec software, -01 denotes the aliquot number, letter suffix indicates the heating step.

b: Ages marked with an asterisk (*) or a pound symbol (#) were those used in the plateau or inverse isochron age calculation, respectively. Run ID#'s that were used are shown in bold.

c: Isotopic abundances corrected for baseline, blank, and detector intercalibration. ^{39}Ar and ^{37}Ar are decay-corrected values. Isotopic abundances are not corrected for nuclear interference reactions.

d: Nominal J (± 0.30%, 1σ) from GSC Irradiation Batch #70 (Cd-shielded), referenced to Fish Canyon Tuff Sanidine = 28.201 ± 0.023 Ma (1σ, Kuiper et al., 2008)

e: Nominal J (± 0.30%, 1σ) from GSC Irradiation Batch #69 (Cd-shielded), referenced to Fish Canyon Tuff Sanidine = 28.201 ± 0.023 Ma (1σ, Kuiper et al., 2008)

Decay Constant (40K λtotal) = 5.463 ± 0.214 x 10-10/yr (2σ, Min et al., 2000)

Atmospheric argon ^{40}Ar/^{36}Ar = 298.56 (Lee et al., 2006)

Nucleogenic interference correction factors (±2σ):

(^{39}Ar/^{37}Ar)Ca = 0.0007 ± 0.000054

(^{36}Ar/^{37}Ar)Ca = 0.00028 ± 0.00017

(^{40}Ar/^{39}Ar)K = 0.003 ± 0.005

^{40}Ar* = radiogenic argon

Plateau and inverse isochron age errors are quoted at 2σ and incorporate the error in J, but *not* the error in decay constants

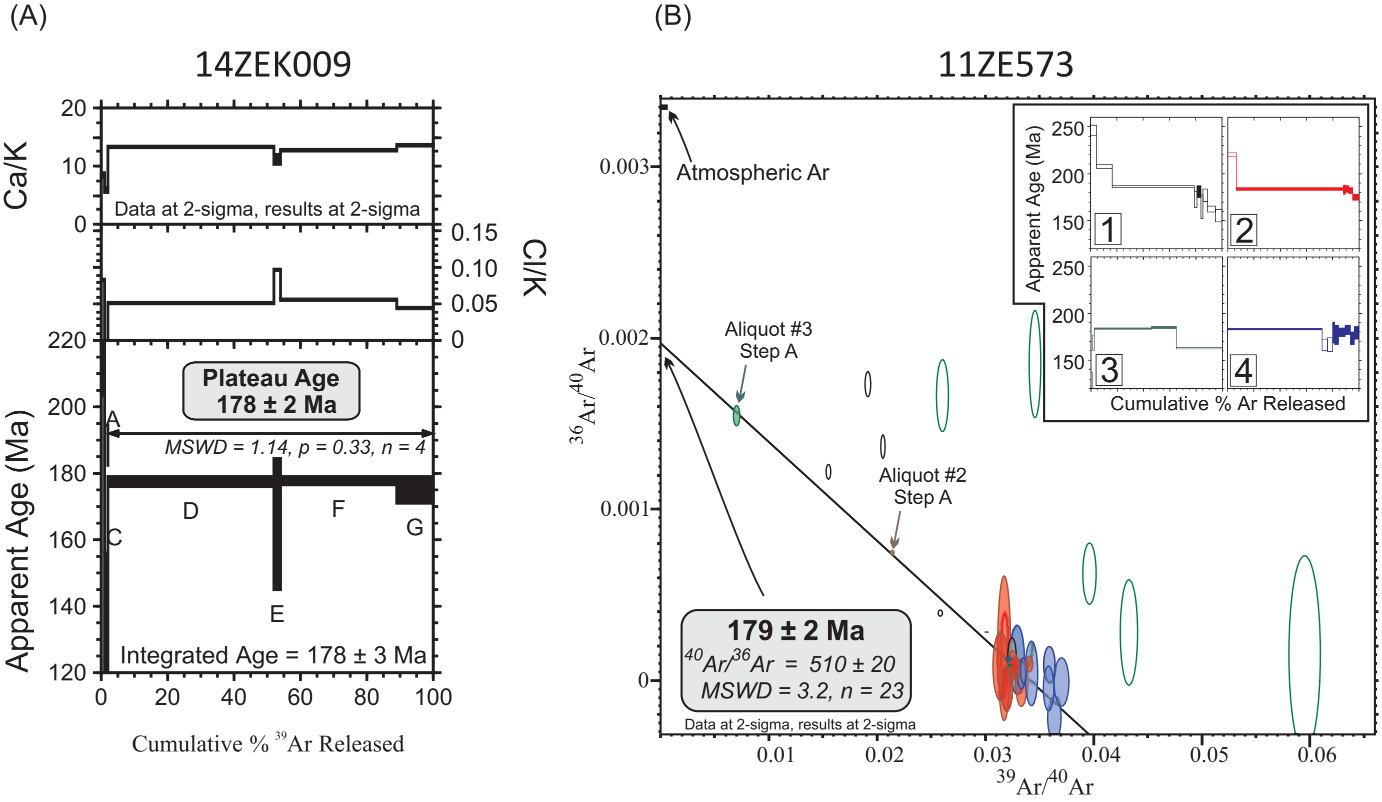

Fig. 9. a) Gas-release spectrum for hornblende from sample 14ZEK009. The integrated age is the total-gas age, calculated by weighting the individual steps by the fraction of ^{39}Ar released. **b)** Inverse isochron plot for hornblende from diorite sample 11ZE573. Colours of ellipses correspond to colours of the aliquots shown in the inset. Filled ellipses are the data points used to calculate the inverse isochron age. Unfilled ellipses were not included in the age calculation. Errors are shown at 2σ. Note that the regression line is heavily controlled by the first heating steps of Aliquots #2 and #3. Inset: Gas-release spectra for Aliquots #1 through #4. The filled boxes are the heating steps that are included in the inverse isochron age calculation. Only the steps comprising greater than 1% of the ^{39}Ar are plotted.

presence of excess ^{40}Ar in the sample (Fig. 9b). The scatter of the 38 data points is likely due to degassing of multiple argon reservoirs of different ^{40}Ar/^{36}Ar composition, such as mineral and/or fluid inclusions. Heterogeneity within the grains is further evidenced by the variable Ca/K measured throughout the analyses; Ca/K values range between ~5 and 22 (Table 1). Using the York (1969) linear least squares regression procedure (invoking the Students' t-test), the inverse isochron age obtained for 23 nearly collinear data points is 179 ±2 Ma (MSWD = 3.2), corresponding to a trapped Ar composition of ^{40}Ar/^{36}Ar = 510 ±20. The regression slope is heavily controlled by only two data points (the first heating steps of Aliquots #2 and #3), whereas the other 21 points are clustered near the x-axis. A more robust inverse isochron age is obtained when the data are spread more evenly along the regression line; however the 179 ±2 Ma age is considered the best approximation of the hornblende cooling age for this sample.

4.3. Re-Os methods

Re-Os age geochronology of molybdenite was conducted at the University of Alberta, Edmonton, Alberta. A molybdenite mineral separate was made for the sample through metal-free crushing, followed by gravity and magnetic concentration methods, which are described in detail by Selby and Creaser (2004). The ^{187}Re and ^{187}Os concentrations in the molybdenite separate were determined through isotope dilution mass spectrometry using Carius-tube, solvent extraction, anion chromatography, and negative thermal ionization mass spectrometry techniques. During this process, a mixed double spike containing known amounts of isotopically enriched ^{185}Re, ^{190}Os, and ^{188}Os analysis was used (Markey et al., 2007). Isotopic analysis used a ThermoScientific Triton mass spectrometer by Faraday collector. Total blanks for Re and Os are less than <3 picograms and 2 picograms, respectively, which are insignificant for the Re and Os concentrations in molybdenite. The molybdenite powder HLP-5 (Markey et al., 1998) was analyzed as a standard, and over a period of two years an average Re-Os date of 221.56 ±0.40 Ma (1SD uncertainty, n = 10) was obtained. This Re-Os age date is identical to that reported by Markey et al. (1998) of 221.0 ±1.0 Ma.

4.3.1. Re-Os results

Sample 142EK-012B is from a massive quartz vein containing minor disseminated sulphides that cuts rocks of the Surprise Mountain intrusion. Some quartz grains have deformation lamellae and display undulose extinction. Bands of small subgrains define minor shear zones in the quartz vein. Pyrrhotite and chalcopyrite occur as inclusions in pyrite. Molybdenite replaces pyrite along fractures and forms aggregates >400μ. The molybdenite mineral separate yielded a Re-Os model age of 180.2 ±0.8 Ma (Table 2). The age uncertainty is quoted at 2σ (95% confidence) level of precision, and includes all known analytical uncertainty (all sources of error), including the uncertainty in the decay constant of ^{187}Re. Because molybdenite overprints other sulphides, mineralization was before 180.2 ±0.8 Ma, as was emplacement of the host quartz diorite.

5. Geochemistry of the Surprise Mountain intrusion

Major and trace element geochemical analysis of samples from the Surprise Mountain intrusion (Table 3) followed sample preparation to remove zones of weathering and alteration using a diamond saw. Samples were analyzed by ICP-ES and ICP-MS following lithium metaborate/tetraborate fusion and nitric acid or Aqua Regia digestion at ACME Laboratories (Vancouver, BC; analytical packages 4A4B and 1DX) and Activation Laboratories (Ancaster, ON; analytical package 4Lithores). The accuracy is typically 5 to 20% if the analyte is at least 10 times the stated detection limit.

Calculated modal mineral contents indicate that the composition of the intrusion varies broadly from granodiorite, quartz diorite to quartz monzodiorite (Fig. 8a; Whalen and Frost, 2013), consistent with modal mineral variations observed in samples. All samples plot along the calc-alkalic magmatic trend (Fig. 10a). Calculated Fe$_2$O$_3$/FeO ratios (Irvine and Baragar, 1971) for all samples exceed 0.5, indicative of magnetite-series granitic rocks (Ishihara 1977, 1981). This is consistent with the common presence of magnetite and high-temperature hematite, and relatively high magnetic susceptibility (average 15.8 x 10^{-3} SI).

On normalized extended trace element plots (Fig. 10) samples yield similar trace element profiles. Samples normalized to primitive mantle (Fig. 10b) show an overall enrichment of large ion lithophile elements (LILE), and an enrichment of light rare earth elements (LREE) relative to heavy rare earth elements (HREE). The samples also display depletion of high field strength elements Nb, Ta, and Ti. Samples normalized to petrographically least altered sample K004, yield very similar trace element profiles, indicating only small differences between samples (Fig. 10c). The largest differences are in Cs, Rb Nb, K and Pb. The homogeneity in major and trace element contents displayed by samples from the Surprise Mountain intrusion suggests limited assimilation, fractionation, and alteration.

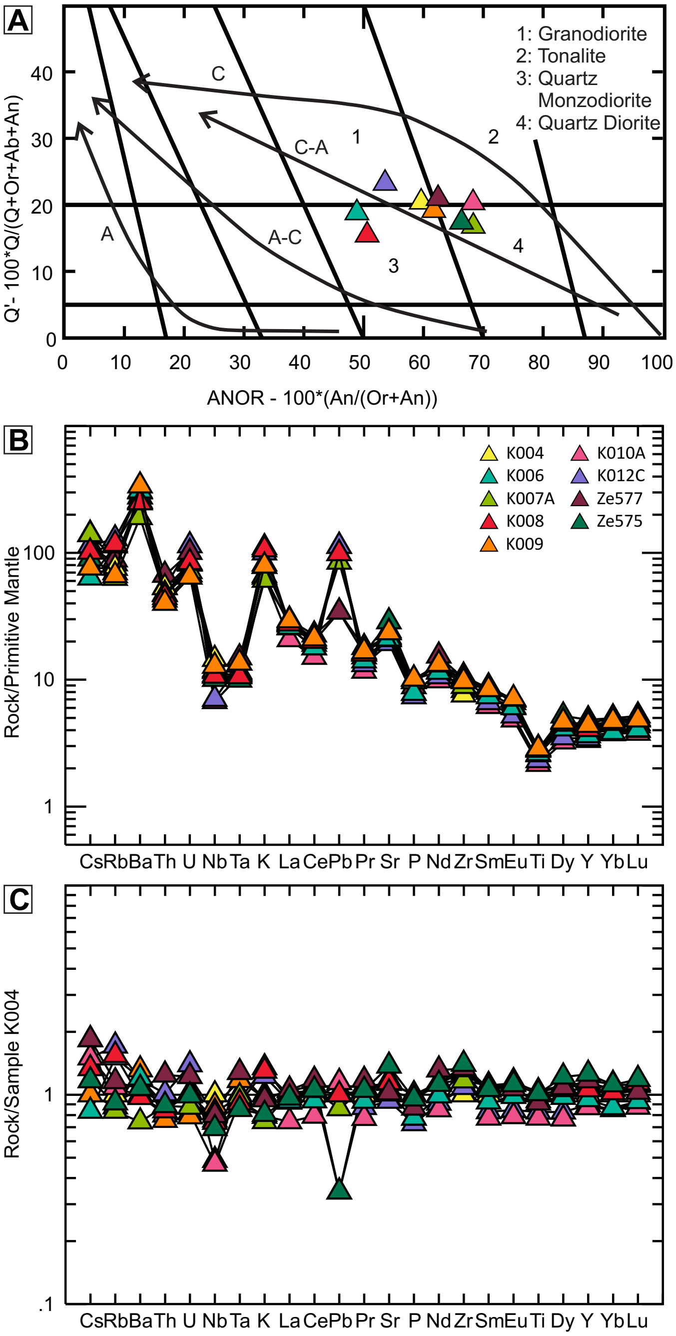

Fig. 10. Geochemical characteristics of quartz diorite. **a)** Normative quartz-feldspar discrimination diagram (Whalen and Frost, 2013). **b)** Primitive mantle-normalized extended trace element plot (values from Sun and McDonough, 1989). **c)** K004-normalized extended trace element plot.

6. Geochemistry of mineralization

We analyzed 12 mineralized samples from the Surprise Mountain intrusion (Table 4). Samples were cut using a diamond saw to retain representative slabs of mineralized zones for petrographic analysis and a split was submitted for geochemistry. Major and trace elements were analyzed using ICP-ES and ICP-MS following lithium metaborate/tetraborate fusion and Aqua Regia digestion at ACME Laboratories (Vancouver, BC; analytical package 1DX) and Activation Laboratories (Ancaster, ON; analytical package AQ251_EXT). Accuracy is typically in the 1-3% range as long as the analyte is present at 20 times the detection limit.

Analytical result show wide variability of all elements, with the exception of Ag, which is consistently elevated in all samples

Table 2. Re-Os istotopic data and ages.

Sample	Re ppm	± 2σ	^{187}Re ppb	± 2σ	^{187}Os ppb	± 2σ	Model Age (Ma)	± 2σ (Ma)
142EK-012B	55.55	0.16	34.92	0.1	105	0.1	180.2	0.8

relative to the host intrusion, in which Ag is consistently below the detection limit (<0.5 ppm). Some samples are elevated in Bi, Pb, Mo, and W relative to host intrusion where these elements are below or at the detection limit (0.1, 5, 2, 0.5 ppm respectively). Au is consistently near the limits of detection in all samples.

7. Discussion

7.1. Relationship between the Surprise Mountain intrusion and the Cone Mountain plutonic suite and timing of thrusting, intrusion, and mineralization

The ^{40}Ar/^{39}Ar (178 ±2 and 179 ±2 Ma) cooling and Re-Os mineralization (180.2 ±0.8 Ma) ages and the lithological characteristics described above suggest that the Surprise Mountain pluton is part of the Cone Mountain plutonic suite (187-180 Ma), and part of a north-trending belt from the Iskut River to Telegraph Creek (Fig. 2). Brown et al. (1996) noted that the Cone Mountain suite characteristically contains abundant angular diorite enclaves, as is seen in the Surprise Mountain quartz diorite, and a common feature in calc-alkaline granitic rocks (Foster and Hyndman, 1990).

Quartz diorite cuts isoclinaly folded Triassic marble and cuts across the thrust contact between this marble and structurally underlying volcano-sedimentary rocks (Fig. 4). Thus thrusting must have been before ~180 Ma (age of the late syn-intrusive mineralization) and after deposition of the footwall volcano-sedimentary rocks that are intercalated with ~187 Ma dacitic tuff breccia to the northeast (Zagorevski et al. unpublished data). This is similar to the relationship observed to the north, where Pliensbachian volcanic rocks (185 +7/-2 Ma: Brown et al., 1996) unconformably overlie folds and thrusts developed in the Stuhini Group. Emplacement of the quartz diorite broadly coincides with the volcanic lull at the transition from the subaerial and marine arc-related Betty Creek formation to rift related submarine magmatism of the Iskut River Formation in the Eskay rift (Fig. 2; Gagnon et al., 2012; Lewis et al., 2013). These stratigraphic relationships are well displayed on the flanks of the McTagg anticlinorium to the east (Fig. 2; Cutts et al., 2015 and references therein). This fundamental tectonic shift was accompanied by a change from porphyry-epithermal styles to volcanogenic massive sulphide styles of mineralization (e.g., Macdonald et al., 1996).

7.2. Polymetallic vein mineralization

Sheeted, subparallel mineralized quartz veins (Fig. 11) suggest emplacement in a dilatational brittle regime. Textural relationships between mineral phases suggest three mineralizing events: 1) early polymetallic mineralization, with mainly pyrite; 2) an overprinting molybdenum-rich event; and 3) a late, more oxidized event leading to Cu remobilization and deposition of chalcocite and covellite. It is unclear if the different compositions recorded by these events resulted from continuous fluid evolution or from distinct fluid pulses overprinting earlier assemblages.

Despite the apparent lack of Au in the polymetallic veins (≤15 ppb), the occurrence displays high concentrations of Au indicator elements including Bi (>2000 ppm) and W (>100 ppm) (Robb, 2005). Strong enrichment of Ag (up to 17 ppm) may be correlated with Au elsewhere within the system (e.g., Robb, 2005). Lack of elevated Au in all 12 samples analyzed suggests that the analyzed Au contents are representative of the sheeted veins in this area. The principal hydrothermal fluids appear to have been lacking Au in this part of the system.

The nature of the mineralization, including association with vein arrays, sulphide mineral assemblage, Ag enrichment, and lack of alteration are most consistent with polymetallic Ag-Pb-Zn±Au or Cu±Ag quartz deposit types (Lefebure and Church, 1996). These deposits typically display limited alteration and an association with calc-alkaline granititic rocks and are contained by steeply dipping, narrow, tabular or splayed subparallel vein sets. These deposits may be peripheral to skarn or porphyry mineralization (Lefebure and Church, 1996) as is observed at Surprise Mountain, where mineralization is close to a garnet, diopside, actinolite ±wollastonite, quartz, carbonate and pyrite exoskarn. The true nature and full regional extent of the alteration and mineralization remains unclear, as pathfinder metals such as Bi and W were not traced outside of the study area, and skarn was not investigated for potential mineralization. However, quartz-carbonate veins with dissseminated galena, sphalerite, tetrahedrite, and arsenopyrite were previously reported on the northeastern margin on this intrusion (MINFILE 104B 130). These yielded assays of up to 1698 grams per tonne silver and up to 12.75 grams per tonne gold (Holbek, 1983).

7.3. Comparison to other Jurassic deposits in the Iskut River area

Significant deposits near the Surprise Mountain body include Red Bluff, Snip, and Johnny Mountain, all of which are older (Fig. 2). The Red Bluff intrusion (195 ±1 Ma; Macdonald et al., 1996) consists of K-feldspar megacrystic, plagioclase porphyritic quartz diorite to quartz monzonite (Burgoyne and Giroux, 2007). In contrast to the Surprise Mountain body, the Red Bluff intrusion is moderately to intensely hydrothermally altered by K-feldspar-biotite-magnetite and later sericite-

Table 3. Whole rock geochemical data.

Sample	DL□*	K003C□	K004□	K006□	K007A□	K008□	K009□	K010A□	K012C□	ZE567*	ZE575*	ZE577*
UTM Easting		351337	351317	351051	350981	350856	350856	350359	349995	352793	351057	350463
UTM Northing		6293238	6293220	6293225	6293237	6293344	6293344	6293434	6293655	6292634	6293284	6293413
Rock Type		Monzogranite Dike	Granodiorite-Quartz Monzodiorite	Quartz Monzodiorite	Quartz Diorite	Quartz Monzodiorite	Quartz Monzodiorite	Quartz Diorite-Tonalite	Granodiorite	Quartz Gabbro Dike	Quartz Diorite	Granodiorite-Tonalite
SiO_2	0.01%	72.64	62.27	63.5	59.68	61.41	62.34	63.17	64.18	60.59	61.23	62.84
Al_2O_3	0.01%	13.43	16.24	16.44	16.98	16.84	16.72	17.48	16.05	17.36	16.9	16.56
Fe_2O_3	0.01/0.04%	1.15	5.34	4.96	5.65	3.81	5.76	4.47	4.37	5.36	5.83	5.31
MnO	0.001/0.01%	0.035	0.147	0.117	0.143	0.087	0.144	0.122	0.122	0.11	0.13	1.75
MgO	0.01%	0.32	1.79	1.53	1.91	1.68	1.96	1.29	1.53	2.05	1.79	0.14
CaO	0.01%	2.01	5.64	4.64	5.56	5.91	5.73	5.86	4.84	6.91	6.17	5.61
Na_2O	0.01%	2.7	3.47	3.65	3.92	3.84	3.57	3.85	3.2	4.41	3.84	3.44
K_2O	0.01%	5.48	2.46	3.31	1.83	3.19	2.37	1.94	3.01	0.39	1.98	2.33
TiO_2	0.001/0.01%	0.178	0.603	0.565	0.625	0.603	0.617	0.466	0.499	0.67	0.61	0.55
P_2O_5	0.01%	0.03	0.22	0.17	0.21	0.22	0.22	0.17	0.16	0.23	0.21	0.19
LOI	0.01/0.1%	0.79	0.98	0.95	2.9	0.88	1.49	0.82	1.24	1.7	1	0.9
Total	%	98.78	99.17	99.84	99.41	98.48	100.9	99.65	99.21	99.8	99.65	99.66
Ba	3/5ppm	1979	1789	2150	1327	1735	2354	1765	2114	526	1917	1911
Be	1ppm	<1	1	1	1	1	1	1	1	1	<1	1
Ce	0.05/0.1ppm	14.2	33.8	31.6	35.4	35.7	37.2	26.7	31.7	36.1	35.6	39.6
Cr	20ppm	80	30	20	30	30	20	40	30	N/A	N/A	N/A
Cs	0.1ppm	0.9	0.6	0.5	1.1	0.8	0.6	0.9	0.9	0.1	0.7	1.1
Dy	0.01/0.05ppm	0.96	3.11	3.02	3.46	3.29	3.42	2.38	2.57	3.87	3.78	3.36
Er	0.01/0.03ppm	0.65	1.93	1.91	2.27	2.04	2.18	1.57	1.58	2.27	2.22	2.08
Eu	0.005/0.02ppm	0.224	1.03	1.01	1.17	1.18	1.19	0.81	0.87	1.18	1.15	1.1
Ga	1/0.5ppm	13	18	17	18	17	18	19	17	16.6	18.9	17.6
Gd	0.01/0.05ppm	0.91	3.1	2.98	3.63	3.42	3.26	2.55	2.54	3.53	3.66	3.54
Ge	0.5ppm	1.4	1.2	1.3	1.4	1.2	1.2	1.5	2	N/A	N/A	N/A
Hf	0.1ppm	1.8	2.4	2.4	2.7	2.2	2.9	2.7	2.3	3.5	3.4	3.4
Ho	0.01/0.02ppm	0.2	0.67	0.61	0.73	0.67	0.69	0.5	0.52	0.75	0.76	0.73
La	0.05/0.1ppm	15.7	19.1	17.8	19.5	18.9	20	14.2	17.6	17.6	18.4	20.1
Lu	0.002/0.01ppm	0.126	0.321	0.298	0.362	0.365	0.356	0.28	0.295	0.36	0.38	0.33
Nb	0.2/0.1ppm	1.2	10.3	7.8	8.5	7.6	9.1	4.8	5	7.3	7.1	8.2
Nd	0.05/0.3ppm	5.36	15.7	15.5	18	17.7	17.9	13.3	14.3	17.4	17.6	20.6
Pr	0.01/0.02ppm	1.62	4.18	3.89	4.5	4.39	4.58	3.22	3.63	4.55	4.39	4.9
Rb	1/0.1ppm	119	48	72	40	74	42	52	82	5.8	43.9	55.4
Sm	0.01/0.05ppm	0.93	3.53	3.26	3.91	3.75	3.71	2.73	2.93	3.92	3.74	3.83
Sr	2/0.5ppm	230	437	441	460	499	495	513	407	519.3	598.7	446.2
Ta	0.01/0.1ppm	0.18	0.47	0.45	0.46	0.43	0.55	0.44	0.55	0.6	0.4	0.6
Tb	0.01ppm	0.15	0.49	0.49	0.56	0.53	0.54	0.41	0.42	0.6	0.61	0.55
Th	0.05/0.2ppm	8.83	4.51	3.99	3.99	3.78	3.4	3.61	4.56	4.4	4	5.6
Tm	0.005/0.01ppm	0.103	0.312	0.294	0.352	0.328	0.334	0.26	0.263	0.37	0.34	0.32
U	0.01/0.1ppm	2.96	1.72	1.74	1.5	1.76	1.35	1.41	2.39	1.7	1.7	2.1
V	5/8ppm	23	119	96	117	103	118	85	103	112	127	96
Y	0.5/0.1ppm	7.1	17.4	16.5	18.8	18.4	19.9	15.1	15.6	22	21.8	20.3
Yb	0.01/0.05ppm	0.75	2.18	1.89	2.41	2.23	2.31	1.86	1.85	2.21	2.43	2.45
Zr	1/0.1ppm	61	85	110	99	112	108	113	92	122	118.7	113.4

UTM Zone 9, NAD 83

□Samples analyzed at Activation Laboratories Ltd., Ancaster, Ontario, 2014

*Samples analyzed at Acme Analytical Laboratories Ltd., Vancouver, British Columbia, 2011

Table 4. Assay data.

Sample	DL□*	K002A□	K003B□	K010B□	K011A□	K011B□	K011C□	K012A3□	K012A2□	K012A4□	K012B□	ZE578A*	ZE578B*
UTM Easting		0351610	0351337	0350359	0350067	0350067	0350067	0349995	0349995	0349995	0349995	0350004	0350004
UTM Northing		6292989	6293238	6293434	6293613	6293613	6293613	6293655	6293655	6293655	6293655	6293637	6293637
Rock Type		Quartz Vein	Quartz Vein	Host & Quartz Vein	Host & Quartz Vein	Quartz Vein	Host & Weak Quartz Vein Stockwork	Quartz Vein	Quartz Vein	Quartz Vein	Quartz Vein	Quartz Vein	Quartz Vein
Ag	100/2ppb	309	387	82	255	74	17549	1331	210	7251	219	2900	300
As	0.5/0.1ppm	<0.1	2.7	0.4	0.8	0.3	0.7	1.2	0.6	<0.1	<0.1	<0.5	<0.5
Au	10/0.2ppb	2.4	3.3	1.3	4.6	0.9	14.8	3	3.7	2.9	2.4	5.5	0.6
Bi	0.1/0.02ppm	0.21	0.11	0.16	0.98	3.9	174.24	2.89	8.63	14.41	1.3	>2000.0	766.6
Cd	0.1/0.01ppm	0.05	0.61	0.06	0.12	<0.01	0.03	0.06	<0.01	0.52	0.47	<0.1	<0.1
Co	0.1ppm	22.1	13.9	8	3.3	0.7	1.4	1.8	0.2	4.2	2.6	2	0.6
Cu	0.1/0.01ppm	210.54	92.46	61.53	66.6	12	36.63	42.37	25.64	55.64	23	28.3	9.7
Fe	0.01%	3.36	2.19	2.15	1.81	1.05	3.31	3.25	1.21	1.69	1.67	2.01	0.89
Mn	1ppm	158	110	397	345	38	59	152	32	192	45	12	11
Mo	0.1/0.01ppm	0.62	6.72	10	0.85	182.24	113.92	67.21	15.33	9.2	764.94	46.2	8
Ni	0.1/0.1ppm	15.5	21.9	1.9	1.4	0.7	0.9	0.9	0.7	1.4	1	3.4	3.8
Pb	0.1/0.01ppm	2.64	40.02	4.15	3.64	3.25	22.84	443.44	5.54	2799.85	6.98	46	22.6
Re	1ppb	<1	16	<1	<1	3	2	<1	<1	<1	62	N/A	N/A
Sb	0.1/0.02ppm	0.11	0.47	0.07	0.02	0.03	0.15	0.58	0.06	0.1	0.08	1.5	0.5
Se	0.5/0.1ppm	6.7	4	0.4	0.6	0.8	8.5	1.8	1.4	2.3	1.8	10.1	4.6
Sn	0.1ppm	<0.1	0.3	0.2	<0.1	<0.1	<0.1	0.6	<0.1	0.3	<0.1	N/A	N/A
Te	0.2/0.02ppm	0.22	0.12	0.03	0.05	0.2	1.93	0.18	0.14	0.27	0.05	3.9	1.5
W	0.1ppm	2	0.3	0.7	53.7	7.5	3.6	0.8	3.1	0.3	>100	41.3	>100.0
Zn	1/0.1ppm	23.6	145	38.1	26.9	7	8.5	20.5	5.6	24.2	5.2	4	2

UTM Zone 9, NAD 83

□Samples analyzed at Activation Laboratories Ltd., Ancaster, Ontario, 2014

*Samples analyzed at Acme Analytical Laboratories Ltd., Vancouver, British Columbia, 2011

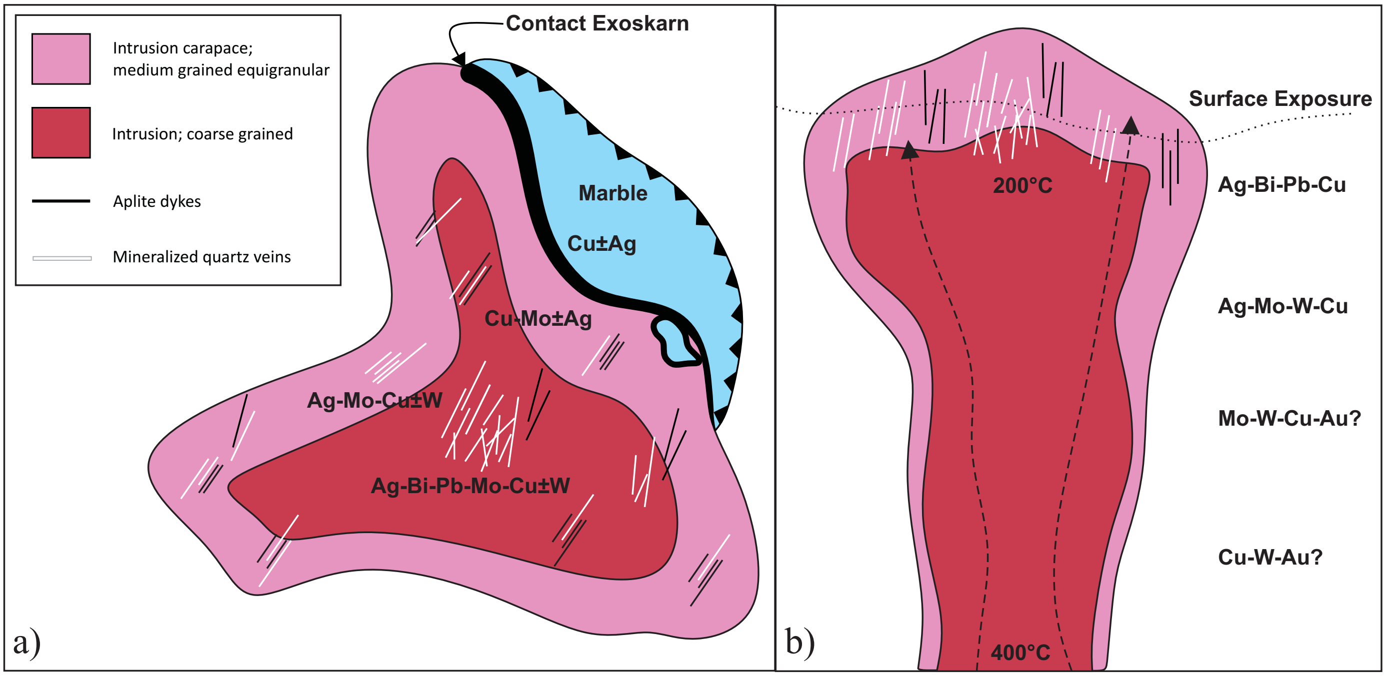

Fig. 11. Schematic model for polymetallic vein mineralization near Surprise Mountain in plan view **a)** and vertical cross-section **b)**. Present erosion level may expose only the shallow, low-temperature part of the mineralizing system.

quartz-pyrite-albite assemblages (Macdonald et al., 1996; Burgoyne and Giroux, 2007). Mineralization comprises quartz-magnetite-hematite stockwork veins, disseminated pyrite-chalcopyrite, quartz-Fe-oxide stockwork, and quartz-pyrite-chalcopyrite veins and veinlets (Burgoyne and Giroux, 2007). The related Snip (Au-Cu-Mo) and Johnny Mountain (Au-Ag-Pb-Zn) deposits are precious metal-rich veins hosted by Triassic and Jurassic sedimentary rocks, and are spatially and genetically related to the Red Bluff porphyry deposit (Burgoyne and Giroux, 2007). At Snip, syn-tectonic quartz and sulphide veins (pyrite-pyrrhotite) were emplaced in a southwest-dipping brittle-ductile fault zone (Macdonald et al., 1996). At Johnny Mountain, auriferous quartz-pyrite veins commonly contain pyrrhotite, chalcopyrite, sphalerite, magnetite, pyrargyrite, and galena (Macdonald et al., 1996). Veins are typically 0.5 to 2 m thick and are surrounded by potassium feldspar alteration envelopes that are up to several times the vein width (Macdonald et al., 1996). The intensity and character of alteration and the potassic character of the host intrusion distinguishes the Red Bluff, Snip, and Johnny Mountain deposits from the Surprise Mountain occurrence, where the alteration is limited to narrow haloes around veins, and the host pluton is a calc-alkalic quartz diorite. Calc-alkalic members of the Cone Mountain plutonic suite at the Strata Glacier pluton (Fig. 2) are associated with polymetallic vein systems (Brown et al., 1996) suggesting that these may be more prospective than previously known.

8. Conclusions

The Surprise Mountain intrusion is a calc-alkaline, I-type, magnetite-series, medium- to coarse-grained, equigranular hornblende quartz diorite. The intrusion cuts a northeast-vergent thrust fault that stacked Permian to Late Triassic marbles above Early Jurassic (<187 Ma) volcaniclastic rocks. Samples from the intrusion yielded ^{40}Ar/^{39}Ar hornblende cooling ages of 178 ±2 and 179 ±2 Ma. An Upper-Lower Jurassic molybdenite Re-Os age of 180.2 ±0.8 Ma defines the minimum age of mineralization, and the minimum age of the host intrusion, implying that thrusting was between ~187 and 180 Ma. Lithological variation and enclave abundance, in conjunction with the minimum 180.2 ±0.8 Ma age, suggest that the intrusion is part of the Cone Mountain plutonic suite (187-180 Ma). Polymetallic mineralization displays high concentrations of indicator elements including Bi (>2000 ppm) and W (>100 ppm), consistent enrichment of Ag (≤17 ppm), significant Pb (>2000 ppm) and Mo (>700 ppm), and trace amounts of Au (≤14.8 ppb). Low Au contents, weak alteration, and lack of metal zonation differentiates this occurrence from nearby porphyry-related vein deposits like Snip and Johnny Mountain, 20 km to the east-southeast. Sheeted quartz veins in the Surprise Mountain quartz diorite are part of a weakly-developed intrusion-hosted polymetallic vein system. This system displays an Ag-Bi-Pb-Mo-Cu elemental association that is not well known in the Iskut River area. Despite the lack of analyzed Au, persistently elevated Ag and other pathfinder elements, especially W and Bi, suggest that the sheeted vein system warrants further investigation. Additionally, strong skarn development in marble in the hanging wall of a thrust fault should be evaluated, especially considering that Au-bearing skarns are documented around other Cone Mountain plutonic suite intrusive rocks (Brown et al., 1996). Further work is necessary to determine the spatial extent of mineralization in the Surprise Mountain intrusion, and to better determine the relationship between Cone Mountain plutonic suite bodies and polymetallic vein mineralization in northwestern British Columbia.

Acknowledgments

This research forms part of K. Martin's B.Sc. thesis at the University of Ottawa, Ottawa that was supported by GEM2: Cordillera Project. J. Nelson and J. Kyba are gratefully acknowledged for providing logistical support for this project. J. Nelson and L. Aspler are thanked for their thoughtful suggestions which improved this manuscript.

References cited

Anderson, R.G., 1993. A Mesozoic stratigraphic and plutonic framework for northwestern Stikinia (Iskut River area), northwestern British Columbia, Canada. In Dunne, G. C., and McDougall, K. A., (Eds.), Mesozoic paleogeography of the western United States - II: Los Angeles. Society of Economic Paleontologists and Mineralogists, Pacific Section, Book 71, p. 477-494.

Anderson, R.G., and Thorkelson, D.J., 1990. Mesozoic stratigraphy and setting for some mineral deposits in Iskut River map area, northwestern British Columbia. Geological Survey of Canada, Paper 90-1E, 131-139.

Brown, D.A., Gunning, M.H., and Greig, C.J., 1996. The Stikine project: geology of western Telegraph Creek map area, northwestern British Columbia (NTS104G/5, 6, 11W 12 and 13). British Columbia Ministry of Energy, Mines and Petroleum Resources, British Columbia Geological Survey Bulletin 95, 183p.

Burgoyne, A.A. and Giroux, G.H., 2007. Technical Report on the Bronson Slope Property, Northwestern British Columbia, Canada. Skyline Gold Corporation, Vancouver, BC. 145 p. (downloaded from http://www.snipgoldcorp.com/s/BronsonSlope.asp on April 27, 2015).

Childe, F.C., 1994. Radiogenic isotopic investigations of the Eskay Creek volcanic hosted massive sulphide deposit, British Columbia, Canada. United States Geological Survey Circular 1107, 58p.

Childe, F.C., 1996. U-Pb geochronology and Nd and Pb isotope characteristics of the Au-Ag-rich Eskay Creek volcanogenic massive sulfide deposit, British Columbia. Economic Geology, 91, 1209-1224.

Cohen, K.M., Finney, S.C., Gibbard, P.L. and Fan, J.-X., 2013. The ICS International Chronostratigraphic Chart. Episodes 36, 199-204.

Colpron, M., and Nelson, J.L., 2011. A Digital Atlas of Terranes for the Northern Cordillera. British Columbia Ministry of Energy and Mines, British Columbia Geological Survey GeoFile 2011-11.

Cutts, J.A., McNicoll, V.J., Zagorevski, A., Anderson, R.G., and Martin, K., 2015. U-Pb geochronology of the Hazelton Group in the McTagg anticlinorium, Iskut River area, northwestern British Columbia. In: Geological Fieldwork 2014, British Columbia Ministry of Energy and Mines, British Columbia Geological Survey Paper 2015-1, pp. 87-101.

Deer, W.A., Howie R.A., and Zussman, J., 1997. Rock Forming Minerals, Volume 1A: Orthosilicates, Geological Society, London, 919p.

Deino, A.L., 2001. Users' manual for Mass Spec v. 5.02. Berkeley Geochronology Center Special Publication 1a, 119p.

Evenchick, C.A., Poulton, T.P., and McNicoll, V.J., 2010. Nature and significance of the diachronous contact between the Hazelton and Bowser Lake Groups (Jurassic), north-central British Columbia. Bulletin of Canadian Petroleum Geology, 58, 235-267.

Evenchick, C.A., Sears, J.W., McMechan, M.E., McNicoll, V.J., Carr, S.D., Harms, T.A., and Evenchick, C.A., 2007. A synthesis of the Jurassic-Cretaceous tectonic evolution of the central and southeastern Canadian Cordillera; exploring links across the orogen. Geological Society of America, Special Paper, 433, 117-145.

Febbo, G.E., Kennedy, L.A., Savell, M., Creaser, R.A., and Friedman, R.M., 2015. Geology of the Mitchell Au-Cu-Ag-Mo porphyry deposit, northwestern British Columbia, Canada. In: Geological Fieldwork 2014, British Columbia Ministry of Energy and Mines, British Columbia Geological Survey Paper 2015-1, pp. 59-86.

Foster, D.A., and Hyndman, D.W., 1990. Magma mixing and mingling between synplutonic mafic dikes and granite in the Idaho-Bitterroot Batholith. Geological Society of America, Memoir, 174, 347-358.

Gagnon, J.F., Barresi, T., Waldron, J.W.F., Nelson, J.L., Poulton, T. P., and Cordey, F., 2012. Stratigraphy of the upper Hazelton Group and the Jurassic evolution of the Stikine Terrane, British Columbia. Canadian Journal of Earth Sciences, 49, 1027-1052.

Holbeck, P., 1983. Report on the geology and geochemistry of the Hoodoo West claim group; BC Ministry of Energy and Mines, Assessment Report 12220, 13p. plus maps.

Irvine, T.N., and Baragar, W.R.A., 1971. A guide to the chemical classification of the common volcanic rocks. Canadian Journal of Earth Sciences, 8, 523-548.

Ishihara, S., 1977. The magnetite-series and ilmenite-series granitic rocks. Mining Geology, 27, 293-305.

Ishihara, S., 1981. The Granitoid Series and Mineralization. Economic Geology 75th Anniversary Volume, 458-484.

Kellett, D. and Joyce, N., 2014. Analytical details of the single- and multicollection ^{40}Ar/^{39}Ar measurements for conventional step-heating and total-fusion age calculation using the Nu Noblesse at the Geological Survey of Canada. Geological Survey of Canada, Technical Note 8, 27p.

Kuiper, K.F., Deino, A., Hilgen, F.J., Krijgsman, W., Renne P.R. and Wijbrans, J.R., 2008. Synchronizing rock clocks of Earth history. Science, 320, 500-504.

Kyba, J., and Nelson, J.L., 2015. Stratigraphic and tectonic framework of the Khyber-Sericite-Pins mineralized trend, lower Iskut River, northwest British Columbia: Geological Fieldwork 2014, British Columbia Ministry of Energy and Mines, British Columbia Geological Survey Paper 2015-1, pp. 41-58.

Lee, J.-Y., Marti, K., Severinghaus, J.P., Kawamura, K., Yoo, H.-S., Lee, J.B., and Kim, J.S. 2006. A redetermination of the isotopic abundances of atmospheric Ar. Geochimica et Cosmochimica Acta, 70, 4507-4512.

Lefebure, D.V. and Church, B.N., 1996. Polymetallic Veins Ag-Pb-Zn+/-Au, in Selected British Columbia Mineral Deposit Profiles, Volume 2 - Metallic Deposits, Lefebure, D.V. and Hõy, T., (Eds.), British Columbia Ministry of Employment and Investment, British Columbia Geological Survey, Open File Report 1996-13, pp. 67-70.

Lewis, P.D., 2013. Iskut River area geology, northwest British Columbia (104B/08, 09, 10 & part of 104B/01,07,11). Geoscience British Columbia Report 2013-05, 3 1:50,000-scale maps, legend and notes, .shp files.

Lewis, P.D., Toma, A., and Tosdal, R.M., 2001. Metallogenesis of the Iskut River Area, Northwestern British Columbia. University of British Columbia, Mineral Deposits Research Unit, Special Publication Number 1, 337p.

Logan, J.M., and Koyanagi, V.M., 1994. Geology and mineral deposits of the Galore Creek area (104G/3, 4). British Columbia Ministry of Energy, Mines and Petroleum Resources, British Columbia Geological Survey, Bulletin 92, 95p.

Logan, J.M., and Mihalynuk, M.G., 2014. Tectonic controls on early Mesozoic paired alkaline porphyry deposit belts (Cu-Au + or - Ag-Pt-Pd-Mo) within the Canadian Cordillera. Economic Geology, 109, 827-858.

Logan, J.M., Drobe, J.R., and McClelland, W.C., 2000. Geology of the Forrest Kerr-Mess Creek area, northwestern British Columbia (NTS 104B/10,15 & 104G/2 & 7W). British Columbia Ministry of Energy and Mines, British Columbia Geological Survey, Bulletin 104, 163p.

Macdonald, A.J., 1993. Lithostratigraphy and Geochronometry, Brucejack Lake, Northwestern British Columbia. In: Ministry of Energy, Mines and Petroleum Resources, British Columbia Geological Survey, Geological Fieldwork 1992, Paper 1993-1, pp. 315-323.

Macdonald, A.J., Lewis, P.D., Thompson, J.F.H., Nadaraju, G., Bartsch, R., Bridge, D.J., Rhys, D.A., Roth, T., Kaip, A., Godwin, C.I., and Sinclair, A.J., 1996. Metallogeny of an Early to Middle Jurassic arc, Iskut River area, northwestern British Columbia. Economic Geology, 91, 1098-1147.

Mark, D.F., Stuart, F.M. and de Podesta, M., 2011. New high-precision measurements of the isotopic composition of atmospheric argon. Geochimica et Cosmochimica Acta, 75, 7494-7501.

Markey R.J., Stein, H.J., and Morgan, J.W., 1998. Highly precise Re-Os dating for molybdenite using alkaline fusion and NTIMS. Talanta, 45, 935– 946

Markey R.J., Stein, H.J., Hannah, J.L., Selby, D., Creaser, R.A., 2007. Standardizing Re-Os geochronology: A new molybdenite Reference Material (Henderson, USA) and the stoichiometry of Os salts. Chemical Geology, 244, 74-87.

Mihalynuk, M., Zagorevski, A., and Cordey, F., 2012. Geology of the Hoodoo Mountain area (NTS 104B/14). In: Geological Fieldwork 2011, British Columbia Ministry of Energy, Mines and Natural Gas, British Columbia Geological Survey, Paper 2012-1, pp. 45-67.

Min, K., Mundil, R., Renne, P.R., and Ludwig, K.R., 2000. A test for systematic errors in ^{40}Ar/^{39}Ar geochronology through comparison with U/Pb analysis of a 1.1 Ga rhyolite. Geochimica Cosmochimica Acta, 64, 73-98.

Monger, J.W.H., 1977. Upper Paleozoic rocks of the western Canadian Cordillera and their bearing on Cordilleran evolution. Canadian Journal of Earth Sciences, 14, 1832-1859.

Nelson, J.L., and Kyba, J., 2014. Structural and stratigraphic control of porphyry and related mineralization in the Treaty Glacier – KSM – Brucejack – Stewart trend of western Stikinia. In: Geological Fieldwork 2013, British Columbia Ministry of Energy and Mines, British Columbia Geological Survey Paper 2014-1, pp. 111-140.

Orchard, M.J., 1993. Report On Conodonts And Other Microfossils. Iskut River (104B). 51 Collections By R.G. Anderson 1985-1986, 1989. 224 Unproductive Samples Collected By R.G. Anderson 1984-1991 (Includes Other Map Areas). Geological Survey of Canada, Paleontological Report OF-1993-1, 25p.

Passchier, C.W., and Trouw, R.A.J., 1998. Microtectonics. Springer-Verlag, Berlin Heidelberg, 289p.

Robb, L., 2005. Introduction to Ore-Forming Processes, Chapter 3: Hydrothermal Ore-Forming Processes, Wiley-Blackwell, United Kingdom, pp. 174-176.

Roddick, J.C., 1988. The assessment of errors in ^{40}Ar/^{39}Ar dating. In: Radiogenic Age and Isotopic Studies, Report 2. Geological Survey of Canada, Paper 88-2, pp. 7–16.

Roddick, J.C., Cliff, R.A., and Rex, D.C., 1980. The evolution of excess argon in alpine biotites - a ^{40}Ar/^{39}Ar analysis. Earth and Planetary Science Letters, 48, 185–208.

Selby, D., and Creaser, R.A., 2004. Macroscale NTIMS and microscale LA-MC-ICP-MS Re-Os isotopic analysis of molybdenite: Testing spatial restrictions for reliable Re-Os age determinations, and implications for the decoupling of Re and Os within molybdenite. Geochimica et Cosmochimica Acta, 68, 3897-3908.

Sun, S.S., and McDonough, W.F., 1989. Chemical and isotopic systematics of oceanic basalts; implications for mantle composition and processes. Geological Society, Special Publication, 42, 313-345.

Tipper, H.W., and Richards, T.A., 1976. Jurassic stratigraphy and history of North-central British Columbia. Geological Survey of Canada, Bulletin, 270, 82p.

Whalen, J., and Frost, C., 2013. The Q-ANOR diagram: A tool for the petrogenetic and tectonomagmatic characterization of granitic suites. Geological Society of America, Abstracts with Programs, 45, 24.

York, D., 1969. Least-squares fitting of a straight line with correlated errors. Earth Planetary Science Letters, 5, 320-324.

Zagorevski, A., Mihalynuk, M.G., Joyce, N.L., Kellett, D.A., Milidragovic, D., 2015. Characterization of volcanic and intrusive rocks across the British Columbia - Yukon border, GEM 2 Cordillera. Geological Survey of Canada, Open File 7956, 2015; 13 pages, doi:10.4095/297272.

Petrology of explosive Middle-Upper Triassic ultramafic rocks in the Mess Creek area, northern Stikine terrane

D. Milidragovic[1, a], N.L. Joyce[2], A. Zagorevski[2], and J.B. Chapman[1]

[1] Geological Survey of Canada, 1500-605 Robson Street, Vancouver, BC, V6B 5J3
[2] Geological Survey of Canada, 601 Booth Street, Ottawa, ON, K1A 0E8
[a] corresponding author: Dejan.Milidragovic@canada.ca

Recommended citation: Milidragovic, D., Joyce, N.L., Zagorevski, A., and Chapman, J.B., 2016. Petrology of explosive Middle-Upper Triassic ultramafic rocks in the Mess Creek area, northern Stikine terrane. In: Geological Fieldwork 2015, British Columbia Ministry of Energy and Mines, British Columbia Geological Survey Paper 2016-1, pp. 95-111.

Abstract

The Mess Lake facies of the Stuhini Group (Middle to Upper Triassic) in northwestern British Columbia includes a unit of pervasively serpentinized, olivine-rich, subaqueous lapilli breccia, lapilli tuff, and ash tuff. Relatively high whole-rock MgO concentrations (29-38 wt.%; loss on ignition-free) of pyroclastic samples from this unit reflect significant accumulation of olivine. These ultramafic pyroclastic rocks also exhibit strong enrichment in Ba and depletion in Nb+Ta relative to La, consistent with derivation from slab-metasomatized mantle asthenosphere in a volcanic arc setting. The restored parental liquid is a primitive, mantle-derived, arc magma that contained up to 16-20 wt.% MgO. The unit contains fresh volcanic glass indicating low-grade regional metamorphism, and suggesting that it postdates emplacement of the nearby Hickman pluton, which yielded $^{40}Ar/^{39}Ar$ hornblende ages of 222.2 ±2.8 Ma, 221.6 ±2.5 Ma, and 220.1 ±2.7 Ma. The Alaskan-type ultramafic plutons of the Polaris suite (Middle to Late Triassic) and a post-Hickman basaltic diatreme, containing picritic fragments, are spatially associated and broadly coeval with the ultramafic pyroclastic rocks of the Mess Lake facies, but a petrogenetic link has yet to be established.

Keywords: Stuhini Group, Triassic, pyroclastic, ultramafic, Stikinia

---

1. Introduction

The Stikine terrane (Stikinia) of the Canadian Cordillera (Fig. 1) is a Mesozoic volcanic arc (see Nelson et al., 2013 for recent overview) that hosts over 1000 Cu ±Au-Mo-Ag porphyry occurrences (British Columbia Geological Survey, 2015; Yukon Geological Survey, 2015). Logan and Mihalynuk (2014) estimated that ≥90% of the Cu mineralization in the Stikine and adjacent Quesnel terrane to the east formed during a relatively short-lived (~6 m.y.) mineralizing epoch centred at ~205 Ma, which spans the Triassic-Jurassic boundary. This episode of porphyry mineralization has been attributed to a thermal spike in the underlying mantle wedge that resulted in mobilization of hydrous, metal-rich fluids. Logan and Mihalynuk (2014) attributed the elevated geothermal gradient to arc-parallel tearing of the Panthalassan oceanic plate as it subducted beneath Stikinia at ~210 Ma, based on the appearance of rare, strongly alkaline lavas and ultramafic (picritic) rocks. In the Mess Lake area, ~130 km southwest of the town of Dease Lake, ultramafic olivine-rich pyroclastic tuff forms the base of the Mess Lake volcanic facies (Logan et al., 2000) of the Stuhini Group (Middle to Upper Triassic), mainly along the eastern margin of the Hickman pluton (Fig. 2). Possibly related to these pyroclastic rocks are the broadly coeval, spatially associated ultramafic intrusions of the Polaris suite (Middle to Late Triassic; Nixon et al., 1989; Logan and Koyanagi, 1994; Brown et al., 1996), which border the Hickman pluton. Establishing a genetic and temporal relationship between the Middle to Late Triassic ultramafic rocks would add further credence to the

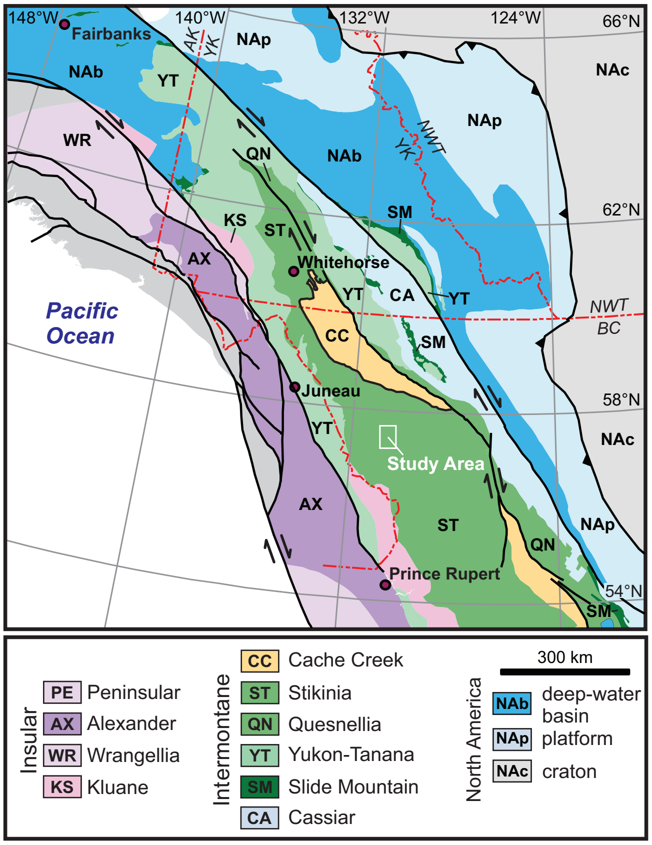

Fig. 1. Terrane map of the northern Canadian Cordillera showing the location of the study area (modified from Nelson et al., 2013).

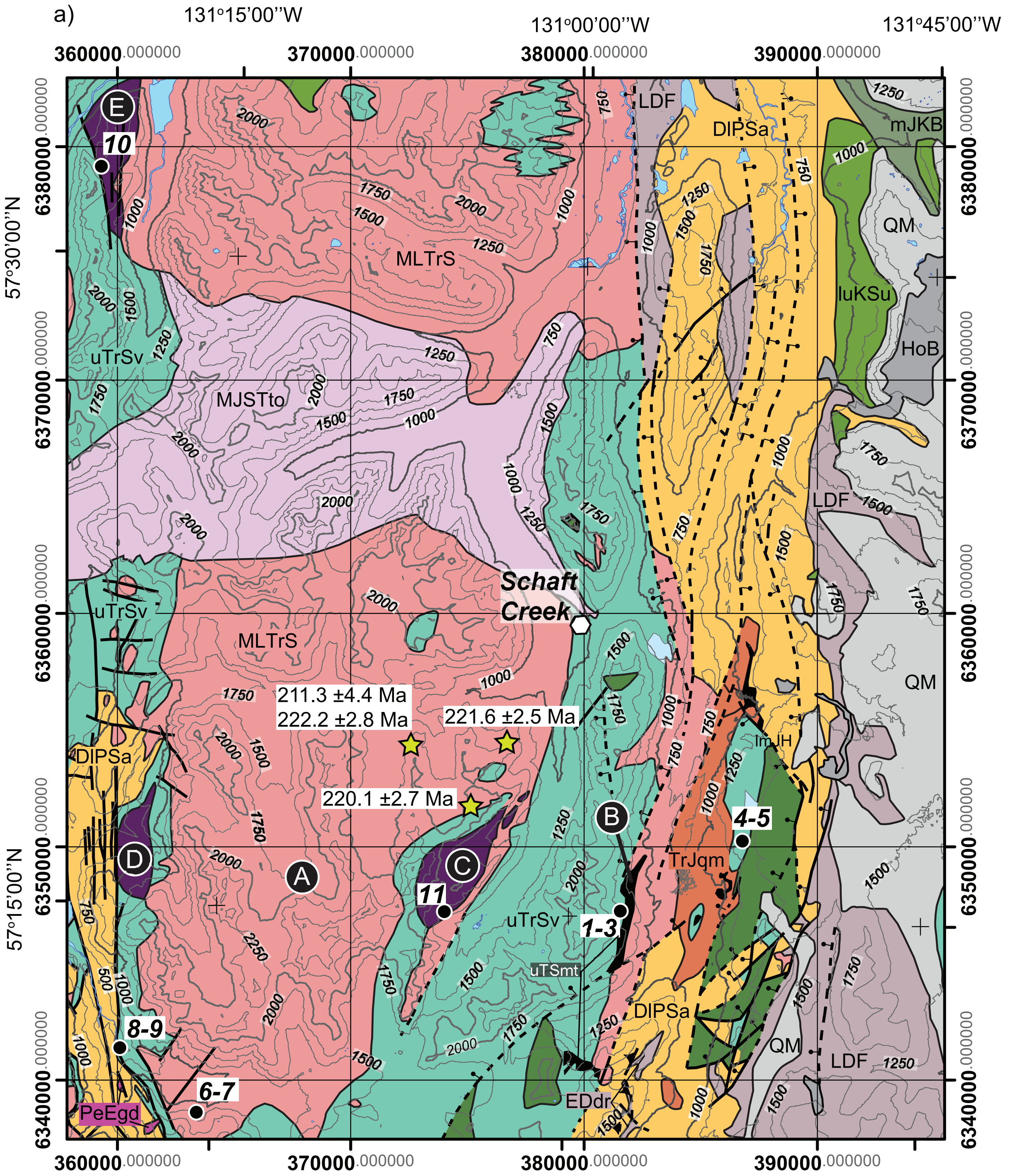

Fig. 2. a) Simplified geological map of the Mess Lake area (parts of NTS 104G 02, 03, 06, 07, 10, and 11; modified from Logan et al., 2000 and Mihalynuk et al., 1996), showing the Schaft Creek exploration camp and locations of samples analyzed for geochemistry (1-11; Table 2) and ^{40}Ar/^{39}Ar geochronology (yellow stars). Key locations discussed in the paper are labeled A-E. **b)** Schematic stratigraphic column illustrating the relationships between stratigraphic and intrusive units in the study area.

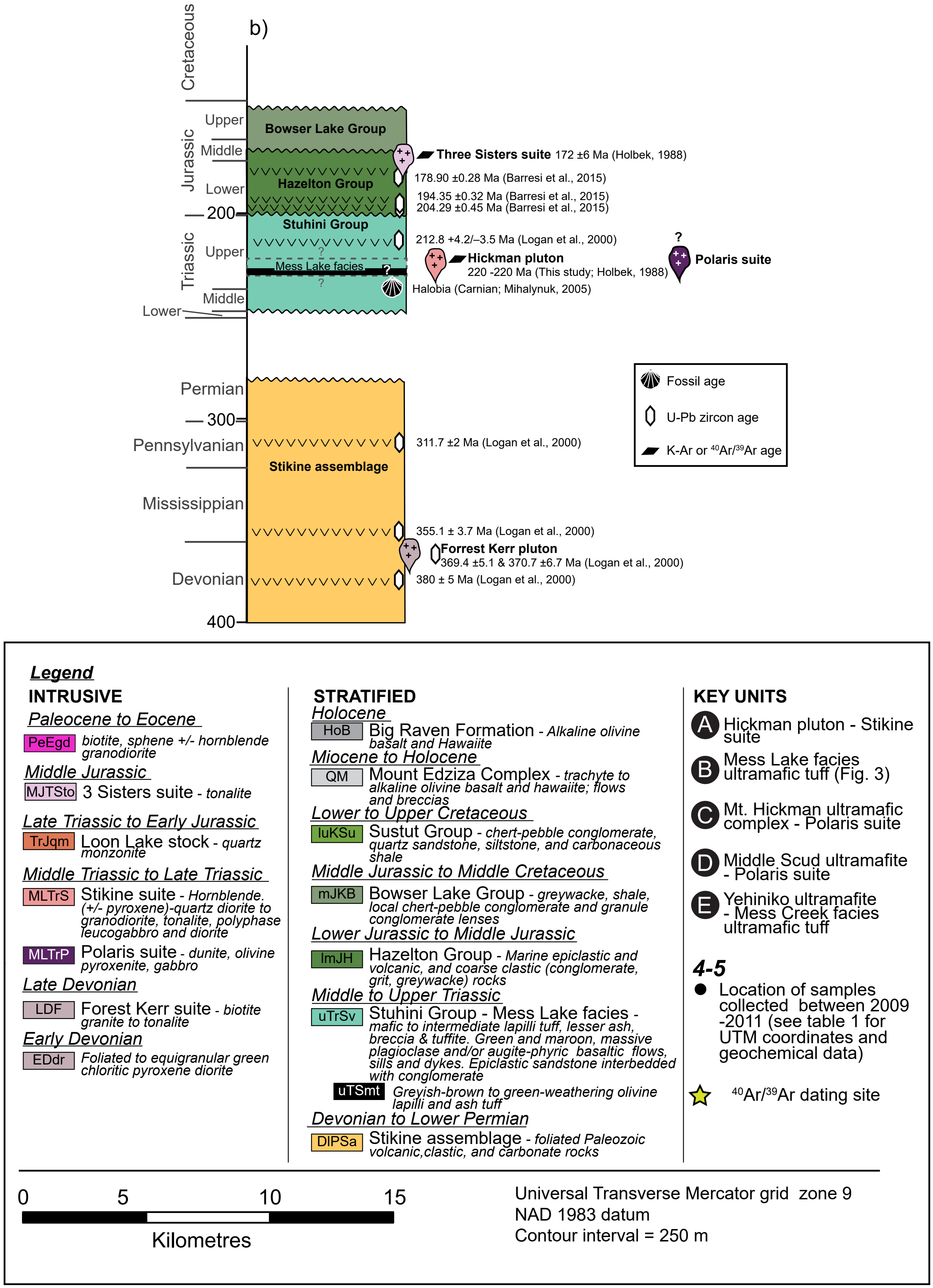
b)
Cretaceous
Jurassic
Upper
Middle
Lower
200
Triassic
Upper
Middle
Lower
Permian
300
Pennsylvanian
Mississippian
Devonian
400
Bowser Lake Group
Hazelton Group
Stuhini Group
Mess Lake facies
?
Stikine assemblage
Three Sisters suite 172 ±6 Ma (Holbek, 1988)
178.90 ±0.28 Ma (Barresi et al., 2015)
194.35 ±0.32 Ma (Barresi et al., 2015)
204.29 ±0.45 Ma (Barresi et al., 2015)
212.8 +4.2/–3.5 Ma (Logan et al., 2000)
Hickman pluton
220 -220 Ma (This study; Holbek, 1988)
Polaris suite
Halobia (Carnian; Mihalynuk, 2005)
Fossil age
U-Pb zircon age
K-Ar or ^{40}Ar/^{39}Ar age
311.7 ±2 Ma (Logan et al., 2000)
355.1 ± 3.7 Ma (Logan et al., 2000)
Forrest Kerr pluton
369.4 ±5.1 & 370.7 ±6.7 Ma (Logan et al., 2000)
380 ± 5 Ma (Logan et al., 2000)
Legend
INTRUSIVE
Paleocene to Eocene
PeEgd biotite, sphene +/- hornblende granodiorite
Middle Jurassic
MJTSto 3 Sisters suite - tonalite
Late Triassic to Early Jurassic
TrJqm Loon Lake stock - quartz monzonite
Middle Triassic to Late Triassic
MLTrS Stikine suite - Hornblende (+/- pyroxene)-quartz diorite to granodiorite, tonalite, polyphase leucogabbro and diorite
MLTrP Polaris suite - dunite, olivine pyroxenite, gabbro
Late Devonian
LDF Forest Kerr suite - biotite granite to tonalite
Early Devonian
EDdr Foliated to equigranular green chloritic pyroxene diorite
STRATIFIED
Holocene
HoB Big Raven Formation - Alkaline olivine basalt and Hawaiite
Miocene to Holocene
QM Mount Edziza Complex - trachyte to alkaline olivine basalt and hawaiite; flows and breccias
Lower to Upper Cretaceous
luKSu Sustut Group - chert-pebble conglomerate, quartz sandstone, siltstone, and carbonaceous shale
Middle Jurassic to Middle Cretaceous
mJKB Bowser Lake Group - greywacke, shale, local chert-pebble conglomerate and granule conglomerate lenses
Lower Jurassic to Middle Jurassic
lmJH Hazelton Group - Marine epiclastic and volcanic, and coarse clastic (conglomerate, grit, greywacke) rocks
Middle to Upper Triassic
uTrSv Stuhini Group - Mess Lake facies - mafic to intermediate lapilli tuff, lesser ash, breccia & tuffite. Green and maroon, massive plagioclase and/or augite-phyric basaltic flows, sills and dykes. Epiclastic sandstone interbedded with conglomerate
uTSmt Greyish-brown to green-weathering olivine lapilli and ash tuff
Devonian to Lower Permian
DlPSa Stikine assemblage - foliated Paleozoic volcanic,clastic, and carbonate rocks
KEY UNITS
A Hickman pluton - Stikine suite
B Mess Lake facies ultramafic tuff (Fig. 3)
C Mt. Hickman ultramafic complex - Polaris suite
D Middle Scud ultramafite - Polaris suite
E Yehiniko ultramafite - Mess Creek facies ultramafic tuff
4-5
● Location of samples collected between 2009 -2011 (see table 1 for UTM coordinates and geochemical data)
★ ^{40}Ar/^{39}Ar dating site
0
5
10
15
Kilometres
Universal Transverse Mercator grid zone 9
NAD 1983 datum
Contour interval = 250 m

catastrophic events in the sub-arc mantle proposed by Logan and Mihalynuk (2014).

Primitive basaltic liquids (MgO >10 wt.%), derived from the Earth's mantle are important carriers of base (e.g., Ni, Cr) and precious (e.g. platinum group element, PGE) metals into the crust, but depending on the fertility, oxidation state, and volatile content of their source regions, primitive basalts may also be important carriers of Cu, Mo, and Au (Richards, 2015). Furthermore, primitive basaltic liquids and their crustal derivatives provide key information about mantle geodynamics and tectonic setting (e.g., Pearce, 2008). Although mafic and ultramafic rocks offer important constraints on the Late Triassic tectonic and metallogenic evolution of Stikinia and seem to be of regional extent, they remain poorly studied. To better understand Late Triassic mantle-sourced magmatism, we examined ultramafic outcrops in the Mess Lake area (Fig. 2) to document field relationships of ultramafic rocks in the Stuhini Group and the Polaris suite, and to collect a representative suite of samples for further petrographic, geochemical, isotopic and geochronological studies. Herein we integrate petrographic and outcrop-scale observations with geochemical data from 11 samples collected during previous reconnaissance sampling. We also present new $^{40}Ar/^{39}Ar$ hornblende ages from four gabbroic to granodioritic samples from the Hickman pluton. We conclude that the ultramafic rocks formed from mantle-derived, primitive arc magmas that likely erupted after ~222 to 220 Ma, when the Hickman pluton was emplaced.

2. Geological background

The Stikine terrane is a composite volcanic arc comprising Devonian to Jurassic volcanic and sedimentary assemblages that are cut by coeval plutonic rocks. Paleozoic rocks of the Stikine assemblage (Monger, 1977) record the first of three episodes of island-arc formation. The second and third episodes are represented by two unconformity-bounded Middle Triassic-Lower Jurassic successions: 1) the Stuhini Group (Middle-Upper Triassic), which consists predominantly of subaqueous, mafic to felsic volcanic and related sedimentary rocks; and 2) the Hazelton Group (Lower-Middle Jurassic) comprising subaqueous to subaerial, volcano-sedimentary rocks (Brown et al., 1996; Logan et al., 2000; Barresi et al., 2015). The Stuhini Group contains voluminous augite and/or plagioclase porphyritic basalt and andesite that are coeval with Carnian to Rhaetian sedimentary rocks (Souther, 1977; Logan et al., 2000; Mihalynuk et al., 1999; Logan and Iverson, 2013). Logan et al. (2000) reported that aplitic dikes extend outward from a hornblende biotite granodiorite to quartz monzonite intrusion on the east-facing slope above Mess Creek and cut the Mess Lake facies of the Stuhini Group. They correlated this plutonic body with the main phase of the Hickman pluton (~221 Ma; Holbek, 1988; this study), implying that the Mess Lake facies is older than ~221 Ma, which may be at odds with our results (see Discussion). The end of Triassic arc building and Stuhini Group deposition is marked by termination of magmatism, deposition of Late Norian to Rhaetian limestones (Sinwa Formation), and deformation.

Plutonic suites coeval with arc volcanism include Forrest Kerr (Late Devonian), More Creek (Early Mississippian), Stikine, Polaris, and Copper Mountain (Late Triassic), Texas Creek, Aishihik, and Long Lake (Early Jurassic), and Three Sisters (Middle Jurassic; Logan et al., 2000; Zagorevski et al., 2014). The Hickman pluton in the eastern half of the study area (Fig. 2) is a composite intrusion and part of the Stikine Suite (Brown et al., 1996; Logan et al., 2000).

2.1. Late Triassic ultramafic magmatism

The Stuhini Group consists mainly of basaltic to andesitic volcanic rocks that are accompanied by rare felsic volcanic rocks. Ultramafic volcanic rocks are volumetrically minor, but seem to be distributed throughout northwestern Stikinia, including the Mess Lake, Telegraph Creek, Endeavour Mountain, and Atlin Lake areas (Brown et al., 1996; Mihalynuk et al., 1999; Logan et al. 2000). In the Mess Creek area, ultramafic volcanic rocks of the Mess Lake facies unconformably overlie Permian Stikine assemblage limestone and are overlain by massive plagioclase-phyric basalts, massive to weakly stratified mafic tuffs, and plagioclase + augite-phyric basaltic andesite.

In addition to these ultramafic pyroclastic deposits, ultramafic plutonic rocks of the Polaris suite, described as Alaskan-type intrusions by Nixon et al. (1989), also occur along the margins of the Hickman batholith (Fig. 2). These ultramafic intrusions comprise chromite-bearing serpentinized dunite and clinopyroxenite (±olivine), and include the Hickman ultramafic complex and Middle Scud ultramafite (Nixon et al., 1989; Brown et al., 1996). Brown et al. (1996) reported a third ultramafic pluton on the western side of the batholith, named the Yehiniko ultramafite.

2.1.1. Ultramafic tuff of the Stuhini Group

The Stuhini Group ultramafic pyroclastic rocks are well exposed ~12 km south-southeast of the Schaft Creek camp (Fig. 2), where they form a 3-5 km long semi-continuous unit that is ≤100 m thick. Although the ultramafic rocks appear to have served as a locus for late brittle faulting and veining, thick sections are relatively undisturbed. One sub-vertical cliff face exposes a section ~35 m thick (Fig. 3a), cut by a thin (<1 m) hornblende-phyric basaltic dike with chilled margins (Fig. 3b). The outcrop exposes four fining-upward sequences, in which beds, normally graded from tuff breccia to olivine lapilli tuff, are capped by units of rhythmically stratified ash tuff (Figs. 3-5). Each fining-upward sequence has a sharp base, locally marked by low-amplitude scouring of underlying ash tuff, and may record a separate eruption event. The contact between fine lapilli tuff and overlying rhythmically-stratified ash tuff is gradational in all cases. The bomb and lapilli-sized fragments contain abundant black-weathering, euhedral to subhedral, serpentine-after-olivine pseudomorphs and have cuspate to embayed margins (Fig. 4a), suggesting minimal deformation during and since deposition. Lapilli are typically vesicular although, in some cases, the internal vesicular microstructure

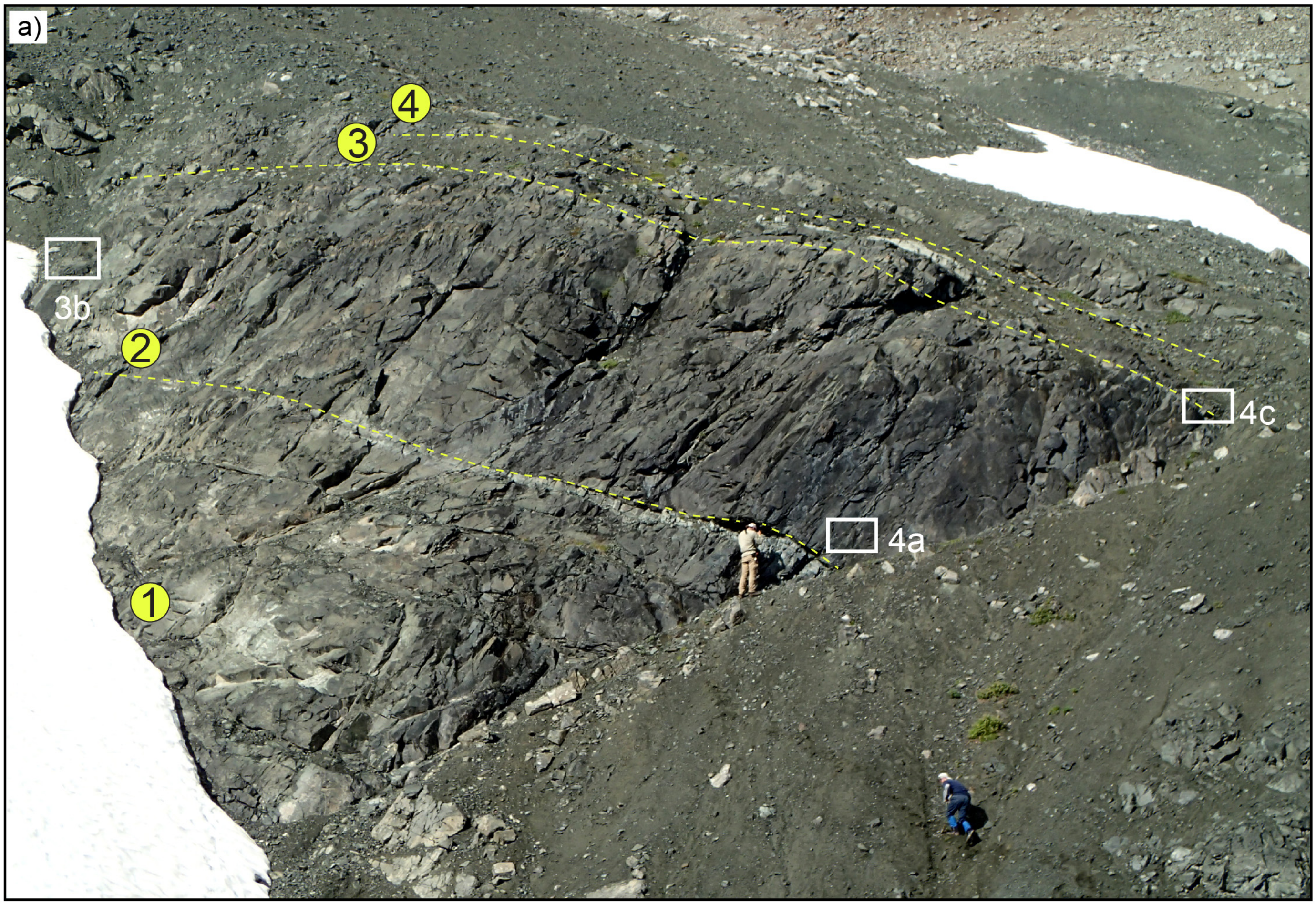

Fig. 3. a) Ultramafic tuffs exposed on a sub-vertical cliff on the west side of the Mess Creek valley, south-southeast of the Schaft Creek exploration camp arranged in four fining-upward sequences (1-4) that follow the order sharp-based tuff breccia to lapilli tuff to ash tuff. White boxes show the positions of Figs. 3b, 4a and 4c. **b)** Hornblende-phyric basaltic dike that cuts pyroclastic rocks on the cliff face in 3a. The size and abundance of hornblende phenocrysts decrease symmetrically from the dike centre.

has been obliterated by devitrification and secondary mineral growth. Some lapilli contain unaltered glass (Fig. 4b), consistent with rapid quenching. The ash tuff is finely to coarsely layered (≤3 mm to ≥5 cm), with individual layers that are continuous and parallel at outcrop scale (Fig. 4c). As observed in thin section, this macroscopic layering is the manifestation of gradational variation in the abundance of partially palagonitized glass shards relative to fragmented serpentinized olivine.

Logan et al. (2000) described the Stuhini Group ultramafic rocks as largely altered to serpentine, chlorite and talc. Most lapilli consist of olivine, pseudomorphed by serpentine ±magnetite and calcite (Fig. 6) in a fine-grained brown groundmass of chlorite, sericite, and other clay minerals; the lapilli float in a matrix of serpentinized olivine, devitrified ash, and chlorite. Less commonly, lapilli are composed entirely of vesicular palagonitized glass (scoria; Fig. 6e). Clinopyroxene is sparse, as are clasts of non-cognate lithologies. Despite pervasive alteration, most ash tuff samples contain bubble-wall shards of partially palagonitized to fresh glass (Fig. 6b).

Brown et al. (1996) mapped ultramafic cumulate rocks at the margin in the Hickman batholith in the Telegraph Creek area, in the northwestern corner of the study area (Yehiniko ultramafite; Fig. 2). Reconnaissance sampling in 2010 indicated that some of these rocks are ultramafic lapilli tuff rather than intrusive rocks. Detailed investigation of the Yehiniko ultramafic body, conducted during this study, revealed abundant ultramafic pyroclastic rocks with ubiquitous, relict olivine (Fig. 6f). Brown et al. (1996) also described other occurrences of Upper

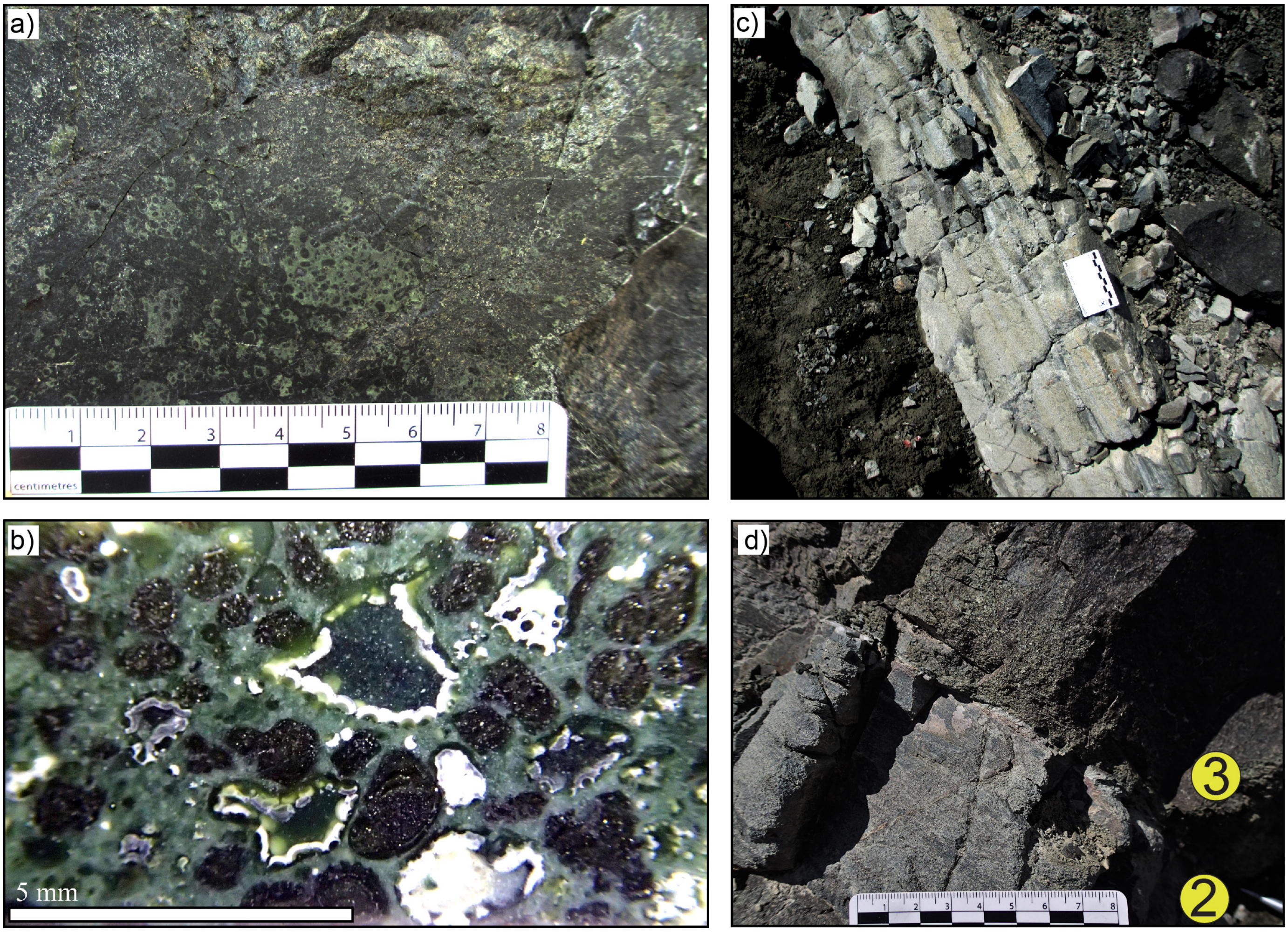

Fig. 4. a) Lapilli tuff near the base of fining-upward sequence 2 (Fig 3). A ~2 cm lapilli, containing subhedral olivine (black) in fine-grained, green matrix is in the centre of the photo. **b)** Close-up of a ~3 cm lapillus. The subhedral black crystals are olivine. The cuspate, green, vitreous features with white rims appear to be fresh volcanic glass. **c)** Thin rhythmic layering in ash tuff at the top of fining-upward sequence 2. **d)** Abrupt contact between lapilli tuff at the base of fining-upward sequence 3 and underlying ash tuff of fining-upward sequence 2.

Triassic or older ultramafic volcanic rocks in the Endeavour Mountain area, ~30 km east-northeast of Schaft Creek (Fig. 2), supporting the idea of widespread ultramafic volcanism in northwestern Stikinia.

2.1.2. The Hickman pluton

The Hickman pluton of the Stikine suite consists mainly of massive to weakly-foliated, medium grained, equigranular, hornblende biotite granodiorite to quartz monzonite with subordinate tonalite and quartz diorite (Brown et al., 1996; Logan et al., 2000). The pluton also contains gabbroic and dioritic phases. Potassium-argon and Rb-Sr geochronology on biotite and hornblende suggests a minimum emplacement age of ~221 Ma for the Hickman pluton (Holbek, 1988; Brown et al., 1996). At the Schaft Creek deposit, quartz and feldspar-porphyritic apophyses of the Hickman pluton, with a U-Pb zircon age of 220 +15/-2 Ma (Logan et al., 2000) cut Stuhini Group country rocks and are associated with mineralization. At its southern limit of exposure, the Hickman pluton is cut by a mafic diatreme breccia of unknown age. The breccia consists of cm- to dm- sized hydrothermally altered granitoid and mafic volcanic clasts in a fine-grained plagioclase-phyric basaltic matrix. The mafic volcanic population includes fragments of augite and olivine (now largely chlorite)-phyric basalt/picrite, which we sampled due to its primitive mineralogy and composition, and possible genetic ties to ultramafic rocks of the Mess Lake facies and/or Polaris suite.

2.1.3. Ultramafic cumulate rocks of the Polaris suite

Evaluating the possibility of a genetic relationship between the Middle to Late Triassic ultramafic intrusions of the Polaris suite (Nixon et al., 1989; Brown et al., 1996) and the ultramafic pyroclastic rocks of the Stuhini Group is important for understanding the extent, timing and duration of the Middle to Late Triassic magmatism in northwestern Stikinia. The Mount Hickman ultramafic complex, on the southeastern margin of the Hickman pluton (Fig. 2), consists mainly of olivine-clinopyroxenite and gabbro; serpentinized dunite is locally

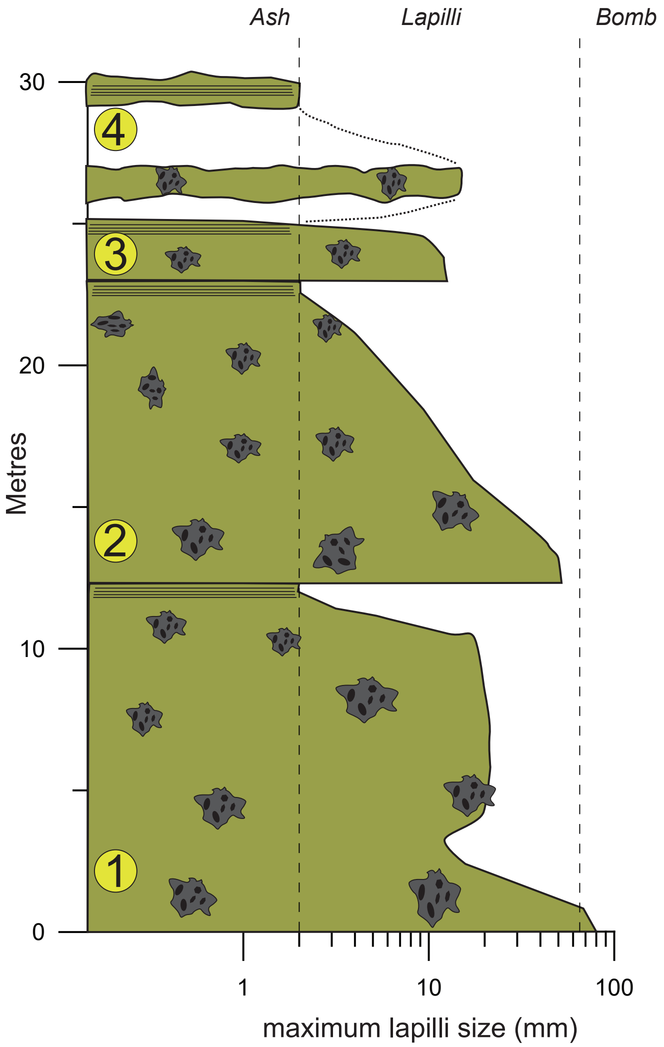

Fig. 5. Measured section of cliff shown in Fig. 3. The numbers on yellow background refer to the four fining-upward sequences.

exposed on its southern and northern flanks. The Middle Scud body on the west side of the Hickman pluton, ~15 km west of Mount Hickman ultramafic complex, contains sheared and pervasively serpentinized biotite-rich peridotite.

3. Methods

3.1. ^{40}Ar/^{39}Ar methodology

Laser ^{40}Ar/^{39}Ar step-heating analysis was carried out at the Geological Survey of Canada Noble Gas laboratory in Ottawa, Ontario. Unaltered pieces (0.25-1.0 mm) of hornblende were picked from four gabbroic to granodioritic samples of the Hickman pluton (Stikine suite). Individual hornblende separates were loaded into aluminum foil packets along with grains of Fish Canyon Tuff Sanidine (FCT-SAN) to act as flux monitor (apparent age = 28.201 ±0.023 Ma; 1σ, Kuiper et al., 2008). The sample packets were arranged radially inside an aluminum canister. The samples were submitted for a 60 MWh irradiation in high flux position 5c at the research reactor of McMaster University in Hamilton, Ontario, Canada.

Upon return from the reactor, samples were split into one or more aliquots each and loaded into individual 1.5 mm-diameter holes in a copper planchet. The planchet was then placed in the extraction line and the system evacuated. Heating of individual sample aliquots in steps of increasing temperature was achieved using a Merchantek MIR10 10W CO_2 laser equipped with a 2 mm x 2 mm flat-field lens. The released Ar gas was cleaned in the extractions line over two hot SAES™ NP-10 getters of St 707 alloy (Zr-V-Fe) held at ~400°C (to remove nitrogen, oxygen, hydrocarbons, water and other active gases) and a room-temperature getter containing HY-STOR® 201 calcium-nickel alloy pellets (to remove hydrogen), and then analyzed isotopically using a Nu Instruments Noblesse noble gas mass spectrometer, equipped with a Faraday detector and three ion counters. For the first aliquots of each sample, the analyses were run in single ion counter peak-hopping mode for small signals (‘SC’ mode as described in Kellett and Joyce, 2014), and in cases where the ^{40}Ar signal exceeded ion counting tolerance, a Faraday plus single ion counter peak-hopping routine was used. For Aliquot #2 of sample ZE09-059A all steps were run in ion counter multi-collection mode (‘MC-Y’ mode of Kellett and Joyce, 2014), except for the 7.5W step for which the ^{40}Ar signal exceeded the ion counter tolerance. This step was run using full multi-collection mode (‘MC-O’ mode of Kellett and Joyce, 2014). Baselines were measured before each analysis. Blank measurements were made throughout the analytical sessions (Table 1). Mass fractionation and detector efficiencies were determined from repeated measurements of air aliquots, whereby ^{40}Ar and ^{36}Ar signals were measured on all collectors. ^{40}Ar/^{36}Ar ratios were then determined for each collector individually, and for each combination of collectors (excluding ^{40}Ar on the Faraday/^{36}Ar on each ion counter). Raw data from the mass spectrometer were processed using in-house Excel® data handling macros that use average, linear or non-linear regression protocols based on the equations of Koppers (2002).

Error analysis on individual steps follows numerical error analysis routines outlined in Scaillet (2000); error analysis on grouped data follows algebraic methods of Roddick (1988). Corrected argon isotopic data are listed in Table 1, and presented in Figure 7 as spectra of gas release or inverse-isochron plots per Roddick et al. 1980. In the case of sample ZE09-059A for which two aliquots were run, the spectrum plotted contains step-heating data from both aliquots, alternately shaded and normalized to the total volume of ^{39}Ar released for each aliquot. Such plots provide a visual image of replicated heating profiles, evidence for ^{40}Ar-loss in the low temperature steps, and the error and apparent age of each step. Reported plateau ages are defined as ages derived from three or more consecutive heating steps that are statistically equivalent, and comprise greater than 50% of the total ^{39}Ar released. MSWD is defined as the mean square of weighted deviates.

Neutron flux gradients throughout the sample canister were evaluated by analyzing the FCT-SAN sanidine flux monitors included with each sample packet and interpolating a linear

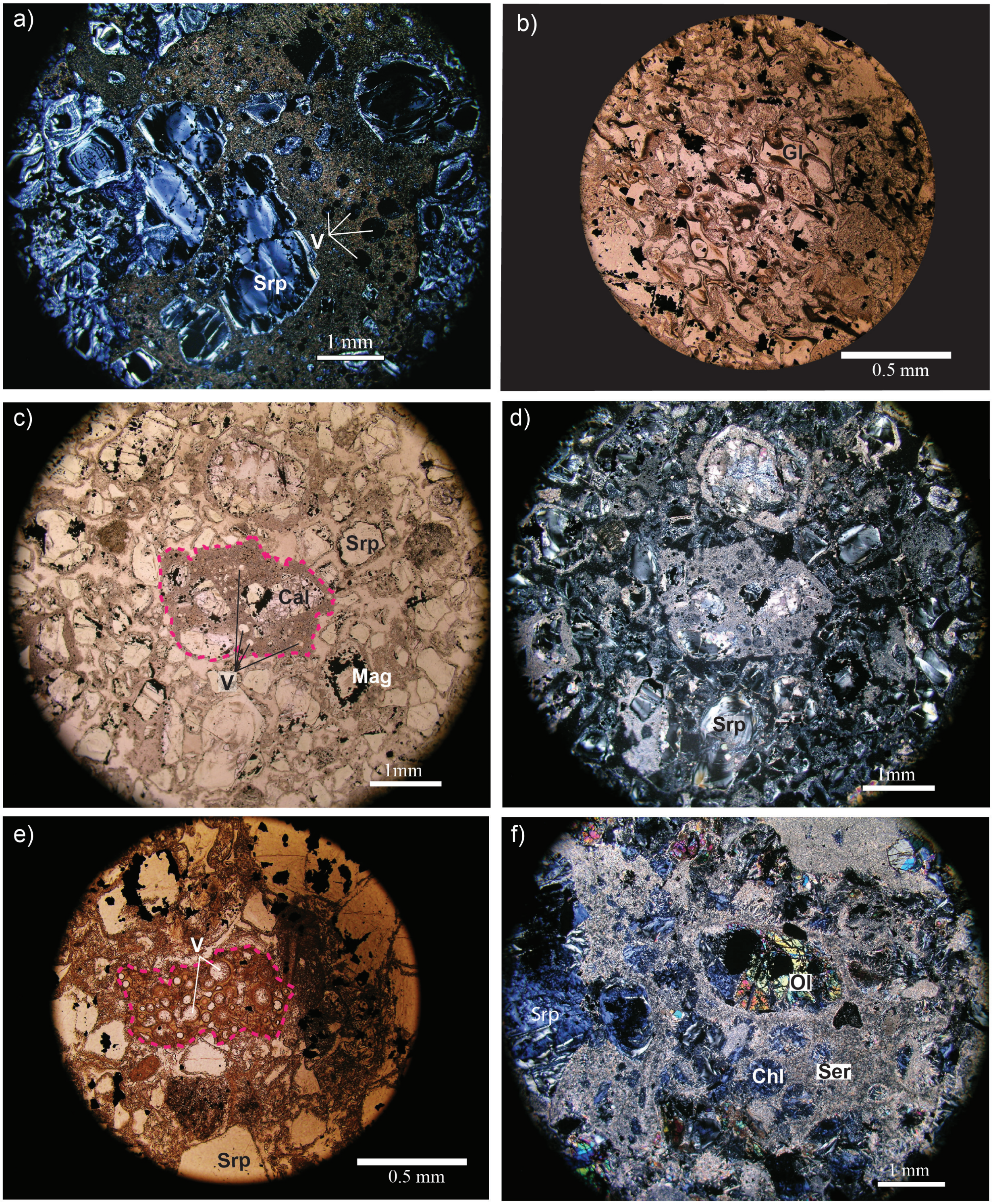

Fig. 6. a) Cross-polarized photomicrograph of a lapilli composed of mm-scale pervasively serpentinized olivine (Srp) that contains fine euhedra of magnetite set in a scoriaceous, very fine-grained groundmass of devitrified glass. Sample 1. **b)** Plane-polarized light image of an ash tuff at the top of fining-upward sequence 1 (Figs. 3 and 5). Concavo-convex, bubble-wall shards of clear to light brown, partially palagonitized, glass (Gl) comprise >40% of the rock. **c)** and **d)** Plane and cross-polarized images of a vesicular lapilli tuff (Sample 4). Olivine, both as part of larger lapilli or as individual crystals has been completely replaced by serpentine, magnetite, and calcite. Dashed pink line in c) outlines the margin of a ~2 mm lapilli. **e)** Plane-polarized light image of a palagonitized lapillius of scoria (dark brown outlined by dashed pink line) in crystal-rich ash tuff at the top of fining-upward sequence 4. **f)** Cross-polarized photomicrograph of a lapilli tuff from the Yehiniko occurrence, previously interpreted as a Polaris suite intrusion. Although the sample has been extensively altered to serpentine (after olivine), sericite, and chlorite, relict fresh olivine is abundant. Cal: calcite, Chl: chlorite, Mag: magnetite, Ol: olivine, Ser: sericite, Serp: serpentine, V: vesicle (now infilled by chlorite).

Table 1. CO_2 laser step-heating ^{40}Ar/^{39}Ar data. All uncertainties quoted at 2σ level unless otherwise indicated.

Power^{a}	Volume ^{39}Ar	^{36}Ar/^{39}Ar	±	^{37}Ar/^{39}Ar	±	^{38}Ar/^{39}Ar	±	^{40}Ar/^{39}Ar	±	%^{4} ^{0}Ar	*^{40}Ar/^{39}Ar	±	f$_{39}$^{c}	App. Age	±		Inverse Isochron Data				
	x10^{-11} cc									ATM			(%)	Ma^{d}			^{39}Ar/^{40}Ar	± % 1σ	^{36}Ar/^{40}Ar	± % 1σ	r
ZE09-059A Hornblende; J=.00745300^{b} Hickman pluton (Z10118) **Inverse Isochron Age = 211.3 ± 4.4 Ma** (Aliquots 1 and 2 combined; Lat/Long 57.31425/ -131.11436)																					
Aliquot: 1																					
3.0	0.0016	0.2208	0.0082	6.533	0.167	0.697	0.019	86.596	1.580	75.3	21.359	2.666	0.7	268.3	30.9	#	0.011548	0.912416	0.002549	1.930474	0.311898
3.5	0.0020	0.0996	0.0062	6.649	0.161	0.169	0.012	40.497	1.112	72.7	11.070	2.077	0.8	143.9	25.8		0.024693	1.372093	0.002459	3.309592	0.361799
3.9	0.0122	0.0622	0.0015	3.751	0.062	0.219	0.012	29.878	0.290	61.5	11.512	0.511	4.9	149.5	6.3		0.033469	0.485716	0.002080	1.264929	0.319293
4.2	0.0128	0.0188	0.0018	8.555	0.130	0.406	0.013	22.791	0.191	24.4	17.237	0.548	5.2	219.5	6.5	#	0.043876	0.419025	0.000825	4.672295	0.067683
4.6	0.0156	0.0090	0.0018	9.281	0.139	0.483	0.014	19.138	0.155	13.9	16.480	0.538	6.3	210.4	6.5	#	0.052252	0.404058	0.000470	9.731073	0.032548
5.0	0.0086	0.0132	0.0021	9.446	0.152	0.335	0.012	20.112	0.293	19.4	16.204	0.687	3.5	207.0	8.2	#	0.049721	0.727794	0.000658	8.019058	0.079435
5.5	0.0663	0.0046	0.0019	11.530	0.164	0.470	0.013	18.715	0.068	7.2	17.364	0.578	26.8	221.0	6.9	#	0.053433	0.182771	0.000244	21.246425	0.005697
6.0	0.0184	0.0037	0.0019	10.650	0.158	0.482	0.013	17.371	0.142	6.3	16.274	0.579	7.4	207.9	7.0	#	0.057566	0.408461	0.000214	25.620646	0.013512
6.5	0.0058	0.0087	0.0027	11.017	0.186	0.332	0.013	18.306	0.422	14.1	15.733	0.912	2.3	201.3	11.0	#	0.054626	1.152899	0.000476	15.778934	0.067746
7.5	0.0366	0.0075	0.0018	10.614	0.155	0.561	0.013	19.256	0.107	11.5	17.047	0.548	14.8	217.2	6.5	#	0.051931	0.278605	0.000388	12.172776	0.014745
15.0	0.0679	0.0024	0.0013	7.390	0.106	0.384	0.012	15.782	0.062	4.4	15.082	0.375	27.4	193.4	4.5		0.063364	0.197334	0.000150	26.440008	0.004635
Aliquot: 2																					
3.0	0.0015	0.1614	0.0078	8.903	3.040	-0.041	-0.013	65.022	1.427	73.3	17.335	2.673	1.3	220.6	31.8	#	0.015379	1.097767	0.002482	2.620440	0.397138
3.5	0.0013	0.0435	0.0078	6.917	3.120	-0.019	-0.011	28.091	1.643	45.8	15.228	2.816	1.1	195.2	34.0	#	0.035598	2.920999	0.001550	9.405879	0.298149
3.9	0.0013	0.0586	0.0076	6.572	4.081	-0.022	-0.011	32.609	1.569	53.1	15.289	2.717	1.1	195.9	32.8	#	0.030666	2.405271	0.001797	6.875240	0.335012
4.2	0.0012	0.0631	0.0081	3.483	3.611	-0.023	-0.012	34.478	1.675	54.1	15.836	2.888	1.0	202.6	34.7	#	0.029004	2.427671	0.001830	6.809965	0.334779
4.6	0.0009	0.0504	0.0118	10.140	4.494	-0.021	-0.011	32.598	2.405	45.7	17.693	4.203	0.8	224.9	49.9	#	0.030677	3.682431	0.001547	12.194885	0.290518
5.0	0.0042	0.0219	0.0027	9.315	0.977	-0.015	-0.011	23.050	0.521	28.0	16.589	0.938	3.5	211.7	11.2	#	0.043384	1.129425	0.000949	6.179897	0.169426
5.5	0.0087	0.0063	0.0020	10.521	0.800	-0.012	-0.011	18.892	0.256	9.8	17.037	0.654	7.3	217.1	7.8	#	0.052933	0.677719	0.000332	16.247860	0.040730
6.0	0.0112	0.0278	0.0024	13.168	0.685	-0.016	-0.011	26.219	0.214	31.4	17.993	0.748	9.4	228.5	8.9	#	0.038140	0.408809	0.001062	4.389982	0.076225
6.5	0.0205	0.0028	0.0020	11.843	0.512	-0.012	-0.011	17.356	0.117	4.8	16.527	0.615	17.3	210.9	7.4	#	0.057618	0.337498	0.000162	36.416034	0.010434
7.5	0.0573	0.0050	0.0017	10.155	0.369	0.781	0.011	18.492	0.074	8.1	17.003	0.513	48.3	216.7	6.1	#	0.054078	0.201232	0.000272	17.050653	0.012445
15.0	0.0106	0.0178	0.0017	9.435	0.502	-0.014	-0.011	21.101	0.215	24.9	15.837	0.548	8.9	202.6	6.6	#	0.047392	0.509907	0.000844	4.833784	0.092081
ZE09-059B Hornblende; J=.00733680^{b} Hickman pluton (Z10119) **Plateau Age = 222.2 ± 2.8 Ma;** Lat/Long 57.31425/ -131.11436																					
Aliquot: 1																					
3.0	0.0033	0.2114	0.0050	4.462	0.108	0.509	0.015	75.991	0.903	82.2	13.531	1.589	1.0	171.9	19.1		0.013160	0.594127	0.002782	1.226595	0.306170
3.5	0.0011	0.0415	0.0105	1.008	0.148	0.063	0.014	26.115	2.178	46.9	13.865	3.780	0.3	175.9	45.4		0.038292	4.160458	0.001587	13.342852	0.300559
3.9	0.0039	0.0926	0.0036	3.036	0.080	0.183	0.012	41.493	0.662	66.0	14.115	1.213	1.2	178.9	14.6		0.024101	0.797124	0.002233	2.050648	0.317603
4.2	0.0032	0.0282	0.0037	1.691	0.072	0.058	0.011	24.028	0.767	34.7	15.685	1.323	1.0	197.8	15.7		0.041618	1.595115	0.001175	6.713847	0.218813
4.6	0.0042	0.0236	0.0028	2.756	0.075	0.091	0.011	23.391	0.584	29.9	16.403	1.004	1.3	206.3	11.9		0.042752	1.247268	0.001011	6.028879	0.188436
5.0	0.0233	0.0170	0.0018	10.384	0.152	0.531	0.014	22.543	0.124	22.3	17.521	0.557	7.0	219.6	6.5	*	0.044360	0.275155	0.000754	5.424043	0.037195
5.5	0.0628	0.0055	0.0016	9.525	0.137	0.689	0.015	19.595	0.077	8.3	17.966	0.482	18.9	224.8	5.6	*	0.051034	0.197007	0.000281	14.633255	0.006711
6.0	0.1195	0.0014	0.0014	8.455	0.119	0.784	0.016	18.086	0.048	2.4	17.659	0.422	36.0	221.2	5.0	*	0.055290	0.132764	0.000080	49.138802	0.001945
6.5	0.0454	0.0025	0.0016	9.281	0.134	0.702	0.015	18.578	0.096	4.0	17.840	0.476	13.7	223.4	5.6	*	0.053827	0.257479	0.000134	31.637550	0.005272
7.5	0.0376	0.0020	0.0016	9.526	0.138	0.688	0.015	18.292	0.098	3.3	17.697	0.491	11.3	221.7	5.8	*	0.054668	0.267584	0.000110	40.387244	0.005074
15.0	0.0273	0.0052	0.0019	10.721	0.156	0.723	0.016	18.032	0.107	8.5	16.508	0.558	8.2	207.6	6.6		0.055456	0.295821	0.000286	17.988349	0.012374

Table 1. Continued.

Power[a]	Volume ^{39}Ar x10^{-11} cc	^{36}Ar/ ^{39}Ar	±	^{37}Ar/ ^{39}Ar	±	^{38}Ar/ ^{39}Ar	±	^{40}Ar/ ^{39}Ar	±	%^{40} Ar ATM	*^{40}Ar/ ^{39}Ar	±	f_{39}[c] (%)	App. Age	±		Inverse Isochron Data				
																	^{39}Ar/^{40}Ar	± % 1σ	^{36}Ar/^{40}Ar	± % 1σ	r
ZE09-060 Hornblende; J=.00733080[b] Hickman pluton (Z10120) **Inverse Isochron Age = 221.6 ± 2.5 Ma;** Lat/Long 57.31402/ -131.0485																					
Aliquot: 1																					
3.0	0.0006	0.2019	0.0183	2.853	0.351	0.586	0.026	93.165	3.430	64.0	33.495	5.941	0.2	398.9	63.1		0.010734	1.840114	0.002167	4.624446	0.243954
3.5	0.0004	0.1764	0.0250	3.403	0.511	0.187	0.022	72.391	4.390	72.0	20.253	8.261	0.2	251.4	95.1	#	0.013814	3.029287	0.002437	7.464110	0.322080
3.9	0.0006	0.0759	0.0154	2.695	0.340	0.050	0.016	41.683	2.692	53.8	19.264	5.204	0.2	239.9	60.3	#	0.023991	3.225428	0.001820	10.544903	0.270588
4.2	0.0002	0.0982	0.0395	0.629	0.785	0.019	0.029	42.518	6.655	68.3	13.496	13.367	0.1	171.3	160.9	#	0.023519	7.760209	0.002310	21.500451	0.351557
4.6	0.0004	0.0638	0.0261	2.896	0.538	0.135	0.021	35.757	4.400	52.7	16.897	8.799	0.2	212.0	103.6	#	0.027966	6.121814	0.001785	21.218806	0.272693
5.0	0.0007	0.0925	0.0156	6.033	0.332	0.417	0.020	46.508	2.979	58.8	19.183	5.389	0.3	238.9	62.5	#	0.021502	3.198464	0.001988	8.896333	0.326352
5.5	0.0050	0.0138	0.0026	7.464	0.141	0.543	0.015	23.791	0.440	17.1	19.720	0.894	2.0	245.2	10.3		0.042033	0.924750	0.000579	9.644968	0.085019
6.0	0.0906	0.0010	0.0010	5.908	0.086	0.497	0.013	18.086	0.048	1.6	17.794	0.299	36.3	222.6	3.5	#	0.055292	0.132186	0.000055	50.528258	0.001795
6.5	0.0408	0.0050	0.0011	6.527	0.098	0.499	0.013	19.556	0.098	7.6	18.067	0.352	16.4	225.9	4.1	#	0.051136	0.250952	0.000258	11.373677	0.012452
7.5	0.0886	0.0013	0.0009	5.549	0.081	0.514	0.013	18.216	0.056	2.1	17.839	0.283	35.5	223.2	3.3	#	0.054896	0.153044	0.000070	36.861940	0.001937
15.0	0.0215	0.0007	0.0012	6.384	0.098	0.542	0.014	17.435	0.112	1.2	17.219	0.370	8.6	215.9	4.4	#	0.057355	0.320644	0.000042	81.517722	0.003218
ZE09-061 Hornblende; J=.00732860[b] Hickman pluton (Z10121) **Plateau Age = 220.1 ± 2.7 Ma;** Lat/Long 57.29168/ -131.0655																					
Aliquot: 1																					
3.0	0.0015	0.3463	0.0100	6.950	0.217	0.575	0.018	125.286	2.076	81.7	22.944	3.051	0.5	282.2	34.5		0.007982	0.828357	0.002764	1.430357	0.265033
3.5	0.0008	0.1506	0.0117	4.784	0.285	0.069	0.015	57.791	2.676	77.0	13.290	4.193	0.3	168.7	50.5		0.017304	2.313974	0.002606	4.351875	0.462234
3.9	0.0014	0.1253	0.0093	3.022	0.181	0.056	0.013	51.597	1.673	71.8	14.560	3.108	0.5	184.1	37.1		0.019381	1.620493	0.002429	3.935871	0.340305
4.2	0.0016	0.1062	0.0076	3.114	0.155	0.060	0.012	45.125	1.408	69.5	13.752	2.569	0.6	174.3	30.9		0.022161	1.559292	0.002353	3.807931	0.344145
4.6	0.0014	0.0316	0.0081	3.348	0.163	0.087	0.013	25.041	1.513	37.3	15.691	2.821	0.5	197.6	33.5		0.039935	3.016409	0.001264	13.154075	0.217199
5.0	0.0033	0.0391	0.0038	7.191	0.157	0.308	0.013	28.199	0.685	41.0	16.632	1.294	1.1	208.8	15.3		0.035462	1.214483	0.001388	4.945848	0.219408
5.5	0.0169	0.0142	0.0017	9.267	0.142	0.448	0.013	21.698	0.149	19.3	17.505	0.509	5.8	219.2	6.0		0.046088	0.343806	0.000654	5.827378	0.044984
6.0	0.0799	0.0022	0.0017	10.164	0.152	0.402	0.012	18.368	0.106	3.5	17.719	0.516	27.5	221.7	6.0		0.054443	0.288156	0.000119	38.978379	0.004034
6.5	0.1050	0.0021	0.0013	8.005	0.116	0.417	0.012	18.326	0.051	3.4	17.703	0.401	36.1	221.5	4.7		0.054568	0.138103	0.000115	31.939381	0.002550
7.5	0.0409	0.0010	0.0011	6.141	0.092	0.386	0.012	17.850	0.094	1.6	17.562	0.330	14.1	219.8	3.9		0.056023	0.263024	0.000055	54.996033	0.003435
15.0	0.0382	0.0013	0.0013	7.660	0.113	0.476	0.013	17.067	0.074	2.3	16.679	0.397	13.1	209.4	4.7		0.058591	0.215781	0.000077	50.325217	0.003141

[a] As measured by laser in % of full nominal power (10W). Ages marked with an asterisk (*) or a pound symbol (#) were those used in the plateau or inverse isochron age calculation, respectively.

[b] Nominal J (±0.30%, 1σ) from GSC Irradiation Batch #61, referenced to Fish Canyon Tuff Sanidine=28.201 ±0.023 Ma (1σ, Kuiper et al., 2008).

[c] Fraction ^{39}Ar as percent of gas in all aliquots.

[d] Errors on ages from each heating step are analytical only and do not reflect error in irradiation parameter J.

Plateau and inverse isochron age errors are quoted at 2σ and incorporate the error in J, but not the error in decay constants

Atmospheric ^{40}Ar/^{36}Ar=295.5

Decay Constant (^{40}K λ_{total})=5.463 ±0.214 x 10^{-10}/yr (2σ, Min et al., 2000)

Blanks were measured before and after aliquot analysis and levels varied between ^{40}Ar=2.5*10^{-7} to 3.9*10^{-7} nmol, ^{39}Ar=1.8*10^{-10} to 5.4*10^{-10} nmol, ^{38}Ar=1.8*10^{-10} to 1.4*10^{-9} nmol, ^{37}Ar=1.3*10^{-9} to 2.3*10^{-9} nmol, ^{36}Ar=1.1* 10^{-9} to 1.4*10^{-9} nmol, all at ±10 % uncertainty (2σ). Nucleogenic interference corrections (±2σ) are (^{40}Ar/^{39}Ar)K=0.025 ±0.005, (^{38}Ar/^{39}Ar)K=0.011 ±0.010, (^{40}Ar/^{37}Ar)Ca=0.002 ±0.002, (^{39}Ar/^{37}Ar)Ca=0.00068 ±0.00004, (^{38}Ar/^{37}Ar)Ca=0.00003 ±0.00003, (^{36}Ar/^{37}Ar)Ca=0.00028 ±0.00016.

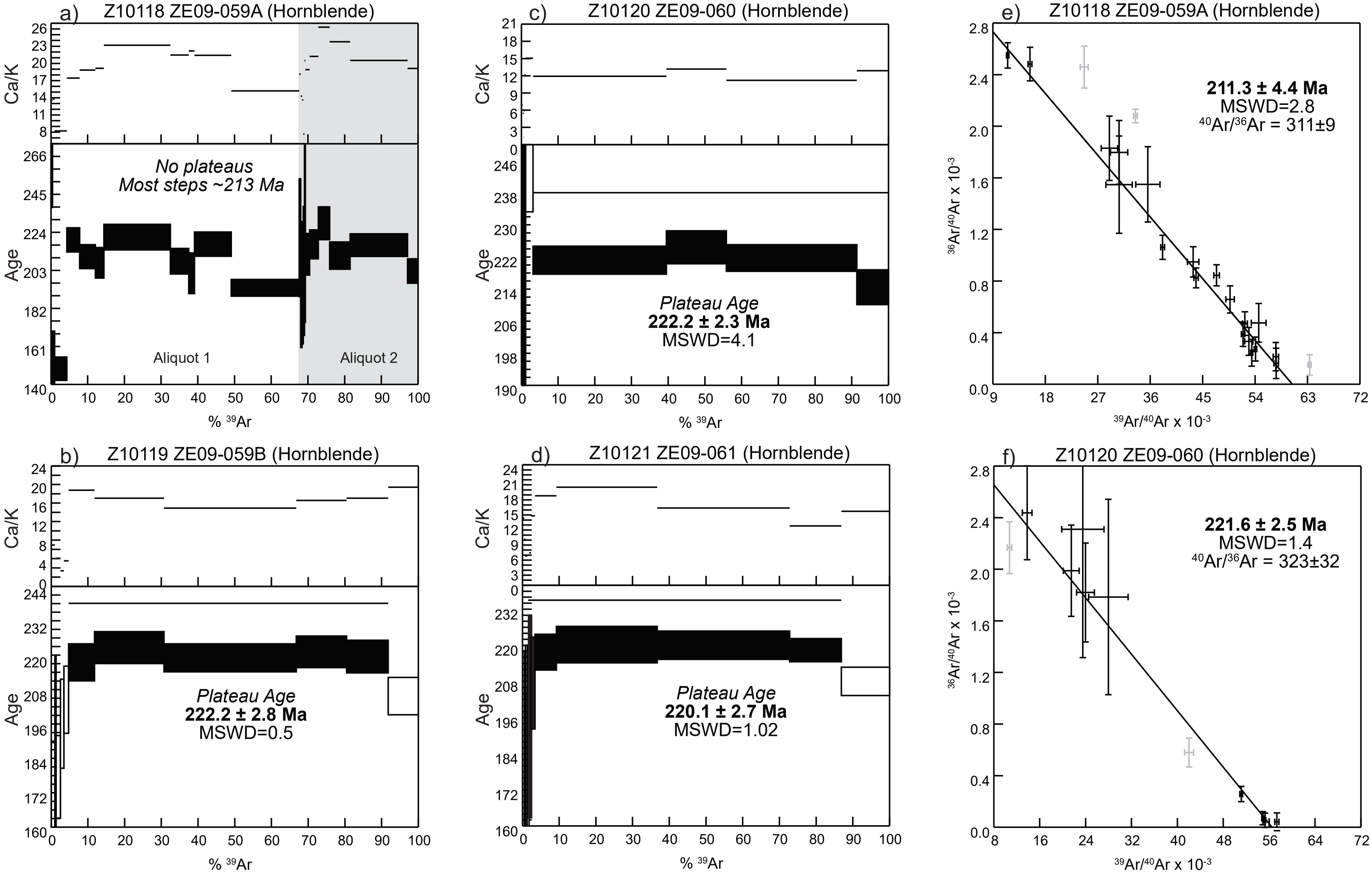

Fig. 7. Hornblende ^{40}Ar/^{39}Ar age spectra and Ca/K ratios as a function of stepped release of ^{39}Ar during heating of samples: **a)** ZE09-059A, **b)** ZE09-059B, **c)** ZE09-060, and **d)** ZE09-061. Inverse ^{36}Ar/^{40}Ar vs. ^{39}Ar/^{40}Ar isochron diagrams for samples: **e)** ZE09-059A and **f)** ZE09-060, respectively.

fit against calculated J-factor and sample position. The error on individual J-factor values is conservatively estimated at ±0.6% (2σ). Because the error associated with the J-factor is systematic and unrelated to individual analyses, correction for this uncertainty is not applied until ages from isotopic correlation diagrams are calculated (Roddick, 1988). Errors in the plateau and inverse isochron ages do not include the errors of decay constants. Nucleogenic interference corrections were $(^{40}Ar/^{39}Ar)_K = 0.025 \pm 0.005$, $(^{38}Ar/^{39}Ar)_K = 0.011 \pm 0.010$, $(^{40}Ar/^{37}Ar)_{Ca} = 0.002 \pm 0.002$, $(^{39}Ar/^{37}Ar)_{Ca} = 0.00068 \pm 0.00004$, $(^{38}Ar/^{37}Ar)_{Ca} = 0.00003 \pm 0.00003$, $(^{36}Ar/^{37}Ar)_{Ca} = 0.00028 \pm 0.00016$. The decay constant used was $^{40}K\ \lambda_{total} = 5.463 \pm 0.214 \times 10^{-10}$/a (2σ) from Min et al. (2000). All errors are quoted at the 2σ level of uncertainty.

3.2. Major and trace element geochemistry

We analyzed 11 samples of Middle-Late Triassic ultramafic rocks that were collected during reconnaissance work in 2009-2011 (Fig. 2). Eight samples from four localities are olivine tuff. One sample, from the Mount Hickman ultramafic complex, is a phlogopite clinopyroxenite. Two clasts of augite-phyric picrite were collected from a diatreme that cuts the Hickman pluton.

The samples were crushed and processed using lithium metaborate/tetraborate fusion and nitric acid dissolution and analyzed using inductively coupled plasma–optical emission spectrometry (ICP-OES) and inductively coupled plasma–mass spectrometry (ICP-MS) at Activation Laboratories (Ancaster, Ontario; 4Lithores analytical package). At a 95% confidence level, the uncertainty in measurement of major elements, significantly exceeding their quantitation limit (defined as 3.33 times the detection limit), is ≤4% relative. The uncertainty in Na_2O, K_2O, and P_2O, which are present in low abundances, is significantly larger ranging between 5 and 30% relative at a 95% confidence level. With the exception of Rb, Pb, Nb, Ta, and Tm, trace elements concentrations in most samples exceed their quantitation limits. The uncertainty in individual measurements, at a 95% confidence level, for transitional metals (e.g. Ni, Cr) is <20%. The relative uncertainty in measurement of rare earth elements (REE) and high field strength elements, at a 95% confidence interval is typically <35%.

4. Results

4.1. $^{40}Ar/^{39}Ar$ results

Sample ZE09-059A is a medium-grained plagioclase porphyritic hornblende-biotite granodiorite. Hornblende occurs as variably altered grains and as fresh hornblende-magnetite clusters. Two aliquots of fresh hornblende were analyzed; both giving disturbed spectra from which no age could be interpreted. Most of the steps, however, fall in the ~213 Ma age range (Fig. 7a; Table 1). Data points on the inverse isochron diagram are generally collinear, plotting along a line that intersects the y-axis at a nearly-atmospheric $^{40}Ar/^{36}Ar$ composition of 311 ±9 and yields an age of 211.2 ±4.4 Ma (Fig. 7e; MSWD = 2.8). We interpret that this is the best approximation of the hornblende cooling age for this sample. Imprecision of the age is due, in part, to elevated and variable Ca/K in the sample; the Ca/K values range between ~7 and 25 (Fig. 7a), suggesting that the grains are compositionally inhomogeneous.

Sample ZE09-059B is from rounded to amoeboid diorite enclaves in medium-grained plagioclase porphyritic hornblende-biotite granodiorite. Hornblende from this sample was clean, fresh, and dark brown to black. One aliquot was analyzed and, although it yielded a slightly hump-shaped spectrum, a robust plateau was obtained for five mid- to high-temperatures steps (excluding the fusion step), giving an age of 222.2 ±2.8 Ma (Fig. 7b; MSWD = 0.5, 87% of total ^{39}Ar). This is the preferred cooling age of the Hickman pluton at this locality.

Sample ZE09-060 is a weakly-foliated, medium-grained, hornblende-biotite diorite. Weakly-zoned hornblende locally contains altered biotite inclusions. Hornblende from this sample selected for analysis was clean, fresh, and dark brown to black. One aliquot was analyzed, and yielded a plateau with four highest-temperatures steps, giving an age of 222.2 ±2.3 Ma (Fig. 7c; MSWD = 4.1, 97% of total ^{39}Ar). When plotted on the inverse isochron diagram, nearly all of the data (9 of 11 heating steps) plot along a line that regresses to an essentially atmospheric $^{40}Ar/^{36}Ar$ composition of 323 ±32, and gives an age of 221.6 ±2.5 Ma (Fig. 7f; MSWD = 1.4). Although indistinguishable from the plateau age, the isochron age includes almost all of the heating steps and has a more acceptable MSWD, and is therefore the preferred cooling age for this sample. This age is indistinguishable from that of sample ZE09-059B (Fig. 7b).

Sample ZE09-061 is a medium-grained to pegmatitic hornblende gabbro. Weakly zoned hornblende is variably altered and locally contains altered biotite inclusions. One aliquot was analyzed, yielding a slightly hump-shaped release spectrum. Six mid- to high-temperatures steps, however, give a plateau age of 220.1 ±2.7 Ma (Fig. 7d; MSWD = 1.02, 85% of total ^{39}Ar). The fusion step, which gives an apparent age of 209 ±5 Ma, was not included.

4.2. Geochemistry

Pyroclastic samples have high volatile contents (7-13 wt.% LOI; Table 2) that reflect, in part, extensive serpentinization of olivine. All pyroclastic samples have high concentrations of MgO (29-38 wt.%, LOI-free) and Ni (1100-1700 ppm), low concentrations of Al_2O_3 (4-6 wt.%) and, with the exception of sample 9, low concentrations of alkalis ($Na_2O+K_2O \leq 0.3$ wt.%). The high absolute MgO and Ni-Cr concentrations and strong negative correlations between MgO and the relatively immobile, conserved oxides (Al_2O_3, TiO_2, P_2O_5; not shown) suggest that the geochemical variability among the ultramafic pyroclastic rocks is mainly controlled by accumulation of olivine. Samples define a nearly vertical array that projects towards ~Fo_{90} on Mg vs. Fe cation unit plot, along an olivine control line (Fig. 8a). Primary liquid compositions were calculated by fractional removal of olivine from each sample at upper crustal pressure (P = 0.1 GPa) until the resulting parental

Table 2. Major and trace element compositions of Late Triassic ultramafic rocks; detection limits in parentheses.

Sample #		1 ZE11-649A	2 ZE11-649D	3 ZE11-649F	4 ZE11-648C	5 ZE11-648D	6 ZE11-644A	7 ZE11-644B	8 ZE11-645A	9 ZE11-645B	10 ZE10-172	11 ZE09-062
Easting		381572	381572	381572	386785	386785	363411	363411	360072	360072	359306	374025
Northing		6347256	6347256	6347256	6350227	6350227	6338573	6338573	6341804	6341804	6379154	6347258
Unit		Stuhini	Stuhini	Stuhini	Stuhini	Stuhini	clast	clast	Stuhini	Stuhini	Stuhini	Polaris suite
Lithology		lapilli tuff	lapilli tuff	lapilli tuff	lapilli tuff	lapilli tuff	Augite picrite	Augite picrite	lapilli tuff	lapilli tuff	lapilli tuff	olivine clinopyroxenite
Major elements (wt. %)												
SiO_2	(0.01)	40.72	40.1	39.98	39.18	39.57	45.6	42.43	40.25	42.46	41.81	44.25
TiO_2	(0.001	0.21	0.27	0.26	0.20	0.31	0.62	0.43	0.20	0.26	0.28	0.91
Al_2O_3	(0.01)	3.97	4.57	4.30	3.82	4.82	9.79	7.99	3.57	5.12	4.70	4.41
Fe_2O_3	(0.01)	9.28	9.53	9.48	8.71	9.39	9.02	9.17	9.25	9.72	9.55	18.62
MnO	(0.001	0.14	0.15	0.14	0.09	0.12	0.15	0.16	0.13	0.15	0.16	0.20
MgO	(0.01)	31.69	29.22	29.9	30.9	25.52	15.42	21.35	33.84	29.47	29.06	13.69
CaO	(0.01)	4.64	6.37	5.83	3.26	9.00	8.61	8.85	3.06	4.44	4.63	16.81
Na_2O	(0.01)	0.03	0.08	0.08	0.07	0.05	1.35	0.22	0.17	0.73	0.22	0.48
K_2O	(0.01)	0.24	0.17	0.14	0.05	0.04	2.81	0.44	0.02	0.65	0.03	0.45
P_2O_5	(0.01)	0.08	0.09	0.09	0.06	0.13	0.42	0.37	0.05	0.08	0.1	0.02
LOI		9.78	10.11	10.25	13.48	10.71	3.86	8.16	8.54	7.39	7.71	0.53
Total	(0.01)	100.80	100.60	100.50	99.82	99.66	97.65	99.57	99.09	100.50	98.25	100.40
Trace elements (ppm)												
Cs	(0.1)	0.2	0.8	0.5	2.1	1.0	4.5	3.3	0.1	1.1	1.2	0.6
Rb	(1)	5	6	3	4	2	84	23	<1	11	2	10
Ba	(3)	138	146	252	59	68	744	118	48	95	13	140
Th	(0.05)	0.17	0.25	0.19	0.22	0.32	1.58	1.24	0.47	0.34	0.15	0.09
U	(0.01)	0.10	0.17	0.13	0.11	0.19	0.97	0.78	0.16	0.23	0.16	0.29
Nb	(0.2)	0.3	0.7	0.3	0.5	0.7	3.1	1.8	0.8	0.7	<0.2	1.0
Ta	(0.01)	<0.01	0.13	0.41	<0.01	0.02	0.14	0.07	<0.01	0.01	<0.01	0.04
Pb	(5)	<5	<5	<5	<5	<5	<5	<5	<5	<5	<5	<5
Sr	(2)	103	183	113	198	94	412	85	73	208	66	113
Zr	(1)	10	12	12	10	17	48	34	27	12	14	20
Hf	(0.1)	0.30	0.40	0.30	0.30	0.50	1.30	1.00	0.70	0.30	0.40	0.70
Y	(0.5)	4.4	5.3	5.0	4.0	7.1	13.7	9.7	4.3	5.4	4.9	8.9
Ga	(1)	5	4	4	4	4	11	8	5	6	5	11
Sc	(1)	16	18	18	14	21	27	21	15	18	19	76
V	(5)	101	123	104	72	106	210	185	98	97	123	461
Co	(1)	60	60	60	70	60	70	70	60	60	70	90
Zn	(30)	98	93	92	97	81	54	69	102	94	94	72
Cu	(10)	40	50	40	30	70	70	70	20	50	30	50
Cr	(20)	2120	2190	1950	1750	1660	950	1660	2400	2100	2120	280
Ni	(20)	1540	1380	1340	1560	1120	580	1070	1700	1380	1260	170
La	(0.05)	1.62	2.74	1.86	2.23	3.15	8.35	6.35	5.31	3.41	1.36	1.80
Ce	(0.05)	3.55	5.96	4.26	4.76	6.68	18.00	13.80	11.00	7.18	3.56	4.66
Pr	(0.01)	0.46	0.72	0.55	0.57	0.82	2.21	1.66	1.19	0.84	0.52	0.77
Nd	(0.05)	2.23	3.16	2.69	2.62	4.17	10.20	7.51	4.34	3.51	2.33	4.19
Sm	(0.01)	0.60	0.84	0.64	0.63	1.13	2.42	1.83	0.90	0.82	0.58	1.50
Eu	(0.005	0.216	0.286	0.260	0.219	0.365	0.815	0.569	0.248	0.315	0.128	0.473
Gd	(0.01)	0.74	0.92	0.86	0.77	1.29	2.66	1.83	0.86	1.03	0.77	1.74
Tb	(0.01)	0.13	0.17	0.14	0.13	0.20	0.45	0.33	0.15	0.18	0.11	0.31
Dy	(0.01)	0.73	0.95	0.88	0.67	1.16	2.50	1.83	0.74	0.94	0.74	1.74
Ho	(0.01)	0.16	0.20	0.17	0.13	0.25	0.49	0.35	0.17	0.18	0.14	0.31
Er	(0.01)	0.44	0.61	0.52	0.42	0.66	1.44	1.04	0.48	0.57	0.42	0.88
Tm	(0.05)	0.060	0.071	0.073	0.064	0.104	0.212	0.138	0.063	0.088	0.065	0.133
Yb	(0.01)	0.42	0.60	0.51	0.43	0.60	1.43	1.02	0.45	0.61	0.47	0.82
Lu	(0.002	0.060	0.085	0.079	0.057	0.103	0.228	0.154	0.073	0.073	0.075	0.113

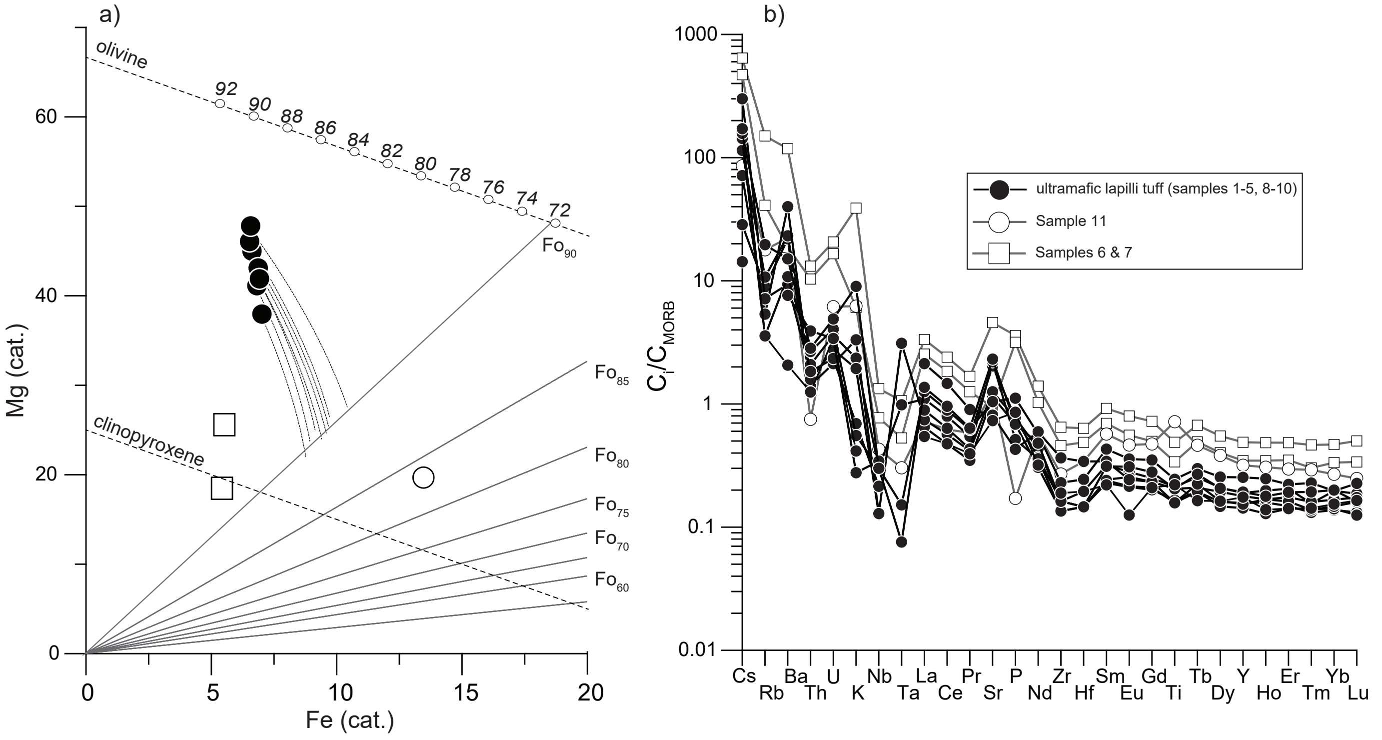

Fig. 8. a) Mg vs. Fe^{TOT} in cation units, showing the compositions of ultramafic lapilli tuff (black circles; samples 1-5, 8-10), olivine clinopyroxenite from Mount Hickman ultramafic complex (white circle; sample 11) and two ultramafic clasts from a basaltic breccia (white squares; samples 6-7). Cation units are calculated by dividing the wt.% oxide value by molecular weight, multiplying by number of cations in oxide formula, and recasting to 100%. The thin dashed lines are the calculated loci of fractional removal of olivine using PRIMELT3 MEGA.XLSM (Herzberg and Asimow, 2015). The radiating lines are isopleths of constant Fo content coexisting with liquids as determined by the Fe-Mg exchange coefficient (K_D=0.30) and adjusted for Fe^{3+}/Fe^{TOT}=0.10. The stoichiometric compositions of olivine and clinopyroxene are shown for reference. **b)** N-MORB normalized trace element patterns of samples collected during 2009-2011 mapping.

liquid is in equilibrium with Fo_{90} (Herzberg and Asimow, 2015). A relatively low Fe^{3+}/Fe^{TOT} ratio (0.05) was chosen to account for the effect of olivine accumulation, which reduces the Fe^{3+}/Fe^{TOT} ratio of the cumulate rock relative to its parental magma. The calculated primary liquids have high MgO concentrations of 16-20 wt.% (LOI-free), consistent with the paucity of clinopyroxene and plagioclase in the pyroclastic rocks. All of the ultramafic samples are orthopyroxene normative (5-25% by weight). However, because of the high mobility of alkalis and the reduction in Mg/Si ratios that result from conversion of olivine (Mg_2SiO_4) to serpentine ($Mg_3Si_2O_5(OH_4)$), the composition of the parental magma cannot be shown to be subalkaline (Si-saturated) with certainty (Kitayama and Francis, 2014).

The high LOI concentrations and pervasive serpentinization, coupled with the lack of correlation between the mobile (e.g., Ba) and immobile (e.g., Zr) elements (not shown), suggest that LILE contents of the Stuhini Group ultramafic rocks should be considered with caution. In nearly all instances, the absolute abundances of the immobile trace elements are lower than those of mid-ocean ridge basalts (MORB), consistent with dilution by olivine accumulation. The ultramafic rocks have relatively flat MORB-normalized heavy rare earth element (HREE) profiles (Tb/Yb_{MORB} = 1.1-1.5), but display relative enrichments in light (L)REE (Ce/Yb_{MORB} = 3-10), and marked depletions in high field strength elements (HFSE) relative to REE of similar compatibility (Nb/La_{MORB} <0.3; Zr/Nd_{MORB} = 0.3-0.6).

The single phlogopite-rich olivine clinopyroxenite sample (sample 11, Table 2) from the Mount Hickman ultramafic complex has a relatively high concentration of MgO (~14 wt.%) and CaO (~17 wt.%) and low concentration of Al_2O_3 (~4.5 wt.%), which reflects the predominant control of clinopyroxene accumulation on the sample's chemistry. The sample also contains abundant cumulus magnetite (>10%), which is reflected in its anomalously high Fe content (Fig. 8a). The phlogopite clinopyroxenite sample is depleted in Nb-Ta relative to the similarly compatible LREE, and strongly enriched in LILE, consistent with derivation from a calc-alkaline parental liquid.

The diatreme clasts (6 and 7, Table 2) are picritic (MgO ≥16 wt.%) and their strongly altered groundmass accounts for the elevated LOI (4-8 wt.%). In addition to containing ubiquitous clinopyroxene, samples 6 and 7 are distinguished from pyroclastic samples by lower concentrations of MgO and FeO and higher concentrations of Al_2O_3, TiO_2, alkalis, and incompatible trace elements. These mineralogical and compositional differences, however, do not preclude a genetic relationship between the clasts and the pyroclastic samples, and future studies may examine possible links.

5. Discussion

5.1. The age of ultramafic volcanism in northern Stikinia

New $^{40}Ar/^{39}Ar$ ages from four granodioritic to gabbroic samples indicate that the Hickman pluton cooled through the hornblende closure temperature (400-600°C; Reiners et al., 2005) at ~220-222 Ma, consistent with the previous determination by Holbek (1988). The observation of fresh to partially palagonitized glass in the ultramafic tuff of the Mess Lake facies < 10 km east of the Hickman pluton indicates that the pyroclastic rocks did not experience significant regional metamorphism (Jakobsson and Moore, 1986), suggesting that they may postdate emplacement of the Hickman pluton. This interpretation contradicts that of Logan et al. (2000) who considered the aplitic dikes cutting volcanic rocks of the Mess Lake facies to be co-magmatic with a granodioritic to quartz monzonitic body that they regarded as part of the Hickman pluton farther west (Fig. 2). However, although direct geochronologic data from this eastern plutonic body are lacking, alkaline geochemistry and associated Cu mineralization suggest that its eastern half includes a Late Triassic-Early Jurassic phase belonging to the ca. 195-210 Ma Copper Mountain plutonic suite (Loon Lake stock; cf. Logan et al., 2000). In short, the relative timing of the Mess Lake ultramafic rocks and the Hickman pluton remains unclear. The issue will be addressed by future work including U-Pb (xenocrystic/detrital zircon) and Sm-Nd (whole rock) geochronology of the ultramafic rocks, and $^{40}Ar/^{39}Ar$ geochronology of crosscutting hornblende-phyric basaltic dikes (Fig. 3b).

5.2. Emplacement and petrology of the Middle to Upper Triassic ultramafic pyroclastic rocks

The ultramafic pyroclastic rocks of the Mess Lake facies were deposited during at least four cycles of explosive eruption, as recorded by four sharp-based fining-upward sequences. Partially palagonitized, highly-vesicular, scoria (Fig. 6e) and the concavo-convex morphology of bubble-wall glass shards suggest that the ultramafic rocks of the Mess Lake facies were fragmented by violent exsolution of volatiles, rather than by hydrovolcanic explosion (McPhie et al., 1993; Thompson-Stiegler, 2008). We speculate that the lack of epiclastic rocks between each sequence might indicate minimal time gaps between eruptive events.

The calculated MgO contents indicate the Mess Lake facies ultramafic pyroclastic rocks were derived from volatile-rich picritic magmas, undergoing olivine crystallization. The immobile trace element profiles of the pyroclastic rocks resemble many arc-related, calc-alkaline magmatic suites, which are widely regarded as melts of sub-arc asthenosphere metasomatized by fluids ±melts emanating from subducted oceanic lithosphere (Pearce and Peate, 1995). Alternatively, calc-alkaline trace element systematics of the tuffs may be attributed to lithospheric contamination of relatively unfractionated (tholeiitic) parental magmas as commonly proposed for Archean and Proterozoic igneous suites (e.g., Maurice et al., 2009; Milidragovic et al., 2014; Sandeman et al., 2014). The mass contribution that is required from such a contaminant may be estimated using reservoir-sensitive trace element ratios that are also insensitive to early stages of olivine-predominant fractional crystallization and accumulation (Pearce, 2008). On a Th/Yb vs. Nb/Yb ratio plot (Fig. 9) the ultramafic pyroclastic rocks of the Mess Lake facies plot above the asthenospheric MORB-ocean island basalt (OIB) array. Their position above the array requires either 1) melting of a fluid/melt metasomatized asthenospheric mantle source; or 2) a depleted N-MORB type magma modified by addition of ~10-20% middle and upper crust. Greater amounts of contamination by lower crust would be required to generate the relatively high Th/Yb ratios of the ultramafic pyroclastic rocks. Although this study is in its preliminary stages, we favour the first alternative, in which melting of slab-metasomatized sub-arc asthenosphere is the main control on the trace element profiles of the ultramafic pyroclastics, for three reasons. First, the relatively high volatile contents required for the buoyant ascent of a picritic magma are more consistent with an arc setting. Second, the pseudomorphed olivine crystals are largely euhedral and show no evidence of disequilibrium, which may be expected from assimilation of Si-rich crustal rocks. Third, Pb, which is strongly enriched in the middle and upper crust (15-17 ppm; Rudnick and Gao, 2003) and depleted in N-MORB (0.30 ppm; Sun and McDonough, 1989), is below detection limit (<5 ppm) in all ultramafic samples.

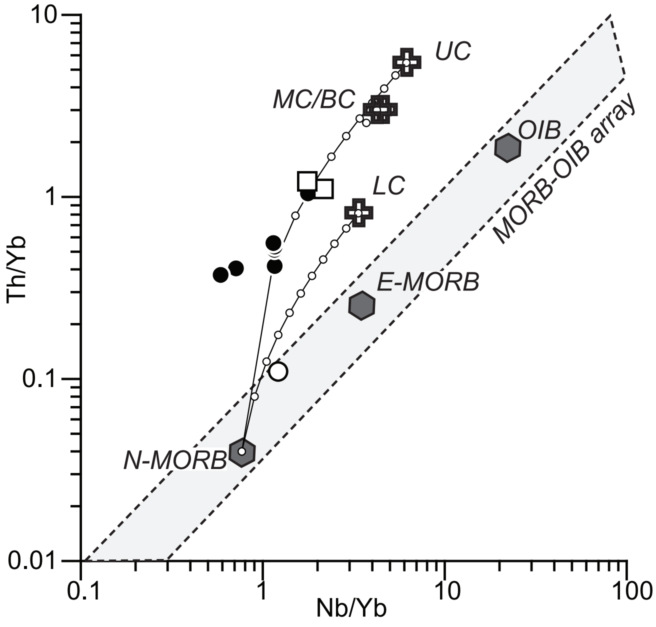

Fig. 9. Th/Yb vs. Nb/Yb (after Pearce, 2008), showing the compositions of ultramafic pyroclastic rocks, olivine clinopyroxenite from the Mount Hickman ultramafic complex, and picritic clasts from a basaltic breccia (symbols as in Fig. 8). The compositions of N-MORB, E-MORB, and OIB are from Pearce (2008); upper continental crust (UC), middle continental crust (MC), lower continental crust (LC) and bulk continental crust (BC) are from Rudnick and Gao (2003). Mixing lines between N-MORB and UC and LC compositions are shown, with small white circles representing 10% mixing steps.

6. Summary and conclusions

Preliminary examination of Middle to Upper Triassic ultramafic volcanic rocks in the Mess Lake area indicates multiple eruptive cycles, evidenced by at least four fining-upward sequences in which sharp-based beds, normally graded from tuff breccia to olivine lapilli tuff, are capped by units of rhythmically stratified ash tuff. Some of the pyroclastic rocks appear to be fresh and contain unaltered glass that is well suited for geochemical studies of magmatic compositions (both major and trace) and volatile contents. Reconstructed primary magma compositions suggest high-MgO (16-20 wt.%) primitive liquids, saturated in olivine only. The ultramafic pyroclastic rocks have typical calc-alkaline trace element signatures (Pearce and Peate, 1995), consistent with derivation from metasomatized, sub-arc asthenospheric mantle. Future studies will examine possible genetic links between the pyroclastic deposits, mafic-ultramafic cumulate intrusions of the Polaris Suite, and diatreme(s) containing picritic clasts.

Fresh volcanic glass in the ultramafic tuffs adjacent to the Hickman pluton and diatreme(s) cutting the Hickman pluton support the idea that ultramafic volcanism, as a whole, is younger than the hornblende age of the Hickman pluton (~222 to 220 Ma). This is at odds with the observations of Logan et al. (2000), who reported that aplitic dikes emanating from a hornblende granodioritic to quartz monzonitic body, which they considered correlative with the Hickman pluton, cut volcanic rocks of the Mess Lake facies. Uranium-lead, ^{40}Ar/^{39}Ar, and Sm-Nd geochronology will be used to better constrain the emplacement age of the ultramafic rocks, and isotopic studies (Rb-Sr and Sm-Nd) will be used to assess the contributions of different reservoirs during ultramafic magma petrogenesis and, ultimately, to help further characterize mantle conditions during the deposition of the Stuhini Group and spatially associated ultramafic plutons.

Acknowledgments

The project is funded by the Geological Survey of Canada's Geomapping for Energy and Minerals program (GSC contribution #2015-0348), with logistical support from Teck Resources. We especially thank Klaus Heppe, Gabe Jutras, and Leif Bailey (Teck) for facilitating our fieldwork out of the Schaft Creek exploration camp. Sebastian Bichlmaier and Simon Carroll provided superb assistance in the field. The manuscript benefited from the attentive reviews by L. Ootes and L. Aspler.

References cited

Barresi, T., Nelson, J.L., Dostal, J., and Friedman, R., 2015. Evolution of the Hazelton arc near Terrace, British Columbia: stratigraphic, geochronological, and geochemical constraints on a Late Triassic-Early Jurassic arc and Cu-Au belt. Canadian Journal of Earth Sciences, 52, 466-494.

British Columbia Geological Survey, 2015. MINFILE—British Columbia mineral deposits database. British Columbia Ministry of Energy and Mines, http://minfile.gov.bc.ca/.

Brown, D.A., Gunning, M.H., and Greig, C.J., 1996. The Stikine project: geology of the western Telegraph Creek map area, Northwestern British Columbia (NTS 104G/5, 6, 11W, 12 and 13). British Columbia Ministry of Energy, Mines and Natural Gas, British Columbia Geological Survey Bulletin 95, 175 p.

Herzberg, C. and Asimow, P.D., 2015. PRIMELT3 MEGA. XLSM software for primary magma calculation: peridotite primary magma MgO contents from the liquidus to the solidus. Geochemistry, Geophysics, Geosystems, 16, 16 p.

Holbek, P.M., 1988. Geology and mineralization of the Stikine Assemblage, Mess Creek Area, northwestern British Columbia. Unpublished M.Sc. thesis, The University of British Columbia, 184 p.

Jakobsson, S. P. and Moore, J.G., 1986. Hydrothermal minerals and alteration rates at Surtsey volcano, Iceland. Geological Society of America Bulletin, 97, 648-659.

Kellett, D. and Joyce, N. 2014. Analytical details of the single- and multicollection ^{40}Ar/^{39}Ar measurements for conventional step-heating and total-fusion age calculation using the Nu Noblesse at the Geological Survey of Canada. Geological Survey of Canada, Technical Note 8, 27 p.

Kitayama, Y. and Francis, D. 2014. Iron-rich alkaline magmatism in the Archean Wawa greenstone belts (Ontario, Canada). Precambrian Research, 252, 53-70.

Koppers, A.A.P. 2002. ArArCALC – software for ^{40}Ar/^{39}Ar age calculations. Computers and Geosciences, 28, 605-619.

Kuiper, K. F., A. Deino, F. J. Hilgen, W. Krijgsman, P. R. Renne and J. R. Wijbrans, 2008. Synchronizing rock clocks of Earth history. Science, 320, 500-504.

Logan, J.M. and Koyanagi, V.M., 1994. Geology and mineral deposits of the Galore Creek area, northwestern British Columbia (104G/3 and 4). British Columbia Ministry of Energy, Mines and Petroleum Resources, British Columbia Geological Survey Bulletin 92, 96 p.

Logan, J.M. and Iverson, O. 2013. Dease Lake geoscience project: geochemical characteristics of Tsaybahe, Stuhini, and Hazelton volcanic rocks, northwestern British Columbia (NTS 104I, J). In: Geoscience BC Summary of Activities 2012, Geoscience BC, Report 2013-1, pp. 11-32.

Logan, J.M. and Mihalynuk, M.G., 2014. Tectonic controls on early Mesozoic paired alkaline porphyry deposit belts (Cu-Au ±Ag-Pt-Pd-Mo) within the Canadian Cordillera. Economic Geology, 109, 827-858.

Logan, J.M., Drobe, J.R., and McClelland, W.C., 2000. Geology of the Forrest Kerr-Mess Creek Area, Northwestern British Columbia (NTS 104B/10, 15 & 104/G2 & 7W). British Columbia Ministry of Energy, Mines and Petroleum Resources, British Columbia Geological Survey Bulletin 104, 164 p.

Maurice, C., David, J., Bedard, J.H, and Francis, D., 2009. Evidence for a widespread mafic cover sequence and its implications for continental growth in the Northeastern Superior Province. Precambrian Research, 168, 45-65.

McPhie, J., Doyle, M., and Allen, R., 1993. Volcanic textures: A guide to the interpretation of textures in volcanic rocks. ARC Centre of Excellence in Ore Deposits, University of Tasmania, 190 p.

Milidragovic, D., Francis, D., Weis, D., and Constantin, M., 2014. Neoarchean (c. 2.7 Ga) plutons of the Ungava craton, Quebec, Canada: parental magma compositions and implications for Fe-rich mantle source regions. Journal of Petrology, 55, 2481-2512.

Mihalynuk, M.G., Bellefontaine, K.A., Brown, D.A., Logan, J.M., Nelson, J.L., Legun, A.S. and Diakow, L.J., 1996. Geological compilation, northwest British Columbia (NTS 94E, L, M; 104F, G, H, I, J, K, L, M, N, O, P; 114J, O, P). BC Ministry of Energy and Mines, British Columbia Geological Survey Open File 1996-11.

Mihalynuk, M.G., Mountjoy, K.J., Smith, M.T., Currie, L.D., Gabites, J.E., Tipper, H.W., Orchard, M.J., Poulton, T.P., and Cordey, F., 1999. Geology and mineral resources of the Tagish

Lake area (NTS 104M/ 8,9,10E, 15 and 104N/ 12W), northwestern British Columbia. British Columbia Ministry of Energy and Mines, British Columbia Geological Survey Bulletin 105, p. 217.

Min, K., Mundil, R., Renne, P.R., Ludwig, K.R., 2000. A test for systematic errors in $^{40}Ar/^{39}Ar$ geochronology through comparison with U/Pb analysis of a 1.1 Ga rhyolite. Geochimica Cosmochimica Acta, 64, 73-98.

Monger, J.W.H., 1977. Upper Paleozoic rocks of the western Canadian Cordillera and their bearing on Cordilleran evolution. Canadian Journal of Earth Sciences, 14, 1832-1859.

Nelson, J., Colpron, M., and Israel, S., 2013. The Cordillera of British Columbia, Yukon and Alaska: tectonics and metallogeny. In: Colpron, M., Bissig, T., Rusk, B., and Thompson, J.F.H., (Eds.), Tectonics, Metallogeny, and Discovery - the North American Cordillera and similar accretionary settings. Society of Economic Geologists, Special Publication 17, pp. 53-109.

Nixon, G.T., Ash, C.H., Connely, J.N., and Case, G., 1989. Alaskan-type mafic-ultramafic rocks in British Columbia: the Gnat Lakes, Hickman, and Menard Creek complexes. In: Geological Fieldwork 1988, British Columbia Ministry of Energy, Mines and Petroleum Resources, British Columbia Geological Survey Paper 1989-1, pp. 429-442.

Pearce, J.A., 2008. Geochemical fingerprinting of oceanic basalts with applications to ophiolite classification and the search for Archean oceanic crust. Lithos, 100, 14-48.

Pearce, J.A. and Peate, D.W., 1995. Tectonic implications of the composition of volcanic arc magmas. Annual Reviews of Earth and Planetary Sciences, 23, 251-285.

Reiners P.W., Ehlers, T.A., and Zeitler, P.K., 2005. Past, present, and future of thermochronology. Reviews in Mineralogy and Geochemistry, 58, 1-18.

Richards, J.P., 2015. The oxidation state, and sulfur and Cu contents of arc magmas: implications for metallogeny. Lithos, 233, 27-45.

Roddick, J. C., Cliff, R. A., and Rex, D. C, 1980. The evolution of excess argon in alpine biotites, Earth and Planetary Science Letters, 48, 185-208.

Roddick, J.C., 1988. The assessment of errors in $^{40}Ar/^{39}Ar$ dating. In: Radiogenic Age and Isotopic Studies, Report 2. Geological Survey of Canada, Paper 88-2, pp. 7-16.

Roddick, J.C., Cliff, R.A., and Rex, D.C., 1980. The evolution of excess argon in alpine biotites -a $^{40}Ar/^{39}Ar$ analysis. Earth and Planetary Science Letters, 48, 185-208.

Rudnick, R.L. and Gao, S., Composition of the continental crust. In: Holland, H.D, Turekian, K.K. (Eds.), Treatise on Geochemistry. Rudnick, R.L. (E.D), The Crust, vol. 3, Elsevier-Pergamon, Oxford, pp. 1-64.

Sandeman, H.A., Ootes, L., Cousens, B., and Killian, T., 2014. Petrogenesis of Gunbarrel magmatic rocks: homogeneous continental tholeiites associated with extension and rifting of Neoproterozoic Laurentia. Precambrian Research, 252, 166-179.

Scaillet, S., 2000. Numerical error analysis in $^{40}Ar/^{39}Ar$ dating, Chemical Geology, 162, 269-298.

Sun, S. and McDonough, W., 1989. Chemical and isotopic systematics of oceanic basalts: implications for mantle composition and processes. In: Saunders, A.D and Norry, M.J (Eds.) Magmatism in the Ocean Basins, Geological Society of London Special Publication 42, pp. 313-435.

Souther, J.G., 1977. Volcanism and tectonic environments in the Canadian Cordillera – A second look. In: Baragar, W. R.A., Coleman, L.C., and Hall, J.M., (Eds.) Volcanic Regimes of Canada. Geological Association of Canada Special Paper 16, pp. 1-24.

Thompson Stiegler, M. Lowe, R., and Byerly, G.R., 2008. Abundant pyroclastic komatiitic volcanism in the 3.5-3.2 Ga Barberton greenstone belt, South Africa. Geology, 36, 779-782.

Yukon Geological Survey, 2015. Yukon MINFILE mineral occurrences and deposits database: Yukon Energy, Mines and Resources, http://ygsftp.gov.yk.ca/httpdocs/minfile/index.html.

Zagorevski, A., Mihalynuk, M.G., Joyce, N., and Martin, K., 2014. Characterization of volcanic and intrusive rocks across the British Columbia-Yukon border, GEM 2 Cordillera. Geological Survey of Canada, Open File 7697, 10 p.

Syncollisional late Early to early Late Jurassic volcanism, plutonism, and porphyry-style alteration on the northeastern margin of Stikinia

Bram I. van Straaten[1, a] and JoAnne Nelson[1]

[1] British Columbia Geological Survey, Ministry of Energy and Mines, Victoria, BC, V8W 9N3
[a] corresponding author: Bram.vanStraaten@gov.bc.ca

Recommended citation: van Straaten, B.I., and Nelson, J., 2016. Syncollisional late Early to early Late Jurassic volcanism, plutonism, and porphyry-style alteration on the northeastern margin of Stikinia. In: Geological Fieldwork 2015, British Columbia Ministry of Energy and Mines, British Columbia Geological Survey Paper 2016-1, pp. 113-143.

Abstract

A previously enigmatic Jurassic volcanic succession on the northeastern margin of Stikinia hosts several early-stage mineral exploration projects, including the Tanzilla porphyry system. Based on new field mapping and preliminary lithogeochemical and geochronological data, we consider these rocks as part of the Hazelton Group and formally define them as the Horn Mountain Formation. The Horn Mountain Formation (ca. 5.4 km thick) consists mainly of green to maroon augite±plagioclase-phyric trachybasalt to trachybasaltic andesite volcanic breccias and lesser plagioclase-phyric to aphyric trachyte to trachyandesite, and is cut by numerous, roughly coeval subvolcanic feeder dikes, sills and stocks. It conformably overlies Toarcian sedimentary rocks of the Spatsizi Formation, which unconformably overlies the Cake Hill pluton (Late Triassic). The Horn Mountain Formation is overlain both conformably and unconformably by Bajocian sedimentary rocks of the Bowser Lake Group. Petrographic observations and major element lithogeochemistry indicate that the volcanic rocks and related subvolcanic intrusions are largely quartz deficient, K-feldspar-rich and alkaline in composition. Regional evaluation indicates that the Horn Mountain Formation extends for least 50 km, and perhaps 110 km, in a west-northwest to east-southeast trending belt that parallels the King Salmon thrust, at the boundary between the Stikine and Cache Creek terranes. A revised structural interpretation extends the Kehlechoa thrust to juxtapose rocks of the Whitehorse trough above Toarcian to Bajocian rocks of the Horn Mountain Formation and Bowser Lake Group. The Snowdrift Creek pluton (early Late Jurassic) stitches the fault and constrains movement to Bajocian-Oxfordian. At the Tanzilla gossan, an advanced argillic lithocap overlies porphyry-style alteration at depth. We report a preliminary 173 Ma U-Pb zircon age for the calc-alkaline plagioclase porphyry that hosts porphyry-style alteration. The alkaline Horn Mountain Formation, calc-alkaline Tanzilla intrusions, Three Sisters plutonic suite, and Snowdrift Creek pluton formed during Stikine-Quesnel arc-arc collision. The protracted late Early to early Late Jurassic syncollisional magmatism represents a potential new metallogenic epoch for the Canadian Cordillera, and is prospective for calc-alkalic to alkalic porphyry- and epithermal-style mineralization.

Keywords: Horn Mountain Formation, Spatsizi Formation, Hazelton Group, Three Sisters plutonic suite, Snowdrift Creek pluton, Takwahoni Formation, Kehlechoa fault, Jurassic, Tanzilla, lithocap, advanced argillic alteration, porphyry copper, Stikinia, arc-arc collision

---

1. Introduction

This paper focuses on a volcano-sedimentary succession east of Dease Lake (northern Stikinia; Fig. 1) that hosts the Tanzilla porphyry copper prospect. Previously, this succession was poorly understood. In published maps, part of it was assigned to the Takwahoni Formation (Lower Jurassic), part to the Stuhini Group (Triassic), and part to a unit of Triassic-Jurassic volcanic rocks that could correlate with either the Stuhini Group or the Hazelton Group (Gabrielse, 1998). To clarify the age and nature of this volcano-sedimentary sequence and to establish a geological framework for alteration and mineralization at Tanzilla, we conducted one month of 1:20,000-scale mapping and stratigraphic analysis northeast of the Tanzilla River, between Gnat Pass and the Tanzilla River, north of Glacial Lake, and east of the McBride River (Figs. 2, 3). Herein we provide the first detailed description of this previously enigmatic volcanic sequence, supported by preliminary igneous rock geochemistry and geochronology. This work demonstrates that the succession represents an unusual late Early to Middle Jurassic volcanic episode coeval with accretion of the Stikine and Cache Creek terranes. Thus far, similar volcanic successions have not been documented elsewhere in northern Stikinia (Fig. 1). We formally define this unit the Horn Mountain Formation, in the upper part of the Hazelton Group, and suggest it extends for at least 50 km, and perhaps 110 km, along the northeastern margin of Stikinia.

2. Geological setting

The study area is near the northeastern margin of the Stikine terrane (Stikinia, Fig. 1), an island arc complex that was accreted to ancestral North America during the Middle Jurassic (Nelson and Mihalynuk, 1993; Mihalynuk et al., 1994; Nelson et al., 2013). The basement of Stikinia contains carbonate and volcanic rocks of the Stikine assemblage (Devonian to Permian) that are overlain by volcanic and related sedimentary rocks of the Stuhini Group (Triassic) and the Hazelton Group (Early to Middle Jurassic; Marsden and Thorkelson, 1992; Currie and Parrish, 1997). The Canadian Cordilleran tectonic

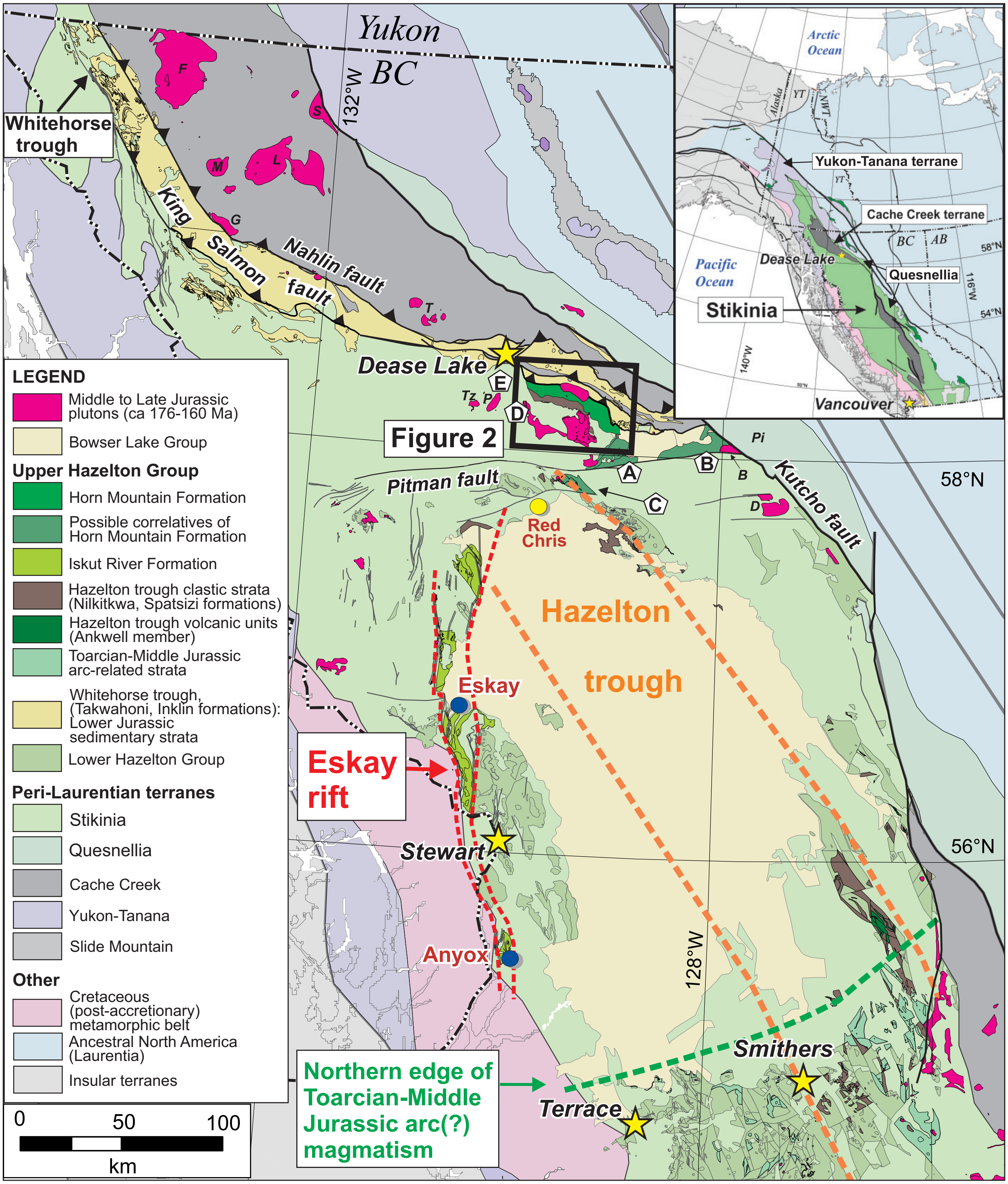

Fig. 1. Geology of northern Stikinia, with emphasis on Middle to Late Jurassic geology and tectonic elements. Boundary of Hazelton trough from Marsden and Thorkelsen (1992); boundary of Eskay rift from Gagnon et al. (2012). Possible correlatives of the Horn Mountain Formation (new volcanic unit proposed herein) are in areas labelled with pentagons 'A' to 'E'. Middle to early Late Jurassic intrusions include F: Fourth of July; S: Slaughterhouse; M: McMaster; L: Llangorse; T: Tachilta Lakes; G: Granite Lake; Tz: Tanzilla; P: Pallen; B: Mt. Blair; D: Mt. Albert Dease; Pi: Pitman.

collage includes the Quesnel terrane (Quesnellia), a volcanic arc with a similar Devonian to Early Jurassic history as Stikinia. The two volcanic arcs are separated by the Cache Creek terrane, an accretionary complex of oceanic crustal rocks, primitive arc ophiolite, pelagic rocks and carbonate rocks (Fig. 1). Combined, Stikinia and Quesnellia host most of the porphyry copper deposits in the Canadian Cordillera (Logan and Mihalynuk, 2014).

The previously enigmatic volcano-sedimentary succession for which we propose the name Horn Mountain Formation (see Section 3.1.2.2.) is exposed in a northwesterly trending belt, about 50 km long and 10 km wide, north and northeast of the Hotailuh batholith (Fig. 2). The succession is on Stikinia, bounded to the north and northeast by the Kehlechoa thrust fault, which separates it from rocks of the Whitehorse trough (Takwahoni Formation) to the north (Fig. 2). The succession is bounded to the west by the Gnat Pass and related faults; its southeastern extent is unknown. Farther northeast, Cache Creek terrane rocks in the hanging wall of the north-dipping King Salmon thrust structurally overlie the Takwahoni Formation (Fig. 2).

The succession unconformably overlies Late Triassic rocks of the Cake Hill pluton, and early workers considered it a part of the Takwahoni Formation (Lower Jurassic) structurally overlain by volcano-sedimentary rocks of the Stuhini Group (Triassic) on an inferred thrust (Hotailuh fault; Anderson, 1983; Gabrielse, 1998). However, recent work by Iverson et al. (2012) demonstrated that rocks previously mapped as part of the Stuhini Group contain Early to Middle Jurassic detrital zircons (ca. 176 Ma peak), leading to the interpretation that the entire volcano-sedimentary succession is part of the Hazelton Group, and removing the need for the putative Hotailuh thrust (Fig. 3; Iverson et al., 2012; van Straaten et al., 2012).

3. Lithostratigraphic units

Rocks in the study area define two tectonostratigraphic domains. Stratigraphic units in the footwall of (south of) the Kehlechoa fault are part of Stikinia; those in the hanging wall (north) are part of the Whitehorse trough (Fig. 2). Most unit descriptions (Table 1) are based on detailed mapping of an area northeast of the Tanzilla River (Figs. 2, 3). We also examined the areas: 1) between Gnat Pass and the Tanzilla River; 2) east of the McBride River; and 3) north of Glacial Lake. Classifications for igneous rocks (Gillespie and Styles, 1999) and sedimentary rocks (Hallsworth and Knox, 1999) are used throughout the following.

3.1. Stikinia

Uniformly north-dipping stratified rocks are present between the Hotailuh batholith and Kehlechoa fault (Figs. 3, 4). As discussed below, we assign the lower predominantly sedimentary succession to the Spatsizi Formation of Thomson et al. (1986) as modified by Evenchick and Thorkelson (2005) and Gagnon et al. (2012). The Spatsizi Formation is overlain by predominantly volcanic rocks of the Horn Mountain Formation (new name, see below). Both formations belong to the upper part of the Hazelton Group as described by Gagnon et al. (2012). In the detailed study area, the Horn Mountain Formation is unconformably overlain by gently north-dipping sedimentary rocks of the Bowser Lake Group.

3.1.1. Stuhini Group (Triassic)

Stuhini Group volcanic rocks were not mapped as part of this study, but a description is included here to document the similarity to the mafic volcanic rocks now assigned to the Horn Mountain Formation. The nearest unequivocal exposures of Stuhini Group are immediately southwest of the study area near Gnat Pass (Fig. 2). Here, poorly exposed dark green, massive augite- and lesser augite-plagioclase-phyric flows, volcanic breccia, tuffaceous conglomerate, volcaniclastic sandstone and siltstone are cut by Late Triassic intrusions (Table 1; Anderson, 1983; Gabrielse, 1998; van Straaten et al., 2012).

3.1.2. Hazelton Group (Lower to Middle Jurassic)

3.1.2.1. Spatsizi Formation

The Spatsizi Group was originally defined by Thomson et al. (1986) based on investigations in the Spatsizi area, ca. 50 km south of the current study area (Area 'C', Fig. 1). The unit was demoted to formational status by Evenchick and Thorkelson (2005) based on its limited geographic extent and to allow inclusion in the Hazelton Group. Gagnon et al. (2012) further modified the Spatsizi Formation to exclude the uppermost Quock Member, a regionally extensive interbedded siliceous mudstone and tuff unit commonly found immediately below Bowser Lake Group sedimentary rocks. They proposed raising the Quock to formational status. The revised Spatsizi Formation comprises shale with minor siltstone, sandstone, tuffaceous beds, conglomerate and limestone; it is Pliensbachian to Aalenian (Thomson et al., 1986; Evenchick and Thorkelson, 2005; Gagnon et al., 2012).

On a more regional scale, the Spatsizi Formation has been correlated with the predominantly siliciclastic Nilkitkwa Formation described east and northeast of Smithers (Fig. 1). The north-northwest trend of siliciclastic rocks of the Spatsizi and Nilkitkwa formations records Pliensbachian to Toarcian marine sedimentation in a back-arc depression (Hazelton trough; Tipper and Richards, 1976; Marsden and Thorkelson, 1992; Gagnon et al., 2012).

The 0.7-1 km thick lower sedimentary sequence between the Hotailuh batholith and Kehlechoa fault (Figs. 3, 4; Table 1) shares many lithological characteristics with the Spatsizi Formation. Both consist mainly of fine-grained siliciclastic rocks, and the Toarcian and younger age of the lower sedimentary sequence in the study area overlaps with published ages for the Spatsizi Formation elsewhere. As a result, we include the lower sedimentary sequence in the Spatsizi Formation. This sequence consists of three main units (Table 1).

In the basal conglomerate unit, subfeldspathic arenites (>75% quartz grains), conglomerate, and quartz-rich feldspathic arenite unconformably overlie the Cake Hill pluton

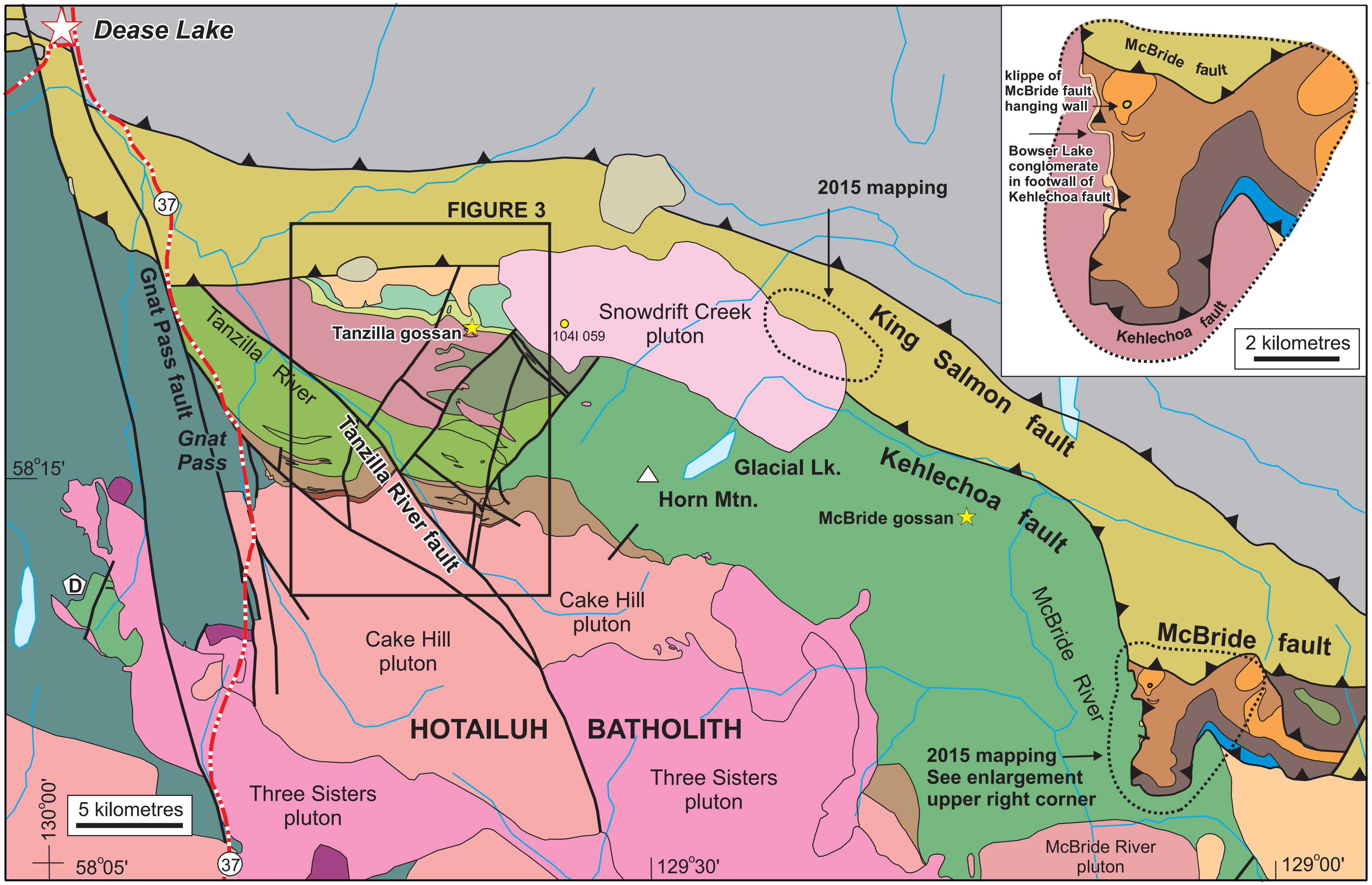

Fig. 2. Regional geology, modified after Gabrielse (1998), Logan et al. (2012b) and van Straaten et al. (2012). See Figure 1 for location. A possible correlative of the Horn Mountain Formation (new volcanic unit proposed herein) is in area 'D'.

LEGEND

Post-accretionary overlap strata

Miocene-Pleistocene Tuya Formation

■ Olivine basalt

Syn- to post-accretionary Middle to Late Jurassic plutons

■ Snowdrift Creek Pluton ca 160-161 Ma: granodiorite, tonalite

■ Three Sisters Pluton ca 170 Ma: diorite, quartz monzonite, granite

Cache Creek terrane

■ Undivided: Late Permian-Early Triassic Kutcho arc sequence, Inklin Formation; ultramafite, basalt, chert, argillite, limestone

—▲—▲—▲—

King Salmon fault

Whitehorse trough

Lower Jurassic Takwahoni Formation

■ Toarcian mudstone, minor sandstone and conglomerate

■ Toarcian conglomerate

■ Pliensbachian greywacke, mudstone, minor conglomerate

■ Sinemurian? Toarcian? andesitic volcanics

■ Sinemurian conglomerate, sandstone, siltstone, mudstone

Upper Triassic Sinwa Formation

■ Upper Norian limestone

—▲—▲—▲—

Kehlechoa fault

Stikinia

Middle Jurassic (Bajocian)

■ Bowser Lake Group

Lower to Middle Jurassic Upper Hazelton Group

Middle Jurassic Horn Mountain Formation

■ Upper mafic volcanics

■ Upper felsic volcanics

Early to Middle Jurassic Horn Mountain intrusions

■ Mafic intrusive complex

Lower to Middle Jurassic Horn Mountain Formation

■ Maroon volcanic rocks

■ Lower mafic volcanic rocks

■ Undivided; also includes cogenetic mafic intrusions

Lower Jurassic (Toarcian) Spatsizi Formation

■ Undivided sedimentary and volcaniclastic strata

■ Basal conglomerate

〰〰〰〰〰〰〰〰

Early Jurassic

■ McBride River Pluton granodiorite

Late Triassic

■ Cake Hill Pluton: quartz monzodiorite, granodiorite, plag(-qtz) porphyry

Late Triassic

■ Gnat Lakes ultramafite pyroxenite, hornblendite, gabbro

Triassic

■ Stuhini Group, undivided

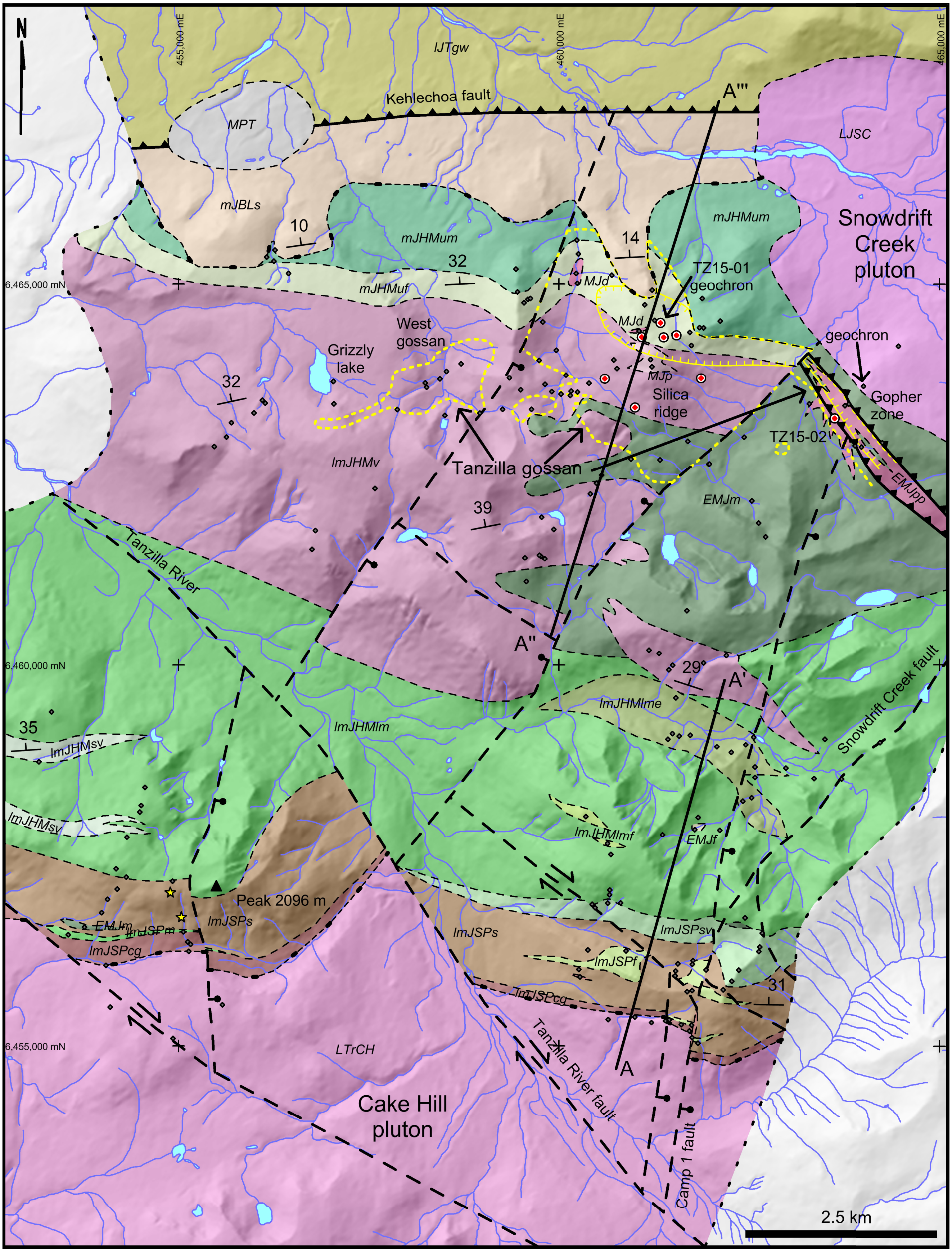

Fig. 3. Geology map of the detailed map area. See Figure 2 for location.

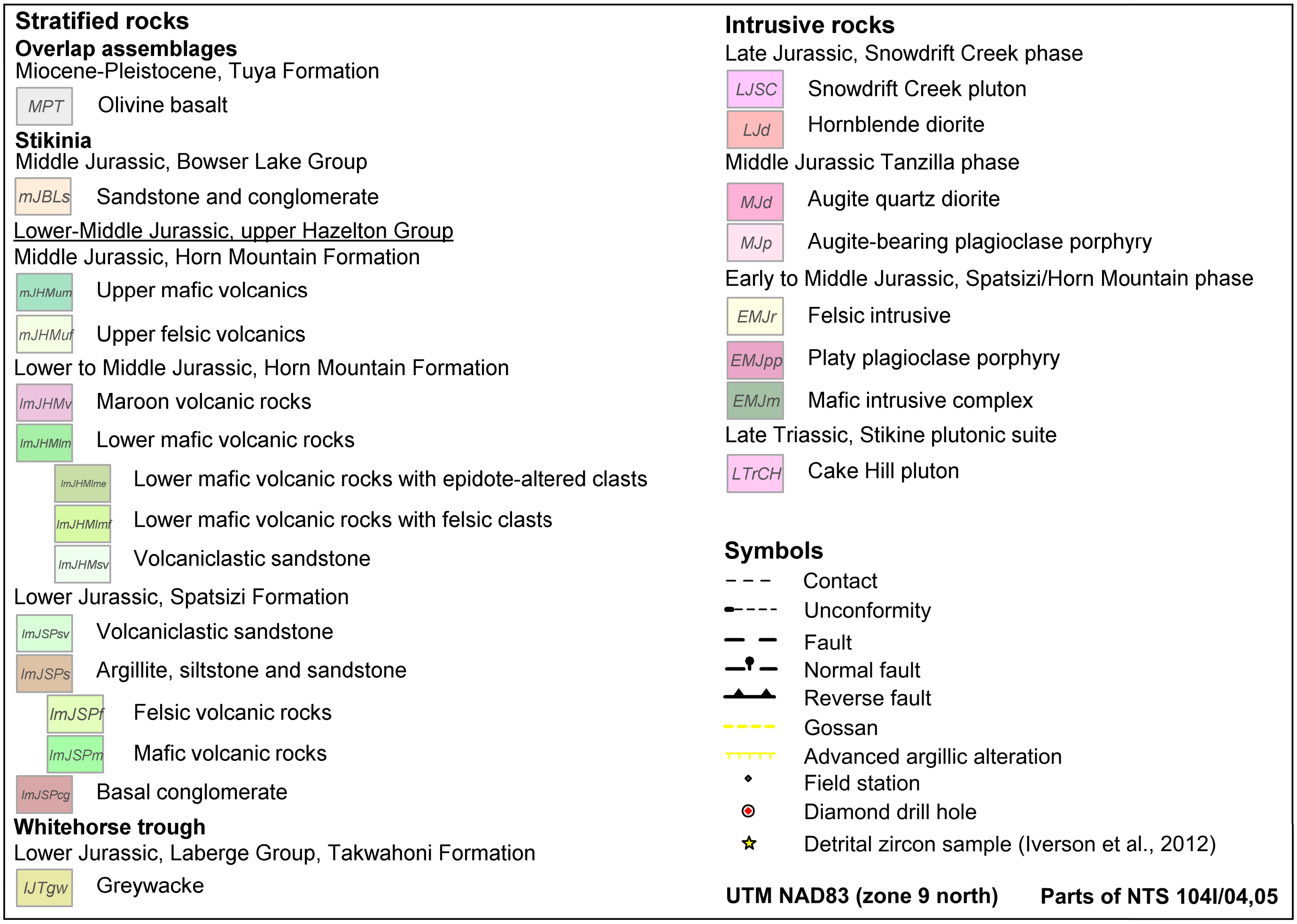

(Late Triassic; Anderson, 1983; Gabrielse, 1998; van Straaten et al., 2012; this study). The conglomerate contains common plutonic clasts of similar composition as the underlying Cake Hill pluton. A calcareous feldspathic arenite bed contains early Toarcian fossils (Henderson and Perry, 1981).

This basal unit fines upward to a unit of argillite, siliceous siltstone, and fine-grained sandstone with minor grey tuff laminae, subordinate mono- to polymictic volcanic breccia intervals, and rare volcaniclastic sandstone (Fig. 5). Detrital zircon samples from this succession yielded Early-Middle Jurassic and Late Triassic age peaks (Iverson et al., 2012). The unit contains two volcanic subunits, felsic coarse platy plagioclase-phyric volcanic breccias northeast of the Tanzilla River (Fig. 6), and a mafic augite-phyric breccia body southwest of the Tanzilla River.

The volcaniclastic unit, at the top of the Spatsizi Formation northeast of Tanzilla River, consists mainly of medium- to coarse-grained volcaniclastic sandstone with lesser siltstone and fine tuff laminae, and subordinate augite-phyric or plagioclase-phyric monomictic volcanic breccia. The contact with the underlying unit is gradational.

3.1.2.2. Horn Mountain Formation (new name)

We propose that the upper, predominantly volcanic succession between the Hotailuh batholith and Kehlechoa fault be called the Horn Mountain Formation, a new formation in the upper part of the Hazelton Group (Figs. 2, 3; Table 1). At its type section (Table 2), the sequence is approximately 5.4 km thick (Fig. 4) and comprises four informal subdivisions. It is middle Toarcian to early Bajocian, based on fossils collected from the underlying Spatsizi Formation and overlying Bowser Lake Group strata. As described below, its base is a transitional contact above the Spatsizi Formation. Its upper contact with Bowser Lake Group conglomerates is unconformable in the detailed map area, and conformable and gradational east of the McBride River. We consider that it extends at least to the first range of mountains east of the McBride River (Fig. 2), based on our work there and on regional mapping by Gabrielse (1998), which included a 684 m-thick stratigraphic section west of the McBride River entirely composed of maroon volcanic rocks (Gabrielse, 1998, p. 126). The Horn Mountain Formation continues along strike for over 50 km.

The Horn Mountain Formation consists of four main units (Figs. 3, 4; Table 1). The lower mafic volcanic unit contains

Table 1. Summary of volcano-sedimentary units. Mineral abbreviations after Kretz (1983).

Age	Unit		Description	Position
Miocene-Pleistocene		Tuya Formation	**Olivine basalt (MPT)** (Gabrielse, 1998)	Overlap
Lower Jurassic	Laberge Group	Takwahoni Formation	**Greywacke (lJTgw).** Interbedded feldspathic wacke, siltstone, argillite, rare feldspathic arenite and rare calcareous feldspathic arenite. Contains common (5%) Qtz grains and minor grey mudstone rip-up clasts. Local predominantly monomictic cobble conglomerate with Hbl diorite clasts. Pliensbachian	Whitehorse trough (N panel)
Lower Jurassic	Laberge Group	Takwahoni Formation	**Argillite and siltstone (lJTs**). Black cherty grey argillite and siltstone, well-stratified, some thinly laminated. Contains minor volcaniclastic sandstone with mainly Pl, lesser Qtz and lithic grains. Minor lighter coloured tuff laminae. Recessive, dark grey-black weathering; forms blocky scree. Toarcian **Upper polymictic conglomerate (lJTucg).** Disorganized polymictic cobble-boulder conglomerate. Common rounded to subangular clasts of light grey recrystallized limestone and black mudstone-siltstone intraclasts. Lesser clasts with 40% 0.5-2 cm equant Pl and 15% 2-3 mm Aug crystals. Minor Aug-Pl-phyric and Pl-phyric clasts. Locally common clasts of equigranular (1-2 mm) Hbl diorite. Rare clasts of Qtz-rich very coarse-grained feldspathic arenite to granule conglomerate, and Qtz diorite clasts with 15% 3-4 mm Qtz eyes. Conglomerate commonly as m- to 100 m-scale blocks and lenses in disrupted bedded to laminated black argillite to dark grey siltstone and feldspathic wacke. Resistant, dark grey weathering. Conglomerate weathers in positive relief relative to enclosing finer grained rocks. Toarcian **Lower polymictic conglomerate (lJTlcg).** Polymictic conglomerate with clasts of limestone (up to 1 m), feldspar porphyry, granitic rock, chert, and argillite. Transitions laterally to black to dark grey shale-tuff beds. Overlain by green andesitic to coarse basaltic breccia, minor tuff, and rare pebble conglomerate (Gabrielse, 1998). Sinemurian	Whitehorse trough (SE panel)
Upper Triassic		Sinwa Fm	**Limestone (uTrS).** Massive limestone with smooth-shelled pelecypods and poorly preserved corals (Gabrielse, 1998). Moderately resistant, white to light grey weathering. Upper Norian	
Middle Jurassic	Bowser Lake Group		**Undivided (mJBL).** Shale, siltstone, tuffaceous shale, feldspathic wacke, breccia, and thick-bedded chert clast-bearing pebble to cobble conglomerate with clasts of green and red radiolarian chert, limestone with fusulinids, aphanitic to porphyritic volcanic rocks and cream-weathering volcanic rocks (Gabrielse, 1998) **Sandstone and conglomerate (mJBLs).** Interbedded calcareous (locally fossiliferous) sandstone, cross-bedded sandstone, and polymictic conglomerate containing mafic volcanic, Pl-phyric, hypabyssal, and pyritic clasts. Moderately resistant, brownish weathering **Chert clast-bearing conglomerate (mJBLcg).** Laminated to medium bedded granule to pebble conglomerate and sandstone. Clasts include abundant rounded 1-2 cm green chert, lesser maroon chert, and limestone. Locally up to 2% very fine-grained greenstone (?). Common Qtz grains. Minor light green laminated to medium bedded tuff and sandstone. Moderately recessive, greenish-grey weathering. Bajocian	Stikinia
Middle Jurassic	upper Hazelton Group	Horn Mountain Formation	**Upper mafic volcanic rocks (mJHMum); >650 m thick.** Aug-Pl-phyric volcanic breccias and flows. Breccia locally contains minor felsic clasts. Includes two thin polymictic conglomerate to breccia beds with Pl-phyric and grey siliceous clasts. Resistant, dark grey weathering **Upper felsic volcanic rocks (mJHMuf); 235 m thick.** Relatively well-stratified crystal tuff, fine tuff, and pyroclastic breccia of sparsely Pl-phyric clasts in a grey glassy groundmass, medium-dark grey aphanitic to glassy clasts and lesser Pl±Aug±Hbl-phyric clasts. Common bomb sags. Includes rare pebble conglomerate with well-rounded clasts, and calcareous sandstone (locally fossiliferous)	

Table 1. Continued.

Age	Unit		Description	Position
Lower-Middle Jurassic	upper Hazelton Group	Horn Mountain Formation	**Middle maroon volcanic rocks (lmJHMv); ≤3000 m thick.** Maroon, pinkish to rare green volcanic breccias and flows, minor pyroclastic rocks; upper volcaniclastic subunit. Maroon breccias are generally massive (locally medium to very thickly bedded ± graded) and contain varicoloured 0.5-5 cm Aug-Pl-phyric clasts, common maroon glassy (felsic?) clasts, local Aug microdiorite clasts, Pl-phyric clasts, rare flow-banded clasts, and very rare platy Pl-phyric clasts. Aug-Pl-phyric flows (pink; rarely green) and rare glassy felsic (?) flows (blood-red to maroon) transition to monomictic autoclastic breccias. Pyroclastic rocks include reddish-maroon laminated to medium bedded tuffs, crystal tuffs, and lapillistone, and at least one welded lapilli-tuff bed with sub-cm fiamme and lithic fragments. Resistant to moderately resistant, dark grey to maroon weathering, moderately to crudely stratified unit in outcrop, except east of the McBride River where it is distinctly thickly bedded. Upper subunit of recessive well-stratified maroon volcaniclastic sandstones and tuffs	Stikinia
			Lower mafic volcanic rocks (lmJHMlm); >1500 m thick. Massive monomictic volcanic breccia with Aug±Pl-phyric 5-10 cm clasts in a sand- to granule crystal matrix or cement; predominantly clast-supported. Rare tuffaceous sandstone interbeds. Very resistant; dark grey to green hackly weathering	
			Lower mafic volcanic rocks with felsic clasts (lmJHMlmf); 0-75 m thick. Similar to middle maroon volcanic rocks, but contains flow-banded Pl-phyric clasts, epidote-altered clasts, and fine-grained to aphyric off-white felsic clasts	
			Lower mafic volcanic rocks with epidote-altered clasts (lmJHMlme); 0-220 m thick. Massive volcanic breccia with epidote-altered clasts, Aug diorite clasts (15-20%, 2-3 mm Aug; 80-85%, 0.5-1 mm Pl) and moderately crystalline Aug-Pl-phyric clasts (15%, 2-3 mm Aug; 20-40%, 0.5-1 mm Pl). Resistant, dark green to green weathering	
			Lower volcaniclastic sandstone (lmJHMsv); 0-150 m thick. Laminated to thickly bedded volcaniclastic sandstone and siltstone. Recessive, brown weathering	
		Spatsizi Formation	**Volcaniclastic sandstone (lmJSPsv); 0-300 m thick.** Medium- to coarse-grained volcaniclastic sandstone with lesser siltstone and fine tuff laminae; subordinate horizons of Aug-phyric or (non-platy) Pl-phyric monomictic volcanic breccia. Well-stratified in outcrop, including prominent resistant horizon up to 100 m thick. Common soft-sediment deformation structures. Resistant, medium-dark brown weathering.	
			Argillite, siltstone and sandstone (lmJSPs); 560 m thick. Argillite, siliceous siltstone, and fine-grained sandstone with minor grey tuff laminae. Subordinate monomictic to polymictic volcanic breccia with Aug-Pl-phyric, Pl-phyric and platy Pl-phyric clasts; rare volcaniclastic sandstone. Mostly recessive, rusty orange-brown weathering. Yielded Early to Middle Jurassic detrital zircon populations (Iverson et al., 2012)	
			Felsic volcanic rocks (lmJSPf); 0-75 m thick. Monomictic clast-supported volcanic breccia with medium grey coarse platy Pl-phyric and pale grey aphyric, common vesicular felsic clasts. Resistant, medium grey weathering	
			Mafic volcanic rocks (lmJSPm); 0-60 m thick. Very thickly bedded Aug±Pl-phyric volcanic breccia. Resistant, dark grey-green weathering	
			Basal conglomerate (lmJSPcg); 140 m thick. Polymictic conglomerate containing aphyric felsic clasts, Aug-phyric clasts, plutonic clasts similar to subjacent Cake Hill pluton, and Qtz clasts. Qtz-rich feldspathic arenite, rare fossiliferous calcareous sandstone and siltstone. Subfeldspathic arenite (likely grus) unconformably overlies the Cake Hill pluton. Recessive, brown weathering. Contains Early Toarcian fossils (Henderson and Perry, 1981)	
Triassic	Stuhini Group		**Basaltic volcanic rocks (TrST).** Massive Aug- and lesser Aug-Pl-phyric flows, volcanic breccia, tuffaceous conglomerate, volcaniclastic sandstone and siltstone (Anderson, 1983; Gabrielse, 1998; van Straaten et al., 2012)	

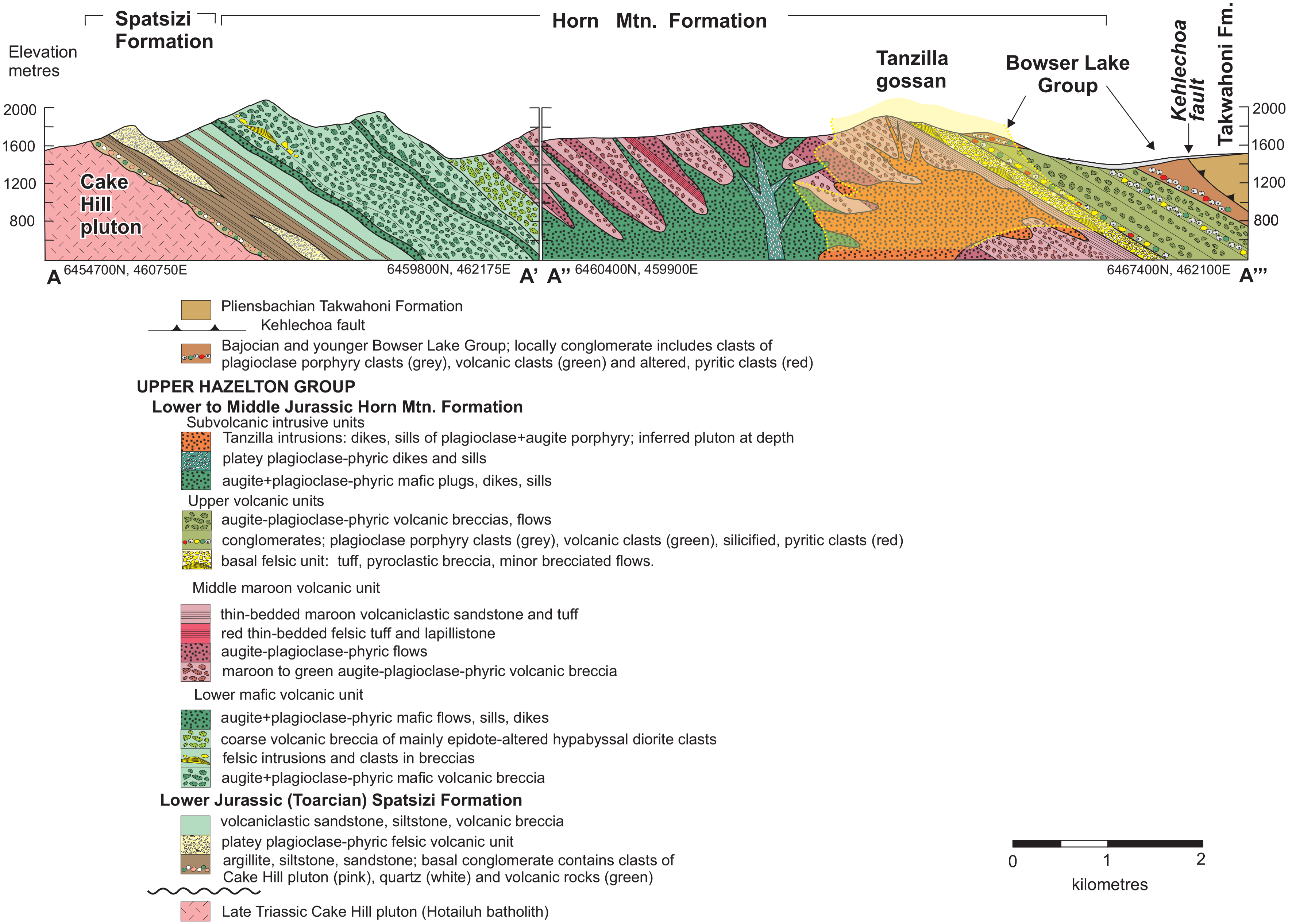

Fig. 4. South (A) to north (A''') cross-section northeast of the Tanzilla River. See Figure 3 for location.

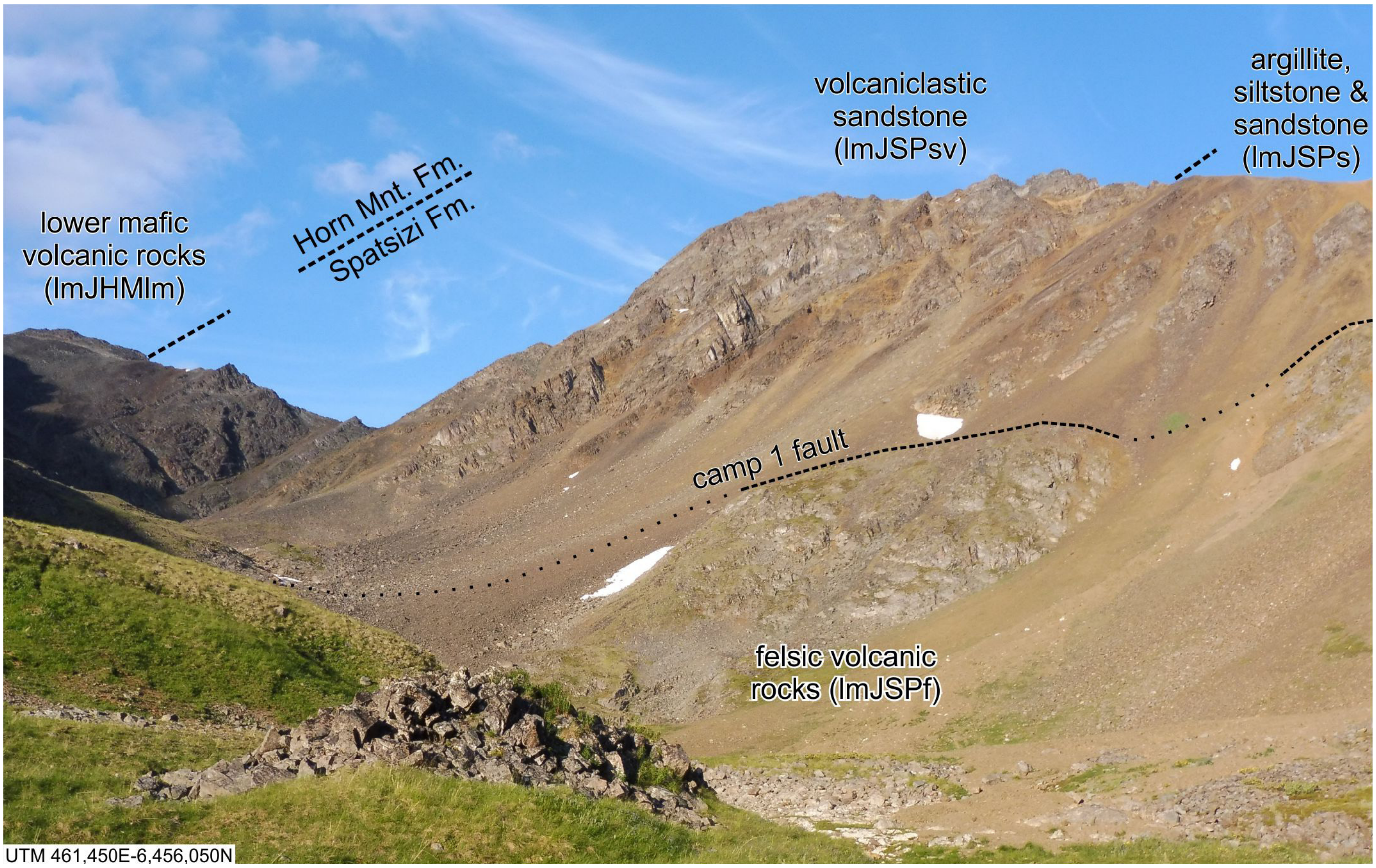

Fig. 5. Outcrop character of Spatsizi and lower Horn Mountain formations. In middle foreground is a ridge-forming felsic platy plagioclase porphyritic volcanic breccia (lmJSPf), part of the argillite, siltstone, and sandstone unit. Behind are recessive, orange-brown weathering rocks of the argillite, siltstone, and sandstone unit (lmJSPs,) and resistant rocks of the volcaniclastic sandstone unit (lmJSPsv). The section is capped by the lower mafic volcanic unit of the Horn Mountain Formation (lmJHMlm). View to the east.

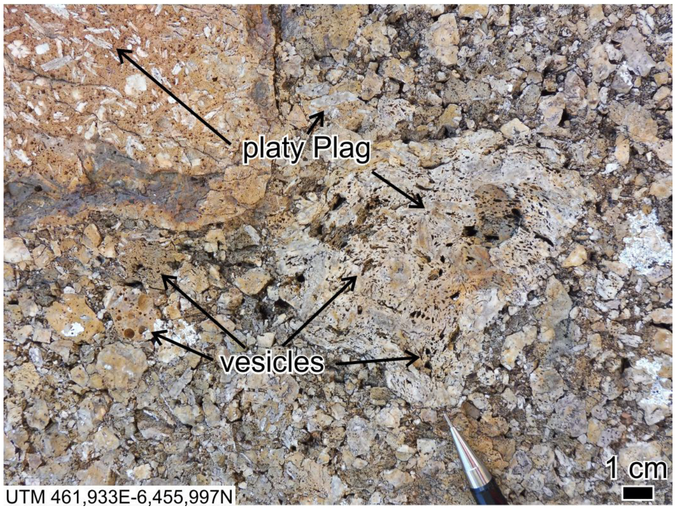

Fig. 6. Spatsizi Formation. Vesicular coarse platy plagioclase-phyric volcanic breccia subunit (lmJSPf) in the argillite, siltstone, and sandstone unit.

generally massive mafic augite±plagioclase-phyric clast-supported volcanic breccias (Fig. 7). It has a minimum thickness of 1.5 km. Its basal contact is considered gradational based on: 1) the common occurrence of augite-phyric volcanic breccia layers and augite-phyric sills in underlying Spatsizi Formation; and 2) a gradual increase in the size and proportion of volcanic debris upsection in the Spatsizi Formation. Two volumetrically minor but distinctive subunits are part of the lower mafic unit northeast of the Tanzilla River; one subunit contains common felsic clasts (Fig. 8), the other contains abundant augite microdiorite and epidote-altered clasts. Southwest of the Tanzilla River, the lower mafic volcanic unit interfingers with a volcaniclastic sandstone subunit.

The middle maroon volcanic rock unit, with an approximate maximum thickness of 3 km, overlies the lower unit of mafic volcanic rocks. The unit contains mainly maroon volcanic breccias, autobreccias, and flows, and includes minor laminated felsic tuffs to bedded lapillistone, and at least one welded lapilli tuff bed. The volcanic breccias and flows are predominantly augite-plagioclase-phyric, suggesting a mafic composition. However, maroon glassy clasts of presumed felsic composition are widespread (although volumetrically minor), and rare blood red to maroon glassy flows and autobreccias of inferred felsic composition were observed in the central part of the detailed map area, suggesting a significant felsic volcanic component. A subaerial origin is suggested by the presence of welded tuff and coherent flows and autobreccias. The contact between this

Table 2. Definition of the Horn Mountain Formation.

Horn Mountain Formation	
Category, rank	Lithostratigraphic unit with the rank of formation.
Name	Named for Horn Mountain, a prominent peak 7.5 km east of the type section.
Description of unit	Resistant dark green weathering massive augite±plagioclase-phyric trachybasalt to basaltic trachyandesite volcanic breccias. Generally overlain by crudely stratified maroon to dark green weathering volcanic breccias with augite±plagioclase-phyric trachybasalt to basaltic trachyandesite clasts and volumetrically lesser plagioclase-phyric and aphyric felsic clasts; rare maroon to red laminated to medium bedded tuff, lapillistone and volcaniclastic sandstone. At the type section, the maroon volcanic rocks are overlain by well-stratified tuff and plagioclase-phyric to aphyric trachyte to trachyandesite volcanic breccia. The volcanic succession is cut by texturally variable augite±plagioclase-phyric trachybasalt to basaltic trachyandesite plugs, sills and dikes. Areas of high intrusion densities (75-99%) cover up to several square kilometres. The intrusions are likely coeval with the lower and middle Horn Mountain volcanic rocks based on similar texture, mineralogy and lithogeochemistry, and a lack of crosscutting relationship with the upper Horn Mountain Formation. In regional studies, these intrusions could be included in the formation.
Geometry, thickness	The unit extends for at least ~50 km in a west to east-southeast trending belt north and northeast of the Hotailuh batholith. The unit is approximately 5.4 km thick at the type section.
Lower contact	Conformable and gradational contact above volcaniclastic sandstone of the Spatsizi Formation. Lower boundary defined where augite±plagioclase-phyric volcanic breccias and related volcanic rocks are more abundant (>50%) than volcaniclastic sandstone and related sedimentary strata (UTM 462,670E-6,456,520N).
Upper contact	At the type section the contact between strongly altered Horn Mountain volcanic rocks and Bowser Lake sedimentary rocks is covered for 100 m, but assumed to be unconformable (UTM 461,130E-6,464,820N). An unconformable contact between upper Horn Mountain mafic volcanic rocks and Bowser Lake conglomerates and sandstones is exposed at a reference section north of Grizzly lake (UTM 456,155E-6,465,355N). At a reference section east of the McBride River, we interpret the contact with overlying chert clast-bearing conglomerates of the Bowser Lake Group as conformable (UTM 493,040E-6,447,048N). Here, the boundary is defined where these conglomerates and related sedimentary strata are more abundant (>50%) than Horn Mountain volcanic rocks.
Age	Late Early Jurassic (Toarcian) to Middle Jurassic (Bajocian), possibly younger.

Coordinates are in UTM NAD 83 (zone 9 north)

unit and the lower mafic volcanic unit is separated by a covered interval of 55 m. In the eastern part of the detailed map area, the unit is cut by abundant (up to 75%) augite-plagioclase-phyric sills, and grades into the mafic intrusive complex discussed in Section 4.2. The uppermost part of this unit contains well-stratified volcaniclastic sandstones and tuffs. The middle maroon volcanic unit was also mapped east of the McBride River (Fig. 2), where it comprises predominantly thickly bedded maroon volcanic breccias with plagioclase-phyric, plagioclase-augite-phyric, aphyric and rare flow-banded clasts, and local flows (Fig. 9).

The upper felsic volcanic unit (about 235 metres thick) overlies the middle maroon volcanic unit. The unit consists mainly of aphanitic and plagioclase-phyric clasts of presumed felsic composition, and lesser plagioclase±augite±hornblende-phyric clasts. Common bomb sags are distributed along a strike length of 3.5 km, suggesting a subaerial pyroclastic origin. On the ridge two kilometres west of Silica ridge (see Fig. 3) the upper felsic volcanic unit contains a bed of pebble conglomerate and (locally fossiliferous) calcareous sandstone, suggesting local erosion and marine deposition.

The upper felsic volcanic unit is capped by the upper mafic volcanic unit, which is up to 650 metres thick. This unit is made up of augite-plagioclase-phyric volcanic breccias and flows, locally containing minor felsic clasts. The contact with the underlying felsic volcanic unit is gradational. On the northeastern spur of Silica ridge, a polymictic conglomerate to breccia contains plagioclase-phyric felsic clasts and grey siliceous clasts in a weakly altered matrix. The siliceous clasts appear to represent strongly silicified rock types derived from the underlying Silica ridge gossan (see Section 6).

The Horn Mountain Formation postdates widespread arc volcanism recorded in the lower part of the Hazelton Group. Volcanic rocks are rare in the upper part of the Hazelton Group. In northern Stikinia, the upper part of the Hazelton Group mainly consists of Pliensbachian and younger sedimentary rocks assigned to the Nilkitkwa and Smithers formations in the south, and the Spatsizi Formation in the north; both are

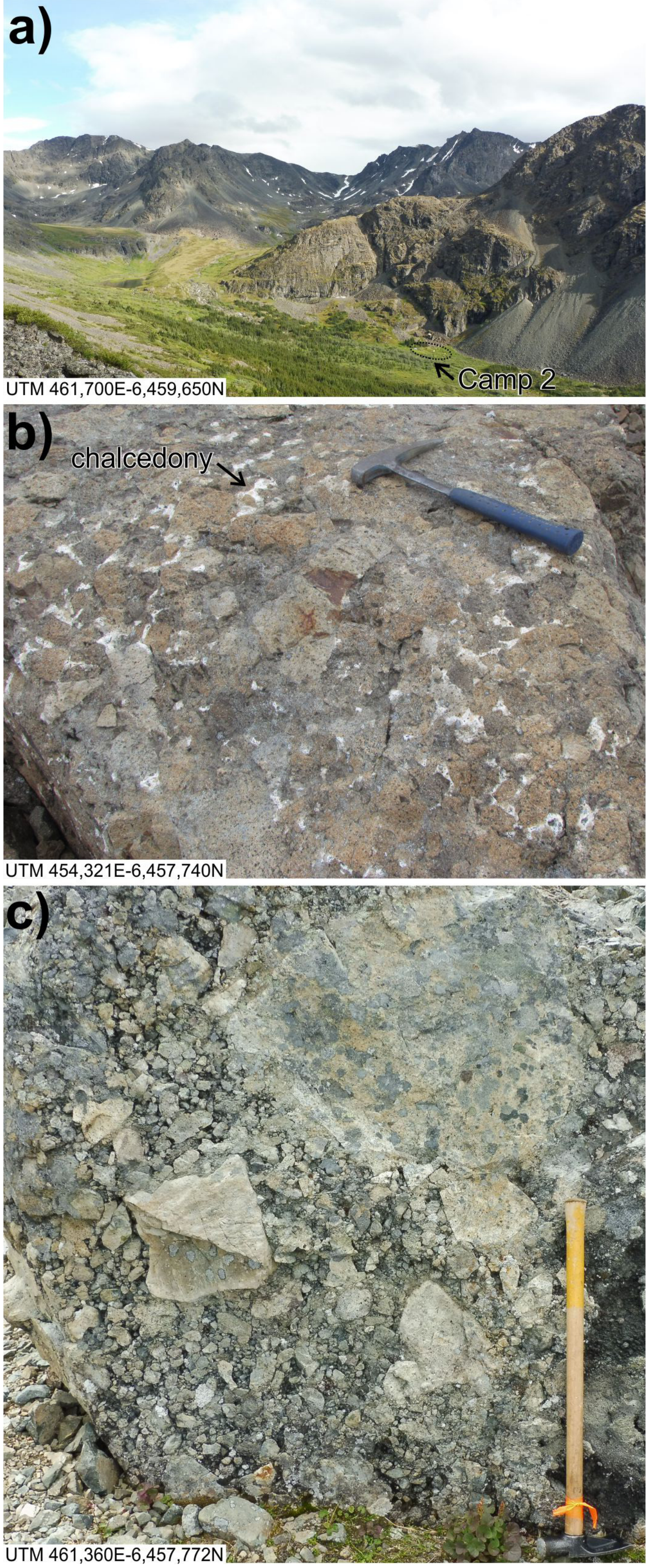

Fig. 7. Horn Mountain Formation, features of the lower mafic volcanic unit (lmJHMlm). **a)** resistant hackly weathering nature of this unit (looking southeast); **b)** chalcedony-cemented augite-phyric volcanic breccia; **c)** clast-supported augite-phyric volcanic breccia.

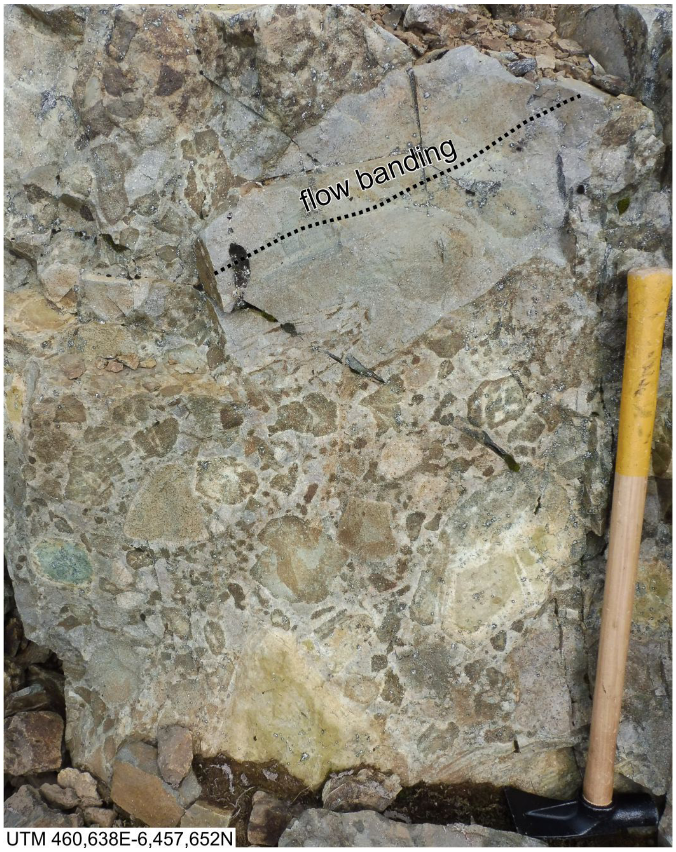

Fig. 8. Horn Mountain Formation, plagioclase-phyric and flow-banded clasts in felsic volcanic breccia subunit (lmJHMlmf). Note chilled margins and reaction rims on smaller clasts.

succeeded by the Quock Formation (Gagnon et al., 2012). Volcanic rocks are mainly in a narrow, north-south oriented belt of tholeiitic pillow basalts, sedimentary rocks, and minor rhyolites assigned to the Iskut River Formation (Gagnon et al., 2012; Barresi et al., 2015b). This Middle Jurassic (Aalenian to Bajocian) succession is interpreted to have formed in a series of sub-basins that define the Eskay rift (Fig. 1). The Iskut River Formation contrasts markedly with the Horn Mountain Formation in lithology, depositional style, structural setting (see Section 5), and lithogeochemistry (see Section 7). The Horn Mountain Formation represents a unique volcanic sequence in the upper part of the Hazelton Group. It is coeval with accretion of the Stikine and Cache Creek terranes, and so far, similar volcanic successions have not been documented elsewhere in northern Stikinia.

3.1.3. Bowser Lake Group (Middle Jurassic)

Sedimentary rocks of the Bowser Lake Group (Table 1) outcrop northeast of the Tanzilla River and east of the McBride River (Fig. 2). Northeast of the Tanzilla River, at Silica ridge (Fig. 3), basal Bowser Lake Group rocks overlie the Hazelton Group. This basal unit comprises interbedded calcareous (locally fossiliferous, including dm-scale ammonites) sandstone, cross-bedded sandstone, and polymictic conglomerate containing

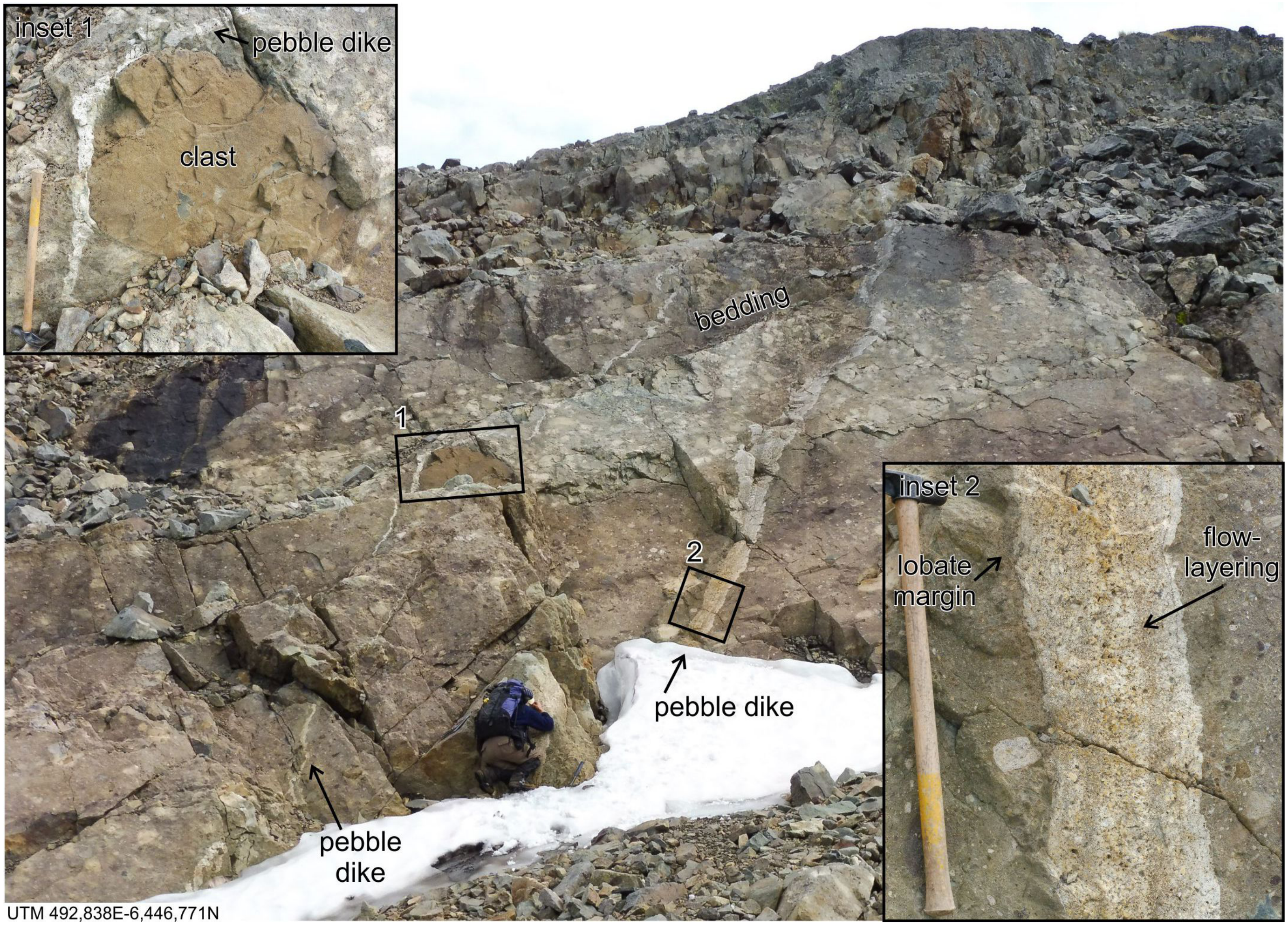

Fig. 9. Horn River Formation, maroon volcanic unit east of the McBride River. Thickly bedded maroon augite-plagioclase-phyric volcanic breccia (lmJHMv) cut by white chert clast-bearing pebble dikes, injected from postulated underlying Bowser Lake Group sediments. **Inset 1)** Close-up of thin pebble dike following large volcanic clast margin. **Inset 2)** Close-up of flow-layered pebble dike with irregular, locally lobate to flame-like, margins.

mafic clasts, plagioclase-phyric clasts and pyrite-altered clasts that appear to have been derived from erosion of Stikinia units. The unit is locally epidote-chlorite-pyrite altered and overlies strongly altered rocks (see Section 6). North of Grizzly lake, a basal pebble to cobble conglomerate directly overlies a mafic flow of the Horn Mountain upper mafic volcanic unit. At both locations, the base of the sedimentary unit and bedding within it dip shallowly to the north, suggesting a 10-15° discordance with the underlying volcanic rocks.

East of the McBride River, chert clast-bearing pebble to granule conglomerate and sandstone of the Bowser Lake Group are interpreted to interfinger with the maroon volcanic unit of the Horn Mountain Formation. The conglomerate contains abundant 1-2 cm green and lesser maroonish-red rounded chert clasts, local limestone clasts, and common quartz grains. In contrast to the Silica ridge section, the McBride River section appears to record an influx of exotic Cache Creek-derived chert clasts. A middle Bajocian age is suggested based on fossils collected from similar Bowser Lake Group units seven kilometres to the south-southeast (Gabrielse, 1998). Steeply east-northeast dipping chert clast-bearing pebble dikes, with dike wall-parallel flow layering, cut the uppermost maroon volcanic rocks (Fig. 9). The dikes display irregular, locally lobate to flame-like, contacts and commonly follow (rather than cut across) volcanic clast boundaries, suggesting that underlying Bowser Lake Group sediments injected into semiconsolidated maroon volcanic deposits. A scree-filled gully 10-15 metres east of the pebble dikes marks the contact between the maroon volcanic rocks and chert clast-bearing conglomerates, likely representing a steeply dipping north-trending minor fault. The lowermost chert clast-bearing conglomerate two metres east of the gully contains maroon volcanic clasts with similar shapes and textures as those in the maroon volcanic unit (Fig. 10). Based on these observations we interpret that the contact between the maroon volcanic rocks and chert clast-bearing conglomerates is conformable, and that the two lithologies interfinger. North to north-northeast trending faults and pebble dikes likely formed while the units were still

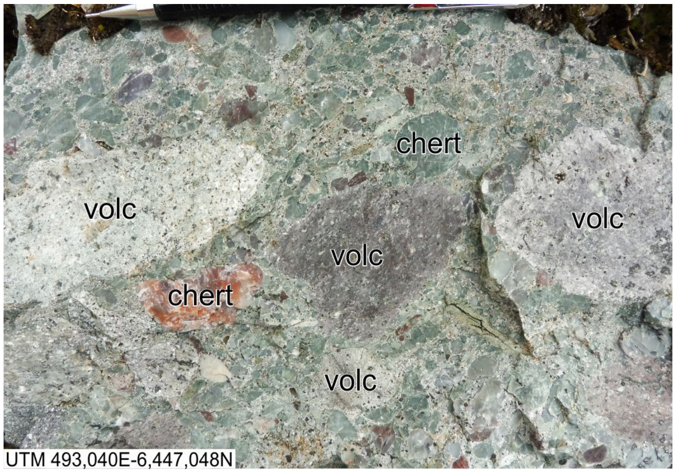

Fig. 10. Base of the Bowser Lake Group east of the McBride River (mJBLcg). Chert clast-bearing pebble conglomerate with green, lesser grey and reddish chert clasts, and maroon to grey volcanic clasts with similar shapes and textures as the underlying maroon volcanic unit.

poorly consolidated. Interbedded maroon volcanic rocks and chert clast-bearing conglomerates are described regionally in two areas to the southeast (see Section 9.1.).

3.2. Whitehorse trough

Between the Kehlechoa and King Salmon thrust faults, sedimentary rocks of the Takwahoni Formation (Laberge Group; Table 1) form a belt at least 90 km long and up to 10 km wide (Fig. 2). The belt represents one of the most southeasterly exposures of the Whitehorse trough (Fig. 1). It was previously interpreted to sit depositionally on undivided Triassic-Jurassic volcanic rocks (Gabrielse, 1998; now assigned to the Horn Mountain Formation), and is re-interpreted here as a sequence above the revised Kehlechoa thrust fault (see Section 5). Feldspathic wackes with Pliensbachian fossils (Gabrielse, 1998) predominate in a northern thrust panel (Fig. 2). A separate thrust panel between the McBride and Kehlechoa faults (east of the McBride River) contains Upper Triassic carbonate rocks overlain by a Lower Jurassic (Sinemurian to Toarcian) sedimentary succession (Fig. 2).

3.2.1. Northern thrust panel

A distinct unit of the Takwahoni Formation was observed north of Glacial Lake (north of the Kehlechoa fault) and east of the McBride River (north of the McBride fault; Fig. 2). The most common lithology at both locations is well-stratified, commonly quartz-bearing (5%), feldspathic wacke, siltstone, and argillite (Fig. 11). East of the McBride River, local monomictic cobble conglomerate with hornblende diorite clasts were observed close to the McBride fault. Numerous fossil collections date this succession as Pliensbachian (Gabrielse, 1998).

3.2.2. Southeastern thrust panel

East of the McBride River, a thrust panel between the McBride and Kehlechoa faults comprises a section of Upper Triassic limestone (Sinwa Formation) and Lower Jurassic sedimentary rocks of the Takwahoni Formation (Fig. 2). Sinwa Formation limestones, with late Norian conodont ages (Gabrielse, 1998), are unconformably overlain by a polymictic conglomerate unit with Sinemurian ammonites (lower polymictic conglomerate, Table 1; Gabrielse, 1998). According to Gabrielse (1998), the conglomerate contains limestone, feldspar porphyry, granitic, chert and argillite clasts. It interfingers with dark, fine-grained siliciclastic strata that also contain Sinemurian ammonites. These units were not investigated as part of this study.

The Sinemurian strata are overlain by laminated black argillite, siltstone and lesser volcaniclastic sandstone (argillite and siltstone unit, Table 1), which surrounds several ca. 1 km lenses of distinctive coarse conglomerate (Fig. 2; upper polymictic conglomerate, Table 1). Although separate, all of the polymictic conglomerate lenses contain similar clast populations (Table 1; Fig. 12). Coarse equant plagioclase-

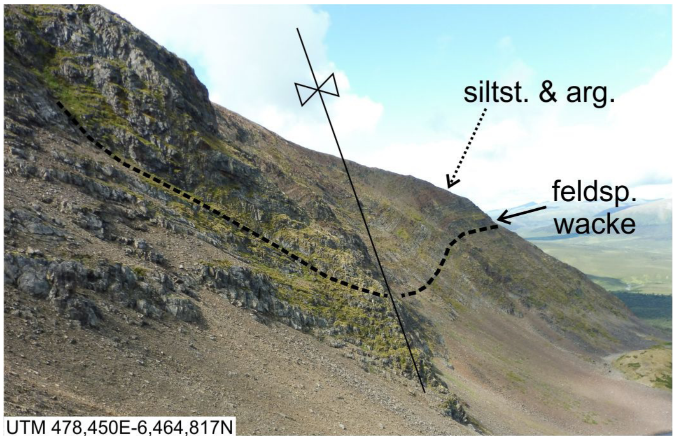

Fig. 11. Syncline in alternating Takwahoni siltstone, argillite (brown) and feldspathic wackes (medium grey), looking west-northwest down the fold axis; in hanging wall of Kehlechoa fault north of Glacial Lake (lJTgw).

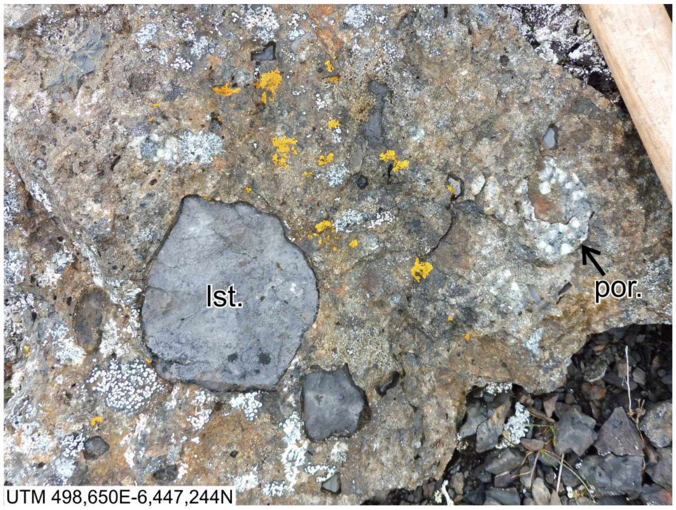

Fig. 12. Takwahoni Formation (Toarcian) polymictic conglomerate (lJTucg) with grey limestone clasts ('lst.') and distinctive coarse equant plagioclase porphyritic clasts ('por.'); east of the McBride River.

phyric clasts (Fig. 12) are a minor but recurring component, distinct from any other clast or igneous unit observed in this study. The conglomerate commonly forms metre to decimetre-scale blocks in disrupted bedded to laminated black argillite, dark grey siltstone, and feldspathic wacke. The irregularity of bedding in the fine-grained sedimentary rocks is likely due to soft-sediment deformation and subsequent tectonic deformation. Toarcian fossils were recovered from both rock units (Gabrielse, 1998).

3.3. Overlap units

3.3.1. Tuya Formation (Miocene to Pleistocene)

Regional aeromagnetic data (Aeroquest Airborne, 2012) show a distinct semi-circular break in a lineament interpreted herein as the Kehlechoa fault (see Section 5). This break might represent a Tuya Formation olivine basalt volcanic centre. Local exposures of olivine basalt have been documented in the region (Fig. 2; Gabrielse, 1998). Alternatively, the aeromagnetic anomaly might represent a post-kinematic intrusive body.

4. Intrusive units

Twelve intrusive units outcrop in the study area including two plutonic phases and a variety of hypabyssal to subvolcanic stocks, sills, and dikes (Table 3). Based on field, petrographic, and preliminary lithogeochemical and geochronological data (see Sections 7, 8) we divide the units into five phases: 1) the Cake Hill pluton (Late Triassic); 2) Early to Middle Jurassic subvolcanic intrusions; 3) Middle Jurassic dikes and stocks coeval with mineralization at Tanzilla; 4) rare dikes correlated with the Three Sisters plutonic suite (Middle Jurassic); and 5) the Snowdrift Creek pluton and associated dikes (Late Jurassic).

4.1. Cake Hill pluton (Late Triassic)

In the southeastern part of the detailed study area, the Cake Hill pluton, which is part of the extensive (2275 km^2) Hotailuh batholith, consists of hornblende quartz monzodiorite and granodiorite. The rocks have lower magnetic susceptibility values (5.9 ±4.0 x 10^3 SI units, average and one standard deviation of 10 measurements at one location) and a lower aeromagnetic response than the rest of the pluton (Aeroquest Airborne, 2012; van Straaten et al., 2012).

4.2. Early to Middle Jurassic subvolcanic intrusions

A mafic intrusive complex extends across an area of at least four by four kilometres in the northeastern part of the detailed map area (Fig. 3). It is made up of texturally variable augite-phyric basalts, augite microdiorite, microdiorite and rare volcanic breccia. Rocks of this complex texturally and compositionally resemble augite-phyric volcanic breccias of the Horn Mountain Formation, and form sills within it (Fig. 4). The complex likely represents a subvolcanic centre that fed Horn Mountain volcanism.

The augite-phyric mafic intrusive complex is cut by coarse platy plagioclase porphyry dikes and stocks that are only found in the northeastern part of the detailed map area. At one location, the porphyry contains diffusely bounded, lobate and flame-like projections of augite microdiorite (Fig. 13) and the microdiorite contains strings of coarse platy plagioclase crystals, suggesting magma mixing between these two phases.

A few felsic dikes and one intrusive felsic breccia occur within the lower mafic volcanic unit of the Horn Mountain Formation. They might represent subvolcanic feeders to the rare felsic volcanic breccias within this unit. Strongly silicified (and locally clay altered) cream to white flow-banded dikes with common ribbon quartz are found higher up in the stratigraphic sequence; they may represent feeder dikes of the Horn Mountain upper felsic volcanic unit.

4.3. Tanzilla intrusions (Middle Jurassic)

Abundant chlorite-epidote-altered plagioclase and augite-plagioclase porphyry dikes and stocks (Fig. 14) cut the Silica

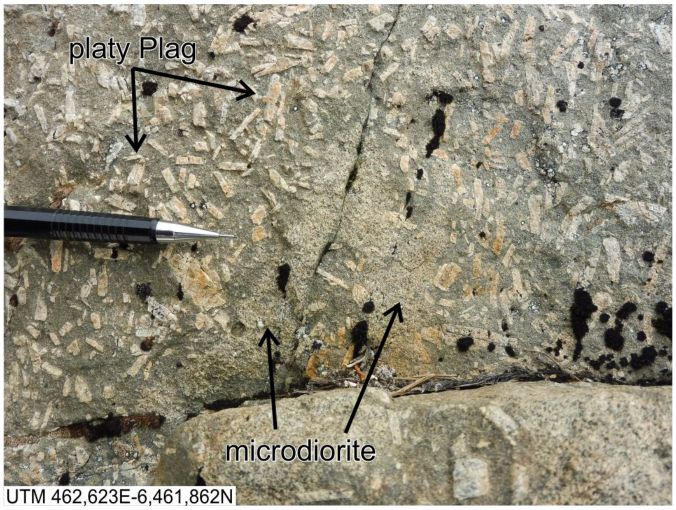

Fig. 13. Coarse platy plagioclase porphyry (EMJpp) with irregular microdiorite (EMJm) projections displaying diffuse boundaries, likely indicating magma mixing.

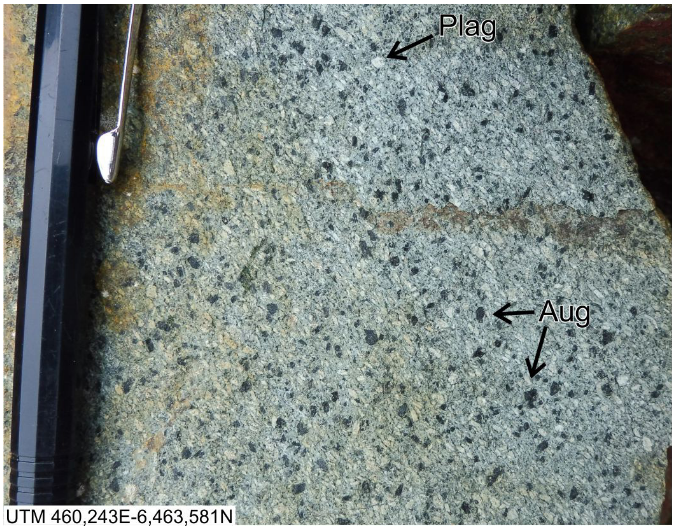

Fig. 14. Tanzilla phase (Middle Jurassic); augite-bearing plagioclase porphyry (MJp).

Table 3. Summary of intrusive units. Mineral abbreviations after Kretz (1983).

Age	Phase	Description	Timing relationships
Late Jurassic	Snowdrift Creek subalkaline	**Snowdrift Creek pluton (LJSC).** Medium-grained (3-4 mm) equigranular Bt-bearing Hbl to Hbl-bearing Bt granodiorite; rare Qtz diorite and tonalite (this study; Gabrielse, 1998). Contains mafic restite xenoliths, trace Mag, Ttn. Recessive to moderately resistant, grey weathering. Preliminary U-Pb zircon age of 160-161 Ma (R. Friedman, pers. comm., 2015)	Cuts Takwahoni greywacke unit, mafic intrusive complex. Interpreted to cut Horn Mountain Formation and Kehlechoa fault
		Hornblende diorite (LJd). Hbl diorite dikes and possible sills. Contains 1-6 mm (generally acicular) Hbl, equant 1-4 mm Pl, rare 2-3 mm Aug, local vesicles, very rare Kfs xenocrysts and Qtz eyes. Resistant, light grey to white weathering	Cuts Spatsizi argillite, siltstone & sandstone unit; Spatsizi felsic volcanic and volcaniclastic sandstone units; Horn Mountain lower mafic volcanic and middle maroon volcanic units. Post-hydrothermal. Follows faults
Middle Jurassic	Three Sisters subalkaline	**Feldspar porphyry (MJfp).** Fsp porphyry dikes with equant to stubby 2-4 mm Fsp phenocrysts set in very fine-grained groundmass. Resistant, commonly orange-pink weathering. Correlated with the Three Sisters – Tees Creek phase of van Straaten et al. (2012)	Cuts Horn Mountain lower mafic volcanic and middle maroon volcanic units; mafic intrusive complex
		Hornblende-bearing syenogranite (MJsg). Hbl-bearing syenogranite dikes (2% Hbl, 3% Mag) with white Pl phenocrysts (3 mm) set in sugary fine- to very fine-grained Qtz-Kfs-rich groundmass. Only observed at one location. Correlated with the Three Sisters – potassic phase of van Straaten et al. (2012)	Cuts Horn Mountain lower mafic volcanic unit
	Tanzilla subalkaline	**Augite quartz diorite (MJd).** Medium-grained equigranular Aug Qtz diorite (and diorite?)	Cuts Horn Mountain middle maroon volcanic and upper felsic volcanic units; Pl porphyry (MJp). Syn-hydrothermal
		Augite-bearing plagioclase porphyry (MJp). Aug-bearing Pl porphyry dikes and stocks with tabular to equant 1-4 mm Pl, 3-5% Aug, minor Mag. Preliminary U-Pb zircon age of 173.25±0.13 Ma (this study)	Interpreted to cut Horn Mountain middle maroon volcanic and upper felsic volcanic units. Syn-hydrothermal
Early-Middle Jurassic	Spatsizi & Horn Mountain alkaline	**Felsic intrusive (EMJf).** Felsic dikes with common dike margin-parallel flow bands and wispy Qtz ribbons. Locally includes m-wide tabular to 100 m-wide bulbous bodies of intrusive breccia containing angular to amoeboid Pl-phyric (20%, 1-2 mm) clasts, some flow-banded autoclasts and rare Aug-Pl-phyric clasts	Cuts Horn Mountain lower mafic volcanic unit; mafic volcanic complex
		Hornblende-bearing plagioclase porphyry (EMJh). Sparse Pl (lath-like to slightly platy) porphyry dikes, locally with minor Hbl, trace Mag. Only observed at two locations	Cuts Horn Mountain middle maroon volcanic unit with indistinct irregular contacts
		Hornblende monzonite (EMJmz). Kfs-Hbl-Pl-phyric monzonite dikes with minor Mag. Only observed at two locations	Cuts mafic intrusive complex
		Platy plagioclase porphyry (EMJpp). Pl-phyric porphyry dikes and stocks with coarse Pl plates (1-3 cm, approximately 5:4:1 aspect ratio) set in a dark green to black aphanitic groundmass. Magnetic to highly magnetic	Cuts mafic intrusive complex, locally with gradational contacts
		Mafic intrusive (EMJm). Variably textured Aug-Pl-phyric intrusive rocks. Generally Aug-phyric (15%, 2-5 mm, locally up to 10 mm), locally comprising well-crystallized Aug microdiorite and microdiorite with up to 85% 0.5-1 mm Pl. Locally amygdaloidal. 1 to 50 m-wide planar to bulbous sills, dikes and intrusive bodies. Resistant, dark grey to green weathering	Cuts Spatsizi argillite, siltstone & sandstone unit; Spatsizi volcaniclastic sandstone unit; Horn Mountain lower mafic volcanic and middle maroon volcanic units
Late Triassic	Stikine subalkaline	**Cake Hill pluton (LTrCH).** Medium- to locally coarse-grained equigranular Hbl Qtz monzodiorite, granodiorite (this study) to Qtz monzonite (van Straaten et al., 2012) containing accessory Ttn. Resistant, blocky, light-medium grey weathering. U-Pb zircon ages of 221±3 Ma, 218.2±1.3 Ma (Anderson and Bevier, 1992; van Straaten et al., 2012)	Unconformably overlain by Spatsizi basal conglomerate unit

ridge gossan. In drill core, a plagioclase (-augite?) porphyry hosts anhydrite-pyrite±chalcopyrite veins. This porphyry returned a preliminary U-Pb zircon age of ca. 173 Ma (see Section 8). Texturally and compositionally the porphyry in drill core resembles the dikes that are exposed on Silica ridge. The intrusions lack the pervasive clay alteration of their wall rocks. They are interpreted as syn-hydrothermal, as they cut (advanced) argillic alteration, and host porphyry-style alteration (see Section 6).

A few medium-grained equigranular augite quartz diorite intrusive bodies are found near Silica ridge (Fig. 15). Texturally similar medium-grained equigranular diorite was intersected in drill core (Section 6). It cuts the plagioclase porphyry described above, and appears to be coeval with porphyry-style hydrothermal alteration (see Section 6).

4.4. Three Sisters intrusions (Middle Jurassic)

Pink feldspar porphyry dikes are locally found in the northern half of the map area. They are tentatively correlated with similar feldspar porphyries described in the Gnat Pass area (Tees Creek intrusive, Three Sisters plutonic suite of van Straaten et al., 2012).

4.5. Snowdrift Creek intrusions (Late Jurassic)

One of the youngest intrusive phases in the area is the Snowdrift Creek pluton, a northwesterly elongate mostly recessive granodiorite, quartz diorite to tonalite body underlying an area of about 100 km^2 (Figs. 2, 3). The pluton hornfelses the mafic intrusive complex and feldspathic wackes of the Takwahoni Formation. The pluton is also interpreted to cut the Kehlechoa fault, which places Takwahoni Formation against Horn Mountain Formation and coeval subvolcanic intrusions. The oldest K-Ar hornblende age on the Snowdrift Creek pluton is 160.8 ±2.5 Ma (Stevens et al., 1982; Hunt and Roddick, 1987). A sample collected for U-Pb zircon analysis returned a preliminary 160-161 Ma age (R. Friedman, pers. comm., 2015).

Hornblende and plagioclase porphyritic diorite dikes and rare sills are found throughout the map area. In them, sizes, shapes and abundance of phenocrysts vary considerably, but acicular hornblende is common (Fig. 16). These intrusions locally follow north-northeast trending faults that cut the Horn Mountain Formation. An unaltered acicular hornblende-phyric diorite dike of this suite cuts the Silica ridge gossan and the plagioclase porphyry.

5. Structure

The structural pattern in the detailed study area is relatively simple, with most bedding in the Spatsizi Formation and Horn Mountain Formation showing right-way-up, uniform moderate northerly dips (Figs. 3, 4). Local variations in bedding attitude are likely related to faulting and/or paleoslopes in a volcanic edifice. The homoclinal Hazelton Group appears to be unconformably overlain by right-way-up, more shallowly north-dipping strata of the Bowser Lake Group (Figs. 3, 4).

Fig. 15. Tanzilla phase (Middle Jurassic); medium-grained equigranular augite quartz diorite (MJd).

Fig. 16. Snowdrift Creek phase (Late Jurassic); acicular hornblende and plagioclase porphyritic dike (LJd).

The Takwahoni feldspathic wacke sequence in the hanging wall of the Kehlechoa fault north of Glacial Lake shows upright open folds with wavelengths of at least 600 metres and subhorizontal west-northwest to northwest plunging fold axes (Fig. 11). Limited cleavage-bedding measurements indicate southwesterly fold vergence.

East of the McBride River the Horn Mountain Formation and overlying Bowser Lake conglomerates show subhorizontal to gentle easterly dips. The Takwahoni units in the hanging wall of the Kehlechoa fault are strongly deformed and sheared. Erratic bedding and cleavage attitudes reflect disharmonic folding and competency contrasts between the conglomerate lenses and surrounding argillites.

5.1. Regional fault systems

Faults and lineaments in the study area comprise two sets. The older set comprises northwest-striking dextral faults and north-northeast to northeast striking normal faults that cut the Hazelton Group and older units of Stikinia. Younger, generally west to northwest striking thrust faults (including the King

Salmon, Kehlechoa and McBride faults), juxtapose the Cache Creek terrane to the north with Whitehorse trough strata and, in turn, Stikinia. They also appear to truncate faults of the older set.

5.1.1. Early dextral and normal faults

A major fault is inferred under Quaternary cover along the valley of the upper Tanzilla River (Figs. 2, 3). The informally named Tanzilla River fault shows about two kilometres of apparent right-lateral offset of the basal unconformity, the largest apparent offset of any early structure in the area. It is projected to join a previously-mapped regional north-northwest trending fault that offsets the Cake Hill pluton and Three Sisters pluton (Gabrielse, 1998; van Straaten et al., 2012; Fig. 2). The fault coincides with a northwest-trending aeromagnetic lineament along the upper Tanzilla River.

A parallel structure to the southwest shows an apparent 750 metre right-lateral offset of the basal unconformity (southwest corner of Fig. 3; Bowen, 2013). A third northwest-striking fault is in the valley of a west-flowing northern tributary of the Tanzilla River (near section A-A', southeast corner of Fig. 3). Slickenfibres on this fault indicate dip-slip, north-side-down movement; those along a subsidiary fault indicate dextral movement. The main fault shows an apparent 580 m right-lateral offset of the felsic volcanic breccia subunit and an inferred decrease in offset towards the northwest (Fig. 3).

Several northeast to north-northeast striking faults have been recognized in the study area. The informally named Camp 1 fault shows an apparent 320 m dextral offset of the basal unconformity. Distant visual observations show only a minor offset of the Spatsizi-Horn Mountain contact, suggesting that that the structure may have been a growth fault with an east side-down movement. A parallel fault 400 m to the west shows only minor offset. Farther north the Camp 1 fault continues as a well-defined lineament that is spatially associated with orange-brown iron-carbonate altered rocks with a well-defined spaced fracture cleavage. A fault immediately west of an unnamed 2096 m high peak (Fig. 3) shows an apparent 230 m dextral offset of the Spatsizi-Horn Mountain contact and underlying basal unconformable contact, and based on the similar orientation is interpreted as an east-side-down normal fault. In the east, the Snowdrift Creek fault along the identically named creek, forms a pronounced lineament and orange-brown altered shear zone. A similarly oriented northeast-trending fault, inferred to occupy the valley east of Silica ridge, appears to define the western boundary of the mafic intrusive complex, and the eastern boundary of widespread alteration at the Silica ridge gossan. Based on the apparent thickening of the maroon volcanic unit to the west, a penecontemporaneous west-side-down movement is inferred. A parallel fault aligns with a northeast trend of orange-brown altered recessive saddles in three ridges west and southwest of Silica ridge (Fig. 17). The fault appears to coincide with the abrupt eastern end of the West gossan, and the westernmost extent of the Silica ridge gossan. A tentative east-side-down normal movement is inferred.

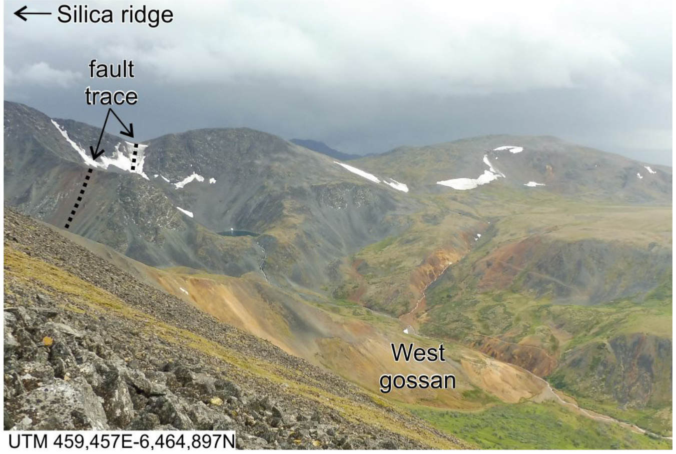

Fig. 17. West gossan looking towards the southwest. The fault west of Silica ridge cuts crudely stratified Horn Mountain Formation maroon volcanic unit (lmJHMv) in the background of the photo.

The normal movement on the north-northeasterly faults is consistent with east-west extension. Their linkage to the west-northwesterly dextral faults suggests that the north-northeasterly faults represent the extension direction in a regime of dextral simple shear in a west-northwest to east-southeast direction.

5.1.2. Late thrust faults

Regional southwest-vergent thrust faults transect the mapped area (Fig. 2; Gabrielse, 1998). They formed in a regime of north-south to north-northeast to south-southwest shortening during accretion of the Quesnel, Cache Creek, and Stikine terranes (Mihalynuk et al., 2004). The King Salmon fault is the master fault that emplaces rocks of the Cache Creek terrane above Stikinia.

The Kehlechoa fault was first recognized by Gabrielse (1998) as a major southerly splay that joins the King Salmon fault 20 km east of the mapped area (Fig. 1). It carries a sequence of Upper Triassic limestones of the Sinwa Formation and Jurassic (Sinemurian to Toarcian) rocks of the Takwahoni Formation in its hanging wall, above younger (Bajocian) rocks of the Bowser Lake Group in its footwall. According to Gabrielse (1998), the western end of the Kehlechoa fault departs from the base of the Takwahoni Formation and loses its definition in the volcanic package near the McBride River. Our interpretation differs from Gabrielse (1998). We recognize a north-striking and steeply to gently east-dipping fault, exposed at several locations on the ridge east of the McBride River. The structure separates sedimentary rocks of the Whitehorse trough (hanging wall) from Stikinia rocks (footwall). Hanging wall fine-grained sedimentary rocks and polymictic conglomerates (Toarcian) are in structural contact with Bowser Lake chert clast-bearing conglomerates (Bajocian) and underlying gently dipping maroon Horn Mountain volcanic rocks. The structure is commonly cut by north-trending, post-kinematic dikes, and is interpreted as a thrust or reverse fault. Its north-south orientation marks a strong departure from the general west-northwest strike of the Kehlechoa fault. It may be a tear fault or lateral ramp.

Previous structural interpretations for the area east of the McBride River included three to five north-dipping thrust panels composed of a variety of Takwahoni sedimentary sequences that are in turn thrust above Bowser Lake sedimentary rocks (Gabrielse, 1998). We propose a simpler explanation that invokes two structural panels. The lower panel includes a stratigraphic succession of Norian limestone, Sinemurian clastic rocks, and a Toarcian unit of mainly argillite and siltstone that contains discrete lenses and blocks of conglomerate. No Pliensbachian faunas have been recovered from this sequence (Gabrielse, 1998). The upper thrust panel contains extensive Pliensbachian feldspathic wackes interbedded with argillite, siltstone, and local conglomerate. The two panels are separated by the McBride River fault, which outcrops on a ridge 4.5 km east of the McBride River. There, it juxtaposes Pliensbachian Takwahoni monomictic conglomerates and underlying Toarcian Takwahoni polymictic conglomerates across a steeply-dipping zone of strongly sheared argillites. The McBride River fault is inferred to join the main Kehlechoa fault between the mapped area and the McBride River (Fig. 2).

Farther west, we infer that the Kehlechoa fault follows the base of the Pliensbachian Takwahoni unit, changing back to a west-northwesterly orientation as it crosses the McBride River. Previously, the contact between the Takwahoni Formation and the structurally underlying and assumed older volcanic rocks was mapped as a depositional contact (Gabrielse, 1998). We interpret this contact as a south-directed thrust fault separating strata of the Whitehorse through from Hazelton and Bowser Lake Group strata based on: 1) the juxtaposition of older rocks (Pliensbachian; Gabrielse, 1998) above younger rocks (Iverson et al., 2012; this study); 2) the presence of a well-developed aeromagnetic lineament (Aeroquest Airborne, 2012) in a wide overburden-filled valley; 3) an orientation that is similar to the King Salmon fault, approximately five kilometres to the north; and 4) the juxtaposition of homoclinal strata against folded Takwahoni units.

Importantly, the Kehlechoa fault is cut by the Snowdrift Creek pluton. The preliminary age on this intrusive body (see Section 8) suggests that shortening related to accretion of Stikinia to the Cache Creek and more inboard terranes was before early Late Jurassic.

In the detailed study area, a west-northwest striking, steeply northeast-dipping ductile shear zone is exposed (northeast corner of Fig. 3). The informally named Gopher shear zone is at least 275 m wide and consists of strongly altered quartz-sericite-clay schist (see Section 6 for details). Strong flattening fabrics parallel the shear zone. The schist contains local porphyroclasts, weakly developed down dip mineral lineations (this study) and northwest-plunging oblique stretched quartz lineations (Luckman et al., 2013). Although kinematic indicators were not observed, a reverse (to reverse oblique) shear sense is inferred based on: 1) a roughly similar orientation as regional-scale thrust faults; 2) its crosscutting relationship with respect to the alteration system at Tanzilla; and 3) the orientation of mineral lineations. This structure is interpreted as a minor shear synthetic with the King Salmon-Kehlechoa thrust system, developed preferentially in a zone of strong alteration. It has no apparent expression west of the valley that separates it from the Silica ridge gossan.

6. The Tanzilla prospect

The Tanzilla gossan, which includes quartz, sericite, clay and/or pyrite alteration, extends along strike for over five kilometres in the northern part of the detailed study area. The gossan includes the main Silica ridge (Fig. 18), the West gossan (Fig. 17) and the Gopher zone (Fig. 3). The earliest documented exploration in the Tanzilla area took place from 1965 to 1976, following discovery of porphyry copper mineralization at Gnat Pass in the early 1960s. The earliest reported activities at Tanzilla included geochemical sampling, geophysical surveys, trenching and diamond drilling, apparently aimed at testing the potential for porphyry copper-molybdenum mineralization (Dolmage, Campbell & Associates Ltd., 1971; Fominoff and Crosby, 1971; Smee, 1971; Stevenson, 1973; BC Department of Mines and Petroleum Resources, 1974, p. 511; Clouthier and Vyselaar, 1975; Schroeter, 1977; British Columbia Geological Survey, 2015). Results from the trenching and drilling were never reported. The property was explored intermittently during the 1980s and 1990s, including geochemical and geological work by Akiko-Lori that focussed on the potential for volcanogenic massive sulphide mineralization (Baker, 1992). More recent exploration interpreted Tanzilla as a high-sulphidation epithermal system, based on the extensive silicification, pyritization and localized argillic and advanced argillic alteration (Travis, 2004; Holbek, 2006; 2008). The Tanzilla property was acquired by West Cirque Resources Ltd. in 2011. West Cirque (now Kaizen Discovery Inc.), in partnership with Freeport-McMoRan Corporation of Canada Limited, carried out a geophysical survey and a Terraspec alteration mineral study. The Terraspec-aided field study confirmed the

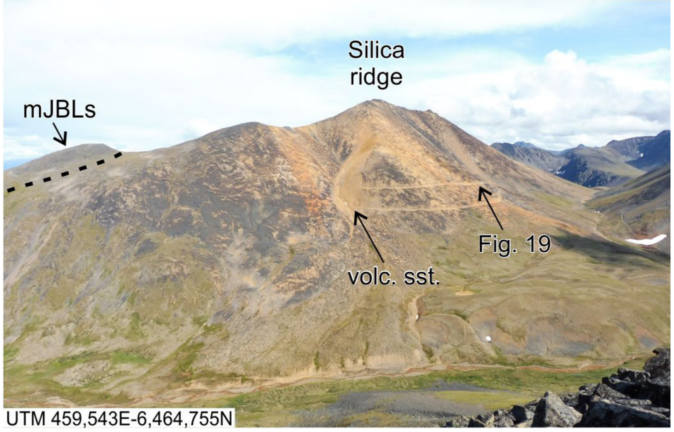

Fig. 18. West side of Silica ridge. Unconformably overlying Bowser Lake sedimentary rocks (mJBLs) are exposed in the far north. Location of Figure 19 indicated, as well as the location where abundant scree of well-stratified volcaniclastic sandstone (‘volc. sst.’, lmJHMv) was observed.

presence of advanced argillic alteration with an assemblage of alunite, pyrophyllite and topaz at the northern part of Silica ridge, and pyrophyllite±topaz at the Gopher zone (Luckman et al., 2013; Fig. 3). Phyllic (quartz-sericite-pyrite), argillic (illite-chlorite-smectite), and intermediate argillic (kaolinite-dickite) alteration assemblages are common throughout the remainder of the Tanzilla gossan. The geophysical and Terraspec study were followed by diamond drilling in 2014 and 2015 (Barresi et al., 2014; Barresi and Luckman, 2015). The goal of the drilling was to test for porphyry-style alteration and mineralization below the strongly altered advanced argillic lithocap exposed at the surface (Barresi et al., 2014).

Field observations made as part of this study focused on establishing protoliths throughout the Tanzilla gossan, and constraining the relationship between alteration, mineralization, and intrusive activity. At Silica ridge, common strong silicification and widespread quartz-clay-pyrite alteration are generally texturally destructive. However, on the northeast ridge, flow-banded rhyolite and rhyolite breccias, and local laminated rocks were observed. On the northwest ridge, local exposures of texturally-intact volcanic breccias were found. We consider these rocks as part of the Horn Mountain Formation upper felsic volcanic unit (Table 1). In the gully northwest of the summit, angular scree of well-stratified volcaniclastic sandstone was observed, similar to the uppermost volcaniclastic interval of the Horn Mountain Formation maroon volcanic unit (see Section 3.1.2.; Fig. 18). On the lower scree slopes west-southwest of the summit, angular blocks of locally layered and felsic flow-banded clast-bearing volcanic breccias were found. The volcanic breccias are themselves hydrothermally brecciated, with angular clasts displaying jigsaw-fit textures set in a dark grey siliceous matrix (Fig. 19). These volcanic breccias are tentatively interpreted as a felsic bed in the Horn Mountain maroon volcanic unit. The Silica ridge alteration system is locally cut by plagioclase and augite-plagioclase porphyries. Based on drill core and surface observations we interpret these porphyries as syn-hydrothermal. In drill core, the porphyries: 1) lack the (advanced) argillic alteration of overlying volcanic rocks; 2) are chlorite-sericite-pyrite, albite to biotite-magnetite altered, and host stockwork veins and hydrothermal breccias; and 3) are cut by a diorite spatially associated with the strongest porphyry-style alteration. At surface exposures, the porphyry dikes lack the intense (advanced) argillic alteration of the surrounding wall rocks, and are chlorite-epidote altered.

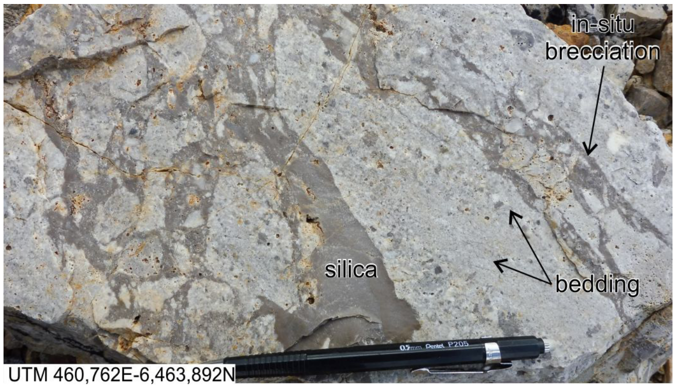

Fig. 19. Faintly bedded felsic volcanic breccias (lmJHMv?) cut by medium-dark grey silica-cemented jigsaw-fit hydrothermal breccia.

The Silica ridge alteration system is overlain in the north by weakly altered to unaltered rock types. On the northeast spur, the Horn Mountain upper mafic volcanic unit marks an abrupt change from strong quartz-clay-pyrite alteration in predominantly texturally destructive altered rocks to overlying essentially unaltered augite-phyric flows. The contact occurs in a talus-covered zone approximately 5 m wide. Slightly higher in the stratigraphy, a polymictic conglomerate to breccia contains plagioclase-phyric felsic clasts and grey siliceous clasts in a weakly altered matrix. The siliceous clasts likely represent strongly silicified rock types derived from the underlying Silica ridge gossan. Mafic volcanic rocks of the upper unit exposed along the creek west of Silica ridge are gossanous and altered. This suggests that, at least locally, the basal part of this unit was deposited before (or during) the main hydrothermal event, or during its waning stages. On the northwest spur, conglomerate and sandstone of the Bowser Lake Group overlie strongly altered rocks; the unit is locally epidote-chlorite-pyrite altered, contains abundant hypabyssal clasts and a few pyritic clasts. An angular discordance suggests an unconformable contact (see Section 3.1.3.). The upper mafic volcanic unit was not observed in this location, either as a result of non-deposition or erosion. The Bowser Lake sedimentary unit appears to have been deposited during the waning stages of the hydrothermal event.

The Gopher zone, 2.5 km east-southeast of Silica ridge, trends northwest and is at least 275 m wide (Fig. 3). It consists of strongly sheared silicified rocks and quartz-sericite-clay schists. Blueish lazulite, an anhydrous phosphate mineral, is commonly observed. Drill core (hole TZ15-02, Barresi and Luckman, 2015) and field observations show that the main protolith at the Gopher zone is a variably sheared and altered coarse platy plagioclase porphyry. Strong flattening fabrics in phyllic-altered rocks parallel the borders of the zone. The zone probably formed during post-alteration reverse shearing.

The West gossan is in a valley system 2.7 km west of Silica ridge (Fig. 17). The area is predominantly quartz-sericite-pyrite altered. Beyond the southern edge of the gossan, the alteration changes to chlorite-epidote (propylitic) assemblages. Protoliths in the gossan are difficult to establish due to texturally destructive alteration. However, beyond the southern edge of the gossan a 120 m wide zone of propylitic chlorite-epidote alteration was observed in green altered volcanic breccias that show identical textures, and grade into, the Horn Mountain maroon volcanic unit farther south.

Two north-northeast trending faults on either side of Silica ridge (see Section 5.1., Figs. 3, 17) appear to coincide with significant changes in the distribution and/or style of alteration at the Tanzilla gossan. At the eastern end of the West gossan, quartz-silica-pyrite alteration and unaltered maroon volcanic rocks are separated by a 50 m wide covered area that lines up with a well-developed lineament marked by orange-brown recessive notches on several ridges. Farther north, the lineament appears to form the western end of the Silica ridge alteration system. A second fault is inferred within the valley east of the Silica ridge alteration system. The fault separates the areally extensive Silica ridge gossan from the linear, and much more areally restricted, Gopher zone alteration. In addition, the fault marks the approximate western end of the Early to Middle Jurassic mafic intrusive complex (Table 3).

Observations from diamond-drill hole TZ15-01 (this study; Barresi and Luckman, 2015), drilled on the northern flanks of Silica ridge, are summarized in Figure 20a. The drill hole first intersects strongly texturally destructive intermediate to advanced argillic alteration that grades down to slightly less intense quartz-clay altered felsic volcanic breccias (Fig. 20b), and then a chlorite-pyrite to chlorite-sericite-pyrite altered plagioclase porphyry intrusion. Petrographic observations show that the chlorite-(sericite-)pyrite altered porphyry contains significant biotite hornfels overprinted by hydrothermal sericite (see Section 7.3). The alteration intensity in the porphyry locally increases in a zone of albite-altered quartz-anhydrite-pyrite±chalcopyrite stockwork (Fig. 20c), before grading back into chlorite-pyrite alteration. The alteration in the plagioclase porphyry transitions downward into albite (Fig. 20e) and then potassic alteration assemblages generally associated with areas of more intense hydrothermal brecciation and a coarser-grained dioritic intrusive phase (Fig. 20f). The plagioclase porphyry was sampled for U-Pb zircon geochronology, and an anhydrite-pyrite-molybdenite vein (Fig. 20d) was sampled for Re-Os geochronology (see Section 8). Assay results indicate anomalous copper and molybdenum values in the top and central portion of the drill hole (Fig. 20a; Kaizen Discovery Inc., 2015).

In summary, the relatively broad advanced argillic lithocap at Silica ridge is hosted at the contact between the middle maroon volcanic unit and the upper felsic volcanic unit of the Horn Mountain Formation. The lithocap and volcanic host rocks are cut by plagioclase porphyry and equigranular diorite intrusions displaying porphyry-style alteration and local chalcopyrite mineralization at depth. The Horn Mountain upper mafic volcanic unit and discordantly overlying Bowser Lake sandstone and conglomerate unit were deposited during the waning stages of, and following, hydrothermal activity. A relatively narrow band of advanced argillic alteration at the Gopher zone (east of Silica ridge; Fig. 3) is hosted in a platy plagioclase porphyry intrusion, which was emplaced in the mafic subvolcanic intrusive complex. Post-hydrothermal shearing has significantly affected the Gopher zone.

7. Petrology and lithogeochemistry

In this section we present observations of 28 petrographic thin sections and summarize the preliminary results from 27 lithogeochemistry samples. Full analytical results, trace element plots and further interpretations will be provided in a later publication. With a few exceptions, samples were taken from representative least altered coherent rocks or igneous clasts. Petrographic examination confirmed that most samples have only been affected by low-grade metamorphism, with a low percentage of hydrous and carbonate minerals. Low-grade metamorphic assemblages were observed in mafic samples from the southern and central parts of the area. They include chlorite, carbonate and epidote, mostly in volcanic breccia matrix, which was excluded from the geochemical samples. Two thin sections contain prehnite-clinozoisite or pumpellyite. Very fine-grained biotite±actinolite and biotite hornfels assemblages are in samples from the mafic intrusive complex and upper mafic volcanic unit in the northern part of the area. Two of the felsic samples are heavily silicified, which disqualified them from chemical classification. One sample was excluded based on a high loss on ignition value.

Samples were processed and analyzed at Bureau Veritas (formerly Acme Labs). Samples were crushed to ≥70% passing 10 mesh (2 mm), homogenized, and riffle split. Then a 250 g subsample was pulverized to ≥85% passing 200 mesh (75 μm). A total of 49 elements were analyzed by lithium metaborate/tetraborite fusion and ICP (18 major and minor elements) or ICP-MS (31 trace elements). Loss on ignition values were determined by igniting a sample split and measuring the weight loss. Carbon and sulphur were determined by combustion and Leco analysis. A total of 14 base metals, precious metals and other volatile elements were analyzed by aqua regia digestion of a 0.5 g sample split and ICP-MS. Results of pulp duplicates and internal standards were monitored to ensure analytical reproducibility and accuracy. Major element lithogeochemical results are portrayed in a total alkali vs. silica plot (Fig. 21).

7.1. Alkaline mafic volcanic and subvolcanic rocks

Ten mafic volcanic rock and mafic subvolcanic intrusive rock samples from the upper Spatsizi Formation, lower Horn Mountain Formation and the mafic intrusive complex all show similar microscopic features. The samples contain euhedral to broken, faintly green-yellow pleochroic (Na-rich?), stubby to equant, up to 1 cm augite crystals. Many of these show delicate concentric growth zones. Augite glomerocrysts are common. Plagioclase phenocrysts are generally smaller than augites, but may be as abundant or more abundant. All plagioclases are andesine in composition. The plagioclase crystals display patchy zoning but not oscillatory zoning. Some of the most mafic samples contain chlorite-carbonate-serpentine-epidote pseudomorphs after olivine. The groundmass consists of plagioclase, interstitial K-feldspar and very fine-grained mafic and opaque minerals. The presence of abundant K-feldspar is predominantly based on the intense sodium cobaltinitrite stain of samples. However, in some samples, groundmass K-feldspar can be readily distinguished from plagioclase. One sample shows platy plagioclase megacrysts set in a K-feldspar-rich groundmass (unit EMJpp). Lithogeochemical results show predominantly trachybasalt (potassic trachybasalt, minor hawaiite) to basaltic trachyandesite (shoshonite) compositions (Fig. 21), which accords well with petrographic observations

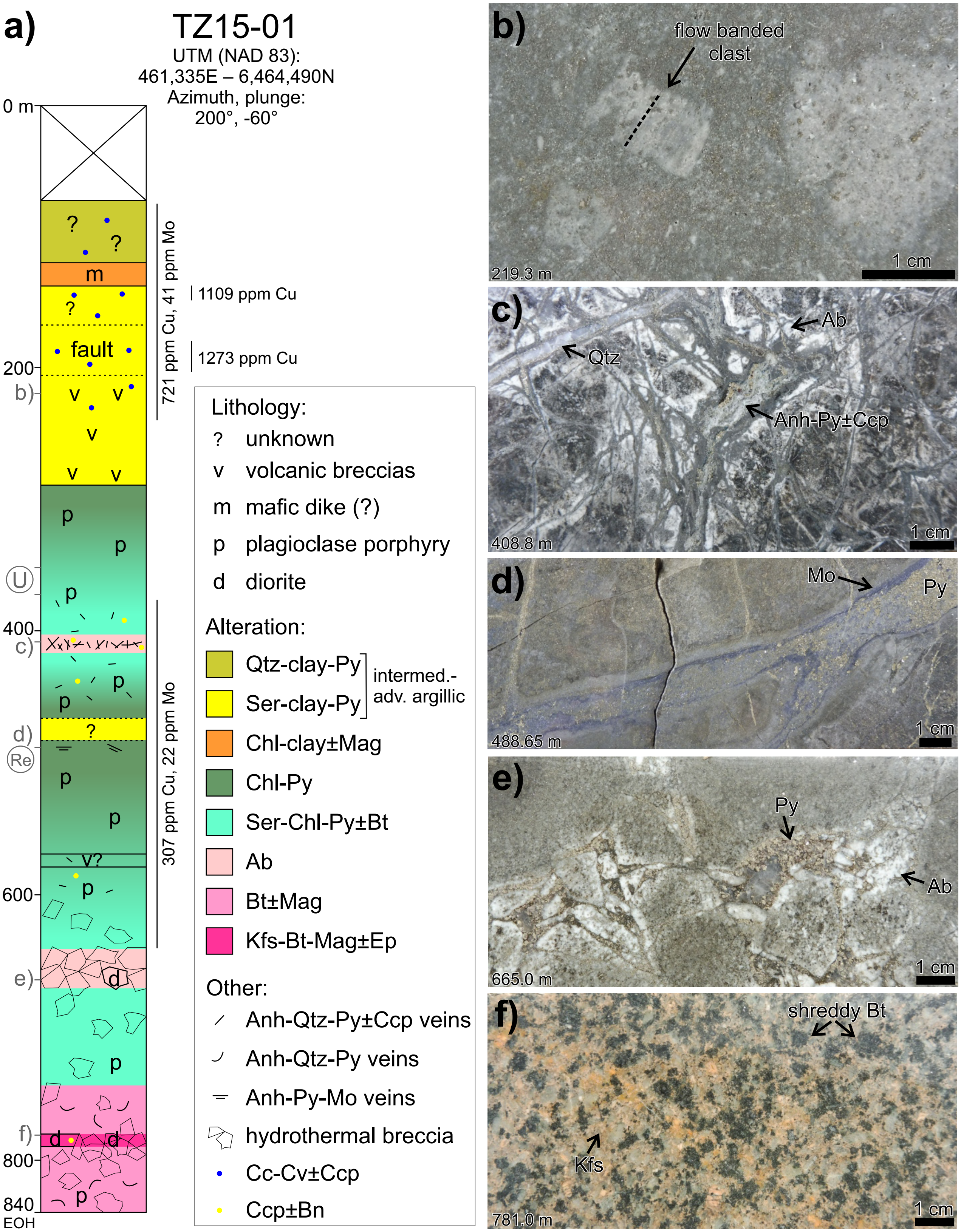

Fig. 20. Diamond-drill hole TZ15-01. **a)** schematic log showing lithology, alteration, veining, hydrothermal brecciation, and mineralization. Photographs illustrate **b)** volcanic breccia texture, including flow-banded clast, **c)** anhydrite-quartz-pyrite-chalcopyrite stockwork with strong albite alteration, **d)** anhydrite-pyrite-molybdenite vein cutting chlorite-pyrite altered rock, **e)** hydrothermally brecciated plagioclase porphyry, and **f)** K-feldspar-biotite altered medium-grained equigranular dioritic intrusive. Sample levels for U-Pb (U) and Re-Os geochronology (Re) indicated. Mineral abbreviations after Kretz (1983); Ser: sericite.

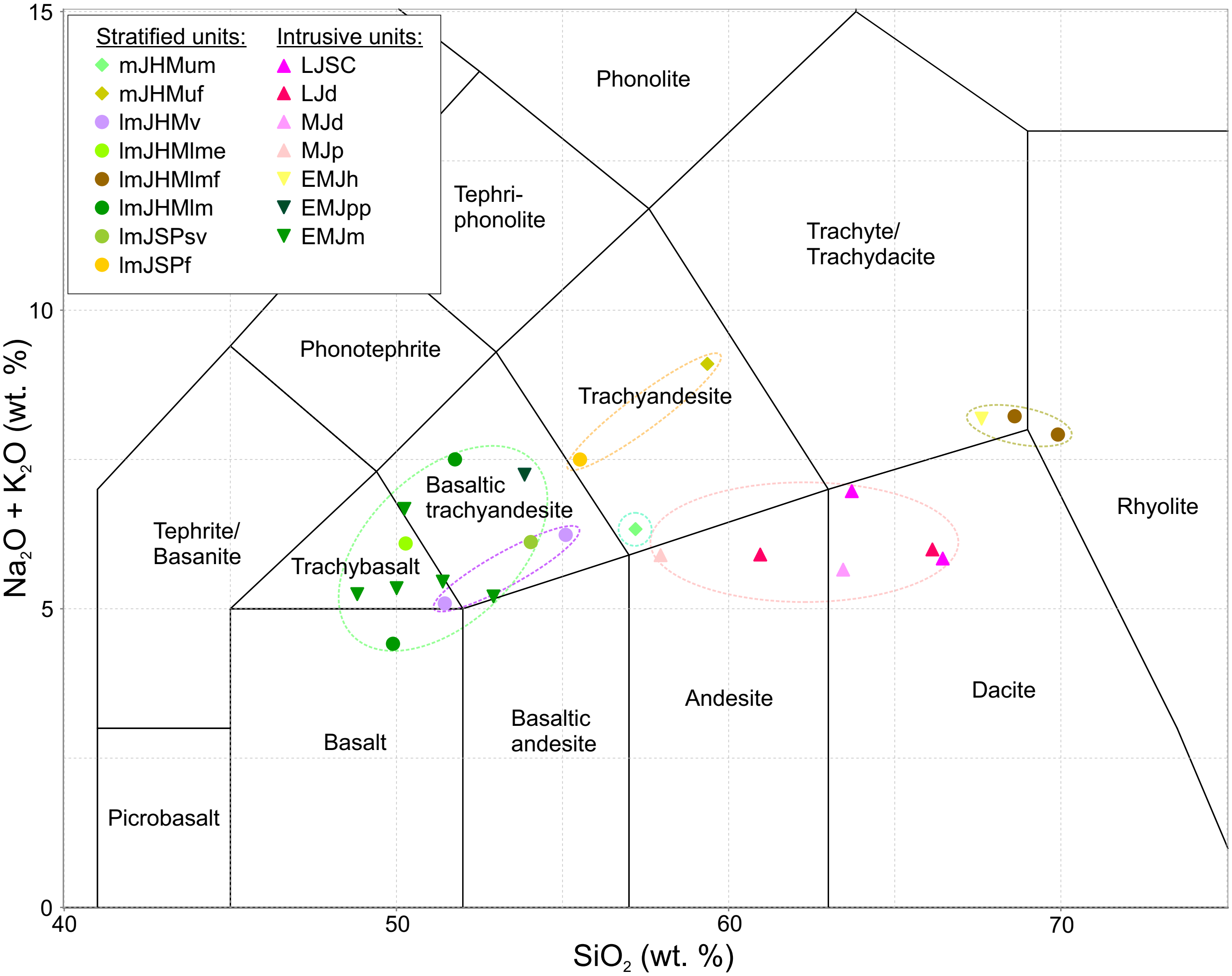

Fig. 21. Total alkalis vs. silica classification diagram (after Le Maitre, 1989) showing results of 24 representative least-altered samples from lithological and intrusive units in the study area.

indicating abundant groundmass K-feldspar in these otherwise mafic rocks.

One sample of the Horn Mountain Formation maroon volcanic unit shows an augite and plagioclase phenocryst population similar to that discussed above. Based on staining, the sample is estimated to contain only small amounts of K-feldspar. This is reflected in the geochemical data showing a trachybasalt composition, with $Na_2O - 2 > K_2O$ resulting in classification as hawaiite (Fig. 21). A sample from a blood red to maroon glassy flow classifies as a basaltic trachyandesite (mugearite), at odds with the original felsic field classification.

A sample from the upper mafic volcanic unit of the Horn Mountain Formation contains plagioclase, augite, and minor hornblende crystals set in a moderately K-feldspar-rich groundmass. The geochemical classification as trachyandesite (latite) is somewhat at odds with the high abundance of augite, dark colour and mafic character of the volcanic unit, and may be caused by biotite hornfelsing, the presence of xenocrystic phases, or cryptic alteration.

7.2. Alkaline felsic volcanic and subvolcanic rocks

Five samples were taken from the Spatsizi felsic volcanic subunit, felsic clasts in the Horn Mountain lower mafic volcanic unit (lmJHMlmf), the Horn Mountain upper felsic volcanic unit and a hornblende-bearing plagioclase porphyritic dike (unit EMJh). In these, plagioclase phenocrysts and (trachytic) plagioclase microcrysts are set in a K-feldspar-rich groundmass. Plagioclase generally lacks oscillatory zoning, except locally in samples from each of unit EMJh and felsic clasts in the lower mafic volcanic unit. The K-feldspar is identified by staining, as it is too fine grained to be resolved optically. The K-feldspar in these rocks is entirely igneous, occurring as a fine-grained, evenly-distributed interstitial component of the groundmass. Only a weak subgreenschist overprint is evident. Plagioclase and augite are generally fresh, veins are absent, and indicators of potassium metasomatism are lacking.

Samples from the Spatsizi platy plagioclase megacrystic volcanic unit and the Horn Mountain upper felsic volcanic unit lie in the trachyandesite field (latites; Fig. 21). This chemical classification captures the potassium-rich nature of these units, but their intermediate (rather than felsic) compositions may be due to abundant large and partly resorbed plagioclase xenocrysts. A more felsic, trachytic, melt composition is suggested based on: 1) a plagioclase and K-feldspar-rich groundmass lacking petrographically observable mafic minerals; 2) trachytic textures, common amygdules, abundant puzzle-fit to clast-supported volcanic breccias and tuffs, indicating hydrous viscous melts and explosive eruptions; and 3) plagioclase-only phenocryst content.

A sample from a moderately plagioclase-phyric dike (unit EMJh) shows abundant very fine-grained groundmass K-feldspar, and is classified as a trachyte. Two samples of felsic clasts in the Horn Mountain lower mafic volcanic unit display plagioclase crystals set in a groundmass with abundant K-feldspar and minor quartz. Based on lithogeochemistry the samples are classified as trachyte and rhyolite (Fig. 21).

7.3. Subalkaline intrusive rocks

The plagioclase porphyry dikes and augite quartz diorite intrusive rocks show little to no modal K-feldspar. Plagioclase is normal and oscillatory zoned, in contrast to the patchy-zoned plagioclase in the alkaline volcanic suite. The plagioclase porphyry samples contain dense mattes of biotite hornfels, or relict biotite hornfels overprinted by sericite. Lithogeochemistry classifies these rocks as andesite to dacite (diorite to granodiorite) and, together with the petrography, suggest a subalkaline affinity.

The Snowdrift Creek pluton was sampled at two locations. Samples are medium-grained equigranular granodiorite to quartz monzodiorite; they contain biotite, hornblende and oscillatory zoned plagioclase. Lithogeochemistry confirms this assignment.

Two samples from post-hydrothermal hornblende diorite dikes show little to no modal K-feldspar and normal- and oscillatory-zoned plagioclase. Lithogeochemical results indicate a diorite to granodiorite composition (Fig. 21).

8. Geochronology

Uranium-lead zircon and argon-argon muscovite studies at the Pacific Centre for Isotopic and Geochemical Research (University of British Columbia) and rhenium-osmium molybdenite studies at the Canadian Centre for Isotopic Microanalysis (University of Alberta) are ongoing and will be reported in detail elsewhere. A sample of plagioclase porphyry (unit MJp) from diamond-drill hole TZ15-01 (Figs. 3, 20) yielded a preliminary U-Pb zircon age of ca. 173 Ma (Fig. 22). R. Friedman (pers. comm., 2015) reports a preliminary U-Pb zircon age of 161-160 Ma from a sample of the Snowdrift Creek pluton collected east of Silica ridge (Fig. 3).

9. Discussion

9.1. Horn Mountain Formation regional correlatives

The Horn Mountain Formation may be more extensive than is presently known. Based on a review of the literature we suggest that equivalent units may be developed more regionally. Taken together, the following occurrences suggest that late Early to Middle Jurassic Horn Mountain volcanism could have occurred over a 110 km-long belt along and near the northeastern margin of Stikinia.

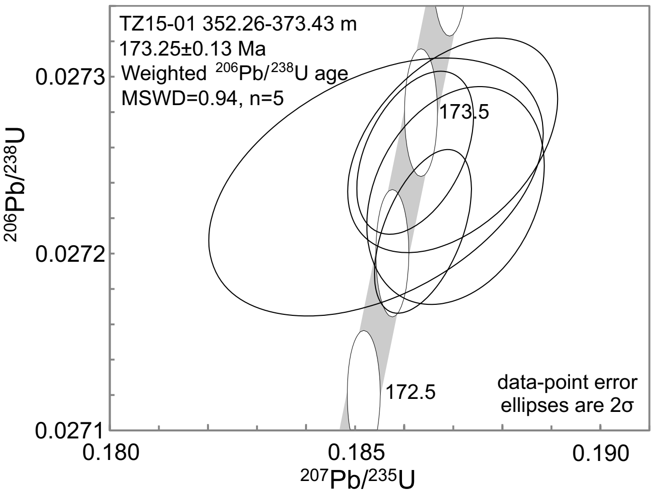

Fig. 22. U-Pb zircon concordia diagram showing chemical abrasion thermal ionization mass spectrometry (TIMS) results for plagioclase porphyry sample (unit MJp) from drill core TZ15-01 (352.26-373.43 m). See Figure 20.

Area 'A'. The area northeast of the junction of the McBride and Stikine rivers has been mapped as undivided Triassic to Jurassic, and Lower Jurassic volcanic rocks (Area 'A', Fig. 1; Gabrielse, 1998; Evenchick and Thorkelson, 2005). In this area a ≥750 m thick succession is composed of red and green epiclastic sandstone, tuff, augite and/or plagioclase-phyric volcanic breccias and flows, rare banded rhyodacite and spherulitic rhyolite (Erdman, 1978; Jones, 1992). The succession lies east of the McBride River pluton, with a 184 ±8 Ma U-Pb zircon age (Anderson and Bevier, 1992). The contact between the pluton and volcanic rocks is not exposed, but apparent contact metamorphic textures may suggest an intrusive relationship (Anderson, 1983). The Lower Jurassic age for some of the volcanic rocks is based on Toarcian fossils and a four-point Rb-Sr whole rock isochron age of 191 ±9 Ma from rocks near Mount Sister Mary (Erdman, 1978). These ages are more consistent with inclusion in the lower part of the Hazelton Group, and may suggest the succession is somewhat older than the Horn Mountain Formation in its type area. However, in the top 100 m of the section, maroon siltstone is interbedded with chert and volcanic clast-bearing conglomerate (Erdman, 1978). Similar maroon volcanic rocks assigned to the Bowser Lake Group are described north of the Pitman fault in the adjacent 1:250,000 scale map sheet (Read and Psutka, 1990; Evenchick and Thorkelson, 2005). The latter two descriptions suggest relationships similar to what we observed between the Horn Mountain maroon volcanic rocks and Bowser Lake chert clast-bearing conglomerates east of the McBride River. Rocks farther west (immediately south of the Hotailuh batholith and north of the Pitman fault) were mapped as undivided Triassic and Jurassic rocks (Evenchick and Thorkelson, 2005). No information is available on the nature of the contacts with the Beggerlay Creek pluton (Late Triassic). They may represent Stuhini Group or Horn Mountain Formation volcanic rocks.

Area 'B'. Volcanic rocks are reported in the northern outlier of Bowser Basin between the Kehlechoa, Kutcho and Pitman faults (Area 'B', Fig. 1). Volcanic rocks assigned to the Bowser Lake Group are well exposed in the east, close to Mount Blair. They are described as dark grey- to mauve- and maroon-weathering feldspar-augite-phyric flows, dark green aphanitic volcanic rocks, and layered pink-, purple- and maroon-weathering tuff (Erdman, 1978; Gabrielse, 1998), similar to the Horn Mountain Formation. Also similar to relationships east of McBride River presented above, near Mount Blair the volcanic rocks are intercalated with chert clast-bearing pebble conglomerate, sandstone, siltstone and shale of the Bowser Lake Group. The volcanic rocks are older than the pluton southeast of Mount Blair, which has a K-Ar hornblende age of 159 ±6 Ma (Erdman, 1978). Sedimentary rocks interpreted as the basal part of the Bowser Lake sequence in the western part of the outlier yielded middle Bajocian fossils (Gabrielse, 1998). If these volcanic rocks correlate to the Horn Mountain Formation, then the upper part of the succession may be as young as late Middle Jurassic.

Area 'C'. Exposed south of the Hotailuh batholith and south of the Pitman fault, the Mount Brock volcanics (Area 'C', Fig. 1) is a >4 km thick succession that conformably overlies Pliensbachian to Toarcian sedimentary rocks of the Spatsizi Formation, which unconformably overlie granitoid rocks correlated with the Railway pluton (Late Triassic; Smith et al., 1984; Read and Psutka, 1990). Strata 100 and 400 m above the base of the Mount Brock volcanics contain early and middle Toarcian ammonites, respectively (Evenchick and Thorkelson, 2005). The succession includes maroon-grey and green volcanic rocks, pink flow-layered rhyodacite, felsic pyroclastic rocks (locally densely welded), grey to light grey bioclastic limestone, and green and maroon tuffaceous sedimentary rocks (Evenchick and Thorkelson, 2005). Phenocrysts in the Mount Brock lava flow deposits are predominantly plagioclase, with subordinate pseudomorphed olivine and augite; they vary from medium-high K basalt to basaltic andesite, to high K andesite, to high K-shoshonitic dacite (Evenchick and Thorkelson, 2005). Intrusions generally concordant with the Mount Brock volcanic strata are correlated with the McEwan Creek pluton, with a U-Pb zircon age of 183.5 ±0.5 Ma (Thorkelson, 1992; Evenchick and McNicoll, 1993). In both stratigraphic position and lithology the Mount Brock volcanics appear similar to the Horn Mountain Formation. Fossil ages from the underlying Spatsizi Formation are similar, or somewhat older. However, the age constraint provided by crosscutting sills correlated with the McEwan Creek pluton suggests that the succession may be slightly older than the Horn Mountain Formation in its type area.

Area 'D'. Immediately west of the Hotailuh batholith Gabrielse (1998) mapped a several square kilometre area underlain by undivided Triassic and Jurassic volcanic rocks that likely represents an erosional remnant of the Horn Mountain Formation (Area 'D' on Figs. 1, 2). Near this area, a stratigraphic section on the north flank of Thenatlodi Mountain, currently interpreted as Lower to Middle Triassic, contains lithologically similar sedimentary strata, with the same stratigraphic architecture, as the Spatsizi Formation section east of Gnat Pass (Iverson et al., 2012).

Area 'E'. Early to Middle Jurassic volcanic rocks have not been reported southwest of Dease Lake (Logan et al., 2012a; b). However, a several square kilometre area of maroon to purple latite, K-feldspar-phyric trachyte, vesicular pyroxene basalt, and minor volcanic sandstone currently interpreted as Late Triassic Stuhini Group are spatially associated with the Hluey Lake biotite-K-feldspar-plagioclase monzonite to syenite (U-Pb zircon age of 166.5 ±0.7 Ma, Logan et al., 2012b; Area 'E', Fig. 1). The maroon volcanic rocks are potassic, mineralogically similar to the intrusive syenite, and have a distinct trace element composition compared to other Late Triassic volcanic rocks (Logan and Iverson, 2013). They may correlate with the Horn Mountain Formation.

9.2. Late Early to early Late Jurassic magmatic activity

The Horn Mountain Formation is part of a broader, multi-stage, alkaline to calc-alkaline Toarcian to Oxfordian magmatic belt that spans the Stikine and Cache Creek terranes in northern British Columbia and southern Yukon.

The late Early to early Middle Jurassic alkaline subvolcanic intrusions related to the Spatsizi Formation and the Horn Mountain Formation represent the earliest stages of magmatism. The belt of volcanic rocks extends for at least 50 km, and perhaps 110 km, in a west-northwest to east-southeast direction (see Section 9.1.).

A later stage includes a northwest to east-southeast trend, at least 300-400 km long, of Middle Jurassic (ca. 170 Ma) quartz-bearing calc-alkaline plutons that span the Cache Creek and Stikine terranes (Fig. 1; van Straaten et al., 2012). In the far northwest of this belt, the Fourth of July batholith (ca. 171 Ma) cuts deformed rocks of the Cache Creek terrane (Fig. 1; Mihalynuk et al., 1992). Several similarly-aged intrusive bodies outcrop between Atlin and Dease Lake, including the Slaughterhouse, McMaster, Llangorse, Tachilta Lakes, Granite Lake, Tanzilla(?) and Pallen plutons (Fig. 1; Gabrielse, 1998; Mihalynuk et al., 2004; Logan et al., 2012a; b). Farther southeast, and immediately south of the study area, is the Three Sisters pluton (Middle Jurassic; Fig. 2). Results from three U-Pb zircon analyses range from 169-171 Ma (Anderson and Bevier, 1992; van Straaten et al., 2012). The 173 Ma calc-alkaline plagioclase porphyry associated with the hydrothermal system at Tanzilla is part of this intrusive phase.

A small quartz-deficient biotite-K-feldspar-plagioclase monzonite to syenite stock spatially associated with local copper and gold mineralization is exposed northeast of Hluey Lakes (Area 'E', Fig. 1; Logan et al., 2012a). The stock yielded a U-Pb zircon age of 166.5 ±0.7 Ma (Logan et al., 2012b) and may represent a feeder system to continued Horn Mountain volcanism during the late Middle Jurassic (see Section 9.1.).

U-Pb zircon ages are lacking for plutons of inferred Middle-Late Jurassic age east of the Three Sisters pluton (Fig. 1), but an intrusive body near Mt. Blair yielded a K-Ar hornblende age of 159 ±6 Ma (Erdman, 1978), and an intrusion near Mt. Albert Dease returned a K-Ar biotite age of 167 ±6 Ma (Wanless et al., 1979). This Middle-Late Jurassic intrusive suite may extend into Quesnellia. An unnamed intrusive body 55 km north of the Snowdrift Creek pluton has yielded K-Ar hornblende ages as old as 157 ±2.4 Ma (Hunt and Roddick, 1987; Gabrielse, 1998). Recent U-Pb zircon geochronology of the Pitman batholith returned 170-171 Ma ages from two samples 3 and 12 km east of the terrane-bounding Kutcho fault (Takaichi and Johnson, 2012).

To date, only one pluton (calc-alkaline Snowdrift Creek) has yielded an early Late Jurassic crystallization age (160-161 Ma, preliminary U-Pb zircon, R. Friedman, pers. comm., 2015). Further work is required to determine how widespread this magmatic pulse is.

9.3. Tectonic evolution and origin of the Horn Mountain Formation

During the Mesozoic, three main phases of magmatic arc development took place in Stikinia, punctuated by collisional events. The Stuhini arc (Late Triassic) was succeeded by the latest Triassic to Early Jurassic main-stage Hazelton arc. The youngest, Toarcian to Middle Jurassic, arc is represented by widespread volcanic rocks in southern and central Stikinia (Fig. 1). In general, the magmatic belts and interpreted arc axes shifted progressively from north to south.

During the Late Triassic, voluminous augite-phyric mafic magmatism was predominant along the northern to eastern margin (current reference frame) of Stikinia, resulting in eruption of Stuhini Group volcanic rocks and intrusion of the Stikine plutonic suite (Woodsworth et al., 1991). The arc likely formed as a result of subduction below the northern to eastern margins of Stikinia (Nelson and Mihalynuk, 1993; Mihalynuk et al., 1994; Colpron et al., 2015). Profound plate rearrangement at the end of the Triassic is marked by the cessation of volcanism on the northern margin of Stikinia, followed by arc uplift and erosion. At this time, the northern end (present coordinates) of Stikinia collided with far northern Quesnellia and the Yukon-Tanana terrane, with strata of the Whitehorse trough deposited in a synorogenic clastic wedge across all three terranes and adjacent parts of the Cache Creek terrane (Colpron et al., 2015).

Reconfigured subduction in the latest Triassic to Early Jurassic created two belts of arc-related lower Hazelton Group volcanic rocks in north-central Stikinia south of the Pitman fault. The volcanic arcs are interpreted to have formed by opposing subduction on either side of the Stikinia microplate, creating a western and eastern volcanic belt separated by a central belt of predominantly sedimentary rocks interpreted as the Hazelton trough (Fig. 1; Marsden and Thorkelson, 1992). Volcanism waned in the Pliensbachian and ended in the late Toarcian (Alldrick, 1993; Brown et al., 1996; Barresi et al., 2015a) as Stikinia accreted with neighbouring terranes to the east and west (Nelson et al., 2013). A final, post-accretionary, episode of arc-related volcanism in Toarcian-Callovian time created a belt of volcanic and intrusive rocks in central and southern Stikinia (Fig. 1; Tipper and Richards, 1976; Diakow and Webster, 1994; MacIntyre et al., 2001). The Horn Mountain Formation rocks are coeval with the youngest arc succession, but the formation is near the northeastern margin of the terrane, proximal to the Cache Creek-Stikinia suture.

Timing of the Cache Creek-Stikinia collision is well constrained as late Early to Middle Jurassic. The youngest Cache Creek cherts that have been overprinted by blueschist facies sodic amphiboles are Pliensbachian to Toarcian (Mihalynuk et al., 2004). Ar-Ar cooling ages on phengite in blueschist mineral assemblages indicate that the central part of the orogenic welt was exhumed by 173.7 ±0.8 Ma (Aalenian; Mihalynuk et al., 2004). Deposition of Cache Creek-derived chert clast-bearing conglomerate in the Bowser Basin started in the early Bajocian (Ricketts et al., 1992). Thus, the Cache Creek accretionary complex became the site of a southwest-vergent tectonic welt that began to shed debris into the Bowser foreland basin in early Bajocian (ca. 169 Ma).

The Horn Mountain Formation volcanic rocks and their local correlatives were probably not the products of normal subduction-related arc magmatism for several reasons. First, subduction was not taking place below northern Stikinia at the time of collision. Subduction below the northern margin of Stikinia ceased in the Late Triassic, followed by slab breakoff soon thereafter (Logan and Mihalynuk, 2014). Subduction below the western and eastern margins of Stikinia waned in the Pliensbachian and ended in the Toarcian. Second, the Horn Mountain Formation rocks are younger than any known volcanic successions of arc affinity in northern Stikinia. In the north, rocks of the upper part of the Hazelton Group are either mainly sedimentary (Spatsizi and Quock formations), or of bimodal volcanic-sedimentary character (Iskut River Formation in the Eskay rift). Third, the Horn Mountain volcanic succession is in the foreland adjacent to the Stikinia-Cache Creek collisional boundary (King Salmon fault), and was erupted between ca. 176 and 169 Ma, during collision. They interfinger with synorogenic clastic strata of the Bowser Lake Group, and are intruded by a 173-160 Ma belt of plutons that cut the Stikinia-Cache Creek suture zone. Finally, their shoshonitic chemistry is suggestive of a syncollisional origin (e.g. Miocene shoshonites on Fiji, Gill and Whelan, 1989). Lithogeochemical data show that the Middle Jurassic calc-alkaline plutons (Mihalynuk et al., 1992; van Straaten et al., 2012), possible Horn Mountain correlatives (Logan and Iverson, 2013) and Horn Mountain Formation (van Straaten and Nelson, unpublished data) are of volcanic arc chemistry. We put forward the preliminary hypothesis that the Horn Mountain Formation formed by re-melting of subduction-modified lithosphere due to collision between the Stikine and Quesnel terranes. Similar to typical subduction-related arc volcanism, postsubduction (syncollisional) arc-like volcanism has been shown to produce porphyry- and epithermal-style mineral deposits (Richards, 2009; see below).

9.4. Alteration and mineralization

The Tanzilla gossan consists of an advanced argillic lithocap overlying porphyry-style alteration at depth. The system includes: 1) multi-phase calc-alkaline porphyritic to equigranular intrusive rocks; 2) zoned potassic to chlorite-sericite to phyllic to intermediate and advanced argillic alteration; 3) local stockwork veins and hydrothermal breccias; and 4) local chalcopyrite, bornite, and molybdenite in veins and stockworks and as disseminations.

The Tanzilla hydrothermal system formed in the foreland of an actively developing fold-and-thrust belt. The structural regime provided the physical trigger for magmatic activity, and likely influenced the hydrothermal system through block faulting, tilting, and erosion. A down-dropped structural block bound by north-northeast trending faults hosts the Silica ridge alteration system. Evidence for erosion within the Horn Mountain volcano-sedimentary strata is found near the top of the middle maroon volcanic unit, locally with the upper felsic volcanic unit, at and near the base of the mafic volcanic unit, and at the unconformable contact with the overlying Bowser Lake conglomerates. The latter two erosional contacts likely developed during the waning stages of the hydrothermal event; these weakly altered lithologies cover the system to the north. The potential for blind mineralization below the late- to post-hydrothermal cover deserves further attention. The angular discordance at the Horn Mountain-Bowser Lake contact may be explained by approximately 15° northward tilting as a result of ongoing arc-arc collision.

Other mineral showings and prospects in the region have been the subject of early-stage exploration. They are associated with late Early to early Late Jurassic alkaline to calc-alkaline magmatic activity, and show characteristics compatible with calc-alkalic to alkalic porphyry systems. Geological mapping at the McBride gossan about 25 km east-southeast of Tanzilla (Fig. 2) by Teck Resources Limited shows that the property is underlain by grey, green and maroon augite- and/or feldspar-phyric volcanic rocks cut by dioritic dikes (Jutras et al., 2014). A petrographic study shows that the dikes lack modal K-feldspar (Jutras et al., 2014), suggesting they may be part of the same calc-alkaline suite as plagioclase porphyry and dioritic intrusions at Tanzilla. The McBride property hosts widespread phyllic alteration, with local areas of potassic (K-feldspar-magnetite) alteration, quartz-magnetite veins, and hydrothermal magnetite breccias returning anomalous copper and gold values in grab samples (Jutras et al., 2014). Notably, the gossan lacks reports of widespread argillic alteration. The alteration and mineralization may be suggestive of the upper levels of a porphyry system.

The Nup prospect (or MO, MINFILE 104I 059; Fig. 2) is in the Snowdrift Creek valley east of the Gopher zone (Fig. 3). Drilling by Paget Moly Corporation in 2008 intersected volcanic tuffs, platy plagioclase porphyritic intrusions, and biotite granodiorite of the Snowdrift Creek pluton. Anomalous molybdenum values were intersected in several drill holes, generally associated with widely spaced quartz-K-feldspar-molybdenite±chalcopyrite veins (Barresi, 2008). The presence of mineralization in the Snowdrift Creek pluton suggests it is early Late Jurassic or younger.

The Hu prospect (MINFILE 104J 013), northwest of Hluey Lakes, is associated with a Middle Jurassic monzonite to syenite stock (Area ‘E’, Fig. 1; Logan et al., 2012a; b). K-feldspar and carbonate alteration are concentrated along intrusive contacts and northeast-trending brittle faults, with grab samples returning elevated copper and gold values (Logan et al., 2012a; b).

Post-subduction (syncollisional) porphyry systems around the world range from calc-alkalic porphyry Cu-Mo (Gangdese belt, Tibet; Yang et al., 2009; Wang et al., 2014) to calc-alkalic porphyry Cu and associated high-sulphidation epithermal Cu-Au (Tampakan, Philippines; Rohrlach and Loucks, 2005) to alkalic porphyry Au-Cu (Cadia, Australia; Holliday et al., 2002; Fox et al., 2015). These deposits may provide analogues for porphyry systems associated with the Horn Mountain Formation of British Columbia and their possible, but as yet untested, regional correlatives.

10. Conclusions

In this paper we describe results from one month of fieldwork and preliminary results from lithogeochemical and geochronological studies on an unusual late Early to Middle Jurassic volcanic succession exposed on the northeastern margin of Stikinia. Before 2012, the sequence was interpreted as Stuhini Group (Triassic) and undivided Triassic to Jurassic volcanic rocks. Our work confirms the suggestion of Iverson et al. (2012) that these volcanic rocks are part of the Hazelton Group. The succession postdates widespread arc volcanism of the lower part of the Hazelton Group, is coeval with deposition of predominantly sedimentary rocks of the upper part of the Hazelton Group, and is concurrent with accretion of the Stikine and Cache Creek terranes.

We formally propose the name Horn Mountain Formation for this ca. 5.4 km thick volcanic succession. It consists mainly of green to maroon augite±plagioclase-phyric trachybasalt to trachybasaltic andesite volcanic breccias and lesser plagioclase-phyric to aphyric trachyte to trachyandesite, and is cut by numerous, roughly coeval subvolcanic feeder dikes, sills and stocks. The succession conformably overlies a 0.7-1 km thick Toarcian predominantly sedimentary sequence that we correlate to the Spatsizi Formation, which unconformably overlies the Cake Hill pluton (Late Triassic). The Horn Mountain Formation is unconformably to conformably overlain by Bajocian conglomerates, chert clast-bearing conglomerates, and sandstones of the Bowser Lake Group. Petrographic observations and major element lithogeochemistry indicate that the Toarcian to Bajocian volcanic rocks and related subvolcanic intrusions are largely quartz deficient, K-feldspar-rich and alkaline in composition. Evaluation of the regional literature indicates that the Horn Mountain Formation may continue for up to 110 km, as a west-northwest to east-southeast trending belt.

A revised structural interpretation extends the Kehlechoa thrust fault to juxtapose rocks of the Whitehorse trough above Toarcian to Bajocian rocks of the Horn Mountain Formation and Bowser Lake Group. The Snowdrift Creek pluton (early Late Jurassic) stitches the thrust fault, and constrains fault movement to Bajocian-Oxfordian.

The Horn Mountain Formation hosts the Tanzilla gossan, composed in part of an advanced argillic lithocap overlying porphyry-style alteration at depth. A calc-alkaline plagioclase porphyry that hosts porphyry-style alteration yielded a preliminary U-Pb zircon age of 173 Ma.

The alkaline Horn Mountain Formation, calc-alkaline Tanzilla intrusions, Three Sisters plutonic suite and Snowdrift Creek pluton formed during Stikine-Quesnel arc-arc collision. The protracted late Early to early Late Jurassic syncollisional magmatic event represents a potential new metallogenic epoch for the Canadian Cordillera and is prospective for calc-alkalic to alkalic porphyry- and epithermal-style mineralization.

Acknowledgments

We thank John Bradford, Tony Barresi, Tyler Ruks, Nigel Luckman, Ingemar Arellano and David Broughton of West Cirque Resources Ltd. (now Kaizen Discovery Inc.) for showing us key outcrops at Tanzilla, rewarding discussions, and providing an opportunity to study and sample drill hole TZ15-01. Safe and courteous flying by Pacific Western Helicopters (now Lakelse Air) is acknowledged. Thanks to Larry Aspler and Mo Colpron for constructive commentary that significantly improved the manuscript. Richard Friedman is thanked for providing preliminary U-Pb TIMS geochronology results.

References cited

Aeroquest Airborne, 2012. Report on a helicopter-borne magnetic survey (Aeroquest Job #11-046) for Geoscience BC. Geoscience BC Report 2012-2, 11p.

Alldrick, D.J., 1993. Geology and metallogeny of the Stewart mining camp, northwestern British Columbia. British Columbia Ministry of Energy, Mines and Petroleum Resources, British Columbia Geological Survey Bulletin 85, 105p.

Anderson, R.G., 1983. Geology of the Hotailuh batholith and surrounding volcanic and sedimentary rocks, north-central British Columbia. Unpublished Ph.D. thesis, Carleton University, Ottawa, Ontario, Canada, 669p.

Anderson, R.G., and Bevier, M.L., 1992. New late Triassic and early Jurassic U-Pb zircon ages from the Hotailuh Batholith, Cry Lake map area, North - Central British Columbia. In: Radiogenic age and isotopic studies: Report 6, Geological Survey of Canada Paper 92-02, pp. 145–152.

Baker, N.W., 1992. Report on the T-Horn claims, Cry Lake area, Liard Mining Division. British Columbia Ministry of Energy and Mines, Assessment Report 22458, 11p.

Barresi, T., Bradford, J., and Luckman, N., 2014. 2014 Diamond drilling report on the Tanzilla property, northwestern British Columbia. British Columbia Ministry of Energy and Mines, Assessment Report 35471, 46p.

Barresi, T., 2008. Diamond drilling report on the MO property (MO mineral claims). British Columbia Ministry of Energy and Mines, Assessment Report 30933, 22p.

Barresi, T., Nelson, J.L., Dostal, J., and Friedman, R., 2015a. Evolution of the Hazelton arc near Terrace, British Columbia: stratigraphic, geochronological, and geochemical constraints on a Late Triassic – Early Jurassic arc and Cu–Au porphyry belt. Canadian Journal of Earth Sciences, 52, 466-494.

Barresi, T., Nelson, J.L., and Dostal, J., 2015b. Geochemical constraints on magmatic and metallogenic processes: Iskut River Formation, volcanogenic massive sulfide-hosting basalts, NW British Columbia, Canada. Canadian Journal of Earth Sciences, 52, 1-20.

Barresi, T., and Luckman, N., 2015. 2015 diamond drilling report on the Tanzilla property, northwestern British Columbia. British Columbia Ministry of Energy and Mines, Assessment Report, 42p.

BC Department of Mines and Petroleum Resources, 1974. Geology, exploration and mining in British Columbia. British Columbia Department of Mines and Petroleum Resources, 642p.

Bowen, B.K., 2013. Technical report on the Galaxie project. Liard Mining Division, British Columbia, Canada. NI 43-101 Report, 140p. Available from http://sedar.com/.

British Columbia Geological Survey, 2015. MINFILE - British Columbia mineral inventory database. Available from http://minfile.gov.bc.ca/.

Brown, D.A., Gunning, M.H., and Greig, C.J., 1996. The Stikine project: Geology of western Telegraph Creek map area, northwestern British Columbia. British Columbia Ministry of Employment and Investment, British Columbia Geological Survey Bulletin 95, 130p.

Clouthier, G.A., and Vyselaar, J., 1975. Geological and geophysical report on the Tom Group 1. BC Ministry of Energy and Mines, Assessment Report 5769, 6p.

Colpron, M., Crowley, J.L., Gehrels, G., Long, D.G.F., Murphy, D.C., Beranek, L., and Bickerton, L., 2015. Birth of the northern Cordilleran orogen, as recorded by detrital zircons in Jurassic synorogenic strata and regional exhumation in Yukon. Lithosphere, 7, 541-562.

Currie, L.D., and Parrish, R.R., 1997. Paleozoic and Mesozoic rocks of Stikinia exposed in northwestern British Columbia: Implications for correlations in the northern Cordillera. Geological Society of America Bulletin, 109, 1402-1420.

Diakow, L.J., and Webster, I.C.L., 1994. Geology of Fawnie Creek map area (NTS 93F/3). In: Geological Fieldwork 1993, British Columbia Ministry of Energy and Mines, British Columbia Geological Survey Paper 1994-1, pp. 15–26.

Dolmage, Campbell & Associates Ltd., 1971. Owl mining claims. Liard Mining division. Physical work for assessment. British Columbia Ministry of Energy and Mines, Property File 19789, 15p.

Erdman, L.R., 1978. Petrology, geochronology and geochemistry of Jurassic volcanic and granitic rocks of the Cry Lake and Spatsizi map sheets, north-central British Columbia. Unpublished B.Sc. thesis, The University of British Columbia, Vancouver, B.C., Canada, 63p.

Evenchick, C.A., and McNicoll, V.J., 1993. U-Pb age for the Jurassic McEwan Creek pluton, north-central British Columbia: regional setting and implications for the Toarcian stage boundary. In: Radiogenic age and isotopic studies: report 7, Geological Survey of Canada Paper 93-2, pp. 91-97.

Evenchick, C.A., and Thorkelson, D.J., 2005. Geology of the Spatsizi River map area, north-central British Columbia. Geological Survey of Canada Bulletin 577, 276p.

Fominoff, P.J., and Crosby, R.O., 1971. Report on magnetometer & induced polarization surveys. Owl Property. Dease Lake area, British Columbia. British Columbia Ministry of Energy and Mines, Assessment Report 3292, 7p.

Fox, N., Cooke, D.R., Harris, A.C., Collett, D., and Eastwood, G., 2015. Porphyry Au-Cu mineralization controlled by reactivation of an arc-transverse volcanosedimentary subbasin. Geology, 43, 811-814.

Gabrielse, H., 1998. Geology of Cry Lake and Dease Lake map areas, North-Central British Columbia. Geological Survey of Canada Bulletin 504, 147p.

Gagnon, J.-F., Barresi, T., Waldron, J.W.F., Nelson, J.L., Poulton, T.P., and Cordey, F., 2012. Stratigraphy of the upper Hazelton Group and the Jurassic evolution of the Stikine terrane, British Columbia. Canadian Journal of Earth Sciences, 49, 1027-1052.

Gillespie, M.R., and Styles, M.T., 1999. BGS rock classification scheme. Volume 1. Classification of igneous rocks. British Geological Survey Research Report RR99-06, 52p.

Gill, J., and Whelan, P., 1989. Early rifting of an oceanic island arc (Fiji) produced shoshonitic to tholeiitic basalts. Journal of Geophysical Research: Solid Earth, 94, 4561-4578.

Hallsworth, C.R., and Knox, R.W.O., 1999. BGS rock classification scheme. Volume 3. Classification of sediments and sedimentary rocks. British Geological Survey Research Report RR99-03, 44p.

Henderson, C.M., and Perry, D.G., 1981. A Lower Jurassic heteroporid bryozoan and associated biota, Turnagain Lake, British Columbia. Canadian Journal of Earth Sciences, 18, 457-468.

Holbek, P., 2006. Tanzilla project. Tan1 to Tan6 and Tanzilla7 mineral claims. British Columbia Ministry of Energy and Mines, Assessment Report 28433, 16p.

Holbek, P., 2008. Tanzilla project. Tan1 to Tan6 and Tanzilla7 mineral claims. British Columbia Ministry of Energy and Mines, Assessment Report 30032, 19p.

Holliday, J.R., Wilson, A.J., Blevin, P.L., Tedder, I.J., Dunham, P.D., and Pfitzner, M., 2002. Porphyry gold–copper mineralisation in the Cadia district, eastern Lachlan Fold Belt, New South Wales, and its relationship to shoshonitic magmatism. Mineralium Deposita, 37, 100-116.

Hunt, P.A., and Roddick, J.C., 1987. A compilation of K-Ar ages: Report 17. In: Radiogenic age and isotopic studies: Report 1, Geological Survey of Canada Paper 87-2, pp. 143-210.

Iverson, O., Mahoney, J.B., and Logan, J.M., 2012. Dease Lake geoscience project, part IV: Tsaybahe group: Lithological and geochemical characterization of Middle Triassic volcanism in the Stikine arch, north-central British Columbia. In: Geological Fieldwork 2011, British Columbia Ministry of Energy and Mines, British Columbia Geological Survey Paper 2012-1, pp. 17–22.

Jones, P.J., 1992. Nun claim group. Geological, geochemical report. British Columbia Ministry of Energy and Mines, Assessment Report 22042, 9p.

Jutras, G., Bickerton, L., Stock, L., Thompson, V., and Beckman, S., 2014. Assessment report on geological, geochemical and geophysical work conducted during July and August 2014 on the McBride mineral tenure. British Columbia Ministry of Energy and Mines, Assessment Report 35038, 40p.

Kaizen Discovery Inc., 2015. Kaizen reports 2015 exploration drill results from its British Columbia projects. Available from http://www.kaizendiscovery.com/.

Kretz, R., 1983. Symbols for rock-forming minerals. American Mineralogist, 68, 227-279.

Le Maitre, R.W., 1989. Classification of igneous rocks and glossary of terms. Oxford University Press, Don Mills, 193p.

Logan, J.M., Moynihan, D.P., and Diakow, L.J., 2012a. Dease Lake geoscienece project, Part I: Geology and mineralization of the Dease Lake (NTS 104J/08) and East-Half of the Little Tuya River (NTS 104J/07E) map sheets, northern British Columbia. In: Geological Fieldwork 2011, British Columbia Ministry of Energy and Mines, British Columbia Geological Survey Paper 2012-1, pp. 23-44.

Logan, J.M., Moynihan, D.P., Diakow, L.J., and van Straaten, B.I., 2012b. Dease Lake - Little Tuya River geology (NTS 104J/08, 07E). British Columbia Ministry of Energy and Mines, British Columbia Geological Survey Open File 2012-04, scale: 1:50,000.

Logan, J.M., and Iverson, O., 2013. Dease Lake geoscience project: Geochemical characterizaiton of Tsaybahe, Stuhini and Hazelton volcanic rocks, northwestern British Columbia (NTS 104I, J). In: Geoscience BC Summary of Activities 2012, Geoscience BC Report 2013-1, pp. 11-32.

Logan, J.M., and Mihalynuk, M.G., 2014. Tectonic Controls on Early Mesozoic Paired Alkaline Porphyry Deposit Belts (Cu-Au ± Ag-Pt-Pd-Mo) Within the Canadian Cordillera. Economic Geology, 109, 827-858.

Luckman, N., Celiz, M.A.D., Wetherup, S., and Walcott, P., 2013. 2013 assessment report. Induced polarization, terraspec and structural surveys on the Tanzilla property. 2013 assessment report. Soil geochemical survey on the Pliny property. British Columbia Ministry of Energy and Mines, Assessment Report 34550, 24p.

MacIntyre, D.G., Villeneuve, M.E., and Schiarizza, P., 2001. Timing and tectonic setting of Stikine Terrane magmatism, Babine-Takla lakes area, central British Columbia. Canadian Journal of Earth Sciences, 38, 579-601.

Marsden, H., and Thorkelson, D.J., 1992. Geology of the Hazelton Volcanic Belt in British Columbia: Implications for the Early to Middle Jurassic evolution of Stikinia. Tectonics, 11, pp. 1266-1287.

Mihalynuk, M.G., Smith, M.T., Gabites, J.E., Runkle, D., and Lefebure, D., 1992. Age of emplacement and basement character of the Cache Creek terrane as constrained by new isotopic and geochemical data. Canadian Journal of Earth Sciences, 29, 2463-2477.

Mihalynuk, M.G., Nelson, J., and Diakow, L.J., 1994. Cache Creek terrane entrapment: Oroclinal paradox within the Canadian Cordillera. Tectonics, 13, 575-595.

Mihalynuk, M.G., Erdmer, P., Ghent, E.D., Cordey, F., Archibald, D.A., Friedman, R.M., and Johannson, G.G., 2004. Coherent French Range blueschist: Subduction to exhumation in <2.5 m.y.? Geological Society of America Bulletin, 116, 910-922.

Nelson, J.L., Colpron, M., and Israel, S., 2013. The Cordillera of British Columbia, Yukon and Alaska: Tectonics and metallogeny. In: Colpron, M., Bissig, T., Rusk, B. G., and Thompson, J. (Eds.), Tectonics, Metallogeny and Discovery: The North American Cordillera and Similar Accretionary Settings, Society of Economic Geologists Special Publication 17, pp. 53-110.

Nelson, J., and Mihalynuk, M., 1993. Cache Creek ocean: Closure or enclosure? Geology, 21, 173-176.

Read, P.B., and Psutka, J.F., 1990. Geology of Ealue Lake East-half (104H/13E) and Cullivan Creek (104H/14) map areas, British Columbia. Geological Survey of Canada Open File 2241.

Richards, J.P., 2009. Postsubduction porphyry Cu-Au and epithermal Au deposits: Products of remelting of subduction-modified lithosphere. Geology, 37, 247-250.

Ricketts, B.D., Evenchick, C.A., Anderson, R.G., and Murphy, D.C., 1992. Bowser basin, northern British Columbia: Constraints on the timing of initial subsidence and Stikinia-North America terrane interactions. Geology, 20, 1119-1122.

Rohrlach, B.D., and Loucks, R.R., 2005. Multi-million-year cyclic ramp-up of volatiles in a lower crustal magma reservoic trapped below the Tampakan copper-gold deposit by Mio-Pliocene crustal compression in the southern Philippines. In: Porter, T. M. (Ed.), Super porphyry copper & gold deposits: A global perspective 2, pp. 369-407.

Schroeter, T.G., 1977. Mineral property examinations. In: Geological Fieldwork 1976, BC Ministry of Energy and Mines Report 1977-1, pp. 68-70.

Smee, B.W., 1971. Geochemical soil survey on the Lotus group of claims. BC Ministry of Energy and Mines, Assessment Report 3538, 6p.

Smith, P.L., Thomson, R.C., and Tipper, H.W., 1984. Lower and

Middle Jurassic sediments and volcanics of the Spatsizi area, British Columbia. In: Current Research, Part A, Geological Survey of Canada Paper 84-1A, pp. 117-120.

Stevens, R.D., DeLabio, R.N., and Lachance, G.R., 1982. Age determinations and geological studies. In: K-Ar isotopic ages, report 15, Geological Survey of Canada Paper 81-2, p. 56.

Stevenson, R.W., 1973. Report on silt and rock geochemical survey. British Columbia Ministry of Energy and Mines, Assessment Report 4661, 9p.

van Straaten, B.I., Logan, J.M., and Diakow, L.J., 2012. Mesozoic magmatism and metallogeny of the Hotailuh Batholith, northwestern British Columbia. British Columbia Ministry of Energy, Mines and Natural Gas, British Columbia Geological Survey Open File 2012-06, 58p.

Takaichi, M., and Johnson, C., 2012. Assessment report on the 2011/2012 geological and geophysical program at the Pitman property, BC, Canada. British Columbia Ministry of Energy and Mines, Assessment Report 33340, 23p.

Thomson, R.C., Smith, P.L., and Tipper, H.W., 1986. Lower to Middle Jurassic (Pliensbachian to Bajocian) stratigraphy of the northern Spatsizi area, north-central British Columbia. Canadian Journal of Earth Sciences, 23, 1963-1973.

Thorkelson, D.J., 1992. Volcanic and tectonic evolution of the Hazelton group in Spatsizi River (104H) map-area, north-central British Columbia. Unpublished Ph.D. dissertation, Carleton University, Ottawa, Ontario, Canada, 281p.

Tipper, H.W., and Richards, T.A., 1976. Jurassic stratigraphy and history of north-central British Columbia. Geological Survey of Canada Bulletin 270, 82p.

Travis, A., 2004. Geological, geochemical and prospecting report undertaken on the Tanzilla property. British Columbia Ministry of Energy and Mines, Assessment Report 27435, 25p.

Wang, R., Richards, J.P., Hou, Z., Yang, Z., Gou, Z., and DuFrane, S.A., 2014. Increasing Magmatic Oxidation State from Paleocene to Miocene in the Eastern Gangdese Belt, Tibet: Implication for Collision-Related Porphyry Cu-Mo ± Au Mineralization. Economic Geology, 109, 1943-1965.

Wanless, R.K., Stevens, R.D., Lachance, G.R., and DeLabio, R.N., 1979. Age determinations and geological studies. In: K-Ar isotopic ages, report 14, Geological Survey of Canada Paper 79-2.

Woodsworth, G.J., Anderson, R.G., Armstrong, R.L., Struik, L.C., and van der Heyden, P., 1991. Chapter 15: Plutonic regimes. In: Gabrielse, H., and Yorath, C. J. (Eds.), Geology of the Cordilleran Orogen in Canada, Geological Survey of Canada, Geology of Canada 4, pp. 491-531.

Yang, Z., Hou, Z., White, N.C., Chang, Z., Li, Z., and Song, Y., 2009. Geology of the post-collisional porphyry copper–molybdenum deposit at Qulong, Tibet. Ore Geology Reviews, Special Issue on Metallogenesis of the Tibetan Collisional Orogen, 36, 133-159.

Application of trace-element compositions of detrital apatite to explore for porphyry deposits in central British Columbia

Alexei S. Rukhlov[1, a], Alain Plouffe[2], Travis Ferbey[1], Mao Mao[1], and Jody Spence[3]

[1] British Columbia Geological Survey, Ministry of Energy and Mines, Victoria, BC, V8W 9N3
[2] Geological Survey of Canada, 601 Booth Street, Ottawa, ON, K1A 0E8
[3] School of Earth and Ocean Sciences, University of Victoria, Victoria, BC, V8P 5C2
[a] corresponding author: Alexei.Rukhlov@gov.bc.ca

Recommended citation: Rukhlov, A.S., Plouffe, A., Ferbey, T., Mao, M., and Spence, J., 2016. Application of trace-element compositions of detrital apatite to explore for porphyry deposits in central British Columbia. In: Geological Fieldwork 2015, British Columbia Ministry of Energy and Mines, British Columbia Geological Survey Paper 2016-1, pp. 145-179.

Abstract

Apatite grains recovered from tills (14 samples) at the Highland Valley, Gibraltar, Mount Polley, and Woodjam porphyry deposits, and mineralized bedrock (2 samples) at the Woodjam Southeast Zone were analysed by electron microprobe and laser ablation-inductively coupled plasma mass spectrometry. The Cl/F and Cl/OH ratios of these grains, assuming molar (F + OH + Cl) = 1, are similar to those of apatites from producing porphyry deposits elsewhere (e.g., Yerrington, Nevada; Bingham, Utah; Henderson, Colorado). Most apatite grains in till from Mount Polley have higher SO_3, SiO_2, Na_2O, Sr, Mg, V, Ba, Zr, Mo, Nb contents and $(La/Sm)_{CN}$, and lower Mn, Y, and ∑HREE (total heavy rare earth elements) contents relative to those from the Highland Valley, Gibraltar and Woodjam deposits. Only apatite grains from till overlying the contact between the Takomkane batholith and Nicola Group volcano-sedimentary rocks at Woodjam show higher As abundances (121–1191 ppm) than those from Mount Polley (mostly 5.5–158 ppm As), perhaps reflecting a sedimentary source. Apatite grains in till from Mount Polley show weak negative Ce anomalies (Ce/Ce*; mostly 0.89–1.03) and moderate to weak negative Eu anomalies (Eu/Eu*; mostly 0.50–0.99). In contrast, those from the Highland Valley, Gibraltar and Woodjam deposits show weak positive Ce anomalies (Ce/Ce* mostly between 1.00 and 1.24) and strong negative Eu anomalies (Eu/Eu* mostly between 0.11 and 0.47). Most apatite grains from tills at Woodjam and a few from other deposits indicate variable degrees of depletion in minor and trace elements and LREEs (light rare earth elements), with highly variable $(Ce/Yb)_{CN}$ (<0.01–47), $(La/Sm)_{CN}$ (0.06–6.0), $(Gd/Yb)_{CN}$ (0.01–39), Ce/Ce* (0.23–3.8) and elevated Eu/Eu* (up to 1.5), probably reflecting metasomatic alteration of primary apatite. The systematic differences in abundances of redox-sensitive SO_3, Mn, V, As, Ce and Eu between apatite grains from Mount Polley and other porphyry deposits are consistent with a more oxidized alkalic porphyry Cu-Au compared to more reduced calc-alkaline porphyry Cu±Mo±Au systems. Although apatite crystallization temperature is needed to quantify the oxidation state of these porphyry deposits, average Mn contents of the pristine apatite grains yield log fO_2 values of -11.2 ±0.5 for Mount Polley, -12.8 ±0.6 for Woodjam Southeast Zone, -14.1 ±0.7 for Gibraltar, and -16.3 ±1.0 for Highland Valley, using an empirical apatite oxybarometer for a given range of temperatures (920–660^{o}C) and compositions (andesitic to rhyolitic). The strong negative Eu anomalies, coupled with higher Mn and lower Mg and Sr contents, of apatite grains at the Highland Valley, Gibraltar and Woodjam deposits also indicate more fractionated, felsic magmas, lacking significant Fe-Mg minerals, compared to the Mount Polley alkalic porphyry Cu-Au system. Classification of the examined apatite grains using discriminant functions correctly identifies the porphyry deposits in all four study areas. Unlike detrital apatite grains at other deposits, those from tills at Woodjam mostly show barren-rock affinity or evidence of metasomatic depletion in most minor and trace elements, suggesting derivation mainly from a higher-level, propylitic alteration zone rather than from mineralized rocks such as at the Woodjam Southeast Zone. Our results show that apatite trace-element chemistry is diagnostic of specific porphyry deposits and their relative oxidation states and thus can be used as an exploration tool for these deposits.

Keywords: Apatite, trace-element compositions, LA-ICP-MS, EMPA, porphyry Cu-Mo, alkalic porphyry Cu-Au, till, indicator mineral, mineral exploration, Gibraltar, Highland Valley Copper, Mount Polley, Woodjam

---

1. Introduction

The Quesnel and Stikine magmatic arc terranes (Late Triassic-Early Jurassic) of the Canadian Cordillera in British Columbia are highly prospective for porphyry Cu±Mo±Au deposits (e.g., Sutherland Brown, 1976; Dawson et al., 1991; Schroeter, 1995; Logan, 2013). However, exploring for these deposits is challenged by glacial deposits that drape much of the Interior Plateau (Ward et al., 2009). In 2010, the Geological Survey of Canada (GSC) launched a five year program (Targeted Geoscience Initiative-4, or TGI-4) to develop methods for targeting buried mineral deposits. As part of this program, the British Columbia Geological Survey and the Geological Survey of Canada conducted till surveys near four porphyry copper deposits in the Interior Plateau: the Highland Valley Copper and Gibraltar mines (calc-alkaline porphyry Cu-Mo); the Mount Polley mine (alkalic porphyry Cu-Au-Ag); and the Woodjam developed prospect (alkalic Cu-Au to calc-alkaline porphyry Cu-Mo; Fig. 1; Anderson et al., 2012a, b, c; Plouffe et al., 2012, 2013a, b, 2014; Ferbey and Plouffe, 2014; Ferbey et al., 2014; Hashmi et al., 2014, 2015; Plouffe and Ferbey, 2015a, d). The objective of these surveys was to develop mineral exploration methods using till geochemistry and mineralogy tied to studies of ice-flow history and glacial dispersion.

Apatite, $Ca_5[PO_4]_3$(F, OH, Cl), is an accessory mineral in porphyry Cu±Mo±Au deposits, and apatite textures, optical properties, and chemical compositions are diagnostic of these deposits (e.g., Carson and Jambor, 1974; Williams and Cesbron, 1977; Belousova et al., 2002; Bath et al., 2006; Liaghat and Tosdal, 2008; Bouzari et al., 2010, 2011a, b, 2015; Celis et al., 2013, 2014; Mao et al., 2015). Most studies have focused on apatite from rock samples and, so far, little research has been done on detrital apatite grains recovered from till. Nonetheless, till sampling near porphyry and IOCG deposits has shown that apatite can survive glacial transport and post-glacial weathering (Kelley et al., 2011; Normandeau et al., 2014; Hashmi et al., 2015). Furthermore, apatite appears to be more abundant in tills deposited down paleoice-flow direction from mineralized zones and thus holds potential as a porphyry indicator mineral (PIM). Given that detrital apatite grains in tills can be derived from multiple sources, apatite trace-element compositions provide criteria to discriminate between porphyry systems and other bedrock sources (Mao et al., 2015).

This study builds on the work of Mao et al. (2015), who proposed a discrimination approach of using trace-element compositions of apatite from many types of ore deposits, including virtually all types of metallic deposits in British Columbia. Here we test the effectiveness of the method to explore for porphyry deposits by analyzing trace-element compositions of apatite grains recovered from till and bedrock samples from the four TGI-4 study areas (Fig. 1). Elsewhere (Rukhlov et al., 2016) we provide full appendices of the new analytical data by electron microprobe (EMPA) and laser ablation – inductively coupled plasma mass spectrometry (LA-ICP-MS). Our results demonstrate that trace-element compositions of detrital apatite grains identify the porphyry deposits in all four study areas and thus confirm the findings of Mao et al. (2015) that detrital apatite chemistry provides a robust tool for mineral exploration.

2. Physiography and glacial history

The four study areas (Fig. 1) are in the Interior Plateau (Holland, 1976). At the onset of the most recent Late Wisconsinan glacial event (Fraser glaciation; Clague, 1989), local valley glaciers formed in mountainous areas of the Interior Plateau (Clague, 1989; Plouffe, 2000). As glaciation proceeded, most of the ice sheet built up from the coalescence of valley and piedmont glaciers flowing into the Interior Plateau from the Coast (west) and Cariboo (east) mountains (Tipper, 1971a, b). Eventually, ice was sufficiently thick to flow outward from the Interior Plateau, independent of topography.

At Highland Valley (Fig. 2), ice-flow indicators suggest a single phase of ice movement from a divide at about 52° north, with flow generally to the south to southeast (Plouffe and Ferbey, 2015b). Glacial striations and clast lithology in the till indicate that ice flowing from the Coast or Cariboo mountains did not reach the area during the build up to the Fraser Glaciation maximum. Farther north, the first glaciers to advance over the Gibraltar (Fig. 3), Mount Polley (Fig. 4), and Woodjam (Fig. 5) areas moved west to southwest from the Cariboo Mountains (Plouffe and Ferbey, 2015d). Glacial striations and landforms indicate a second phase of flow, directed north to northwest, likely from an ice divide near 52° north during the glacial maximum (Ferbey et al., 2013). Evidence for a third phase, to the south-southeast, is preserved at Gibraltar. Although the origin and timing of this movement remain unclear, it could be related to an early ice flow out of an unnamed mountain ridge marked with cirques and arêtes north of the deposit (Plouffe and Ferbey, 2015c). Multiple ice-flow movements in these three areas imply multiple detrital transport histories (Plouffe and Ferbey, 2015d).

The Cordilleran ice sheet left a glacial sediment cover of variable thickness. In addition to multiple transport paths, this variation needs to be considered when interpreting till geochemistry and mineralogy. Although mineralization at Gibraltar, Mount Polley and Highland Valley is generally covered by glacial deposits 2-10 metres thick, local mineralized outcrops were exposed before mining in each case (Rotherham et al., 1972; Casselman et al., 1995; Byrne et al., 2013; Rees, 2013). Any mineralized zone that was protected from glacial erosion by a cover of pre-glacial sediment or non-mineralized rock will not yield a geochemical or mineralogical signal in Late Wisconsinan till (Plouffe et al., 2012; Plouffe and Ferbey, 2015d). For example, at Woodjam, the Southeast Zone is covered by more than 200 m of unconsolidated sediments, probably in part pre-glacial (J.W. Morton, pers. comm. 2014; see profiles in del Real et al., 2014). Similarly, unconsolidated sediments form a 40-100 m thick blanket over the Three Firs prospect at Woodjam, which is also partly covered by up to 20 m of Cenozoic basaltic flows of the Chilcotin Group (Bissig et al., 2013; see Figure 6 in Vandekerkhove et al., 2014).

3. Geology and porphyry mineralization

The four porphyry deposits in this study are hosted by the Late Triassic to Early Jurassic alkaline (alkalic porphyry Cu-Au) and calc-alkaline (porphyry Cu-Mo±Au) intrusions of the Quesnel terrane. Three of these deposits (Highland Valley, Gibraltar, and Mount Polley) are producing open-pit mines, and the Woodjam is a developed prospect. The following briefly summarizes the geology of the deposits.

3.1. Highland Valley

The Guichon Creek batholith (Late Triassic) hosts at least five economic porphyry Cu-Mo deposits comprising the Highland Valley porphyry district, about 54 km southwest of Kamloops (Fig. 2; McMillan, 1985, 2005; Casselman et al., 1995; McMillan et al., 2009; Byrne et al., 2013). The batholith cuts volcanic and sedimentary rocks of the Nicola Group (Late Triassic) and is made up of a core of granodiorite to quartz monzonite that is rimmed by older diorite to quartz diorite (McMillan, 1985;

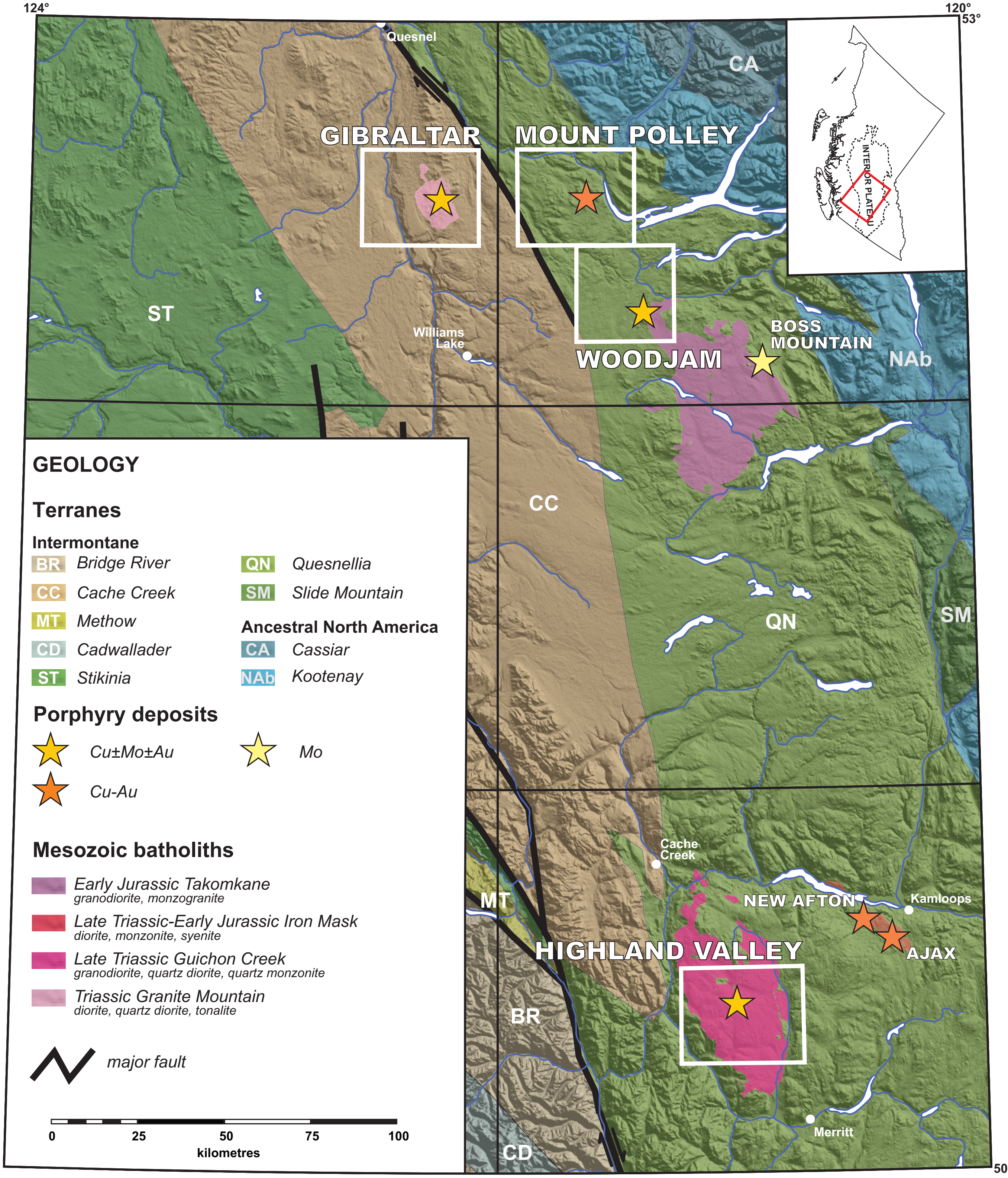

Fig. 1. Terranes (after Nelson et al., 2013), Mesozoic batholiths (after Massey et al., 2005; Logan et al., 2010), major porphyry deposits, and locations of Highland Valley, Gibraltar, Mount Polley, and Woodjam study areas in south-central British Columbia.

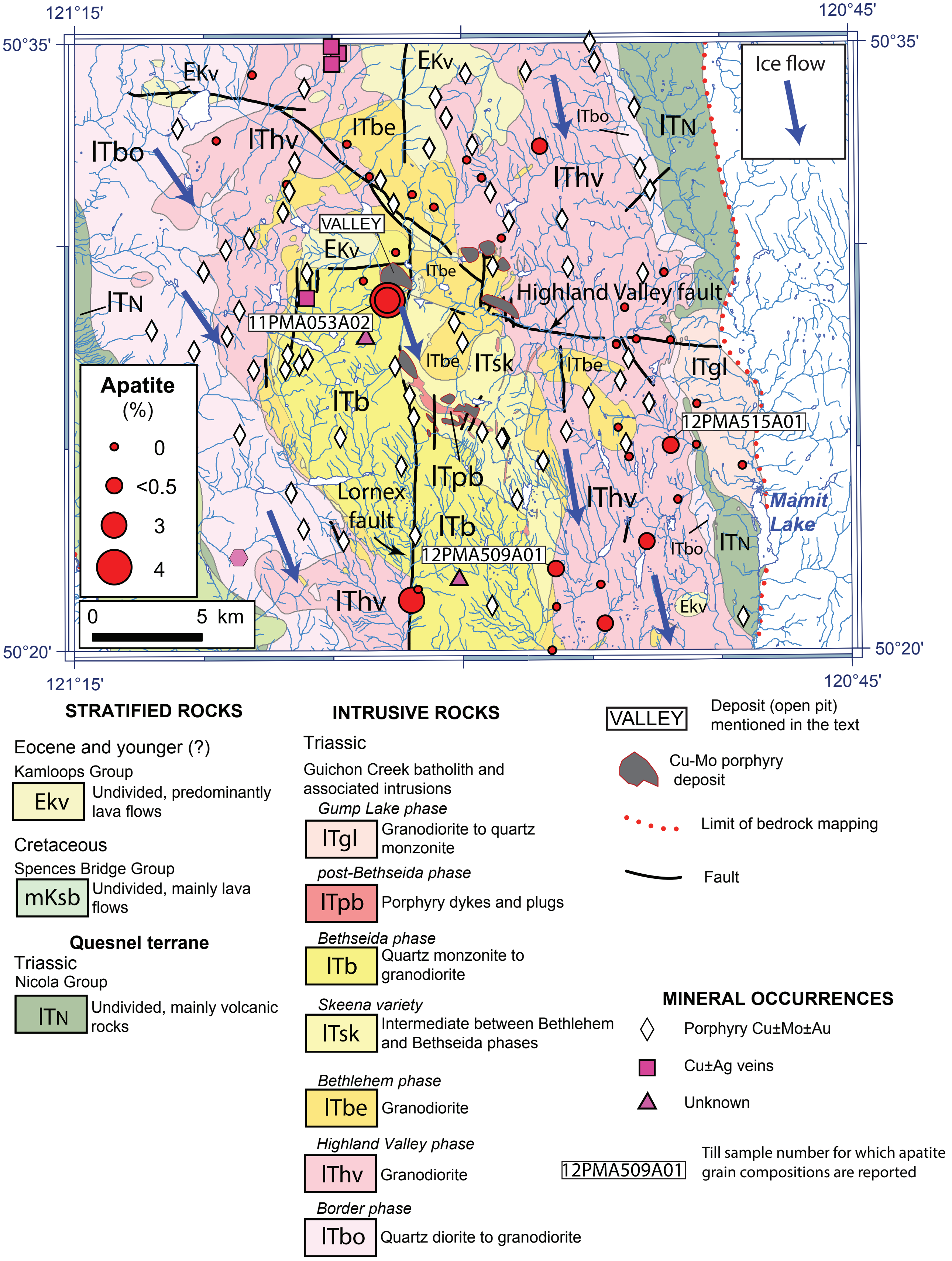

Fig. 2. Geology, sample locations, generalized ice-flow directions, mineral occurrences and apatite content of till (0.25–0.50 mm, >3.2 g·cm^{-3}, >1.0 A fraction), Highland Valley calc-alkaline porphyry Cu-Mo district. Geology after McMillan (1985) and McMillan et al. (2009).

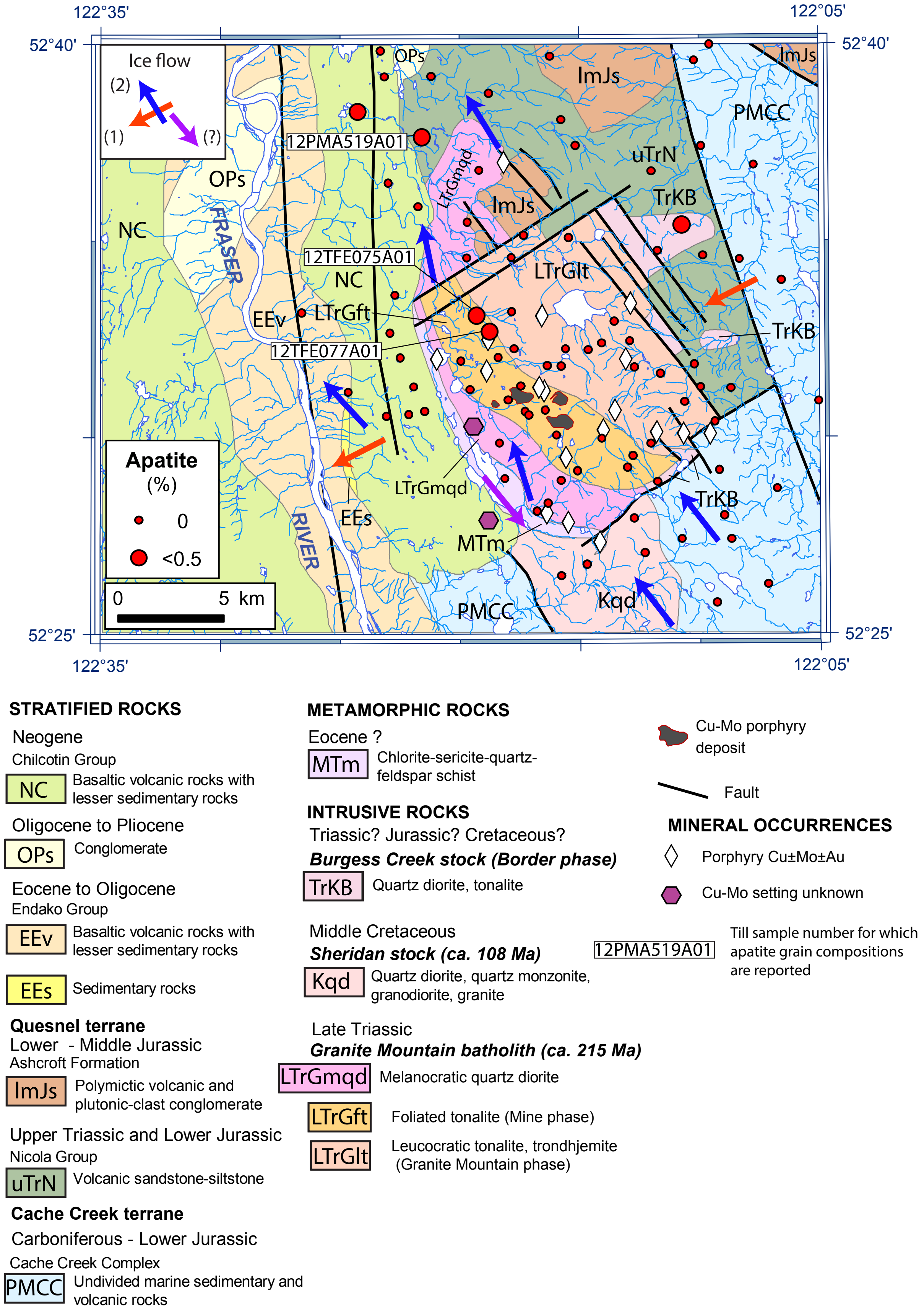

Fig. 3. Geology, sample locations, generalized ice-flow directions, mineral occurrences and apatite content of till (0.25–0.50 mm, >3.2 g·cm^{-3}, >1.0 A fraction), Gibraltar calc-alkaline porphyry Cu-Mo mine area. Geology after Ash et al. (1999a) and Schiarizza (2014).

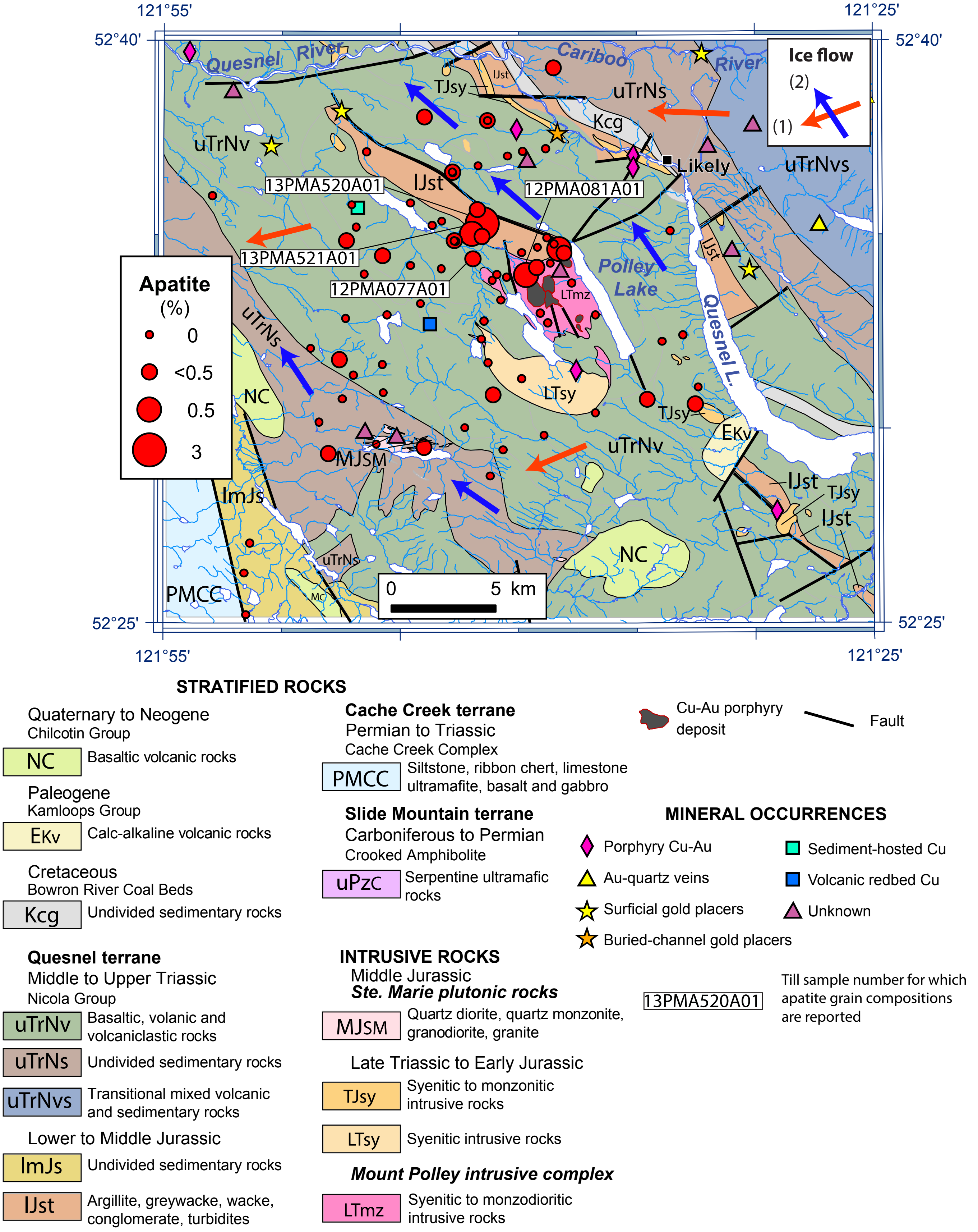

Fig. 4. Geology, sample locations, generalized ice-flow directions, mineral occurrences and apatite content of till (0.25–0.50 mm, >3.2 g·cm^{-3}, >1.0 A fraction; after Hashmi et al., 2015), Mount Polley alkalic porphyry Cu-Au mine area. Geology after Logan et al. (2007a, 2010).

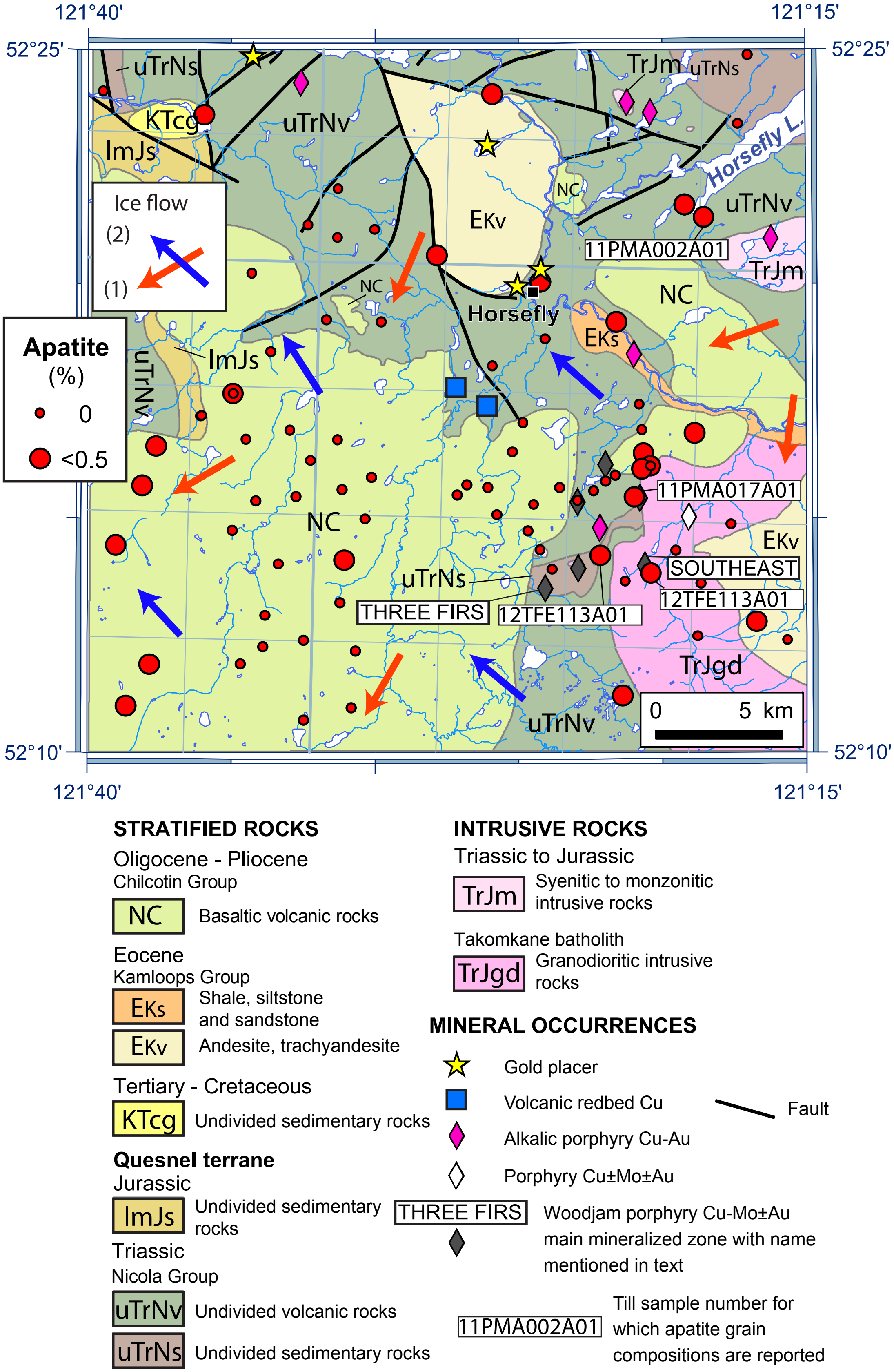

Fig. 5. Geology, sample locations, generalized ice-flow directions, mineral occurrences and apatite content of till (0.25–0.50 mm, >3.2 g·cm^{-3}, >1.0 A fraction), Woodjam high-K, calc-alkaline porphyry Cu-Mo±Au developed prospect area. Geology after Logan et al. (2007b, 2010) and Schiarizza et al. (2009a, b).

Casselman et al., 1995). A total of 1615.16 million tonnes of ore grading 0.40% Cu and 0.010% Mo have been processed from the Highland Valley deposits, with reserves (as of December 2012) estimated to be 697 million tonnes grading 0.29% Cu and 0.008% Mo (Byrne et al., 2013). The major deposits are at the intersection of the Lornex and Highland Valley faults (Fig. 2; Casselman et al., 1995). The main ore minerals include chalcopyrite, bornite and molybdenite. Regional hydrothermal vein alteration, with green sericite, chlorite and epidote, is prominent at Highland Valley, extending approximately 10 km to the northwest, north and southeast from the intersection of the Lornex and Highland Valley faults (see Figure 14 in Casselman et al., 1995). Sedimentary and volcanic rocks of the Kamloops Group (Eocene) locally overlie the northern part of the intrusion. Apatite has been reported as an accessory mineral in both K-silicate and muscovite alteration zones, and in fresh Guichon batholith intrusive rocks (Casselman et al., 1995; Bouzari et al., 2011b).

3.2. Gibraltar

The Granite Mountain batholith (Late Triassic) hosts the Gibraltar calc-alkaline porphyry Cu-Mo deposit, approximately 50 km north of Williams Lake, and comprises an intrusive complex made up of diorite to quartz diorite, tonalite, and trondhjemite (Fig. 3; Drummond et al., 1973, 1976; Bysouth et al., 1995; Ash et al., 1999a, b; Ash and Riveros, 2001; Schiarizza, 2014, 2015). Most of the mineralization is hosted by foliated tonalite (Mine phase) in the core of the intrusion (van Straaten et al., 2013). Supergene ore was mined from two of the pits in the initial phases of mining (Rotherham et al., 1972). Combining the past production and the current resources, the Gibraltar deposit comprises 1.22 billion tonnes of ore with a Cu grade of 0.317% and an estimated Mo grade of 0.010% (van Straaten et al., 2013). The predominant ore minerals include chalcopyrite and molybdenite, and chalcocite in the supergene zones (Ash et al., 1999b).

Sutherland Brown (1974), Drummond et al. (1976), and Bysouth et al. (1995) originally assigned host rocks of the Granite Mountain batholith to the Cache Creek oceanic terrane (Late Paleozoic to Early Mesozoic), unlike other porphyry deposits in southern British Columbia, which are in the Quesnel terrane. However, part of the batholith and the mineralization underwent ductile deformation and were metamorphosed to greenschist grade, which raised questions as to whether the mineralization is a porphyry style (e.g., Sutherland Brown, 1974; Ash et al., 1999b). Recently, Schiarizza (2014, 2015) found that the Granite Mountain batholith cuts the Nicola Group, the defining stratigraphic unit of Quesnel terrane, and concluded that it occupies a panel of Quesnel terrane that was juxtaposed against Cache Creek rocks along later faults. Ductile strain features in the ore bodies imply that mineralization was before or during deformation (van Straaten et al., 2013). Apatite was reported in the tonalite of the Mine phase (Ash and Riveros, 2001).

3.3. Mount Polley

The Mount Polley intrusive complex (Late Triassic), made up of diorite, monzodiorite, monzonite, and plagioclase porphyry, hosts the Mount Polley alkalic porphyry Cu-Au deposit, approximately 45 km east of the Gibraltar mine (Fig. 4). The complex cuts sedimentary and volcanic rocks of the Nicola Group (Middle to Late Triassic; Hodgson et al., 1976; Logan et al., 2007a, b, 2010). Production includes 452 million pounds of Cu, 0.695 million ounces of Au, and 2.2 million ounces of Ag from 80 million tonnes of ore (Rees, 2013). The reserves (as of January 2013) were estimated to be 93 million tonnes grading 0.297% Cu, 0.299 g/t Au, and 0.620 g/t Ag (Rees, 2013). Three Cu-Au mineralized zones are present at Mount Polley, one in the core of the intrusion, a second in the southeast sector, and a third, higher-grade zone, in the northeast sector. Part of the mineralization is spatially associated with hydrothermal breccias cemented by magnetite and disseminated chalcopyrite. The main ore minerals include chalcopyrite and bornite. Gold forms inclusions in pyrite and chalcopyrite (Fraser et al., 1995; Pass, 2010). Apatite is present in both the calc-potassic alteration zone (‘alteration zone III’ of Rees, 2013) and fresh monzonite (Bouzari et al., 2011b). Celis et al. (2014) also reported ubiquitous subhedral to anhedral apatite grains (0.5 mm) in intrusive rocks and alteration zones.

3.4. Woodjam

Satellite intrusions about 1.5 km north of the Takomkane batholith (Late Triassic to Early Jurassic) host six porphyry-style mineralized zones comprising the Woodjam developed prospect, about 45 km east of Williams Lake and 35 km southeast of the Mount Polley mine (Fig. 5; Logan et al., 2007a, b, 2010; Schiarizza et al., 2009a, b; Schroeter, 2009). The intrusive rocks vary from monzodiorite to quartz monzonite (Schroeter, 2009). The batholith cuts sedimentary and volcanic rocks of the Nicola Group (Late Triassic). Mineralization in the camp is mainly of the high-K, calc-alkaline porphyry Cu-Mo±Au variety (Vandekerkhove et al., 2014) similar to that at Red Chris (Rees et al., 2015) and Kemess South (Duuring et al., 2009). Texturally variable quartz monzonite intrusions host the Southeast Zone deposit and display alteration and mineralization typical of calc-alkaline porphyry deposits, although other mineralized zones such as the Deerhorn prospect may have some alkalic porphyry features (del Real et al., 2014). Epidote-chlorite-pyrite, illite and hematite overprint both pervasive K-feldspar-biotite-magnetite alteration assemblage in the centre of the Southeast Zone and albite±epidote assemblage along its margins. The latter also occurs near the contact between the Takomkane batholith and rocks of the Nicola Group (del Real et al., 2014). Inferred resources for three of the mineralized zones are 221.7 million tonnes of ore with grades ranging from 0.22 to 0.31% Cu and from 0.26 to 0.49 g/t Au (Sherlock et al., 2013; Sherlock and Trueman, 2013; del Real et al., 2014). Ore minerals include chalcopyrite with minor bornite, and small amount of molybdenite and native copper. Gold is mainly related to chalcopyrite and bornite and is only visible microscopically (Sherlock et al., 2013; see Figure 19 in Vandekerkhove et al., 2014). A large portion of the Woodjam area is underlain by volcanic and subordinate sedimentary rocks of the Kamloops (Eocene) and Chilcotin (Oligocene to Pliocene) groups (Fig. 5). Potassic, propylitic, and tourmaline alteration styles are present at Woodjam, but apatite has not been reported in any of the alteration zones or fresh intrusive rocks.

4. Samples

We examined 147 apatite grains recovered from 14 till samples and 2 mineralized bedrock samples at Highland Valley, Gibraltar, Mount Polley, and Woodjam (Table 1). From each area, three to four till samples were selected, mainly down-ice from known mineralization (for details of the till sampling, see Plouffe and Ferbey, 2015d). Figures 2–5 show the percentage of apatite in the 0.25–0.50 mm, >3.2 g·cm^{-3}, >1.0 A (non-magnetic) fraction of till samples, determined, along with other porphyry indicator minerals (e.g., visible gold, chalcopyrite, epidote), as part of the TGI-4 studies (Plouffe et al., 2013a; Plouffe and Ferbey, 2015a, d). These mineralogical data guided our selection of till samples for this study.

The two rock samples from the Woodjam Southeast Zone (Table 1) are mineralized quartz monzonites from Gold Fields Limited's diamond-drill hole SE11-27. Sample 258404 is from the 115.8 to 117.0 m depth interval; sample 258405 is from the interval 117.0 to 119.0 m. Based on a binocular microscope description of the rock fragments (2–6 mm; S.A. Averill, pers. comm. 2014), the rocks are massive and porphyritic to equigranular. The porphyritic varieties contain 15-30% euhedral, albite-twinned plagioclase and 5% biotite phenocrysts (1–2 mm) in a fine-grained (0.15–0.50 mm) granophyric groundmass made up of 65% alkali feldspar (perthite), 30% quartz, 0–5% biotite, 0–1% magnetite, and 0–0.2% pyrrhotite. The equigranular quartz monzonite is medium grained (1–2 mm) and consists of 40% euhedral, fresh and commonly albite-twinned plagioclase, 35% interstitial, anhedral, perthitic alkali feldspar, 20% quartz, and 5% biotite. The rocks are stained by hematite and contain 1–2% chalcopyrite along hairline fractures, and lining or filling fractured quartz veinlets (1–5 mm wide). Biotite is mostly altered to chlorite, and calcite (1%) fills younger, unmineralized fractures. Other accessory minerals, in the heavy mineral concentrates (HMC), include apatite > pyrite > chalcocite > molybdenite > titanite ≈ rutile. Bornite (0.10–0.25 mm) and visible gold (15–125 μm) were identified in the panned fraction of heavy mineral concentrates.

We also examined thin sections from five rock samples from the Gibraltar mine (not listed in Table 1) to determine if apatite separation would be feasible. Although rare apatite is in four of these, we failed in our attempt to recover apatite grains from two Gibraltar mine samples (mineralized, sheared tonalite, sample SVA75-7-14.6, and massive quartz diorite, sample GSC-2). Based on a binocular microscope description of hand specimens (S.A. Averill, pers. comm. 2014) and petrographic examinations, the sheared tonalite is a medium-grained (2–4 mm), augen schist made up of pervasively sericitized and saussuritized plagioclase (40%), quartz (30%), and retrograde chlorite after biotite (30%) with trace leucoxene after primary titanite. Chlorite forms folded wisps and locally continuous seams separating quartz and feldspar augen. Chalcopyrite (1%) and trace amounts of molybdenite, pyrite, and rutile are restricted to the chlorite±quartz±albite veins or seams and are similarly foliated and folded, possibly suggesting that mineralization was before deformation. Carbonate and epidote are also common. Rare euhedral to subhedral apatite (0.10–0.28 mm by 0.08–0.14 mm) forms clusters in chlorite±quartz±albite veins, with traces of chalcopyrite and rutile, and along feldspar-quartz boundaries. The massive quartz diorite is an equigranular, medium-grained (1–2 mm) rock made up of euhedral, pervasively sericitized and saussuritized plagioclase (70%), chlorite (20%), and quartz (10%), with traces of titanite, pyrite, sphalerite, chalcopyrite, and covellite. Traces of supergene azurite and malachite coat fractures. Rare, mostly euhedral apatite (0.10–0.26 mm by 0.04–0.12 mm) occurs along quartz-chlorite and plagioclase-epidote-chlorite boundaries. Zircon is an accessory mineral in both rocks.

5. Methods

5.1. Sample preparation

Apatite separation and identification were completed at Overburden Drilling Management Ltd. (Ottawa, ON) following the protocol adopted at the Geological Survey of Canada (Plouffe et al., 2013c). Blind quality controls, including blank samples from a weathered granite (to monitor laboratory cross-contamination), field duplicate samples (to test sampling site variability), and spiked samples (to evaluate the reproducibility of the heavy mineral separation and the identification of indicator minerals) were inserted. Till samples (~10 kg) were processed to recover heavy minerals (>2.8 g·cm^{3} fraction) as follows. First, the samples were wet sieved to the <2 mm fraction and concentrated by gravity on a shaking table. Shaking table concentrates were then separated with methylene iodide diluted with acetone into 2.8–3.2 g·cm^{-3} and >3.2 g·cm^{3} fractions. Next, ferromagnetic minerals were removed with a hand magnet before re-sieving into three size fractions (0.25–0.50 mm, 0.5–1.0 mm, and 1–2 mm). The 0.25–0.50 mm fraction was processed on a Carpco High-Intensity Lift electro-magnetic separator (model MLH) set at 0.6, 0.8 and 1.0 A. Apatite grains (Fig. 6) were hand-picked from the 0.25–0.50 mm, >3.2 g·cm^{-3}, >1.0 A fraction under a binocular microscope. Apatite contents in this fraction of the till and rock samples vary from trace (<0.5%) to 3% (Table 1, Fig. 6). No apatite grains were observed in the 0.5–2.0 mm fraction of the till samples, nor was apatite found in the finer (0.18–0.25 mm) and 2.8–3.2 g·cm^{-3} fractions of the two rock samples from Gibraltar. Because apatite has a density that varies from 3.17 to 3.23 g·cm^{-3} (Berry et al., 1983), it is typically recovered from the 2.96–3.32 g·cm^{-3} fraction (Mao et al., 2015), but we analyzed only grains recovered from the >3.2 g·cm^{-3} fraction, a separation adopted in other apatite studies (Normandeau et

Table 1. Summary of estimated apatite contents in till and bedrock samples, recovered apatite grains, and the analyses performed on apatite grains.

N	Sample[1]	Northing[2]	Easting[2]	Type	Apatite[3] %	Grains picked	EDS checked	Grains used	EMPA	LA-ICP-MS	Area	Main deposit type
1	12PMA519A01	5830965	543370	Till	<0.5 (8)	8	8	8	7	5	Gibraltar	Calc-alkaline porphyry Cu-Mo
2	12TFE075A01	5822574	546002	Till	<0.5 (~30)	25	15	10	10	8		
3	12TFE077A01	5821831	546631	Till	<0.5 (~50)	27	7	10	10	10		
4	11PMA053A02	5593549	638475	Till	3 (~600)	30	5	10	10	10	Highland Valley	Calc-alkaline porphyry Cu-Mo
5	12PMA509A01	5581422	646465	Till	<0.5 (16)	16	16	10	6	6		
6	12PMA515A01	5587223	651586	Till	<0.5 (5)	5	5	5	5	5		
7	12PMA077A01	5825591	588194	Till	<0.5 (~30)	23	23	10	9	9	Mount Polley	Alkalic porphyry Cu-Au
8	12PMA081A01	5824874	590751	Till	0.5 (~150)	33	3	10	10	10		
9	13PMA520A01	5827291	588619	Till	0.5 (~100)	27	17	10	10	10		
10	13PMA521A01	5826794	588125	Till	0.5 (~100)	25	25	10	10	10		
11	11PMA002A01	5802049	615155	Till	<0.5 (~30)	20	20	10	9	7	Woodjam	High-K, calc-alkaline porphyry Cu-Mo±Au
12	11PMA017A01	5790909	612652	Till	<0.5 (~40)	25	25	10	10	10		
13	12TFE113A01	5787923	613380	Till	<0.5 (~30)	21	6	10	10	9		
14	12TFE116A01	5788577	611357	Till	<0.5 (10)	10	10	10	10	8		
15	258404	5788122	613121	Rock [4]	<0.5 (~50)	22	7	11	11	11	Woodjam (Southeast Zone)	High-K, calc-alkaline porphyry Cu-Mo±Au
16	258405	5788122	613122	Rock [4]	1 (~200)	27	7	10	10	10		
17	MAD standard			Fragments of large crystal				10	10	26*	First Mine Discovery, Madagascar	Pegmatite
18	DUR standard			Fragments of large crystal				7	7	26	Cerro de Mercado, Durango	Kiruna-type

Footnotes:

[1] Details of the samples from the regions of the Gibraltar, Highland Valley and Mount Polley mines, and the Woodjam deposits and prospects in south-central British Columbia can be found in Plouffe et al. (2013a) and Plouffe and Ferbey (2015a, d); for details on Madagascar and Durango reference apatites, see Thomson et al. (2012) and Young et al. (1969).

[2] NAD83, UTM Zone 10 coordinates.

[3] Estimated apatite content (%) and total number of apatite grains (in parentheses) in the heavy mineral concentrate, i.e. 0.25–0.50 mm, >3.2 $g \cdot cm^{-3}$, >1.0 A (non-magnetic) fraction.

[4] Core samples of mineralized quartz monzonites from Gold Fields Limited's diamond-drill hole SE11-27; sample 258404 from 115.8 to 117.0 m depth below surface; sample 258405 from 117.0 to 119.0 m depth below surface. See text for details.

* Includes 14 new LA-ICP-MS analyses of fragments in a grain mount used by Mao et al. (2015).

EDS = number of grains confirmed by energy dispersive X-ray spectrometry, EMPA = number of electron microprobe analyses, LA-ICP-MS = number of analyses by laser ablation - inductively coupled plasma mass spectrometry; one EMPA and LA-ICP-MS analysis each per grain, except for some large fragments of Durango and Madagascar apatites on which multiple LA-ICP-MS analyses were performed.

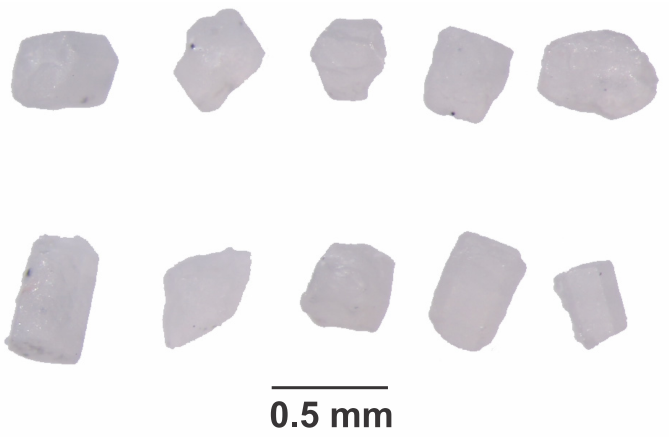

Fig. 6. Colourless apatite grains recovered from till in the southern part of the Highland Valley study area.

al., 2014). More than 50% of the recovered apatite grains were confirmed on a scanning electron microscope (SEM) equipped with an energy-dispersive X-ray spectrometer (EDS) (Table 1).

To evaluate the reproducibility of apatite identification in the mineral concentrates, 21 concentrates were resubmitted with new numbers. Table 2 presents results from these replicates, which demonstrate good reproducibility of apatite identification at the processing laboratory. Throughout this report, the percentage of apatite in till samples refers to the amount of apatite in the 0.25–0.50 mm, >3.2 g·cm^{-3}, >1.0 A fraction.

Selected apatite grains (up to 10 per sample) were mounted in epoxy mounts for electron microprobe analysis (EMPA) and laser ablation-inductively coupled plasma mass spectrometry (LA-ICP-MS). Fragments of two large natural apatite crystals from Cerro de Mercado, Durango (Young et al., 1969) and First Discovery Mine, Madagascar (Thomson et al., 2012), used as the matrix-matched standards by Mao et al. (2015), were mounted together with the apatite grains (Table 1). The grain mounts were polished by hand using BuehlerMet II lapping papers P400, P1200, P4000, and Buehler lapping powder 1 µm and 0.3 µm. All grain mounts were rinsed thoroughly using deionized water between polishing steps and cleaned in an ultrasonic bath for about 30 minutes before analysis. EMPA and LA-ICP-MS analyses were performed using procedures for apatite developed by Mao et al. (2015), which are summarized below.

5.2. EMPA analysis

All electron probe analyses (EMPA) were performed on a fully automated Cameca SX50 electron microprobe equipped with four wavelength-dispersive spectrometers at the Department of Earth, Ocean and Atmospheric Sciences, University of British Columbia (UBC). Apatite grains (n = 147; Table 1) were analyzed using the wavelength-dispersion mode with a 15 kV excitation voltage, 10 nA beam current, and 10 µm beam diameter. Flat surface regions, free of any inclusions or fractures, where possible, were chosen for the beam spot (one per grain). Although some apatites display complex zoning in cathodoluminescence or back-scattered electron (BSE) imaging, reflecting magma mixing, intracrystalline diffusion or complex dissolution-reprecipitation (e.g., Tepper and Kuehner, 1999; Bath et al., 2006; Liaghat and Tosdal, 2008; Bouzari et al., 2011b), the examined apatite grains lacked prominent internal zonation in BSE. Peak and background counting times were 20 seconds for F, S, Cl and Fe, and 10 seconds for Na, Si, P and Ca. Fluorine was always measured on the first cycle because of migration during analysis. The background values for F were fixed and based on the first measured result. Data reduction was done using the 'PAP' Φ(ρZ) method (Pouchou and Pichoir, 1985). The following standards (locations), X-ray lines, and crystals were used: topaz (Topaz Valley, UT, U.S.A.), FKα, TAP; albite (Rutherford Mine, Amelia County, VA, U.S.A.), NaKα, TAP; diopside (C.M. Taylor Company, locality unknown), SiKα, TAP; apatite (Wilberforce, ON, Canada), PKα, PET; barite (C.M. Taylor Company, locality unknown), SKα, PET; scapolite (Lot 32, Con. XVII, Monmouth, ON, Canada), ClKα, PET; apatite (Wilberforce, ON, Canada), CaKα, PET; and synthetic fayalite (Los Alamos National Laboratory, NM, U.S.A.), FeKα, LIF.

The detection limits, based on counting statistics, were 0.85 wt.% for F, 0.05 wt.% for Na, 0.04 wt.% for Si and S, 0.08 wt.% for P, 0.03 wt.% for Cl, 0.06 wt.% for Ca, and 0.07 wt.% for Fe. The relative precision (2σ), based on the analyses of Durango (n = 7) and Madagascar (n = 10) apatites, was 1% for Ca, 4% for P, from 11% to 40% for F, Si, S, and Cl, and from 23% to >100% for Na and Fe (Appendix 1, Rukhlov et al., 2016). Therefore, Na and Fe values close to the EMPA detection limit are semi-quantitative to qualitative.

5.3. LA-ICP-MS analysis

All laser ablation analyses (LA-ICP-MS) were performed using He as the carrier gas and a New Wave UP-213 coupled to a Thermo X-Series II (X7) quadrupole ICP-MS at the School of Earth and Ocean Sciences, University of Victoria (SEOS). We adopted the LA-ICP-MS analytical and data reduction procedures from Mao et al. (2015). Apatite grains (n = 138; Table 1) were analyzed with a 30 µm laser spot diameter, a pulse rate of 10 Hz, and measured fluence from 8.5 to 12.5 J·cm^{-2}. A pre-ablation warm-up of 5 seconds was used to avoid unstable laser energy at the beginning of each ablation. All LA-ICP-MS spectra were recorded for 120 s, including ~30 s gas blank before ablation started, 60 s during ablation, and ~30 s post ablation. At least 60 s of gas flushing was allowed between analyses. The ICP-MS was optimized to maximize sensitivity and minimize oxide formation. Forward RF was 1400 watts. The dwell time was 3 ms for all REE elements and 5 ms for all other elements.

We used ^{43}Ca as the internal standard for LA-ICP-MS calibration and Ca concentrations determined directly by EMPA. NIST glasses 611, 613, and 615 (Jochum et al., 2011) were used as the external calibration standards. Madagascar and Durango apatites were analyzed 26 times each (multiple

Table 2. Results of apatite identification in replicate pairs of heavy mineral concentrates from till samples.

Sample	Apatite (%)	Sample	Apatite (%)
11PMA018A1	0	12PMA560A1	0
11PMA100A1	0	12PMA705A1	0
11PMA053A1	4	12PMA564A1	0
11PMA10011	4	12PMA706A1	0
11PMA010A1	<0.5	12PMA567A1	0
11PMA102A1	<0.5	12PMA707A1	0
11PMA017A1	<0.5	12PMA571A1	0
11PMA103A1	<0.5	12PMA708A1	0
11PMA003A2	<0.5	12PMA585A1	0
11PMA104A1	<0.5	12PMA709A1	0
11PMA051A1	0	12PMA586A1	0
11PMA105A1	<0.5	12PMA710A1	<0.5
12PMA515A1	<0.5	12PMA588A1	0
12PMA700A1	0	12PMA711A1	0
12PMA528A1	0	12PMA595A1	0
12PMA701A1	0	12PMA712A1	0
12PMA535A1	0	12PMA596A1	0
12PMA702A1	0	12PMA713A1	0
12PMA547A1	0	12PMA606A1	0
12PMA703A1	0	12PMA714A1	0
12PMA559A1	0		
12PMA704A1	0		

Heavy mineral concentrates (HMC) are 0.25-0.50 mm, >3.2 g·cm^{-3}, >1 A (non-magnetic) fraction of till samples.

analyses per crystal fragment) to monitor accuracy and precision of the analyses (Appendix 1, Rukhlov et al., 2016). Appendix 3 (Rukhlov et al., 2016) provides complete analytical data for the standards. A typical session started with NIST glasses 615, 613, and 611, followed by Madagascar and Durango apatites, then 6 unknowns, and then all five standards were repeated. During offline data reduction, time-resolved count rates were carefully checked and any spectra with spikes, indicating possible inclusions, were discarded. The data reduction procedure for each element included: 1) selecting the time intervals for the background and signal region of each spectrum; 2) calculating the mean CPS (count per second) of these intervals; 3) correcting for background of the signal CPS; 4) normalizing to the internal standard; 5) correcting for drift using a linear drifting factor determined from repeat analysis of NIST 611; 6) calibrating using sensitivities for each element determined from the initial analyses of NIST 615, 613 and 611 in each load (i.e. analytical session) to obtain the concentration value of each element.

We analyzed 30 elements by LA-ICP-MS in the apatite grains. The instrument detection limit (IDL) has been estimated as:

$$\text{IDL} = 3\sigma\ \text{background}/\text{Sensitivity}$$

where 3σ background is the 3 times standard deviation of the signal for a given element collected before ablation for each sample (gas blank), and Sensitivity is the slope of calibration curve (i.e. internal-standard– and drift–corrected cps versus ‘true’ concentration for external standards) determined from NIST 615, 613 and 611 for a given element in each session. Appendix 1 (Rukhlov et al., 2016) provides the detection limits per element, which varied between individual analyses due to instrument background variations. The detection limits are <200 ppm for Mn, As and Ce; <75 ppm for Mg, Ti, Sr, Y, Zr, La, and Nd; <25 ppm for Cu, Zn, Mo, Ba, Pr, Sm, Gd, and Dy; <9 ppm for V, Rb, Nb, Eu, Yb, Pb, and Th; and <5 ppm for Lu, W, and U. Although Si and P were analyzed by both EMPA and LA-ICP-MS, the latter results are less precise and, therefore, will not be discussed further.

The experimental precision was determined by repeat analyses (n = 26) of NIST glasses 611 and 613 and the Madagascar and Durango apatites. Based on NIST 613 and Durango and Madagascar apatites, the relative precision (2σ) varies from 3% to 18% for elements with concentrations >10 ppm, except for As in NIST glass 613 (52%), and from 10% to 110% for elements with lower concentrations (Appendix 1, Rukhlov et al., 2016). For NIST 611, with order of magnitude higher concentrations of all elements than those in NIST 613, the precision is 2%-12% for all elements. The precision for NIST 615 (from 15% to 96%) shows that values close to the instrument detection limit are semi-quantitative to qualitative (Appendix 1, Rukhlov et al., 2016). Our results for the Madagascar and Durango apatites (Appendix 1, Rukhlov et al., 2016) are in excellent agreement with those reported by Mao et al. (2015).

6. Results

6.1. Apatite in till

Given that the abundance of apatite in till was determined in the heavy mineral fraction (>3.2 g·cm^{-3}), our results represent only the partial abundance of apatite in till. Regardless, it demonstrates that apatite survives glacial transport and post-glacial weathering and that its composition is worth studying to fingerprint a mineralized source.

Our limited dataset from the Highland Valley area shows that most samples taken from tills overlying the Guichon Creek batholith lack apatite or contain only trace amounts (<0.5%; Fig. 2). Two samples immediately down ice from porphyry Cu-Mo mineralization in the Valley open pit and one sample in the southern part of the study area contain 3%–4% apatite. The two samples near the Valley pit also contain large numbers of chalcopyrite (2300 and 4600 grains per 10 kg of bulk material <2 mm) in the 0.25–0.50 mm, >3.2 g·cm^{-3} fraction and high Cu contents (987 and 1056 ppm) in the clay-sized fraction (<0.002 mm) of till (Plouffe et al., 2013a; Plouffe and Ferbey, 2015d).

Most till samples from the Gibraltar area (Fig. 3) lack apatite grains. However, five contain trace (<0.5%) apatite, four of which were collected northwest of the deposit, i.e. down-ice with respect to the glacial maximum ice flow. The fifth, from till overlying the Burgess Creek quartz diorite-tonalite stock, is 9 km to the northeast of the deposit. The paucity of apatite grains in the tills reflects low abundances in local bedrock (Mao et al., 2015), and makes it difficult to define down-ice dispersion from the mineralized or altered bedrock (Fig. 3). On the other hand, Cu and Mo concentrations in till clay fractions, and chalcopyrite grain abundances in till, are elevated near the Gibraltar deposit compared to tills derived from surrounding barren bedrock (Plouffe et al., 2011, 2013a; Plouffe and Ferbey, 2015a, d). The resulting amoeboid dispersion pattern may reflect the three directions of ice flow in the region (Plouffe and Ferbey, 2015d).

Hashmi et al. (2015) characterized the distribution of apatite grains in till of the Mount Polley mine area (Fig. 4). Although most of the till samples lack apatite or contain only trace amounts (<0.5%), some samples to the northwest (down-ice) of the Mount Polley deposit contain up to 3% apatite. Hashmi et al. (2015) suggested that tills with more abundant apatite were derived from the alteration zones associated with Mount Polley alkalic porphyry Cu-Au mineralization. Other indicator minerals (chalcopyrite, visible gold grains, and jarosite) are also dispersed northwest of the mineralized zones (Hashmi et al., 2015).

Tills at Woodjam contain only trace amounts (<0.5%) of apatite (Fig. 5). Similar to the Gibraltar region, the spatial distribution of apatite grains in till does not clearly define dispersion from known mineralized zones. The distribution of chalcopyrite and epidote grains in till and Cu concentrations in till clay fraction better indicate dispersion from the porphyry mineralization and alteration zones; grain counts and Cu values are elevated within 2 km of the mineralized zones compared to those farther away (Ferbey and Plouffe, 2014; Plouffe and Ferbey, 2015a, d).

6.2. Apatite chemistry

A total of 147 apatite grains, excluding the Durango and Madagascar apatites, were analyzed by EMPA (Table 3; see Appendix 2 in Rukhlov et al., 2016 for full analytical results). Of these grains, 138 were analyzed by LA-ICP-MS. A few grains were too small or thin for the LA-ICP-MS analysis. Results below detection limits (DL) were arbitrarily set to half of the DL value per element for plotting. Results <DL in the whole data set constitute 1% for Mg, La, Ce, Th, and U; 4% to 6% for V, As, and Ba; 8% to 9% for Zn, Rb, and Zr; 12% to 19% for Ti, Cu, and W; 45% for Mo; 59% for Nb; and 0% for the remaining elements. Results from abnormal spectra or below abnormally high detection limits for individual elements in some analyses are meaningless and therefore were discarded. Nulls (i.e. discarded values) due to poor results in the whole data set comprise 1% to 3% for Cu, Zn, Mo, Ba, Pb, and Th; 4% for Cl, 7% to 9% for Na, Si, As, and Rb; 14% to 21% for S, Fe, and Ti, and 0% for the rest of the elements.

6.2.1. Major elements

Calcium, phosphorous, fluorine, and chlorine are the main constituents in calcium phosphate apatites with the general formula $Ca_5(PO_4)_3(F,Cl,OH)$ (Pan and Fleet, 2002; Hughes and Rakovan, 2015). Calcium occupies two distinct cation sites (M polyhedra) in the apatite structure: two 9-fold coordinated (CaO_9) M1 and three 7-fold coordinated (CaO_6X_1) M2 sites per half the unit cell, where X = F^-, Cl^-, OH^-, CO_3^{2-}, and O^{2-} anions in columns along the edges of the unit cell. Phosphorous is in a third, tetrahedral (PO_4) cation site (Hughes and Rakovan, 2015).

Table 3. EMPA and LA-ICP-MS data summary for apatite grains.

	Highland Valley till				Gibraltar till				Mount Polley till				Woodjam till				Woodjam SE Zone bedrock			
	Min	Max	Mean	N	Min	Max	Mean	N	Min	Max	Mean	N	Min	Max	Mean	N	Min	Max	Mean	N
EMPA																				
SiO_2 (wt%)	0.021	0.369	0.147	21	0.024	0.433	0.108	26	0.015	0.864	0.495	39	0.006	0.225	0.062	30	0.054	0.246	0.137	20
FeO (wt%)	0.007	0.261	0.069	21	0.009	0.265	0.074	27	0.001	0.204	0.066	39	0.002	0.219	0.065	39	0.010	0.142	0.072	21
CaO (wt%)	53.38	55.04	54.20	21	53.08	55.25	54.36	26	53.43	55.34	54.46	38	54.11	55.69	54.92	36	53.43	55.16	54.43	21
Na_2O (wt%)	0.014	0.317	0.130	21	0.014	0.181	0.102	27	0.041	0.389	0.178	39	0.007	0.120	0.057	39	0.020	0.178	0.095	21
P_2O_5 (wt%)	39.78	42.79	41.26	21	39.66	43.66	41.37	24	38.68	43.12	40.38	39	39.61	42.65	41.51	33	39.18	42.66	41.45	21
SO_3 (wt%)	0.046	0.471	0.183	21	0.020	0.318	0.127	27	0.267	1.115	0.783	39	0.005	0.215	0.075	39	0.046	0.307	0.127	21
F (wt%)	0.13	3.54	2.35	21	1.68	4.07	2.91	27	0.73	5.44	3.18	39	1.16	5.27	2.89	39	1.38	3.71	2.26	21
Cl (wt%)	0.056	1.642	0.283	18	0.010	0.156	0.050	22	0.011	1.121	0.300	38	0.003	0.905	0.176	26	0.222	0.894	0.503	21
LA-ICP-MS																				
Mg (ppm)	24	494	135	21	3.1	142	38	23	21	711	229	39	<3	240	67	34	41	253	168	21
Ti (ppm)	<0.2	4.8	1.2	18	0.03	15	1.2	22	0.17	7.9	1.8	36	0.04	32	2.2	28	<0.2	4.1	1.2	17
V (ppm)	1.3	93	14	21	0.06	57	8.5	23	<0.2	323	151	39	0.02	58	9.4	34	8.5	24	18	21
Mn (ppm)	518	8057	2999	21	45	6067	1973	23	275	1890	670	39	52	3332	622	34	768	1747	1392	21
Cu (ppm)	<0.2	94	5.6	20	<0.2	8.2	1.5	23	<0.2	10	1.5	38	<0.2	9.1	0.70	34	0.07	2.7	0.60	19
Zn (ppm)	0.02	3.4	0.80	20	0.03	3.2	0.55	23	<0.1	3.8	0.87	39	<0.1	21	1.4	34	<0.1	2.9	0.57	21
As (ppm)	<1	42	7.7	21	0.15	34	11	22	<1	158	30	38	0.37	1191	236	26	<1	42	18	20
Rb (ppm)	<0.01	0.26	0.079	21	0.0003	0.13	0.062	21	<0.01	0.71	0.16	34	<0.01	1.3	0.20	33	0.010	0.32	0.11	19
Sr (ppm)	179	563	335	21	158	5733	548	23	167	3640	1854	39	140	3440	485	34	139	298	258	21
Y (ppm)	270	2032	749	21	3.1	2051	899	23	129	848	550	39	12	1699	551	34	386	1617	986	21
Zr (ppm)	0.09	2.0	0.47	21	0.002	0.92	0.30	23	0.08	9.2	3.2	39	<0.02	1.1	0.13	34	<0.02	0.83	0.25	21
Nb (ppm)	<0.01	0.035	0.009	21	<0.01	0.033	0.010	23	<0.01	0.12	0.019	39	<0.01	0.14	0.014	34	<0.01	0.031	0.008	21
Mo (ppm)	0.012	0.36	0.071	21	<0.04	0.32	0.048	23	<0.04	0.62	0.15	38	<0.04	0.15	0.045	34	<0.04	0.69	0.11	19
Ba (ppm)	<0.1	5.9	1.1	20	<0.1	2.7	0.55	23	0.66	50	13	39	0.013	7.7	0.86	34	0.29	1.6	0.75	21
La (ppm)	59	1569	567	21	0.37	1084	300	23	0.77	1461	594	39	0.066	694	121	34	195	1006	551	21
Ce (ppm)	444	4524	1706	21	<1	3037	1059	23	2.9	2637	1206	39	<1	1533	296	34	533	2345	1337	21
Pr (ppm)	94	593	238	21	0.031	342	163	23	0.35	279	147	39	0.20	195	41	34	74	283	168	21
Nd (ppm)	402	2365	1012	21	0.34	1255	758	23	3.8	969	597	39	0.66	807	184	34	348	1111	691	21
Sm (ppm)	78	476	211	21	0.26	348	190	23	1.3	191	123	39	0.71	161	58	34	93	239	152	21
Eu (ppm)	8.1	44	19	21	0.084	119	20	23	0.37	48	30	39	0.13	45	10	34	9.3	18	12	21
Gd (ppm)	71	399	180	21	0.18	377	183	23	3.4	186	124	39	1.2	266	82	34	102	238	157	21

Table 3. Continued.

	Highland Valley till				**Gibraltar till**				**Mount Polley till**				**Woodjam till**				**Woodjam SE Zone bedrock**			
	Min	Max	Mean	N	Min	Max	Mean	N	Min	Max	Mean	N	Min	Max	Mean	N	Min	Max	Mean	N
Dy (ppm)	44	331	133	21	0.21	346	150	23	8.7	140	93	39	1.1	271	93	34	71	231	141	21
Yb (ppm)	16	244	57	21	0.65	147	63	23	14.3	66	34	39	0.58	158	40	34	25	155	83	21
Lu (ppm)	2.3	38	8.4	21	0.12	22	9.0	23	2.0	9.8	4.5	39	0.035	25	6.0	34	3.5	23	12	21
W (ppm)	0.007	0.36	0.12	21	0.032	1.2	0.33	23	0.0003	0.84	0.10	39	<0.02	4.5	0.47	34	<0.02	0.35	0.055	21
Pb (ppm)	0.9	2.5	1.5	21	0.14	20	5.4	23	1.1	25	2.8	39	0.20	47	8.3	34	0.37	4.6	1.8	20
Th (ppm)	1.0	80	15	21	<0.05	34	4.9	23	0.012	26	13	37	0.006	28	5.3	34	1.3	42	20	21
U (ppm)	1.9	55	11	21	0.095	23	5.8	23	0.090	16	5.5	39	0.024	26	7.4	34	2.8	25	11	21
Eu/Eu*	0.15	0.55	0.33	21	0.15	1.5	0.39	23	0.36	1.0	0.74	39	0.11	1.1	0.47	34	0.18	0.34	0.25	21
Ce/Ce*	1.0	1.5	1.2	21	0.98	1.6	1.2	23	0.89	1.4	1.0	39	0.23	3.8	1.2	34	1.0	1.2	1.1	21
$(Ce/Yb)_{CN}$	1.3	27	14	21	0.027	17	5.1	23	0.024	16	10.2	39	0.006	47	5.9	34	2.6	14	5.0	21
$(La/Sm)_{CN}$	0.22	3.7	1.8	21	0.031	4.0	1.0	23	0.36	5.2	3.0	39	0.058	6.0	1.3	34	1.3	3.6	2.3	21
$(Gd/Yb)_{CN}$	0.85	5.2	3.5	21	0.23	13	2.7	23	0.086	4.4	3.2	39	0.014	39	3.8	34	1.2	3.5	1.7	21
∑LREE	596	6685	2511	21	1.0	4463	1522	23	4.0	4377	1947	39	1.6	2422	458	34	803	3633	2056	21
∑MREE	559	3264	1423	21	0.87	1974	1151	23	8.8	1352	874	39	2.7	1132	334	34	553	1549	1013	21
∑HREE	71	613	198	21	0.97	515	222	23	46	202	131	39	1.9	406	139	34	99	406	236	21
∑REE	1680	10322	4132	21	2.9	6052	2895	23	59	5932	2952	39	6.7	3697	932	34	1512	5519	3305	21

Footnote:
EMPA = electron microprobe analysis; **LA-ICP-MS** = laser ablation-inductively coupled plasma mass spectrometer analysis; **N** = total number of values; **wt.%** = weight per cent; **ppm** = parts per million.

$Ce/Ce^* = Ce_{CN}{*}(La_{CN}{*}Pr_{CN})^{-0.5}$, $Eu/Eu^* = Eu_{CN}{*}(Sm_{CN}{*}Gd_{CN})^{-0.5}$; normalization (CN) values from Lodders (2010).

∑LREE = La + Ce + Pr, ∑MREE = Nd + Sm + Eu + Gd, ∑HREE = Dy + Yb + Lu, ∑REE = La + Ce + Pr + Nd + Sm + Eu + Gd + Dy + Yb + Lu; all totals are multivariate (i.e. all variables must be not null).

Apatite grains from till at Woodjam show slightly higher CaO contents (54.11–55.69 wt.%) than those in apatite grains from mineralized quartz monzonite at the Woodjam Southeast Zone and till at the Highland Valley, Gibraltar, and Mount Polley deposit areas, which contain 53.08–55.34 wt.% CaO (Table 3). Phosphorous contents in apatite grains from the Mount Polley area (38.68–43.12 wt.% P_2O_5) are slightly lower than those of apatite grains from other areas (39.18–43.66 wt.% P_2O_5) (Table 3). Bouzari et al. (2011b) attributed increased CaO contents (by ~1%) of apatites in altered rocks relative to those of pristine apatites in fresh rocks from porphyry Cu-Mo-Au deposits to the loss of minor and trace elements from apatite during hydrothermal alteration.

Accurate analysis of apatite by EMPA, particularly for F and Cl, is difficult due to anisotropy effects (Stormer et al., 1993; Raudsepp, 1995). About 14% of our apatite analyses (Appendix 2, Rukhlov et al., 2016) have F concentrations (up to 5.44 wt.%) in excess of the maximum F content of ~3.77 wt.% in end-member fluorapatite (Webster and Piccoli, 2015), indicating problematic EMPA analyses, or excess F bound to CO_3^{2-} (Piccoli and Candela, 2002). Without measured CO_3^{2-}, we made no attempt to calculate the concentration of F bound to the assumed carbonate anion. Furthermore, relatively high EMPA detection limit (0.85 wt.%) and poor precision (34-38% at 2σ level) render the F results largely semi-quantitative compared with more precise data for other elements. Precision for Cl (14–33% at 2σ level) is generally better and the detection limit is lower (~0.03 wt.%) than those for F (see Appendices 1 and 3, Rukhlov et al., 2016).

Figure 7a shows F-Cl-OH variability in the halogen-site of the examined apatite grains. The mole fractions of fluor-, chlor- and hydroxylapatite end members were calculated directly from the measured F and Cl concentrations, assuming that F^-, Cl^-, and OH^- fill the X-site and that CO_3^{2-}, O^{2-}, other anions, and vacancies in this site are not significant. For discussion of the methods to calculate the mole fractions in apatite, we refer the reader to Piccoli and Candela (2002). Apatite grains in this study contain between 3.4–100 mol% F, 0–73 mol% OH, and <24 mol% Cl, indicating mainly F–OH exchange (Fig. 7a), partly due to the similarity in radius for F^- and OH^- as compared to Cl^- (Piccoli and Candela, 2002; Kusebauch et al., 2015). Most of the apatite grains show molar F/Cl ratios of >1, except for one apatite grain from till in the eastern part of the Highland Valley area (sample 12PMA515A01) with 1.64 wt.% Cl and 0.13 wt.% F (Fig. 7a; Table 3). Apatite grains from the Gibraltar deposit area and most apatite grains at Highland Valley, Woodjam and Mount Polley contain <0.32 wt.% Cl. However, some apatite grains at Woodjam (from Southeast Zone mineralized quartz monzonite and till sample 11PMA017A01) and Mount Polley (mainly from till sample 13PMA521A01) have generally higher Cl contents, ranging from 0.17 to 1.12 wt.% (Table 3; Fig. 7a).

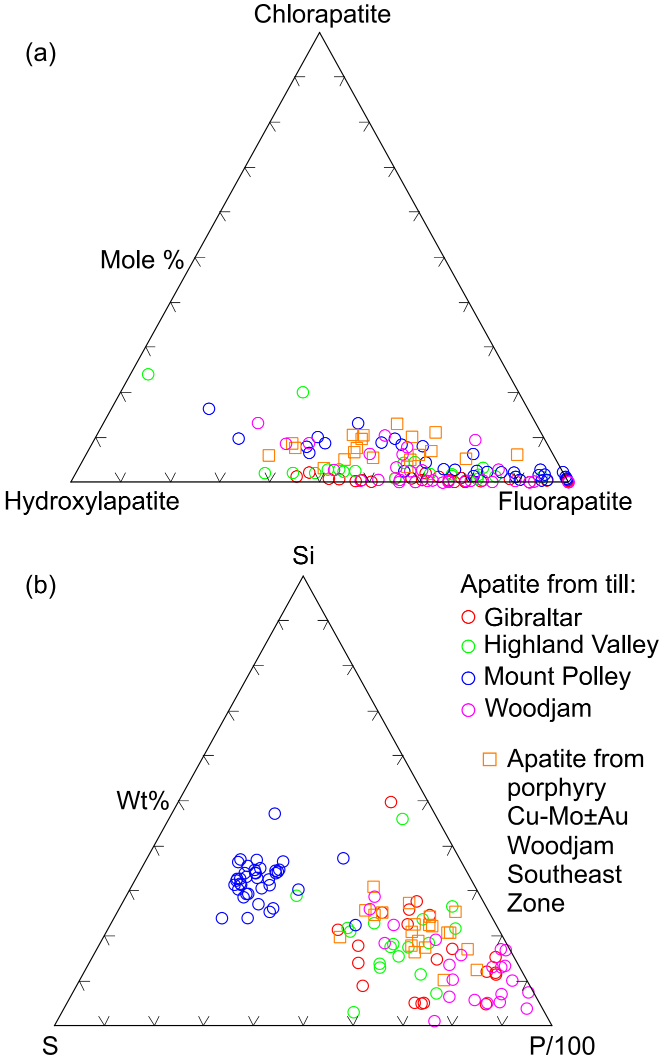

Fig. 7. Ternary plots for apatite. **a)** Fluorapatite-Chlorapatite-Hydroxylapatite recast as mole fractions so that F, Cl, and OH fill the halogen-site in apatite; X_F^{Ap} (fluorapatite mole fraction) = $C_F^{Ap}/3.767$, X_{Cl}^{Ap} (chlorapatite mole fraction) = $C_{Cl}^{Ap}/6.809$, X_{OH}^{Ap} (hydroxylapatite mole fraction) = $1 - X_F^{Ap} - X_{Cl}^{Ap}$, where C_F^{Ap} = F concentration in wt.% in apatite, C_{Cl}^{Ap} = Cl concentration in wt.% in apatite (after Piccoli and Candela, 2002); for a few analyses with $(X_F^{Ap} + X_{Cl}^{Ap}) > 1$, the fluorapatite and chlorapatite mole fractions were normalized to unity. **b)** P/100-Si-S cations (in wt.%) in the tetrahedral site.

6.2.2. Minor and trace elements

Calcium phosphate apatite structure can incorporate most elements in minor or trace amounts. The tetrahedral site occupied by P^{5+} can incorporate Si^{4+} and redox-sensitive As^{5+}, V^{5+}, and S^{6+} (Pan and Fleet, 2002; Hughes and Rakovan, 2015). The M1 and M2 polyhedra in the apatite structure can accommodate substitution by many divalent cations (e.g., Mg, Mn, Fe, Cu, Zn, Sr, Ba, and Pb), with many substituents showing a strong site preference (e.g., Sr for M2 site, whereas Mn for M1 site; Pan and Fleet, 2002; Hughes and Rakovan, 2015). Because Mn^{2+} substitutes directly for Ca^{2+} due to similarities in charge and ionic radius, apatite incorporates Mn^{2+} in preference to Mn^{3+} or Mn^{4+} (Marshall, 1988; Pan and Fleet, 2002). Therefore, elevated Mn contents in apatite may reflect high Mn^{2+}/Mn in a reduced magma, or low abundances of other Mn-bearing phases such as biotite, amphibole, and magnetite in highly fractionated, felsic magmas, which forces Mn substitution into apatite (Sha and Chappell, 1999; Belousova et al., 2002; Piccoli and Candela, 2002; Miles et al., 2014). Trivalent rare-earth elements (REE) and Y, and tetravalent U and Th substitute in the M1 and M2 sites via coupled substitution reactions to maintain charge balance (e.g., $Na^+ + REE^{3+} \leftrightarrow 2Ca^{2+}$ and $Si^{4+} + REE^{3+} \leftrightarrow P^{5+} + Ca^{2+}$; Rønsbo, 1989; Pan and Fleet, 2002; Hughes and Rakovan, 2015). Light REEs (LREE) prefer the M2 site, whereas heavy REEs (HREE) prefer the M1 site, and the middle REEs (MREE), with ionic radii close to that of Nd, show no site preference (Hughes and Rakovan, 2015).

Unlike other REEs, Ce and Eu can exist in two valency states (Ce^{3+} and Ce^{4+} and Eu^{2+} and Eu^{3+}) due to redox sensitivity and thus behave differently than adjacent REEs (Roeder et al., 1987; Smythe and Brenan, 2015). Because apatite structure shows strong preference for Eu^{3+} relative to Eu^{2+} (Prowatke and Klemme, 2006; Cao et al., 2012), the lack of significant depletions in Eu relative to adjacent REEs or 'Eu anomalies' (quantified as $Eu/Eu^* = Eu_{CN}/(Sm_{CN} \cdot Gd_{CN})^{-0.5}$ using chondrite normalization, Lodders, 2010) may indicate low Eu^{2+}/Eu^{3+} in oxidized magmas, or early crystallization of feldspars, which preferentially incorporate Eu^{2+} (Budzinski and Tischendorf, 1989; Sha and Chappell, 1999; Belousova et al., 2002; Piccoli and Candela, 2002; Tollari et al., 2008; Miles et al., 2014). Likewise, because Ce^{3+} is more compatible in apatite than Ce^{4+} (Miles et al., 2014), enrichments in Ce relative to the adjacent REEs or 'Ce anomalies' ($Ce/Ce^* = Ce_{CN}/(La_{CN} \cdot Pr_{CN})^{-0.5}$ using chondrite normalization, Lodders 2010) may reflect high Ce^{3+}/Ce^{4+} in reduced magmas. Unlike Eu anomalies, Ce anomalies are insensitive to feldspar fractionation. However, Ce/Ce* variations in apatite also may result from partitioning of Ce in other accessory phases such as monazite, fluorite and zircon, that in turn partly reflects redox conditions (Ballard et al., 2002; Belousova et al., 2002; Piccoli and Candela, 2002; Colombini et al., 2011; Miles et al., 2014).

The relationships between Si, S and P, with a median atomic Si/S ratio of about 1.0, in the analyzed apatite grains (Fig. 7b) suggest the substitution $Si^{4+} + S^{6+} \leftrightarrow 2P^{5+}$ (Harada et al., 1971; Piccoli and Candela, 2002). A weak positive correlation also exists between Na and S contents (correlation coefficient = 0.62) of the examined apatite grains, suggesting the coupled substitution reaction $S^{6+} + Na^+ \leftrightarrow P^{5+} + Ca^{2+}$ (Kreidler and Hummel, 1970), although apparently less significant than the Si-S-P substitution. Both SiO_4^{2-} and Na^+ can be incorporated in the apatite structure as charge compensators via the coupled substitutions of REE^{3+} and Y^{3+} for Ca^{2+} (Rønsbo, 1989; Sha and Chappell, 1999; Pan and Fleet, 2002; Hughes and Rakovan, 2015), and can be removed out of the apatite-fluid system in preference to REEs during metasomatic alteration of apatite by a Na- and Si-poor fluid such as $H_2O \pm CO_2$, HCl, H_2SO_4, or KCl brine (Harlov, 2015). Sulfur substitution for P in apatite is redox sensitive, readily incorporating S^{6+} in oxidizing conditions, unlike sulfide-bound S^{2-} in reducing conditions (Sha and Chappell, 1999; Piccoli and Candela, 2002; Webster and Piccoli, 2015).

Spider diagrams (Fig. 8) show minor- and trace-element compositions of analyzed apatite grains normalized to the average apatite composition of Mao et al. (2015). Figure 9 provides chondrite-normalized REE profiles for these apatite grains. Figures 8 and 9 also show average apatite compositions from porphyry deposits after Mao et al. (2015). The distribution of minor and trace elements and the chondrite-normalized REE profiles, characterized by a relative enrichment in LREEs with $(Ce/Yb)_{CN} < 47$, $(La/Sm)_{CN} < 6.0$, and $(Gd/Yb)_{CN} < 5.2$, strong to weak negative Eu anomalies (Eu/Eu* = 0.11–0.87), and lack of significant Ce anomalies (Ce/Ce* = 0.89–1.30), for most of the analyzed apatite grains (Figs. 8 and 9; Table 3) are consistent with the findings of Mao et al. (2015) on apatites from porphyry deposits. Trace-element abundances of apatites at Woodjam cover much wider range of values (up to 4 orders of magnitude) than those from the Highland Valley, Gibraltar and Mount Polley (Figs. 8 and 9).

Apatite grains from mineralized bedrock at the Woodjam Southeast Zone show Si, S, Mn, V, and other trace-element abundances and the chondrite-normalized REE patterns typical of apatites from the calc-alkaline porphyry Cu±Mo±Au deposits studied by Mao et al. (2015). However, apatite grains from till at Woodjam display much wider variations in trace-element composition, ranging from concentration levels similar to those in Southeast Zone bedrock, with the LREE-enriched chondrite-normalized REE patterns, to less than detection limit for most trace elements, with LREE-depleted chondrite-normalized REE patterns (Figs. 8d and 9d; Table 3). A few apatite grains at Highland Valley, Gibraltar and Mount Polley also show similar LREE-depleted chondrite-normalized REE patterns (Figs. 9a-c), coupled with depletions in Na, Mg, Si, S, Cl, V, Mn, As, Y, Zr, Ba, Th and U (Figs. 8a-c), which are distinct from the average apatite compositions from these deposits as reported by Mao et al. (2015). These depletions probably reflect hydrothermal alteration, which is extensive near the Woodjam mineralized zones (Schiarizza et al., 2009a; del Real et al., 2014; Vandekerkhove et al., 2014) and resulted in metasomatic removal of S, Cl and many trace elements, with LREEs in preference to HREEs and Y, from primary apatite (e.g., Harlov, 2015). The metasomatic removal of LREEs from these apatite grains also resulted in the extreme variations in their Ce/Ce* (0.23–3.8) and elevated Eu/Eu* (up to 1.5) (Fig. 9; Table 3). Bouzari et al. (2011b) also attributed a decrease in Na_2O, SiO_2, SO_3, Cl, and MnO contents and MnO/FeO of apatites in altered rocks relative to those of apatite in fresh rocks from several porphyry Cu-Mo-Au deposits to the metasomatic removal of these elements from primary apatite. Below we summarize some of the characteristic trace-element features of apatite grains from the four porphyry deposit areas.

Apatite grains from all four study areas have similar FeO contents (from <0.09 to 0.27 wt.%) and most have similar levels of Cu (<10 ppm) and Zn (<3.8 ppm), except for one grain from till sample 11PMA017A01 at Woodjam (21 ppm Zn) and one

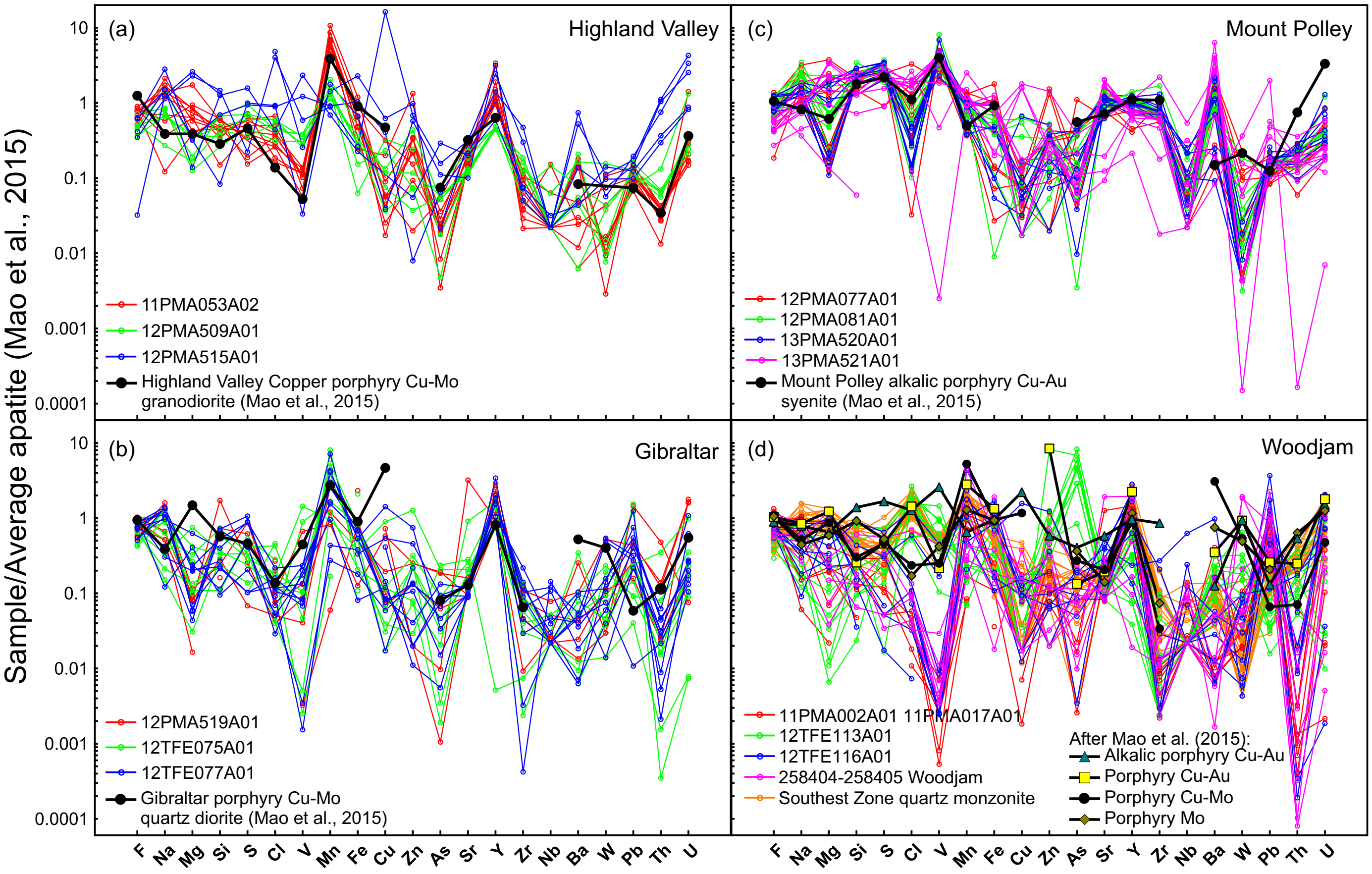

Fig. 8. Spider diagrams for apatite grains normalized to the average apatite of Mao et al. (2015). **a)** Highland Valley porphyry district. Average apatite from mineralized granodiorite, Highland Valley Copper calc-alkaline porphyry Cu-Mo deposit (after Mao et al., 2015) is shown for comparison. **b)** Gibraltar mine area. Average apatite from mineralized quartz diorite, Gibraltar calc-alkaline porphyry Cu-Mo deposit (after Mao et al., 2015) is shown for comparison. **c)** Mount Polley mine area. Average apatite from mineralized syenite, Mount Polley alkalic porphyry Cu-Au deposit (after Mao et al., 2015) is shown for comparison. **d)** Woodjam developed prospect area. Average apatite compositions for alkalic porphyry Cu-Au and calc-alkaline porphyry Cu-Au, porphyry Cu-Mo, and porphyry Mo deposits (after Mao et al., 2015) are shown for comparison.

from till sample 12PMA515A01 at Highland Valley (94 ppm Cu; Table 3). Apatite grains from Mount Polley have higher Ti contents (0.17–7.9 ppm) and those from Gibraltar have lower Ti (0.03–2.3 ppm) relative to other apatites in this study, except for one grain from Gibraltar (till sample 12TFE075A01) with 15 ppm Ti and one from Woodjam (sample 12TFE113A01) with 32 ppm Ti. Tungsten concentrations are higher in apatite grains from till at Gibraltar (up to 1.2 ppm W) and Woodjam (up to 4.5 ppm W) than those of other studied grains. Average Rb contents in apatite in till from Mount Polley (0.16 ppm) and Woodjam (0.20 ppm) are similar, and higher than those of apatite grains from bedrock at the Woodjam Southeast Zone and from till at the Highland Valley and Gibraltar deposits (Table 3). Only ~30% of the analyzed apatite grains have detectable Nb >0.01 ppm (up to 0.14 ppm), and ~47% of the apatite grains have detectable Mo >0.04 ppm (up to 0.69 ppm; Appendix 2, Rukhlov et al., 2016).

The trace-element chemistry of apatite grains from the Mount Polley deposit area is distinct relative to other apatite grains examined here. At Mount Polley (Fig. 7b; Table 3), apatite grains contain much higher SO_3 (mostly 0.56–1.12 wt.%) and SiO_2 (mostly 0.32–0.86 wt.%) than those from other deposit areas (<0.47 wt.% SO_3 and <0.43 wt.% SiO_2), in agreement with the findings of Bouzari et al. (2011b). Most have higher Na_2O (0.04–0.39 wt.%), Sr (1107–3640 ppm), Mg (21–711 ppm), V (80–323 ppm), Ba (0.7–50 ppm), Zr (1.9–9.2 ppm), Mo (up to 0.62 ppm), Nb (up to 0.12 ppm), and low Mn (275–1890 ppm), Y (129–848 ppm), and total HREE (∑HREE = Dy + Yb + Lu; 46–202 ppm) contents relative to those from other areas (Table 3). Bouzari et al. (2011b) also reported MnO abundances below EMPA detection limit (~0.15 wt.% MnO) for most of apatites in rocks from the Mount Polley deposit. Their chondrite-normalized REE patterns show higher LREE/MREE, with $(La/Sm)_{CN}$ ranging mostly from 2.0 to 5.2, much higher Eu/Eu* (mostly 0.50–0.99), and lower Ce/Ce* (mostly 0.89–1.03; Fig. 9; Table 3). Apatite grains from the Mount Polley deposit area also have higher As contents (mostly 5.5–158 ppm) compared with others analyzed here, except for those with anomalously high As from till sample 11PMA017A01 at Woodjam (Fig. 8; Table 3). Three apatite grains at Mount Polley (all from sample

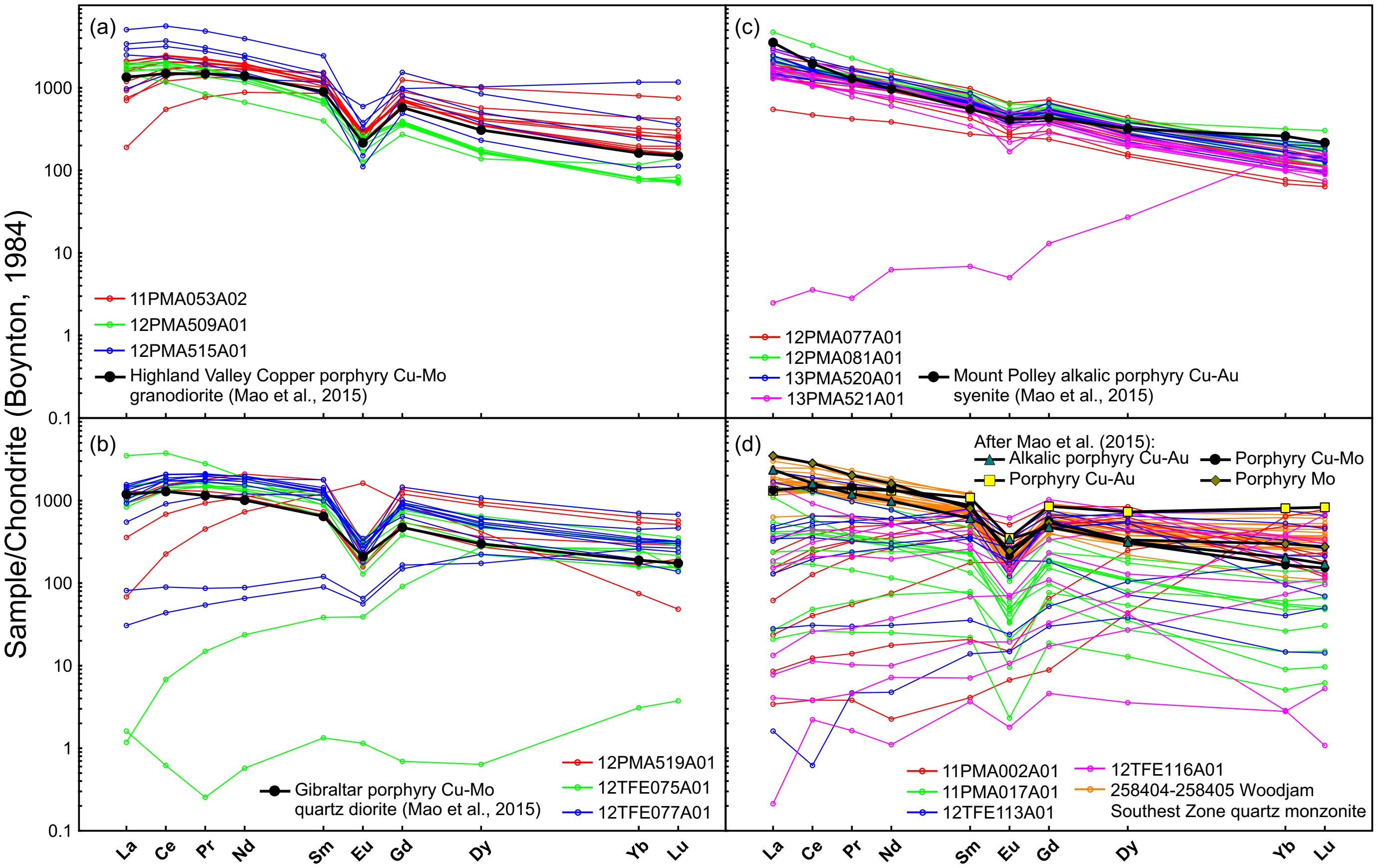

Fig. 9. Chondrite-normalized rare earth element plots for apatite grains, using normalization of Boynton (1984). **a)** Highland Valley porphyry district. Average apatite from mineralized granodiorite, Highland Valley Copper calc-alkaline porphyry Cu-Mo deposit (after Mao et al., 2015) is shown for comparison. **b)** Gibraltar mine area. Average apatite from mineralized quartz diorite, Gibraltar calc-alkaline porphyry Cu-Mo deposit (after Mao et al., 2015) is shown for comparison. **c)** Mount Polley mine area. Average apatite from mineralized syenite, Mount Polley alkalic porphyry Cu-Au deposit (after Mao et al., 2015) is shown for comparison. **d)** Woodjam developed prospect area. Average apatite compositions for alkalic porphyry Cu-Au and calc-alkaline porphyry Cu-Au, porphyry Cu-Mo, and porphyry Mo deposits (after Mao et al., 2015) are shown for comparison.

13PMA521A01) with much lower Sr (167–350 ppm) and V (<73.5 ppm), including two grains with low Zr (<0.75 ppm) and one grain with low LREE/HREE (e.g., $(Ce/Yb)_{CN}$ = 0.02; $(La/Sm)_{CN}$ = 0.36), low Eu/Eu* of 0.36, and high Ce/Ce* of 1.4, were likely metasomatically altered. The lack of significant Eu anomalies, coupled with the elevated S, V, and As but low Mn contents and low Ce/Ce* values, of apatite grains at Mount Polley relative to those from other deposit areas are indicative of the highly oxidized nature of the magmatic-hydrothermal systems that form alkalic porphyry Cu-Au deposits (e.g., Lang et al., 1995; Mao et al., 2015).

Apatite grains from till at the Highland Valley and Gibraltar calc-alkaline porphyry Cu-Mo deposits are distinguished by their much higher Mn (mostly 518–8057 ppm) and total MREE (∑MREE = Nd + Sm + Eu + Gd; mostly 559–3264 ppm) contents, higher Ce/Ce* values (0.98–1.30), and by lower As contents (<1–42 ppm) relative to those from other porphyry deposit areas in this study (Figs. 8 and 9; Table 3). Notably, all apatite grains from till sample 11PMA053A02, immediately down-ice from the Highland Valley Copper deposit (Fig. 2), have the highest Mn concentrations, ranging from 3635 to 8057 ppm, in agreement with the range of values (334–10934 ppm Mn) reported by Bouzari et al. (2011b) and Mao et al. (2015) for apatites in the ore rocks at the Highland Valley porphyry Cu-Mo deposits. Compared to apatite from the Gibraltar deposit area, most grains at Highland Valley have higher Na_2O (0.01–0.32 wt.%), Mg (24–494 ppm), and $(Ce/Yb)_{CN}$ (1.3–27), and lower Nb (<0.03 ppm) and Pb (<2.5 ppm) contents. In addition, apatite grains from till near the eastern margin of the Guichon Creek batholith (sample 12PMA515A01; Fig. 2), have the highest total REE (∑REE = La + Ce + Pr + Nd + Sm + Eu + Gd + Dy + Yb + Lu; 3555–10322 ppm), Th (21–80 ppm), and U (10–55 ppm) contents (Table 3).

For the Woodjam deposits and prospects, apatite grains from till sample 11PMA017A01 contain the highest As concentrations (121–1191 ppm; Fig. 8d; Table 3). Mao et al. (2015) attributed high As contents in some hydrothermal ore deposits (e.g., Kiruna-type) to sedimentary sources that had accumulated As. Because the till sample with As-rich apatite grains overlies volcano-sedimentary Nicola Group rocks in contact with the Takomkane batholith, the elevated values may record precipitation from melt or hydrothermal fluid that scavenged As from the Nicola Group. Apatite grains from till at Woodjam have generally lower Zr contents (average 0.13 ppm) than those from the Southeast Zone mineralized rocks (average 0.25 ppm Zr). Compared to grains from other areas, apatite from till at Woodjam have highly variable abundances of trace elements, with generally high Pb (0.2–47 ppm) and Rb (up to 1.3 ppm) contents, and the low SO_3 (<0.22 wt.%), SiO_2 (<0.23 wt.%), Na_2O (<0.17 wt.%), V (<58 ppm), and ∑REE (<3697 ppm) contents (Figs. 8d and 9d; Table 3). These apatites cover the widest range of $(Ce/Yb)_{CN}$ (<0.01–47), $(La/Sm)_{CN}$ (0.06–6.0), $(Gd/Yb)_{CN}$ (0.01–39), Ce/Ce* (0.23–3.8), and Eu/Eu* (0.11–1.11) in this study (Fig. 9d; Table 3), probably reflecting the loss of LREE in preference to HREE due to the extensive hydrothermal alteration in the Woodjam area (Schiarizza et al., 2009a; del Real et al., 2014; Vandekerkhove et al., 2014). In contrast, concentrations of most trace elements in apatite grains from mineralized quartz monzonites at the Woodjam Southeast Zone show a more restricted range, with generally higher abundances than those from till at Woodjam, except for As, Sr, and Pb (Table 3; Figs. 8d and 9d). Compared to apatite grains from the Highland Valley and Gibraltar deposit areas, those from mineralized rocks at the Woodjam Southeast Zone show more restricted range of Mn (768–1747 ppm), V (mostly 15–24 ppm), Y (mostly 595–1617 ppm), $(Ce/Yb)_{CN}$ (2.6–14), $(Gd/Yb)_{CN}$ (1.2–3.5), Ce/Ce* (1.00–1.18), and Eu/Eu* (0.18–0.34) values (Table 3). These grains also have higher Mg (mostly 117-253 ppm), As (mostly 5.7–42 ppm), Mo (mostly 0.05–0.69 ppm), Th (mostly 9.6–42 ppm), U (2.8–25 ppm), and $(La/Sm)_{CN}$ (1.3–3.7), and lower W (<0.36 ppm) and MREE (559–1549 ppm) values relative to those at Highland Valley and Gibraltar (Table 3). The strong negative Eu anomalies, coupled with low S, V, As but high Mn contents and higher Ce/Ce* values, of apatite grains from Highland Valley, Gibraltar, and Woodjam are opposite to those from Mount Polley and characterize the less oxidized magmas and fluids that form typical calc-alkaline porphyry Cu±Mo±Au deposits (Mao et al., 2015).

7. Discussion

7.1. Apatite as a proxy for fluid composition in magmatic-hydrothermal systems

Apatite in most igneous rocks is commonly F-rich, whereas high-Cl apatites are found in some magmatic-hydrothermal ore systems and may record metasomatic alteration of primary fluorapatite in mafic and mantle rocks (Roegge et al., 1974; Piccoli and Candela, 2002; Patiño Douce et al., 2011; Harlov, 2015; Webster and Piccoli, 2015). Variations in relative abundances of halogens and OH in apatite reflect the behaviour of these volatiles during magma-fluid evolution (Boyce and Hervig, 2009) and depend on many factors, including the melt and/or fluid composition, P-T conditions, and the presence of other halogen-bearing phases (Harlov, 2015; Kusebauch et al., 2015). Experimental evidence also suggests that OH is more compatible than Cl in apatite regardless of the Cl concentration in the hydrothermal fluid (Kusebauch et al., 2015). Webster and Piccoli (2015) found that Cl partitioning between apatite and melt depends on both Cl content in coexisting fluid and pressure. For example, in rhyolitic melts at a temperature range of 850–950°C, Cl becomes more compatible in apatite as pressure decreases from 2000 to 275 bars (Webster and Piccoli, 2015). The Cl/F ratio in apatite decreases with decreasing temperature and as a result of volatile exsolution, which lowers H_2O/F and Cl/F ratios in the melt due to preferential partitioning of Cl into a fluid relative to F (Webster, 1990; Piccoli and Candela, 2002; Kusebauch et al., 2015). Assuming ideal mixing of F, Cl, and OH in apatite and that CO_3^{2-}, O^{2-}, other anions, and vacancies in the X site are insignificant, the calculated molar Cl/OH ratios in the studied apatite grains suggest up to 0.15 m HCl in the aqueous vapour in equilibrium with these apatites and host melts at a T = 800°C and a P = 1000 bars, using a technique after Piccoli and Candela (2002). At a higher temperature of 1000°C, the vapour phase would contain up to 0.36 m HCl. However, recent studies have shown that mixing of halogens in apatite is nonideal, with anion substitutions resulting in significant changes in the apatite structure, especially in the M2 polyhedra (Hughes and Rakovan, 2015; Webster and Piccoli, 2015). Nevertheless, the calculated molar Cl/OH ratios in the examined apatite grains agree with those of apatites from some of the producing porphyry deposits elsewhere (e.g., Yerrington, Nevada; Bingham, Utah; Henderson, Colorado; Piccoli and Candela, 2002 and references therein).

7.2. Redox and other controls on apatite trace-element chemistry

Sulfur, vanadium, manganese, arsenic, cerium and europium exist in variable oxidation states and substitute significantly in apatite. Under oxidizing conditions, some S is present as SO_4^{2-}, which can easily substitute for PO_4^{3-} in apatite, whereas under reducing conditions, S mainly occurs as S^{2-}, which forms sulfides (Sha and Chappell, 1999; Piccoli and Candela, 2002). Similarly, under oxidizing conditions, As and V readily substitute for PO_4^{3-} as AsO_4^{3-} and VO_4^{3-} in the presence of As^{5+} and V^{5+}. In contrast, under more reducing conditions, As^{3+} crystallizes as (arseno)sulfide and V^{3+} enters Fe-Mg minerals (Kutoglu, 1974; Sha and Chappell, 1999). Experiments on S partitioning between apatite and trachyandesitic and rhyolitic melts have determined that S partitions preferentially into apatite relative to melt with increasing oxygen fugacity and with decreasing pressure and S abundances in the melt (Piccoli and Candela, 2002; Webster and Piccoli, 2015 and references therein). Peng et al. (1997) found that S concentrations of apatite in intermediate rocks increase dramatically as a function of oxygen fugacity from <0.04 wt.% SO_3 in reducing conditions (quartz-fayalite-magnetite, QFM) up to 2.6 wt.% SO_3 in oxidizing conditions (magnetite-hematite, MH). Therefore, the elevated SO_3, V, and As abundances in apatite grains from the Mount Polley alkalic porphyry Cu-Au deposit area suggest crystallization in an oxidizing magmatic-hydrothermal system. In contrast, the much lower concentrations of these elements in apatite grains at the Highland Valley, Gibraltar and Woodjam deposits likely reflect the somewhat less oxidizing conditions that are typical of the calc-alkaline porphyry Cu-Mo±Au systems, consistent with the findings of Mao et al. (2015) on bedrock apatites from porphyry deposits. In addition, zoned apatites with sulfur-rich core mantled by sulfur-poor rim, documented at the Mount Polley and Galore Creek porphyry Cu-Au deposits, may indicate SO_3 depletion in the evolved host magma due to anhydrite precipitation (Bath et al., 2006; Liaghat and Tosdal, 2008).

Manganese exchange in apatite differs from that of S, V and As. Because Mn^{2+} substitutes for Ca in apatite more readily than Mn^{3+} or Mn^{4+}, which favour Fe-Mg minerals (Marshall, 1998; Pan and Fleet, 2002), elevated Mn abundances in apatite may reflect not only the degree of magma fractionation (i.e. the lack of abundant Fe-Mg phases in highly fractionated, felsic melt) but also higher Mn^{2+}/Mn in reducing conditions (Sha and Chappell, 1999; Belousova et al., 2002; Piccoli and Candela, 2002; Miles et al., 2014). Because Sr abundance in apatite is a function of whole-rock Sr, it reflects the degree of magma fractionation (Sha and Chappell, 1999; Belousova et al., 2002; Piccoli and Candela, 2002). Early fractionation of Fe-Mg minerals results in low Mg contents in apatite, whereas hydrothermal apatites may inherit high Mg contents from the breakdown of Mg-rich primary minerals (Mao et al., 2015). A weak positive correlation between Sr and Mg contents in the studied apatites (correlation coefficient = 0.41) suggests fractionation of both plagioclase and Fe-Mg minerals. Although apatite grains at Mount Polley contain much higher Sr and Mg than those from the other deposit areas, relatively poor negative correlation between Sr and Mn in the analyzed apatites (correlation coefficient = -0.29), therefore, suggests that variations in their Mn abundances mainly reflect redox control (Sha and Chappell, 1999; Belousova et al., 2002; Piccoli and Candela, 2002; Miles et al., 2014). The lower Mn contents of apatite grains from Mount Polley relative to those from Highland Valley, Gibraltar and Woodjam, in agreement with the findings of Bouzari et al. (2011b), are consistent with the more oxidized state of the former alkalic porphyry Cu-Au deposit relative to the calc-alkaline porphyry Cu-Mo±Au systems. Using empirical relationship between oxygen fugacity (fO_2) and Mn contents in apatite from andesitic to rhyolitic melts for a range of temperatures (920–660°C) after Miles et al. (2014), apatite grains in till at Mount Polley indicate an average log fO_2 = -11.2 ±0.5 (calibration error), in agreement with the average log fO_2 of -10.6 ±0.5 for bedrock apatites from Mount Polley (Mao et al., 2015), which is close to the magnetite-hematite (MH) buffer. For apatites from calc-alkaline porphyry Cu±Mo±Au deposits, the average log fO_2 values range from -12.8 ±0.6 (Woodjam Southeast Zone) to -14.1 ±0.7 (Gibraltar) and -16.3 ±1.0 (Highland Valley) in till. Apatites from mineralized rocks at the Gibraltar and Highland Valley Copper deposits (after Mao et al., 2015) yield similar average log fO_2 values of -14.3 ±0.8 and -16.2 ±1.0, respectively, indicating transition to relatively more reducing conditions (fO_2 < NNO + 1). However, without constrained temperature of apatite crystallization, these log fO_2 values, tied to a wide range of temperatures (920–660°C), provide only relative estimates of the oxidation state for these deposits.

Cerium and europium are the only REEs with two oxidation states (Ce^{3+} and Ce^{4+}; Eu^{2+} and Eu^{3+}); both Ce^{3+} and Eu^{3+} are preferred in the apatite structure (Prowatke and Klemme, 2006; Cao et al., 2012). Therefore, variations in Ce and Eu abundances relative to the adjacent REEs, expressed as Ce/Ce* and Eu/Eu*, in apatite reflect Eu^{2+}/Eu^{3+} and Ce^{3+}/Ce^{4+} in the host magmatic-hydrothermal system as controlled by both redox state and minerals such as feldspars (concentrating Eu^{2+}) and zircon, monazite, and fluorite (concentrating Ce; Budzinski and Tischendorf, 1989; Sha and Chappell, 1999; Ballard et al., 2002; Belousova et al., 2002; Piccoli and Candela, 2002; Tollari et al., 2008; Colombini et al., 2011; Miles et al., 2014). Residual feldspar retained in source rocks would have the same effect on Eu^{2+}/Eu^{3+} of the anatectic melt. Therefore, the lack of significant Eu anomalies in apatite grains from Mount Polley, in contrast to the pronounced negative Eu anomalies in those from the Highland Valley, Gibraltar and Woodjam deposits, are consistent with the more oxidized state of the former alkalic porphyry Cu-Au deposit compared to the more reduced calc-alkaline porphyry Cu±Mo±Au deposits. A positive correlation between Eu/Eu* values and Sr contents in the studied apatites (correlation coefficient = 0.73) also suggests some control of the early feldspar fractionation on Eu^{2+}/Eu^{3+} of the host magmas and fluids. Thus, the low-Sr, low-Eu/Eu* apatite grains at Highland Valley, Gibraltar and Woodjam may also imply apatite crystallization after significant plagioclase fractionation in the host melts, whereas high-Sr apatites lacking significant Eu anomalies at Mount Polley may indicate apatite crystallization before most other minerals. Unlike Eu anomalies, Ce anomalies are insensitive to feldspar fractionation. Although apatites in this study do not show significant Ce anomalies, except those with low LREE/HREE perhaps due to the metasomatic alteration (mostly apatite grains from till at Woodjam), the lower Ce/Ce* values of apatite grains from Mount Polley relative to those from Highland Valley, Gibraltar, and Woodjam are consistent with low Ce^{3+}/Ce^{4+} in the oxidized alkalic porphyry system. In addition to low fO_2, depolymerized melts and higher H_2O contents favour stabilization of Ce^{3+}, resulting in higher Ce^{3+}/Ce^{4+} relative to more polymerized or anhydrous melts (Smythe and Brenan, 2015). In summary, the systematic contrasts in abundances of redox-sensitive elements between apatite grains from the alkalic porphyry Cu-Au and the calc-alkaline porphyry Cu±Mo±Au deposits, at least in part, could be attributed to the more oxidized state of the former.

7.3. Apatite trace-element chemistry as a tool for mineral exploration

7.3.1. Method

Here we apply the stepwise discrimination approach of Mao et al. (2015) to apatite grains recovered from tills at the Highland Valley, Gibraltar, Mount Polley and Woodjam porphyry deposits, and from mineralized rocks at the Woodjam Southeast Zone. Mao et al. (2015) subdivided apatites from barren rocks versus different deposit types using a three-step series of discriminant-function diagrams, based on a discriminant projection analysis (DPA; Flury, 1997) of many apatite trace-element compositions from numerous deposits. For projecting into the discrimination diagrams, compositions of apatite grains are recast as scores of a series of linear discriminant functions (DP), calculated as a sum of constant and log10-transformed concentrations of up to 11 elements (Mg, V, Mn, Sr, Y, La, Ce, Eu, Dy, Yb, Pb, Th and U) in ppm, except for Mg which is in wt.%, multiplied by a coefficient for each element for a given function (Mao et al., 2015). The numbering of functions reflects the discrimination step, set (if more than one discrimination diagram is used for a given step), and DP function number. For example, DP2-1-1 represents discrimination step 2, the first set of functions, and the first discriminant function. First, the DP1-1 versus DP1-2 discrimination diagram separates apatites from ore deposits, carbonatites, and barren rocks. This discrimination is final for apatites from carbonatites and barren rocks. Second, only the apatites determined to be derived from ore systems in the first step are further subdivided into six main deposit types: undivided porphyry Cu-Au-Mo and epithermal Au-Ag; undivided iron-oxide copper-gold (IOCG) and Kiruna-type; skarn; orogenic Au; and orogenic Ni-Cu±PGE ore systems, using six discriminant functions (DP2-1-1 versus DP2-1-2, DP2-2-2 versus DP2-2-3, and DP2-3-1 versus DP2-3-2 diagrams). This step identifies apatites derived from the orogenic Au, orogenic Ni-Cu±PGE, and undivided IOCG and Kiruna-type deposits. Finally, only apatites determined to have affinities to porphyry Cu-Au-Mo or skarn deposits in the second step are subdivided into alkalic porphyry Cu-Au, porphyry Mo, porphyry Cu±Mo±Au, porphyry-related Cu-Au breccia, W skarn, and undivided Au±Co±Cu±Pb±Zn skarn types using DP3-1 versus DP3-2 and DP3-1 versus DP3-3 diagrams (Step 3a), which are different binary projections of the same 3-D discriminant space.

7.3.2. Discrimination of apatite grains

Equations for each DP function and their calculated scores for apatite grains analyzed in the present study are presented by Rukhlov et al. (2016). Figure 10 shows the DP1-1 versus the DP1-2 discrimination diagram for apatite grains examined here. Most of the data from each deposit area plot within the field of ore deposits, including all apatite grains from till at the Highland Valley deposit and from mineralized bedrock at the Woodjam Southeast Zone. Apatite grains from tills showing a barren-rock affinity are higher at Woodjam and Gibraltar (both ~35%) compared to Mount Polley (~14%). Two data points fall marginally in the field of carbonatites; one (sample 12PMA519A01 at Gibraltar) is at the boundary with barren rocks, the second (sample 11PMA017A01 at Woodjam) is at the boundary with ore systems (Fig. 10). Although the former apatite grain has the highest Sr in this study (5733 ppm), its low $(\text{La/Sm})_{CN}$ and a positive Eu anomaly (Rukhlov et al., 2016) suggest that it was derived from metasomatically altered barren rock. Likewise, despite being enriched in LREE (with the highest $(\text{Ce/Yb})_{CN}$ ratio in this study) the low absolute abundances of REEs (∑REE = 713 ppm) and Sr (339 ppm; Rukhlov et al., 2016) of the second apatite grain are atypical of apatites from carbonatites (>930 ppm ∑REE and >1840 ppm Sr; Mao et al., 2015).

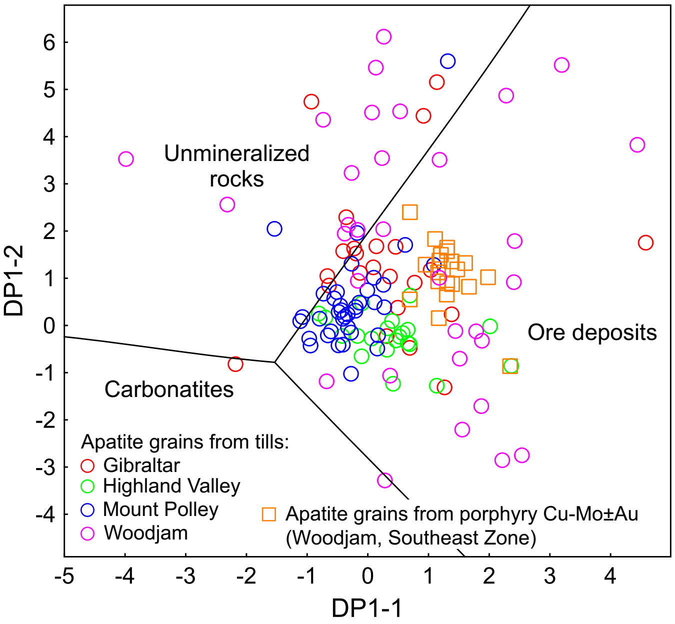

Fig. 10. The first discriminant function (DP1-1) versus the second discriminant function (DP1-2) discrimination diagram for apatite (Step 1) after Mao et al. (2015); DP1-1 = -0.06461·LogMn - 1.56·LogSr + 2.609·LogY + 0.3631·LogLa - 1.766·LogCe + 0.6243·LogEu - 3.642·LogDy + 0.7086·LogYb - 1.178·LogPb + 0.4161·LogTh + 0.963·LogU + 6.589; DP1-2 = 0.2073·LogMn - 1.035·LogSr + 15.1·LogY + 4.995·LogLa - 5.804·LogCe + 0.1741·LogEu - 8.771·LogDy - 4.326·LogYb + 2.022·LogPb - 0.6719·LogTh + 0.02096·LogU - 10.45. Variables are log10-equivalents of element concentrations in parts per million (ppm).

Apatite grains that have trace-element chemistry consistent with ore systems (Fig. 10) are plotted in the discrimination diagrams for general ore deposits (Fig. 11). Excluding Woodjam, most of the data plot within the field of undivided porphyry Cu-Mo-Au and epithermal Au-Ag deposits. Data for detrital apatite grains from Woodjam spread into the adjacent fields of skarn deposits due to their highly variable trace-element compositions, which reflect extensive hydrothermal alteration (Schiarizza et al., 2009a; del Real et al., 2014; Vandekerkhove et al., 2014). Two apatite grains from till sample 11PMA017A01 overlying the contact between the Takomkane batholith and rocks of the Nicola Group (Fig. 5) plot within the field of orogenic Ni-Cu±PGE deposits (Fig. 11). Other than monzonite stocks and dikes, mafic-ultramafic intrusions suitable for this deposit-type are unknown in the Woodjam area but occur >20 km to the south and southeast, up-ice from this till sample, along the contacts of the Takomkane batholith, (Schiarizza et al., 2009a; Sherlock et al., 2013; del Real et al., 2014). High As contents of these two apatite grains, similar to those of other apatite grains from this till sample, suggest a common source

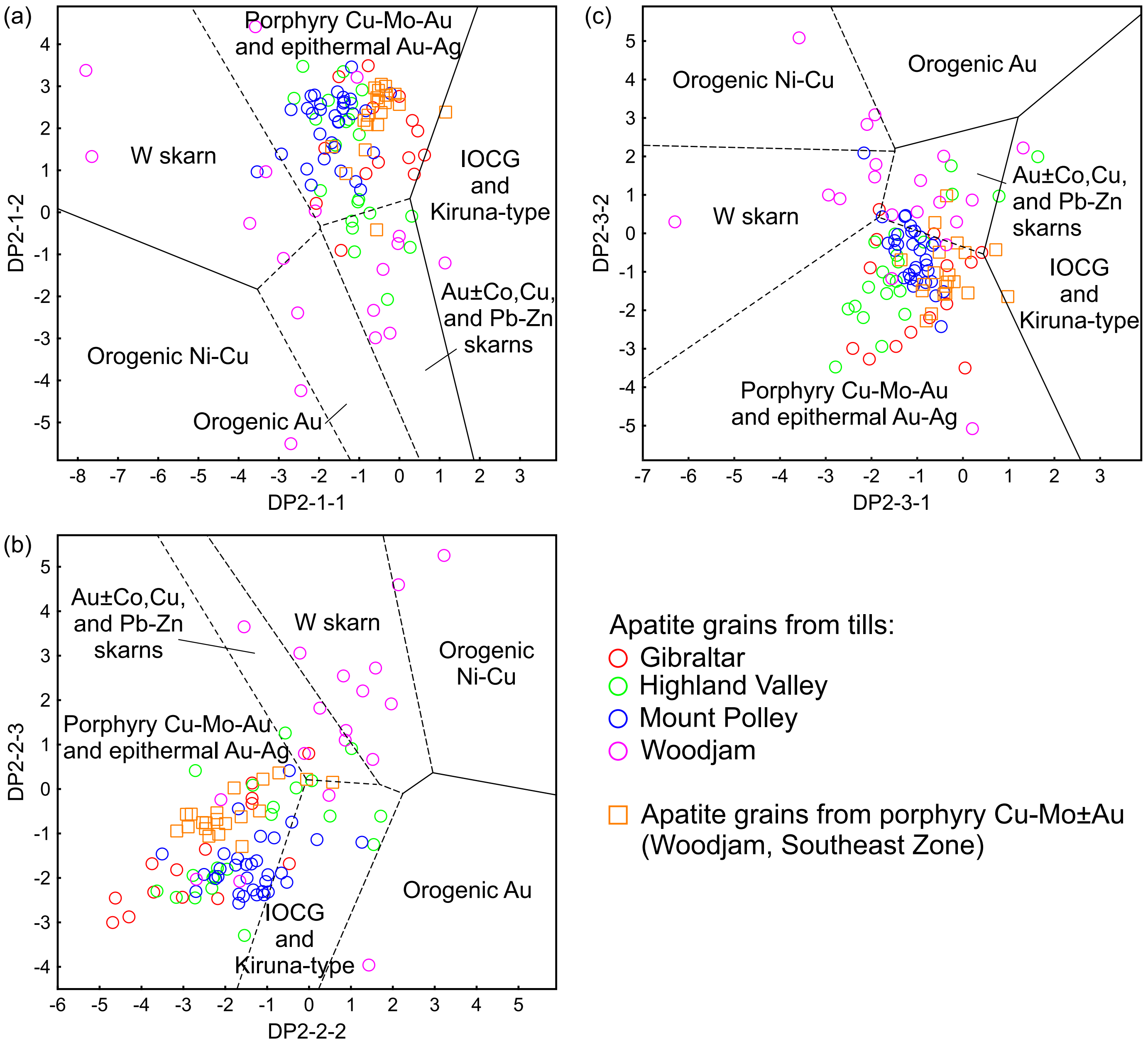

Fig. 11. Discrimination diagrams for apatite from ore deposits (Step 2) after Mao et al. (2015). IOCG = iron oxide copper-gold deposits; porphyry Cu-Mo-Au = undivided calc-alkaline porphyry Cu±Mo±Au and porphyry Mo, and alkalic porphyry Cu-Au deposits. a) The first discriminant function (DP2-1-1) versus the second discriminant function (DP2-1-2); DP2-1-1 = -2.275·LogMn - 1.429·LogSr + 1.504·LogY + 3.247·LogCe - 1.088·LogEu + 0.1925·LogDy + 0.7636·LogYb - 0.05301·LogTh - 1.538·LogU - 3.655; DP2-1-2 = 1.321·LogMn + 1.576·LogSr + 14.63·LogY - 0.005804·LogCe + 1.605·LogEu - 16.53·LogDy + 3.251·LogYb - 0.2426·LogTh - 1.155·LogU - 20.3. **b)** The second discriminant function (DP2-2-2) versus the third discriminant function (DP2-2-3); DP2-2-2 = 1.882·LogMg - 1.872·LogMn - 0.8039·LogSr - 12.21·LogY - 0.6912·LogCe - 2.014·LogEu + 14.84·LogDy - 3.946·LogYb - 0.734·LogTh + 2.513·LogU + 24.20; DP2-2-3 = -0.3009·LogMg - 0.078·LogMn - 1.591·LogSr - 6.697·LogY - 0.6125·LogCe - 0.2912·LogEu + 0.722·LogDy + 2.686·LogYb + 1.466·LogTh + 0.4239·LogU + 16.26. **c)** The first discriminant function (DP2-3-1) versus the second discriminant function (DP2-3-2); DP2-3-1 = 1.034·LogMg - 3.069·LogMn + 4.045·LogY + 3.368·LogCe - 3.127·LogEu - 0.2322·LogDy - 0.7732·LogYb - 0.1035·LogPb - 1.228·LogTh - 0.2231·LogU - 4.263; DP2-3-2 = 1.888·LogMg - 1.839·LogMn - 4.813·LogY - 0.3218·LogCe - 3.421·LogEu + 10.67·LogDy - 5.662·LogYb + 1.706·LogPb - 1.043·LogTh + 1.803·LogU + 14.24. Variables are log10-equivalents of element concentrations in parts per million (ppm) for all elements, except Mg which is in weight per cent (wt.%).

of elevated As, probably in underlying sedimentary rocks of the Nicola Group.

Compositions of apatite grains shown in Figure 11, except for the two apatite grains at Woodjam indicating orogenic Ni-Cu±PGE affinity, are projected into DP3-1 versus DP3-2 and DP3-1 versus DP3-3 discrimination diagrams with fields of different sub-types of porphyry Cu-Mo-Au, porphyry-related Cu-Au breccia, and skarn deposits (Fig. 12). As expected, data for apatite grains from Mount Polley fall in the alkalic porphyry Cu-Au field (Fig. 12a). For the Highland Valley and Gibraltar deposits, apatite data straddle the porphyry Cu±Mo±Au and porphyry Mo fields in the DP3-1 versus DP3-2 projection (Fig. 12a) or the porphyry Cu±Mo±Au and alkalic porphyry Cu-Au fields in the DP3-1 versus DP3-3 projection (Fig. 12b). Note that the DP3-1 versus DP3-2 diagram better discriminates alkalic porphyry Cu-Au from other deposit types than the DP3-1 versus DP3-3 diagram, which best separates porphyry Mo deposits from others (Mao et al., 2015). However, all these deposit types are separated from each other in the 3-D discriminant space, with the apparent overlaps between some of the deposits in Figure 12 resulting from projection of their fields into 2-D diagrams (Mao et al., 2015).

In combination, the discrimination diagrams (Figs. 12a, b) reveal that most of the apatite grains at the Highland Valley and Gibraltar deposit areas have the porphyry Cu±Mo±Au affinity, as expected for these deposits. A few data points from these areas that do plot within porphyry Mo or alkalic porphyry Cu-Au fields are within the 95% confidence uncertainty of the field boundaries in these diagrams (Mao et al., 2015). Likewise, by eliminating alkalic porphyry Cu-Au plus W skarn (Fig. 12a) and porphyry Mo (Fig. 12b), apatite grains from mineralized bedrocks at the Woodjam Southeast Zone indicate porphyry Cu±Mo±Au source, consistent with their trace-element and REE features as outlined above. As we have already seen in all other diagrams, compositions of apatite grains from till at Woodjam also show the widest spread in Figure 12, scattering from porphyry Cu±Mo±Au field across porphyry-related Cu-Au breccia field to the field of undivided Au±Co-, Cu-, and Pb-Zn skarns. As discussed above, the wide variations of trace-element compositions of apatite grains from till at Woodjam likely reflect their metasomatic overprint due to the extensive hydrothermal alteration documented in this area (Schiarizza et al., 2009a; del Real et al., 2014; Vandekerkhove et al., 2014). In addition, six apatite grains from till at Woodjam and one at Gibraltar have trace-element compositions with low $(Ce/Yb)_{CN}$ ratios of <0.85 (probably due to the metasomatic alteration) and fall beyond the limits of the discrimination diagrams of Mao et al. (2015). Therefore, they are not classified here (i.e. labelled "unknown" in Appendix 4; Rukhlov et al., 2016).

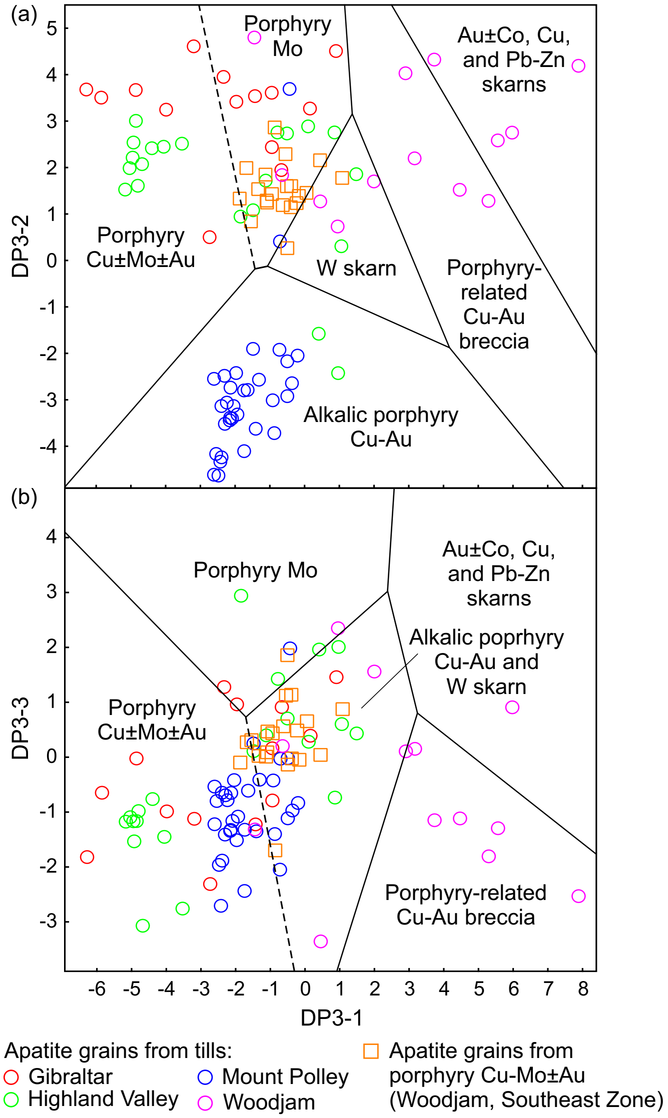

Fig. 12. Discrimination diagrams for apatite from porphyry and skarn deposits (Step 3) after Mao et al. (2015). **a)** The first discriminant function (DP3-1) versus the second discriminant function (DP3-2). **b)** The first discriminant function (DP3-1) versus the third discriminant function (DP3-3). $DP3\text{-}1 = 0.8718 \cdot LogMg - 4.156 \cdot LogMn - 3.065 \cdot LogSr + 6.341 \cdot LogY - 1.704 \cdot LogCe - 1.806 \cdot LogEu - 7.320 \cdot LogYb - 0.2802 \cdot LogPb + 0.6948 \cdot LogTh + 1.698 \cdot LogU + 21.07$; $DP3\text{-}2 = -1.473 \cdot LogMg + 2.550 \cdot LogMn - 2.981 \cdot LogSr - 5.398 \cdot LogY + 0.5600 \cdot LogCe - 2.898 \cdot LogEu + 3.780 \cdot LogYb + 2.108 \cdot LogPb - 0.4108 \cdot LogTh - 0.1375 \cdot LogU + 8.534$; $DP3\text{-}3 = 0.1617 \cdot LogMg - 1.173 \cdot LogMn - 4.364 \cdot LogSr + 2.634 \cdot LogY + 0.8452 \cdot LogCe + 3.378 \cdot LogEu - 3.184 \cdot LogYb + 1.619 \cdot LogPb + 1.956 \cdot LogTh - 0.6212 \cdot LogU + 4.471$. Variables are log10-equivalents of element concentrations in parts per million (ppm) for all elements, except Mg which is in weight per cent (wt.%).

7.3.3. Spatial patterns

The abundance of chalcopyrite grains (0.25–0.50 mm, >3.2 $g \cdot cm^{-3}$ fraction; normalized to 10 kg of <2 mm-size bulk sediment) in tills (after Hashmi et al., 2015; Plouffe et al., 2013a; Plouffe and Ferbey, 2015a, d) for each study area highlights glacial dispersion from known porphyry deposits (Figs. 13-16). Notably, all apatite grains in metal-rich till (with up to 2500 chalcopyrite grains), immediately down-ice from the Highland Valley Copper deposit, show consistent porphyry Cu±Mo±Au features (Fig. 13). Till with <51 chalcopyrite

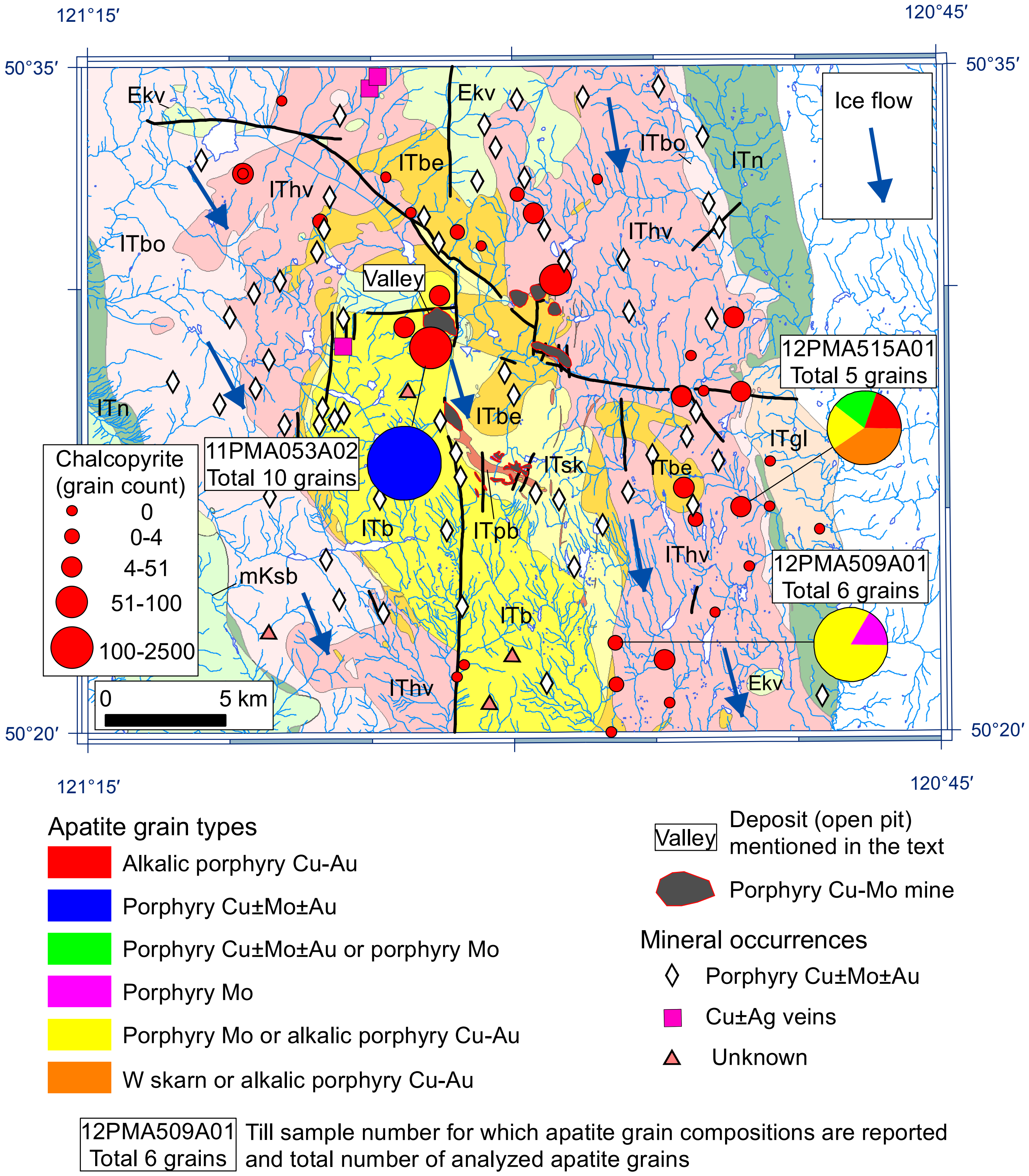

Fig. 13. Affinity of apatite grains (0.25–0.50 mm, >3.2 g·cm^{-3}, >1.0 A fraction), based on the classification of Mao et al. (2015), and number of chalcopyrite grains (0.25–0.50 mm, >3.2 g·cm^{-3} fraction; normalized to 10 kg of <2 mm-size bulk sediment; after Plouffe et al., 2013a; Plouffe and Ferbey, 2015d) from till samples, Highland Valley calc-alkaline porphyry Cu-Mo district. Bedrock legend and other symbols as in Figure 2.

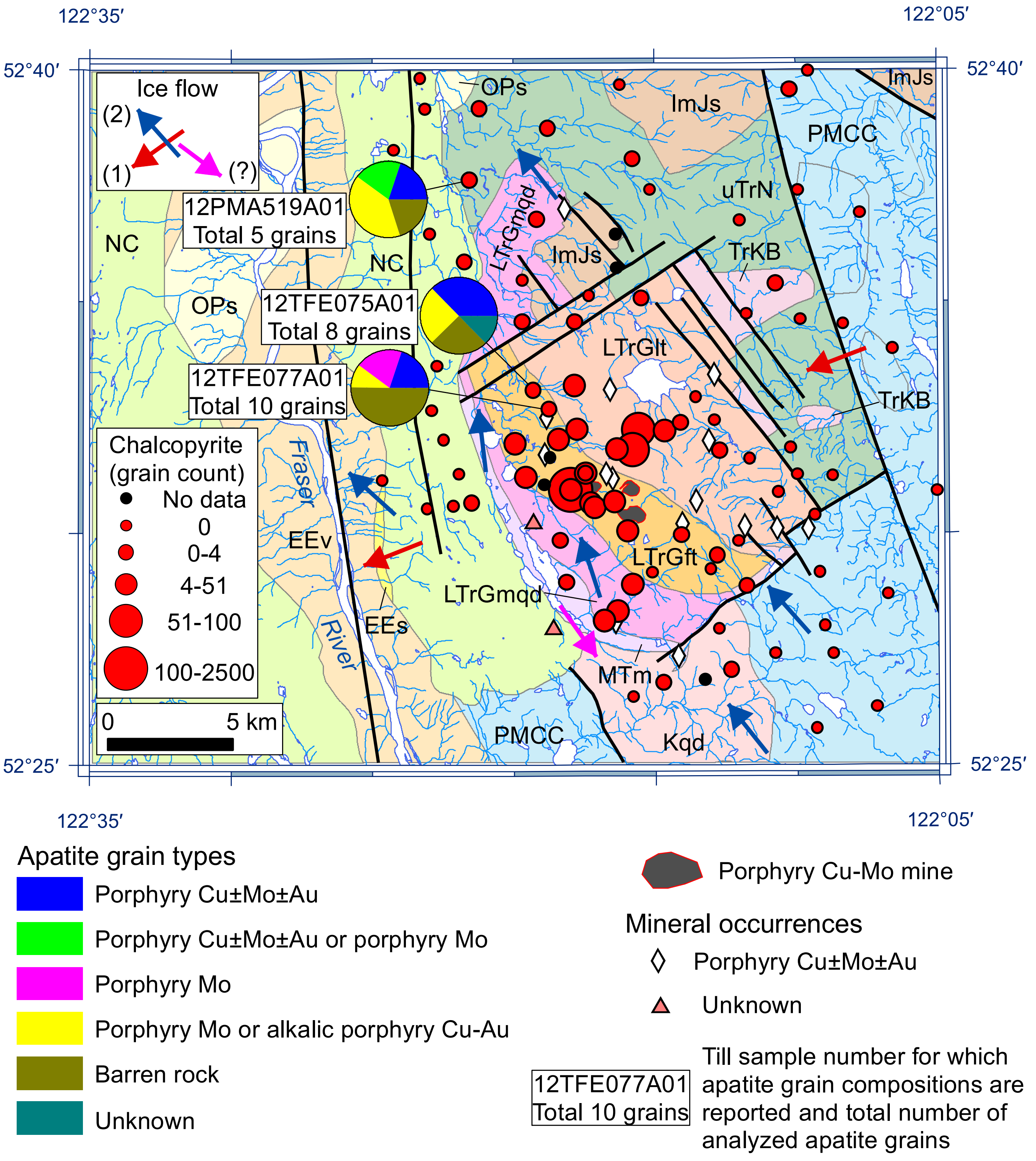

Fig. 14. Affinity of apatite grains (0.25–0.50 mm, >3.2 g·cm^{-3}, >1.0 A fraction), based on the classification of Mao et al. (2015), and number of chalcopyrite grains (0.25–0.50 mm, >3.2 g·cm^{-3} fraction; normalized to 10 kg of <2 mm-size bulk sediment; after Plouffe et al., 2013a; Plouffe and Ferbey, 2015a, d) from till samples, Gibraltar calc-alkaline porphyry Cu-Mo mine area. Bedrock legend and other symbols as in Figure 3.

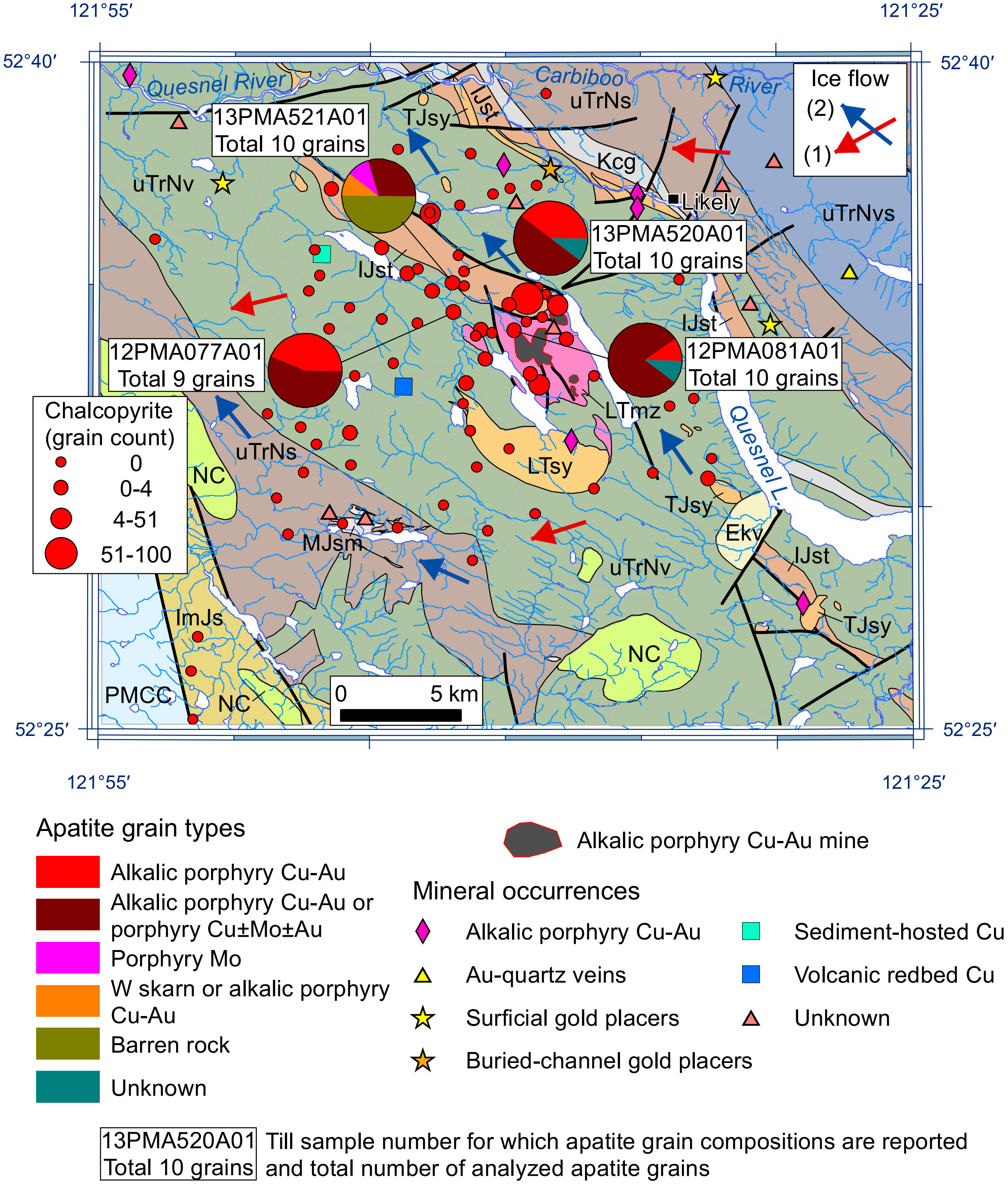

Fig. 15. Affinity of apatite grains (0.25–0.50 mm, >3.2 g·cm^{-3}, >1.0 A fraction), based on the classification of Mao et al. (2015), and number of chalcopyrite grains (0.25–0.50 mm, >3.2 g·cm^{-3} fraction; normalized to 10 kg of <2 mm-size bulk sediment; after Hashmi et al., 2015) from till samples, Mount Polley alkalic porphyry Cu-Au mine area. Bedrock legend and other symbols as in Figure 4.

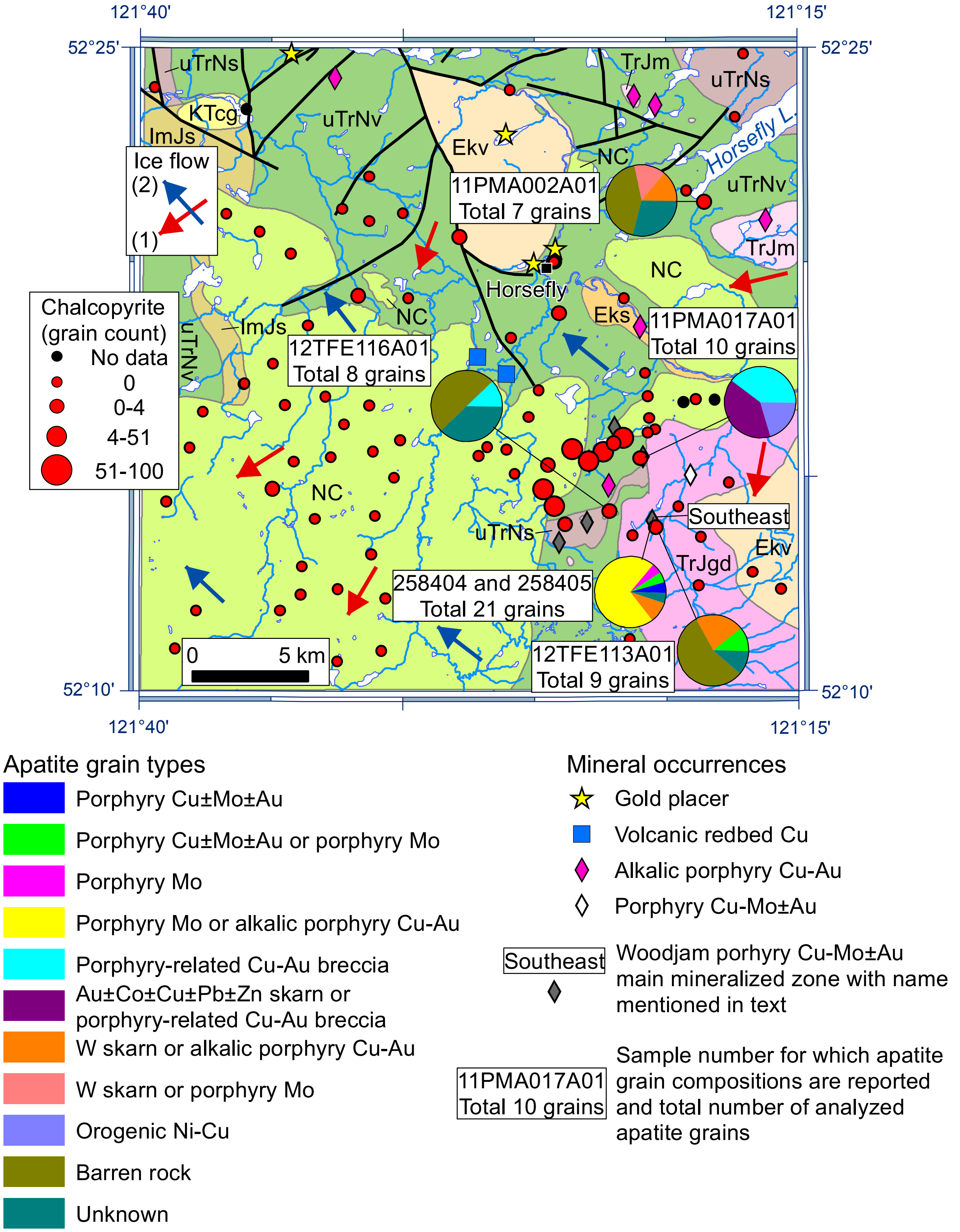

Fig. 16. Affinity of apatite grains (0.25–0.50 mm, >3.2 g·cm^{-3}, >1.0 A fraction) from till and bedrock samples, based on the classification of Mao et al. (2015), and number of chalcopyrite grains from till samples (0.25–0.50 mm, >3.2 g·cm^{-3} fraction; normalized to 10 kg of <2 mm-size bulk sediment; after Plouffe and Ferbey, 2015a, d), Woodjam high-K, calc-alkaline porphyry Cu-Mo±Au developed prospect area. Bedrock legend and other symbols as in Figure 5.

grains in the eastern part of the Highland Valley district contains less abundant apatite, with all examined grains indicating ore systems, ranging from porphyry Cu±Mo±Au to porphyry Mo or alkalic porphyry Cu-Au (Fig. 13; Table 4).

At Gibraltar, till with <4 chalcopyrite grains, deposited 5 to 15 km down-ice from the porphyry Cu-Mo deposit, contains apatite grains that mostly show the trace-element characteristics consistent with porphyry Cu±Mo±Au deposits (Fig. 14). Two apatite grains from till sample 12TFE077A01 indicate a porphyry Mo source, and one unclassified apatite grain from a nearby till sample 12TFE075A01 has the trace-element chemistry (e.g., low LREE/HREE) indicating metasomatic alteration. All till samples from Gibraltar contain apatite grains with the chemical attributes of barren rocks (20–50%; Fig. 14; Table 4). Grains of predominantly porphyry Cu±Mo±Au affinity are from till samples roughly aligned along the late-phase ice-flow direction (northwest), away from the Gibraltar deposit, and may indicate glacial transport as far as 15 km. Such dispersion is not recorded in the amounts of chalcopyrite grains in these tills, perhaps due to the limited preservation of chalcopyrite during glacial transport and postglacial weathering relative to apatite.

The chalcopyrite-poor (0–4 grains) but relatively apatite-rich (up to 3% of the HMC fraction) till samples within 0 to ~5 km down-ice (northwest) from the Mount Polley alkalic porphyry Cu-Au deposit all contain apatite grains with the trace-element signature of alkalic porphyry Cu-Au deposits (Fig. 15). The proportion of the alkalic porphyry Cu-Au–type apatite grains decreases from 90% to 40% with distance down-ice from the Mount Polley deposit, consistent with increasing dilution of tills by barren-rock material farther away from the mineralization. Half of the apatite grains (0.5% in the HMC fraction) in till sample 13PMA521A01, ~5 km down-ice from the deposit, are inferred to be from barren rocks, and one apatite grain from this sample shows chemical signature of porphyry Mo deposits.

Apatite grains from mineralized quartz monzonites at the Woodjam Southeast Zone indicate porphyry Cu±Mo±Au affinity, consistent with the high-K, calc-alkaline character of the mineralization (del Real et al., 2014; Vandekerkhove et al., 2014). Apatite grains showing barren-rock affinity or highly variable degrees of depletion in most of trace-elements with low LREE/HREE ratios, perhaps due to the extensive hydrothermal alteration of their source rocks (Schiarizza et al., 2009a; del Real et al., 2014; S.M. Vandekerkhove et al., 2014) are predominant in tills at Woodjam (Fig. 16). Three apatite grains from till sample 12TFE113A01 immediately above the Southeast Zone show porphyry Cu±Mo±Au or alkalic porphyry Cu-Au affinities. Two apatite grains from till sample 11PMA002A01, ~2.5 km down-ice from an alkalic porphyry Cu-Au occurrence, ~15 km northeast of the Southeast Zone, indicate an alkalic porphyry Cu-Au source (Fig. 16; Table 4). Apatite grains from till (sample 11PMA017A01) overlying the Takomkane batholith-Nicola Group contact show the highest As in this study and a wide range of Mg and ∑REE abundances, with compositions falling mostly within the porphyry-related Cu-Au breccia field in the DP3-1 versus DP3-3 diagram (Fig. 12b), except for two apatite grains showing orogenic Ni-Cu±PGE affinity (Fig. 16). As discussed above, the trace-element chemistry of these apatite grains suggest crystallization in a hydrothermal environment with elevated As perhaps derived from sedimentary rocks of the Nicola Group. Their porphyry-related Cu-Au breccia-type affinity indicates probable derivation from breccias related to monzonite stocks and dikes at the Woodjam porphyry camp (del Real et al., 2014). The clear Cu±Mo±Au signature displayed by apatite from mineralized bedrock at the Woodjam Southeast Zone is lacking in most till grains. The latter are predominantly metasomatically altered apatites, even in tills proximal to the known mineralized zones, implying derivation from higher-level, low-temperature alteration halos related to the Takomkane batholith and its satellite intrusions.

8. Conclusions

Our EMPA and LA-ICP-MS examination of 147 apatite grains recovered from 14 till samples at the Highland Valley, Gibraltar, Mount Polley, and Woodjam porphyry deposits, and from two mineralized bedrock samples at the Woodjam Southeast Zone, reveals systematic trace-element patterns characteristic of both the degree of fractionation and the relative redox state of these magmatic-hydrothermal ore systems. Apatite grains from Mount Polley show higher SO_3, SiO_2, Na_2O, Sr, Mg, V, Ba, Zr, Mo, Nb contents, $(La/Sm)_{CN}$, and Eu/Eu*, and lower Mn, Y, ∑HREE contents and Ce/Ce* relative to those of apatite grains from the Highland Valley, Gibraltar and Woodjam deposits. They also have systematically higher As contents, except for apatite grains from one till sample at the Woodjam porphyry camp, above the contact between the Takomkane batholith and Nicola Group volcano-sedimentary rocks, likely As sources. The lack of significant Eu anomalies, coupled with higher SO_3, V, and As, and lower Mn abundances and Ce/Ce* values, of apatite grains at Mount Polley than those from Highland Valley, Gibraltar and Woodjam are consistent with the generally more oxidized alkalic porphyry Cu-Au deposits compared to the calc-alkaline porphyry Cu±Mo±Au systems. Average Mn abundances in primary apatite grains yield log fO_2 values of -11.2 ±0.5 for Mount Polley, -12.8 ±0.6 for Woodjam Southeast Zone, -14.1 ±0.7 for Gibraltar, and -16.3 ±1.0 for Highland Valley, using an empirical calibration for a range of temperatures (920–660 ^{o}C) and compositions (andesitic to rhyolitic) after Miles et al. (2014). These log fO_2 values provide relative estimates of the oxidation state for these porphyry deposits within a given range of temperatures. However, they will quantify the redox state (relative to mineral buffers) with an estimated temperature of apatite crystallization for a given sample. The Mn in apatite oxybarometer does not apply to metasomatically altered apatites with low minor- and trace-element abundances and low LREE/HREE. Strong negative Eu anomalies, combined with higher Mn and lower Mg and Sr contents, of apatite grains at Highland Valley, Gibraltar and Woodjam, compared to those at Mount Polley,

Table 4. Summary of apatite grains from till and mineralized bedrock in the Highland Valley, Gibraltar, Mount Polley, and Woodjam study areas, subdivided by barren-rock or deposit-type affinity using the apatite classification after Mao et al. (2015).

Sample	Type	Area	Total apatite grains	Alk. pry Cu-Au	Alk. pry Cu-Au or pry Cu±Mo±Au	Pry Cu±Mo±Au	Pry Cu±Mo±Au or pry Mo	Pry Mo	Pry Mo or alk. pry Cu-Au	W skarn or alk. pry Cu-Au	W skarn or pry Mo	Pry-related Cu-Au breccia	Skarn* or pry-related Cu-Au breccia	Skarn*	Orogenic Ni-Cu±PGE	Unknown	Barren rock
12PMA519A01	Till	Gibraltar	5			1	1		2								1
12TFE075A01	Till		8			3			2							1	2
12TFE077A01	Till		10			2		2	1								5
11PMA053A02	Till	Highland Valley	10			10											
12PMA509A01	Till		6					1	5								
12PMA515A01	Till		5	1			1		1	2							
12PMA077A01	Till	Mount Polley	9	4	5												
12PMA081A01	Till		10	1	8											1	
13PMA520A01	Till		10	4	5											1	
13PMA521A01	Till		10		3			1		1							5
11PMA002A01	Till	Woodjam	7							1	1					2	3
11PMA017A01	Till		10									4	3	1	2		
12TFE113A01	Till		9				1			2						1	5
12TFE116A01	Till		8									1				3	4
258404	Rock	Woodjam Southeast Zone	11			1	1	1	8								
258405	Rock		10						7	2						1	

Alk. = alkalic, **Pry** = porphyry.

Details of till samples can be found in Plouffe et al. (2013a) and Plouffe and Ferbey (2015a, d). We refer the reader to Mao et al. (2015) for details of the deposit types and their discrimination using apatite trace-element chemistry. The "unknown" group includes apatite grains with missing values for some elements due to poor analysis and extreme compositions falling beyond the bounds of the discrimination diagrams after Mao et al. (2015).

* Includes Au-Co skarn, Cu skarn, and Pb-Zn skarn types (after Mao et al., 2015).

may also indicate early plagioclase and pyroxene fractionation (which lower Sr, Mg and Eu^{2+}/Eu^{3+} in the melt) and lack of significant Fe-Mg minerals (which accommodate Mn) in the evolved calc-alkaline magma. Most apatite grains from tills at Woodjam, along with a few apatite grains at Highland Valley, Gibraltar, and Mount Polley, show variable degrees of depletion in most of minor and trace elements and LREEs, yielding extreme ranges in $(Ce/Yb)_{CN}$ (<0.01–47), $(La/Sm)_{CN}$ (0.06–6.0), $(Gd/Yb)_{CN}$ (0.01–39), Ce/Ce* (0.23–3.8) and elevated Eu/Eu* (up to 1.5). The trace-element and REE patterns of these grains, distinct from those in mineralized rocks at Woodjam and other porphyry deposits (Mao et al., 2015), probably reflect metasomatic alteration, which is extensive at the Woodjam high-K, calc-alkaline Cu-Mo±Au porphyry camp (Schiarizza et al., 2009a; del Real et al., 2014;Vandekerkhove et al., 2014). Calculated molar Cl/F and Cl/OH ratios in the examined apatite grains, assuming molar (F + OH + Cl) = 1, agree with those of apatites from some producing porphyry deposits elsewhere (Piccoli and Candela, 2002). The trace-element chemistry of apatite grains correctly identifies the porphyry systems in all four study areas. Paucity of porphyry Cu±Mo±Au-type apatite grains in Woodjam tills implies protection of the mineralized zones from erosion during the most recent glaciation by a cover of pre-glacial sediment or unmineralized rock (Bissig et al., 2013; del Real et al., 2014; Vandekerkhove et al., 2014; J.W. Morton, pers. comm. 2014).

Our study indicates that apatite can survive glacial transport and post-glacial weathering. It presents the first test of the apatite classification by Mao et al. (2015) on grains from till, and demonstrates that apatite trace-element chemistry can be an effective mineral exploration tool. Future research should test the effectiveness of the method on apatite from other deposit types, including carbonatites, orogenic Au, IOCG, porphyry Mo, orogenic Ni-Cu±PGE, and barren rocks. Our study was limited to the heavy (>3.2 $g \cdot cm^{-3}$) apatite fraction; separation and identification methods need to be further developed to incorporate less dense fractions.

Acknowledgments

We thank Overburden Drilling Management Limited for help with recovering and identifying apatite grains from heavy mineral concentrates. Edith Czech (University of British Columbia) and Mati Raudsepp (University of British Columbia) are acknowledged for their assistance with the electron microprobe analysis (EMPA). We are grateful to Beth McClenaghan (Geological Survey of Canada), Stephen Rowins (British Columbia Geological Survey), and Larry Aspler (British Columbia Geological Survey) for thorough reviews of the paper. ESS contribution # 20150382.

References cited

Anderson, R.G., Plouffe, A., Ferbey, T., and Dunn, C.E., 2012a. The search for surficial expressions of buried Cordilleran porphyry deposits; a new TGI4 activity in the southern Canadian Cordillera. Geological Survey of Canada Open File 7081, poster.

Anderson, R.G., Plouffe, A., Ferbey, T., and Dunn, C.E., 2012b. The search for surficial expressions of buried Cordilleran porphyry deposits: background and progress in a new TGI-4 activity in the southern Canadian Cordillera. In: Current Research 2012-7, Geological Survey of Canada, 15p.

Anderson, R.G., Plouffe, A., Ferbey, T., and Dunn, C.E., 2012c. The search for surficial expressions of buried Cordilleran porphyry deposits: preliminary findings in a new TGI4 activity in the southern Canadian Cordillera. Geological Survey of Canada Open File 7266, 82p.

Ash, C.H. and Riveros, C.P., 2001. Geology of the Gibraltar copper-molybdenite deposit, east-central British Columbia (93B/9). In: Geological Fieldwork 2000, British Columbia Ministry of Energy and Mines, British Columbia Geological Survey Paper 2001-1, pp. 119–134.

Ash, C.H., Panteleyev, A., MacLellan, K.L., Payne, C.W., and Rydman, M.O., 1999a. Geology of the Gibraltar Mine area (93B/6&9). British Columbia Ministry of Energy and Mines, British Columbia Geological Survey Open File 1999-7, 1:50,000 scale.

Ash, C.H., Rydman, M.O., Payne, C.W., and Panteleyev, A., 1999b. Geological setting of the Gibraltar mine south central British Columbia (93B/8, 9). In: Exploration and Mining in British Columbia - 1998, Part B - Geological Descriptions of Selected Properties, British Columbia Ministry of Energy and Mines, pp. A1–A15.

Ballard, J.R., Palin, J.M., and Campbell, I.H., 2002. Relative oxidation states of magmas inferred from Ce(IV)/Ce(III) in zircon: application to porphyry copper deposits of northern Chile. Contributions to Mineralogy and Petrology, 144, 347–364.

Bath, A.B., Logan, J.M., and Kamenetsky, V.S., 2006. Apatite in Cu-sulfide ore from Mount Polley alkalic porphyry, BC Canada. Geochimica et Cosmochimica Acta, 70, A40.

Belousova, E.A., Griffin, W.L., O'Reilly, S., and Fisher, N.I., 2002. Apatite as an indicator mineral for mineral exploration: trace element compositions and their relationship to host rock type. Journal of Geochemical Exploration, 76, 45–69.

Berry, L.G., Mason, B., and Dietrich, R.V., 1983. Mineralogy. W.H. Freeman and Company, San Francisco, 561p.

Bissig, T., Heberlein, D.R., and Dunn, C.E., 2013. Geochemical techniques for detection of blind porphyry copper-gold mineralization under basalt cover, Woodjam prospect, south-central British Columbia (NTS93A/03, /06). In: Summary of Activities 2012, Geoscience BC Report 2013-1, pp. 63–78.

Bouzari, F., Hart, C.J.R., Barker, S., and Bissig, T., 2010. Porphyry indicator minerals (PIMs): exploration for concealed deposits in south central British Columbia (NTS 092I/06, 093A/12, 093N/01, /14). In: Summary of Activities 2009, Geoscience BC Report 2010-1, pp. 25–32.

Bouzari, F., Hart, C.J.R., Barker, S., and Bissig, T., 2011a. Exploration for concealed deposits using porphyry indicator minerals (PIMs): Application of apatite texture and chemistry. In: 25th International Applied Geochemistry Symposium, Series B 92-1, Rovaniemi, Finland, Vuorimiesyhdistys-Finnish Association of Mining and Metallurgical Engineers, pp. 89–90.

Bouzari, F., Hart, C.J.R., Barker, S., and Bissig, T., 2011b. Porphyry indicator minerals (PIMS): a new exploration tool for concealed deposits in south-central British Columbia. Geoscience BC Report 2011-17, 31p.

Bouzari, F., Hart, C.J.R., and Bissig, T., 2015. Mineralogical characteristics of porphyry-fertile plutons: Guichon Creek, Takomkane, and Granite Mountain batholiths, south central British Columbia. In: Summary of Activities 2014, Geoscience BC Report 2015-1, pp. 63–68.

Boyce, J.W. and Hervig, R.L., 2009. Apatite as a monitor of late-stage magmatic processes at Volcán Irazú, Costa Rica. Contributions to Mineralogy and Petrology, 157, 135–145.

Boynton, W.V., 1984. Geochemistry of the rare earth elements:

Meteorite studies. In: Henderson, P., (Ed.), Rare Earth Element Geochemistry, Elsevier, New York, pp. 63–114.

Budzinski, H. and Tischendorf, G., 1989. Distribution of REE among minerals in the Hercynian postkinematic granites of Westerzgebirge-Vogtland, GDR. Zeitschrift für Geologische Wissenschaften, 17, 1019–1031.

Byrne, K., Stock, E., Ryan, J., Johnson, C., Nisenson, J., Alva Jimenez, T., Lapointe, M., Stewart, H., Grubisa, G., and Syroka, S., 2013. Porphyry Cu-(Mo) deposits in the Highland Valley district, south-central British Columbia. In: Logan, J.M. and Schroeter, T.G., (Eds.), Porphyry Systems of Central and Southern British Columbia: Tour of Central British Columbia Porphyry Deposits from Prince George to Princeton. Society of Economic Geologists Field Trip Guidebook Series 43, pp. 99–116.

Bysouth, G.D., Campbell, K.V., Barker, G.E., and Gagnier, G.K., 1995. Tonalite-trondhjemite fractionation of peraluminous magma and the formation of syntectonic porphyry copper mineralization, Gibraltar mine, central British Columbia. In: Schroeter, T.G., (Ed.), Porphyry Deposits of the Nortwestern Cordillera of North America. Canadian Institute of Mining, Metallurgy and Petroleum Special Volume 46, pp. 201–213.

Cao, M., Li, G., Qin, K., Seitmuratova, E.Y., and Liu, Y., 2012. Major and trace element characteristics of apatite in granitoids from central Kazakhstan: implications for petrogenesis and mineralization. Resource Geology, 62, 63–83.

Carson, D.J.T. and Jambor, J.L., 1974. Mineralogy, zonal relationships and economic significance of hydrothermal alteration at porphyry copper deposits, Babine Lake area, British Columbia. Canadian Institute of Mining and Metallurgy Bulletin, 67, 110–133.

Casselman, M.J., McMillan, W.J., and Newman, K.M., 1995. Highland Valley porphyry copper deposits near Kamloops, British Columbia: A review and update with emphasis on the Valley deposit. In: Schroeter, T.G., (Ed.), Porphyry Deposits of the Nortwestern Cordillera of North America. Canadian Institute of Mining, Metallurgy and Petroleum Special Volume 46, pp. 161–191.

Celis, M.A., Bouzari, F., Bissig, T., Hart, C.J.R., and Ferbey, T., 2014. Petrographic characteristics of porphyry indicator minerals from alkalic porphyry copper-gold deposits in south-central British Columbia (NTS 092, 093). In: Summary of Activities 2013, Geoscience BC Report 2014-1, pp. 53–62.

Celis, M.A., Hart, C.J.R., Bouzari, F., Bissig, T., and Ferbey, T., 2013. Porphyry indicator minerals (PIMs) from alkalic porphyry copper-gold deposits in south-central British Columbia (NTS 092, 093). In: Summary of Activities 2012, Geoscience BC Report 2013-1, pp. 37–46.

Clague, J.J., compiler, 1989. Chapter 1. Quaternary geology of the Canadian Cordillera. In: Fulton, R.J., (Ed.), Quaternary Geology of Canada and Greenland. Geological Survey of Canada, Geology of Canada Series 1, pp. 15–96.

Colombini, L.L., Miller, C.F., Gualda, G.A.R., Wooden, J.L., and Miller, J.S., 2011. Sphene and zircon in the Highland Range volcanic sequence (Miocene, southern Nevada, USA): elemental partitioning, phase relations, and influence on evolution of silicic magma. In: Broska, I., Finger, F., and Harlov, D., (Eds.), Accessory Minerals in Igneous and Metamorphic Rocks. Mineralogy and Petrology, 102, pp. 29–50.

Dawson, K.M., Panteleyev, A., Sutherland Brown, A., and Woodsworth, G.J., 1991. Regional metallogeny. In: Gabrielse, H. and Yorath, C.J., (Eds.), Geology of the Cordilleran Orogen in Canada. Geological Survey of Canada, Geology of Canada Series 4, pp. 709–768.

del Real, I., Hart, C.J.R., Bouzari, F., Blackwell, J.L., Rainbow, A., and Sherlock, R., 2014. Relationships between calcalkalic and alkalic mineralization styles at the copper-molybdenum Southeast Zone and copper-gold Deerhorn porphyry deposits, Woodjam property, central British Columbia (NTS 093A). In: Summary of Activities 2013, Geoscience BC Report 2014-1, pp. 63–82.

Drummond, A.D., Sutherland Brown, A., Young, R.J., and Tennant, S.J., 1976. Gibraltar - regional metamorphism, mineralization, hydrothermal alteration and structural development. In: Sutherland Brown, A., (Ed.), Porphyry Deposits of the Canadian Cordillera. Canadian Institute of Mining and Metallurgy Special Volume 15, pp. 195–205.

Drummond, A.D., Tennant, S.J., and Young, R.J., 1973. The interrelationship of regional metamorphism, hydrothermal alteration and mineralization at the Gibraltar mines copper deposit in B.C. Canadian Mining and Metallurgical Bulletin, 66, 48–55.

Duuring, P., Rowins, S.M., McKinley, B.S.M., Dickinson, J.M., Diakow, L.J., Young-Seog, K., and Creaser, R.A., 2009. Magmatic and structural controls on porphyry-style Cu-Au-Mo mineralization at Kemess South, Toodoggone District of British Columbia, Canada. Mineralium Deposita, 44, 435–462.

Ferbey, T. and Plouffe, A., 2014. Lifting the burden of overburden in British Columbia: recent advances in till geochemical surveys. In: Mineral Exploration Roundup 2014 Conference, Abstract Volume, Association for Mineral Exploration British Columbia, Vancouver, B.C., pp. 26–28.

Ferbey, T., Arnold, H., and Hickin, A.S., 2013. Ice-flow indicator compilation, British Columbia. British Columbia Ministry of Energy and Mines, British Columbia Geological Survey Open File 2013-06, 1:1,650,000 scale.

Ferbey, T., Plouffe, A., and Anderson, R.G., 2014. An integrated approach to search for buried porphyry-style mineralization in central British Columbia using geochemistry and mineralogy: a TGI-4 project. In: Current Research 2014-2, Geological Survey of Canada, 12p.

Flury, B., 1997. A First Course in Multivariate Statistics. Springer-Verlag, New York, 715p.

Fraser, T.M., Stanley, C.R., Nikic, Z.T., Pesalj, R., and Gorc, D., 1995. The Mount Polley alkalic porphyry copper-gold deposit, south-central British Columbia. In: Schroeter, T.G., (Ed.), Porphyry Deposits of the Nortwestern Cordillera of North America. Canadian Institute of Mining and Metallurgy Special Volume 46, pp. 609–622.

Harada, K., Nagashima, K., Nakao, K., and Kato, A., 1971. Hydroxylellestadite, a new apatite from Chichibu Mine, Saitama prefecture, Japan. American Mineralogist, 56, 1507–1518.

Harlov, D.E., 2015. Apatite: a fingerprint for metasomatic processes. Elements, 11, 171–176.

Hashmi, S., Ward, B.C., Plouffe, A., Ferbey, T., and Leybourne, M.I., 2014. Geochemical and mineralogical dispersal in till from the Mount Polley Cu-Au porphyry deposit, central British Columbia, Canada. Geological Survey of Canada Open File 7589, poster.

Hashmi, S., Ward, B.C., Plouffe, A., Leybourne, M.I., and Ferbey, T., 2015. Geochemical and mineralogical dispersal in till from the Mount Polley Cu-Au porphyry deposit, central British Columbia, Canada. Geochemistry: Exploration, Environment, Analysis, 15, 234–249.

Hodgson, C.J., Balles, R.J. and Verzosa, R.S., 1976. Cariboo-Bell. In: Sutherland Brown, A., (Ed.), Porphyry Deposits of the Canadian Cordillera. Canadian Institute of Mining and Metallurgy Special Volume 15, pp. 388–396.

Holland, S.S., 1976. Landforms of British Columbia, a physiographic outline. British Columbia Department of Mines and Petroleum Resources Bulletin 48, 138p.

Hughes, J.M. and Rakovan, J.F., 2015. Structurally robust, chemically diverse: apatite and apatite supergroup minerals. Elements, 11, 165–170.

Jochum, K.P., Weis, U., Stoll, B., Kuzmin, D., Yang, Q., Raczek, I., Jacob, D.E., Stracke, A., Birbaum, K., Frick, D.A., Günther, D., and Enzweiler, J., 2011. Determination of reference values for NIST SRM 610–617 glasses following ISO guidelines.

Geostandards and Geoanalytical Research, 35, 397–429.

Kelley, K.D., Eppinger, R.G., Lang, J., Smith, S.M., and Fey, D.L., 2011. Porphyry Cu indicator minerals in till as an exploration tool: example from the giant Pebble porphyry Cu-Au-Mo deposit, Alaska, USA. Geochemistry: Exploration, Environment, Analysis, 11, 321–334.

Kreidler, E.R. and Hummel, F.A., 1970. The crystal chemistry of apatite: structure fields of fluor- and chlorapatite. American Mineralogist, 55, 170–184.

Kusebauch, C., John, T., Whitehouse, M.J., Klemme, S., and Putnis, A., 2015. Distribution of halogens between fluid and apatite during fluid-mediated replacement processes. Geochimica et Cosmochimica Acta, 170, 225–246.

Kutoglu, A., von, 1974. Structure refinement of the apatite $Ca_5(VO_4)_3(OH)$. Neues Jahrbuch für Mineralogie – Monatshefte, 5, 210-218.

Lang, J.R., Stanley, C.R., and Thompson, J.F.H., 1995. Porphyry copper-gold deposits related to alkalic igneous rocks in the Triassic-Jurassic arc terranes of British Columbia. In: Wahl Pierce, F., and Bolm, J.G., (Eds.), Porphyry Copper Deposits of the American Cordillera, Arizona Geological Society, Digest 20, p. 219–236.

Liaghat, S. and Tosdal, R., 2008. Apatite chemical composition and textures as a probe into magmatic conditions at Galore Creek porphyry copper-gold deposit, British Columbia. Geochimica et Cosmochimica Acta, 72, A550.

Lodders, K., 2010. Solar system abundances of the elements: Principles and Perspectives in Cosmochemistry. In: Astrophysics and Space Science Proceedings, Springer-Verlag, Berlin, Heidelberg, pp. 379–417.

Logan, J.M., 2013. Porphyry systems of central and southern BC: Overview and field trip road log. In: Logan, J.M. and Schroeter, T.G., (Eds.), Porphyry Systems of Central and Southern British Columbia: Tour of central British Columbia Porphyry Deposits from Prince George to Princeton. Society of Economic Geologists Field Trip Guidebook Series 43, pp. 1–45.

Logan, J.M., Bath, A.B., Mihalynuk, M.G., and Rees, C.J., 2007a. Regional geology of the Mount Polley area, central British Columbia. British Columbia Ministry of Energy and Mines, British Columbia Geological Survey Geoscience Map 2007-1, 1:50,000 scale.

Logan, J.M., Mihalynuk, M.G., Ullrich, T., and Friedman, R.M., 2007b. U-Pb ages of intrusive rocks and $^{40}Ar/^{39}Ar$ plateau ages of copper-gold-silver mineralization associated with alkaline intrusive centres at Mount Polley and the Iron Mask batholith, southern and central British Columbia. In: Geological Fieldwork 2006, British Columbia Ministry of Energy, Mines and Petroleum Resources, British Columbia Geological Survey Paper 2007-1, pp. 93–116.

Logan, J.M., Schiarizza, P., Struik, L.C., Barnett, C., Nelson, J.L., Kowalczyk, P., Ferri, F., Mihalynuk, M.G., Thomas, M.D., Gammon, P., Lett, R., Jackaman, W., and Ferbey, T., compilers, 2010. Bedrock geology of the QUEST map area, central British Columbia. Geoscience BC Report 2010-5, British Columbia Ministry of Forests, Mines and Lands, British Columbia Geological Survey Geoscience Map 2010-1, Geological Survey of Canada Open File 6476, 1:500,000 scale.

Mao, M., Rukhlov, A.S., Rowins, S.M., Spence, J., and Coogan, L.A., 2015. Detrital apatite trace-element comopsitions: a robust new tool for mineral exploration. British Columbia Ministry of Energy and Mines, British Columbia Geological Survey GeoFile 2015-9 (poster).

Marshall, O.J., 1988. Cathodoluminescence of Geological Materials. Unwin Hyman, Boston, 146p.

Massey, N.W.D., MacIntyre, D.G., Desjardins, P.J., and Cooney, R.T., 2005. Geology of British Columbia. British Columbia Ministry of Energy, Mines and Petroleum Resources, British Columbia Geological Survey Geoscience Map 2005-3, 1:1,000,000 scale.

McMillan, W.J., 1985. Geology and ore deposits of the Highland Valley camp. Geological Association of Canada, Mineral Deposits Division, Field Guide and Reference Manual Series 1, 121p.

McMillan, W.J., 2005. Porphyry Cu-Mo deposits of the Highland Valley district, Guichon Creek batholith, British Columbia, Canada. In: Porter, T.M. (Ed.), Super Porphyry Copper & Gold Deposits: A Global Perspective, PGC Publishing, Adelaide, 1, p. 259–274.

McMillan, W.J., Anderson, R.G., Chan, R., and Chow, W., 2009. Geology and mineral occurrences (Minfile), Guichon Creek Batholith and Highland Valley porphyry copper district, British Columbia. Geological Survey of Canada Open File 6079, 2 sheets, 1:100,000 and 1:150,000 scale.

Miles, A.J., Graham, C.M., Hawkesworth, C.J., Gillespie, M.R., Hinton, R.W., Bromiley, G.D., and EMMAC, 2014. Apatite: a new redox proxy for silicic magmas? Geochimica et Cosmochimica Acta, 132, 101–119.

Nelson, J.L., Colpron, M., Israel, S., 2013. The Cordillera of British Columbia, Yukon and Alaska: tectonics and metallogeny. In: Colpron, M., Bissig, T., Rusk, B.G., and Thompson, F.H., (Eds.), Tectonics, Metallogeny, and Discovery: The North American Cordillera and Similar Accretionary Settings. Society of Economic Geologists, Inc. Special Publication 17, pp. 53–109.

Normandeau, P.X., Corriveau, L., Paquette, J., and McMartin, I., 2014. Apatite as an indicator mineral to IOCG deposits in the Great Bear magmatic zone, Northwest Territories, Canada. In: 42nd Annual Yellowknife Geoscience Forum, Yellowknife, November 25-27, 2014. Northwest Territories Geoscience Office, Yellowknife Geoscience Forum Abstracts 2014, p. 53-54.

Pan, Y. and Fleet, M.E., 2002. Compositions of the apatite-group minerals: substitutions mechanisms and controlling factors. Reviews in Mineralogy and Geochemistry, 48, 13–49.

Pass, H.E., 2010. Breccia-hosted chemical and mineralogical zonation patterns of the Northeast Zone, Mt. Polley Cu-Ag-Au alkalic porphyry deposit, British Columbia, Canada. Unpublished Ph.D. thesis, The University of Tasmania, Hobart, Tasmania, Australia, 276p.

Patiño Douce, A.E., Roden, M.F., Chaumba, J., Fleisher, C., and Yogodzinski, G., 2011. Compositional variability of terrestrial mantle apatites, thermodynamic modeling of apatite volatile contents, and the halogen and water budgets of planetary mantles. Chemical Geology, 288, 14–31.

Peng, G., Luhr, J.F., and McGee, J.J., 1997. Factors controlling sulfur concentrations in volcanic apatite. American Mineralogist, 82, 1210–1224.

Piccoli, P.M. and Candela, P.A., 2002. Apatite in igneous systems. Reviews in Mineralogy and Geochemistry, 48, 255–292.

Plouffe, A., 2000. Quaternary geology of the Fort Fraser and Manson River map areas, central British Columbia. Geological Survey of Canada Bulletin 554, 62p.

Plouffe, A. and Ferbey, T., 2015a. Discovering buried copper porphyry mineralization: geochemistry and indicator minerals in till. Geological Survey of Canada Open File 7680, 45p.

Plouffe, A. and Ferbey, T., 2015b. Surficial geology, Gnawed Mountain area, British Columbia, parts of NTS 92I/6, I/7, I/10 and I/11. Geological Survey of Canada Canadian Geoscience Map 214 (preliminary), British Columbia Geological Survey Geoscience Map 2015-3, 1:50,000 scale.

Plouffe, A. and Ferbey, T., 2015c. Surficial geology, Granite Mountain area, British Columbia, parts of NTS 93-B/8 and 93-B/9. Geological Survey of Canada Canadian Geoscience Map 223 (preliminary), British Columbia Geological Survey Geoscience Map 2015-4, 1:50,000 scale.

Plouffe, A. and Ferbey, T., 2015d. Till composition near Cu-porphyry deposits in British Columbia: Highlights for mineral exploration. In: Rogers, N., (Ed.), TGI 4 - Intrusion Related Mineralisation

Project: New Vectors to Buried Porphyry-Style Mineralisation. Geological Survey of Canada Open File 7843, pp. 15–37.

Plouffe, A., Anderson, R.G., and Dunn, C.E., 2011. Till composition and biogeochemistry near a porphyry Cu-Mo deposit: Gibraltar Mine, British Columbia. Geological Survey of Canada Open File 6755, 25p.

Plouffe, A., Bednarski, J.M., Huscroft, C.A., Anderson, R.G., and McCuaig, S.J., 2011c. Late Wisconsinan glacial history in the Bonaparte Lake map area, south central British Columbia: implications for glacial transport and mineral exploration. Canadian Journal of Earth Sciences, 48, 1091–1111.

Plouffe, A., Ferbey, T., and Anderson, R.G., 2014. Till composition and ice-flow history in the region of the Gibraltar Mine: developing indicators for the search of buried mineralization. Geological Survey of Canada Open File 7592, poster.

Plouffe, A., Ferbey, T., Anderson, R.G., Hashmi, S., and Ward, B.C., 2013a. New TGI-4 till geochemistry and mineralogy results near the Highland Valley, Gibraltar, and Mount Polley mines, and Woodjam District: An aid to search for buried porphyry deposits. Geological Survey of Canada Open File 7473, 58p.

Plouffe, A., Ferbey, T., Anderson, R.G., Hashmi, S., Ward, B.C., and Sacco, D.A., 2013b. The use of till geochemistry and mineralogy to explore for buried porphyry deposits in the Cordillera - preliminary results from a TGI-4 intrusion-related ore systems project. Geological Survey of Canada Open File 7367, poster.

Plouffe, A., Ferbey, T., Levson, V.M., and Bond, J.D., 2012. Glacial history and drift prospecting in the Canadian Cordillera: recent developments. Geological Survey of Canada Open File 7261, 51p.

Plouffe, A., McClenaghan, M.B., Paulen, R.C., McMartin, I., Campbell, J.E., and Spirito, W.A., 2013c. Processing of glacial sediments for the recovery of indicator minerals: protocols used at the Geological Survey of Canada. Geochemistry: Exploration, Environment, Analysis, 13, 303–316.

Pouchou, J.L. and Pichoir, F., 1985. "PAP" Φ(ρZ) procedure for improved quantitative microanalysis. In: Armstrong, J.T., (Ed.), Microbeam Analysis. San Francisco Press, San Francisco, USA, pp. 104–106.

Prowatke, S. and Klemme, S., 2006. Trace element partitioning between apatite and silicate melts. Geochimica et Cosmochimica Acta, 70, 4513–4527.

Raudsepp, M., 1995. Recent advances in the electron-probe microanalysis of minerals for the light elements. The Canadian Mineralogist, 33, 203–218.

Rees, C., 2013. The Mount Polley Cu-Au deposit, south-central British Columbia, Canada. In: Logan, J.M. and Schroeter, T.G., (Eds.), Porphyry Systems of Central and Southern British Columbia: Tour of Central British Columbia Porphyry Deposits from Prince George to Princeton. Society of Economic Geologists Field Trip Guidebook Series 43, pp. 67–98.

Rees, C., Riedell, K.B., Proffett, J.M., MacPherson, J., and Robertson, S., 2015. The Red Chris copper-gold deposit, northern British Columbia, Canada: Igneous phases, alteration, and controls of mineralization. Economic Geology, 110, 857–888.

Roeder, P.L., MacArthur, D., Ma, X.-P., Palmer, G.R., and Mariano, A.N., 1987. Cathodoluminescence and microprobe study of rare-earth elements in apatite. American Mineralogist, 72, 801–811.

Roegge, J.S., Logsdon, M.J., Young, H.S., Barr, H.B., Borcsik, M., and Holland, H.D., 1974. Halogens in apatite from the Providencia area, Mexico. Economic Geology, 69, 229–240.

Rønsbo, J.G., 1989. Coupled substitution involving REEs and Na and Si in apatite in alkaline rocks from the Ilímaussaq intrusion, South Greenland, and the petrological implications. American Mineralogist, 74, 896–901.

Rotherham, D.C., Drummond, A.D., and Tennant, S.J., 1972. Exploration of Gibraltar. Western Miner, 45, 25–28.

Rukhlov, A.S., Plouffe, A., Ferbey, T., Mao, M., and Spence, J., 2016. Supplementary data for application of trace-element compositions of detrital apatite to explore for porphyry deposits in central British Columbia. British Columbia Ministry of Energy and Mines, British Columbia Geological Survey GeoFile 2016-1.

Schiarizza, P., 2014. Geological setting of the Granite Mountain batholith, host to the Gibraltar porphyry Cu-Mo deposit, south-central British Columbia. In: Geological Fieldwork 2013, British Columbia Ministry of Energy and Mines, British Columbia Geological Survey Paper 2014-1, pp. 95–110.

Schiarizza, P., 2015. Geological setting of the Granite Mountain batholith, south-central British Columbia. In: Geological Fieldwork 2014, British Columbia Ministry of Energy and Mines, British Columbia Geological Survey Paper 2015-1, pp. 19–39.

Schiarizza, P., Bell, K., and Bayliss, S., 2009a. Geology and mineral occurrences of the Murphy Lake area, south-central British Columbia (NTS 093A/03). In: Geological Fieldwork 2008, British Columbia Ministry of Energy, Mines and Petroleum Resources, British Columbia Geological Survey Paper 2009-1, pp. 169–187.

Schiarizza, P., Bell, K., and Bayliss, S., 2009b. Geology of the Murphy Lake area, NTS 93A/03. British Columbia Ministry of Energy, Mines and Petroleum Resources, British Columbia Geological Survey Open File 2009-03, 1:50,000 scale.

Schroeter, T.G., 2009. Woodjam copper-molybdenum-gold porphyry project: the exciting South East Zone discovery and beyond. In: Mineral Exploration Roundup 2009 Conference, Abstract volume, Association for Mineral Exploration British Columbia, Vancouver, B.C., pp. 37–38.

Schroeter, T.G., editor, 1995. Porphyry deposits of the northwestern Cordillera of North America. Canadian Institute of Mining, Metallurgy and Petroleum Special Volume 46, 888p.

Sha, L.-K. and Chappell, B.W., 1999. Apatite chemical composition, determined by electron microprobe and laser-ablation inductively coupled plasma mass spectrometry, as a probe into granite petrogenesis. Geochimica et Cosmochimica Acta, 63, 3861–3881.

Sherlock, R. and Trueman, A., 2013. NI 43-101 technical report for 2012 activities on the Woodjam South property. Gold Fields Horsefly Exploration Group and Consolidated Woodjam Copper Corporation, Cariboo Mining Division, British Columbia, 158p.

Sherlock, R., Blackwell, J., and Skinner, T., 2013. NI 43-101 technical report for 2012 activities on the Woodjam North property. Gold Fields Horsefly Exploration Group and Consolidated Woodjam Copper Corporation, Cariboo Mining Division, British Columbia, 275p.

Smythe, D.J. and Brenan, J.M., 2015. Cerium oxidation state in silicate melts: Combined fO_2, temperature and compositional effects. Geochimica et Cosmichimica Acta, 170, 173–187.

Stormer, J.C., Jr., Pierson, M.L., and Tacker, R.C., 1993. Variation of F and Cl X-ray intensity due to anisotropic diffusion in apatite during electron microprobe analysis. American Mineralogist, 78, 641–648.

Sutherland Brown, A.E., 1974. Gibraltar Mine (93B-12, 13). In: Geology, Exploration and Mining in British Columbia 1973, British Columbia Ministry of Mines and Petroleum Resources, pp. 299–318.

Sutherland Brown, A.E., editor, 1976. Porphyry deposits of the Canadian Cordillera. Canadian Institute of Mining and Metallurgy Special Volume 15, 510p.

Tepper, J.H. and Kuehner, S.M., 1999. Complex zoning in apatite from the Idaho batholith: a record of magma mixing and intracrystalline trace element diffusion. American Mineralogist, 84, 581–595.

Thomson, S.N., Gehrels, G.E., Ruiz, J., and Buchwaldt, R., 2012. Routine low-damage apatite U-Pb dating using laser ablation–multicollector–ICPMS. Geochemistry, Geophysics, Geosystems, 13, doi:10.1029/2011GC003928.

Tipper, H.W., 1971a. Glacial geomorphology and Pleistocene history of central British Columbia. Geological Survey of Canada Bulletin 196, 89p.

Tipper, H.W., 1971b. Multiple glaciations in central British Columbia. Canadian Journal of Earth Sciences, 8, 743–752.

Tollari, N., Barnes, S.-J., Cox, R.A., and Nabil, H., 2008. Trace element concentrations in apatite from the Sept-Îles Intrusive Suite, Canada — Implications for the genesis of nelsonites. Chemical Geology, 252, 180–190.

Vandekerkhove, S., Rowins, S.M., and Johnston, S.T., 2014. Geology and physicochemical conditions of copper-gold mineralization at the Three Firs porphyry prospect, Woodjam district, south-central British Columbia. In: Geological Fieldwork 2013, British Columbia Ministry of Energy and Mines, British Columbia Geological Survey Paper 2014-1, pp. 67-94.

van Straaten, B.I., Oliver, J., Crozier, J., and Goodhue, L., 2013. A summary of the Gibraltar porphyry copper-molybdenum deposit, south-central British Columbia, Canada. In: Logan, J.M. and Schroeter, T.G., (Eds.), Porphyry Systems of Central and Southern British Columbia: Tour of Central British Columbia Porphyry Deposits from Prince George to Princeton. Society of Economic Geologists Field Trip Guidebook Series 43, pp. 55–66.

Ward, B., Maynard, D., Geertsema, M., and Rabb, T., 2009. Iceflow history, drift thickness and drift prospecting for a portion of the QUEST Project area, central British Columbia (NTS 093G, H[west half], J). In: Summary of Activities 2008, Geoscience BC Report 2009-1, pp. 25-32.

Webster, J.D., 1990. Partitioning of F between H_2O and CO_2 fluids and topaz rhyolite melt: Implications for mineralizing hydrothermal fluids in F-rich granitic systems. Contributions to Mineralogy and Petrology, 104, 424–438.

Webster, J.D. and Piccoli, P.M., 2015. Magmatic apatite: a powerful, yet deceptive, mineral. Elements, 11, 177–182.

Williams, S.A. and Cesbron, F.P., 1977. Rutile and apatite: useful prospecting guides for porphyry copper deposits. Mineralogical Magazine, 41, 288–292.

Young, E.J., Myers, A.T., Munson, E.L., and Conklin, N.M., 1969. Mineralogy and geochemistry of fluorapatite from Cerro de Mercado, Durango, Mexico. In: US Geological Survey Paper 650D, pp. 84–93.

Trace element composition of fluorite and its potential use as an indicator in mineral exploration

Mao Mao[1, a], George J. Simandl[1, 2], Jody Spence[2], Michaela Neetz[1], and Daniel Marshall[3]

[1] British Columbia Geological Survey, Ministry of Energy and Mines, Victoria, BC, V8W 9N3
[2] School of Earth and Ocean Sciences, University of Victoria, Victoria, BC, V8P 5C2
[3] Department of Earth Sciences, Simon Fraser University, Burnaby, BC, V5A 1S6
[a] corresponding author: Mao.Mao13@outlook.com

Recommended citation: Mao, M., Simandl, G.J., Spence, J., Neetz, M., and Marshall, D., 2016. Trace element composition of fluorite and its potential use as an indicator in mineral exploration. In: Geological Fieldwork, 2015, British Columbia Ministry of Energy and Mines, British Columbia Geological Survey Paper 2016-1, pp. 181-206.

Abstract

Fluorite is an accessory and a gangue mineral in many metalliferous deposits, and the trace element composition of fluorite has been used to discriminate different deposit types. We examined fluorite from 14 North American deposits by performing 514 LA-ICP-MS analyses for thirty-four elements, to improve our database. This database will be required for future studies aiming to produce reliable discrimination diagrams for use in mineral exploration. Results of this study revealed that fluorite from sedimentary-hosted deposits (Liard, Kootenay Florence, vein; Hastie Quarry, Barnett mine, Elmwood, Gordonsville, Young mine, MVT) has Sr concentrations less than 200 ppm (with the exception of two outliers), and Y concentrations less than 31 ppm. REE chondrite-normalized patterns are convex or have a negative slope; 75% of the data have a chondrite-normalized REE ratio below 3. Seventy-five percent of fluorite analyses from peralkaline/alkaline-related deposits (Kipawa, Rexspar, Eaglet, Rock Candy), and Rock Canyon Creek have chondrite-normalized ratios higher than 2 for each lanthanide, and flat to weakly negative patterns. The 4th tetrad portion of the chondrite-normalized REE plots of sedimentary-hosted deposits has a weakly negative to negative slope, whereas the pattern for alkaline/peralkaline-related deposits varies from weakly negative to positive. Fifty percent of the data (between the 1st and 3rd quartile) from carbonatite-related deposits (Eldor and Wicheeda Lake) show sinusoidal patterns on chondrite-normalized REE plots, with wide element ranges in their first tetrad. Barium, Th, and U also show potential for use in indicator mineral discrimination diagrams. Analyses of single crystals reveals compositional zoning that may not be optically apparent. Fifty analyses on a single Rock Candy fluorite crystal identified three compositional zones. One of these zones shows variations of trace elements (Ce, 14.5%; Pr, 13.9%; Nd, 14.9%; Sm, 16.9%; Eu 11.4%; Gd, 19.2%; Dy, 18.8%) with similar or lower variability than NIST glass (615). This zone may be useful as a matrix-matched secondary standard. Intra-grain chemical zoning is unlikely to be a major cause of elemental variation within a deposit and, by extrapolation, between deposit types. Our results suggest that Y, Sr and REE are essential for constructing discrimination diagrams that use fluorite as an indicator mineral.

Keywords: Fluorite, REE, indicator mineral, exploration, LA-ICP-MS

---

1. Introduction

Fluorite (CaF_2) belongs to the isometric crystal system, with a cubic, face-centred lattice. Fluorite commonly forms cubes or octahedrons, and less commonly dodecahedrons. Single crystal fluorite is transparent to translucent, and has vitreous luster. Although fluorite can be colourless, it occurs in a variety of colours, including purple, green, blue, yellow, and can exhibit colour zoning (Staebler et al., 2006). Fluorite from many localities is fluorescent (Verbeek, 2006).

Fluorite density varies from 3.0-3.6 g/cm^3, depending to a large extent on inclusions and impurities in the crystal lattice (Staebler et al., 2006). The Ca^{2+} ion in the fluorite crystal structure can be replaced by Li^+, Na^+, K^+, Mg^{2+}, Mn^{2+}, Fe^{2+}, Fe^{3+}, Zn^{2+}, Sr^{2+}, Y^{3+}, Zr^{4+}, Ba^{2+}, Pb^{2+}, Th^{4+}, U^{4+}, and lanthanide ions (Bailey et al., 1974; Bill and Calas, 1978; Gagnon et al., 2003; Schwinn and Markl, 2005; Xu et al., 2012; Deng et al., 2014). It is expected that the colour zoning observed in many fluorite crystals is manifested by corresponding variations in concentrations of trace elements. Sector zoning (e.g., [111] relative to [100] sector), reflecting preferential substitution and incorporation of trace elements was described by Bosze and Rakovan (2002). Concentrations of impurities in fluorite commonly do not exceed 1% (Deer et al., 1965).

Fluorite, as an accessory and a gangue mineral, occurs in many metalliferous deposits and, in exceptional cases, it can be the main ore of an economic deposit (Simandl, 2009). Fluorite commonly occurs adjacent to or in: carbonatites and alkaline complexes (Kogut et al., 1998; Hagni,1999; Alvin et al., 2004; Xu et al., 2004; Salvi and Williams-Jones, 2006); Mississippi Valley-type (MVT) Pb-Zn-F-Ba deposits; F-Ba-(Pb-Zn) veins (Grogan and Bradbury, 1967,1968; Baxter et al., 1973; Kesler et al., 1989; Cardellach et al., 2002; Levresse et al., 2006); hydrothermal Fe (±Au, ±Cu) and rare earth element (REE) deposits (Borrok et al., 1998; Andrade et al.,1999; Fourie, 2000); precious metal concentrations (Hill et al., 2000); skarns (Lu et al., 2003); Sn-polymetallic greissen-type deposits (Bettencourt et al., 2005); and uranium deposits (Cunningham et al., 1998; Min et al., 2005).

Based on its physical and chemical properties, and its association with diverse deposit types, fluorite can be used as a proximal indicator mineral for mineralization if appropriate discrimination diagrams are established. The trace element distribution in fluorite of ore deposits has been previously studied by Möller et al. (1976), Bau et al. (2003), Gagnon et al. (2003), Schwinn and Markl (2005), and Deng et al. (2014). The benchmark paper by Möller et al. (1976) divided the Tb/Ca vs Tb/La diagram into sedimentary, hydrothermal, and pegmatitic fields. Eppinger and Closs (1990) investigated fluorite in south-central New Mexico, showing that Sr, Ba, Y, and U composition and Eu anomalies are useful in identifying fluorite from epithermal Au-Ag-Cu-Pb-Zn veins, W-Be-Fe skarns, epithermal Ba-Pb veins, and epithermal calcite-silica-fluorite veins. Gagnon et al. (2003) studied the Gallinas Mountains (New Mexico), Rock Canyon Creek (British Columbia), South Platte (Colorado), and St. Lawrence (Newfoundland) deposits. They concluded that chondrite-normalized REE patterns for fluorite from granite-related deposits and alkaline rock-related deposits are distinct. Schwinn and Markl (2005) investigated the REE behaviors of hydrothermal fluorite, showing that the REE are carried by basement-derived hydrothermal fluids, and not from the country rock adjacent to fluorite mineralization. More recently, Makin et al. (2014) compiled trace-element concentrations of fluorite from MVT, fluorite-barite veins, peralkaline-related, and carbonatite-related deposits to validate the previously published diagram by Möller et al. (1976).

A preliminary survey (Mao et al., 2015) investigated fluorite from the Rock Candy deposit (British Columbia), Kootenay Florence (British Columbia), Eaglet (British Columbia), Eldor (Quebec), and the Hastie quarry (Illinois) by laser ablation-inductively coupled mass spectrometry (LA-ICP-MS) analysis of individual grains and powder fused beads, and by X-ray fluorescence (XRF) analysis. Their results showed that Sr, Y, and lanthanides concentrations in fluorite can be reliably measured by LA-ICP-MS, and these elements have the potential to discriminate fluorite from different deposit types. Other elements, such as Mn, Ba, and Th are present in detectable levels in some deposits and may further contribute to discriminating deposit types. The same study confirmed that the stoichiometric Ca content of fluorite can be used as the internal standard for LA-ICP-MS analysis of fluorite.

A matrix-matched standard of fluorite for LA-ICP-MS analysis is currently unavailable because reference minerals with homogeneous trace element contents are scarce (Klemme et al., 2008). Previous LA-ICP-MS studies on trace elements in fluorite used National Institute of Standards and Technology (NIST) glasses as the main external standard and Ca as the internal standard (Gagnon et al., 2003; Schwinn and Markl 2005; Dimitrova et al., 2011; Baele et al., 2012). Jackson (2008) showed that fluorite REE contents analyzed by LA-ICP-MS using non-matrix-matched standards (10-100 ppm) agree well with results from solution nebulization-ICP–MS. However, Jackson (2008) and Sylvester (2008) also revealed that large errors can occur when the fractionation indices of elements differ substantially from those of the internal standard. Therefore, finding a matrix-matched secondary standard would improve the accuracy of LA-ICP-MS analyses.

For this study, we analyzed samples from 14 North American deposits by LA-ICP-MS (Fig. 1; Table 1). The main objectives were to: 1) examine trace element variations in crystals; 2) evaluate the element composition of fluorite on a deposit scale; 3) document variations in chemical composition of fluorite from different deposit types; and 4) assess fluorite from Rock Candy as a matrix-matched secondary standard for LA-ICP-MS.

2. Laboratory methods

2.1. Sample preparation

In total, 36 rock samples from 14 deposits in North America were selected for use in this study (Table 2). Twenty-eight samples were broken to select fluorite fragments of sizes 0.2-2.5 cm. These fluorite fragments were then crushed and examined under a binocular microscope to select only inclusion-free fluorite fragments (0.5 mm to 3 mm). Grains from each inclusion-free fluorite concentrate were mounted and polished on epoxy pucks for trace element analysis of individual grains by LA-ICP-MS (Table 2). Another nine rock samples were prepared as polished thin sections 200 μm thick. These polished thin sections were analyzed by LA-ICP-MS for trace element concentrations.

Two single fluorite crystals were covered by 57 LA-ICP-MS analyses to determine the trace element variations on the crystal scale. One of these, a dodecahedron green fluorite (~1 cm in diameter) from the Rock Candy deposit, named RC-08-8X (from sample RC-08-8), was split close to its {111} cleavage and mounted with the cleavage face upward (Fig. 2). This Rock Candy crystal was selected because of its centimetre size and

Fig. 1. Location of the 14 deposits examined in this study.

Table 1. Summary of the fluorite-bearing deposits sampled for this study.

Deposit name	**Deposit-type**	**Local Geology**	**Additional information**	**Mineral assemblage**
Rock Canyon Creek, BC	Carbonatite or peralkaline intrusion related (fl±REE)	Cambro-Ordovician to Devonian carbonate rocks (Leech, 1979) disseminated and veinlet fl and brt associated with REE mineralization occurs in dolomite (Pell, 1992; Samson et al., 2001).	fl bearing rocks have high F, REE, Ba, Nb, Mo, Zn, Pb, Mg, Ag by whole-rock geochemistry (Samson et al., 2001; Gagnon et al., 2003).	Main zone: fl, brt, dol, qz, synchysite, parasite, bastnäesite, py, cal, gorceixite, ilt, ap. Float zone: fl, qz, brt, ms, crl, prosopite, elpasolite, goyazite, gorceixite (Samson et al., 2001).
Eldor, QC	Carbonatite-hosted REE ± Nb ±Ta ±fl ± ap	carbonatite complex (1.88-1.87 Ga, U-Pb); pcl and columbite in the middle stage carbonatite; REE minerals and fl in the late stage carbonatite (Gagnon et al., 2012).	fl as intergrowths with mnz,; may incorporate aggregates of anhedral bastnaesite and small veins of xtm (Gagnon et al., 2012).	mnz, bastnaesite, parasite, synchysite, xtm, fl, dol, qz, ms, Accesssory minerals are ap, py, sp, mag, Nb-bearing rt, nioboaeschynite, ferrocolumbite and ilm (Wright et al., 1998; Gagnon et al., 2012).
Wicheeda lake, BC	Carbonatite-related LREE±Nb	steeply dipping lens of carbonatite in metasedimentary rocks (Trofanenko et al., 2014).	trace fl (Trofanenko et al., 2014); relationship to REE mineralization uncertain	Bastnäesite(Ce), mnz(Ce), pcl, cal, bt, py, ab, ap, fl (Trofanenko et al., 2014).
Rock Candy, BC	fl-brt vein	fl veins hosted by Tertiary andesites (adjacent to Coryell syenite) consisting of ab, oligoclase, act, bt, mag. altered andesite adjacent to veins contains chl, ser, qz, cal, py, clay minerals (Pell, 1992).	breccia and composite veins with multiple generations of green and purple fl are exposed in a trench, containing fragments of severely altered country rock (Pell, 1992).	fl, brt, chalcedony, kln, py, qz, and cal (Pell, 1992; Mauthner and Melanson, 2006).
Eaglet, BC	Mo- and fl-bearing granite-syenite	granitic orthogneiss (375-335 Ma, U-Pb zircon; Mortensen et al., 1987) with dikes and pods of aplite, pegmatite, lamprophyre, and feldspar porphyry dikes, adjacent to contact with the Neoproterozoic biotite-garnet metapelite (Pell, 1992).	fl veinlets, veins, and pods; disseminated mol near the fl mineralization but not overlapping (Hora et al., 2008).	qz, mol, fl, carbonate minerals, clt, prismatic REE-bearing carbonates, gn, sp, py, gp, dck, aln, pcl (Pell, 1992; Hora et al., 2008).
Rexspar, BC	Volcanic hosted fl	Devonian-Mississippian trachytic rocks host one fl and five uranium zones (Preto, 1978).	fl zone is affected by a fine-grained, brecciated, tuffaceous trachyte with pervasive potassic alteration (McCammon, 1955; Preto, 1978; Pell, 1992).	fl associated with qz, brt, mol, clt, str, ccp, gn, and bastnaesite (Pell, 1992); fl from banded py-fl facies was analysed.
Kipawa, QC	Peralkaline-related REE±Zr	eudialyte, mosandrite, britholite-bearing syenite gneisses (Allan, 1992).		foliated leucocratic syenite with15-20% amphiboles, and 80-85% feldspar ± fl, vlasovite, gittensite, mosandrite, zircon, titanite?, fosterite?, baestnasite? (Saucier et al., 2013)

Table 1. Continued.

Deposit name	Deposit-type	Local Geology	Additional information	Mineral assemblage
Kootenay Florence, BC	Sedimentary-hosted Ag-Pb-Zn veins and replacements	veins and replacements along contact of limestone and overlaying schist; fl was recovered from a cave (Fyles, 1967).	sample selected for this study was a coarse, open space filling fl.	qz, ca, sp, ga, py, ± fl (Pell, 1992; Schofield, 1920).
Liard, BC	Carbonate-hosted fl±wth±brt (MVT)	irregular lenses, veins, breccia zones, and replacements in limestone or along limestone- mudstone contacts (Woodcock, 1972; Pell, 1992).	morphology of the mineralized zones, association with an unconformity and temperature of homogenization (T_h) suggest affinity with MVT deposits. T_h in cal, sp , brt = 62-240°C; salinity ~6.4-17.0 wt% NaCl equivalent (Changkakoti et al., 1987).	fl, wth, and brt ± barytocalcite; gangue qz and cal (Pell, 1992).
Barnett mine, IL	MVT (fl±wth±brt ±Pb±Zn)	mineralization follows a fault in a Mississippian interlayered greenish gray shale and sandstone unit (Baxter et al., 1967; Denny and Counts, 2009).	detailed geological descriptions unavailable.	
Hastie Quarry, IL	MVT (fl±wth±brt ±Pb±Zn)	bedded replacement zones in Mississippian oolitic or fossiliferous limestones underlying a sandstone unit (Pelch et al., 2015) age of mineralization is 272±17 Ma (fl, Sm-Nd; Chesley et al., 1994).	steeply dipping faults and fractures interpreted as feeders for mineralizing fluids (Pelch et al., 2015).	fl in hydrothermal stage II and III with sp, gn, qz, and ccp; gangue minerals brt, wth, and cal in stage IV (Richardson and Pinckney, 1984; Pelch et al., 2015).
Gordonsville, TN	MVT (sp±fl±cal±brt)	mineralization in collapse breccias in Lower Ordovician dolostone; deposits in dolomitized limestones (Misra and Lu, 1992).	massive, open space-filling, and disseminated sp T_h in cal, sp , brt = 100-150°C; salinity ~18-23 wt% NaCl equivalent (Misra and Lu, 1992).	sp, fl, cal, brt, and minor ± dol, gn, and py (Misra and Lu, 1992).
Elmwood, TN	MVT (sp±fl±cal±brt)	same as Gordonsville	same as Gordonsville	same as Gordonsville
Young mine, TN	MVT (sp±fl±cal±brt)	dolostone and limestone	detailed geological descriptions unavailable.	

Mineral abbreviations according to Whitney and Evans (2010): ab (albite), aln (allanite), ap (apatite), brt (barite), bt (biotite), cal (calcite), ccp(chalcopyrite), chl (chlorite), clt (celestite), crl (cryolite), dck (dickite), dol (dolomite), fl (fluorite), gp (gypsum), gn (galena), ilm (ilmenite), ilt (illite), kln (kaolinite), mag (magnetite), mol (molybdenite), ms (muscovite), pcl (pyrochlore), py (pyrite), qz (quartz), rt (rutile), ser (sericite) sp (sphalerite), str (strontianite), wth (witherite), xtm (xenotime).

Table 2. Statistical summary of fluorite samples and analyses.

Deposit name/Location	Sample Name	Fluorite Colour	No. of Analyses LA-ICP-MS	Total analysis
Rock Canyon Creek, BC	RC-9A-1	Purple	8	
	RC-9A-2	Colourless/purple	11	
	RC-9C	Purple	12	
	DP-08-1	Purple	8	
	DP-08-2A	Purple	10	49
Eldor, QC	ELDOR2	Colourless/purple	23	
	ELDOR3	Colourless/purple	9	
	ELDOR4	Colourless/purple	8	40
Wicheeda lake, BC	WI	Purple	7	7
Rock Candy, BC	RC-08-1	Green	10	
	RC-08-5	Purple/Green	26	
	RC-08-7	Pale	12	
	RC-08-8	Green	13	
	RC-08-8X	Green	50	111
Eaglet, BC	EAGLET7	Purple	17	
	EAGLET9	Colourless	12	
	EAGLET11	Colourless/purple	9	38
Rexspar, BC	08-GS-FL	Purple	18	
	08-GS-61A	Colourless	13	31
Kipawa, QC	Kipawa1	Colourless/purple	22	22
Kootenay Florence, BC	AHS-1	Colourless	13	13
Liard, BC	Liard-1	Colourless/purple	24	
	Liard-2	Colourless/purple	9	33
Hastie Quarry, IL	HQ-12S-9E	Yellow/purple	24	
	HQ-12S-9EB	Yellow/purple	4	28
Barnett mine, IL	BM-28-12S-8EV(W)	Colourless	20	
	BM-28-12S-8EMV(P)	Purple	24	44
Gordonsville, TN	204-4	Colourless/purple	12	
	205-4	Colourless/blue	6	
	293-4	Colourless/blue	12	
	58-15	Colourless/blue	6	
	58#11	Colourless/blue	12	48
Elmwood, TN	20-78#8	Colourless/blue	13	13
Young mine, TN (Mascot-Jefferson city)	YM9215-01	Colourless/purple	4	
	YM9215-02	Colourless/purple	10	
	YM9215L-01	Colourless/purple	8	
	YM9215L-02	Colourless/purple	8	
	YM9215-1X	Colourless/purple	7	37
				514

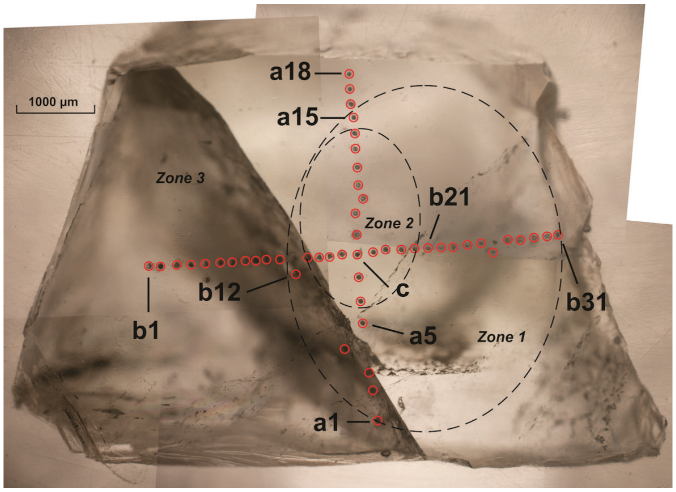

Fig. 2. Composite photo of sample RC-08-8X (Rock Candy Mine) in epoxy puck under plane-polarized light. The red circles indicate the location of LA-ICP-MS analyses along lines systematically numbered from 'a1-a18' (bottom to top) and 'b1-b31' (left to right) intersecting at point 'c'. Three analytical points (a4, b12, and b26) are offset from the lines 'a1-a18' and 'b1-b31'; to avoid impurities, original analyses on the line were discarded due to abnormal signals. Compositional zones delineated by dashed lines.

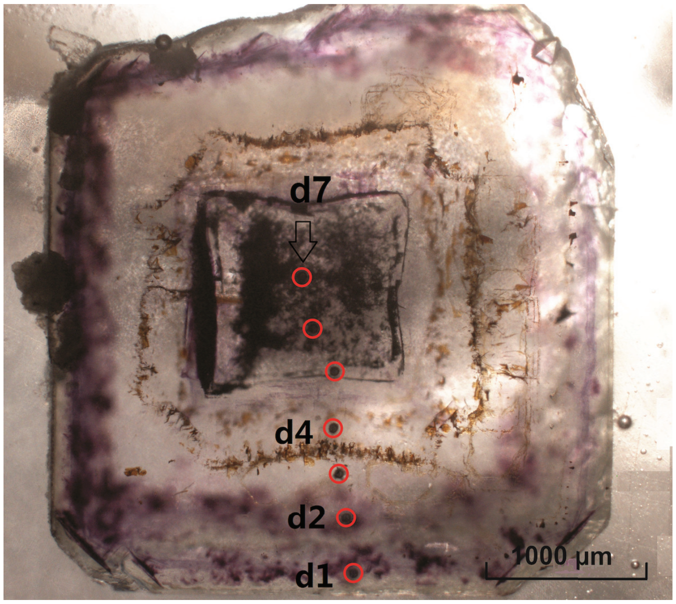

Fig. 3. Photo of the sample YM9215-1X in epoxy puck. The red circles indicate analytical points systematically numbered from 'd1-d7' (bottom to top).

lack of visible zoning using a petrographic microscope. The second sample is a cubic fluorite crystal with macroscopically visible colour zoning from Young mine, named YM9215-1X (derived from sample YM9215-01), which was mounted with the (001) face upward (Fig. 3).

2.2. LA-ICP-MS analysis

LA-ICP-MS analyses of fluorite grains were performed on a Thermo X-Series II (X7) quadrupole ICP-MS at the School of Earth and Ocean Sciences, University of Victoria. A New Wave UP-213 was coupled to the X-Series II with Helium as the carrier gas.

Fluorite grains were analyzed with a 55 µm diameter laser spot, a pulse rate of 10 Hz, and a measured fluence ranged from 7.69 to 12.55 J/cm^2. A pre-ablation warm-up of 5 seconds was used to avoid unstable laser energy at the beginning of each ablation. All spectra were recorded for 120 seconds including ~30 seconds gas blank before ablation started, 60 seconds during ablation, and ~30 seconds after ablation. At least 60 seconds of gas flushing occurred between analyses. The ICP-MS was optimized to maximize sensitivity and minimize oxide formation. Forward radio frequency ablation was carried out at 1400 watts. The dwell time was 10 ms for all elements.

The stoichiometric Ca content (51.33 wt.%) of fluorite was used as the internal standard for LA-ICP-MS calibration (Mao et al., 2015), whereas NIST glass standards (611, 613, 615) were used for external calibration (Jochum et al., 2011). Each analysis session started with NIST glasses 615, 613, and 611, followed by sample RC-08-8X, and then six to seven unknowns, before all four standards were repeated. During data reduction, time-resolved count rates were carefully checked and any spectra with spikes, indicating possible inclusions, were excluded. The data reduction procedure for each element was as follows: 1) selection of the time intervals for the background and signal region of each spectrum; 2) calculation of the mean CPS (counts per second) of these intervals; 3) background correction of the signal CPS; 4) external and internal standard normalizations; 5) drift correction using a linear drifting factor determined from repeat analysis of NIST 611; and 6) calibration using sensitivities for each element determined from the initial analyses of NIST 615, 613 and 611 in each load.

Thirty-four trace elements were analyzed by LA-ICP-MS for reconnaissance. The experimental precision was determined by repeat analyses of NIST glasses 613 and 615. Based on NIST 613, the 2σ precision for elements with concentrations ranging from tens to several hundred ppm is <5% for Mn, Sr, and Nb; from 5% to 10% for Mg, Sc, Ti, V, Cu, Zn, Rb, Y, Zr, Mo, Ba, lanthanides, W, Pb, and Th; and from 10% to 20% for Fe and U. For NIST 615, which contains lower concentrations of all elements than NIST 613, the 2σ precision is <15% for Mg, Pr, Eu, Tb, Ho, Tm, Lu, Pb, and Th; between 15-20% for Rb, Sr, Y, Zr, Nb, Ba, La, Nd, Sm, Dy, Er, Yb, and W; from 20% to 30% for V, Ce, Gd, and U; and >30% for other elements.

The limit of detection (LOD) was determined for each element using the following:

$$\mathrm{LOD} = \frac{3 \text{ x } (\text{STDev background signal})}{\text{Sensitivity}(\text{per analyte element, per session})}$$

Where 'STDev background signal' is the standard deviation of the signal for a given element collected before ablation for each sample (gas blank), and 'Sensitivity' is the calibrated sensitivity determined from NIST 615, 613 and 611 in each session. Sensitivity = (corrected signal / element concentration).

The lower limits of detection are typically <20 ppm for Fe;

<15 ppm for Sr; <5 ppm for Mg; <3 ppm for Mn and Y; <2 ppm for Ba; <1 for Rb, Ce, Nd, and Pb; <0.5 for La, Pr, Sm, Gd, Dy, Th, and U; <0.2 for Zr, Nb, Mo, Eu, Tb, Ho, Er, Tm, Yb, Lu, and W.

3. Results

A total of 514 analyses were obtained from 38 samples (Table 2). The number of analyses per sample varied from 4 to 26, and many individual grains in these samples were analyzed twice to estimate trace element variations. At least 80% of the analyses have detectable levels of Sr, Y, and all lanthanides except Tm and Lu, which were detected in approximately 70% of analyses. In a few analyses, Mg, Mn, Zr, Ba, W, Th, and U are in concentrations above the detection limits. Iron is detectable in almost all analyses, but shows little variation in concentration. Few of the remaining elements are above their detection limits (Sc, V, Cu, Zn, Rb) or show little variations (Na, Ti, Nb, Mo, Pb) and hence will not be discussed further because they show limited potential for establishing discrimination diagrams.

3.1. Analytical results of trace elements by deposit (±2σ)

Strontium concentrations in analyzed fluorite grains vary from 3.41 (±0.57) to 3,530 (±180) ppm (Table 3; Fig. 4a). Fluorite from Eaglet has the highest Sr contents (1,830 ±90 – 3,530 ±180 ppm), followed by fluorite from Rexspar (1,110 ±60 – 1,640 ±80 ppm), Eldor (886 ±45 – 3,360 ±170 ppm), and Kipawa (952 ±48 – 1,240 ±60 ppm). Fluorite from Kootenay Florence, Liard, Hastie Quarry, Barnett mine, Young mine, Elmwood, Gordonsville, and Wicheeda Lake have Sr concentrations less than 200 ppm. Fluorite from the Elmwood has the lowest Sr contents (5.07 ±0.85 – 21.0 ±3.5 ppm), and the Gordonsville fluorite has the second lowest Sr contents (3.41 ±0.57 – 38.6 ±6.4 ppm). The range of Sr concentrations (3.41 ±0.57 – 808 ±40 ppm) in the Rock Canyon Creek samples overlap with the other deposits except for Eaglet, Rexspar, Eldor, and Kipawa. Fluorite from Rock Candy has a variation in Sr content from 125 (±6) to 701 (±35) ppm (Table 3; Figure 4a).

The term 'REE', as used in this paper, includes all lanthanides and Y (Sc will not be discussed due to its low concentrations in fluorite). The light REE (LREE) analyses include La, Ce, Pr, Nd, Sm, and Eu, and the heavy REE (HREE) analyses include Gd, Tb, Dy, Ho, Er, Tm, Yb, and Lu (Y is not included). From La to Eu, the general trends of element concentrations for all deposits do not show significant variations, and are summarized by the results of Ce (Fig. 4b). The deposits with consistently high Ce contents (Table 3; Fig. 4b) are Kipawa (15.1 ±0.8 – 120 ±7 ppm), and Rexspar (18.2 ±1.0 – 70.2 ±3.9 ppm). The Ce contents of fluorite from Rock Canyon Creek (0.01 ±0.003 – 205 ±11.2 ppm), Rock Candy (2.07 ±0.55 – 123 ±7 ppm), and Eldor (0.01 ±0.003 – 54.4 ±3.0 ppm) all show wide variations. Fluorite from Wicheeda Lake, Young mine, Kootenay Florence, Liard, Elmwood, Gordonsville, Barnett mine, and Hastie Quarry mostly have Ce contents less than 2 ppm (Fig. 4b). The lowest Ce contents are in Hastie Quarry fluorite (0.005 ±0.001 – 0.04 ±0.01 ppm), followed by Barnett mine (0.007 ±0.002 – 0.38 ±0.01 ppm). Neodymium shows similar concentration trends to Ce in all the deposits (Figs. 4b, c).

The element concentrations of HREE are summarized by the results of Gd (Fig. 4d). The highest contents of Gd are most commonly from Rexspar (5.95 ±0.42 – 32.4 ±2.3 ppm), followed by Kipawa (4.63 ±0.50 – 12.9 ±0.9 ppm), and are only surpassed by outliers of Eldor and values above the 3rd quartile from Rock Canyon Creek and Rock Candy. Fluorite from Rock Canyon Creek (0.76 ±0.16 – 45.4 ±3.2 ppm) and Rock Candy (0.06 ±0.01 – 109 ±7.7 ppm) show wide variations in Gd. The Young mine fluorite has the lowest Gd concentrations (0.01 ±0.002 – 0.27 ±0.05 ppm). Ytterbium shows similar concentration trends to Gd in all the deposits (Figs. 4d, e).

Yttrium ranges from 0.03 (±0.006) to 1,450 (±120) ppm (Table 3; Fig. 4f), with wide variations in samples from Rock Candy (0.50 ±0.09 – 1,450 ±120 ppm) and Rock Canyon Creek (1.15 ±0.22 – 946 ±77 ppm), which overlap with all other deposits except Young mine, which has the lowest Y concentrations (0.03 ±0.006 – 4.2 ±0.8 ppm, mostly <1 ppm). Besides Y in fluorite from Rock Candy and Rock Canyon Creek, there are very high Y contents in fluorite from Kipawa (132 ±11 – 304 ±25 ppm), Rexspar (92.8 ±7.5 – 645 ±52 ppm), and Eldor (104 ±8 – 866 ±70 ppm). Fluorite from Kootenay Florence, Liard, Hastie Quarry, Barnett mine, Young mine, Elmwood, Gordonsville, and Wicheeda Lake have less than 31 ppm Y. The Y concentrations in Eaglet samples vary from 27.7 (±2.2) to 74.1 (±6.0) ppm (Table 3; Fig. 4f).

The behaviours of Ce and Eu can differ to those of the adjacent REEs due to their redox sensitivity. Large variations in Ce anomalies

($\mathrm{Ce/Ce}^{*} = \frac{(\mathrm{Ce/Ce_{ch}})}{\sqrt{[(\mathrm{La/La_{ch}})\mathrm{x}(\mathrm{Pr/Pr_{ch}})]}}$; Taylor and McLennan, 1985)

are seen in Hastie Quarry (0.43-1.25), Barnett mine (0.5-1.12), Rock Candy (0.69-1.05), and Eldor (0.6-1.06; Fig. 5a) samples. Sixty percent of the Ce anomalies from Eaglet are positive (>1). Fluorite from Young mine, Elmwood and Kipawa have Ce anomalies less than 0.93. Fluorite from Kootenay Florence (0.48-0.64) and Liard (0.51-0.68) have the strongest negative (<1) Ce anomalies.

The Eu anomalies

($\mathrm{Eu/Eu}^{*} = \frac{(\mathrm{Eu/Eu_{ch}})}{\sqrt{[(\mathrm{Sm/Sm_{ch}})\mathrm{x}(\mathrm{Gd/Gd_{ch}})]}}$; Taylor and McLennan, 1985)

of fluorite range from 0.17 to 4.1, but most are between 0.2 and 2.8 (Fig. 5b). Fluorite from the Barnett mine shows the widest range in Eu anomalies, which are all positive (1.07-4.0). Generally, fluorite from Eldor and Rock Canyon Creek has very small Eu anomalies (Eu/Eu* = 0.8–1.3, median = 1.05). Most of the fluorite from Rock Candy, Elmwood, and Gordonsville has weak, positive Eu anomalies with magnitudes from 0.82 to 2.2. The remaining deposits generally have negative Eu anomalies. Kipawa has consistently strong negative Eu anomalies (Eu/Eu* = 0.32–0.37).

The main discriminations for lanthanides and Y in fluorite from the different deposits are listed below.

Table 3. Summary of trace-element contents (ppm) in fluorite grains. M.D.L.: Minimum Detection Limit. For each element, results below detection limit have been replaced with half the minimum detection limit from all analysis sections.

			Rock Canyon Creek		n=49			**Eldor**		n=40	**M.D.L.**
(ppm)	Minimum	1st quartile	Median	3rd quartile	Maximum	Minimum	1st quartile	Median	3rd quartile	Maximum	
Na	1.200	61.000	188.000	467.000	1730.000	1.200	1.200	13.200	17.400	64.100	2.402
Mg	0.470	0.470	22.500	97.400	582.000	0.470	0.470	0.470	2.780	23.200	0.942
Sc	0.130	0.130	0.130	1.120	11.100	0.130	0.130	0.130	0.130	0.130	0.267
Ti	0.060	0.410	0.510	0.510	5.070	0.020	0.070	0.510	0.510	0.510	1.021
V	0.020	0.040	0.040	0.040	0.470	0.040	0.040	0.040	0.040	3.390	0.082
Mn	0.360	0.360	0.360	2.210	39.000	0.360	0.360	0.360	0.360	0.360	0.717
Fe	129.000	154.000	171.000	234.000	281.000	104.000	119.000	134.000	166.000	219.000	2.800
Cu	0.120	0.160	0.160	0.160	8.290	0.160	0.160	0.160	0.160	9.260	0.317
Zn	0.040	0.040	0.040	0.040	0.120	0.040	0.040	0.040	0.040	2.810	0.074
Rb	0.020	0.030	0.030	0.030	8.070	0.030	0.030	0.030	0.030	0.030	0.059
Sr	3.410	59.200	212.000	357.000	808.000	886.000	982.000	1010.000	1120.000	3360.000	0.300
Y	1.150	9.310	70.400	118.000	946.000	104.000	152.000	167.000	197.000	866.000	0.065
Zr	0.002	0.030	0.030	1.470	11.300	0.002	0.003	0.010	0.030	0.040	0.004
Nb	0.003	0.020	0.020	1.010	6.230	0.001	0.003	0.020	0.020	0.050	0.003
Mo	0.010	0.080	0.110	0.340	0.740	0.004	0.010	0.070	0.110	0.110	0.215
Ba	0.010	0.010	1.890	11.500	83.700	0.010	0.010	0.020	0.560	2.200	0.027
La	0.010	0.740	8.380	27.600	124.000	0.010	0.110	0.280	0.940	56.800	0.027
Ce	0.010	2.440	16.400	41.600	205.000	0.010	0.440	0.720	1.910	54.400	0.023
Pr	0.010	0.600	1.820	4.450	15.800	0.010	0.110	0.150	0.330	4.920	0.016
Nd	0.050	4.490	6.740	18.300	76.000	0.050	0.860	1.070	1.810	18.400	0.091
Sm	0.240	1.480	2.400	4.750	15.600	0.050	0.680	0.770	0.910	5.790	0.105
Eu	0.120	0.560	0.840	2.270	6.850	0.010	0.460	0.490	0.560	3.590	0.029
Gd	0.760	1.720	2.730	7.160	45.400	1.460	2.300	2.430	2.790	18.200	0.110
Tb	0.110	0.230	0.350	1.040	4.260	0.010	0.460	0.490	0.550	4.460	0.014
Dy	0.460	1.570	2.600	9.390	41.400	2.380	3.550	3.940	4.430	39.200	0.083
Ho	0.060	0.250	0.580	1.560	11.200	0.010	0.790	0.890	0.990	8.220	0.020
Er	0.140	0.550	2.070	3.810	38.400	1.330	2.310	2.640	2.940	20.800	0.042
Tm	0.010	0.050	0.280	0.450	5.600	0.010	0.260	0.300	0.340	1.960	0.013
Yb	0.030	0.340	1.770	2.750	37.600	0.810	1.720	1.910	2.110	8.700	0.050
Lu	0.010	0.040	0.230	0.340	4.820	0.010	0.210	0.260	0.280	1.240	0.011
W	0.000	0.020	0.070	0.230	0.710	0.001	0.020	0.030	0.080	0.240	0.048
Pb	0.010	0.240	0.590	1.770	10.500	0.010	0.010	0.010	0.020	1.530	0.020
Th	0.420	2.490	7.770	53.500	108.000	0.003	0.010	0.010	0.030	0.260	0.012
U	0.001	0.005	0.020	0.080	3.220	<0.001	0.005	0.005	0.005	0.005	0.010

Table 3. Continued.

			Wicheeda lake		n=7			**Eaglet**		n=38	**M.D.L.**
(ppm)	Minimum	1st quartile	Median	3rd quartile	Maximum	Minimum	1st quartile	Median	3rd quartile	Maximum	
Na	1.200	1.200	1.200	39.000	75.400	1.200	1.200	15.000	19.200	40.000	2.402
Mg	0.470	0.470	0.470	0.470	82.000	0.470	0.470	0.470	0.470	3.290	0.942
Sc	0.130	0.130	0.130	0.130	0.130	0.030	0.130	0.130	0.130	0.130	0.267
Ti	0.030	0.390	0.510	0.510	0.510	0.030	0.090	0.510	0.510	0.510	1.021
V	0.040	0.040	0.040	0.040	0.040	0.040	0.040	0.040	0.040	0.040	0.082
Mn	0.360	0.360	0.360	0.360	32.100	0.360	3.940	4.770	5.490	7.960	0.717
Fe	193.000	222.000	234.000	246.000	258.000	120.000	139.000	151.000	169.000	201.000	2.800
Cu	0.120	0.150	0.160	0.160	0.170	0.110	0.160	0.160	0.160	0.160	0.317
Zn	0.040	0.040	0.040	0.040	0.080	0.040	0.040	0.040	0.040	1.790	0.074
Rb	0.030	0.030	0.030	0.080	0.230	0.030	0.030	0.030	0.030	0.030	0.059
Sr	12.400	14.400	37.000	53.900	60.200	1830.000	2350.000	2600.000	2810.000	3530.000	0.300
Y	3.540	4.540	6.080	10.800	17.500	27.700	30.200	49.300	55.000	74.100	0.065
Zr	0.030	0.030	0.030	0.030	0.030	0.002	0.010	0.030	0.030	0.030	0.004
Nb	0.002	0.003	0.020	0.050	0.070	0.001	0.010	0.020	0.020	0.230	0.003
Mo						0.010	0.070	0.110	0.190	0.520	0.215
Ba	0.010	0.630	3.560	5.440	5.840	0.010	0.010	0.010	0.020	0.080	0.027
La	0.010	0.010	0.010	0.180	3.060	0.830	1.480	2.530	3.250	5.090	0.027
Ce	0.010	0.010	0.010	0.190	2.040	2.660	5.400	7.890	8.890	11.700	0.023
Pr	0.010	0.010	0.010	0.010	0.280	0.010	0.910	1.180	1.330	2.440	0.016
Nd	0.050	0.050	0.050	0.070	1.000	4.430	5.120	5.640	6.340	14.400	0.091
Sm	0.020	0.020	0.050	0.050	0.310	0.950	1.140	1.360	2.250	4.180	0.105
Eu	0.010	0.010	0.010	0.020	0.080	0.010	0.330	0.370	0.710	1.610	0.029
Gd	0.050	0.050	0.060	0.300	0.390	1.350	1.580	1.880	3.440	5.170	0.110
Tb	0.010	0.020	0.030	0.040	0.060	0.010	0.220	0.250	0.400	0.650	0.014
Dy	0.100	0.120	0.240	0.260	0.280	1.310	1.510	1.720	2.600	3.550	0.083
Ho	0.020	0.030	0.050	0.060	0.070	0.010	0.350	0.410	0.550	0.680	0.020
Er	0.060	0.070	0.110	0.180	0.200	0.970	1.130	1.340	1.560	2.210	0.042
Tm	0.003	0.010	0.010	0.020	0.020	0.010	0.120	0.160	0.190	0.280	0.013
Yb	0.020	0.030	0.040	0.060	0.080	0.030	0.920	0.990	1.110	1.610	0.050
Lu	0.002	0.002	0.010	0.010	0.010	0.010	0.090	0.110	0.140	0.180	0.011
W	0.010	0.010	0.010	0.010	0.010	0.020	0.100	0.120	0.150	0.200	0.048
Pb	0.010	0.010	0.010	0.010	0.010	0.010	0.010	0.010	0.030	0.070	0.020
Th	0.010	0.010	0.330	4.310	22.700	0.001	0.003	0.010	0.010	11.000	0.012
U	0.003	0.004	0.005	0.080	0.270	0.003	0.005	0.010	0.020	0.150	0.010

Table 3. Continued.

			Kipawa		n=22			Rexspar		n=31	M.D.L.
(ppm)	Minimum	1st quartile	Median	3rd quartile	Maximum	Minimum	1st quartile	Median	3rd quartile	Maximum	
Na	1.200	45.900	64.700	86.500	168.000	1.200	58.100	77.100	122.000	683.000	2.402
Mg	0.470	0.470	0.470	0.470	4.110	0.470	0.470	0.470	3.810	10.100	0.942
Sc	0.130	0.130	0.130	0.130	0.130	0.130	0.130	0.130	0.130	0.130	0.267
Ti	0.020	0.120	0.510	0.510	2.200	0.040	0.070	0.180	0.510	0.510	1.021
V	0.010	0.040	0.040	0.040	0.040	0.040	0.040	0.040	0.040	0.040	0.082
Mn	0.360	0.360	0.360	1.220	1.920	2.920	4.360	4.980	5.470	7.510	0.717
Fe	122.000	136.000	148.000	152.000	170.000	109.000	124.000	138.000	176.000	199.000	2.800
Cu	0.160	0.160	0.160	0.160	0.160	0.160	0.160	0.160	0.160	0.160	0.317
Zn	0.040	0.040	0.040	0.040	0.040	0.040	0.040	0.040	0.040	1.810	0.074
Rb	0.030	0.030	0.030	0.030	0.030	0.030	0.030	0.030	0.030	0.190	0.059
Sr	952.000	1040.000	1090.000	1130.000	1240.000	1110.000	1280.000	1380.000	1430.000	1640.000	0.300
Y	132.000	162.000	203.000	269.000	304.000	92.800	112.000	151.000	194.000	645.000	0.065
Zr	0.001	0.010	0.010	0.030	0.030	0.002	0.030	0.030	0.030	0.610	0.004
Nb	0.001	0.010	0.020	0.020	0.060	0.003	0.020	0.020	0.020	0.040	0.003
Mo	0.010	0.010	0.020	0.040	0.110	0.020	0.090	0.110	0.110	0.190	0.215
Ba	0.540	0.620	0.700	0.930	1.390	0.010	0.010	0.010	0.270	3.400	0.027
La	7.320	11.400	20.900	31.900	49.500	8.150	13.300	17.300	23.500	29.200	0.027
Ce	15.100	25.100	41.700	62.800	120.000	18.200	31.800	39.100	56.800	70.200	0.023
Pr	2.610	4.050	5.820	8.730	14.500	2.710	4.950	5.660	8.350	11.800	0.016
Nd	14.200	19.600	28.000	42.300	56.700	14.900	25.200	29.000	42.700	71.900	0.091
Sm	3.490	4.680	6.860	9.300	11.000	4.570	6.040	7.850	10.200	22.700	0.105
Eu	0.500	0.590	0.880	1.150	1.350	1.550	2.060	2.540	3.560	7.410	0.029
Gd	4.630	6.370	8.750	10.800	12.900	5.950	8.010	9.330	12.700	32.400	0.110
Tb	0.690	0.920	1.220	1.650	1.910	0.720	0.930	1.160	1.480	3.960	0.014
Dy	4.900	6.640	8.670	11.700	13.300	4.300	5.540	6.810	8.430	23.300	0.083
Ho	1.120	1.570	2.020	2.580	3.050	0.870	1.080	1.360	1.730	4.840	0.020
Er	3.520	4.930	6.090	8.030	9.500	2.250	2.850	3.710	4.750	13.400	0.042
Tm	0.460	0.610	0.780	1.050	1.230	0.010	0.340	0.420	0.550	1.420	0.013
Yb	2.490	3.670	4.540	6.320	7.180	1.620	2.060	2.630	3.470	8.050	0.050
Lu	0.290	0.410	0.510	0.690	0.790	0.010	0.270	0.350	0.460	1.110	0.011
W	0.020	0.180	0.250	0.440	0.570	0.020	0.220	0.330	0.420	1.310	0.048
Pb	0.010	0.010	0.010	0.010	0.530	0.010	0.010	0.010	0.010	4.330	0.020
Th	0.010	0.010	0.010	0.010	12.800	0.010	0.010	0.020	0.070	0.200	0.012
U	0.005	0.005	0.030	0.080	0.100	0.005	0.005	0.090	0.130	0.240	0.010

Table 3. Continued.

			Rock Candy		n=60			**RC-08-8X**		n=51	**M.D.L.**
(ppm)	Minimum	1st quartile	Median	3rd quartile	Maximum	Minimum	1st quartile	Median	3rd quartile	Maximum	
Na	1.200	1.200	1.200	1.200	5.900	1.200	1.200	1.200	1.200	1.200	2.402
Mg	0.240	0.470	0.470	0.470	0.470	0.290	0.470	0.470	0.470	3.790	0.942
Sc	0.130	0.130	0.130	0.130	0.130	0.130	0.130	0.130	0.130	0.130	0.267
Ti	0.020	0.070	0.510	0.510	0.510	0.020	0.510	0.510	0.510	0.510	1.021
V	0.010	0.040	0.040	0.040	0.040	0.040	0.040	0.040	0.040	0.040	0.082
Mn	0.360	0.360	0.360	0.360	6.470	0.360	0.360	0.360	0.360	0.360	0.717
Fe	126.000	146.000	151.000	158.000	178.000	71.700	116.000	142.000	158.000	292.000	2.800
Cu	0.140	0.160	0.160	0.160	0.160	0.160	0.160	0.160	0.160	0.210	0.317
Zn	0.040	0.040	0.040	0.040	0.040	0.040	0.040	0.040	0.040	0.040	0.074
Rb	0.030	0.030	0.030	0.030	0.120	0.030	0.030	0.030	0.030	0.030	0.059
Sr	125.000	288.000	415.000	535.000	674.000	323.000	380.000	449.000	520.000	701.000	0.300
Y	0.500	5.030	16.800	35.300	1450.000	3.150	10.000	20.300	33.000	42.000	0.065
Zr	0.001	0.010	0.030	0.030	0.730	0.001	0.030	0.030	0.030	0.030	0.004
Nb	0.001	0.003	0.010	0.020	0.020	0.001	0.020	0.020	0.020	0.020	0.003
Mo	0.004	0.010	0.020	0.110	0.110	0.004	0.010	0.110	0.110	0.110	0.215
Ba	0.010	0.060	0.120	0.410	3.060	0.010	0.010	0.010	0.010	0.230	0.027
La	1.330	2.500	7.020	10.700	52.000	2.480	3.280	6.140	8.330	11.700	0.027
Ce	2.070	4.440	12.200	16.200	123.000	5.070	6.210	9.480	11.600	19.800	0.023
Pr	0.270	0.580	1.440	2.350	21.000	0.010	0.990	1.140	1.410	2.390	0.016
Nd	1.080	2.570	6.950	11.200	135.000	2.260	5.020	5.780	6.360	11.100	0.091
Sm	0.050	0.690	1.650	3.390	65.800	0.050	0.950	1.280	1.880	2.740	0.105
Eu	0.010	0.410	0.700	2.000	29.600	0.010	0.420	0.620	1.050	1.380	0.029
Gd	0.050	0.750	1.930	4.170	109.000	0.050	1.080	1.590	2.700	3.720	0.110
Tb	0.010	0.140	0.280	0.900	19.600	0.010	0.100	0.210	0.380	0.460	0.014
Dy	0.040	0.910	1.820	7.020	136.000	0.040	0.790	1.430	2.470	3.070	0.083
Ho	0.010	0.170	0.330	1.260	26.400	0.010	0.100	0.300	0.520	0.710	0.020
Er	0.020	0.510	0.900	3.830	67.800	0.020	0.410	0.920	1.550	2.060	0.042
Tm	0.000	0.070	0.140	0.570	6.930	0.010	0.010	0.120	0.190	0.250	0.013
Yb	0.030	0.500	1.040	4.050	36.000	0.030	0.510	0.850	1.330	1.790	0.050
Lu	0.010	0.070	0.160	0.510	3.980	0.010	0.010	0.130	0.210	0.290	0.011
W	0.001	0.003	0.020	0.020	0.270	0.001	0.020	0.020	0.020	0.020	0.048
Pb	0.003	0.010	0.010	0.010	0.100	0.010	0.010	0.010	0.010	0.010	0.020
Th	<0.001	0.010	0.010	0.040	0.970	0.010	0.010	0.010	0.010	0.070	0.012
U	0.002	0.005	0.010	0.030	3.170	0.005	0.005	0.005	0.090	0.430	0.010

Table 3. Continued.

	Kootenay Florence				n=13	**Liard**				n=33	**M.D.L.**
(ppm)	Minimum	1st quartile	Median	3rd quartile	Maximum	Minimum	1st quartile	Median	3rd quartile	Maximum	
Na	1.200	1.200	1.200	1.200	1.200	1.200	137.000	198.000	278.000	546.000	2.402
Mg	0.470	0.470	0.470	0.470	0.470	0.470	0.470	0.470	5.780	7.480	0.942
Sc	0.130	0.130	0.130	0.130	0.130	0.130	0.130	0.130	0.130	0.700	0.267
Ti	0.040	0.050	0.060	0.510	0.510	0.060	0.150	0.510	0.510	0.510	1.021
V	0.040	0.040	0.040	0.040	0.040	0.010	0.040	0.040	0.040	0.040	0.082
Mn	0.360	0.360	0.360	0.360	0.360	0.360	0.360	0.360	0.360	1.170	0.717
Fe	138.000	147.000	150.000	155.000	164.000	118.000	140.000	152.000	205.000	234.000	2.800
Cu	0.160	0.160	0.160	0.160	0.160	0.120	0.160	0.160	0.160	0.240	0.317
Zn	0.040	0.040	0.040	0.040	0.040	0.040	0.040	0.040	0.040	0.130	0.074
Rb	0.010	0.030	0.030	0.030	0.030	0.010	0.030	0.030	0.030	0.050	0.059
Sr	83.700	90.400	96.700	128.000	142.000	43.800	70.600	87.400	107.000	533.000	0.300
Y	6.040	13.500	16.000	20.600	31.500	6.140	20.400	22.300	23.800	28.700	0.065
Zr	0.003	0.004	0.030	0.030	0.030	0.004	0.360	0.540	0.670	0.890	0.004
Nb	0.020	0.020	0.020	0.020	0.020	0.002	0.010	0.020	0.020	0.020	0.003
Mo	0.010	0.080	0.110	0.110	0.110	0.010	0.010	0.090	0.110	0.110	0.215
Ba	0.010	0.010	0.010	0.040	0.510	0.010	3.200	15.400	31.500	474.000	0.027
La	0.010	0.430	0.780	0.970	1.130	0.010	0.160	0.220	0.280	0.370	0.027
Ce	0.010	0.480	0.780	1.100	1.370	0.010	0.320	0.370	0.410	0.490	0.023
Pr	0.010	0.040	0.160	0.210	0.230	0.010	0.010	0.080	0.100	0.120	0.016
Nd	0.050	0.780	0.940	1.220	1.600	0.050	0.360	0.560	0.670	0.810	0.091
Sm	0.050	0.130	0.300	0.370	0.590	0.030	0.050	0.200	0.250	0.280	0.105
Eu	0.010	0.010	0.080	0.110	0.220	0.010	0.010	0.070	0.090	0.110	0.029
Gd	0.050	0.340	0.760	0.880	1.080	0.050	0.600	0.720	0.840	3.460	0.110
Tb	0.010	0.010	0.070	0.110	0.150	0.010	0.050	0.100	0.110	0.140	0.014
Dy	0.040	0.420	0.630	0.760	1.080	0.040	0.600	0.730	0.800	1.040	0.083
Ho	0.010	0.010	0.100	0.160	0.240	0.010	0.140	0.170	0.180	0.210	0.020
Er	0.020	0.070	0.230	0.320	0.670	0.080	0.380	0.470	0.510	0.620	0.042
Tm	0.010	0.010	0.010	0.010	0.020	0.010	0.010	0.040	0.050	0.070	0.013
Yb	0.030	0.030	0.030	0.070	0.250	0.030	0.160	0.210	0.250	0.400	0.050
Lu	0.003	0.010	0.010	0.010	0.020	0.010	0.010	0.010	0.030	0.040	0.011
W	0.001	0.003	0.020	0.020	0.100	0.002	0.020	0.020	0.020	0.020	0.048
Pb	0.010	0.010	0.010	0.010	0.050	0.010	0.010	0.010	0.010	0.070	0.020
Th	0.010	0.010	0.120	0.240	0.290	0.010	0.100	0.190	0.270	0.810	0.012
U	<0.001	0.004	0.005	0.005	0.005	0.005	1.320	1.530	2.220	6.750	0.010

Table 3. Continued.

			Hastie quarry		n=28			Barnett Mine		n=44	M.D.L.
(ppm)	Minimum	1st quartile	Median	3rd quartile	Maximum	Minimum	1st quartile	Median	3rd quartile	Maximum	
Na	1.200	1.200	44.800	80.300	243.000	1.200	1.200	1.200	15.200	291.000	2.402
Mg	0.150	0.470	0.470	0.470	5.930	0.390	0.470	0.470	0.470	4.960	0.942
Sc	0.130	0.130	0.130	0.130	0.130	0.130	0.130	0.130	0.130	0.130	0.267
Ti	0.030	0.110	0.510	0.510	0.510	0.020	0.050	0.110	0.510	0.510	1.021
V	0.020	0.040	0.040	0.040	0.040	0.010	0.040	0.040	0.040	0.040	0.082
Mn	0.360	0.360	0.360	0.360	0.360	0.360	0.360	0.360	0.360	0.360	0.717
Fe	14.400	142.000	145.000	151.000	158.000	118.000	129.000	138.000	152.000	179.000	2.800
Cu	0.160	0.160	0.160	0.160	0.160	0.160	0.160	0.160	0.160	1.090	0.317
Zn	0.040	0.040	0.040	0.040	0.040	0.040	0.040	0.040	0.040	0.040	0.074
Rb	0.010	0.030	0.030	0.030	0.030	0.030	0.030	0.030	0.030	0.030	0.059
Sr	10.900	12.700	49.700	84.500	104.000	3.410	11.600	13.000	45.800	59.500	0.300
Y	2.620	3.050	9.970	12.200	13.100	0.970	2.110	2.670	6.140	8.220	0.065
Zr	0.002	0.002	0.010	0.030	0.030	0.001	0.010	0.030	0.030	0.030	0.004
Nb	0.001	0.001	0.020	0.020	0.020	0.001	0.002	0.020	0.020	0.030	0.003
Mo	0.005	0.010	0.110	0.110	0.110	0.003	0.010	0.020	0.110	0.110	0.215
Ba	0.002	0.010	0.040	0.140	0.170	0.001	0.010	0.010	0.010	0.550	0.027
La	0.001	0.003	0.010	0.010	0.010	0.001	0.010	0.010	0.040	0.100	0.027
Ce	0.005	0.010	0.010	0.040	0.040	0.010	0.010	0.020	0.150	0.380	0.023
Pr	0.001	0.010	0.010	0.020	0.020	0.002	0.010	0.010	0.050	0.090	0.016
Nd	0.040	0.050	0.150	0.260	0.290	0.050	0.050	0.080	0.370	0.550	0.091
Sm	0.050	0.050	0.150	0.240	0.270	0.050	0.050	0.050	0.130	0.280	0.105
Eu	0.010	0.010	0.070	0.100	0.120	0.010	0.050	0.080	0.230	0.330	0.029
Gd	0.050	0.170	0.500	0.660	0.740	0.050	0.110	0.160	0.350	0.620	0.110
Tb	0.010	0.010	0.070	0.090	0.100	0.010	0.010	0.020	0.030	0.050	0.014
Dy	0.040	0.120	0.450	0.560	0.610	0.040	0.100	0.140	0.230	0.360	0.083
Ho	0.010	0.010	0.090	0.110	0.120	0.010	0.010	0.020	0.040	0.080	0.020
Er	0.020	0.020	0.210	0.250	0.270	0.020	0.030	0.050	0.100	0.170	0.042
Tm	0.003	0.010	0.010	0.020	0.030	0.002	0.010	0.010	0.010	0.010	0.013
Yb	0.004	0.030	0.030	0.100	0.120	0.010	0.020	0.030	0.030	0.030	0.050
Lu	0.001	0.010	0.010	0.010	0.020	0.001	0.003	0.010	0.010	0.010	0.011
W	0.001	0.010	0.020	0.020	0.030	0.001	0.003	0.020	0.020	0.060	0.048
Pb	0.010	0.010	0.010	0.010	0.070	0.001	0.010	0.010	0.010	3.270	0.020
Th	0.010	0.010	0.180	0.300	0.380	0.010	0.010	0.010	0.020	0.040	0.012
U	0.001	0.005	0.005	0.010	0.010	<0.001	0.005	0.005	0.005	0.005	0.010

Table 3. Continued.

			Elmwood		n=13			Gordonsville		n=48	M.D.L.
(ppm)	Minimum	1st quartile	Median	3rd quartile	Maximum	Minimum	1st quartile	Median	3rd quartile	Maximum	
Na	1.200	1.200	1.200	1.200	17.400	1.200	1.200	1.200	8.240	149.000	2.402
Mg	0.470	0.470	0.470	0.470	0.470	0.310	0.470	0.470	0.470	25.000	0.942
Sc	0.130	0.130	0.130	0.130	0.130	0.130	0.130	0.130	0.130	0.130	0.267
Ti	0.510	0.510	0.510	0.510	0.510	0.510	0.510	0.510	0.510	0.510	1.021
V	0.040	0.040	0.040	0.040	0.040	0.010	0.040	0.040	0.040	0.040	0.082
Mn	0.360	0.360	0.360	0.360	0.360	0.360	0.360	0.360	0.360	0.360	0.717
Fe	74.500	79.400	89.200	101.000	108.000	89.200	106.000	121.000	129.000	150.000	2.800
Cu	0.160	0.160	0.160	0.160	0.160	0.160	0.160	0.160	0.160	0.830	0.317
Zn	0.040	0.040	0.040	0.040	0.040	0.040	0.040	0.040	0.040	53.100	0.074
Rb	0.030	0.030	0.030	0.030	0.030	0.010	0.030	0.030	0.030	0.030	0.059
Sr	5.070	6.710	10.700	15.800	21.000	3.410	8.490	10.600	14.300	38.600	0.300
Y	0.710	1.530	2.110	2.960	3.330	0.030	1.930	2.480	3.010	4.940	0.065
Zr	0.003	0.020	0.030	0.030	0.030	0.002	0.003	0.010	0.030	0.030	0.004
Nb	0.002	0.010	0.020	0.020	0.020	0.001	0.002	0.010	0.020	0.020	0.003
Mo	0.010	0.010	0.010	0.010	0.010	0.010	0.010	0.110	0.110	0.110	0.215
Ba	0.002	0.010	0.010	0.050	0.460	0.001	0.004	0.010	0.010	13.000	0.027
La	0.010	0.010	0.130	0.180	0.250	0.010	0.010	0.020	0.080	0.260	0.027
Ce	0.010	0.010	0.360	0.530	0.650	0.010	0.090	0.220	0.290	0.730	0.023
Pr	0.010	0.010	0.080	0.110	0.140	0.010	0.010	0.050	0.060	0.140	0.016
Nd	0.030	0.150	0.460	0.680	0.920	0.050	0.290	0.380	0.540	0.870	0.091
Sm	0.020	0.050	0.180	0.240	0.320	0.020	0.050	0.150	0.230	0.350	0.105
Eu	0.010	0.050	0.120	0.140	0.190	0.000	0.050	0.090	0.130	0.200	0.029
Gd	0.050	0.230	0.300	0.340	0.430	0.010	0.220	0.300	0.380	0.500	0.110
Tb	0.010	0.010	0.030	0.040	0.050	0.001	0.010	0.030	0.040	0.060	0.014
Dy	0.020	0.040	0.120	0.180	0.200	0.010	0.050	0.140	0.180	0.330	0.083
Ho	0.010	0.010	0.010	0.020	0.030	0.001	0.010	0.010	0.030	0.050	0.020
Er	0.020	0.020	0.020	0.050	0.080	0.003	0.020	0.020	0.050	0.090	0.042
Tm	0.002	0.003	0.004	0.010	0.010	<0.001	0.004	0.010	0.010	0.010	0.013
Yb	0.002	0.010	0.010	0.020	0.030	0.002	0.010	0.020	0.030	0.040	0.050
Lu	0.002	0.002	0.010	0.010	0.010	<0.001	0.002	0.004	0.010	0.010	0.011
W	0.003	0.003	0.020	0.020	0.020	0.001	0.001	0.004	0.020	0.020	0.048
Pb	0.001	0.005	0.010	0.010	0.010	0.001	0.010	0.010	0.010	0.810	0.020
Th	0.004	0.010	0.010	0.010	0.020	0.001	0.004	0.010	0.010	0.020	0.012
U	0.001	0.005	0.005	0.005	0.010	<0.001	0.001	0.005	0.005	0.005	0.010

Table 3. Continued.

			Young mine		n=30			YM9215-1X		n=7	M.D.L.
(ppm)	Minimum	1st quartile	Median	3rd quartile	Maximum	Minimum	1st quartile	Median	3rd quartile	Maximum	
Na	1.200	1.200	1.200	1.200	72.600	1.200	1.200	1.200	19.200	31.000	2.402
Mg	0.470	0.470	0.470	0.470	23.000	0.470	0.470	0.470	0.470	0.470	0.942
Sc	0.130	0.130	0.130	0.130	0.130	0.130	0.130	0.130	0.130	0.130	0.267
Ti	0.510	0.510	0.510	0.510	0.510	0.510	0.510	0.510	0.510	0.510	1.021
V	0.005	0.040	0.040	0.040	0.040	0.040	0.040	0.040	0.040	0.040	0.082
Mn	0.360	0.360	0.360	0.360	0.360	0.360	0.360	0.360	0.360	0.360	0.717
Fe	78.900	87.800	93.500	103.000	109.000	80.400	82.400	85.400	88.800	95.400	2.800
Cu	0.160	0.160	0.160	0.160	0.160	0.160	0.160	0.160	0.160	0.160	0.317
Zn	0.040	0.040	0.040	0.040	0.040	0.040	0.040	0.040	0.040	0.040	0.074
Rb	0.000	0.030	0.030	0.030	0.030	0.030	0.030	0.030	0.030	0.030	0.059
Sr	3.410	10.600	12.800	21.800	178.000	10.500	10.600	11.200	19.100	29.400	0.300
Y	0.030	0.030	0.090	0.210	4.200	0.030	0.030	0.030	0.080	0.240	0.065
Zr	0.002	0.003	0.030	0.030	0.140	0.002	0.002	0.002	0.002	0.002	0.004
Nb	0.001	0.002	0.003	0.020	0.020	0.001	0.001	0.001	0.010	0.020	0.003
Mo	0.005	0.005	0.010	0.110	0.110	0.110	0.110	0.110	0.110	0.110	0.215
Ba	0.002	0.010	0.010	0.010	0.260	0.004	0.004	0.010	0.010	0.010	0.027
La	0.010	0.710	1.160	1.700	12.900	0.010	0.460	1.140	1.600	1.940	0.027
Ce	0.010	0.950	1.410	1.940	10.300	0.640	0.650	1.300	1.830	2.220	0.023
Pr	0.070	0.110	0.150	0.180	0.720	0.090	0.090	0.150	0.180	0.190	0.016
Nd	0.050	0.380	0.500	0.550	2.060	0.050	0.240	0.460	0.610	0.670	0.091
Sm	0.010	0.020	0.050	0.050	0.210	0.010	0.010	0.020	0.050	0.060	0.105
Eu	0.001	0.010	0.010	0.010	0.040	0.002	0.005	0.010	0.010	0.010	0.029
Gd	0.010	0.020	0.030	0.050	0.270	0.010	0.010	0.020	0.050	0.050	0.110
Tb	<0.001	0.001	0.004	0.010	0.030	0.001	0.001	0.002	0.003	0.010	0.014
Dy	0.003	0.010	0.010	0.040	0.140	0.001	0.003	0.010	0.040	0.040	0.083
Ho	<0.001	0.001	0.005	0.010	0.040	0.001	0.001	0.003	0.010	0.010	0.020
Er	0.001	0.003	0.010	0.020	0.110	0.002	0.002	0.010	0.020	0.020	0.042
Tm	<0.001	0.001	0.010	0.010	0.010	0.001	0.001	0.010	0.010	0.010	0.013
Yb	0.001	0.002	0.004	0.030	0.060	0.001	0.002	0.004	0.020	0.030	0.050
Lu	<0.001	0.001	0.010	0.010	0.010	<0.001	<0.001	0.010	0.010	0.010	0.011
W	0.001	0.002	0.020	0.020	0.020	0.020	0.020	0.020	0.020	0.020	0.048
Pb	0.001	0.010	0.010	0.010	0.020	0.001	0.001	0.010	0.010	0.010	0.020
Th	<0.001	0.001	0.010	0.010	0.990	<0.001	<0.001	0.010	0.010	0.010	0.012
U	<0.001	<0.001	0.005	0.005	0.020	<0.001	<0.001	0.005	0.005	0.005	0.010

M.D.L.: Minimum Detection Limit. For each element, results below detection limit have been replaced with half the minimum detection limit from all analysis sections.

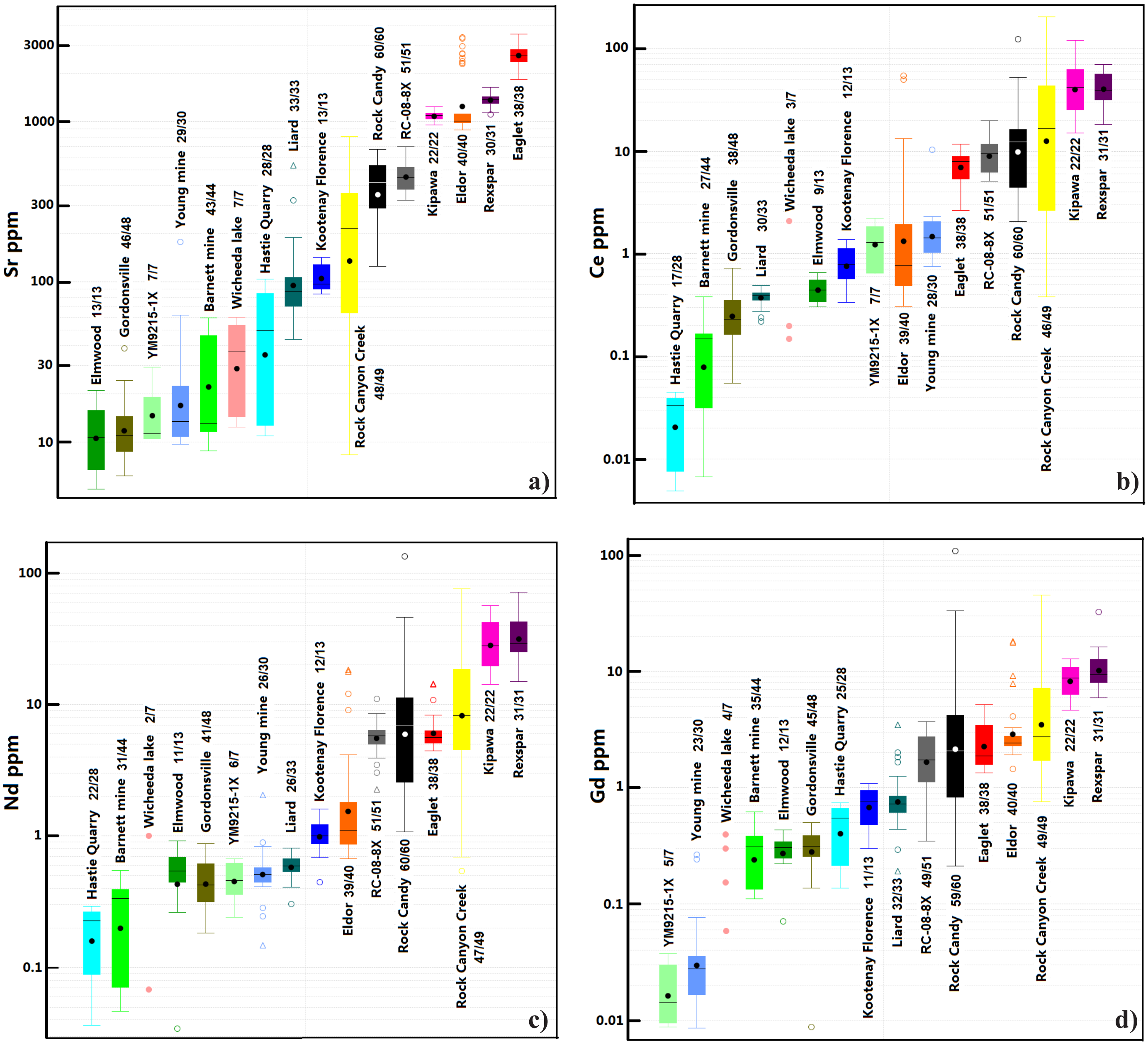

Fig. 4. Box plots of selected elements from fluorite of each deposit with the ratio of analyses above detection limit to total analyses. **a)** Sr; **b)** Ce; **c)** Nd; **d)** Gd; **e)** Yb; **f)** Y. Line: median value; solid dot: mean value; box: interquartile range (1st-3rd quartiles); open circle (outlier); farther than 1.5 x (1st-3rd quartiles); open triangle (outlier): farther than 3 x (1st-3rd quartiles); whiskers: extreme values that are not outliers. If there are less than five analyses above the detection limit, solid colour dots represent individual analyses.

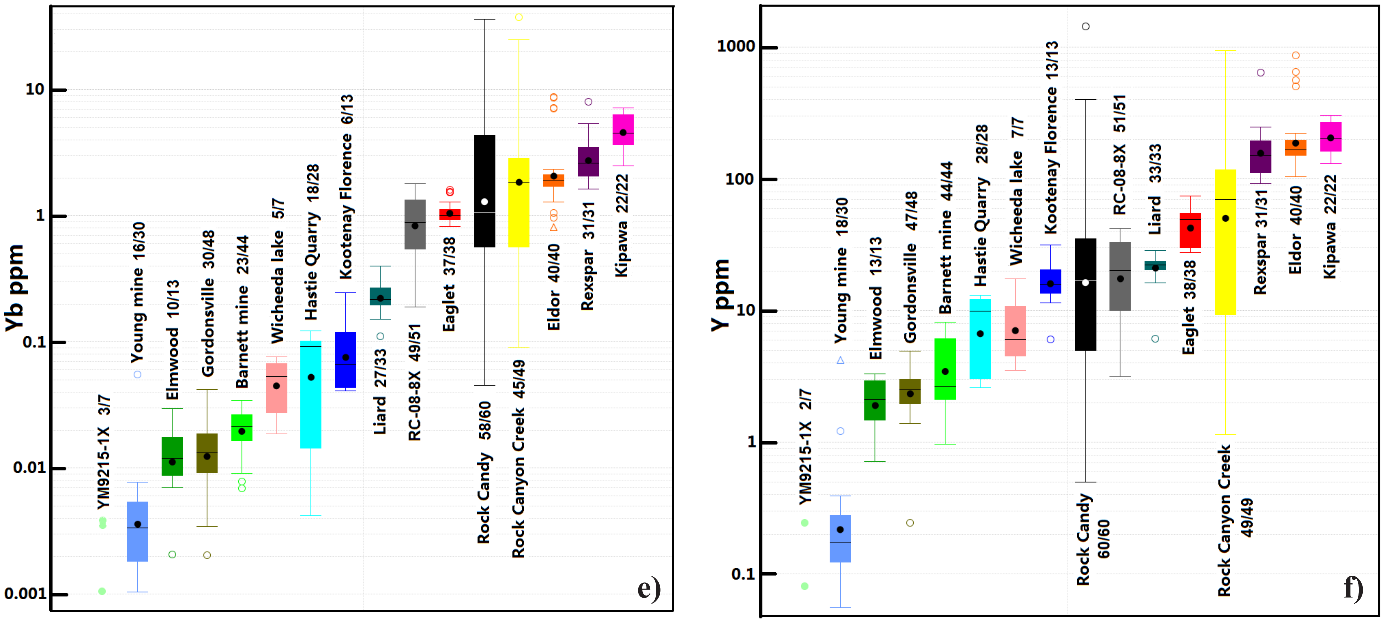

Fig. 4 continued. Box plots of selected elements from fluorite of each deposit with the ratio of analyses above detection limit to total analyses. **a)** Sr; **b)** Ce; **c)** Nd; **d)** Gd; **e)** Yb; **f)** Y. Line: median value; solid dot: mean value; box: interquartile range (1st-3rd quartiles); open circle (outlier); farther than 1.5 x (1st-3rd quartiles); open triangle (outlier): farther than 3 x (1st-3rd quartiles); whiskers: extreme values that are not outliers. If there are less than five analyses above the detection limit, solid colour dots represent individual analyses.

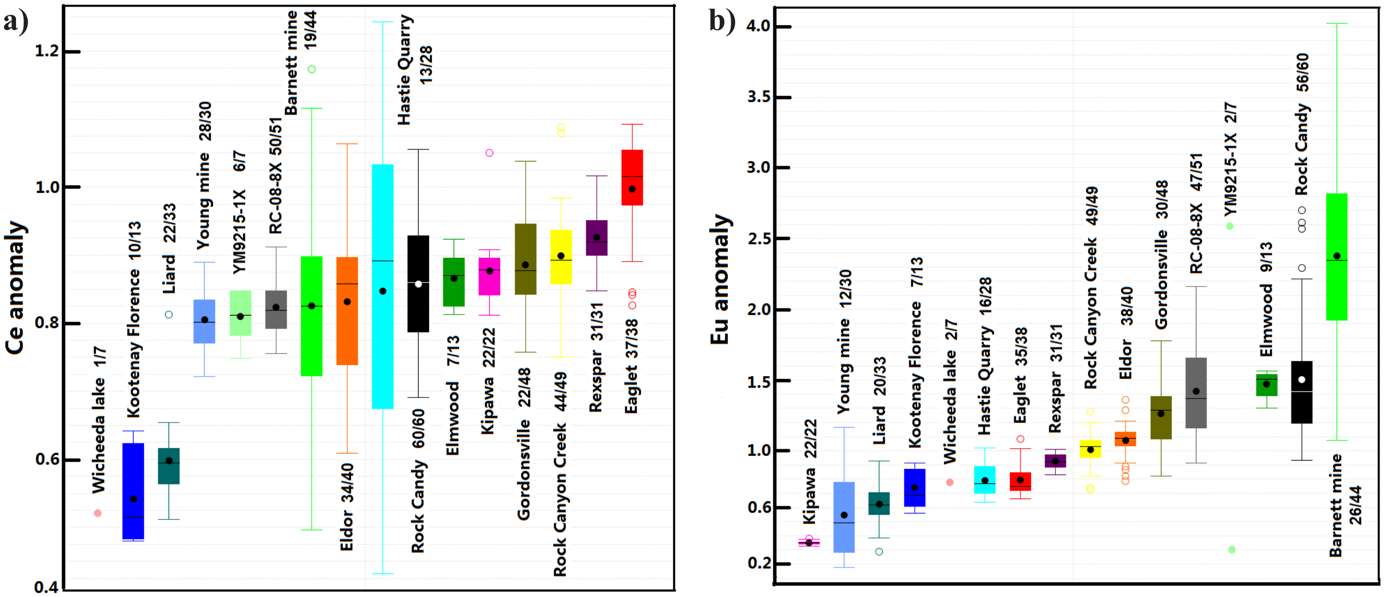

Fig. 5. Box plots of **a)** Ce anomalies and **b)** Eu anomalies from fluorite of each deposit. The ratios indicate the number of analyses for which anomalies could be determined, relative to the total number of analyses. Positive anomalies on these diagrams are higher than 1, conversely negative anomalies are lower than 1. Line: median value; solid dot: mean value; box: interquartile range (1st-3rd quartiles); open circle (outlier); farther than 1.5 x (1st-3rd quartiles); open triangle (outlier): farther than 3 x (1st-3rd quartiles); whiskers: extreme values that are not outliers. If there are less than five analyses above the detection limit, solid colour dots represent each individual analyses.

- The Eldor fluorite shows a large variation in La and progressively smaller variations in concentrations of Ce, Pr, Nd, Sm, and Eu (Figs. 4b, c, Fig. 6a; Table 3).
- Fluorite from Kipawa and Rexspar always has the highest contents (3rd quartile) of lanthanides except Eu; only Kipawa has prominent negative Eu anomalies (Figs. 4b, c, d, e, Fig. 5b; Fig. 6b).
- Hastie Quarry and Barnett mine fluorite has the lowest contents of La, Ce, Pr, and Nd (Figs. 4b, c, Fig. 6b; Table 3).
- Rock Candy and Rock Canyon Creek fluorite shows very wide ranges of lanthanide and Y concentrations (Figs. 4b, c, d, e, f; Figs. 6a, c).
- Elmwood and Gordonsville fluorite shows similar behaviors for all lanthanides and Y (Figs. 4b, c, d, e, f; Fig. 6c).
- The chondrite-normalized LREE contents of Young mine fluorite decreases from La to Eu (Fig. 6c).
- Fluorite from the Young mine contains the lowest concentrations of Eu, and many of analyses show that Eu contents are less than detection limits (Table 3).
- The chondrite-normalized patterns from Gd to Ho (excluding Y) of fluorite are flat in all deposits except for Elmwood, Gordonsville, and the Young mine (Fig. 6).
- Rexspar, Kipawa, Eldor, Rock Canyon Creek, Rock Candy, and Eaglet fluorite have flat or slightly negatively sloped chondrite-normalized patterns from Er to Lu, and their concentrations of Er, Tm, Yb, and Lu are elevated relative to those from other deposits in which the patterns from Er to Lu show a notable negative slope (Fig. 6).

Magnesium concentrations in fluorite are generally less than 10 ppm. Five to 45% of the analyses from each deposit contained detectable Mg, except for fluorite from Rock Canyon Creek (>60%). Detectable Mg concentrations in Rock Canyon Creek are between 2.10 (±0.26) – 582 (±47) ppm, and most are above 10 ppm (Table 3).

Manganese was detected in 20% of all the analyses. More than 85% of the analyses from Rexspar and Eaglet yielded between 2.92 (±0.14) and 7.96 (±0.39) ppm Mn, and fluorite grains from Eldor, Kipawa, Rock Candy, and Rock Canyon Creek contain detectable Mn, typically less than 10 ppm (Table 3).

Zirconium is detectable in 40% of all the analyses, and it is commonly present in concentrations less than 0.1 ppm. More than 85% of analyses from Liard have detectable Zr, ranging from 0.004 to 0.89 ppm. Approximately 75% of the analyses from Rock Canyon Creek contain Zr and have a large variation from 0.002 (±0.0003) to 11.3 (±0.9) ppm (Table 3).

More than half of all the analyses have detectable Ba, ranging from 0.001 (±0.0002) to 474 (±24) ppm, many of which are less than 1 ppm. Barium can be detected in 85% of analyses from Liard which has the highest content range (0.99 ±0.16 and 474 ±24 ppm). Barium is also commonly detected in concentrations above 1 ppm in fluorite from Rock Canyon Creek (60% detectable, 0.1 ±0.02 – 83.7 ±4.3 ppm) and Wicheeda Lake

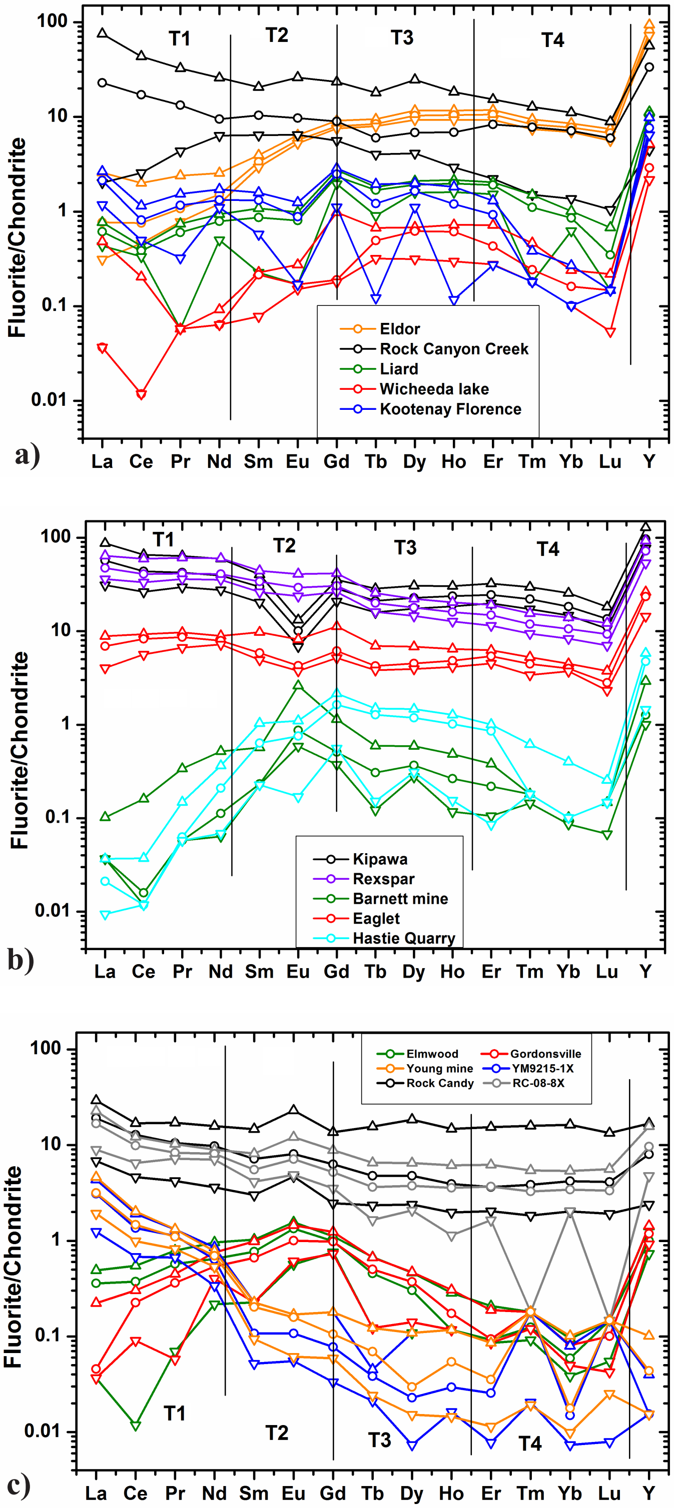

Fig. 6. Chondrite-normalized REE plots of fluorite for each deposit (chondrite data from Taylor and McLennan, 1985). **a)** Fluorite from Eldor, Rock Canyon Creek, Wicheeda Lake, Liard, and Kootenay Florence; **b)** Fluorite from Kipawa, Rexspar, Hastie Quarry, Barnett mine, and Eaglet; **c)** Fluorite from Rock Candy, RC-08-8X, Elmwood, Gordonsville, Young mine, and YM9215-1X. Lines split lanthanides into the four tetrads (McLennan, 1994). Solid line with open circle: median value; solid line with open downward triangle 1st quartile and upward triangle 3rd quartile.

(85% detectable, 0.63 ±0.10 – 5.84 ±0.93 ppm; Table 3).

Tungsten was detected in about half of all the analyses, although it rarely exceeds 1 ppm. Fluorite from Rexspar (90% detectable) has the highest W contents from 0.16 (±0.02) to 1.31 (±0.20) ppm. Fluorite from Kipawa has similar W contents (75% detectable, 0.14 ±0.02 – 0.57 ±0.09 ppm) to Rexspar. Eighty-two percent of fluorite analyses from Eaglet, and 63% from Eldor yield detectable concentrations of W, but values are rarely above 0.2 ppm. Fluorite from Rock Canyon Creek has detectable W in the 0.002 (±0.0003) to 0.71 (±0.1) ppm range. Detectable W is uncommon in other deposits (Table 3).

Thorium is detectable in 55% of all the analyses and concentrations are less than 1 ppm in most deposits. Rock Canyon Creek has the highest Th levels in fluorite (95% detectable analyses) with values ranging from 0.42 (±0.06) to 108 (±9) ppm (Table 3).

Uranium is detectable in more than 40% of all the analyses, mostly in concentrations less than 1 ppm. More than 85% of the analyses of Liard fluorite contain detectable U with values ranging from 0.7 (±0.15) to 6.75 (±0.92) ppm. The Liard fluorite has the highest U concentrations found in this study. The Rexspar deposit fluorite also has detectable U in 75% of the analyses (0.02 ±0.01 – 0.24 ±0.05 ppm). Fluorite samples from Rock Canyon Creek area also have a large range of U values, from 0.001 (±0.0002) to 3.22 (±0.44) ppm (Table 3).

Iron is detectable in most of the sample analyses, with concentrations ranging from 14.4 (±5.0) to 291 (±51) ppm. There are large overlaps in Fe concentrations between individual deposits. Twenty-five to seventy-seven percent of the analyses from Rock Canyon Creek show detectable levels of Sc, Ti, V, Nb, Mo, Ag, and Pb (Table 3). Other trace elements were not consistently detected in fluorite from the studied deposits.

3.2. Variation of trace elements within particular crystals

Numerous analyses of fluorite RC-08-8X and YM9215-1X were performed (Table 3) to test the homogeneity of trace elements in single fluorite crystals. Fifty sites were analyzed on the RC-08-8X crystal along two approximately perpendicular lines (a1-a18 and b1-b31, Fig. 2). Three compositional zones were identified along line a1-a18 (Fig. 7a). The first zone, from a1 to a5, contains lower Sr (320-420 ppm) and Ce (6 ppm), and higher Y (30-40 ppm), Gd (2-3 ppm), and Yb (1-2 ppm). The second zone, from a6 to a14, displays high Sr (450-650 ppm), varying Ce (10-20 ppm), and lower Y (8-20 ppm), Gd (1-2 ppm), and Yb (0.3-0.8 ppm). The third zone, from a15 to a18, has intermediate Sr and Y contents. Analytical line b1-b31 also shows three compositional zones (Fig. 7b). The first zone, from b1 to b11, has trace element contents that are between the compositions of the first and second zones on line a1-a18 (Fig. 7b). The second zone contains the highest Sr (500-700 ppm), highly variable Ce (5-16 ppm), and the lowest Y (3-25 ppm, mostly <10 ppm), Nd (2-5 ppm), Gd (0.3-2 ppm), and Yb (0.2-1.3 ppm), from b12 to b20. The third zone, from b21 to b31, contains the lowest Sr (320-400 ppm) and Ce (5-6 ppm), and the highest Y (30-40 ppm), Nd (5-6 ppm), Gd (2-3 ppm), and Yb (1-2 ppm). In summary, the RC-08-8X crystal shown in Fig. 2 displays three compositional zones.

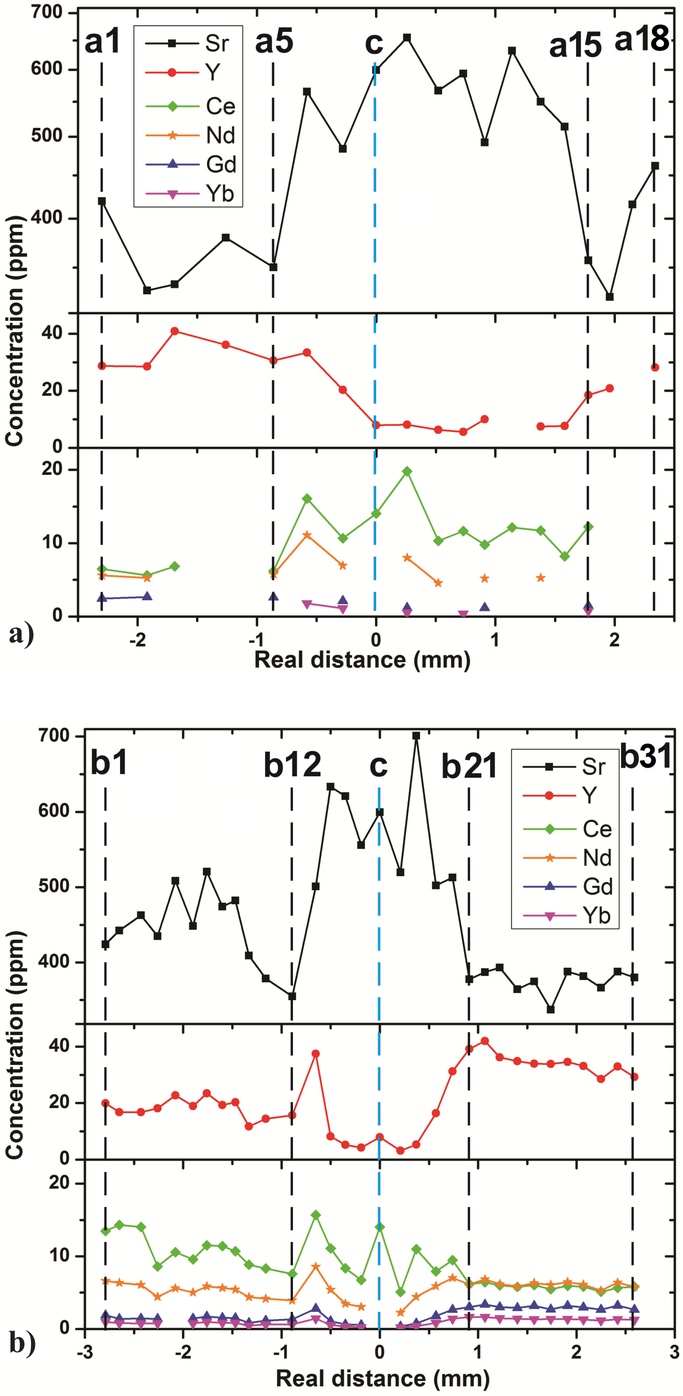

Fig. 7. Concentration variation of selected elements in fluorite along the analysis lines of RC-08-8X: **a)** line 'a1-a18' and **b)** line 'b1-b31' (see Fig. 2). The x axis represents the distances between the analytical points, '0' is the intersection point of the analytical lines, the 'c' point. Black dashed lines indicate the critical analytical points defining compositional zones, and blue dashed line indicates the central 'c' point (see also Fig. 2).

Because trace element concentrations are generally low in fluorite from the Young mine (Table 3), Sr, Ce, Pr, Nd, Tb, and Er were selected to test for intra-grain variation (sample YM9215-1X). In the purple rim (Fig. 3) from d1 to d2, Sr and Tb contents decrease, whereas Ce, Pr, and Nd contents increase (Fig. 8). In the colourless zone from d3 to d4, Sr and Ce contents decrease, and Pr contents increase slightly. In the dark core from d5 to d7 (Fig. 3), the contents of Sr, Ce, Nd, and Tb show notable variations (Fig. 8), and Er content increases. More analyses would be required to establish a clear relationship between compositional and colour zonings

4. Discussion

Our discussion of the results will focus on comparing trace element concentrations in fluorite of specific deposits and groups of deposits, trace element variations within single fluorite crystals and the potential use of Rock Candy fluorite as a matrix-matched secondary standard.

4.1. Trace element composition of fluorite from individual deposits

For the purpose of this discussion, deposits under consideration can be divided into: 1) Sedimentary-hosted deposits (Liard, Hastie Quarry, Barnett mine, Young mine, Gordonsville, Elmwood, Kootenay Florence), 2) Peralkaline/alkaline rock-related deposits (Eaglet, Kipawa, Rexspar, Rock Candy, Rock Canyon Creek), and 3) Carbonatite-related deposits (Eldor, Wicheeda Lake).

Concentrations of Sr, Y, and lanthanides are consistently above LA-ICP-MS detection limits (Table 3) and show geochemical variations between deposits. To facilitate the comparisons between chondrite-normalized REE profiles, we adopted the 'tetrad' terminology as discussed by McLennan (1994), and Monecke et al. (2002). Lanthanides are divided into four tetrads: the 1st tetrad (T1) consists of La, Ce, Pr, Nd, the 2nd tetrad (T2) consists of Sm, Eu, Gd, the 3rd tetrad (T3) corresponds to Gd, Tb, Dy, Ho, and the 4th tetrad (T4) groups Er, Tm, Yb, Lu. Ratios between specific lanthanides, and lanthanide tetrads may be useful for constructing discrimination diagrams in addition to Ce and Eu anomalies and to Sr and Y contents,.

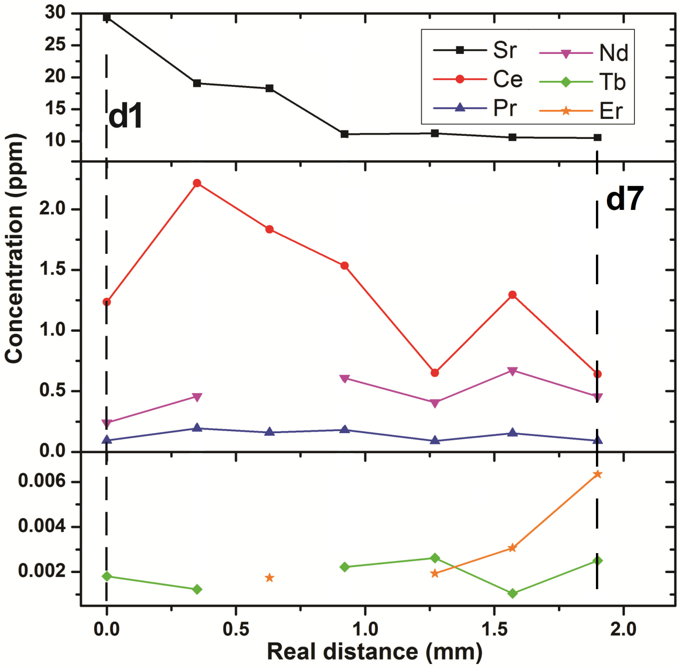

Fig. 8. Concentration variation of selected elements in fluorite along the analysis line of YM9215-1X. The '0' on the x axis is the analytical point on the edge of the crystal (d1, Fig. 3).

4.1.1. Trace element behaviors of fluorite from sedimentary-hosted deposits

Fluorite from sedimentary-hosted deposits has low trace element concentrations, which plot mostly below 3 on chondrite-normalized REE ratio diagrams (Fig. 6). Strontium concentrations are typically less than 200 ppm (Fig. 4a), and Y concentrations are all less than 31 ppm (Fig. 4f). All sedimentary-hosted fluorite, except from the Young mine, have nearly flat or convex-shaped chondrite-normalized REE patterns; flat or positively sloping T1, positively sloping T2, flat or negatively sloping T3, and negatively sloping T4 (Fig. 6; Table 5). The Young mine fluorite has a negatively sloping chondrite-normalized REE pattern, where T1 and T2 are notably negative, and T3 and T4 weakly negative.

The Hastie Quarry and the Barnett mine (Illinois-Kentucky mining district) both have convex shaped chondrite-normalized REE patterns, with strong positively sloping T1, positively sloping T2, flat T3, and negatively sloping T4 (Fig. 6b; Table 5). Hastie Quarry has negative Eu anomalies, whereas Barnett mine has the strongest positive Eu anomalies and largest Eu variation in this study (Fig. 5b). Due to the lack of detailed geological information for Barnett mine, the origin of the high Eu source is unclear. However, Eu enrichment is generally associated with changes of oxidation state (Möller and Holzbecher, 1998; Bau et al., 2003).

The Elmwood and Gordonsville deposits (central Tennessee zinc district) both have similar convex chondrite-normalized REE patterns with positive slopes in T1, T2, and negatively sloping T3 and T4 (Table 5). The negatively sloping T3 is distinct from the flat T3 of most other deposits (Fig. 6; Table 5). The Elmwood and Gordonsville deposits are only a few kilometres apart (Lewchuk, 1996), and are likely to have formed from fluid of the same composition and similar temperatures.

Liard (carbonate/shale-hosted fluorite±witherite±barite deposit) and Kootenay Florence (sedimentary-related Ag-Pb-Zn deposit) both have generally flat to slightly convex shape chondrite-normalized REE patterns with similar REE contents (Fig. 6a). Tetrad patterns, T1 and T3 are flat, T2 is positively sloping and T4 is negatively sloping. Unlike the other sedimentary-hosted (MVT) deposits discussed above, Liard and Kootenay Florence are not close to each other (Fig. 1).

The Young mine (Eastern Tennessee zinc district) is the only deposit that shows enriched LREE and depleted HREE (all tetrads are negative; Table 5, Fig. 6c). The reason for this distinct chondrite-normalized REE pattern is unclear due to the lack of available information.

4.1.2. Trace element behaviors of fluorite from peralkaline/alkaline-related deposits

Fluorite from peralkaline/alkaline rock-related deposits have chondrite-normalized ratios higher than 2 (Fig. 6, Table 5), and Sr contents higher than 100 ppm, except for Rock Canyon Creek (Fig. 4a). Eaglet, Kipawa, Rexspar, Rock Candy are relatively flat in T1, have flat or weakly sloping T2 and T3 with variable Eu anomalies, and weakly negative or positive T4 slopes. The La to Nd of the Rock Canyon Creek fluorite displays negative T1 and T2 slopes.

Fluorite from Kipawa and Rexspar has higher lanthanide contents than other deposits, and they have similar chondrite-normalized REE patterns, with the exception of Eu anomalies (Fig. 6b). Rexspar fluorite is commonly hosted by tuffaceous trachyte with pervasive potassic alteration (Pell 1992). The Rexspar fluorite has a flat chondrite-normalized REE pattern with weakly negative Eu anomalies. This pattern is similar to those of fluorite from alkaline rocks (Gagnon et al., 2003). Kipawa fluorite has a flat chondrite-normalized REE pattern, with a strong negative Eu anomaly. The fluorite REE pattern is very similar to the syenite REE pattern in this region (Currie and Van Breemen, 1996), suggesting that the fluorite is directly related to the syenite nearby.

Rock Candy (fluorite ±barite vein) and Eaglet (Mo- and fluorite-bearing) are deposits related to alkaline rocks (Table 1). They have flat chondrite-normalized REE patterns and lower REE contents than Rexspar and Kipawa (Figs. 6b, c). Their tetrad patterns are similar to Rexspar and Kipawa with the exception of a weakly positive T4 for Rock Candy fluorite. Rock Candy has wide ranges of REE and Y contents (Figs. 4b, c, d, e, f) with notably positive Eu anomalies (Fig. 5b), and varying Y relative to HREE (Fig. 6c). This variation may reflect the evolution of fluid composition or change in temperature over time (Bau and Dulski, 1995). Positive Eu anomalies of fluorite are usually associated with enriched Eu hydrothermal fluids. The Eaglet fluorite has negative Eu anomalies (Fig. 5b) and prominent high Sr concentrations (Fig. 4a). The elevated Sr contents are likely due to high Sr contents in fluid suggested by co-existing celestite in mineralized zones (Hora et al., 2008). The flat or nearly flat chondrite-normalized REE patterns in the four deposits are similar to the REE patterns of fluorite associated with alkaline rocks at Gallinas Mountains (Gagnon et al., 2003).

Rock Canyon Creek deposit contains disseminated and fine veinlet fluorite hosted by dolostone. Although, no igneous rocks outcrop (Pell and Hora, 1987; Samson et al., 2001), mineralization may be carbonatite or peralkaline intrusion-related (Pell and Hora, 1987). The presence of Al-F minerals (cyrolite and prosopite) in float has been taken as evidence of an alkaline rock association (Samson et al., 2001). Fluorite from Rock Canyon Creek shows large variations in Sr, Y, and lanthanides (Figs. 4, 6a). The chondrite-normalized REE patterns show a very wide range (especially in the LREE), lack Eu anomalies, and have a weakly negative slope; however, the median values show a weak sinusoidal shape. These variations in trace element concentrations probably reflect the difference in origin between fluorite from the main zone and the float of unknown provenance.

4.1.3. Trace element behaviors of fluorite from carbonatite-related deposits

Fluorite from carbonatite-related deposits has widely varying trace element contents. The chondrite-normalized REE patterns show sinusoidal shapes. They both have wide content ranges for T1, positively sloped T2, weakly positively sloped or flat T3, and negatively sloped T4 (Fig. 6a; Table 5).

Fluorite at Eldor may contain intergrown monazite and aggregated bastnaesite (Wright et al 1998; Gagnon et al., 2012). It is enriched in HREE (and Y) and depleted in LREE (Fig. 6a). The fluorite shows large variations in concentrations of La, Ce, Pr, and Nd relative to HREE. The depletion of LREE in fluorite from Eldor may be due to preferential incorporation of LREE into monazite and bastnaesite, relative to fluorite. Furthermore, the large range of negative Ce anomalies in Eldor fluorite (Fig. 5a) may be explained by the effect of a change in oxidation-reduction conditions as fluorite crystallization progressed. At the Wicheeda Lake carbonatite, fluorite is only a local accessory mineral (Trofanenko et al., 2014). There are not enough data to make a concrete interpretation for the Wicheeda Lake fluorite and this is reflected in the erratic relationship between upper and lower quartiles on figure 6a. Concentrations of REE are in the same range as fluorites from sedimentary-hosted deposits (Fig. 6). But, the wide variations of LREE contents and sinusoidal shapes of REE patterns are similar to the carbonatite-related deposit, Eldor.

4.1.4. Characteristics of other trace elements

Magnesium, Mn, Zr, Ba, W, Th, and U in fluorite have rarely been reported in the literature, due to their very low abundances in the mineral, but the presence of these elements in detectable concentrations may be specific to some deposit types. For example, Rock Canyon Creek fluorite has very high concentrations of ‘uncommon’ trace elements including Mg, Mn, Pb, Th, V, Nb, Mo, Sc, W, Zr, and Ba (Table 3). In Liard fluorite, the Ba varies from 0.01 to 474 ppm; and U from 0.01 to 6.75 ppm (Table 3). This fluorite crystallized from the same fluid as co-existing witherite and barite (Changkakoti et al., 1987), explaining its high Ba content. The fluid may have been similar to modern waters at Liard Hot springs which are slightly radioactive (Holland, 1955) explaining detectable U content in fluorite.

4.2. Trace element variations in single crystals vs. multiple crystals of the same deposit

Sample RC-08-8X is a single crystal (Fig. 2) from Rock Candy, a vein type deposit (Table 1). This sample has no visually identifiable zoning and was analyzed 50 times. The

Table 4. The compositional variations for analyses in each zone of sample RC-08-8X, and analytical variations from NIST 613 and 615 through all analyses. All values in percent unless otherwise indicated.

	Sr	Y	La	Ce	Pr	Nd	Sm	Eu	Gd	Tb	Dy	Ho	Er	Tm	Yb	Lu
Zone 1: a1-a5, b21-b31, 16 analyses	13.0	25.1	23.1	14.5	13.9	14.9	16.9	11.4	19.2	16.8	18.8	25.4	28.3	30.5	22.7	24.0
Zone 2: a6-a14, c, b13-b20, 18 analyses	21.9	171.4	63.9	63.1	81.6	81.8	107.4	84.1	124.5	135.9	148.8	131.5	184.2	101.4	141.4	108.5
Zone 3: a15-a18, b1-b12, 16 analyses	26.1	41.6	34.5	41.1	40.1	34.1	39.1	46.2	37.0	25.5	36.6	33.9	37.3	30.7	38.8	33.9
Precision from NIST 613	5.0	8.1	6.3	5.5	5.5	6.4	6.2	5.7	7.1	6.9	7.9	8.2	8.7	8.0	7.3	8.8
Precision from NIST 615	16.7	18.7	15.9	26.3	14.3	19.1	19.4	12.7	20.9	10.7	15.8	12.8	16.9	12.0	15.6	12.4

The compositional variations are determined by 2 x standard deviation divided by average value.

Table 5. The characteristics of chondrite-normalized REE plots for each deposit.

Deposit name	Lanthanide/Chondrite	General pattern	Ce anomalies	Eu anomalies	T1 shape	T2 shape	T3 shape	T4 shape
Sedimentary-hosted:								
Liard	3rd quartile <3	Nearly flat, very weak convex	- - -	- -	Flat	+ +	Flat	- -
Kootenay Florence	3rd quartile <3	Nearly flat, very weak convex	- - -	- -	Flat	+ +	Flat	- -
Hastie Quarry	3rd quartile <3	Convex	- - Wide range	- -	+ + +	+ +	Flat	- -
Barnett mine	3rd quartile <3	Convex	- - Wide range	+ + + Wide range	+ + +	+ +	Flat	- -
Elmwood	3rd quartile <2	Convex	- -	+ + +	+ +	+ +	- -	- -
Gordonsville	3rd quartile <2	Convex	- -	+ +	+ +	+ +	- -	- -
Young mine	3rd quartile <3 except La	Negative slope, enriched LREE	- -	- -	- -	- -	-	-
Peralkaline/alkaline-related:								
Kipawa	1st quartile >6	Nearly flat, very weak negative slope	- -	- - -	Nearly flat (-)	Flat	Flat	-
Rexspar	1st quartile >7	Nearly flat, very weak negative slope	-	-	Flat	Flat	Flat	-
Eaglet	1st quartile >2	Nearly flat, very weak negative slope	No anomaly	- -	Flat	Nearly flat (+)	Flat	-
Rock Candy	1st quartile >2	Nearly flat, very weak negative slope	- - Wide range	+ +	Nearly flat (-)	Nearly flat (-)	Flat	+
Rock Canyon Creek	1st quartile >2	Weak negative slope	- -	No anomaly	Undetermined	Nearly flat (-)	Flat	-
Carbonatite-related:								
Eldor	0.4<1st quartile, 3rd quartile<10.4	Sinusoidal	- - Wide range	+	Undetermined	+ +	+	-
Wicheeda lake[1]	0.06<1st quartile, 3rd quartile<10	Sinusoidal	- - -	- -	Undetermined	+ +	Flat	- -

Positive and negative anomalies or slope are indicated by '+' and '-'. A single notation (e.g. +) refers to a 'weak' signature, double notation (e.g. ++) refers to a 'medium' signature and triple notation refers to a 'strong' signature. [1] The Wicheeda Lake sample has only one analysis showing a Ce anomaly, and two analyses showing Eu anomalies.

results obtained from this sample are compared with 61 analyses from 35 different Rock Candy grains (Fig. 4; Fig. 6c). The compositional ranges of Sr, Y, La, Ce, Pr, Nd, Sm, Eu, Gd, and Yb, constrained by the 1st and 3rd quartile concentrations, show that variations within a single grain are less than those of multiple grains from the same deposit. The 1st quartile values are less than those of multiple grains from the same deposit for Tb, Dy, Ho, Er, Tm, and Lu in sample RC-08-8X (Fig. 6c). The blank signal of some analyses for sample RC-08-8X generated very high background signals (e.g., 0-1,000 counts-per-seconds vs. 0-250 counts-per-seconds, for Tm) resulting in high detection limits affecting ~10-30% of analyses for Tb, Dy, Ho, Er, Tm, and Lu. In our statistical representation of the data, the analyses less than the detection limit are replaced by half of the minimum detection limit (M.D.L./2), thus the true contents of some elements in RC-08-8X may be underestimated. To exaggerate this point, when comparing all detectable analyses (without filtering via detection limits) of Tm and Lu, the 1st and 3rd quartiles of RC-08-8X are all within the1st and 3rd quartile range of the Rock Candy fluorite (Figs. 9a, b). For Rock Candy fluorite, the intra-grain trace element variations are smaller than those from multiple fluorite grains.

Sample YM9215-1X is a single crystal with visible colour zoning (Fig. 3) from the Young mine, a MVT deposit (Table 1). We compare 7 analyses of this crystal to other Young mine grains (30 analyses from 9 grains). For Sr, La, Ce, Pr, Nd, Sm, Gd, and Tb, the total concentration variation of each element in YM9215-1X is less than the Young mine fluorite (Table 3), however the ranges of the 1st and 3rd quartiles are greater (Fig. 6c). The same comparison of 1st and 3rd quartile ranges cannot be applied for Y, Eu, Dy, Ho, Er, Tm, Yb, and Lu, because more than 40% of the data are below the detection limit in all the Young mine samples, causing the 1st quartile values to be unreliable. However, the 3rd quartile values show that the contents of Y, Eu, Dy, Ho, Er, Tm, Yb, and Lu in sample YM9215-1X are less than other Young mine grains. Although the elemental variations for YM9215-1X are not restricted within variations for the Young mine fluorite, the chondrite-normalized REE patterns are similar (Fig. 6c), as expected. These results show that intra-grain trace element variations are small when elemental concentrations are notably higher than the detection limits. But, when element concentrations are close to the detection limits, the intra-grain trace element variations are close to or larger than variations between multiple grains. One cause of this could be the relatively large uncertainty associated with low precision and high detection limits. For this reason, it

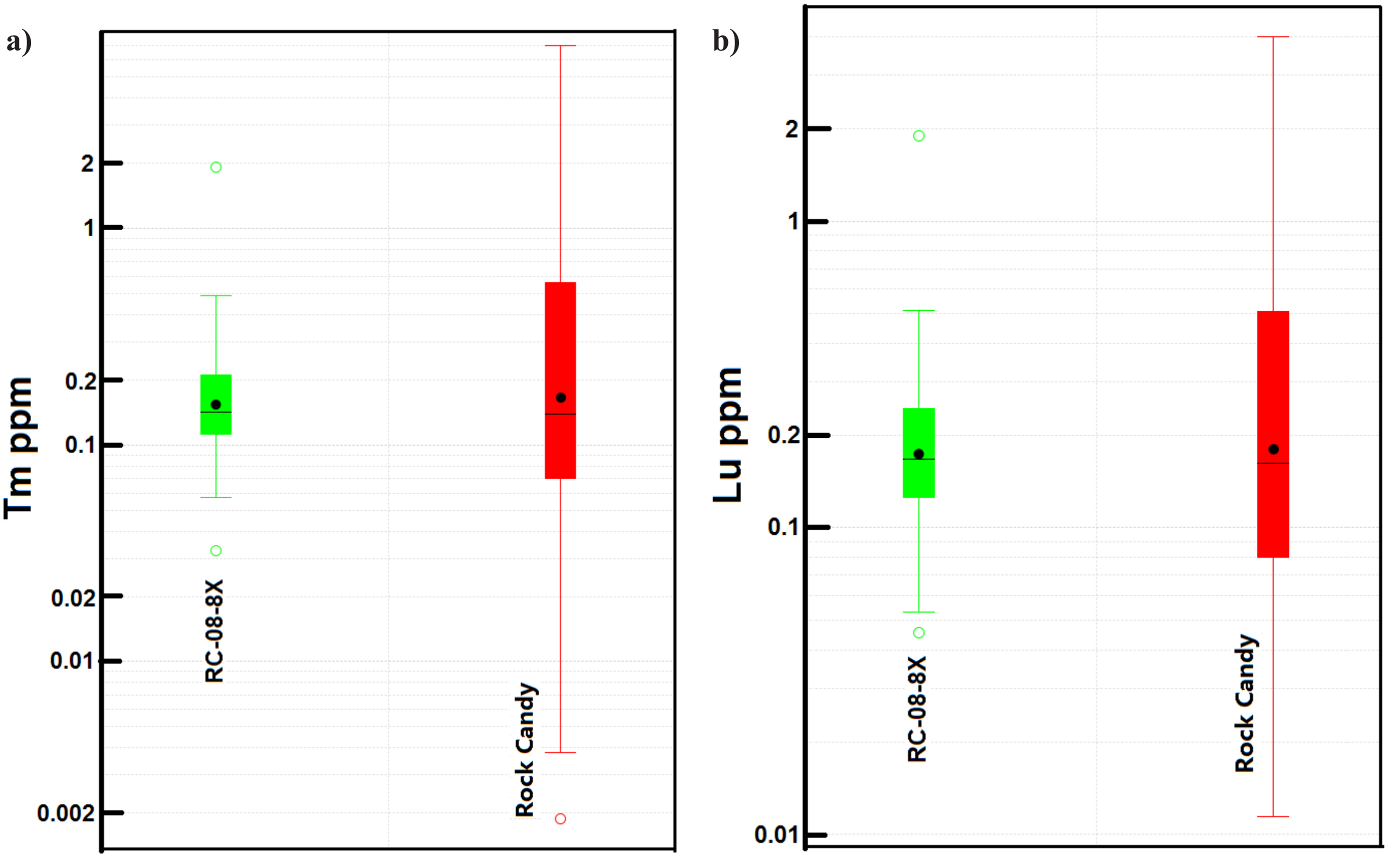

Fig. 9. Box plots of **a)** Tm and **b)** Lu from RC-08-8X and other Rock Candy fluorite with all analyses including those less than the detection limits. For Tm, high detection limits were determined for 30% of all analyses and are between 0.14-0.49 ppm. For Lu, high detection limits were determined for 25% of all analyses and are between 0.11-0.51 ppm. Line: median value; solid dot: mean value; box: interquartile range (1st-3rd quartiles); open circle (outlier); further than 1.5 x (1st-3rd quartiles); whiskers: extreme values that are not outliers.

is important to take note of the uncertainty for analyses that are close to the detection limit.

4.3. Potential use of Rock Candy fluorite as a matrix-matched secondary standard for LA-ICP-MS

The fractionation indices of elements in NIST glass differ substantially from those of the internal standard, so non-negligible error may be introduced (Jackson, 2008; Sylvester, 2008). When NIST glass is used to calibrate fluorite analyses, a matrix-matched secondary standard enhances quality-control. Unfortunately, a commercial synthetic fluorite standard is currently unavailable, and natural minerals are rarely homogeneous. The LA-ICP-MS, results from crystal RC-08-8X indicate three zones defined by Sr, Y, and lanthanides (Figs. 2, 7). Most of the compositional variations (2σ) in Zone 1 are less than 20%, and all are less than 30.5% (Table 4). With the exception of Sr, the analyses of all elements considered in Zone 2 have 2σ above 60% (Table 4, Fig. 7).The compositional variations of Zone 3 range between 25%-45%. Comparing Zone 1 with NIST 613, the compositional variations for Sr (328-419 ppm, 13%) and Y (28-41 ppm, 25%) are approximately three times higher than the analytical variations (determined precision, Sr ppm, 5%; Y ppm, 8%). The concentrations of lanthanides in Zone 1 are similar to NIST 615, and many of the compositional variations are comparable to the analytical variations (Table 4). The small compositional variations detected in Zone 1 of the RC-08-8X make it a candidate for a matrix-matched secondary standard. The adjacent areas, between the a1-a5 and b21-b31 lines, are currently the best option for use as a matrix-matched secondary standard.

5. Summary

Fluorite from sedimentary-hosted deposits (Liard, the Hastie Quarry, the Barnett mine, the Young mine, Gordonsville, Elmwood, Kootenay Florence) can be characterized by lanthanide/chondrite ratios <3, convex or negatively sloped REE patterns, negatively sloped T4, and low concentrations of Sr, Y, and lanthanides. Fluorite from peralkaline/alkaline rock-related deposits (Eaglet, Kipawa, Rexspar, Rock Candy, Rock Canyon Creek) mainly show elevated Sr, Y, and lanthanide contents and lanthanide/chondrite >2, flat to weakly negative sloping patterns on REE chondrite-normalized plots and weakly sloping T4. Fluorite from carbonatite-related deposits (Eldor, Wicheeda Lake) has sinusoidal REE chondrite-normalized patterns, with wide ranges of LREE contents. High concentrations of other elements such as Ba, Th, and U are distinctly related to particular deposits (Rock Canyon Creek and Liard).

Trace elemental variations in single fluorite crystals are less than the variations between crystals from the same deposit, and are unlikely to significantly affect the use of fluorite trace element contents to distinguish deposits. Detailed analyses of single fluorite crystals revealed compositional zoning regardless of presence or absence of visible zoning. A compositional zone was identified in a fluorite crystal (RC-08-8X) from Rock Candy that could be used as a matrix-matched secondary standard for fluorite. A larger data compilation is required to produce valid discrimination diagrams.

Acknowledgments

This project was partly funded by the Targeted Geoscience Initiative 4 (TGI4), a Natural Resources Canada programme carried out under the auspices of the Geological Survey of Canada in collaboration with the British Columbia Geological Survey. Samples from the Cave-in-Rock District were collected by F. Brett Denny and Zak Lasemi of the Illinois State Geological Survey, Prairie Research Institute, IL. Samples from the Tennesse MVT deposits were donated by Jason K. Dunning of Nyrstar US Inc., Fort Lauderdale, FL. The Eldor samples were provided by Daren Smith of Dahrouge Geological Consulting Ltd., Edmonton, AB. Access to the drill core from the Wicheeda Lake carbonatite was provided by Chris Graf of Spectrum Mining Corporation, Wardner, BC. Matamec Explorations Inc., and Frédéric Fleury (Gestion Aline Leclerc, Inc,) are thanked for their hospitality at the Zeus project (Kipawa).

References cited

Allan, J.F., 1992. Geology and Mineralization of the Kipawa Yttrium-Zirconium Prospect, Quebec. Exploration Mining and Geology, 1, 283-295.

Alvin, M.P., Dunphy, J.M. and Groves, D.I., 2004. Nature and genesis of a carbonatite-associated fluorite deposit at Speewah, East Kimberley region, Western Australia. Mineralogy and Petrology, 80, 127-153.

Andrade, F.R.D., Möller, P., Lüders, V., Dulski, P., and Gilg, H.A., 1999. Hydrothermal rare earth elements mineralization in the Barra do Itapirapuã carbonatite, southern Brazil: behaviour of selected trace elements and stable isotopes (C,O). Chemical Geology, 155, 91-113.

Baele, J-M., Monin, L., Navez, J., and André, L., 2012. Syetematic REE partitioning in cubo-dodecahedral fluorite from Belgium revealed by cathodoluminescence spectral imaging and laser ablation-ICP-MS. In: Broekmans, M. A. T. M. (Ed.), Proceedings of the 10th International Congress for Applied Mineralogy, 23-30.

Bailey, A.D., Hunt, R.P., and Taylor, K.N.R., 1974. An ESR study of natural fluorite containing manganese impurities. Mineralogical Magazine, 39, 705-708.

Bau, M. and Dulski, P., 1995. Comparative study of yttrium and rare-earth element behaviours in fluorine-rich hydrothermal fluids. Contributions to Mineralogy and Petrology, 199, 213-223.

Bau, M., Romer, R.L., Lüders, V., and Dulski, P., 2003. Tracing element sources of hydrothermal mineral deposits: REE and Y distribution and Sr-Nd-Pb isotopes in fluorite from MVT deposits in the Pennine Orefield, England. Mineralium Deposita, 38, 992-1008.

Baxter, J.W., Bradbury, J.C., and Hester, N.C., 1973. A Geologic Excursion to Fluorspar Mines in Hardin and Pope Counties, Illinois. Illinois State Geological Survey, Guidebook Series II, 28p.

Bettencourt, J.S., Leite Jr., W.B., Goraieb, C.L., Sparrenberger, I., Bello, R.M.S. and Payolla, B.L., 2005. Sn-polymetallic greissen-type deposits associated with late-stage rapakivi granites, Brazil: fluid inclusion and stable isotope characteristics. Lithos, 80, 363-386.

Bill, H. and Calas, G., 1978. Color centers, associated rare-earth ions and the origin of coloration in natural fluorites. Physics and Chemistry of Minerals, 3, 117-131.

Borrok, D.M., Kesler, S.E., Boer, R.H., and Essene, E.J., 1998. The Vergenoeg Magnetite-Fluorite Deposit, South Africa: Support for a Hydrothermal Model for Massive Iron Oxide Deposits. Economic Geology, 93, 564-586.

Bosze, S. and Rakovan J., 2002. Surface-structure-controlled sectoral zoning of the rare earth elements in fluorite from Long Lake, New York, and Bingham, New Mexico, U.S.A. Geochimica et Cosmochimica Acta, 66, 997-1009.

Cardellach, E., Canal, A., and Grandia, F., 2002. Recurrent hydrothermal activity induced by successive extensional episodes: the case of the Berta F-(Pb-Zn) vein system (NE Spain). Ore Geology Reviews, 22, 133-144.

Changkakoti, A., Gray, J., and Morton, R.D., 1987. The role of basinal brines and thermal springs in the genesis of carbonate-hosted fluorite-witherite mineralization in the Liard river area, British Columbia, Canada. Neues Jahrbuch für Mineralogie. Monatshefte, 5, 217-232.

Chesley, J.T., Halliday, A.N., Kyser, T.K., and Spry, P.G., 1994. Direct dating of Mississippi Valley-type mineralization: Use of Sm-Nd in fluorite. Economic Geology, 89, 1192-1199.

Cunningham, C.G., Rassmussen, J.D., Steven, T.A., Rye, R.O., Rowley, P.D., Romberger, S.B. and Selverstone, J., 1998. Hydrothermal uranium deposits containing molybdenum and fluorite in the Marysvale volcanic field, west-central Utah. Mineralium Deposita, 33, 477-494.

Currie, K.L. and Van Breemen, O., 1996. The origin of rare minerals in the Kipawa syenite complex Western Quebec. The Canadian Mineralogist, 34, 435-451.

Deer, W.A., Howie, R.A., and Zussman, J., 1965. Rock-forming minerals. Halsted Press, London, 347-353.

Deng, X., Chen, Y., Yao, J., Bagas, L., and Tang, H., 2014. Fluorite REE-Y (REY) geochemistry of the ca. 850 Ma Tumen molybdenite-fluorite deposit, eastern Qinling, China: Constraints on ore genesis. Ore Geology Reviews, 63, 532-543.

Denny, F.B., and Counts, R.C., 2009. Bedrock Geology of Shetlerville Quadrangle, Pope and Hardin Counties, Illinois: Illinois State Geological Survey, STATEMAP, Shetlerville-BG, 1:24,000 scale; report, 6p.

Dimitrova, D., Mladenova, V., and Vassilkyoka, R., 2011. LA-ICP-MS study of fluorite from the Lukina Padina deposit, NW Bulgaria. Bulgarian Geological Society, National Conference with international participation “GEOSCIENCES 2011”, 15-16.

Eppinger, R.G., and Closs, L.G., 1990. Variation of trace elements and rare earth elements in fluorite: A possible tool for exploration. Economic Geology, 85, 1896-1907.

Fourie, P.J., 2000. The Vergenoeg fayalite Fe-oxide fluorite deposit, South Africa: some new aspects. In: Porter, T.M. (Ed.), Hydrothermal Fe-oxide copper–gold and related deposits: a global perspective. Australian Mineral Foundation, Adelaide, pp. 309–320.

Fyles, J.T., 1967. Geology of the Ainsworth-Kaslo area, British Columbia. British Columbia Geological Survey Bulletins, 53.

Gagnon, J.E., Samson, I.M., Fryer, B.J., and Williams-Jones, A.E., 2003. Compositional heterogeneity in fluorite and the genesis of fluorite deposits: Insights from LA-ICP-MS analysis. The Canadian Mineralogist, 41, 365-382.

Gagnon, G., Rousseau, G., Camus, Y., and Gagné, J., 2012. NI 43-101 Technical Report, Preliminary Economic Assessment: Ashram rare earth deposit for Commerce Resources Corporation. <http://www.commerceresources.com/assets/docs/reports/2015-01-07_GG-PEA-Report.pdf> Accessed on 12th Sep. 2015.

Grogan, R.M., and Bradbury, J.C., 1967. Origin of the stratiform fluorite deposits of southern Illinois. Economic Geology Monograph, 3, 40-51.

Grogan, R.M., and Bradbury, J.C., 1968. Fluorite-zinc-lead deposits of the Illinois-Kentucky mining district. In: Ridge, J.D., (eds.), Ore deposits of the United States, 1933–1967: New York. American Institute of Mining, Metallurgy, and Petroleum Engineers, pp. 370–399.

Hagni, R.D., 1999. Mineralogy of beneficiation problems involving fluorspar concentrates from carbonatite-related fluorspar deposits. Mineralogy and Petrology, 67, 33-44.

Hill, G.T., Campbell, A.R., and Kyle, P.R., 2000. Geochemistry of the southwestern New Mexico fluorite occurrences, implications for precious metals exploration in fluorite-bearing systems. Journal of Geochemical Exploration, 68, 1-20.

Holland, S.S., 1955. Fluorite-Witherite: Gem; B.C. Minister of Mines, Annual Report 1954, A178-179.

Hora, Z.D., Langrova, A., and Pivec, E., 2008. Eaglet property revisited: fluorite-molybdenite porphyry-like hydrothermal system, east-central British Columbia (NTS 093A/10W). Geological Fieldwork 2007, British Columbia Geological Survey, 17-30.

Jackson, S.E., 2008. Calibration strategies for elemental analysis by LA-ICP-MS. In: Sylvester, P. (Eds.), Laser Ablation–ICP–MS in the Earth Sciences current practices and outstanding issues. Mineralogical Association of Canada Short Course 40, Vancouver, B.C., pp. 169-188.

Jochum, K.P., Weis, U., Stoll, B., Kuzmin, D., Yang, Q., Raczek, I., Jacob, D.E., Stracke, A., Birbaum, K., Frick, D.A., Günther, D., and Enzweiler, J., 2011. Determination of Reference Values for NIST SRM 610–617 Glasses Following ISO Guidelines. Geostandards and Geoanalytical Research, 35, 397-429.

Kesler, S.E., Gesink, J.A. and Haynes, F.M., 1989. Evolution of mineralizing brines in the east Tennessee Mississippi Valley-type ore fields. Geology, 17, 466-469.

Klemme, S., Prowatke, S., Münker, C., Magee,C., Lahaye, Y., Zack, T., Kasemann, A., Cabato, E.J. and Kaeser, B., 2008. Synthesis and preliminary characterization of new silicate, phosphate and titanite reference glasses. Geostandards and Geoanalytical Research, 32, 39-54.

Kogut, A.I., Hagni, R.D., and Schneider, G.I.C., 1998. Geology, mineralogy, and paragenetic sequence of the Okorusu carbonatite-related fluorite ores, Namibia. In: Schweizerbart’sche, E. (Ed.), Proceedings of the Quadrennial IAGOD Symposium, 9, pp. 555-573.

Levresse, G., Trittla, J., Villareal, J. and González-Partida, E., 2006. The “El Pilote” fluorite skarn: A crucial deposit in the understanding and interpretation of the origin and mobilization of F from northern Mexico deposits. Journal of Geochemical Exploration, 89, 205-209.

Lewchuk, M.T., 1996. Genesis of the central Tennessee Mississippi Valley-type ore deposits and host rock dolomitization from Paleomagnetism. Digitized Theses, Paper 2618.

Lu, H.-Z., Liu,Y., Wang, C., Xu, Y., and Li, H., 2003. Mineralization and Fluid Inclusion study of the Shizhuyuan W-Sn-Bi-Mo-F Skarn deposit, Hunan Province, China. Economic Geology, 98, 955-974.

Makin, S.A., Simandl, G.J., and Marshall, D., 2014. Fluorite and its potential as an indicator mineral for carbonatite-related rare earth element deposits. In: Geological Fieldwork 2013, British Columbia Ministry of Energy and Mines, British Columbia Geological Survey Paper 2014-1, 207-212.

Mao, M., Simandl, G.J., Spence, J., and Marshall, D., 2015. Fluorite trace element chemistry and its potential as an indicator mineral: Evaluation of LA-ICP-MS method. In: Simandl, G.J. and Neetz, M., (Eds.), Symposium on Strategic and Critical Materials Proceedings, November 13-14, 2015, Victoria, British Columbia. British Columbia Ministry of Energy and Mines, British Columbia Geological Survey Paper 2015-3, pp. 251-264.

Mauthner, M. and Melanson, F., 2006. Fluorite occurrences in Canada. Rocks & Minerals, 81, 114-120.

McCammon, J.W., 1955. Rexspar Uranium and Metals mining Co. Limited. Minister of Mines, B.C., Annual report, 1954, pp. 108-111.

McLennan, S.M., 1994. Rare earth element geochemistry and the "tetrad" effect. Geochimica et Cosmochimica Acta, 58, 2025-2033.

Min, M., Fang, C., and Fayek, M., 2005. Petrography and genetic history of coffinite and uraninite from the Liueryiqi granite-hosted uranium deposit, SE China. Ore Geology Reviews, 26, 187-197.

Misra, K.C. and Lu, C., 1992. Hydrothermal calcites from the Mississippi Valley-type Elmwood-Gordonsville zinc deposits, Central Tennessee, U.S.A.: Fluid inclusion and stable isotope data. European Journal of Mineralogy, 4, 977-988.

Monecke, T., Kempe, U., Monecke, J., Sala, M., and Wolf, D., 2002. Tetrad effect in rare earth element distribution patterns: A method of quantification with application to rock and mineral samples from granite-related rare metal deposits. Geochimica et Cosmochimica Acta, 66, 1185-1196.

Mortensen, J.K., Montgomery, J.R. and Fillipone, J., 1987. U-Pb zircon, monazite, and sphene ages for granitic orthogneiss of the Barkerville Terrane, east-central British Columbia. Canadian Journal of Earth Sciences, 24, 1261–1266.

Möller, P., Holzbecher, E., 1998. Eu anomalies in hydrothermal fluids and minerals. A combined thermochemical and dynamic phenomenon. Freiberger Forschungshefte, 475, 73– 84.

Möller, P., Parekh, P.P., and Schneider, H.-J., 1976. The application of Tb/Ca-Tb/La abundance ratios to problems of fluorspar genesis. Mineralium Deposita, 11, 111-116.

Pelch, M.A., Appold, M.S., Emsbo, P., and Bodnar, R.J., 2015. Constraints from fluid inclusion compositions on the origin of Mississippi Valley-Type mineralization in the Illinois-Kentucky district. Economic Geology, 110, 787-808.

Pell, J., 1992. Fluorspar and fluorine in British Columbia. British Columbia Geological Survey, Open file 1992-16.

Pell, J. and Hora, Z.D., 1987. Geology of the Rock Canyon Creek fluorite/rare earth element showing southern Rocky Mountains. In: Geological Fieldwork 1986, British Columbia Ministry of Energy and Mines, British Columbia Geological Survey Paper 1987-1, pp. 255-258.

Preto, V.A., 1978. Rexspar Uranium Deposit (82M/12W), B.C.. Ministry of Energy and Mines, Geological Fieldwork 1977, Paper 1978-1, 19-22.

Richardson, C.K. and Pinckney, D.M., 1984. The chemical and thermal evolution of the fluids in the Cave-in-Rock fluorspar district, Illinois: Mineralogy, paragenesis and fluid inclusions. Economic Geology, 79, 1833-1856.

Samson, I.M., Kerr, I.D., and Graf, C., 2001. The Rock Canyon Creek fluorite-REE deposit, British Columbia. In: Industrial Minerals in Canada. Canadian Institute of Mining, Metallurgy and Petroleum, Special Volume 53, 1-10.

Salvi, S. and Williams-Jones, A.E., 2006. Alteration, HFSE mineralization and hydrocarbon formation in peralkaline igneous systems: Insights from Strange Lake Pluton, Canada. Lithos, 90, 19-24.

Schofield, S.J., 1920. Geology and ore deposit of Ainsworth Mining Camp, British Columbia. Geological Survey of Canada, Memoir 117, 73p.

Schwinn, G. and Markl, G., 2005. REE systematics in hydrothermal fluorite. Chemical Geology, 216, 225-248.

Simandl, G.J., 2009. World fluorspar resources, market and deposit examples from British Columbia, Canada. British Columbia Geological Survey, Information Circular, 2009-4, 16p.

Staebler, G., Deville, J., Verbeek, E., Richards, R.P., and Cesbron, F., 2006. Fluorite: From ancient treasures to modern labs and collections. In: Fisher, J., Jarnot, M., Neumeier, G., Pasto, A., Staebler, G., and Wilson, T. (Eds.), Fluorite - the collector's choice. Lithographie, LLC, Connecticut, U.S.A. pp. 4-12.

Sylvester, P., 2008. Matrix effects in LA-ICP-MS. In: Sylvester, P. (Ed.), Laser Ablation–ICP–MS in the Earth Sciences current practices and outstanding issues. Mineralogical Association of Canada Short Course 40, Vancouver, B.C., pp. 67-79.

Taylor, S.R. and McLennan, S. M., 1985. The continental crust: its composition and evolution. Blackwell scientific publications, Oxford, 312p.

Trofanenko, J., Williams-Jones, A.E., and Simandl, G.J., 2014. The nature and origin of the carbonatite-hosted Wicheeda Lake rare earth element deposit. In: Geological Fieldwork 2013, British Columbia Ministry of Energy and Mines, British Columbia Geological Survey Paper 2014-1, pp. 213-225.

Verbeek, E., 2006. Fluorite Luminescence. In: Fisher, J., Jarnot, M., Neumeier, G., Pasto, A., Staebler, G., and Wilson, T. (Eds.), Fluorite - the collector's choice. Lithographie, LLC, Connecticut, U.S.A., pp. 13-19.

Whitney, D.L. and Evans, B.W., 2010. Abbreviations for names of rock-forming minerals. American Mineralogist, 95, 185-187.

Woodcock, J.R., 1972. Geology - Liard Fluospar Project, Mineral Claims TEE, TAM, FIRE, WEST, GEM, Liard Mining Division. British Columbia Ministry of Energy Mines and Petroleum Resources, Assessment report, No. 3975, 61p.

Wright, W.R., Mariano, A.N. and Hagni, R.G., 1998. Pyrochlore, mineralization, and glimmerite formation in the Eldor (Lake LeMoyne) carbonatite complex, Labrador Trough, Quebec, Canada. In: Proceedings of the 33rd Forum on the Geology of Industrial Minerals. Canadian Institute of Mining, Metallurgy and Petroleum; Special Volume, 50, pp. 205-213.

Xu, C., Taylor, R.N., Li, W., Kynicky, J., Chakhmouradian, A.R., and Song, W., 2012. Comparison of fluorite geochemistry from REE deposits in the Panxi region and Bayan Obo, China. Journal of Asian Earth Sciences, 57, 76-89.

Xu, C., Zhang, H., Huang, Z., Liu, C., Qi, L., Li, W., and Guan, T., 2004. Genesis of the carbonatite-syenite complex and REE deposit at Maoniuping, Sichuan Province, China: Evidence from Pb isotope geochemistry. Geochemical Journal, 38, 67-76.

Appendix: British Columbia Geological Survey publications and peer-reviewed journal papers authored by BCGS staff and released in 2015

All BCGS publications are available for download, free of charge, from:
www.empr.gov.bc.ca/Mining/Geoscience/PublicationsCatalogue/Pages/default.aspx

To receive notification of our latest releases email:
Geological.Survey@gov.bc.ca

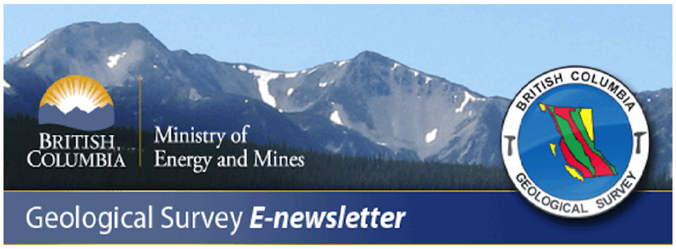

Papers

Paper 2015-1
Geological fieldwork 2014, a summary of field activities and current research, 200p.

Han, T., and Nelson, J., 2015. Mapping hydrothermally altered rocks with Landsat 8 imagery: A case study in the KSM and Snowfield zones, northwestern British Columbia. In: Geological Fieldwork 2014, British Columbia Ministry of Energy and Mines, British Columbia Geological Survey Paper 2015-1, pp. 103-112.

Hickin, A.S., Jones, L.D., Rowins, S.M., and Clarke, G., 2015. British Columbia Geological Survey annual program review In: Geological Fieldwork 2014, British Columbia Ministry of Energy and Mines, British Columbia Geological Survey Paper 2015-1, pp. 1-17.

Kyba, J., and Nelson, J.L., 2015. Stratigraphic and tectonic framework of the Khyber-Sericite-Pins mineralized trend, lower Iskut River, northwest British Columbia. In: Geological Fieldwork 2014, British Columbia Ministry of Energy and Mines, British Columbia Geological Survey, Paper 2015-1, pp. 41-58.

Mackay, D.A.R., Simandl, G.J., Luck, P., Grcic, B., Li, C., Redfearn, M., and Gravel, J., 2015. Concentration of carbonatite indicator minerals using Wilfley gravity shaking table: A case history from the Aley carbonatite, British Columbia, Canada. In: Geological Fieldwork 2014, British Columbia Ministry of Energy and Mines, British Columbia Geological Survey Paper 2015-1, pp. 189-195.

Mihalynuk, M.G., Diakow, L.J., Logan, J.M, and Friedman, R.M., 2015. Preliminary geology of the Shrimpton Creek area (NTS 092H/15E, 16W) Southern Nicola Arc Project. In: Geological Fieldwork 2014, British Columbia Ministry of Energy and Mines, British Columbia Geological Survey Paper 2015-1, pp. 129-163.

Rukhlov, A.S., Han, T., Nelson, J., Hickin, A., and Ferri, F., 2015. Carlin-type geochemical signal in lake and stream sediments from the Kechika trough, north-central British Columbia. In: Geological Fieldwork 2014, British Columbia Ministry of Energy and Mines, British Columbia Geological Survey Paper 2015-1, pp. 165-188.

Ryan, J.J., Nelson, J.L., and van Staal, C., 2015. Fieldwork in the Sylvester allochthon, Cassiar Mountains, British Columbia: Investigations of the Rapid River tectonite and the Slide Mountain terrane In: Geological Fieldwork 2014, British Columbia Ministry of Energy and Mines, British Columbia Geological Survey, Paper 2015-1, pp. 113-128.

Schiarizza, P., 2015. Geological setting of the Granite Mountain batholith, south-central British Columbia. In: Geological Fieldwork 2014, British Columbia Ministry of Energy and Mines, British Columbia Geological Survey Paper 2015-1, pp. 19-39.

Paper 2015-2
Rukhlov, A.S., and Ferbey, T., 2015. Application of lead isotopes in till for mineral exploration: A simplified method using ICP-MS, 93p.

Paper 2015-3
Simandl, G.J., and Neetz, M. (Eds.), 2015. Symposium on strategic and critical materials proceedings, November 13-14, 2015, Victoria, British Columbia, 273p.

Fajber, R., Simandl, G.J., Luck, O., and Neetz, M., 2015. Biogeochemical methods to explore for carbonatites and related mineral deposits: An orientation survey, Blue River area, British Columbia, Canada. In: Simandl, G.J. and Neetz, M., (Eds.), Symposium on Strategic and Critical Materials Proceedings, November 13-14, 2015, Victoria, British Columbia. British Columbia Ministry of Energy and Mines, British Columbia Geological Survey Paper 2015-3, pp. 241-243.

Mackay, D.A.R., and Simandl, G.J., 2015. Niobium and tantalum: Geology, markets, and supply chains. In: Simandl, G.J. and Neetz, M., (Eds.), Symposium on Strategic and Critical Materials Proceedings, November 13-14, 2015, Victoria, British Columbia. British Columbia Ministry of Energy and Mines, British Columbia Geological Survey Paper 2015-3, pp. 13-22.

Mackay, D.A.R., Simandl, G.J., Ma, W., Gravel, J., and Redfearn, M. 2015. Indicator minerals in exploration for specialty metal deposits: A QEMSCAN® approach. In: Simandl, G.J. and Neetz, M., (Eds.), Symposium on Strategic and Critical Materials Proceedings, November 13-14, 2015, Victoria, British Columbia. British Columbia Ministry of Energy and Mines, British Columbia Geological Survey Paper 2015-3, pp. 211-217.

Mao, M., Simandl, G.J., Spence, J., and Marshall, D., 2015. Fluorite trace element chemistry and its potential as an indicator mineral: Evaluation of LA-ICP-MS method. In: Simandl, G.J. and Neetz, M., (Eds.), Symposium on Strategic and Critical Materials Proceedings, November 13-14, 2015, Victoria, British Columbia. British Columbia Ministry of Energy and Mines, British Columbia Geological Survey Paper 2015-3, pp. 251-264.

Rukhlov, A.S., Bell, K., and Amelin, Y., 2015. Carbonatites, isotopes and evolution of the subcontinental mantle: An overview. In: Simandl, G.J. and Neetz, M., (Eds.), Symposium on Strategic and Critical Materials Proceedings, November 13-14, 2015, Victoria, British Columbia, British Columbia Ministry of Energy and Mines, British Columbia Geological Survey Paper 2015-3, pp. 39-64.

Simandl, G.J., 2015. Carbonatites and related exploration targets. In: Simandl, G.J., and Neetz, M., (Eds.), Symposium on Strategic and Critical Materials Proceedings, November 13-14, 2015, Victoria, British Columbia. British Columbia Ministry of Energy and Mines, British Columbia Geological Survey Paper 2015-3, pp. 31-37.

Simandl, G.J., Akam, C., and Paradis, S., 2015. Which materials are 'critical' and 'strategic'. In: Simandl, G.J. and Neetz, M., (Eds.), Symposium on Strategic and Critical Materials Proceedings, November 13-14, 2015, Victoria, British Columbia. British Columbia Ministry of Energy and Mines, British Columbia Geological Survey Paper 2015-3, pp. 1-4.

Simandl, G.J., Paradis, S., and Akam, C., 2015. Graphite deposit types, their origin, and economic significance. In: Simandl, G.J. and Neetz, M., (Eds.), Symposium on Strategic and Critical Materials Proceedings, November 13-14, 2015, Victoria, British Columbia, British Columbia Ministry of Energy and Mines, British Columbia Geological Survey Paper 2015-3, pp. 163-171.

Geoscience Maps

GM 2015-1
Manor, M.J., Wall, C.J., Friedman, R.M., Gabites, J., Nixon, G.T., Scoates, J.S., and Ames, D.E., 2015. Geology, geochronology and Ni-Cu-PGE orebodies of the Giant Mascot ultramafic intrusion, Hope, southwestern British Columbia, scale 1:10,000.

GM 2015-2
Hashmi, S., Plouffe, A., and Ward, B.C., 2015. Surficial geology of Bootjack Mountain area, British Columbia, Parts of NTS 93A/5, A/6, A/11 and A/12 (also Geological Survey of Canada, Canadian Geoscience Map 209), scale 1:50,000.

GM 2015-3
Plouffe, A., and Ferbey, T., 2015. Surficial geology, Gnawed Mountain area, British Columbia, Parts of NTS 92-I/6, NTS 92-I/7, NTS 92-I/10, and NTS 92-I/11 (also Geological Survey of Canada, Canadian Geoscience Map 214, scale 1:50,000.

GM 2015-4
Plouffe, A., and Ferbey, T., 2015. Surficial geology, Granite Mountain area, British Columbia, Parts of NTS 93-B/8 and 93-B/9 (also Geological Survey of Canada, Canadian Geoscience Map 223), scale 1:50,000.

Open Files

OF 2015-1
Clarke, G., Britton, J., Jago, P., Katay, F., Kyba, J., and Northcote, B., 2015. Operating Mines and Selected Exploration Projects in British Columbia, 2014.

OF 2015-2
Cui, Y., Miller, D., Nixon, G., and Nelson, J., 2015. British Columbia digital geology.

GeoFiles

GF 2015-1
Rukhlov, A.S., and Ferbey, T., 2015. Using lead isotopes and elemental abundances in till for mineral exploration in the Cordillera.

GF 2015-2
Mihalynuk, M.G., Friedman, R.M., and Logan, J.M., 2015. Southern Nicola arc project 2014: Geochronological data.

GF 2015-3
Rukhlov, A.S., and Naziri, M., 2015. Regional Geochemical Survey database 2015.

GF 2015-4
Nelson, J., and Kyba, J., 2015. Structural and stratigraphic controls on mineralization in the Bronson corridor, Iskut region, NW BC (poster).

GF 2015-5
Schiarizza, P., 2015. Geological setting of the Granite Mountain batholith, south-central British Columbia (poster).

GF 2015-6
Mackay, D.A.R., Simandl, G.J., Ma, W., Grcic, B., Redfearn, M., Luck, P., and Li, C., 2015. Assessment of Mozley and Wilfley shaking tables for concentrating carbonatite indicator minerals, Aley carbonatite, British Columbia, Canada (poster).

GF 2015-7
Mackay, D.A.R., Simandl, G.J., Grcic, B., Luck, P., Li, C., Ma, W., Redfearn, M., and Gravel, J., 2015. Assessment of Mozley C800 laboratory mineral separator for specialty metal indicator mineral exploration: Aley carbonatite, British Columbia, Canada (poster).

GF 2015-9
Mao, M., Rukhlov, A.S., Rowins, S.M., Spence, J., and Coogan, L.A., 2015. Detrital apatite trace-element compositions: A robust new tool for mineral exploration (poster).

GF 2015-12
Jago, C.P., 2015. Exploration and mining in the Omineca and Northeast regions, British Columbia (poster).

GF 2015-13
Katay, F., 2015. 2014 Exploration and mining, Kootenay-Boundary Region (poster)

GF 2015-15
Northcote, B.K., 2015. Exploration and mining in the South and West Coast regions, 2014 (poster).

Information Circulars

IC 2015-1
Clarke, G., Britton, J., Jago, P., Katay, F., Kyba, J., and Northcote, B., 2015. Provincial overview of mines and mineral exploration, 2014, 33p.

IC 2015-2
Exploration and mining in British Columbia, 2014, 114p.

IC 2015-3
British Columbia coal industry overview, 2014, 14p.

IC 2015-4
Coal in British Columbia (pamphlet).

IC 2015-5
Copper in British Columbia (pamphlet).

IC 2015-6
Gold in British Columbia (pamphlet).

IC 2015-7
Molybdenum in British Columbia (pamphlet).

IC 2015-8
Nickel in British Columbia (pamphlet).

IC 2015-9
Jade in British Columbia; IC 2015-9c in Chinese (pamphlet).

IC 2015-10
The East Kootenay Coalfields (poster).

IC 2015-11
The Northeastern Coalfields (poster)

IC 2015-12
Zinc in British Columbia (pamphlet).

IC 2015-13
British Columbia Geological Survey (brochure).

Peer-reviewed journal publications

Barresi, T., Nelson, J.L., and Dostal, J., 2015. Geochemical constraints on magmatic and metallogenic processes: Iskut River Formation, volcanogenic massive sulfide-hosting basalts, NW British Columbia, Canada. Canadian Journal of Earth Sciences, 52, 1-20.

Barresi, T., Nelson, J.L., Dostal, J., and Friedman, R., 2015. Evolution of the Hazelton arc near Terrace, British Columbia: stratigraphic, geochronological, and geochemical constraints on a Late Triassic – Early Jurassic arc and Cu–Au porphyry belt. Canadian Journal of Earth Sciences, 52, 466-494.

Bell, K., Zaitsev, A.N., Spratt, J., Frojdo, S., and Rukhlov, A.S., 2015. Elemental, lead and sulfur isotopic compositions of galena from Kola carbonatites, Russia; implications for melt and mantle evolution. Mineralogical Magazine, 79, 219-241.

Hashmi, S., Ward, B.C., Plouffe, A., Leybourne, M.I., and Ferbey, T., 2015. Geochemical and mineralogical dispersal in till from the Mount Polley Cu-Au porphyry deposit, central British Columbia, Canada. Geochemistry: Exploration, Environment, Analysis, 15, 234-249.

Hickin, A.S., Lian, O.B., Levson, V.M., and Cui, Y., 2015. Pattern and chronology of glacial Lake Peace shorelines and implications for isostacy and ice-sheet configuration in northeastern British Columbia, Canada. Boreas, 44, 288-304.

Mackay, D.A.R., and Simandl, G.J., 2015. Pyrochlore and columbite-tantalite as indicator minerals for specialty metal deposits. Geochemistry: Exploration, Environment, Analysis, 15, 167-178.

Paradis, S., Keevil, H., Simandl, G.J., and Raudsepp, M., 2015. Carbonate-hosted nonsulphide Zn-Pb mineralization of southern British Columbia, Canada. Mineralium Deposita, 50, 923-921.

Shuguang, Z., Kefa, Z., Cui, Y., Jinlin, W., and Jianli, D., 2015. Exploratory data analysis and singularity mapping in geochemical anomaly identification in Karamay, Xinjiang, China. Journal of Geochemical Exploration, 154, 171-179.

Contributions to partner publications

Chapman, J.B., Plouffe, A., Jackson, S.E., Ryan, J.J., and Ferbey, T., 2015. Mineral markers of porphyry processes: regional and local signatures of porphyry prospectivity. In Rogers, N. (Ed.), TGI 4 - Intrusion Related Mineralisation Project: New vectors to buried porphyry-style mineralisation. Geological Survey of Canada, Open File 7843, pp. 521-534.

Ferbey, T., Levson, V.M., and Kerr, D.E., 2015. Reconnaissance surficial geology, Nonacho Lake, Northwest Territories, NTS 75-F. Geological Survey of Canada, Canadian Geoscience Map 207, scale 1:250,000.

Jackson-Brown, S., Scoates, J.S., Nixon, G.T., and Ames, D.E., 2015. Geology, mineralogy, and geochemistry of the Cu-PGE (DJ/DB) zone of the Turnagain Alaskan-type intrusion, north-central British Columbia: Supporting databases for the convergent margin Ni-Cu-PGE study. Geological Survey of Canada, Open File 7871.

Mackay, D.A.R., Simandl, G.J., Grcic, B., Li, C., Luck, P., Redfearn, M., and Gravel, J., 2015. Evaluation of Mozley C800 laboratory mineral separator for heavy mineral concentration of stream sediments in exploration for carbonatite-hosted specialty metal deposits: case study at the Aley carbonatite, northeastern British Columbia (NTS 094B); in Geoscience BC Summary of Activities 2014, Geoscience BC, Report 2015-1, pp. 111–122.

Manor, M.J., Scoates, J.S., Nixon, G.T., and Ames, D.E., 2015. Geology, geochronology, mineral chemistry, and geochemistry: Supporting databases for the convergent margin Ni-Cu-PGE deposit study, Giant Mascot magmatic sulphide deposit, Hope, southwestern British Columbia. Geological Survey of Canada, Open File 7727.

Nixon, G.T., Manor, M.J., Jackson-Brown, S., Scoates, J.S., and Ames, D.E., 2015. Magmatic Ni-Cu-PGE sulphide deposits at convergent margins. In: D.E. Ames and M.G. Houlé (Eds.) Targeted Geoscience Initiative 4: Canadian nickel-copper-platinum group elements-chromium ore systems - fertility, pathfinders, new and revised models. Geological Survey of Canada, Open File 7856, pp. 19–34.

Pisiak, L.K., Canil, D., Grondahl, C., Plouffe, A., Ferbey, T., and Anderson, R.G., 2015. Magnetite as a porphyry copper indicator mineral in till: a test using the Mount Polley porphyry copper-gold deposit, south-central British Columbia (NTS 093A). In: Geoscience BC Summary of Activities 2014, Geoscience BC, Report 2015-1, pp. 141–150.

Plouffe, A., and Ferbey, T., 2015. Discovering buried copper porphyry mineralization: geochemistry and indicator minerals in till. Geological Survey of Canada, Open File 7680, 44p.

Plouffe, A., and Ferbey, T., 2015. Till composition near Cu-porphyry deposits in British Columbia: highlights for mineral exploration. In Rogers, N. (Ed.), TGI 4 - Intrusion Related Mineralisation Project: new vectors to buried porphyry-style mineralisation. Geological Survey of Canada, Open File 7843, pp. 15-37.

Plouffe, A., Ferbey, T., Hashmi, S., and Ward, B.C., 2015. Till geochemistry and mineralogy near Cu-Au and Cu-Mo porphyry deposits in British Columbia; indicators of buried mineralization. Geological Survey of Canada, Open File 7861, 1 sheet (poster).

Zagorevski, A., Corriveau, A.-S., McGoldrick, S., Bédard, J.H., Canil, D., Golding, M.L., Joyce, N., and Mihalynuk, M.G., 2015. Geological framework of ancient oceanic crust in northwestern British Columbia and southwestern Yukon, GEM 2 Cordillera. Geological Survey of Canada, Open File 7957, 12p.

Zagorevski, A., Mihalynuk, M.G., Joyce, N., Kellett, D.A., and Milidragovic, D., 2015. Characterization of volcanic and intrusive rocks across the British Columbia - Yukon border, GEM 2 Cordillera. Geological Survey of Canada, Open File 7956, 13p.